Lecture Notes in Electrical Engineering 852

Shailendra Kumar
Bhim Singh
Arun Kumar Singh *Editors*

Recent Advances in Power Electronics and Drives

Select Proceedings of EPREC 2021

Springer

Lecture Notes in Electrical Engineering

Volume 852

The book series *Lecture Notes in Electrical Engineering* (LNEE) publishes the latest developments in Electrical Engineering - quickly, informally and in high quality. While original research reported in proceedings and monographs has traditionally formed the core of LNEE, we also encourage authors to submit books devoted to supporting student education and professional training in the various fields and applications areas of electrical engineering. The series cover classical and emerging topics concerning:

- Communication Engineering, Information Theory and Networks
- Electronics Engineering and Microelectronics
- Signal, Image and Speech Processing
- Wireless and Mobile Communication
- Circuits and Systems
- Energy Systems, Power Electronics and Electrical Machines
- Electro-optical Engineering
- Instrumentation Engineering
- Avionics Engineering
- Control Systems
- Internet-of-Things and Cybersecurity
- Biomedical Devices, MEMS and NEMS

For general information about this book series, comments or suggestions, please contact leontina.dicecco@springer.com.

To submit a proposal or request further information, please contact the Publishing Editor in your country:

China

Jasmine Dou, Editor (jasmine.dou@springer.com)

India, Japan, Rest of Asia

Swati Meherishi, Editorial Director (Swati.Meherishi@springer.com)

Southeast Asia, Australia, New Zealand

Ramesh Nath Premnath, Editor (ramesh.premnath@springernature.com)

USA, Canada:

Michael Luby, Senior Editor (michael.luby@springer.com)

All other Countries:

Leontina Di Cecco, Senior Editor (leontina.dicecco@springer.com)

**** This series is indexed by EI Compendex and Scopus databases. ****

More information about this series at https://link.springer.com/bookseries/7818

Shailendra Kumar · Bhim Singh ·
Arun Kumar Singh
Editors

Recent Advances in Power Electronics and Drives

Select Proceedings of EPREC 2021

Springer

Editors
Shailendra Kumar
Department of Electrical Engineering
MANIT
Bhopal, India

Bhim Singh
Department of Electrical Engineering
Indian Institute of Technology Delhi
Delhi, India

Arun Kumar Singh
Department of Electrical Engineering
National Institute of Technology Jamshed
Jamshedpur, India

ISSN 1876-1100 ISSN 1876-1119 (electronic)
Lecture Notes in Electrical Engineering
ISBN 978-981-16-9238-3 ISBN 978-981-16-9239-0 (eBook)
https://doi.org/10.1007/978-981-16-9239-0

Contents

About the Editors

Dr. Shailendra Kumar is an Assistant Professor in the Department of Electrical Engineering at MANIT Bhopal, India. He received his M.Tech. and a Ph.D. degree from the Indian Institute of Technology (IIT) Delhi, India, in 2015 and 2019, respectively. His research interest areas are power quality, grid integration, and microgrid. Dr. Kumar received POSOCO Power System Awards (PPSA) in 2016 and 2019. Dr. Kumar has got four patents (filed) and over 80 publications to his credit.

Prof. Bhim Singh is a Professor in the Department of Electrical Engineering at IIT Delhi. He received his B.E. degree in electrical engineering from the University of Roorkee (now IIT Roorkee), Roorkee, India, in 1977. He obtained his M.Tech. degree in power apparatus and systems, and a Ph.D. degree in electrical engineering from IIT Delhi, in 1979 and 1983, respectively. Prof. Singh has guided 84 Ph.D. dissertations and 168 M.E./M.Tech./M.S.(R) theses. He has filed 58 patents and has executed over 80 sponsored and consultancy projects. His areas of interest are solar PV grid interface systems, microgrids, power quality monitoring, and mitigation, solar PV water pumping systems, and improved power quality AC/DC converters.

Dr. Arun Kumar Singh is a Professor in the Department of Electrical Engineering, National Institute of Technology Jamshedpur, India. He received his B.Sc. (Engg.) from Kurukshetra University, M.Tech. from the Banaras Hindu University, Varanasi, and a Ph.D. degree in electrical engineering from the IIT Kharagpur, India. He has over 30 years of teaching experience and research experience. Dr. Singh's research areas are control systems, control system applications in different areas, and non-conventional energy.

Fuzzy Controlled Multi-converter-UPQC for Power Quality Improvement in Distribution System

S. Joyal Isac and S. Srinath

1 Introduction

A UPQC derives from the UPFC [1] that is present at the level of distribution. It is composed of joined shunt and series converters for the consequent adjustment of current and voltage unbalance available in a supply feeder [2]. It restricts the reactive, unbalances, and harmonic power that is being demanded by the load. The best solution to attain a healthy power distribution system is to use the MC-UPQC [3].

The power electronics-oriented devices draw the reactive and harmonic power from the supply owing to their inherent non-linearity. In the case of three-phase systems, they create unbalance and produce a vast amount of neutral currents [4]. The excessive neutral currents, unbalance, reactive power burden, and injected harmonics create worst power factor and less system efficiency. Additionally, the power system is given to several transients such as flickers, swells, and voltage sags. These transients damage the voltage that is present at the distribution levels [5]. The excessive reactive power in the loads enhances the transmission losses of the lines and also enhances the producing capacity of generating stations. Therefore, it becomes necessary to supply the reactive power at the load ends [6].

Power quality enhancement by means of Artificial Intelligence (AI)-controlled strategies is the recent research field in the area of custom power devices that are related to the electrical distribution systems. The intelligent control strategies, which employ AI approaches like artificial bee colony algorithm, fuzzy logic, and Artificial Neural Networks (anns) are the best substitutes for the traditional control strategies in identifying the power quality enhancement in the traditional scenarios [7]. The power

S. Joyal Isac (✉)
Department of EEE, Saveetha Engineering College, Chennai, India
e-mail: joyalisac@saveetha.ac.in

S. Srinath
Department of EEE, COE, Velammal Engineering College, Chennai, India

S. Kumar et al. (eds.), *Recent Advances in Power Electronics and Drives*, Lecture Notes in Electrical Engineering 852, https://doi.org/10.1007/978-981-16-9239-0_1

quality identification is composed of performing load balancing, eradicating the harmonics that occur because of the non-linear loads, and handling the voltage quality with respect to the constant frequency and load imperfections [3, 8, 9]. Nowadays, due to the enhancement in the non-linear power electronic equipment usage, power quality seems to be the main conflict, and hybrid AI approaches are in the area of research for the UPQCS.

The major improvement of the paper is as follows.

- To manage the power quality in the distribution system by means of a novel controller-oriented MC-UPQC.
- To implement the control schemes of MC-UPQC by means of the fuzzy theory with SRF, thereby reducing the THD.
- To evaluate the effectiveness of the developed fuzzy controlled-MC-UPQC by comparing it with the existing models.

The organization of the paper is shown as Sect. 1 provides the introduction of the MC-UPQC. The literature related works of the MC-UPQC are described in Sect. 2. The enhanced MC-UPQC for power quality improvement is explained in Sect. 3. Section 4 provides the fuzzy controller-oriented MC-UPQC for power quality improvement. The results and discussions are explained in Sect. 5. Section 6 ends the paper.

2 Literature Survey

2.1 Related Works

In 2018, Nagireddy et al. [10] have proposed a model of the hybrid fuzzy backpropagation control strategy. The reference currents were described with the help of the back-propagation algorithms that contain the load and source currents as the input control parameters. This investigation was done in a multilevel UPQC. The outcomes of the mitigation of the voltage sag, load balancing, dynamic performance, and total harmonic distortion were examined by means of the MATLAB/Simulink.

In 2015, Boddepalli and Sangameswara [11] have addressed the control and design operation of MC-UPQC. A series VSC was included in the nearby feeder. The device was joined among multiple feeders that arise from distinct substations. The combined system was used to reduce the voltage and the current fluctuations. The control schemes used here were the p-q theory and d-q method that were composed of extended mathematical modeling. The artificial intelligence techniques were used to reduce the harmonics by means of the MATLAB/SIMULINK Software.

In 2013, Boddepalli and Raju [12] have developed a new structure for a three-phase four-wire (3P4W) distribution system that employed the MC-UPQC. It also proposed a novel control scheme for handling the unbalanced load currents. The

simulation outcomes revealed the efficiency of the MC-UPQC-oriented 3P4W distribution system. The control schemes were based on Neuro-Fuzzy controller, FUZZY, and PI of the MC-UPQC.

In 2015, Mahanty [13] has introduced a new MC-UPQC for continuous adjustment of current and voltage in multifeeder/multibus distribution systems. A MC-UPQC joined multiple apfs and one shunt APF. MC-UPQC compensated load current unbalances and supply voltage on the main feeder and complete adjustment of supply voltage unbalances on the remaining feeders. Here, a two-feeder MC-UPQC was employed that was composed of two series apfs and one shunt APF. The entire apfs shared a common DC-link capacitor. A new hybrid fuzzy-PI controller was modeled that was non-linear and robust to parameter variations and was composed of a quick dynamic response together with the superior steady-state response. The outcomes showed that the MC-UPQC compensated load current and supply voltage imperfections on feeder 1 and completely protected the critical/sensitive load on feeder 2 against the interruption, swell/sag, and distortion.

In 2015, Gaikwad et al. [14] have proposed a MC-UPQC that has the capability of consequent compensation for the current and voltage in multifeeder/multibus systems. It consisted of multiple VSCS and one shunt VSC. The power compensated for the interruption and swell/sag. It was simulated in MATLAB Simulink and power transfer was compared among the two nearby feeders for the interruption compensation. It returned minimum Total Harmonic Distortion (THD). The major problem solved was the voltage dip.

2.2 Review

The MC-UPQC offers high current and voltage, minimizes the cost since series transformer is not necessary, easier capacity expansion, redundancy, and working at maximum rating, etc. But, it lacks from high conduction loss, centralized approach, difficult capacity expansion, etc. These challenges must be handled quickly. Few features with the challenges are shown in Table 1. Hybrid fuzzy-backpropagation control [10] regulates the DC voltage without any undershoot or overshoot beneath abnormal conditions and also estimates the gating signals for the shunt as well as the series VSCS of the multilevel UPQCS. But, within distinct levels, voltage unbalance occurs. NFC [11] achieves better compensation functions and also reduces the THD with the current and the voltage. Still, it cannot be utilized in multilevel operations. Power quality theory [12] frees the load currents from the distortion and can be executed with the help of simple analog hardware. Yet, it returns less efficiency near the nominal operating point. Hybrid Fuzzy-PI control [13] can be extended to multifeeder/multibus distribution systems with the addition of several series apfs and is robust to parameter variations, non-linear, and is composed of quick dynamic response together with steady-state performance. But, high DC-link losses are resulted. Novel multifeeder distribution system approach [14] shares the power compensation capabilities among the two nearby feeders and also handles the

Table 1 Features and challenges of state-of-the-art MC-UPQC methods

Author [citation]	Methodology	Features	Challenges
Nagireddy et al. [10]	Hybrid fuzzy-backpropagation control	• The gating signals are estimated for the shunt as well as the series VSCS of the multilevel UPQCS • It regulates the DC voltage without any undershoot or overshoot beneath abnormal conditions	• Voltage unbalance happens among distinct levels
Boddepalli and Sangameswara [11]	NFC	• It minimizes the THD with the current and the voltage • It achieves better compensation functions	• It cannot be utilized in multilevel operations
Boddepalli and Raju [12]	Power quality theory	• It can be executed by means of simple analog hardware • The load currents are free from the distortion	• Less efficiency is returned near the nominal operating point
Mahanty [13]	Hybrid Fuzzy-PI control	• It is robust to parameter variations, non-linear, and is composed of quick dynamic response together with steady-state performance • It can be extended to multifeeder/multibus distribution systems with the addition of several series apfs	• It results in high dc-link losses
Gaikwad et al. [14]	Novel multifeeder distribution system approach	• It handles the problem of voltage dip • It shares the power compensation capabilities among the two nearby feeders	• It produces heavy and bulky dc inductor

voltage dip problem. Still, heavy and bulky dc inductor is produced in some cases. Hence, these challenges are acted as a motivation in developing a fuzzy controlled MC-UPQC for power quality improvement.

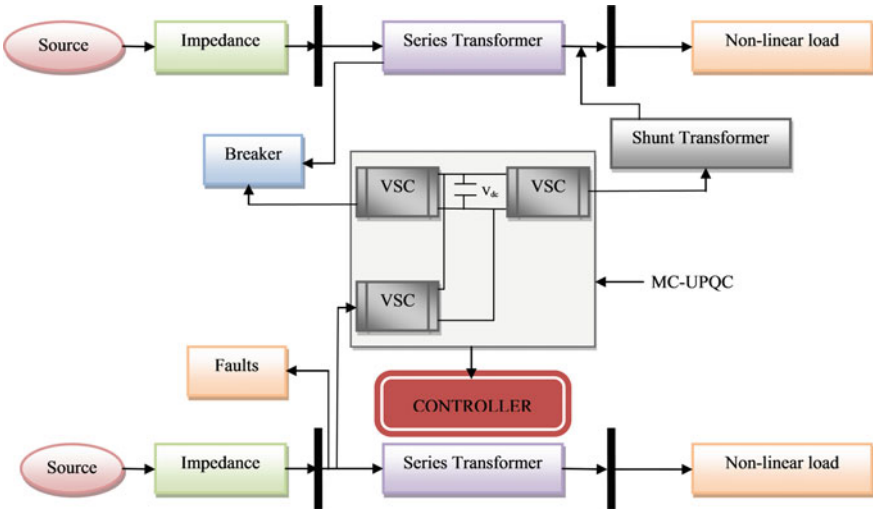

Fig. 1 Diagrammatic illustration of MC-UPQC

3 Power Quality Improvement Using Improved MC-UPQC

3.1 MC-UPQC

The reactive current coming from the source is likely to be in-phase with the currently present feeder voltages. The feeder 1 is linked to a non-linear load and feeder 2 is linked to a linear load, hence both these feeders are joined in the MC-UPQC. This is used to handle the power quality related problems. As non-linear load is present in feeder 1, it gets affected by the unbalanced currents/voltage, harmonic distortions, and the feeder sources. Feeder 2 is composed of linear load, and so it is not composed of any interruption, current/voltage unbalance, harmonic distortion, swell, and sag. Thus, both the feeders do not contain any effects. The two series VSCs are linked by means of a series transformer. The switching harmonics get rejected by power RC high pass filter that contains a communication reactor L with the complete VSCs. It is done by verifying the single strategy of the MC-UPQC with the FLC. The diagrammatic model of the MC-UPQC is portrayed in Fig. 1.

3.2 Control Strategies

The suggested method generates the reference signals for the shunt as well as series voltage source converter. The current as well as the voltage unbalance, voltage sags, load currents of feeders, reactive and harmonic component, swell and harmonics, and source voltage distributions are extracted by the control technique.

The control algorithm that is associated with the shunt VSC block is explained here. The shunt VSC is composed of the MSRF theory and Fuzzy Logic Classifier (FLC) technique. Synchronization is achieved by a PLL with the help of the supply voltage. At every phase, it calculates the 120° phase displacement. Depending on the unit vector template, the shunt VSC follows the MSRF theory approach. The phase angle is extracted using three independent two-phase system that is denoted by lag or $\Pi/2$. The theory exists independently for the three-phase of the entire phase system. It is displayed in Eqs. (1) and (2).

$$\begin{bmatrix} i_{n-d} \\ i_{n-q} \\ i_{n-0} \end{bmatrix} = \begin{bmatrix} I_d \\ I_q \\ I_0 \end{bmatrix} \begin{bmatrix} i_{n-a} \\ i_{n-b} \\ i_{n-c} \end{bmatrix} \tag{1}$$

$$\begin{bmatrix} I_d \\ I_q \\ I_0 \end{bmatrix} = \frac{2}{3} \begin{bmatrix} \sin\ \omega z & \sin\left(\omega z - \frac{2\pi}{3}\right) & \sin\left(\omega z + \frac{2\pi}{3}\right) \\ \cos\ \omega z & \cos\left(\omega z - \frac{2\pi}{3}\right) & \cos\left(\omega z + \frac{2\pi}{3}\right) \\ \frac{1}{2} & \frac{1}{2} & \frac{1}{2} \end{bmatrix} \begin{bmatrix} I_a \\ I_b \\ I_c \end{bmatrix} \tag{2}$$

The primary direct axis component current is given to the DC as portrayed in Eqs. (3) and (4).

$$i_{g-d}^{rce} = \bar{i}_{nd} + \Delta I_{dc} \tag{3}$$

$$i_{g-q}^{rce} = i_{n-q} \tag{4}$$

The power released from the DC-link capacitor minimizes the average value that is present in the DC bus voltage. These are given to the FLC that is used to lessen the error between the measured as well as the desired capacitor voltage. The controlling signal output is used as input to the shunt VSC's current control system. The power is returned from the source and the DC capacitor voltage is stabilized with the help of the shunt VSC. Hence, feeder 1 does not contain harmonic as well as reactive component. This behavior is shown in Eq. (5).

$$\begin{bmatrix} i_{g-a}^{rce} \\ i_{g-b}^{rce} \\ i_{g-c}^{rce} \end{bmatrix} = \begin{bmatrix} I_a \\ I_b \\ I_c \end{bmatrix} \begin{bmatrix} i_{g-d}^{rce} \\ i_{g-q}^{rce} \\ i_{g-0}^{rce} \end{bmatrix} \tag{5}$$

The addition of shunt currents to the *abc* reference currents takes place. The controlling of currents occurs by the sensation of the reference frame currents. The current in the shunt VSC is given to the controller part. The series VSC is composed of the MSRF theory as well as the enhanced PWM generator. The series VSC block is operated by the MSRF theory. This performance is depicted in Eqs. (6) and (7).

$$\begin{bmatrix} v_{n-d} \\ v_{n-q} \\ v_{n-0} \end{bmatrix} = \begin{bmatrix} v_d \\ v_q \\ v_0 \end{bmatrix} \begin{bmatrix} v_{n-a} \\ v_{n-b} \\ v_{n-c} \end{bmatrix} \tag{6}$$

$$\begin{bmatrix} v_d \\ v_q \\ v_0 \end{bmatrix} = \frac{2}{3} \begin{bmatrix} \sin\ \omega z & \sin\left(\omega z - \frac{2\pi}{3}\right) & \sin\left(\omega z + \frac{2\pi}{3}\right) \\ \cos\ \omega z & \cos\left(\omega z - \frac{2\pi}{3}\right) & \cos\left(\omega z + \frac{2\pi}{3}\right) \\ \frac{1}{2} & \frac{1}{2} & \frac{1}{2} \end{bmatrix} \begin{bmatrix} v_a \\ v_b \\ v_c \end{bmatrix} \tag{7}$$

The load voltage is kept sinusoidal with the stable amplitude. Equation (8) shows the subtraction of the forecasted load synchronous reference $dq0$ voltages from the V_{m-dq0}. This is depicted in Eq. (9).

$$\begin{bmatrix} v_{g-d}^{rce} \\ v_{g-q}^{rce} \\ v_{g-0}^{rce} \end{bmatrix} = \begin{bmatrix} v_{n-d} \\ v_{n-q} \\ v_{n-0} \end{bmatrix} \begin{bmatrix} v_{g-d}^{\exp o} \\ v_{g-q}^{\exp o} \\ v_{g-0}^{\exp o} \end{bmatrix} \tag{8}$$

$$\begin{bmatrix} v_{tg-a}^{rce} \\ v_{tg-b}^{rce} \\ v_{tg-c}^{rce} \end{bmatrix} = \begin{bmatrix} v_d \\ v_q \\ v_0 \end{bmatrix}^{-1} \begin{bmatrix} v_{g-d}^{rce} \\ v_{g-q}^{rce} \\ v_{g-0}^{rce} \end{bmatrix} \tag{9}$$

4 Fuzzy Controller-Based MC-UPQC for Power Quality Improvement

4.1 Proposed Fuzzy Controller

The main concept of the developed technique is to design a MC-UPQC that can perform the power quality issues present in the distribution system. This technique works on the principle of the SRF theory. Normally, the MC-UPQC consists of two series VSC, in which the power transformation from other feeders eliminates the "voltage sag, swell, interruption, and transient response of the system". The Fuzzy logic controllers are very cheaper to develop. It is very useful for Natural language processing. It is also used for the modern control systems. Here, the power quality is managed by the novel controller-oriented MC-UPQC. The control strategies related to the MC-UPQC are implemented by the fuzzy theory that contains the SRF. The major aim of the fuzzy controlled-MC-UPQC is to reduce the THD. The effectiveness is measured by comparing it over the existing models. The block diagram for fuzzy controller is shown in Fig. 2.

FLC [15, 16] models a system by means of the MC-UPQC with the concept of fuzzy theory. The logical variables are examined as input values that consider the continuous variables from 0 to 1. The controllers offer the linguistic schemes by

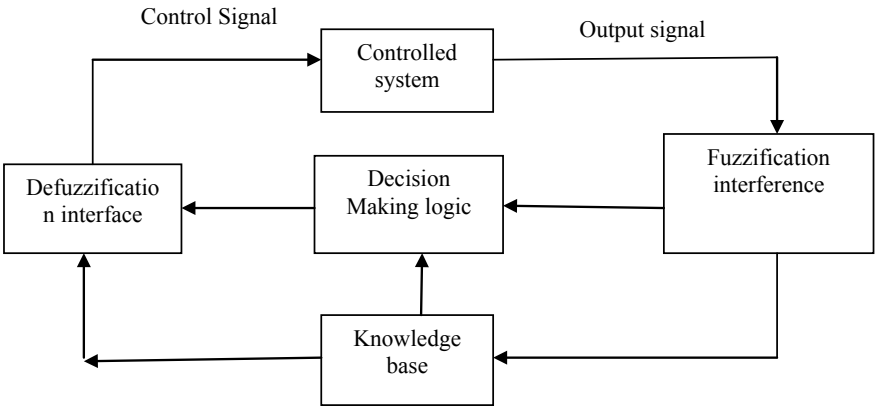

Fig. 2 Block diagram for fuzzy controller

means of the expert knowledge. FLC was introduced by Professor Lotfia Zadeh at California University in the year 1965. The inaccurate data is processed here. The applications cannot be revealed without the computers as well as the controllers. The controller operation works on the principle of the fuzzy rules that are made by the fuzzy set theory. Fuzzy controller compensates the power quality problem. The phases available in the fuzzy controller are the "decision-making, defuzzification, and fuzzification". In fuzzification, the crisp value is altered to the fuzzy value. It is got by several types of fuzzifier. The fuzzy set shapes exist as triangular, trapezoidal, etc. The fuzzified process output is produced by the rule creation. The FLC model returns the dynamic performance of the small and the large signal, but it is impossible with the linear control approach. The FLC input represents the alteration of error as well as the voltage error. The membership functions are assumed to be triangular. The fuzzy approach is assumed to be the area center.

The knowledge base rules and the database output create the inference relation CS as displayed in Eq. (10). The variables are assumed to consist of fuzzy set description. The fuzzy memberships are shown in Eq. (10).

$$\begin{aligned} CS^{(QO)} = IF\ U_1\ is\ GH_1\ AND\ U_2\ is\ GH_2 \cdots U_{oi}\ is\ GH_{oi} \\ then\ V\ is\ DS^{(QO)} \end{aligned} \tag{10}$$

In the above equation, the term $QO = 1, 2, 3 \cdots OI$, where OI denotes the rule count, $GH_1, GH_2, \cdots GH_{oi}$ defines the fuzzy sets, oi defines the fuzzy variable count, $U_1, U_2, \cdots U_{oi}$ defines the input variable vector, and V defines the output variable that is also called as control variable. The fuzzy controller computes the input signals to define the efficient control action. The FLC is implemented by the two input state variables as portrayed in Eq. (11).

$$v_{err}\ fuzz = v_{dc} - v_{dc}^{rce} \tag{11}$$

The fuzzy control rules are used for V_{dc} and ΔV_{dc}. It regulates the voltage using less real loss quantity that is being taken as the output of FLC. The MSRF-oriented currents are provided to the relay and a sensing takes place in the shunt VSC control circuit.

5 Results and Discussions

5.1 Simulation Setup

The proposed fuzzy controller MC-UPQC was performed in MATLAB 2019a and the tests were carried out. The transmission of power from feeder 1 to feeder 2 was done to eliminate the "voltage sag, swell, interruption and transient response of the system". The proposed method was compared with distinct models like "MC-UPQC, FLC-MC-UPQC, and NN-MC-UPQC" for describing that the THD is reduced in the developed method.

5.2 MC-UPQC Performance in Connection with Feeder 1 with Different Controllers

The proposed method was compared with the traditional models that are connected with feeder 1 as portrayed in Fig. 3. The outcomes revealed the "bus 1 voltage, series compensation voltage and load 1 voltage". The source voltage is provided with sag from 0.1 to 0.2 s and it tends to swell from 0.2 to 0.3 s. If fault happens in feeder 1, then there occurs an effect in feeder 1 with voltage across the linear load having interruptions, swell, and sag. This problem is handled by connecting an FLC to the shunt VSC. This is efficiently handled by the FLC than the remaining controllers.

5.3 MC-UPQC Performance in Connection with Feeder 2 with Different Controllers

The proposed method is compared over the state-of-the-art models that are linked with the feeder 2 as in Fig. 4. It clearly portrays the "bus 1 voltage, series compensation voltage and load 1 voltage". The disturbances and voltage sag swell are reduced by joining the system with the two-feeder system. The source voltage is applied that contains the sag from 0.1 to 0.2 s and swelling from 0.2 to 0.3 s. If fault occurs in feeder 2, then the effect of voltage occurs along the linear load that contains the interruptions, sag, and swell. This problem is solved by linking the FLC with the shunt

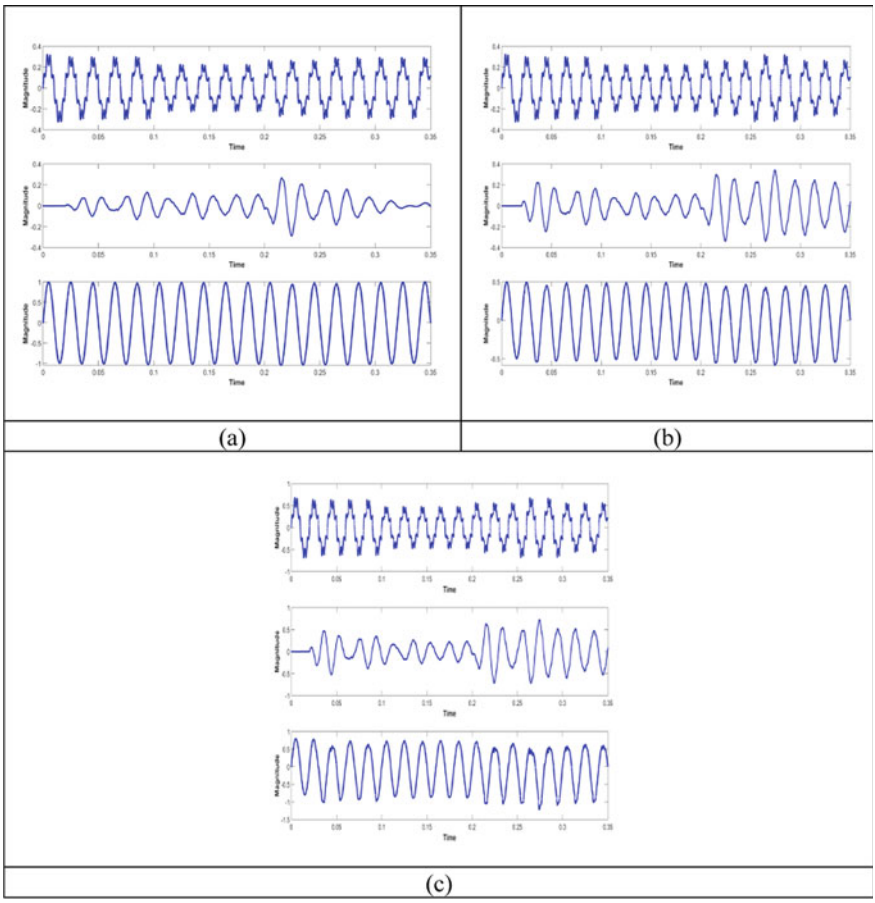

Fig. 3 Analysis of proposed and existing MC-UPQC **a** General MC-UPQC system, **b** NN-MC-UPQC, and **c** FLC-MC-UPQC for "Bus 1, series compensation, and load 1 voltages in feeder 1"

VSC. It is effectively portrayed in the load voltage that is solved by the proposed method in an efficient manner than the various controllers.

5.4 Harmonic Analysis

The harmonic analysis of the proposed method over the traditional models that are linked with the feeder 1 and feeder 2 is portrayed in Fig. 5, respectively. It portrays the THD of the general MC-UPQC, FLC-MC-UPQC, and NN-MC-UPQC at distinct seconds. Here, the THD of the developed method is minimized over the time sequence when compared with the existing models. At 0.15 s, the THD of the proposed method

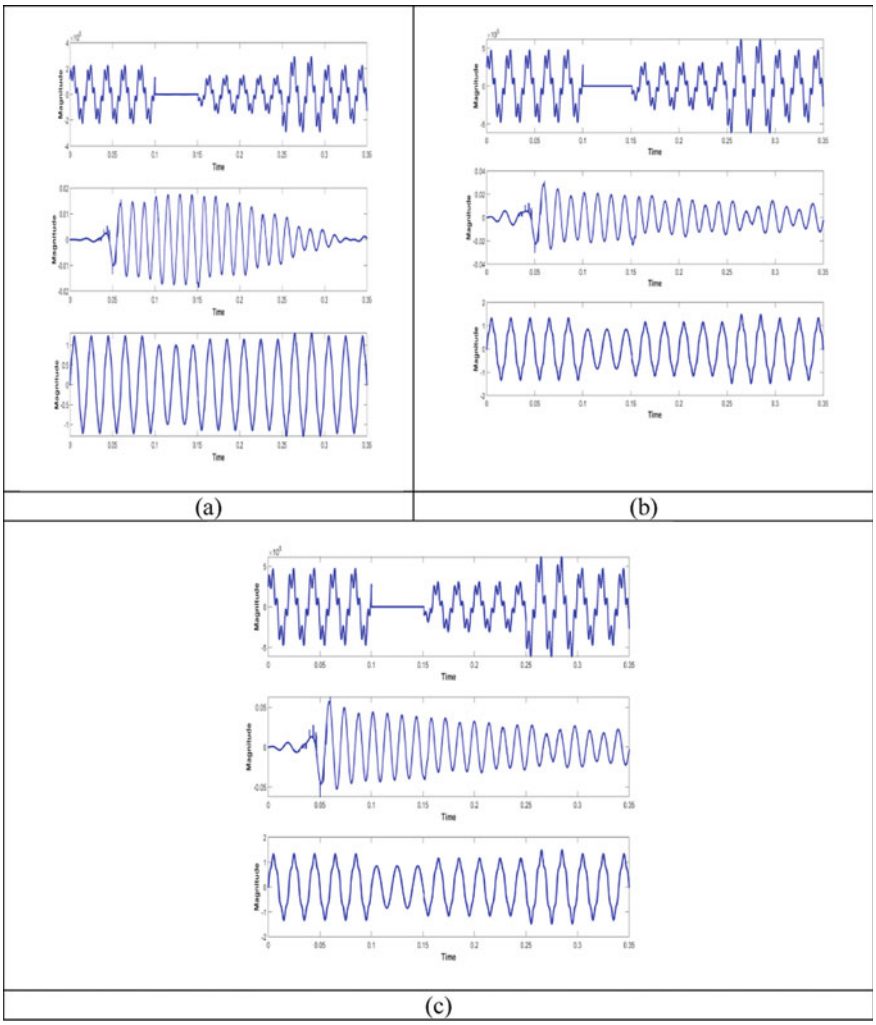

Fig. 4 Analysis of proposed and existing MC-UPQC **a** General MC-UPQC system, **b** NN-MC-UPQC, and **c** FLC-MC-UPQC for "Bus 1, series compensation, and load 1 voltages in feeder 2"

is 33.33 and 20% better than general MC-UPQC and NN-MC-UPQC system. Therefore, MC-UPQC reduced the THD in the developed method than the traditional models when it is joined with the feeder 1 and feeder 2.

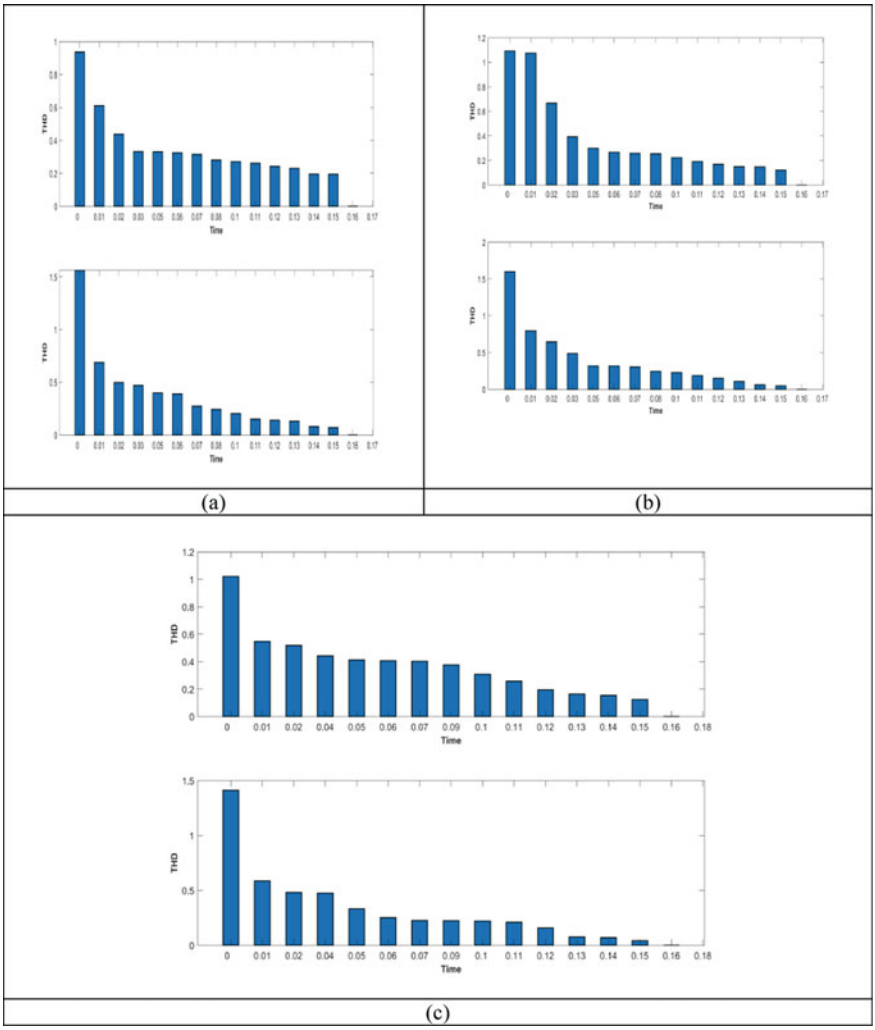

Fig. 5 Harmonic Analysis of proposed and existing MC-UPQC **a** General MC-UPQC system, **b** NN-MC-UPQC, and **c** FLC-MC-UPQC for feeder 1 and feeder 2

6 Conclusion

This paper has managed the power quality in distribution system by means of a new controller-oriented MC-UPQC. The fuzzy theory containing the SRF implemented the control schemes of MC-UPQC. As a major objective, the fuzzy controlled-MC-UPQC minimized the THD. MC-UPQC is used to mitigate voltage and current harmonics and for improving the voltage regulation and to compensate reactive power. The effectiveness was described by comparing it with traditional models.

From the analysis, at 0.15 s, the THD of the proposed method was 33.33% and 20% better than general MC-UPQC and NN-MC-UPQC system. Hence, MC-UPQC reduced the THD in the proposed method than the traditional models when it was combined with the feeder 1 and feeder 2.

References

1. Mohammadi HR, Varjani AY, Mokhtari H (2009) Multiconverter unified power-quality conditioning system: MC-UPQC. IEEE Trans Power Deliv 24(3)
2. Rezaeipour R, Kazemi A (2008) Review of Novel control strategies for UPQC. Int J Electr Power Eng 2(4):241–247
3. Basu M, Das SP, Dubey GK (2007) Comparative evaluation of two models of UPQC for suitable interface to enhance power quality. Elect Power Syst Res 821–830
4. Khadkikar V, Chandra A (2009) A Noval structure for three-phase four-wire distribution system utilizing unified power quality conditioner (UPQC). IEEE Trans Ind Appl 45(5):1897–1902
5. Abdelkhalek O, Benachaiba C, Gasbaoui B, Nasri A (2010) Using of ANFIS and FIS methods to improve the UPQC performance. Int J Eng Sci Technol 2(12):6889–6901
6. Ghosh A, Ledwich G (2001) A unified power quality conditioner (UPQC) for simultaneous voltage and current compensation. Elect Power Syst Res 55–63
7. Zerikat M, Chekroun S (2007) Design and implementation of a hybrid fuzzy controller for a high perforance induction motor. World Acad Sci Eng and Technol 20:263
8. Sajedi S, Khalifeh F (2011) Modeling and application of UPQC to power quality improvement considering loading of series and shunt converters. Aust J Basic Appl Sci 5(5):300–309
9. Aredes M, Heumann K, Watanabe EH (1998) An universal active power line conditioner. IEEE Trans Power Del 13(2):545–551
10. Nagireddy VV, Kota VR, Kumar DVA (2018) Hybrid fuzzy back-propagation control scheme for multilevel unified power quality conditioner. Ain Shams Eng J 9(4):2709–2724
11. Boddepalli R, Sangameswara P (2015) Performance analysis of MC-UPQC using artificial intelligence. Int J Emerg Eng Res Technol 3(6):141–156
12. Boddepalli R, Raju PS (2013) Power quality improvement using multi converter unified power quality conditioner with Pq theory. Int J Electr Electron Eng Res 3(2):185–201
13. Mahanty R (2015) Hybrid fuzzy-PI controller based MC-UPQC for power quality enhancement. Int J Adv Res Electr Electron Instrum Eng 4(11)
14. Gaikwad SN, Singh H, Jha RK (2015) MC-UPQC-A novel approach in multifeeder distribution system for improvement of power quality issues. IJARIIE 1(5):2395–4396
15. Rajani B, Raju PS (2013) Neuro-fuzzy controller based multi converter unified power quality conditioner with PQ theory. Int Electr Eng J 4(1):926–938
16. Paduchuri CB, Dash SS, Chinnamuthu S (2014) A new control strategy based multi converter UPQC using fuzzy logic controller to improve the power quality issues. Power Eng Electr Eng 12(2)

Modified BBO-Based PV Integrated Reduced Component Multilevel Inverter for Mitigating THD

Debanjan Mukherjee and Sourav Mallick

1 Introduction

Over the recent years, research fraternity in power electronics domain has been engrossed toward the modification and extensive usage of multilevel inverters (MLIs). Though the MLI was first developed almost three decades ago, it has gained popularity over the time for its wide applications in various fields, viz., renewable energy source integration, electric drives, Flexible AcTransmission Systems (FACTS) compensation, electric vehicles, medium or high-power industrial applications, etc. Total Harmonic Distortion (THD) in output voltage, electro-magnetic interference (EMI), and total standing voltage (TSV) are high in case of the usual two-stage inverter [1]. These disadvantages of such inverters have been alleviated with the advent of MLI. There are mainly three kinds of MLI, i.e., Cascaded H-Bridge (CHB) type, Neutral Point Clamped (NPC) type, and Flying Capacitor (FC) type. A large number of component requirements of NPCMLI for producing higher voltage level has restricted its usage. On the other hand, capacitor voltage tuning problem increases complexity of circuitry of FCMLI, thereby, increasing the size and cost. The CHBMLI has won the attention of the industry for such drawbacks of the NPCMLI and FCMLI [2]. Furthermore, the provision of isolated DC sources in CHBMLI topology is also advantageous for integrating the renewable energy sources [3].

With the fast depletion of fossil fuels, usage of renewable sources is increasing to satisfy the world's growing demand of power. Solar energy, being the largest source of renewable energy, is under the consideration. The solar irradiation when fall on photovoltaic cell (PV cell) releases electrons which creates a potential difference and

D. Mukherjee (✉) · S. Mallick
National Institute of Technology Sikkim, Ravangla, South Sikkim 737139, India

S. Mallick
e-mail: s.mallick@nitsikkim.ac.in

S. Kumar et al. (eds.), *Recent Advances in Power Electronics and Drives*, Lecture Notes in Electrical Engineering 852, https://doi.org/10.1007/978-981-16-9239-0_2

the solar energy is thus trapped in the form of electrical energy. But, as the solar irradiation varies with time, constant power is not available. Hence, a battery is connected with PV cell in such a fashion that the battery will get charged when solar radiation is available and will deliver power in the absence of solar power. The delivery of power from the battery can be possible if it is connected to electrical grid through inverter. Hence, the PV systems are being integrated with the MLIs. Moreover, the traditional MLI configuration having large number of switches becomes bulky and expensive with low efficiency. The recent state-of-the-art literatures emphasized on various MLI topologies with reduced number of devices to increase efficiency [4–10]. The recent research trend also aims at improving the quality by reducing harmonics. To avoid switching loss, low frequency switching is preferred over high frequency switching [11]. To overcome the lacunae of available inverter topologies, a reduced component count topology of 5-level MLI with integration of PV system is proposed in this work. To increase the output power quality, suppression of the lower order harmonic components is essential which can be aptly done by the Selective Harmonic Elimination (SHE) technique. The SHE technique can efficiently mitigate the selected lower order harmonics by resolving the trigonometric transcendental equations which are nonlinear in nature [12]. Traditional iterative methods like Newton Raphson (NR), Resultant Theory (RT), etc. are not so good in solving the nonlinear problems as they are sensitive to the initial guess and involve complex mathematical expressions [13–15]. Hence, the SHE problem is generally solved by different bio-inspired metaheuristic techniques efficiently [16]. The modified biogeography-based optimization (MBBO) technique is developed in this work for improving the output quality by optimizing firing angles and its performance is compared by using popular metaheuristic techniques like Butterfly Optimization Algorithm (BOA) [17], BBO [18], gravitational search algorithm (GSA) [19], Particle Swarm Optimization (PSO) [20]. All the simulations are experimentally validated using Hardware In Loop (HIL) setup which has high security, fidelity, and effectiveness [21–23]. In this work, the PV system has been designed according to the datasheet of commercially available SLP080-12 [24, 25].

In the following section of the paper, PV system and the proposed MLI topology are discussed sequentially. Then, in the subsequent section, the SHE scheme is conceptualized followed by the discussion on the BBO and the proposed techniques. In the next sections, simulation and hardware in loop details are described consecutively. At last, the conclusion section is presented after thorough discussions of the available results in the result section.

2 Description of the Photovoltaic System

Advantages of photovoltaic system as a viable source of energy motivate this work to utilize it. A commercial PV panel, viz., SLP080-12 [24, 25], is replicated for simulation in MATLAB and HIL in this research work. The essential functional parameters of that replicated PV system are presented in Table 1. In that modeled

Table 1 Description of the PV system parameters

Parameters	SLP080-12
Number of parallel strings	3
Modules in series per string	1
Open circuit voltage V_{OC} (V)	21.5
Voltage at maximum power point V_M (V)	17.2
Short circuit current I_{SC} (A)	5.17
Current at maximum power point I_M (A)	4.65
Temperature co-efficient of V_{OC} (%/°C)	−0.31
Temperature co-efficient of I_{SC} (%/°C)	0.03
Cells per module	36

Input parameters are irradiance = 1000 w/m^2 and temperature = 25 °C

PV system, 3mF DC link capacitor has the initial voltage 0f 21.5 V which is same as the output voltage of PV panel.

In order to get good quality AC from the PV, proper MLI scheme is needed to be used; otherwise, large number of harmonics will distort the output voltage and current. There are several MLI topologies used to get proper output. The traditional MLI suffers from the losses due to the presence of large number of switches and driver circuits. Hence, the necessity of the reduced switch MLI has got the attention of the researchers. In this work, the authors proposed to integrate the modeled PV system with a reduced switch MLI topology without sacrificing the efficiency. Detailed discussion regarding the proposed topology is presented in the following section.

3 Proposed Topology of Single Phase 5-Level MLI

To generate 5-level voltage output, the proposed MLI scheme requires 1 diode (D_1), 5 switches (T_1 to T_5), an isolated DC source (V_{DC}) and a PV system with the twice voltage output that of the DC source as shown in Fig. 1. D_1 is used to make unidirectional current flow. Presentation of switching states to generate 5-level output voltage in the proposed topology is shown in Table 2 where 1 and 0 indicate ON state and OFF state of the switches, respectively.

Thus, the proposed topology is able to produce the desired 5-level staircase output voltage which is similar to that of the traditional MLI. But due to the switching of MLIs, output voltage is contaminated with harmonics. Due to those harmonics, voltage quality and system's efficiency are dropped down. Therefore, harmonics suppression is very essential to achieve the required efficiency. The above objective can be fulfilled by utilizing optimized switching. Adaptation of the SHE scheme can fulfill the above-mentioned goal.

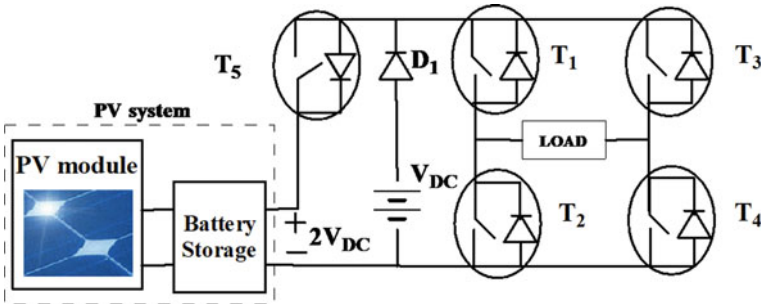

Fig. 1 Proposed topology of single phase 5-level PV integrated MLI with 5 switches

Table 2 Switching states of the proposed MLI for producing 5-level output voltage

T_1	T_2	T_3	T_4	T_5	D_1	V_{out}
0	1	1	0	1	0	−2Vdc
0	1	1	0	0	1	−Vdc
1	0	1	0	0	0	0
1	0	0	1	0	1	Vdc
1	0	0	1	1	0	2Vdc

4 Selective Harmonic Elimination as an Optimization Problem

Expression of output voltage by expanding through Fourier series is necessary for realizing the theory of SHE [2] which is considering quarter wave symmetry as presented in Eq. (1); whereas, the peak magnitude of voltage at kth harmonic is expressed by Eq. (2).

$$V(\omega t) = \sum_{k=1,3,5}^{\infty} V_k \sin(k\omega t) \tag{1}$$

$$V_k = \frac{4V_{DC}}{k\pi}(\cos(k\alpha_1) + \cos(k\alpha_2)) \tag{2}$$

subjected to, $0 < \alpha_1 < \alpha_2 < 90°$.

Where α_1, α_2 are the firing angles for generating the 5-level output, V_{DC} is the voltage of single DC source in symmetric MLI. According to SHE, the transcendental equations are used, presented in (3) and (4) to suppress the kth harmonic at a specific Modulation Index (MI).

$$\frac{1}{2}(\cos\alpha_1 + \cos\alpha_2) = MI \tag{3}$$

$$(\cos(k\alpha_1) + \cos(k\alpha_2)) = 0 \tag{4}$$

where MI can be computed as Eq. (5).

$$MI = \frac{\pi V_{desired}}{4N_{source}V_{DC}} \tag{5}$$

where $V_{desired}$ is the desired voltage magnitude at fundamental frequency.

Thus, Eq. (6) provides the objective function (OF) derived using the SHE problem and applied in the various optimization techniques used in this paper.

$$OF = \min\left\{\left(2 \times S \times \frac{V_{desired} - V_1}{V_{desired}}\right)^4 + \sum_{k=3}^{13} \frac{1}{k}\left(S \times \frac{V_k}{V_1}\right)^2\right\} \tag{6}$$

subject to, $0 < \alpha_1 < \alpha_2 < 90°$ and S is a positive non-zero integer and k to be an odd integer, where V_1 is the voltage magnitude of fundamental frequency.

In this work, the chosen value of S is 50. The first term of the above equation ensures fundamental voltage magnitude with 1% error; whereas, the second term helps to suppress the voltage magnitudes of lower order harmonics from as 3rd to 13th. In OF, $(1/k)$ is the weight factor. Thus, Eq. (6) satisfies the IEEE-519 harmonic standard. As Eqs. (1)–(4) contain nonlinear elements, metaheuristic techniques are well-suited to find the optimal solution. In this work, biogeography-based optimization (BBO) is initially used to find the optimal solution. The following subsection describes the BBO technique.

5 Brief Discussion on Biogeography-Based Optimization

The biogeography-based optimization (BBO) technique was developed by D. Simon in the year 2008. This metaheuristic technique is inspired from the natural way of species accumulation phenomena in biogeography. Natural tendency of the species is to move in the habitat which is favorable for inhabitants. The surrounding factors that attract the species toward habitat are temperature, weather, humidity, etc. In BBO, the said factors are termed as suitability index variables (SIVs); whereas, the particular habitat quality is named as habitat suitability index (HSI). The species are moved from one habitat to other according to migration process which involves the concepts of emigration and immigration procedures. The species are further upgraded through mutation process. The mutation phase helps to break the trap of local optima. The flow chart, presented in Fig. 2, demonstrates the concept of BBO. This technique may provide good result but still having limitation of local optima stuck problem which have been reduced by modifying its mutation phase in the proposed technique.

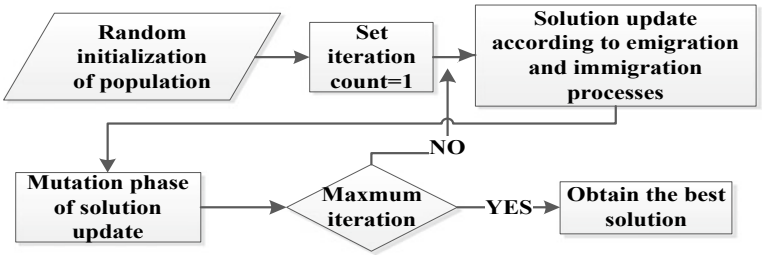

Fig. 2 Flow chart of BBO technique

6 The Proposed Technique

In the mutation phase of BBO technique, few solutions are updated randomly within the search space but the rest are kept intact which may cause local trapping problem. To get rid of such issue of BBO, modification of mutation phase is introduced in this work. Firstly, the mutation rate (*mu*) is calculated for all species [18]. If the mutation rate becomes less than a generated random number, then a new species will be generated randomly within the search space. The authors propose here to use the rest of the species (solutions) which will be updated with random walk surrounding the best species. The step length of that random walk is derived from the exponential distribution in Eq. (7).

$$S \sim Exp(l) \tag{7}$$

where l is the decay parameter.

$$H_i(SIV) = \eta * \mathrm{S}^*(H_i(SIV) - H_{best}(SIV)) \tag{8}$$

where $H_{best}(SIV)$: The best species so far, η: scale factor to adjust the step length according to the requirement of the problem.

Species updating approach using Eqs. (7, 8) explores the local search surrounding the best species so far. In addition, the extended tail of exponential distribution curve creates the probability of generating long step which can overcome the local trapping issue. Thus, the balanced exploration and exploitation abilities are achieved which helps to provide better solution and speed of convergence in the proposed MBBO technique than the original one. Proposed mutation phase is realized by the pseudo-code in Fig. 3. Here, N, D are the species number and dimension of each species, respectively.

```
for i=1 to N
    Dynamic probability and mutation rate (mu_i) are evaluated by using α_i and β_i.
    for SIV = 1 to D do
        Produce a random number denoted by RAND
        if RAND < mu_i then
            Randomly generate a new H_i(SIV) by replacing the previous one
        else
            update the H_i(SIV) by using equations (7, 8)
        end if
    end for
end for
```

Fig. 3 Pseudo-code of the modified mutation phase in the MBBO technique

6.1 Flowchart for Firing Angle Optimization

The proposed and the other metaheuristic techniques are employed to optimize the firing angles of 5-level MLI in different modulation indexes. The entire process is depicted in the following flowchart (Fig. 4).

7 Hardware in Loop (HIL)

Hardware in loop is the real-time emulator to mimic the actual experimental setup. Due to high security and fidelity, HIL is being used in recent research works to validate the simulation [21–23]. This work employed Typhoon HIL [22] to validate the simulated work. The PC is interfaced with the device (HIL-402) where the simulations are modeled in "Typhoon HIL control center" which is an open-source

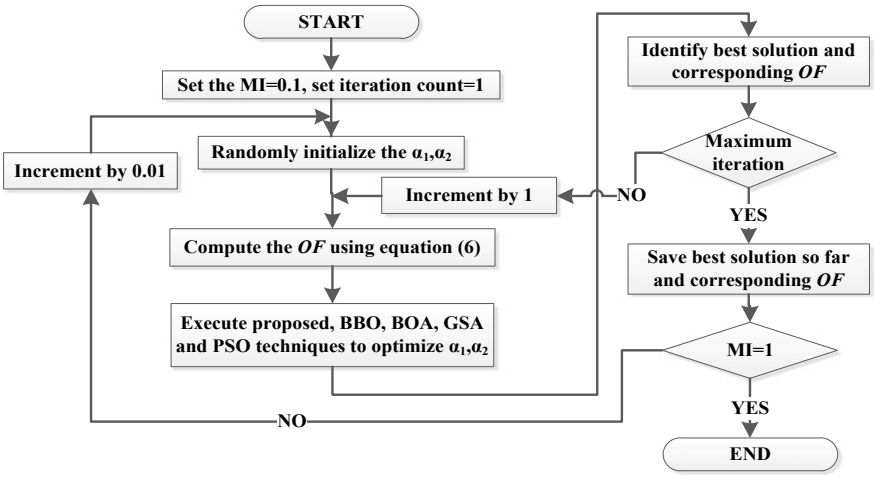

Fig. 4 Flow chart of entire process for firing angle optimization in variable MI

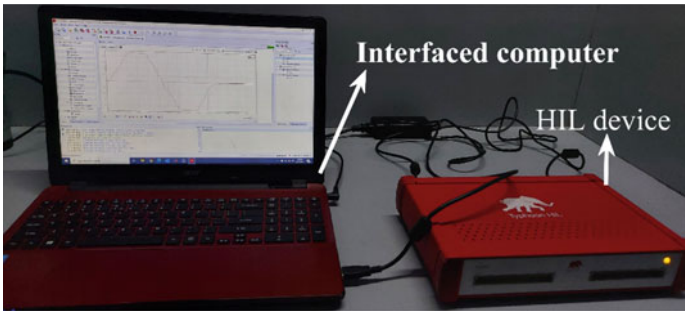

Fig. 5 Experimental setup of hardware in loop

software. The HIL SCADA in the HIL basically provides the scope of controlling, monitoring, and capturing the simulation outcome. Figure 5 shows the experimental setup of HIL.

8 Simulation Details

All the simulations in this work are done in the MATLAB R2013a software platform. The firing angles of the proposed MLI are optimized by using the BOA, the BBO, the GSA, and the PSO techniques and their optimizing performances are compared with the proposed technique. For all the techniques, maximum iteration number is set as 25. And population size is taken as 50. The default values of control variables for the BOA, the BBO, and the GSA are taken in this research as the authors suggested in [17, 18] and [19], respectively. The control variables in the proposed technique are same as in [18] but the additional parameters required for modification, i.e., decay parameter (l), scale factor (η) are assigned as 1 and 0.01, respectively. In the PSO technique, chosen set of control parameters are inertia weight (w) = 0.5 and constriction factors, i.e., $c_1 = c_2 = 2.03$.

9 Results and Discussions

This section arranges all the simulated and hardware in loop validated results. Discussions on the obtained results are categorized in the subsequent sub-sections.

Table 3 Comparison of available single phase 5-level MLI topologies with proposed MLI

Design parameters	MLI 1 [5]	MLI 2 [6]	MLI 3 [7]	MLI 4 [8]	MLI 5 [9]	MLI 6 [10]	Proposed MLI
N_{SWITCH}	8	8	8	7	7	6	5
N_{DRIVER}	8	8	8	7	7	6	5
V_{LS}	$4V_{DC}$	$4V_{DC}$	$4V_{DC}$	$3V_{DC}$	$3V_{DC}$	$2V_{DC}$	V_{DC}
TSV	$12V_{DC}$	$12V_{DC}$	$12V_{DC}$	$11V_{DC}$	$11V_{DC}$	$10V_{DC}$	$9V_{DC}$

9.1 Comparison of Reduced Switch MLIs with the Proposed MLI Topology

The comparisons among some of the available MLIs [5–10] and proposed MLI in terms of component counts and total standing voltage (TSV) are shown in Table 3. TSV is the summation of the maximum withstand voltage appearing across all switches. In all test cases, number of levels ($N_{LEVEL} = 5$), number of sources ($N_{SOURCE} = 2$), and the sum of the withstand voltages across the switches of H-bridge ($V_{HS} = 8V_{DC}$) are kept at the same values. From the comparative study, it can be said that the required number of switches (N_{SWITCH}), driver circuits (N_{DRIVER}), sum of the withstand voltages across level producing switches (V_{LS}), and TSV are of the least values in case of the proposed method. This clearly indicates the superiority of the proposed MLI over available MLIs.

9.2 Comparison of Results of Different Optimization Techniques with the Proposed MBBO

Figure 6a–e shows the comparison of the results of percentage reduction in THD with change of MI from 0.1 to 1 obtained from the BBO, the BOA, the GSA, and the PSO techniques with the proposed MBBO technique. Figure 6f shows that the minimum THD is obtained when MI is 0.87. It also exhibits the supremacy of the proposed technique in achieving the least value of THD among all the techniques.

Figure 7 portrays the variation of lower order harmonic components and total percentage of THD with the change in MI. When MI equals to 0.87, the 3rd, 5th, 7th, and 9th harmonics are at their lower values. Therefore, minimum value of THD is achieved. This clearly justifies the claim mentioned earlier. In Fig. 8, at MI = 0.87 convergence curves of the optimization techniques, used in this paper, are compared. This comparison confirms the better accuracy of the MBBO over the other techniques.

Using the different optimization techniques and the proposed MBBO, the optimized values of firing angles, i.e., α_1 *and* α_2, are obtained for different values of MI. For sake of brevity, only the variations of firing angles obtained by MBBO are depicted in Fig. 9. The comparison of firing angles with %THD for different

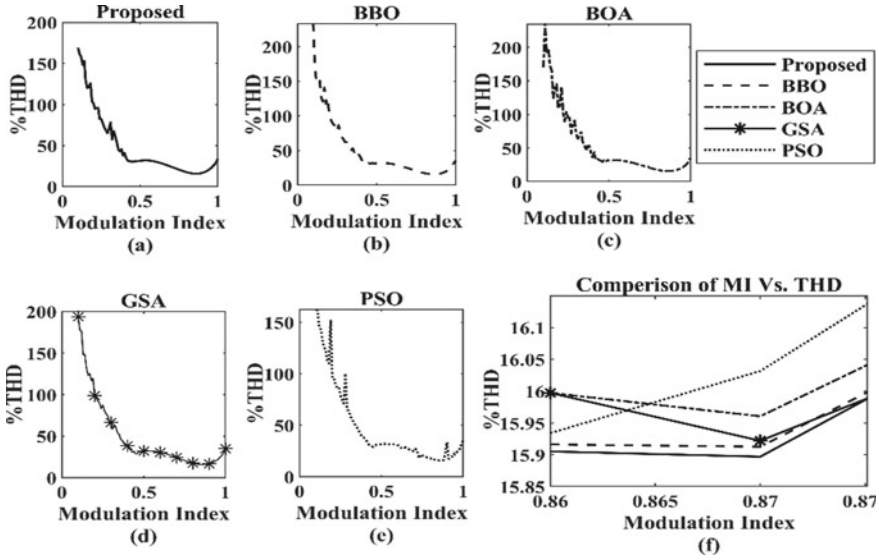

Fig. 6 Comparison of MI versus THD for different techniques

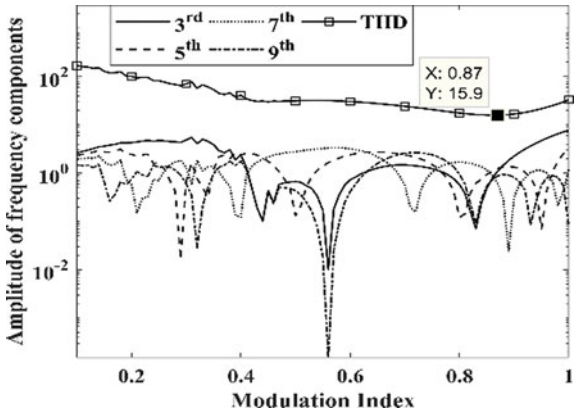

Fig. 7 Frequency components versus MI

techniques when MI is 0.87 is shown in Table 4. The results clearly indicate the supremacy of the proposed MBBO technique among all the techniques (used in this work) to mitigate THD.

The firing angles which are obtained from the proposed MBBO technique, corresponding to MI at 0.87 are fed to the Simulink model of the proposed 5-level MLI. The attained output voltage waveform and its corresponding FFT spectrum have been presented in Fig. 10. It is observed from the figure that the lower order dominating harmonics are being suppressed substantially. Moreover, the percentage of THD is reduced to 16.74% which matches the aimed percentage THD, shown in Table 4. The

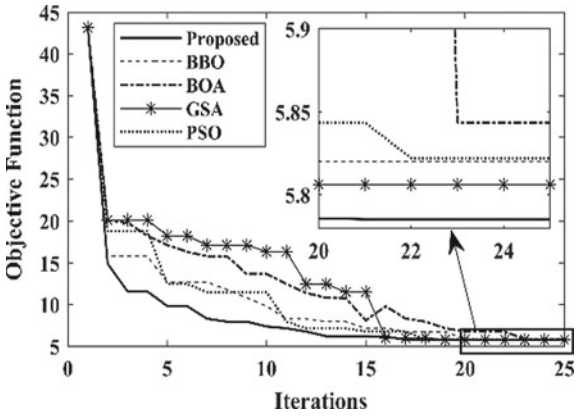

Fig. 8 Convergence curves at MI = 0.87

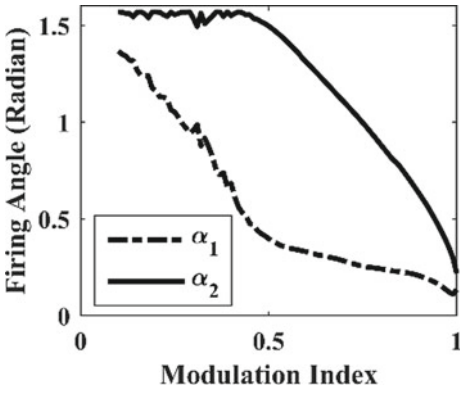

Fig. 9 Firing angles versus MI

Table 4 Comparison of firing angles (in radian) with %THD for different techniques at MI = 0.87

Techniques	α_1	α_1	%THD
BBO	0.2287	0.7154	15.9127
BOA	0.2348	0.7109	15.9606
GSA	0.2257	0.7115	15.9221
PSO	0.2291	0.7152	16.0317
Proposed MBBO	0.2213	0.7154	**15.897**

Load current versus Time and the corresponding FFT spectrum, depicted in Fig. 11, clearly points out to the reduction of percentage THD to 6.30%, when the load is R-L type whose R = 24 Ω, L = 20 mH.

In order to validate the MATLAB simulation results, the same parameters of load along with the system model are applied in HIL.

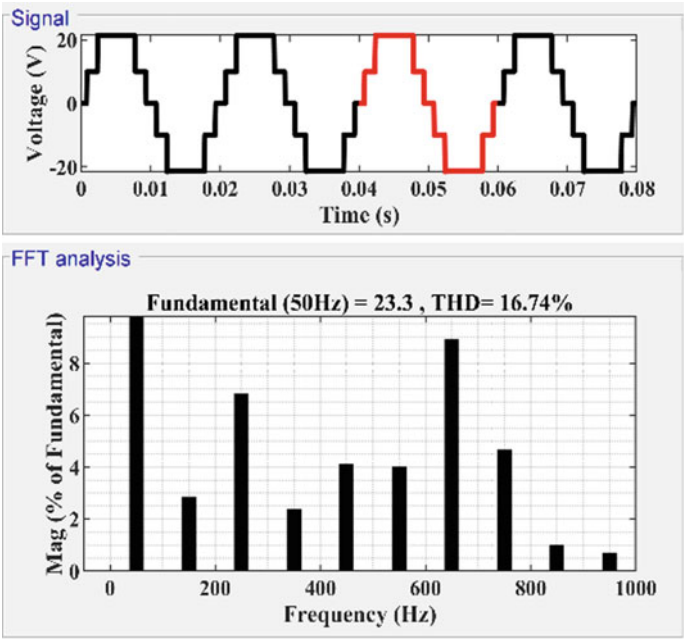

Fig. 10 Output voltage with FFT spectrum

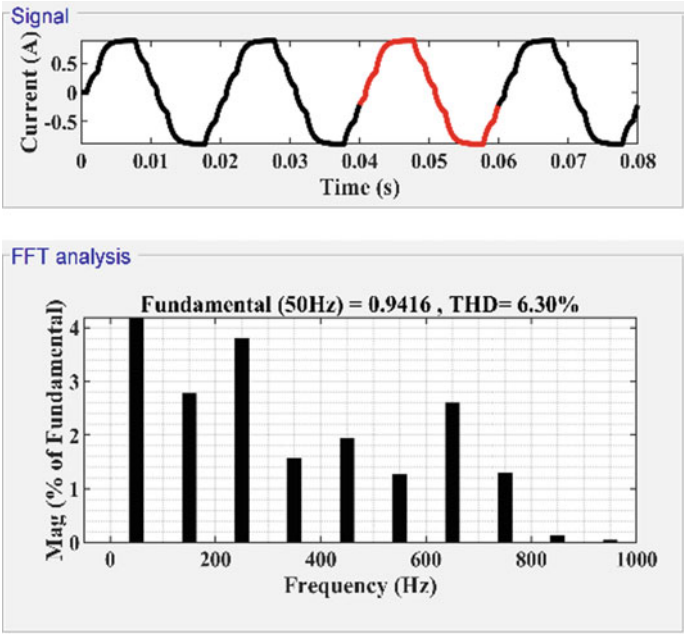

Fig. 11 Output current with FFT spectrum

9.3 Hardware in Loop (HIL) Validated Results

The test conditions for the experiments in HIL are kept the same as that of the simulations. The obtained output voltage and current waveforms using HIL setup and their corresponding fast Fourier transform (FFT) are presented in Figs. 12, 13, 14 and 15. In the FFT spectrum of voltage shown in Fig. 10 and Fig. 13, the 13th harmonic component is the largest. Moreover, the %THD obtained from HIL (16.9%) is very close to MATLAB simulation result (16.74%). Similar pattern can be seen for the load current in Figs. 11 and 14. This clearly proves the advantages of proposed MLI. Thus, it can be concluded that the simulation of the proposed MLI with optimized firing angle using proposed MBBO technique is successfully validated through the HIL setup.

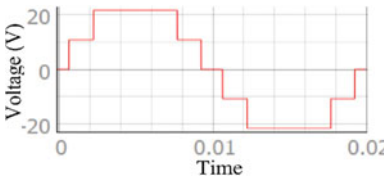

Fig. 12 Output voltage waveform of HIL for one cycle

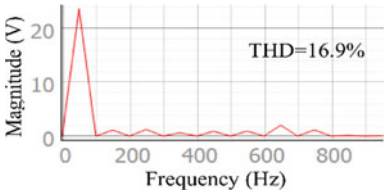

Fig. 13 FFT spectrum of output voltage of HIL

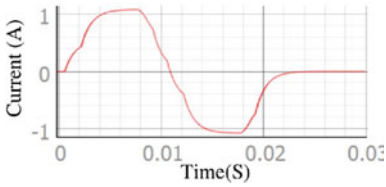

Fig. 14 Output current waveform of HIL for one cycle

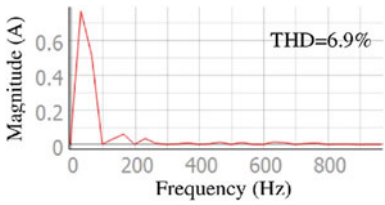

Fig. 15 FFT spectrum of output current of HIL

10 Conclusions

In this article, the proposed MLI topology has successfully produced 5-level voltage output with reduced switch count. The proposed topology is suitable for PV system integration. Moreover, the proposed optimization technique namely modified biogeography-based optimization (MBBO) shows better performance than other well-known techniques, i.e., the BBO, the BOA, the GSA, and the PSO techniques in THD mitigation. All the simulated results are successfully validated through hardware in loop setup.

References

1. Benedetto M, Lidozzi A, Solero L, Crescimbini F, Grbović PJ (2018) Five-level E-type inverter for grid-connected applications. IEEE Trans Ind Appl 54(5):5536–5548
2. Panda KP, Panda G (2018) Application of swarm optimisation-based modified algorithm for selective harmonic elimination in reduced switch count multilevel inverter. IET Power Electron 11(8):1472–1482
3. Panda KP, Lee SS, Panda G (2019) Reduced switch cascaded multilevel inverter with new selective harmonic elimination control for standalone renewable energy system. IEEE Trans Ind Appl 55(6):7561–7574
4. Gupta KK, Ranjan A, Bhatnagar P, Sahu LK, Jain S (2016) Multilevel inverter topologies with reduced device count: a review. IEEE Trans Power Electron 31(1):135–151
5. Lee SS, Chu B, Idris NRN, Goh HH, Heng YE (2015) Switched-battery boost-multilevel inverter with GA optimized SHEPWM for standalone application. IEEE Trans Industr Electron 63(4):2133–2142
6. Babaei E, Hosseini SH (2009) New cascaded multilevel inverter topology with minimum number of switches. Energy Convers Manag 50(11):2761–2767
7. Najafi E, Yatim AHM (2011) Design and implementation of a new multilevel inverter topology. IEEE Trans Industr Electron 59(11):4148–4154
8. Nedumgatt JJ, Kumar DV, Kirubakaran A, Umashankar S (2012) A multilevel inverter with reduced number of switches. In: 2012 IEEE students' conference on electrical, electronics and computer science. IEEE, Bhopal, pp 1–4
9. Wang L, Wu QH, Tang W (2017) Novel cascaded switched-diode multilevel inverter for renewable energy integration. IEEE Trans Energy Convers 32(4):1574–1582
10. Sen P, Bana PR, Panda KP (2019) Firefly assisted genetic algorithm for selective harmonic elimination in PV interfacing reduced switch multilevel inverter. Int J Renew Energy Res 9(1):32–43
11. Rotella M, Peñailillo G, Pereda J, Dixon J (2008) PWM method to eliminate power sources in a nonredundant 27-level inverter for machine drive applications. IEEE Trans Industr Electron 56(1):194–201
12. Bana PR, Panda KP, Naayagi RT, Siano P, Panda G (2019) Recently developed reduced switch multilevel inverter for renewable energy integration and drives application: topologies, comprehensive analysis and comparative evaluation. IEEE Access 7:54888–54909
13. Sun J, Grotstollen H (1992) Solving nonlinear equations for selective harmonic eliminated PWM using predicted initial values. In: Proceedings of the 1992 international conference on industrial electronics, control, instrumentation, and automation, vol 1. IEEE, San Diego, CA, pp 259–264
14. Chiasson JN, Tolbert LM, McKenzie KJ, Du Z (2005) Elimination of harmonics in a multilevel converter using the theory of symmetric polynomials and resultants. IEEE Trans Control Syst Technol 13(2):216–223

15. Du Z, Tolbert LM, Chiasson JN (2006) Active harmonic elimination for multilevel converters. IEEE Trans Power Electron 21(2):459–469
16. Memon MA, Mekhilef S, Mubin M, Aamir M (2018) Selective harmonic elimination in inverters using bio-inspired intelligent algorithms for renewable energy conversion applications: a review. Renew Sustain Energy Rev 82(3):2235–2253
17. Arora S, Singh S (2019) Butterfly optimization algorithm: a novel approach for global optimization. Soft Comput 23(3):715–734
18. Simon D (2008) Biogeography-based optimization. IEEE Trans Evol Comput 12(6):702–713
19. Rashedi E, Nezamabadi-Pour H, Saryazdi S (2009) GSA: a gravitational search algorithm. Inf Sci 179(13):2232–2248
20. Eberhart R, Kennedy J (1995) A new optimizer using particle swarm theory. In: Proceedings of the sixth international symposium on micro machine and human science. IEEE, Nagoya, pp 39–43
21. Li F, Wang Y, Wu F, Huang Y, Liu Y, Zhang X, Ma M (2020) Review of Real-time simulation of power electronics. J Mod Power Syst Clean Energy 8(4):796–808
22. Typhoon HIL Homepage. https://www.typhoon-hil.com. Accessed 18 Jan 2021
23. Ahmad J, Pervez I, Sarwar A, Tariq M, Fahad M, Chakraborty RK, Ryan MJ (2020) Performance analysis and hardware-in-the-loop (HIL) validation of single switch high voltage gain DC-DC converters for MPP tracking in solar PV system. IEEE Access
24. Agwa AM, El-Fergany AA, Maksoud HA (2020) Electrical characterization of photovoltaic modules using farmland fertility optimizer. Energy Convers Manag 217:1–12
25. SLP080-12 Datasheet. https://www.solarland.com.tr/main/media/poly/SLP080-12.pdf. Accessed 18 Jan 2021

Power Quality Improvement of an Interconnected Grid System Using PWM Technique of D-STATCOM

Manoj Kumar Kar, Sanjay Kumar, and Arun Kumar Singh

1 Introduction

In general, power squality (PQ) is the maintenance of a sinusoidal voltage waveform at nominal voltage and frequency. It is the power supply characteristics that allow the equipment to operate properly. Any faults on transmission lines, capacitor switching, switching of large loads, use of power electronic devices cause distortion due to its non-linearity nature. At the generation point, the electric power waveform is strictly sinusoidal and is free from distortion. The same power would be available in the load side if there is no distortion. But, in practical case due to the presence of transmission line reactance, the power to be transmitted gets affected. The current flowing through the system's impedance can cause a number of voltage disruptions. The voltage is often skewed by distorted currents from harmonic production loads as they pass through the impedance of the system. These distortions spread all over the network.

In the early days, the quality of power was mainly concerned with the continuity of the supply of electricity at appropriate voltage and frequency. AC distribution systems are faced with a number of problems in the quality of power. In particular, because of the use of sensitive equipment in the majority of production, residential, industrial, and traction applications. Not only can non-linear loads cause problems with power efficiency, but they are also extremely susceptible to voltage deviations. The ability to monitor both actual and reactive power exchanges can be effectively used to damp power oscillation damping, and for providing uninterrupted power to essential loads.

M. K. Kar (✉) · S. Kumar · A. K. Singh
EE Department, NIT Jamshedpur, Jamshedpur, Jharkhand, India

S. Kumar
e-mail: sanjay.ee@nitjsr.ac.in

A. K. Singh
e-mail: aksingh.ee@nitjsr.ac.in

S. Kumar et al. (eds.), *Recent Advances in Power Electronics and Drives*, Lecture Notes in Electrical Engineering 852, https://doi.org/10.1007/978-981-16-9239-0_3

Nonlinear loads cause distortions in currents and voltages in the supply mains, leading to deterioration of power quality [1]. Different approaches have been applied for compensating the effect of these non-linear loads [2]. The performance can be improved with different algorithms [3, 4]. A new unified method was proposed for the manipulation of power system waveform parameters such as magnitude, phaseaangle, and ffrequency [5]. Though variation of load has effect on PQ, still based on the different environmental conditions PQ disruptions are also classified [6]. The power quality can be improved by using D-STATCOM near the load [7]. In order to produce the reference load voltage for a voltage-controlled DSTATCOM, a control algorithm was proposed [8]. In VSC-based DSTATCOM, an adaptive fuzzy logic controller with IRPT control algorithm has been used [9]. A control algorithm based on SRF theory is implemented to control DSTATCOM efficiently in grid level PQ improvement [10]. A hybrid technique-based icosϕ control algorithm has been used for analyzing the performance [11]. Taking into consideration the costs of DSTATCOM, the optimal location is chosen for loss minimization and enhancement of voltage profile [12]. A DSTATCOM integrated with distribution transformer is used for reactive power compensation [13]. An optimal allocation model of DSTATCOM with multi-objective functions is described [14]. The methods to protect critical loads from voltage-based PQ issues are presented [15]. The PCC voltage and the reactive power are taken care by the DSTATCOM [16]. The mitigation of harmonics and power factor improvement is done by using D-STATCOM [17]. The distorted voltage and hence, the power quality is improved [18].

2 Operation and Control of DSTATCOM

Static compensators connecting at distributed system and operating for mitigating of multiple current power quality problems commonly known as distributed STATCOM (DSTATCOM). It is typically used to boost power quality in low or medium voltage distribution systems. It is often used in three-phase systems to control the terminal vvoltage, dominate the voltage flicker and enhance voltage balance. The basic purpose of DSTATCOM is to alleviate all current power-based problems such as VAR, unbalanced currents, neutral currents, and harmonics. An IGBT dependent current controlled VSC is used as the DSTATCOM with a DC bus capacitor to provide sinusoidal balanced currents in the supply. The VSC uses PWM power, so small ripple filters are needed to minimize switching ripples.

A control algorithm is generally used to control directly the reference currents of the DSTATCOM. By using PWM current ccontrol, which results in an indirect current control, the gating pulses to the DSTATCOM are produced. In all control algorithms, the reactive power and the unbalanced current are being compensated using DSTATCOM.

The main purpose of DSTATCOM's control algorithm is to use feedback signals to calculate the reference currents. In PWM current controllers, these reference currents are used, along with corresponding sensed currents, to generate PWM gating signals

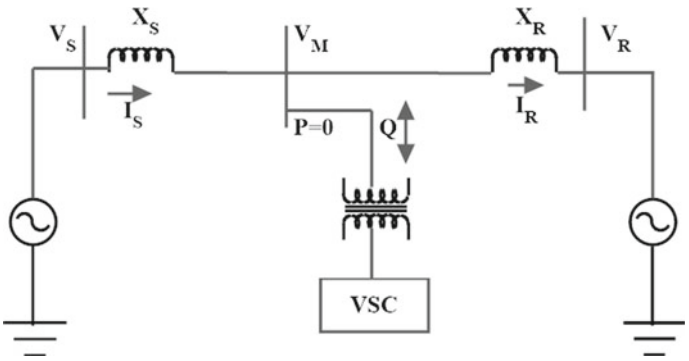

Fig. 1 Schematic diagram of the DSTATCOM

for VSC switching devices used as DSTATCOM. Figure 1 shows the reactive power generation using the basic VSC scheme.

A coupling transformer is installed to match the voltage level because the device rating may not match with system rating. The DC storage capacitor is used to keep the instantaneous output and input powers equal. Semiconductor switches having some losses in a practical converter. These losses are being compensated by the stored energy in the dc capacitor. Thus, to replenish the internal losses, the converter consumes a small amount of active power from the system, maintaining the desired capacitor voltage.

The schematic diagram of the DSTATCOM is shown in Fig. 1. If the voltage magnitude of the VSC is more than the system AC voltage V_M, the reactive current starts flowing from the converter to the ac system through the tie line reactance, and the VSC produces reactive power for the ac system which is capacitive in nature. If the output voltage amplitude is less than that of the ac system, then the current flows from the AC system to the converter and the reactive power is absorbed by the converter which is inductive in nature. If the amplitude of both is equal, then there is no exchange of reactive power.

3 Modeling

The basic diagram of the DSTATCOM based on VSC is shown in Fig. 2.

The three-phase AC system voltage V_s lags the STATCOM output voltage by an angle and is given by Eq. (1).

$$V_{s,abc} = \begin{bmatrix} V_{sa}(t) \\ V_{sb}(t) \\ V_{sc}(t) \end{bmatrix} = \sqrt{\frac{2}{3}} V_s \begin{bmatrix} \sin \omega t \\ \sin(\omega t - \frac{2\pi}{3}) \\ \sin(\omega t + \frac{2\pi}{3}) \end{bmatrix} \tag{1}$$

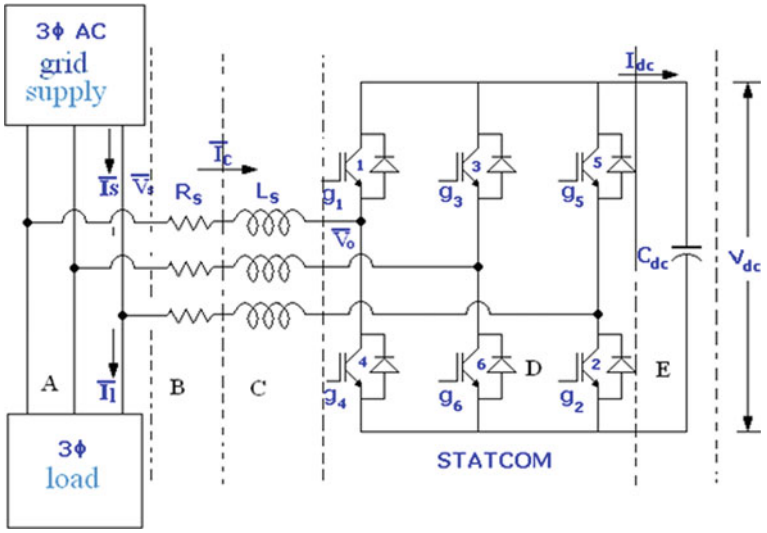

Fig. 2 Block diagram of the VSC-based DSTATCOM

The STATCOM currents are given by Eq. (2).

$$L_s \frac{d}{dt}\begin{bmatrix} i_{ca}(t) \\ i_{cb}(t) \\ i_{cc}(t) \end{bmatrix} = R_s \begin{bmatrix} i_{ca}(t) \\ i_{cb}(t) \\ i_{cc}(t) \end{bmatrix} + \begin{bmatrix} V_{sa}(t) \\ V_{sb}(t) \\ V_{sc}(t) \end{bmatrix} - \begin{bmatrix} V_{oa}(t) \\ V_{ob}(t) \\ V_{oc}(t) \end{bmatrix} \tag{2}$$

The above voltage and currents are transformed into α-β axis as below:

$$\begin{bmatrix} v_\alpha \\ v_\beta \end{bmatrix} = \sqrt{\frac{2}{3}} \begin{bmatrix} 1 & -1/2 & -1/2 \\ 0 & \sqrt{3}/2 & -\sqrt{3}/2 \end{bmatrix} \begin{bmatrix} v_a \\ v_b \\ v_c \end{bmatrix} \tag{3.1}$$

$$\begin{bmatrix} i_\alpha \\ i_\beta \end{bmatrix} = \sqrt{\frac{2}{3}} \begin{bmatrix} 1 & -1/2 & -1/2 \\ 0 & \sqrt{3}/2 & -\sqrt{3}/2 \end{bmatrix} \begin{bmatrix} i_a \\ i_b \\ i_c \end{bmatrix} \tag{3.2}$$

where α and β are the orthogonal coordinates.

These currents can be transformed from α-β to d-q by using Park's transformation defined as

$$\begin{bmatrix} i_d \\ i_q \end{bmatrix} = \begin{bmatrix} \cos\theta & \sin\theta \\ -\sin\theta & \cos\theta \end{bmatrix} \begin{bmatrix} i_\alpha \\ i_\beta \end{bmatrix} \tag{4}$$

The STATCOM model in d-q frame is given in Eq. (5).

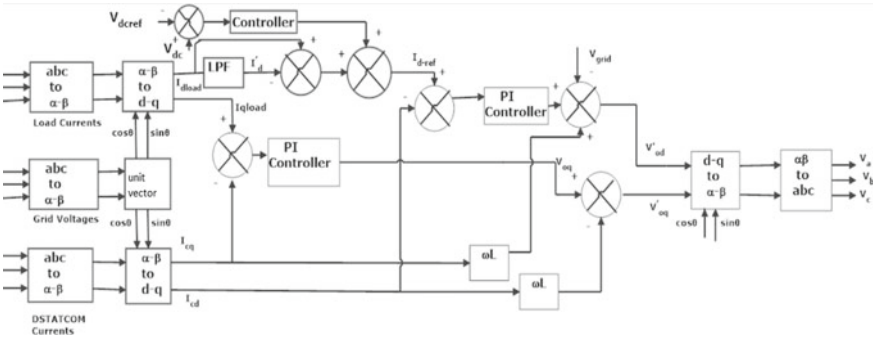

Fig. 3 Transformation block diagram

$$\frac{d}{dt}\begin{bmatrix} i_{cd}(t) \\ i_{cq}(t) \\ v_{dc}(t) \end{bmatrix} = \begin{bmatrix} -R_s/L_s & \omega & -m/L_s \\ -\omega & -R_s/L_s & 0 \\ m/C & 0 & 0 \end{bmatrix} \begin{bmatrix} i_{cd}(t) \\ i_{cq}(t) \\ v_{dc}(t) \end{bmatrix} + \frac{V_s}{L_s}\begin{bmatrix} \cos\alpha \\ -\sin\alpha \\ 0 \end{bmatrix} \tag{5}$$

The transformation block diagram is shown in Fig. 3.

4 Controller Design

Two controllers namely voltage and current controller are used to analyze the performance.

Equation (5) can be rewritten as

$$\frac{d}{dt}\begin{bmatrix} i_{cq} \\ i_{cd} \end{bmatrix} = \begin{bmatrix} -R_s/L_s & -\omega \\ \omega & -R_s/L_s \end{bmatrix} \begin{bmatrix} i_{cq} \\ i_{cd} \end{bmatrix} + \frac{1}{L_s}\left[\begin{bmatrix} V_{sq} \\ V_{sd} \end{bmatrix} - \begin{bmatrix} V_{oq} \\ V_{od} \end{bmatrix}\right] \tag{6}$$

4.1 Current Controller Design

The harmonic current is supplied by the d-axis controller and a small amount of active current is drawn to meet the switching losses where as both harmonic and reactive current are supplied by the q-axis controller.

$$v_{oq} = -v_{oq}^{*} - \omega L_s i_{cd} + v_{sq} \tag{7.1}$$

$$v_{od} = -v_{od}^{*} - \omega L_s i_{cq} + v_{sd} \tag{7.2}$$

Applying the Laplace transformation and then rearranging, the transfer function can be obtained as follows

$$G_i(s) = \frac{I_{cq}(s)}{v^*_{oq}(s)} = \frac{I_{cd}(s)}{v^*_{od}(s)} = \frac{1}{R_s + L_s} \tag{8}$$

4.2 Voltage Controller Design

The DC link voltage is maintained constant using voltage controller

$$V_{dc} = \frac{1}{C} \int i_{dc}(t) \tag{9}$$

$$G_v(s) = \frac{V_{dc}}{I_{dc}} = \frac{1}{sC} \tag{10}$$

5 Simulation Results

The performance of the 3-ϕ grid-connected system with nonlinear load has been studied with MATLAB/SIMULINK and the results have been presented. The 3-ϕ source voltage waveform is given in Fig. 4. Due to the non-linearity nature of the load, the current waveform gets distorted and is shown in Fig. 5. When the DSTATCOM is enabled at t = 0.1 s, it injects the harmonic current and thus maintains sinusoidal source current by compensating the distortion. The injected current waveform with enabled DSTATCOM at t = 0.1 s is shown in Fig. 6. The power factor is found to be unity after the DSTATCOM is enabled thus improves the power quality of the system which is shown in Fig. 7. The THD of the grid current is found to be 31.08% and 2.67% without and with compensation which is given in Fig. 8 and Fig. 9 respectively.

6 Conclusion

The analysis of DSTATCOM and design of controllers are presented in this paper. A DSTATCOM based on VSI is used to provide the load with both VAR and harmonic current so that the source current becomes sinusoidal and has a unit power factor. The controllers are designed on the basis of parameters of the STATCOM and time constant. THD is reduced from 31.08 to 2.67% after connecting DSTATCOM. Thus, the effectiveness of DSTATCOM with PI controller to improve the power factor

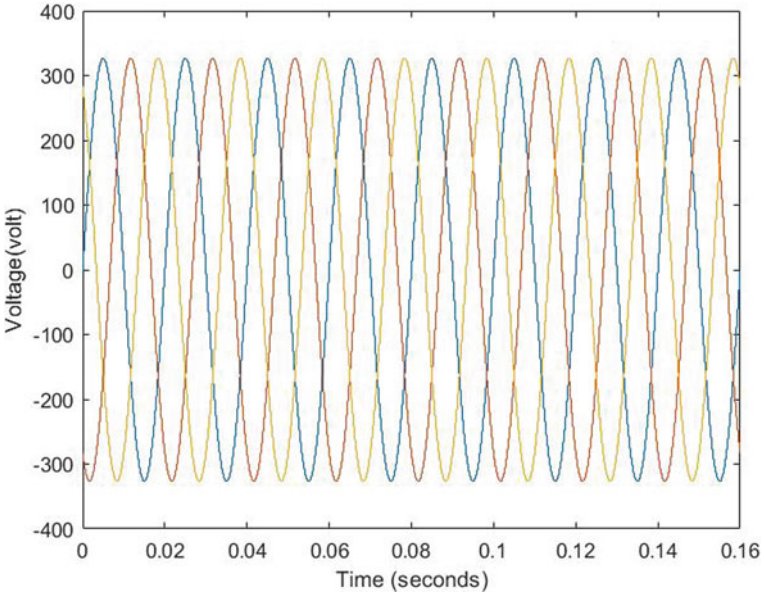

Fig. 4 Three-phase source voltage waveforms

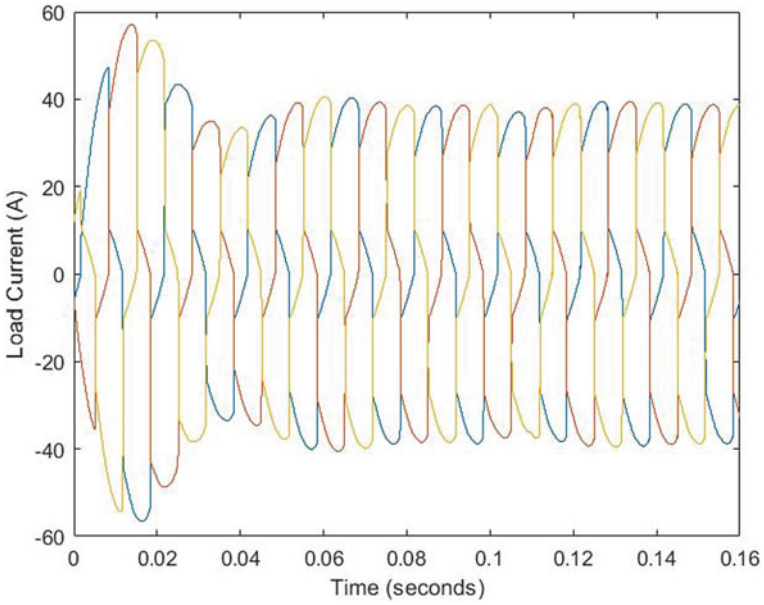

Fig. 5 Load current waveform

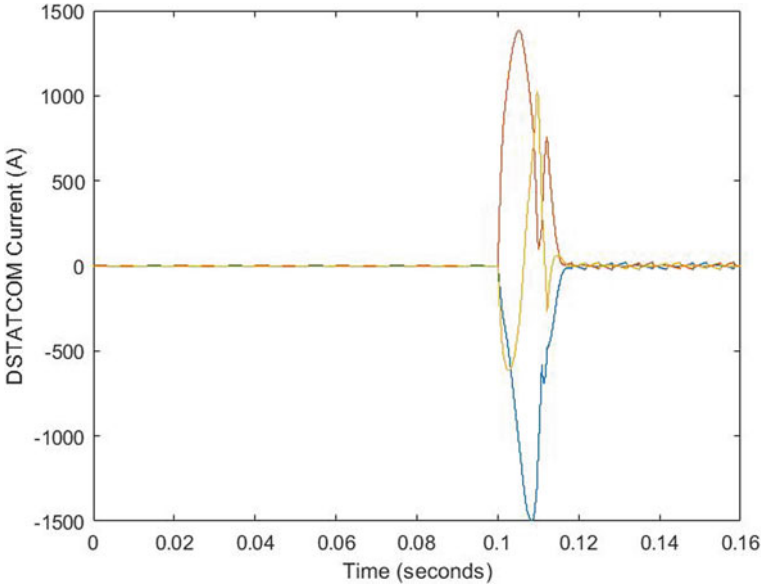

Fig. 6 Current injected by DSTATCOM

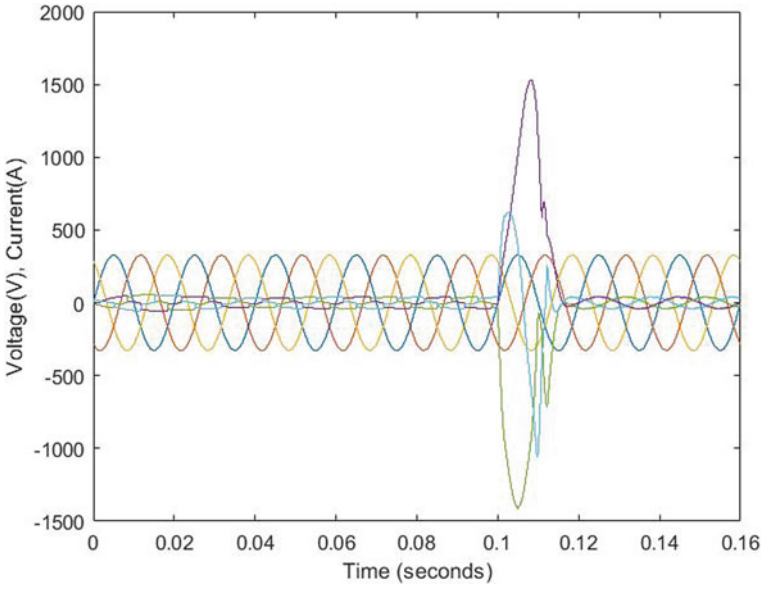

Fig. 7 UPF operation after using DSTATCOM

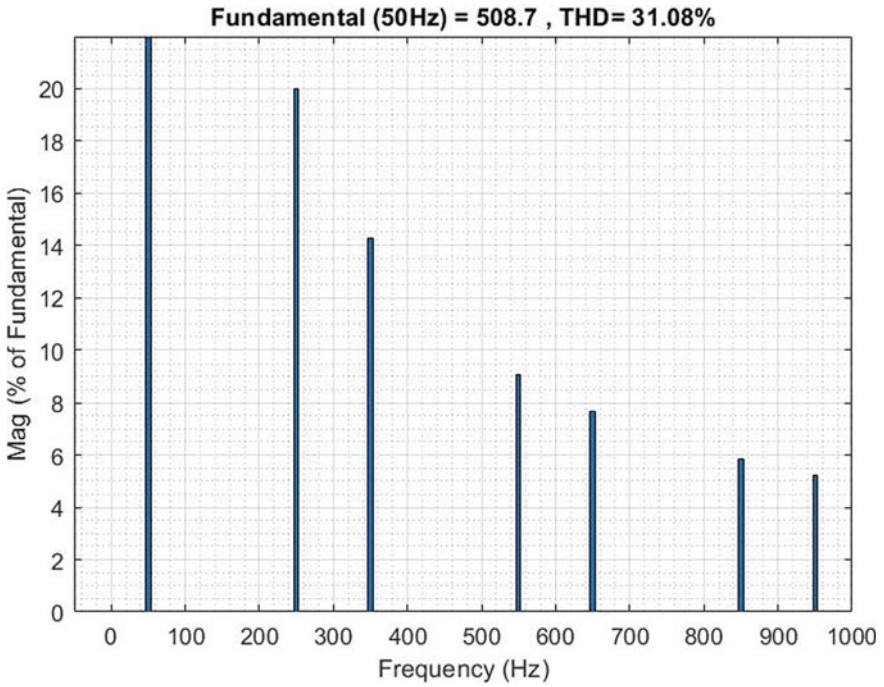

Fig. 8 THD before using DSTATCOM

is also investigated. Unity power factor operation is observed after 0.1 s when the DSTATCOM is enabled. The proposed DSTATCOM model effectively reduces the current harmonics injected by the load into the distribution network and hence enhances the power quality of the system.

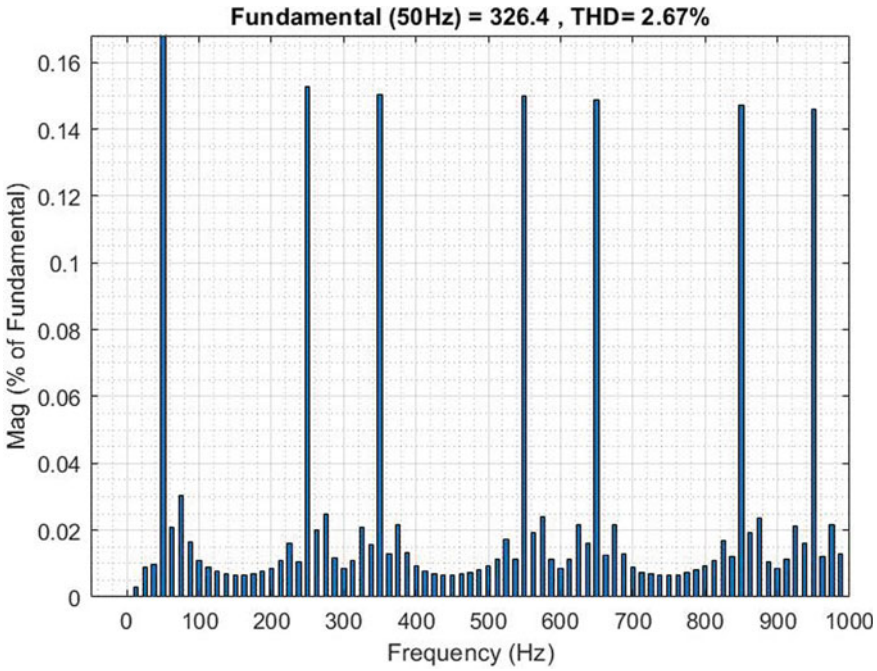

Fig. 9 THD after using DSTATCOM

References

1. Padiyar KR (2008) FACTS controllers in power transmission and distribution. New Age International, New Delhi
2. Herrera RS, Salmeron P, Kim H (2008) Instantaneous reactive power theory applied to active power filter compensations: different approaches, assessment, and experimental results. IEEE Trans Ind Electron 55(1):184–196
3. Masand D, Jain S, Agnihotri G (2008) Control strategies for distribution static compensator for power quality improvement. IETE J Res 54(6):421–428
4. Singh B, Solanki J (2009) A comparison of control algorithms for DSTATCOM. IEEE Trans Ind Electron 56(7):2738–2745
5. Dash P, Padhee M, Barik S. Estimation of power quality indices in distributed generation systems during power islanding conditions. Int J Elect Power Energy Syst 36(1):18–30
6. Ray PK, Mohanty SR, Kishore N (2013) Classification of power quality disturbances due to environmental characteristics in distributed generation system. IEEE Trans Sust Energy 4(2):302–313
7. Kar MK, Rout BD, Moharana JK (2014) Improvement of power factor of a grid connected load system using a static compensator. J Found Appl Phys 1(1):5–10
8. Kumar C, Mishra MK (2014) A voltage controlled DSTATCOM for power quality improvement. IEEE Trans Power Deliv 29(3)
9. Singh B, Dube SK, Arya SR (2015) An improved control algorithm of DSTATCOM for power quality improvement. Electr Power Energy Syst 64:493–504
10. Mahela OP, Shaik AG (2016) Power quality improvement in distribution network using DSTATCOM with battery energy storage system. Int J Electr Power Energy syst 83:229–240

11. Mangaraj M, Panda AK (2017) Performance analysis of DSTATCOM employing various control algorithms. IET Gener Transm Distrib 11(10):2643–2653
12. Iqbal F, Khan MT, Siddiqui AS (2018) Optimal placement of DG and DSTATCOM for loss reduction and voltage profile improvement. Alex Eng J 755–765
13. Chen Y, Wen M, Xianggen Yin EL, Lai J, Wang Z (2018) Passivity-based control of cascaded multilevel converter based DSTATCOM integrated with distribution transformer. Electr Power Syst Res 154:1–12
14. Pradhan M, Mishra MK (2019) Dual P-Q Theory based energy-optimized dynamic voltage restorer for power quality improvement in a distribution system. IEEE Trans Ind Electron 66(4)
15. Zhang T, Yu L (2020) Optimal allocation of DSTATCOM considering the uncertainty of photovoltaic systems. IEEJ Trans Electr Electron Eng 15:355–363
16. Sayahi K, Kadri A, Bacha F, Marzougui H (2020) Implementation of a DSTATCOM control strategy based on direct power control method for grid connected wind turbine. Electr Power Energy Syst 121:1–14
17. Rohouma W, Balog RS, Peerzada AA, Begovic MM (2020) D-STATCOM for harmonic mitigation in low voltage distribution network with high penetration of nonlinear loads. Renew Energy 145:1449–1464
18. Abas N et al (2020) Power quality improvement using dynamic voltage restorer. IEEE Access 8:164325–164349

Speed Control of a Three-Phase IM with Closed-Loop Control Scheme

Rajkumar Yadav, Manoj Kumar Kar, and Arun Kumar Singh

1 Introduction

Induction motor runs at rated speed, when it is connected to main supply. However, depending on various applications, there is a need to regulate the speed of the IM. Various methods are available to control the speed of IM from both sides either stator side or rotor side. The voltage and frequency are varied simultaneously but the v/f ratio is kept constant so that the air-gap flux remains constant and to avoid the saturation. v/f control method reduces steady-state error as discussed in [1, 2]. A sensor less strategy with the help of direct torque control (DTC) was discussed in [3], and it reduces the perturbations of speed, torque, and current around steady state. An intelligent technique with PI controller deal with real-time estimation, improve performance and decrease the sensitivity with changing in parameter and load [4]. An automated PLC system was used for better speed regulation in induction motor drive with variable load [5]. The PLC control system is more efficient than open-loop control of IM fed by inverter. The closed loop control scheme has been used to control the speed of a permanent magnet synchronous machine [6] . The hybrid PWM technique [7] reduces ripple present in torque with improving the harmonics distortion in current. The hybrid PWM technique has good result in such areas as compared to conventional SVPWM technique. Mathematical modeling and simulation of VSI-fed IM with closed-loop control method is done by maintaining v/f as constant to control speed of IM drive discussed in [8]. The same approach is implemented in laboratory with the help of PC and add-on card. The idea of Z-source inverter (ZSI) useful for the speed control of IM using v/f control method [9]. The ZSI diminishes the stress voltage across such capacitor, hence this topology makes drive system economical. The traditional model-based design replaced after the development of model-based embedded system design in MATLAB is described in [10]. SPWM control method is developed based on MATLAB platform and implemented using

R. Yadav (✉) · M. K. Kar · A. K. Singh
NIT Jamshedpur, Jamshedpur 831014, India

S. Kumar et al. (eds.), *Recent Advances in Power Electronics and Drives*, Lecture Notes in Electrical Engineering 852, https://doi.org/10.1007/978-981-16-9239-0_4

model-based design which saves both effort and time. A sensor less approach is established on the application of Lueberger observer for flux and rotor speed calculations [11]. In case of open path errors take place in switches of inverter with sensor less induction motor must be detected quickly and disconnect the healthy drive system from faulty system. In SPWM, closed-loop control and open-loop control methods converters are used which provide output waveforms inclosing some ripples, now to eliminate this problem converters use PI-controlled elementary positive output lift Luo converter (EPOLLC) [12] for speed control of IM. The whole drive systems are assembled through field programmable gate array spartan-6 computer. The paper [13] discusses a scheme where it proposes about vector organized squirrel cage IM drive with synchronized SPWM providing wide range of speed variations suitable for drive applications. The paper [14] explains SVPWM method for speed control of TIM drive with open-loop and closed-loop control approach. In SVPWM technique the output voltage almost similar as sinusoidal provides good concert and becomes more efficient to the drive systems [15]. A new idea for speed control of IM known as direct matrix converter (DMC) which is controlled by global synchronous PWM (GSPWM) approach. The proposed idea is used to keep the input power factor as a unity from rectifier side of DMC. In this way the drive system becomes very simple and free from maintenance [16]. To control the speed of squirrel cage IM, the practical setup is done by v/f scalar control with two methods, one is open-loop control and the other is closed-loop control. During experiment, it is essential to monitor the behavior of current to escape from possible damages. In [17], various loss minimization techniques are discussed, the losses arise due to the switching devices used in Inverter-fed drive systems. The component-level loss minimization method does not guarantee about minimization of total losses. But system-level loss method provides a true minimum total loss in the motor drive systems. On the basis of performance, the comparative examination for speed control of IM drive is done by SVM and SPWM based VSI-fed motor drive having PI controller as in feedback path with v/f ratio same. Analyzing the result [18, 19], it is found that SVPWM technique has better performance compare to SPWM technique with closed-loop control approach. A digital basis FPGA controller gives the signals for switching devices used in drive [20]. The idea of SPWM used with FPGA controller into the application of IM drive system and also enhance the routine in variable-voltage/variable-frequency (VVVF). The closed-loop speed control method with PI controller limits the starting current of motor within range. PI controller reduces steady-state error and provides smooth speed but does not limit the dynamic behavior. The complete policy and establishment of close-loop and open-loop control method is done in [21] by using PI controller. The digital signal controller (DSC) reduces the circuit complexity, hence decrease the overall cost of the IM drive system. An algorithm is designed in [22] for a digital signal PIC microcontroller in VSI-fed IM. A comparative study is done in [23] to enhance the efficiency of three-phase induction motor (TIM). Another advanced controller proposed with switching topology to monitor the harmonics, flux, voltage, current, and frequency control during the speed control of TIM. The paper [24] elaborates the difficulties that arise during speed control for IM through a

literature survey. There are many techniques available for IM drive system, the troubles faced by such techniques as variations in speed, harmonics, or ripples present in voltage and current waveforms. By adjusting the duty cycles of switches, the stator terminal voltage of VSI-fed IM is to be controlled [25]. Hence the speed and torque can be adjusted easily. Without any speed control scheme, IM runs at its own speed after connecting with supply. Among the various schemes, VVVF method is most popular to find the variable speed for such motor drive system. The developed torque is related to the flux which is associated with ratio of change in voltage and change in frequency having the v/f ratio constant [26]. The paper [27] discusses a comparative analysis among the various PWM approaches such as space vector PWM, sinusoidal PWM, and multiple PWM having different power rating of machine. All these PWM methods help to produce gate signals for VSI-fed IM drive. To reduce the THD and find better quality of voltage sine waves at output terminals of Diode Clamped Multilevel Inverter, different modulation schemes have been implemented [28, 29]. A 15-level diode clamped MLI was used to control the speed of TIM with improving the performance characteristics.

In this work, the speed control of 3-Φ IM is achieved by adjusting the pulse width in case of variable-voltage method whereas in case of VVVF method, by maintaining the v/f ratio constant throughout the entire speed range, the machine performance and hence efficiency is improved. In VVVF method, the motor reference speed is compared with the actual speed, the error obtained produces a reference frequency of PWM. Then, the motor speed can be changed according to the reference speed.

2 Sinusoidal PWM Technique

Among the various modulation approaches, SPWM is popular in industries to control the speed of an IM. Three references sinusoidal waves (120° apart in phase) are compared by a saw tooth wave signal used to produce gate pulses for three-phase inverters. A squirrel cage IM with ratings 5.4 HP, 400 V, 50 Hz, 1430 RPM is used. The Simulink block diagram of SPWM control scheme is depicted in Fig. 1. The gate pulses are generated using SPWM technique. The inverter output is fed to the IM for analyzing the performance. In this case, the speed control of the IM is achieved only by varying the voltage.

The idea about on/off Inverter has six switches and a DC voltage source as an input. Now after comparison between reference and carrier wave, six gate signals (A1, A2, A3, A4, A5, A6) are generated by the SPWM technique. These pulses are given to the switching devices shown in Fig. 2.

The above diagram gives switching pattern of the devices. Switch pair (S1-S4, S3-S6, and S5-S6) from the same leg cannot conduct at the similar time to escape the short circuit. In this case, the output voltage becomes zero and it may cause explosion.

The speed and torque of the IM related with supply frequency and voltage are represented as following:

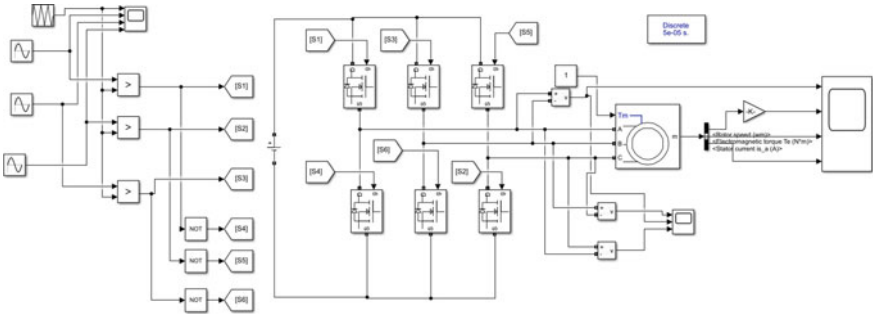

Fig. 1 Simulink diagram with SPWM inverter

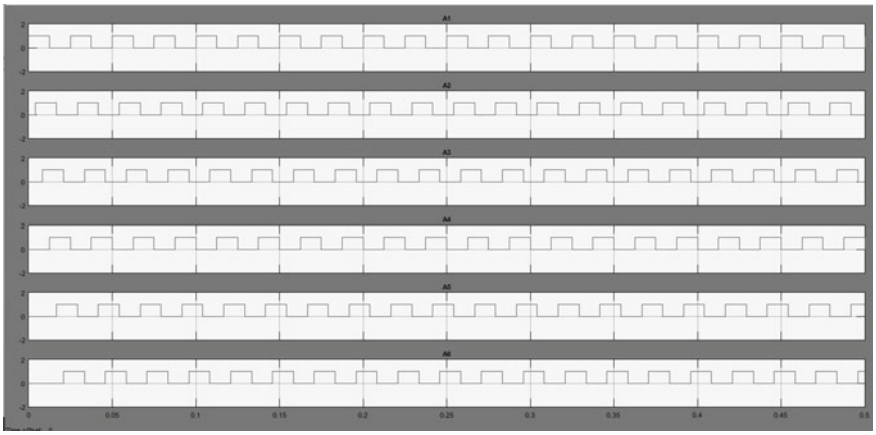

Fig. 2 Gate signals of switching devices

$$N = 120 * f/p \tag{1}$$

$$V = 4.44 * \varphi * f * N_p \tag{2}$$

$$T = \frac{3 * \left(V^2 * R_2'/s\right)}{\omega_s * \left((R_1 + R_2'/s)^2 + (X_1 + X_2')^2\right)} \tag{3}$$

where N = speed in rpm, f&V are supply frequency and voltage respectively, Φ&T are flux per pole and torque (N-m) respectively, ω_s = angular speed (rad/s), s = slip. It is clear from the above equations, the torque and speed of TIM can be changed by altering the frequency, voltage, or both at a time.

3 Simulation Result and Discussion for SPWM Scheme

Figure 3 shows the inverter line voltage achieved by SPWM method which is fed to the induction motor for controlling the speed.

Figure 4 shows the rotor speed characteristic waveform w.r.t the time implementing SPWM scheme. The settling time for rotor speed is 0.12 s. The rotor speed changes between 1475 and 1425 rpm after steady state.

Figure 5 explains the behavior of torque w.r.t time implementing SPWM scheme. The torque has transient nature at starting but it settles after 0.1 s. From Eq. 3, torque is proportional to the square of voltage. Hence torque is also varied. Hence the torque and voltage relation are satisfied. From speed and torque wave form, it is seen that as speed is higher at the same time torque has a minimum value to make the drive system under steady state.

During the speed control of IM, one of the important parameters is known as stator. To avoid the damage due to excess heat produced by the current must have the safe limit during drive application. IM draws the high amount of current just at starting as shown in Fig. 6. The stator current has direct relation to the supply voltage generated by SPWM inverter.

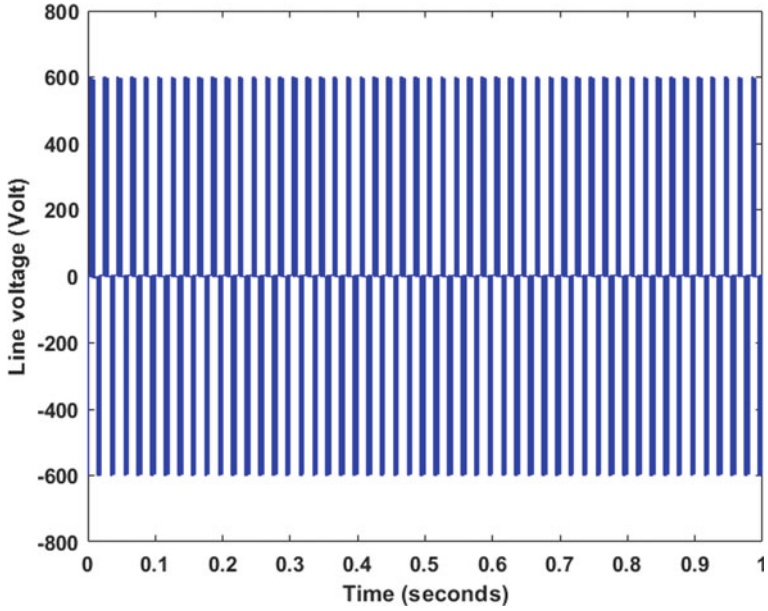

Fig. 3 Response of line voltage

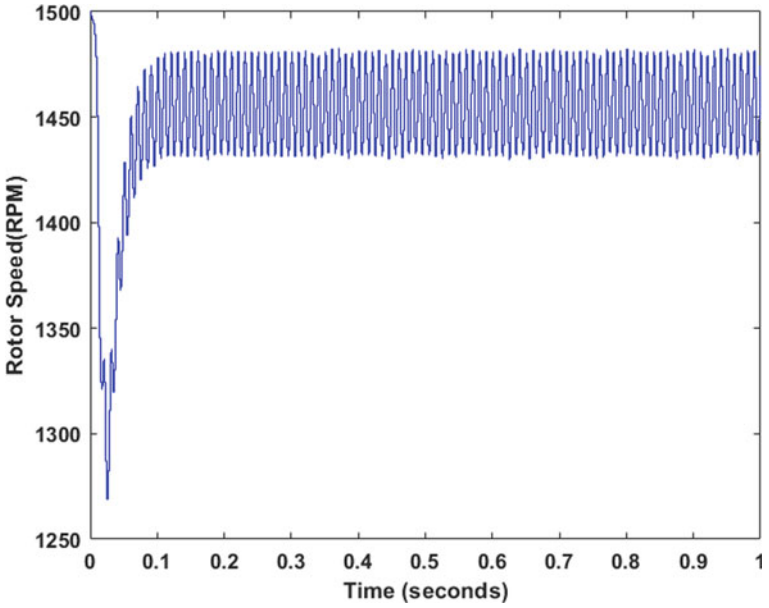

Fig. 4 Response of rotor speed using SPWM scheme

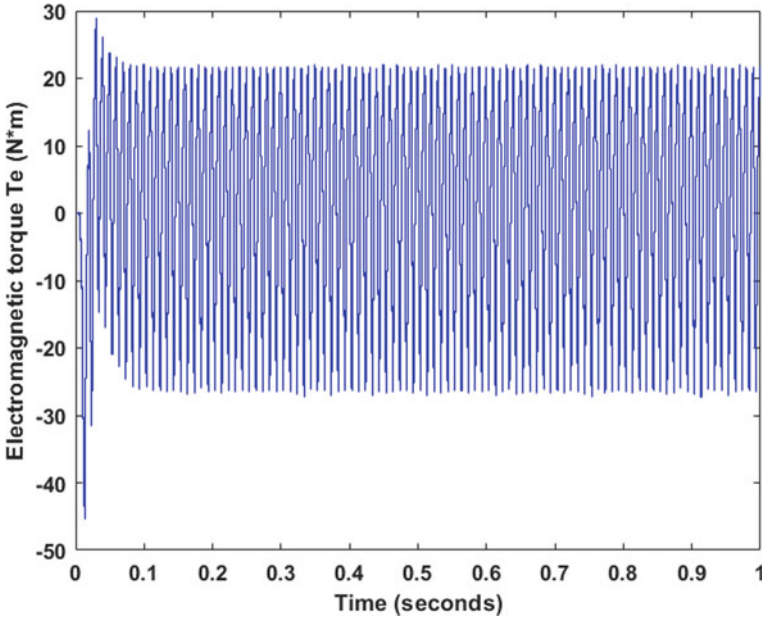

Fig. 5 Response of electromagnetic torque using SPWM scheme

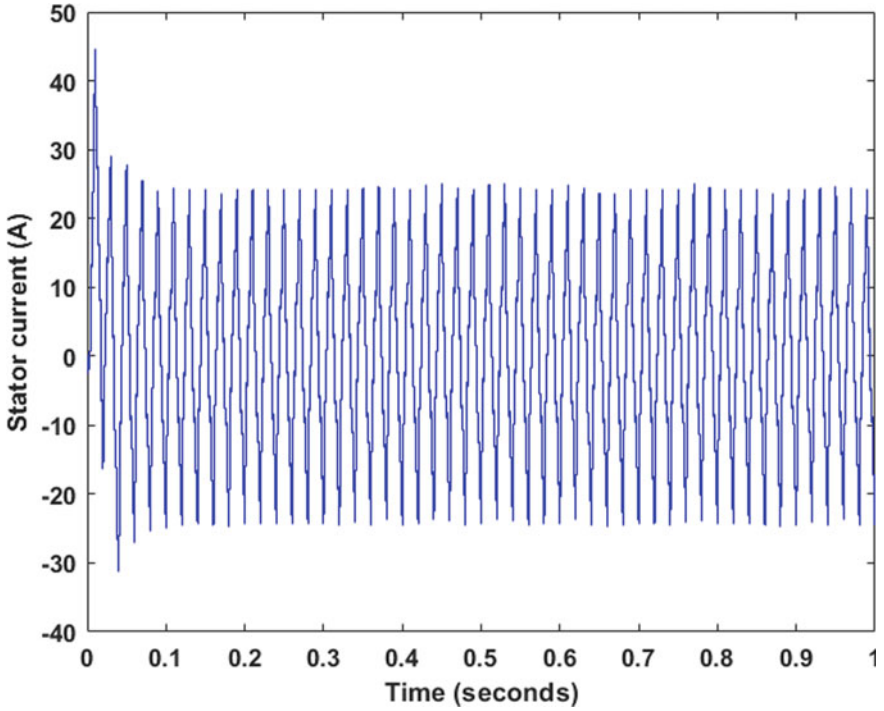

Fig. 6 Response of stator current using SPWM scheme

4 Advantages of Sinusoidal SPWM Scheme

- It is less costly. Because the result is found without need of any filter by keeping frequency as the constant parameter.
- It is simple for design and implementation. There is no requirement of controller and look-up table like SVPWM.

5 Speed Control by Closed-Loop V/F Approach

As the frequency changes, speed also changes in the same proportion which is clear from Eq. 1. Since the flux has an inverse relationship with frequency, the frequency cannot be changed beyond the limit to take care of air-gap flux. From Eq. 2, the voltage is directly proportional to flux means supply voltage must vary within the limit for the same reason. The slip speed being the difference between the synchronous speed and rotor speed can't be maintained. It leads to the unstable operation of Torque-Speed characteristics. As a result, the stator current exceeds the rated value of current which

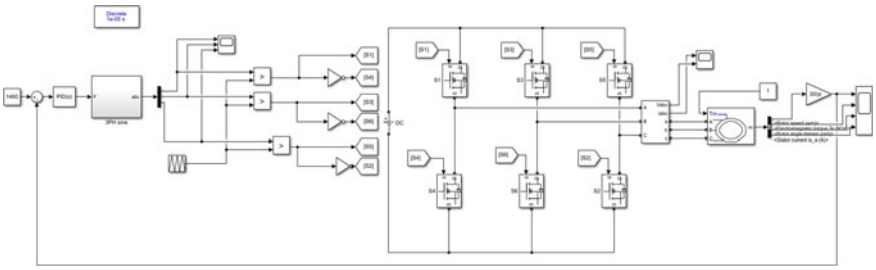

Fig. 7 Simulink model implementing v/f scheme with closed-loop control

may have adverse effect on the inverter-converter combination. The above problem can be overcome by using an outer loop in the IM shown in Fig. 7.

The scheme consists of a PID controller, VSI, and speed sensing feedback. The actual rotor speed is compared with the reference value to generate an error. This error is passed through a controller and its output sets the inverter frequency. This frequency generates the reference signal for the closed-loop control of the IM.

6 Result and Discussion for Closed-Loop V/F Control Method

The frequency of supply voltage fed to the IM can be varied by varying the width of pulses. The frequency has a direct relation with the speed from Eq. 1. Hence speed of IM is regulated by controlling the supply frequency. Figure 8 shows the nature of rotor speed w.r.t. time implementing closed loop v/f control scheme.

The speed-time graph settles after 2 s. Before that time, speed is under transient condition. At starting difference between actual and reference speed is high. It shows the larger error signal, the error is given to the controller. The PID controller has advantage to limit speed difference until the error signal becomes zero. Variation in speed is going to be controlled within the fixed range.

The electromagnetic torque w.r.t. time using closed loop v/f control scheme is shown in Fig. 9. It shows the fluctuations just at starting. From the graph, it can be seen that torque has more fluctuations between (0–0.8) s and after that it is settled down between (0.8–1.8) s having less fluctuation. But for fractions of second (1.8–2.2) again transient occurs and finally achieve the steady-state condition after 2.2 s. v/f ratio is maintained as constant in closed-loop control so that flux setup to become unchanged and torque would be free from the supply frequency. Now in such case speed of IM allowed to vary with a larger range by changing the frequency. It does not affect the torque operated under loaded condition.

The rotor angle (rad) graph is shown in Fig. 10. The rotor angle is related to the stator current and slip. It can be adjusted from 0 to a fixed angle. It is a straight-line

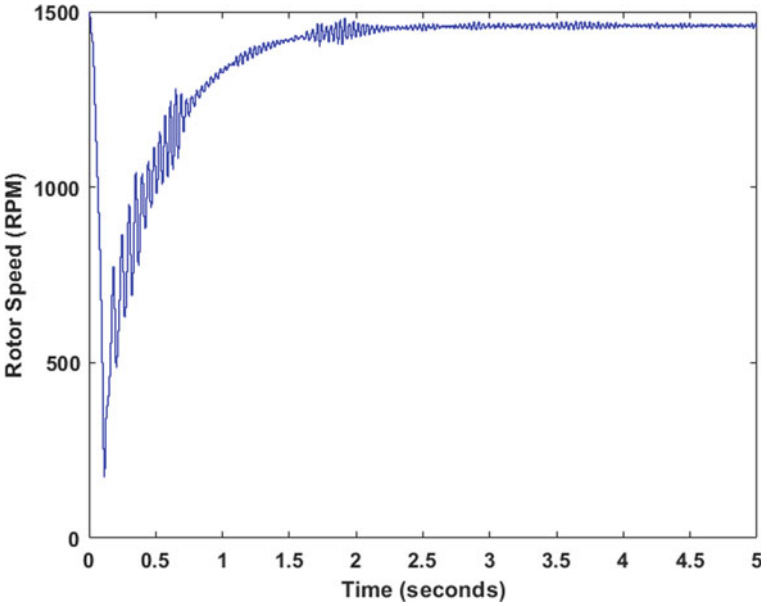

Fig. 8 Response of rotor speed using closed loop v/f control scheme

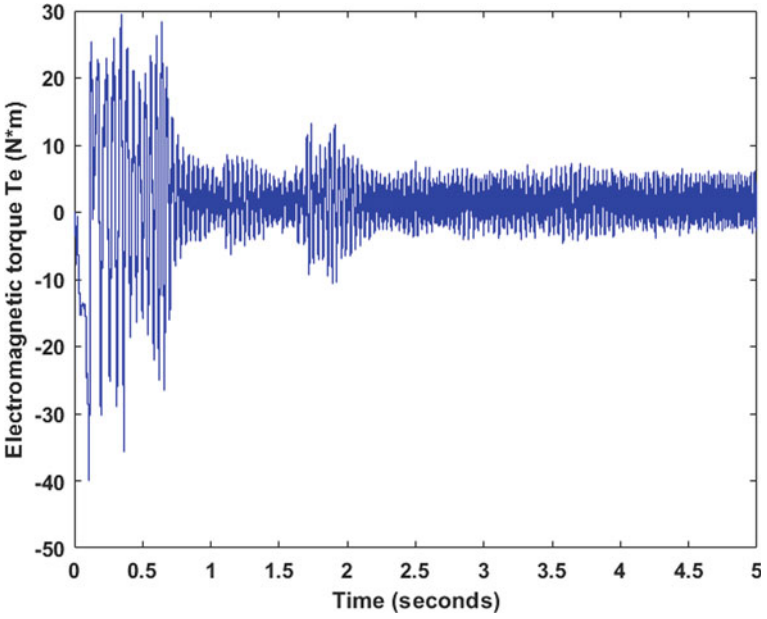

Fig. 9 Response of electromagnetic torque using closed loop v/f control scheme

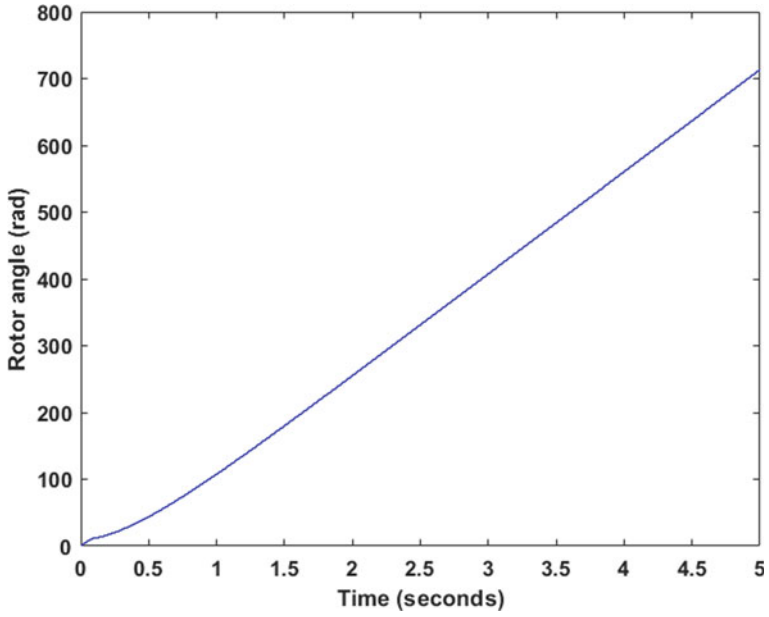

Fig. 10 Response of rotor angle

graph starting from zero. IM behaves as a load itself, so the rotor current drawn by the motor should be under control during closed-loop v/f control.

The response of the stator current using closed loop v/f control scheme is presented in Fig. 11. It is found that stator current has a direct relation with supply voltage. So, at the time of starting favorable supply given to the drive system. The stator current is found to be within the limit of the rated value. Distortion in current waveform is improved as compared to the open-loop scheme.

7 Advantages of Closed-Loop V/F Control Method

- Maximum torque is constant throughout the operation due to flux unchanged having voltage to frequency ratio constant.
- IM can run as greater than base speed, if increase the frequency only where voltage cannot go higher than rated value.

8 Conclusion

The speed control of IM by variable voltage and by VVVF method is achieved using MATLAB/SIMULINK. To analyze the performance by speed control of IM,

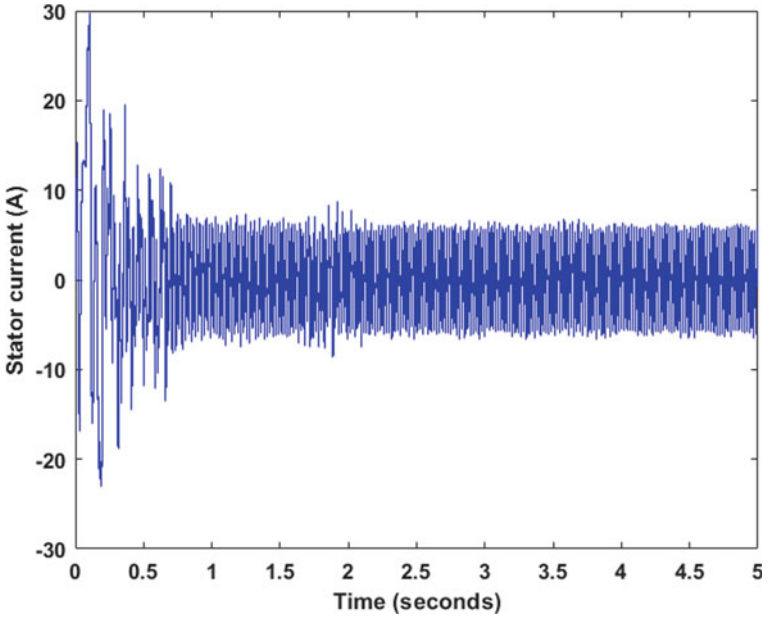

Fig. 11 Response of stator current using closed loop v/f control scheme

two cases are considered. The different motor parameters such as voltage, rotor speed, electromagnetic torque, and stator current waveform are observed by each method. The demerits of earlier method are compensated by the later discussed method. It is clear from the obtained result that the application of closed-loop control scheme enhances the performance as compared to open-loop control because the motor parameters have less harmonics.

References

1. Koga K, Ueda R, Sonoda T (1992) Constitution of V/f control for reducing the steady-state speed error to zero in induction motor drive system. IEEE Trans Ind Appl 28(2):463–471. https://doi.org/10.1109/28.126757
2. Munoz-Garcia A, Lipo TA, Novotny DW (1997) A new induction motor open-loop speed control capable of low frequency operation. In: IEEE Industry applications society annual meeting, New Orleans, Louisiana, 5–9 October 1997
3. Lascu C, Boldea I, Blaabjerg F (2000) A modified direct torque control for induction motor sensor less drive. IEEE Trans Ind Appl 36(1):122–130. https://doi.org/10.1109/28.821806
4. Chen T-C, Sheu T-T (2002) Model reference neural network controller for induction motor speed control. IEEE Trans Energy Convers 17(2):157–163. https://doi.org/10.1109/TEC.2002.1009462
5. Ioannides MG (2004) Design and implementation of PLC-based monitoring control for induction motor. IEEE Trans Energy Convers 19(3):469–476. https://doi.org/10.1109/TEC.2003.822303

6. Yadav R, Kar MK, Singh AK (2021) Controlling speed of a permanent magnet synchronous machine using closed loop control scheme. In: Emerging trends in industry 4.0 (ETI 4.0) pp 1-6. https://doi.org/10.1109/ETI4.051663.2021.9619448
7. Harsha Vardhan Reddy M, Jegathesan V (2011) Open loop V/F control of induction motor based on hybrid PWM with reduced torque ripple. In: International conference on emerging trends in engineering and technology ICETET-2011
8. Vijay Babu K, Magajikondi SJ, Raju AB (2011) Modeling, simulation and PC based implementation of a closed lopp speed control of VSI fed induction motor drive. IEEE
9. Amudhavalli D, Narendran L (2012) Speed control of an induction motor by V/F method using an improved Z source inverter. In: 2012 International conference on emerging trends in electrical engineering and energy management (ICETEEEM), Chennai, 2012, pp 436–440. https://doi.org/10.1109/ICETEEEM.2012.6494486
10. Li H, Li W, Cui D (2013) Automatic code generation of SPWM for single phase inverter by model-based design. In: Proceedings of 2013 2nd international conference on measurement, information and control, Harbin, pp 1035–1038. https://doi.org/10.1109/MIC.2013.6758136
11. Trabelsi M, Boussak M (2014) Sensorless speed control of VSI-FED induction motor drive under IGBT open-switch damage: performances and fault tolerant analysis. In: 2014 International conference on electrical sciences and technologies in Maghreb (CISTEM), Tunis, 2014, pp 1–8. https://doi.org/10.1109/CISTEM.2014.7368727
12. Elangovan P, Mohanty NK (2015) FPGA based V/F control of three phase induction motor drives. Int J Power Electron Drives Syst (IJPEDS) 5(3):393–403. ISSN: 2088-8694
13. Sahoo SK, Bhattacharya T (2016) Rotor flux-oriented control of induction motor with synchronized sinusoidal PWM for traction application. IEEE Trans Power Electron 31(6):4429–4439. https://doi.org/10.1109/TPEL.2015.2475398
14. Abdul M, Biabani KA, Ali SM (2016) Control of induction motor drive using space vector PWM. In: International conference on electrical electronics and optimization techniques (ICEEOT)-2016
15. Singh AK, Kumar NM, Pattnaik S, Vinay Reddy K (2016) Speed control of 3-phase induction motor fed through direct matrix converter using GSPWM technique with unity input power factor. In: International conference on electrical power and energy systems (ICEPES), 14–16 Dec 2016
16. Pena JM, Diaz EV (2016) Implementation of V/F scalar control for speed regulation of a three-phase induction motor. IEEE
17. Sridharan S, Krein PT (2017) Minimization of system-level losses in VSI-based induction motor drives: offline strategies. IEEE Trans Ind Appl 53(2):1096–1105. https://doi.org/10.1109/TIA.2016.2631513
18. Alizadeh M, Masoumi M, Ebrahim E (2017) Closed loop speed control of induction motor using constant V/F applying SPWM and SVM based inverter. Int J Eng Adv Technol (IJEAT) 6(5). ISSN: 2249-8958
19. Shukla NK, Srivastava R (2017) SVPWM and SPWM controller based performance evaluation of three phase induction motor. Int J Eng Sci Res Technol (IJESRT)
20. Selvabharathi P, Kamatchi Kannan V, Sathish Kumar S (2018) SPWM base FPGA controller. Int J Pure Appl Math (IJPAM) 119(18)
21. Naveed I, Sabir A (2018) Design and implementation of open and close loop speed control of three phase induction motor using PI controller. Int J Eng Res Gen Sci 6(2)
22. Moundekar PC, Goyal GN, Hatwar PS (2018) Generation of SPWM control pulses for voltage source inverter sing dcPIC 33EP256MU 810. In: International conference on smart electric drives and power system
23. Hannan MA, Ali JA, Jern KP, Mohamed A, Hossain Lipu MS, Hussain A (2018) Switching techniques and intelligent controllers for induction motor drives: issues and recommendations. IEEE Access
24. Agrawal A, Lodhi RS, Nema P (2018) A review of speed control methods of induction motor. IOSR J Electr Electron Eng (IOSR-JEEE) 13(3):09–14. e-ISSN: 2278-1676, p-ISSN: 2320-3331

25. Bhagat B, Singh G (2019) Performance and evaluation of voltage source inverter feed induction motor drives. Int Res J Eng Technol (IRJET) 6(2)
26. Gawade O, Utekar O, Rajane S, Raut A, Sonune R (2019) V/F speed control technique of three phase induction motor. Int J Innov Res Electr Electron Instrum Control Eng 7(1)
27. Divyam, Saxena A, Rai JN, Singh B (2020) Comparative analysis of PWM techniques and SVPWM operated V/F control of induction motor having different power ratings. In: Fifth international conference on communication and electronics systems (ICCES)
28. Kar MK, Giri P, Gupta NK, Singh AK (2021) Control of a three-phase diode clamped multilevel inverter using phase disposition modulation scheme. In: Kumar J, Jena P (eds) Recent advances in power electronics and drives. Lecture notes in electrical engineering, vol 707. Springer, Singapore. https://doi.org/10.1007/978-981-15-8586-9_6
29. Sumathi S, Bhavani C (2020) Sinusoidal pulse width modulation based speed control of induction motor using fifteen level diode clamped multilevel inverter. Int J Innov Technol Explor Eng (IJITEE)

A Review on Recent Technologies in Power Electronic Drives for Hybrid Electric Vehicles

Rajakumar Sakile and Umesh Kumar Sinha

1 Introduction

Nowadays, fuel cost is gradually increasing and it will create more burden on the human and the ecosystem [1]. To overcome the above-said disadvantages electrical vehicles are a promising solution for transportation [2]. Due to the lack of fossil fuel, alternate energy sources are required, the oil price index is gradually increasing day by day and International Energy Agency conducted a survey on the oil price index as shown in Fig. 1. When electrical vehicles are introduced then the consumption of crude oil is predominantly reduced. Therefore, air pollution is also reduced [3]. To reduce global warming all countries are encouraged by automobile industries to develop zero-emission vehicles and also provide incentives such as road tax-free and zero insurance. Some countries started fast-charging stations to attract customers [4].

(i) Plug in electrical vehicle (PEV); the construction of PEV is very easy, it consists of a battery, converter, motor, and gear system. But it has one major disadvantage is that the battery is discharged suddenly, and therefore for long transportation it is not suitable [5].

(ii) Hybrid electrical vehicle (HEV); the HEV has three types.

(1) Series HEV: It is the extension of Battery Electrical Vehicle (BEV) by adding the Internal Combustion Engine (ICE) in series with the system. In the urban area, the ICE can be OFF mode to reduce Greenhouse Gas (GHG) emission. When the battery energy is low then turn ON the ICE, mostly on the highways. To maintain the higher efficiency the ICE is operated as a constant output power source [6]. Therefore, the ICE can be turned ON or OFF there is an improvement in the fuel economy. The power rating of the ICE is depending

R. Sakile (✉) · U. K. Sinha
Electrical Engineering Department, NIT Jamshedpur, Jamshedpur, Jharkhand, India

U. K. Sinha
e-mail: uksinha.ee@nitjsr.ac.in

S. Kumar et al. (eds.), *Recent Advances in Power Electronics and Drives*, Lecture Notes in Electrical Engineering 852, https://doi.org/10.1007/978-981-16-9239-0_5

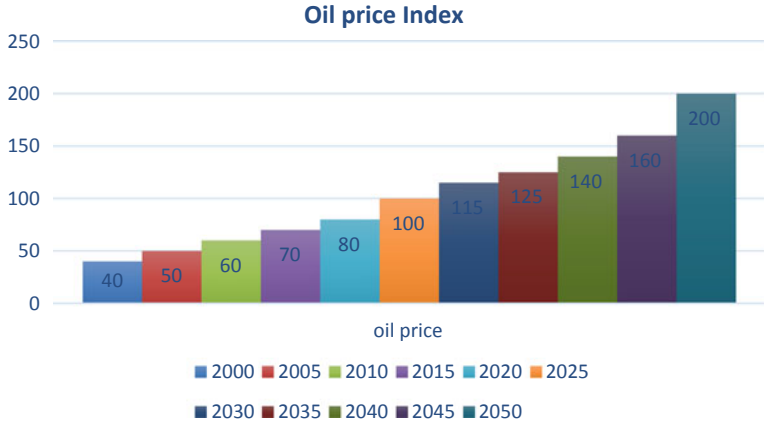

Fig. 1 Oil price index (*Source* International Energy Agency)

upon the characteristics of the series vehicle. Series HEV needs three rotating parts and its cost is high and construction is easy. Series HEV required a bigger internal combustion engine compared to parallel HEV. According to driving performance, the acceleration of the series electrical vehicle is poor. The fuel consumption of series EV is more. An example of a series hybrid electrical vehicle is the Chevrolet volt [7]. The series HEV is shown in Fig. 2.

(2) Parallel HEV: In the parallel HEV, the ICE is always in ON mode and operated at maximum efficiency point. Therefore, it will greatly improve the fuel economy. Parallel one needs only two rotating parts and its cost is lesser than the series HEV. The internal combustion engine size should be less and therefore the fuel consumption of parallel HEV is less [8, 9]. The parallel HEV is shown in Fig. 3.

(3) Dual mode HEV/series–parallel HEV: To overcome the drawbacks of both series, parallel HEV, the dual-mode HEV is introduced. To achieve more

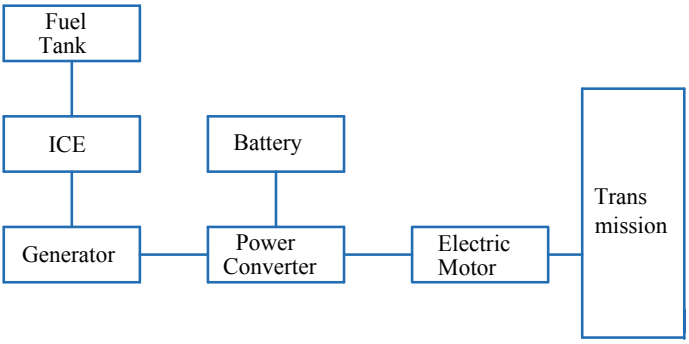

Fig. 2 Series HEV

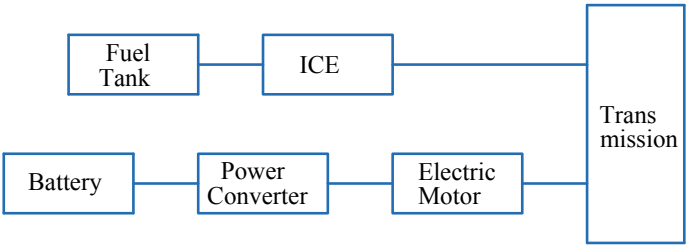

Fig. 3 Parallel HEV

power/torque a flywheel may be added to the output of the motor. It can be operated for both series/parallel HEV. Therefore, using dual-mode HEV will get more flexible operation, the construction is difficult and the cost is also high [10–12]. The dual-mode HEV is shown in Fig. 4 and the comparison of series, parallel and dual-mode HEV is discussed in Table 1.

In this paper, Sect. 1 is discussing the introduction of Hybrid Electric Vehicles (HEV) and different types of HEVs. Section 2 discusses about the different types of motor drives and power electronic interface circuits in hybrid electric vehicles

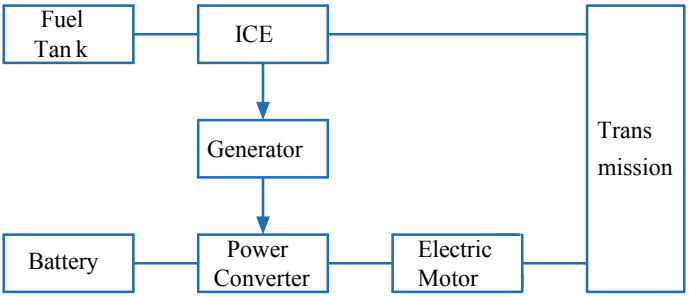

Fig. 4 Series–parallel HEV

Table 1 Comparison table for hybrid electrical vehicles [9]

Classification of HEVs	Fuel economy improvement				Driving performance	
	Idling stop	Energy recovery	High efficiency operation control	Total efficiency	Acceleration	Continuous high output
Series	●	∇	●	●	■	■
Parallel	●	●	■	●	●	■
Series/parallel	∇	∇	∇	∇	●	●

∇ Excellent ● Superior ■ Somewhat unfavorable

are discussed. Section 3 discusses about the electrical configuration of the HEV, and Sects. 4 and 5 discuss about the electrical propulsion system of the Evs and the conclusion of the paper.

2 Types of Motors and Power Electronic Interface Circuits

Based on the vehicle requirements both AC and DC motors can be used in HEV. DC motors can be powered directly from the battery. Whereas AC motors need converters to convert DC voltage into AC voltage. Due to the presence of brushes and commutators, DC motors have been rarely used in HEV. Although brushless DC motors can be used in HEV, compared to DC motors AC motors are used in HEV because AC motors are more reliable, lightweight, and high efficiency [13, 14].

Recently three popular motors are used in HEV, those are permanent magnet synchronous motor (PMSM), induction motor (IM), and switched reluctance motor (SRM). PMSM is similar to the brushless DC motor. It has higher power density, high starting torque, and high efficiency under operation. In [3], the detailed comparison of various motors used in HEV is discussed in the below table at a various speed of operation (Table 2).

Power electronics will play a vital role in HEVs for the conversion of DC voltage to AC voltage and vice versa. Normally power electronics has several advantages and those are low cost, low weight, and high reliability. Nowadays, HEVs configurations required many converters, like Toyota Prius there exists a DC/DC converter between the battery and inverter. The schematic diagram of the power train in HEVs is shown in Fig. 5. HEVs required two inverters; inverter 1 is connected to the motor to drive the ICE. During regenerative braking, it also acts as a generator to recharge the battery. Inverter 2 is connected to the generator which will transfer the power from ICE to battery [8, 15–17].

Table 2 Comparison of various electrical specifications at different speeds [10]

Speed 1500 rpm			
Various specifications	PMSM	IM	SRM
Torque (Nm)	303	297	294
Iron loss (W)	198	148	404
Copper loss (W)	4328	8591	7653
Efficiency (%)	91.3	83.1	85.2
Speed 6000 rpm			
Various specifications	PMSM	IM	SRM
Torque (Nm)	45.6	50.8	52.1
Iron loss (W)	953	439	4074
Copper loss (W)	219	730	306
Efficiency (%)	96.1	95.2	88.2

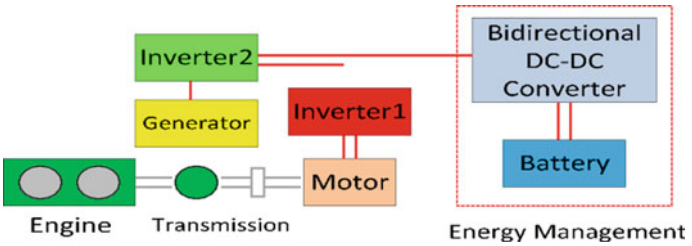

Fig. 5 Schematic of power train in HEVs

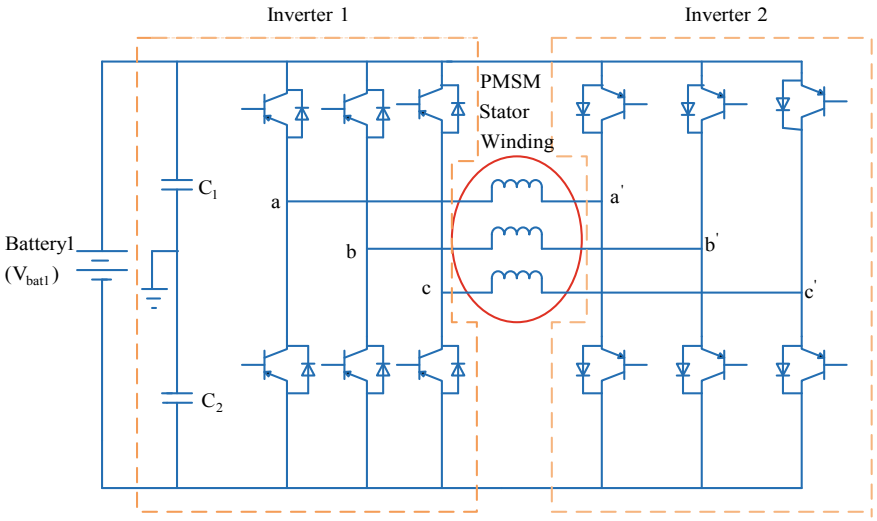

Fig. 6 Dual-inverter PMSM drive with single source [12]

Figure 6 shows the power electronic interface in HEVs. The diagram shows that the power flows from the battery to the motor and also grid to the battery to charge battery [18, 19]. Figures 6 and 7 are different types of drives used in hybrid electric vehicles. The DC to DC boost converter used increases the output voltage. If the motor is operating with high voltage then it means batteries which do not achieve the high voltage for that boost converters will be used to step up the voltage level up to the motor voltage level.

If AC motor is used in an HEV then it means AC drives will be used. In Figs. 6 and 7, dual-inverter PMSM drive with single and two sources is used for the operation of AC drives. DC source is connected to the inverter, and then it will be converted as an AC by using the above configuration. Recently, dual-inverter PMSM drives with two source AC drive is mostly used because of many advantages [20].

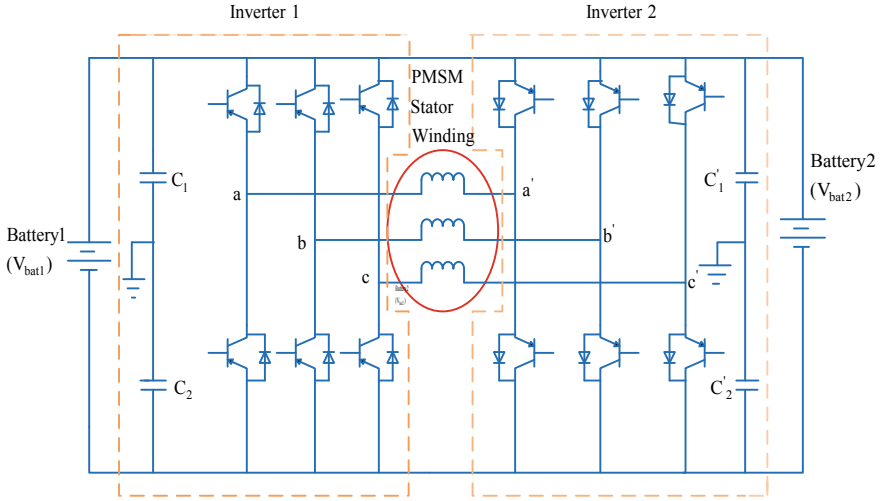

Fig. 7 Dual-inverter PMSM drive with two sources

3 Configuration of the EVs

Battery Management System (BMS) plays a key role in the electric vehicles control and operation of the battery. The battery remaining power is obtained by the state of charge (SOC) and an accurate SOC value gives the best performance of the EV. The SOC is obtained by considering the battery voltage, temperature, and other parameters such as polarization and concentrated effects and discharge current [21, 22]. The obtained SOC is sent to the Hybrid Control Unit (HCU) by the communication lines. From the SOC information, the HCU operates and controls the motor with the best performance and safe operation of the battery. The configuration of the EVs is shown in Fig. 8.

4 Electric Propulsion System of HEVs

An electric propulsion system is the heart of Hybrid Electrical Vehicles (HEV). It consists of an electric motor, power converter, electric controller, and energy storage system. Electric motor converts electrical energy into mechanical energy to drive the system [23]. Power converters will give reliable voltage and current to the electric motor, and lastly the electronic controller gives commands to the power converter to give fruitful power, torque, and speed to the transmission system. During regenerative braking, the battery is charged with Battery Management System (BMS), and in that time vehicle is operated with Internal Combustion Engine (ICE). If the battery is

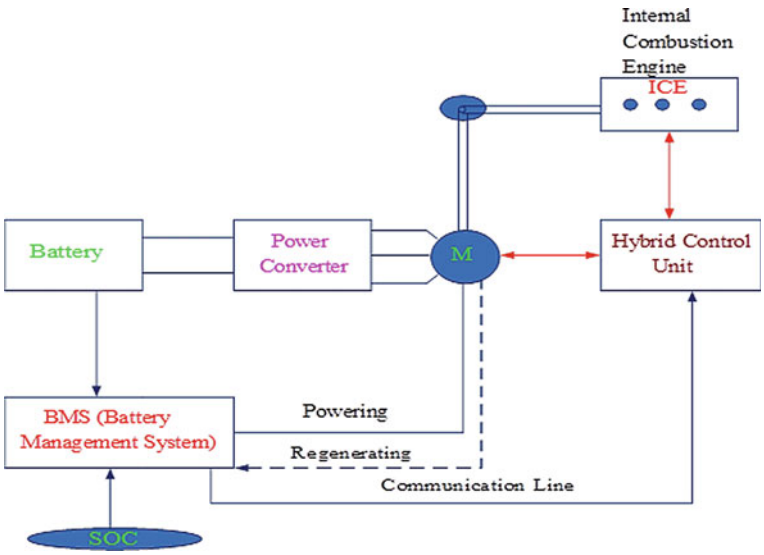

Fig. 8 Configuration of the electric vehicle

charged fully then the vehicle is converted into battery running mode to achieve maximum speed [24].

Drives used in HEVs:

Many motor drives are used in EVs and HEVs to drive the vehicle with frequent starts and stops and also provide a wide speed range of operation. There are two types of drives which are utilized in HEVs, those are commutator drives and commutator-less drives. Commutator drives are normally called DC drives and commutator-less drives are known as AC drives.

(A) DC Drives:

Due to the presence of a commutator sparking will take place at brush contacts, which leads to motor damage [25]. Therefore, the DC drives are not suitable for HEVs applications. To increase efficiency and higher power density, AC drives are preferred. AC drives are free from the commutator, and therefore AC drives cost is less, more reliable, and maintenance-free as compared to DC drives.

(B) Induction Motor Drives:

For the electric propulsion purpose, in Electric Vehicles (EVs) and Hybrid Electric Vehicle (HEVs), the induction motor drives are used. In the present scenario, these types of motor drives employed many advantages compared to commutator motor drives. Basically, induction motor drives are two types and those are wound-rotor and squirrel-cage motors. Due to the lack of applications, wound-rotor induction

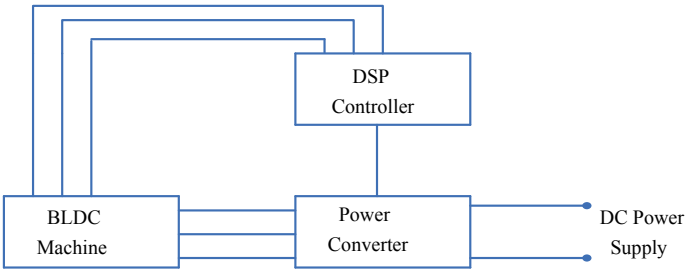

Fig. 9 BLDC motor

motor drives are not suitable for HEV. Therefore, squirrel-cage induction motors are themselves treated as induction motor drive [26].

(C) BLDC Motor Drives*:*

A BLDC motor drive mainly consists of brushless DC machine, DSP controller, and power converter, As shown in Fig. 9, permanent magnet brushless DC motor drive can be designed with the higher power density and high operation efficiency. Due to this advantage the BLDC motor drives are most suitable for EV and HEV applications (Fig. 10).

Advantages of BLDC Motor Drives:

- BLDC motors are more efficient machines compared to all-electric motors. Due to the absence of a mechanical commutator and brushes, low frictional losses will have occurred in the machine which leads to higher efficiency.
- BLDC motors are achieving very high flux densities because of the recent introduction of rare-earth magnets.
- Easy to control, the control variables are constant throughout the working operation of the motor.
- Less noise will be present at commutation.
- More reliable and less maintenance.

BLDC motor drives also suffer from some drawbacks which are of more cost, limited constant power, less safety, demagnetization, and fault tolerance. To avoid the above-said disadvantages replace the BLDC motors with SRM drives [27, 28].

(D) SRM Drive:

Switched Reluctance Motor (SRM) drive is the best suitable candidate for EV or HEV applications due to its simple structure, rugged structure, low cost, and wide range of speed control compared to all discussed electrical drives [29, 30]. It does not have any permanent magnets on its rotor side and therefore capable of high-speed operation. It consists of SRM; various sensors like voltage, current, and position sensing units; power converter; and DSP-related control peripherals are connected as shown in Fig. 11. The total estimation cost is explained in Table 3.

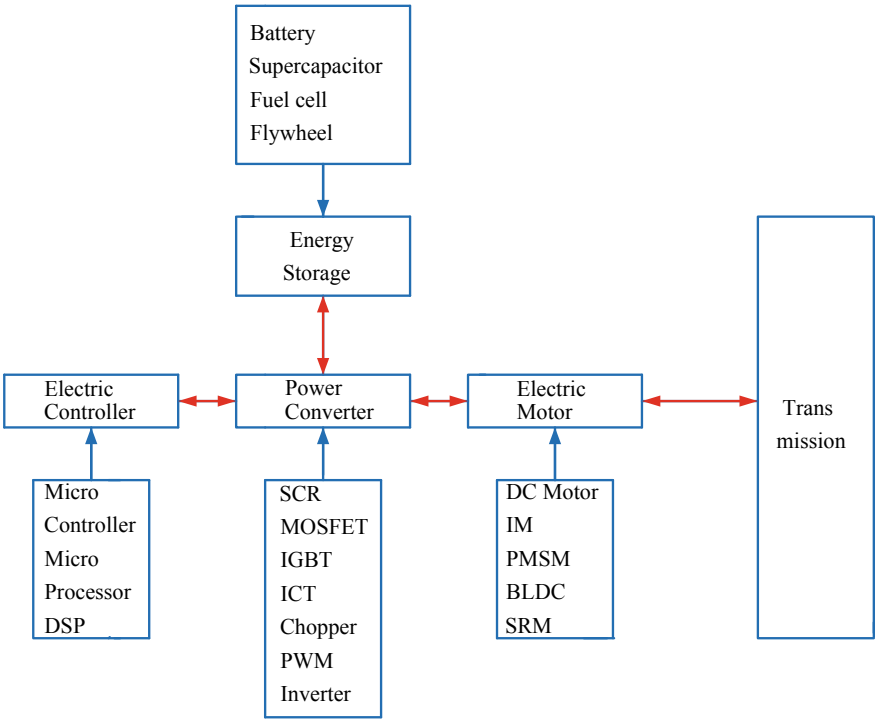

Fig. 10 Block diagram of electric propulsion system

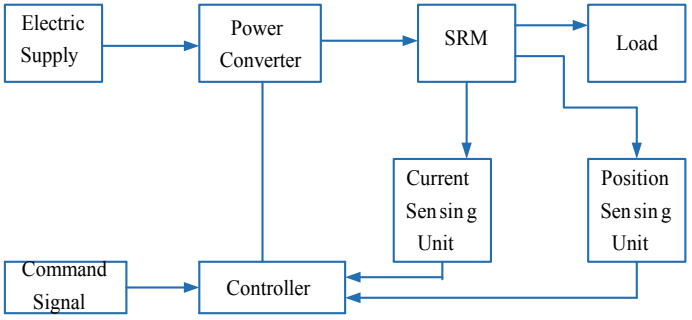

Fig. 11 SRM motor drive

5 Conclusion

In this paper, the working operation and different motor drives used in HEVs are discussed. According to motor drives, the SRM has many advantages compared to IM, PMSM, and BLDC motor drives. It shows clearly that the SRM motor drives

Table 3 Comparison of special electrical motors

Items	Maximum	BLDC motor	PMSM	SRM
Power density	10	9	10	8
Overload	10	7	7	8
High-speed range	20	9	10	8
Control	20	15	15	16
Noise	10	8	8	6
Size and weight	10	6	8	5
Ruggedness	10	8	9	7
Torque ripple	20	14	12	18
Maintenance	10	8	8	9
Manufacturing	20	14	12	18
Cost	30	20	18	26
Total	180	128	135	146

are highest in number compared to all-electric motor drives. The power electronic converters are used for the conversion and control of HEV, and dual-inverter PMSM drive with two sources has given better dynamic characteristics compared to a single source. The electrical configuration of the HEVs is explained with a neat block diagram and the electric propulsion system of HEVs was discussed with various drives.

References

1. Hoque MM, Hannan MA, Mohamed A, Ayob A (2017) Battery charge equalization controller in electric vehicle applications: a review. Renew Sustain Energy Rev 75:1363–1385
2. Hannan MA, Lipu MSH, Hussain A, Mohamed A (2017) A review of lithium-ion battery state of charge estimation and management system in electric vehicle applications: challenges and recommendations. Renew Sustain Energy Rev 78:834–854
3. Fotouhi A, Auger DJ, Propp (2016) A review on electric vehicle battery modelling: from lithium-ion toward lithium–sulphur. Renew Sustain Energy Rev 56(2016):1008–1021
4. Sakile R, Sinha UK (2020) Estimation of SOC (state-of-charge) and SOH (state-of health) of lithium-ion battery by using adaptive techniques. IJITEE J 9(3)
5. Maggetto G, Van Mierlo J (2011) Electrical hybrid vehicle technology; a survey. InTech
6. Ehsani M, Gao Y, Gay SE, Emadi A (2004) Modern electric, hybrid electric and fuel cell vehicles book. CRC Press
7. Mehmet Ugras Cuma (2015) Tahsin Koroglu, A comprehensive review on estimation strategies used in hybrid and battery electric vehicles. Renew Sustain Energy Rev 42:517–531
8. Vasebi A, Bathaee SMT, Partovibakhsh M (2008) Predicting state of charge of lead-acid batteries for hybrid electric vehicles by extended Kalman filter. Energy Convers Manag 49:75–82
9. Edward WCLO (2009) Review on the configurations of Hybrid Electric vehicles. In: IEEE conference on power electronics systems and applications

10. Liu D, Li L, Song Y, Wu L, Peng Y (2019) Hybrid state of charge estimation for lithium-ion battery under dynamic operating conditions. Electr Power Energy Syst 0142-0615
11. Lulhe AM, Date TN (2015) A technology review paper for drives used in electrical vehicle (EV) & hybrid electrical vehicles (HEV). In: 2015 International conference on control, instrumentation, communication and computational technologies (ICCICCT)
12. Alagarsamy T, Moulik B (2018) A review on optimal design of hybrid electric vehicles and electric vehicles. In: 2018 3rd international conference for convergence in technology (I2CT), The Gateway Hotel, XION Complex, Wakad Road, Pune, India, 06–08 Apr 2018
13. Yao LW, Aziz JA, Kong PY, Idris NRN. Modelling of lithium-ıon battery using MATLAB/Simulink. In: IEEE conference. 978-1-4799-0224-8
14. Kim S (2008) Nonlinear state of charge estimator for hybrid electric vehicle battery. IEEE Trans Power Electron 23(4)
15. Yang L, Cai Y, Yang Y, Deng Z (2019) Supervisory long-term prediction of state of available power for lithium-ion batteries in electric vehicles. Appl Energy 0306-2619
16. Shen Y (2009) Adaptive online state-of-charge determination based on neuro-controller and neural network. Energy Convers Manag 0196-8904
17. Cuma MU, Koroglu T (2015) A comprehensive review on estimation strategies used in hybrid and battery electric vehicles. Renew Sustain Energy Rev 42:517–531
18. Ma Z, Murgovski N, Cui S (2019) Predictive energy management for electric variable transmission HEV. IFAC Papers Online 52–5:417–422
19. Sakile R, Kumar P, Sinha UK (2020) Modelling of lithium-ion battery using matlab/simulink for electric vehicle applications. Recent Adv Power Electron Drives 291–299
20. Messier P, Nguyen B-H et al (2020) Disturbance observer-based state-of-charge estimation for Li-ion battery used in light electric vehicles. J Energy Storage 27:101144
21. Chen Q, Jiang J, Raun H, Zhang C (2017) Simply designed and universal sliding mode observer for the SOC estimation of lithium-ion batteries. IET Power Electron 10(6):697–705
22. Sakile R, Sinha UK (2020) Estimation of SOC (state- of-charge) and SOH (state-of-health) of lithium-ion battery by using adaptive techniques. IJITEE J 9(3)
23. Spurgeon SK (2008) Sliding mode observers: a survey. Int J Syst Sci 39(8):751–764. https://doi.org/10.1080/00207720701847638
24. Hannan MA, Lipu MSH, Mohamed HA (2017) A review of lithium-ion battery state of charge estimation and management system in electric vehicle applications: challenges and recommendations. Renew Sustain Energy Rev 2017(78):834–854
25. Hoque MM, Hannan MA, Mohamed AA (2017) Battery charge equalization controller in electric vehicle applications: a review. Renew Sustain Energy Rev 2017(75):1363–1385
26. Yan W, Zhang B, et al (2018) Battery management system with Lebesgue sampling-based extended Kalman filter. IEEE Trans Industr Electron. https://doi.org/10.1109/TIE.2018.2842782
27. Tang X, Wang Y, Chen Z (2015) A method for state-of-charge estimation of LiFePO4 batteries based on a dual-circuit state observer. J Power Sources 296(2015):23–29
28. Tian Y, Chen C, Xia B et al (2014) An adaptive gain nonlinear observer for state of charge estimation of lithium-ıon batteries in electric vehicles. Energie*s* 7:5995–6012. https://doi.org/10.3390/en7095995
29. Zou Y, Hu X, Ma H, Li SE (2017) Combined state of charge and state of health estimation over lithium-ion battery cell cycle lifespan for electric vehicles. J Power Sources 273(2015):793–803
30. Zhang ZL, Cheng X, Lu ZY, Gu DJ (2017) SOC estimation of lithium-ion batteries with AEKF and wavelet transform matrix. IEEE Trans Power Electron 2017(32):7626–7634

Comparative THD Analysis of Multilevel Inverter Using Different Multicarrier PWM Schemes

Shashi Shekhar Tripathi, Manoj Kumar Kar, and Arun Kumar Singh

1 Introduction

Modified MLI topology seven-level pack u-cell inverter for seven-level output voltage with lower harmonic distortion for photovoltaic (PV) application is discussed in [1]. Based on input DC voltage sources cascaded H-bridge MLI has two configurations symmetric (equal magnitude) and asymmetric (unequal magnitude). For same higher levels, output asymmetric configuration has less THD as per IEEE standard than symmetric configuration [2]. High-frequency magnetic link (HFML)-based cascaded H-bridge MLI has advantages of reduced device count, size, and cost than conventional invertors is discussed in [3]. The cascaded H-bridge topology of MLI is more competent than diode clamped and capacitor clamped MLI. With increase in number of levels in output waveform of CHBMLI the harmonic distortion and voltage stress dv/dt reduce [4]. A new cascaded switch-ladder MLI topologies gives more number of output voltage levels with decreased switch count and voltage rating of components which is discussed in [5]. Different MLI topologies and its application are discussed in [6]. Three-phase CHBMLI topology with reduced power electronic components and hybrid control technique to produce gate pulses for switches are discussed in [7]. Cascaded H-bridge MLI topology with different control techniques for output voltage level generates less THD which is discussed in [8]. A self-balanced step-up MLI topology to reduce total standing voltage and PIV for switches is discussed in [9]. Different reduced switch MLI topologies give higher voltage levels to improve power quality and reduce filter requirements which are discussed in [10]. A new three-phase modular multilevel inverter (MMLI) topology using both SPWM and staircase modulation techniques generates output voltage levels with reduced switch count, voltage stress, and harmonic distortion than other MLI topologies which are discussed in [11]. New cascade MLI topology generating both even and odd voltage levels at output with reduced power electronic components and cost by using

S. S. Tripathi (✉) · M. K. Kar · A. K. Singh
EE Department, NIT Jamshedpur, Jamshedpur, Jharkhand, India

S. Kumar et al. (eds.), *Recent Advances in Power Electronics and Drives*, Lecture Notes in Electrical Engineering 852, https://doi.org/10.1007/978-981-16-9239-0_6

series connection of extended sub-multilevel units is discussed in [12]. A novel MLI topology using sinusoidal pulse width modulation techniques to generate gate pulses and filters to reduce THD is discussed in [13]. The advantages of multilevel inverter and various compromises for reducing power semiconductor components are discussed in [14]. The novel unified power flow controller (UPFC) with cascaded H-bridge MLI offers many advantages and applications than conventional configuration which is discussed in [15]. For large power and medium voltage application, a modified three-phase MLI configuration using PWM technique is discussed in [16]. Cascaded MLI giving positive and negative voltage levels at output by using different algorithm is discussed in [17]. Symmetric MLI with reduced switch count, cost, and loss compared to cascaded H-bridge MLI generates higher levels of output voltage which are discussed in [18]. In MLI, SHEPWM techniques diminish more THD value related to ordinary PWM techniques which are discussed in [19]. A new MLI topology using in-phase disposition (IPD) SPWM techniques for high-voltage and high-power application is discussed in [20, 21]. Modern advancement in MLI topologies, modulation, and control techniques is discussed in [22]. Symmetric and asymmetric topologies of MLI producing all levels of output voltage with reduction in switches, cost, and size are discussed in [23]. A current control algorithm with discrete-time model for CHBMLI generating all levels of output voltage is discussed in [24]. Particle swarm optimization (PSO) method to solve harmonic elimination problems with unequal DC sources in cascaded H-bridge MLI is discussed in [25]. Series connection of CHB cells with photovoltaic (PV) module for MPPT is discussed in [26]. The three-phase configuration of CHBMLI circuits and various forms of multi-carrier sinusoidal pulse width modulation (MCSPWM) techniques are discussed in [27]. Emerging topologies, the most important methods of control and modulation, and recent MLI applications are discussed in [28].

2 Cascaded H-bridge MLI

A seven-level CHBMLI is depicted in Fig. 1. It consists of two stages: (i) DC-DC converter and (ii) inverter. Every H-bridge cell has four switches. Single phase full bridge inverters with separate DC source are connected in series to form CHBMLI. The objective of series connection is to increase the number of levels of output voltage and to reduce THD. When 'K' H-bridges are linked in series, a maximum KE output voltage of $2K + 1$ separate output voltage level is obtained, where E is input voltage of single H-bridge. When $K = 3$, the output voltage has seven levels 3E, $-3E$, 2E, $-2E$, E, $-E$, and 0, respectively. Switching state of seven-level output waveform which is given in Table 1.

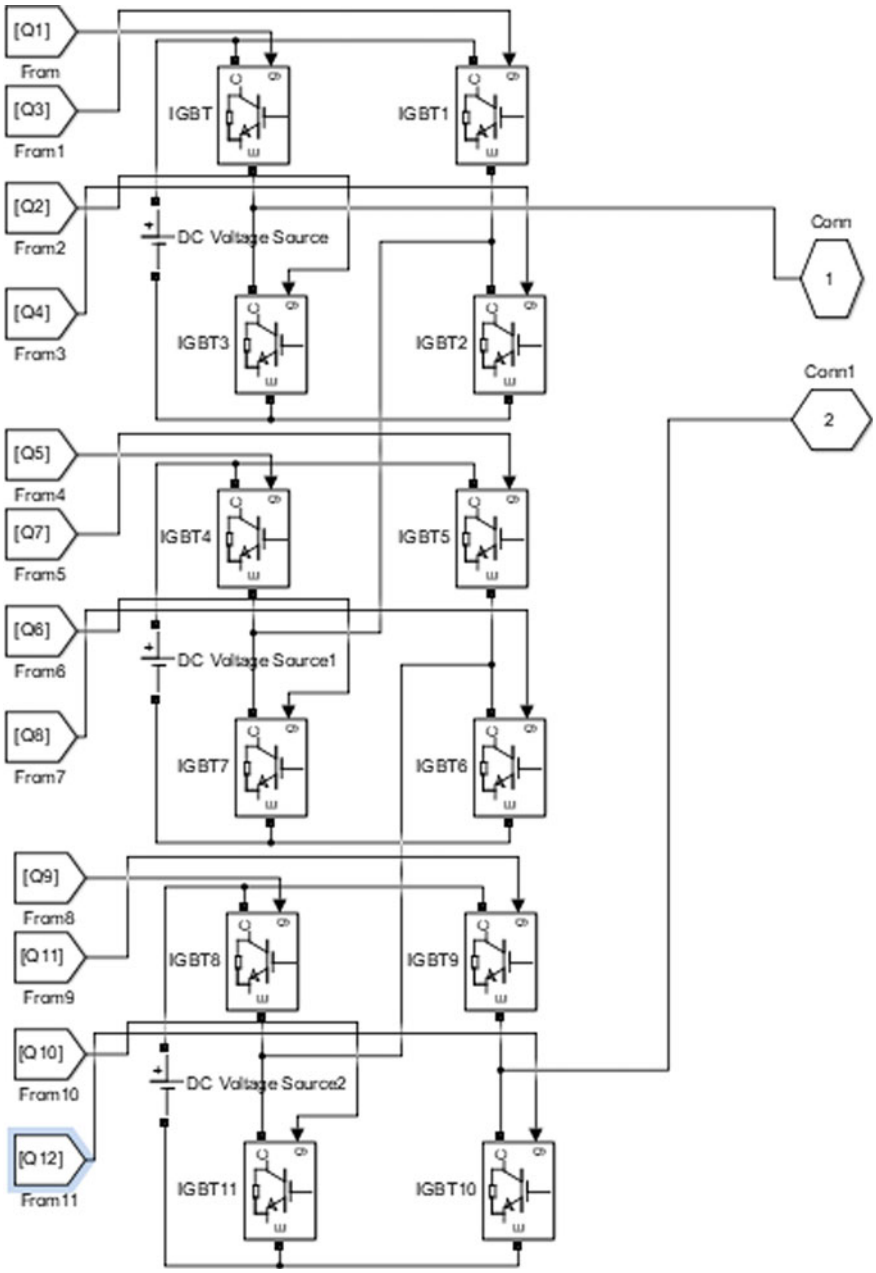

Fig. 1 Circuit for seven-level CHBMLI

Table 1 Switching table for seven-level CHBMLI

Voltages	Q11	Q2	Q33	Q44	Q55	Q66	Q77	Q88	Q99	Q110	Q111	Q112
3*E	1	0	0	1	1	0	0	1	1	0	0	1
2*E	1	0	0	1	1	0	0	1	1	0	1	0
E	1	0	0	1	1	0	1	0	1	0	1	0
0	0	0	0	0	0	0	0	0	0	0	0	0
−E	0	1	1	0	1	0	1	0	1	0	1	0
−2*E	0	1	1	0	0	1	1	0	1	0	1	0
−3*E	0	1	1	0	0	1	1	0	0	1	1	0

3 Problem Definition

The inverter has attracted a great interest to be used in heavy duty industries and large power applications, but it is difficult to connect a single power semiconductor switch directly to medium voltage grids, even the two-level inverter with high-voltage grids. Two-level inverter has greater harmonics distortion that requires a complicated filtering circuit to obtain the sinusoidal waveform. To overcome these drawbacks of two-level inverter, multilevel inverter is used. MLI has lesser harmonic distortion and does not need a filtering circuit to produce smoother sinusoidal waveform. Cascaded H-bridge topology of MLI is preferred compared to flying capacitor and diode clamped topologies because it includes small number of semiconductors components. Therefore, the weight and price of this type of topology are lower than that of other two topologies.

In this study, out of different carrier-based PWM techniques, a pure sine wave is obtained by providing appropriate carrier frequency. The model is designed with minimum number of switches to reduce the complexity, cost, and switching losses. The performance of the proposed technique is analyzed using IPD, POD, and APOD techniques. The proposed technique also gives lesser torque ripples which is clear from the FFT analysis.

4 Sinusoidal PWM Scheme for Inverter

PWM (pulse width modulation) is the inverter's internal control tool. A sinusoidal (reference) wave of low frequency is compared with a triangular (carrier) wave of high frequency in the PWM scheme to produce gate pulses for switches.

The output pulses are not identical, i.e., they are having the variable width of pulses. The width of pulse varies in accordance with the magnitude of sinusoidal waveform. Pulses are generated using SPWM scheme and provided to switches for different levels of output voltage. THD percentage for 3, 5, 7, 9, 11, and 13 levels of output voltage is discussed and compared in table below.

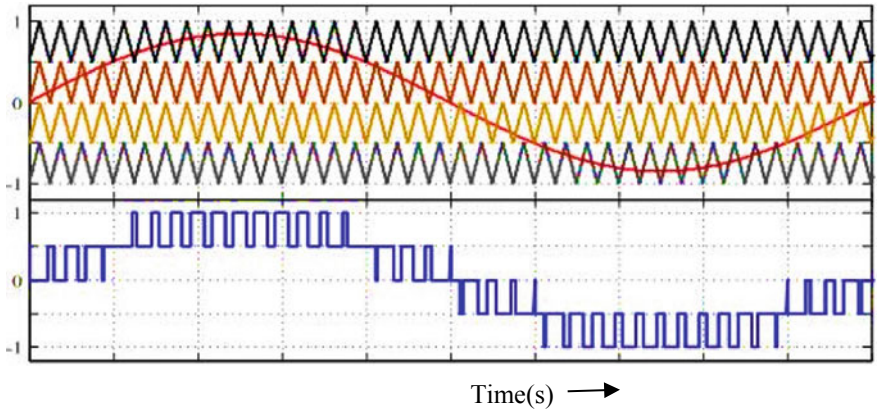

Fig. 2 IPD modulation technique

5 Multicarrier PWM (MCPWM) Scheme for Inverter

To get output waveform with reduced harmonic contents of MLI, it is necessary to implement a proper modulation technique. MCPWM scheme is one of the best methods of pulse generation for switches due to simple architecture and simpler implementation. In MCPWM scheme, the reference wave is a sinusoidal signal and the carrier wave is a triangular signal. 'm − 1' numbers of triangular carriers are required for an MLI having 'm' number of voltage levels. For all carrier signals, the frequency and the Vp-p remain same. The signal of reference and carrier are compared and therefore the gate pulses are generated.

MCPWM schemes are categorized as 'level shifted', 'phase shifted', and 'hybrid' PWM. Level-shifted PWM is of three types: in-phase disposition (IPD), phasekop-positekdisposition (POD), and alternative phase opposite disposition (APOD). In IPD, signal is in phase for all carriers (Fig. 2).

The carriers above zero reference in POD are in phase but are in reverse to those present below the null reference. All carriers in APOD are alternatively in reverse disposition (Figs. 3 and 4).

6 Benefits of IPD Modulation Technique

In the IPD modulation technique, the voltage (L-L) is reduced because the fcarrier harmonics are made as common mode voltage of fcarrier and thus cancelled out in voltage (L-L) [21]. It is advantageous over POD and APOD techniques. This approach is valid for all types of multilevel inverters.

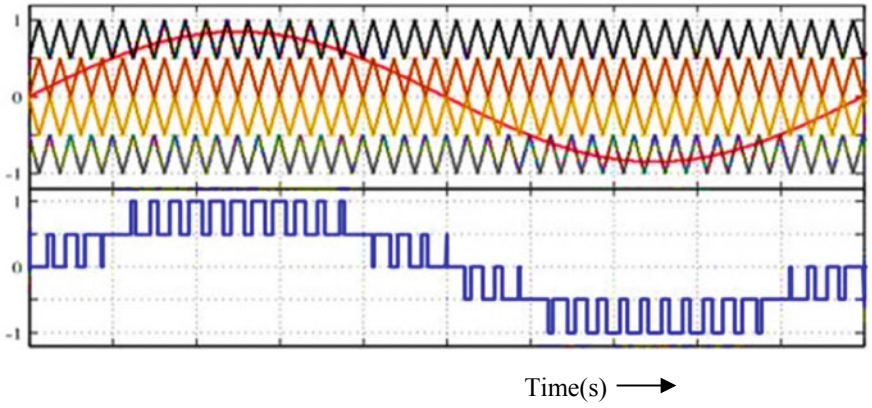

Fig. 3 POD modulation technique

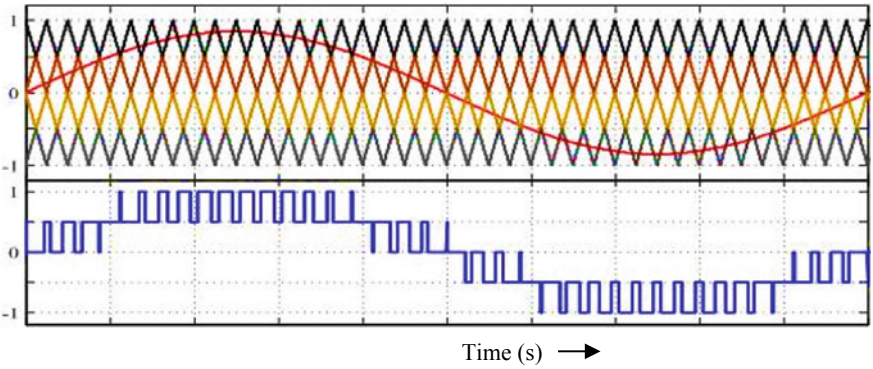

Fig. 4 APOD modulation technique

7 Simulation Result

The simulation result using MATLAB technique is discussed in this paper. The frequency of carrier signal is 1 kHz. The frequency of reference signal is 50 Hz. The reference signal (sinusoidal) is compared with carrier signal (triangular) to produce gate pulses for the switches of CHBMLI. The voltage output of 13-level using IPD, POD and APOD schemes are shown in Figs. 5, 7 and 9 respectively. The THD% of 13-level CHBMLI using IPD, POD, and APOD PWM schemes are shown in Figs. 6, 8 and 10 respectively. In IPD scheme, THD is 8.91%. In POD scheme, THD is 9.37%. For E = 50 V, voltage output waveform of 13-level CHBMLI using APOD scheme is depicted in Fig. 9. In APOD scheme, THD is found to be 9.67%.

The value of modulation index is always kept one.

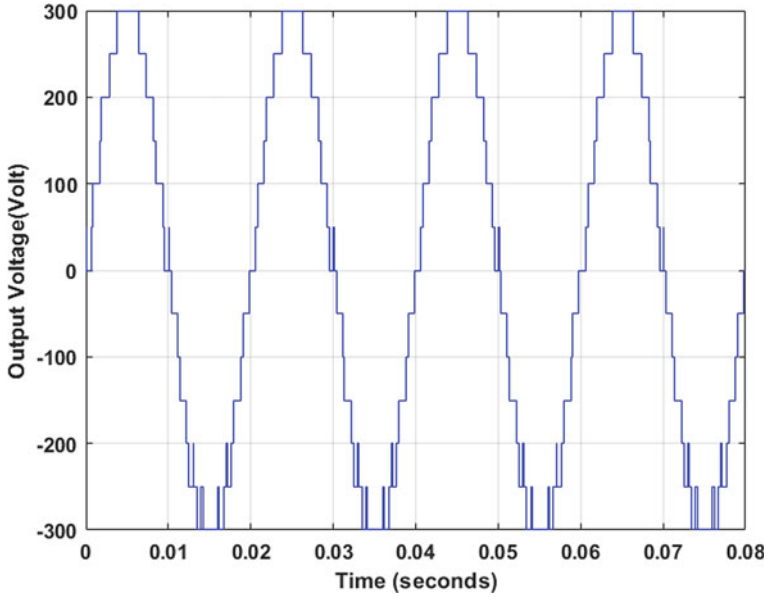

Fig. 5 Voltage output of 13-level using IPD scheme

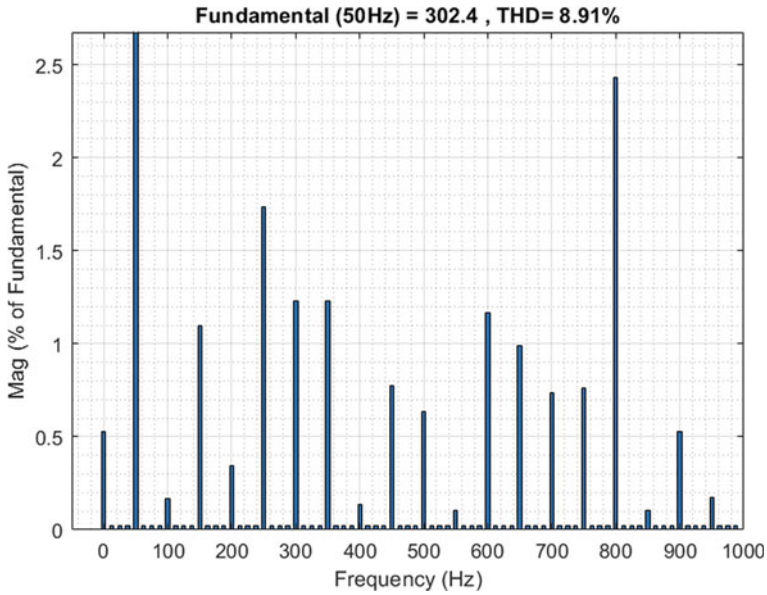

Fig. 6 THD of 13-level CHBMLI using IPD scheme

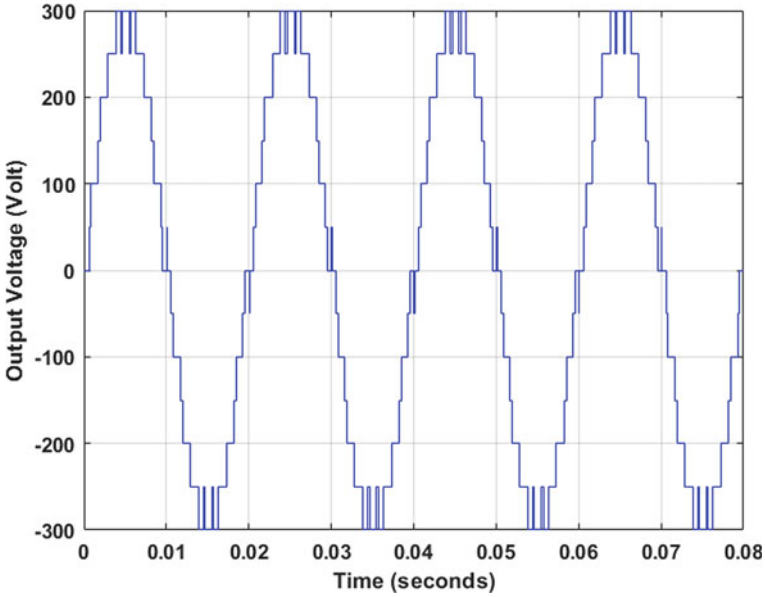

Fig. 7 Voltage output of 13-level using POD scheme

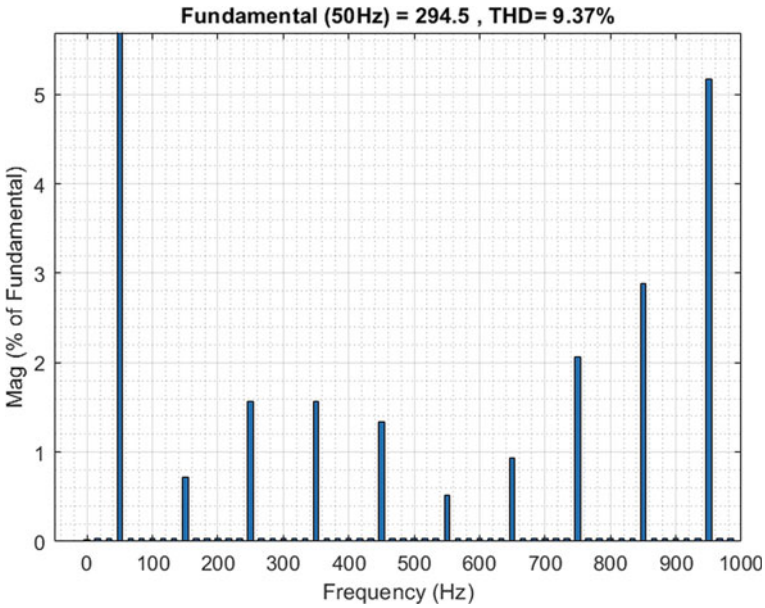

Fig. 8 THD of 13-level CHBMLI using POD scheme

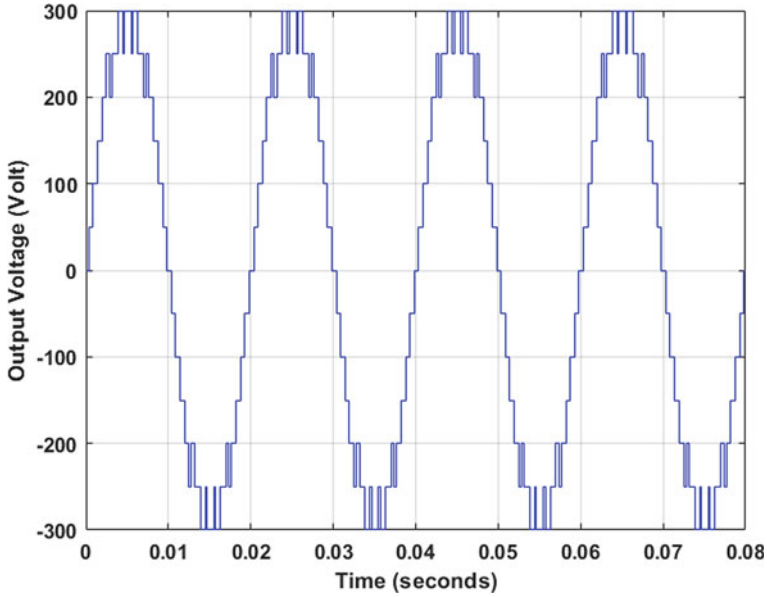

Fig. 9 Voltage output of 13-level using APOD scheme

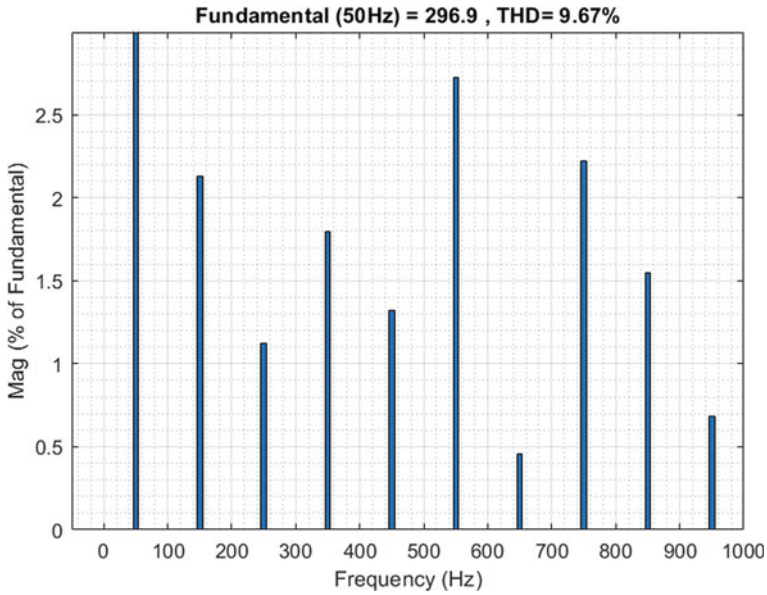

Fig. 10 THD of 13-level CHBMLI using APOD scheme

Table 2 THD percentage for different levels of output voltage

No. of levels	THD percentage (%)
3	55.88
5	26.89
7	16.43
9	16.79
11	14.04
13	8.58

Table 3 Comparative analysis of THD percentage after using different schemes for different levels of output voltage

No. of levels	THD%		
	IPD	POD	APOD
3	53.21	55.87	54.03
5	24.98	26.89	28.16
7	16.49	18.07	18.98
9	12.94	17.59	15.37
11	10.31	10.55	12.16
13	8.91	9.37	9.67

8 Conclusion

IPD, POD, and APOD schemes which are based on MCPWM have been effectively applied for 3, 5, 7, 9, 11, and 13 levels of output voltage in CHBMLI. THD percentage for these different levels is depicted in Table 3. THD percentage for different levels of output voltage using SPWM schemes is depicted in Table 2. From Tables 2 and 3, it is obvious that as the number of levels enhances THD% reduces. Among all MCPWM schemes, IPD has the lowest THD% for same level output voltage.

References

1. Vahedi H, Sharifzadeh M, Al-Haddad K (2018) Modified seven level pack u-cell inverter for photovoltaic application. IEEE Trans Emerg Sel Topics Power Electron 6(3):1508–1516
2. Dhanamjayulum C, Meikandasivam S (2018) Implementation and comparison of symmetric and asymmetric multilevel inverters for dynamic loads. IEEE Access 6:738–746
3. Hasan M, Abu-siada A, Islam SM, Dahidah M (2018) A new cascaded multilevel inverter topology with galvanic isolation. IEEE Trans Ind Appl
4. Singh G, Garg VK (2017) THD analysis of cascaded h-bridge multilevel inverter. In: 4th IEEE International conference on signal proccessing, computing, and control, 21–23 Sept 2017
5. Alishah RS, Hosseini SH, Babaei E, Sabahi M (2017) Optimal design of new cascaded switch-ladder multilevel inverter structure. IEEE Trans Ind Electron 64(3):2072–2080
6. Akagi H (2017) Multilevel converters: fundamental circuits and systems. Proc IEEE 105(11):2048–2065

7. Sabayasachi S, Borghate VB, Karasani RR, Suryawanshi HM (2017) Hybrid control technique based three-phase cascaded multilevel inverter topology. IEEE Access 5:26912–26921
8. Kannan C, Mohanty NK, Selvarasu R (2017) A new topology for cascaded h-bridge multilevel inverter with PI and fuzzy control. In: 1st International conference on power engineering, computing and control, pp 917–926
9. Taghvaie A, Adabi J, Rezanejad M (2017) A self-balanced step-up multilevel inverter based on switched-capacitor structure. IEEE Trans Power Electron 33(1):199–209
10. Natarajan P, Kaliannah P (2017) A comprehensive review on reduced switch multilevel inverter topologies, modulation techniques and applications. Renew Sustain Energy Rev 76:1248–1282
11. Salem A, Ahmad M, Orabi M, Ahmed EM (2016) Study and analysis of new three-phase modular multilevel inverter. IEEE Trans Ind Electron
12. Alishah RS, Hosseini SH, Babaei E, Sabahi M, Gharehkoushan AZ (2016) Optimal design of new cascaded multilevel converter topology based on series connection of extended sub-multilevel units. IET Power Electron 9(7):1341–1349
13. Hsieh C, Liang T, Chen S, Tsai S (2016) Design and implementation of a novel multilevel dc-ac inverter. IEEE Trans Ind Electron
14. Gupta KK, Ranjan A, Bhatnagar P, Sahu LK, Jain S (2016) Multilevel inverter topologies with reduced device count: a review. IEEE Trans Power Electron 31(1):135–151
15. Peng F, Lui Y, Yang S, Zhang S, Gunasekaran D, Karki U (2015) Transformer-less unified power flow controller using the cascaded multilevel inverter. IEEE Trans Power Electron
16. Sanjeevikumar P, Blaabjerg F, Wheeler PW, Olorunfemi J (2015) Three-phase multilevel inverter configuration for open winding high-power application. IEEE
17. Babaei E, Laali S (2015) Optimum structures of proposed new cascaded multilevel inverter with reduced number of components. IEEE Trans Ind Electron 62(11):6887–6895
18. Oskuee MJ, Karimi M, Ravadanegh SN, Gharehpetian GB (2015) An innovative scheme of symmetric multilevel voltage source inverter with lower number of circuit devices. IEEE Trans Ind Electron
19. Ashok B, Rajendran A (2013) Selective harmonic elimination of multilevel inverter using SHEPWM technique. Int J Soft Comput Eng 3:79–82
20. Najafi E, Yatim AH (2012) Design and implementation of a new multilevel inverter topology. IEEE Trans Ind Electron 59(11):4148–4154
21. Kar MK, Giri P, Gupta NK, Singh AK (2021) Control of a three-phase diode clamped multilevel ınverter using phase disposition modulation scheme. In: Kumar J, Jena P (eds) Recent advances in power electronics and drives. Lecture notes in electrical engineering, vol 707. Springer, Singapore. https://doi.org/10.1007/978-981-15-8586-9_6
22. Kouro S, Malinowski M, Pou J, Lenon JI, Franquelo LG, Perez A (2010) Recent advances and industrial applications of multilevel converters. IEEE Trans Ind Electron 57(8):2553–2580
23. Ahmed RA, Mekhilef S, Ping H (2010) New multilevel inverter topology with minimum no. of switches. In: IEEE TENCON, pp 1862–1867
24. Cortes P, Wilson A, Rodriguez J, Abu-Rub H (2010) Model predictive control of multilevel cascaded h-bridge inverters. IEEE Trans Ind Electron 57:2691–2699
25. Taghizadeh H, Tarafdar M (2010) Harmonic elimination of cascade multilevel inverters with nonequal dc sources using particle swarm optimization. IEEE Trans Ind Electron 57(11):3678–3684
26. Villanneva E, Correa P, Rodriguez J, Pacas M (2009) Control of a single-phase cascaded h-bridge multilevel inverter for grid connected photo-voltaic systems. IEEE Trans Ind Electron 56(11):4399–4406
27. Kar MK, Mansoori M, Kumar S, Gupta SK (2021) Harmonic elimination of a T-type multilevel ınverter based on multistate switching cell. In: Kumar J, Jena P (eds) Recent advances in power electronics and drives. Lecture notes in electrical engineering, vol 707. Springer, Singapore. https://doi.org/10.1007/978-981-15-8586-9_9
28. Rodriguez J, Slai J, Peng FZ (2002) Multilevel inverters: a survey of topologies, control, and applications. IEEE Trans Ind Electron 49(4):724–738

Design and Implementation of Two-Phase Interleaved Boost Converter with Voltage Multiplier for Fuel Cell Hybrid Electric Vehicles

Melisa Miranda, M. Komal, and Shweta P. Hegde

1 Introduction

Fuel Cell (FC) technologies can be considered an imminent power source for automobile applications because they are clean, highly efficient, and highly reliable. The power capability of FC systems is considerably good while operating in steady state. But the instantaneous power demands of FCs are relatively slow. Therefore, FCs are incorporated with Energy Storage Systems (ESS) like batteries and supercapacitors to meet the demands of the Hybrid Electric Vehicles (HEV). And also, fuel cells generally have low voltage ratings. But higher voltage level is required for driving the motors. So, there is a need for boosting the power and the voltage by using boost converter like a DC system of multiple DC-DC converters to interface between FC or ESS and the DC bus in the drivetrain of FCHEVs [1].

In this application, maintaining high efficiency using the traditional DC-DC boost converter becomes a major challenge. Simultaneously, for high-power applications such as electric vehicles, handling the large input current and large output voltage becomes difficult [2]. An effective way is to use a two-phase Interleaved Boost Converter (IBC) with a Voltage Multiplier (VM) cell.

Various converter circuits with which a higher gain in voltage can be achieved are discussed in [3, 4]. The major drawbacks of these circuits are the large number of components, the complexity, and the remarkably high input current ripple. In this paper, we are adding a voltage multiplier to overcome these disadvantages.

Powertrain system of FCHEV comprises a DC-DC boost converter linking the FC system and DC-AC inverter, and also a bidirectional DC-DC boost converter that joins the ESS to the DC-AC inverter as shown in Fig. 1.

M. Miranda · M. Komal (✉) · S. P. Hegde
Department of Electronics and Communication Engineering, PES University, Bengaluru, India

M. Miranda
e-mail: melisamiranda@pes.edu

S. Kumar et al. (eds.), *Recent Advances in Power Electronics and Drives*, Lecture Notes in Electrical Engineering 852, https://doi.org/10.1007/978-981-16-9239-0_7

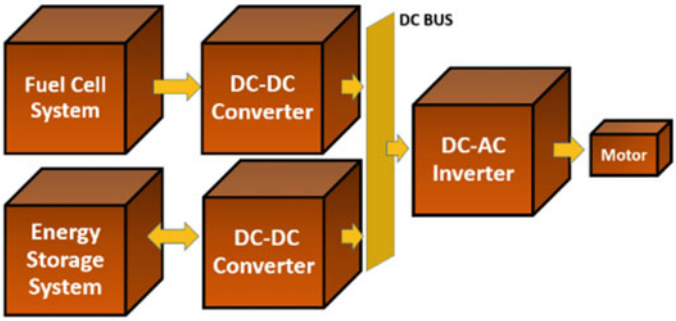

Fig. 1 Block diagram of the drivetrain system in FCHEV

Two conventional DC-DC boost converters connected in parallel with each other form an IBC. The proposed structure of two-phase IBC is composed of two parallel phases each having a diode and a power switch. With this approach, the passive component size can be scaled down easily. This structure also improves the transient response and efficiency of the FCHEV system [5].

Voltage multiplier circuits are simple circuits consisting of switched capacitors and diodes. They are efficient and have a low cost. They are designed in such a way so as to acquire large output DC voltage. The distribution of the current in the voltage multiplier lowers the effective current decreasing the conduction losses. Also, the currents through the diodes becomes zero before turning off alleviating the diode recovery losses. There are two ways of connecting the VM cells to the DC-DC converter circuit.

- The VM cell can be connected in the middle of the circuit preferably after the power switch, so as to scale down the voltage stress.
- The VM cell can be connected in between the output of the FC system, i.e., at the input stage of the proposed converter design and the input inductors, in order to rectify pulsating DC or AC voltages.

The design of a two-phase IBC incorporated with a VM cell in the middle of the circuit is implemented in this paper. Adding VM cell reduces input current ripple and also a high voltage gain can be obtained without adding to the complexity. This is one of the main advantages of adding a VM cell. A comprehensive simulation analysis is conducted by using MATLAB-SIMULINK to test the performance of the system.

2 Modeling of the Converter

The converter put forward in this paper comprises a two-phase IBC integrated with VM cell as shown in Fig. 2.

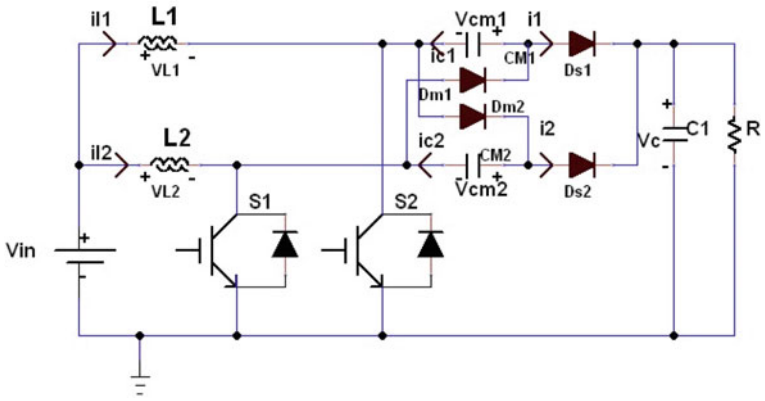

Fig. 2 Two-phase IBC with VM cell

The proposed structure is inferred from the DC-DC boost converter and the structure has two input inductors (L1, L2), one for each parallel phase. The inductor is designed in the same way as that of traditional DC-DC boost converter. The ripple in the input current can be scaled down by increasing the number of stages that operate in different phases. The proposed converter is composed of two parallel stages, i.e., $S = 2$ and one VM cell, i.e., $N = 1$. The number of VM cells and parallel stages is obtained by analyzing the interdependence of input and output voltages and also the peak voltage of the power switch and current stress. There is a major difference between the conventional low-frequency voltage multipliers that usually operate at low-frequency range and the voltage multipliers incorporated with DC-DC boost converters put forward in this paper. Increasing the number of cells in the traditional VM increases the total number of diodes connected in series and also increases the losses occurred due to conduction. Hence, the efficiency of the system gets reduced with the increment in the number of VM cell. But this does not occur in the proposed VM cell, since the current gets distributed between the diodes in the VM cell. Thus, the addition in the number of VM cells does not result in large conduction losses of the diodes.

3 Design and Working of the Converter

From Fig. 4, it can be deduced that the two power stages have a phase difference by 180°, which results in the reduction of peak-to-peak ripple current which is shown in Fig. 3.

The individual power stages of the converter operate at the same frequency of about 20 kHz as that of single-phase design. But input and output ripple frequencies are effective at 40 kHz.

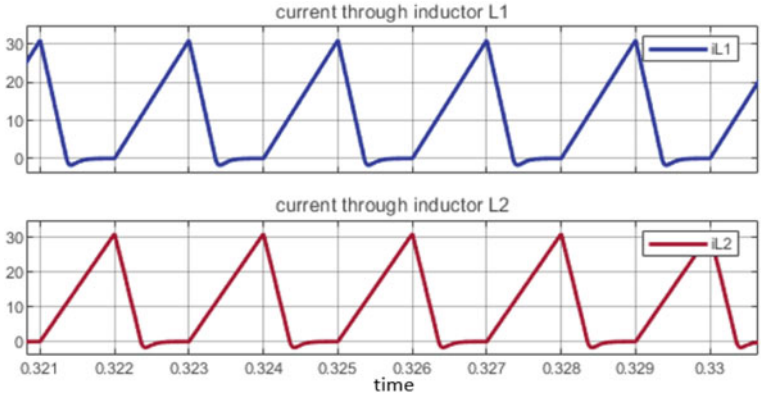

Fig. 3 Inductor currents i_{L1} and i_{L2}

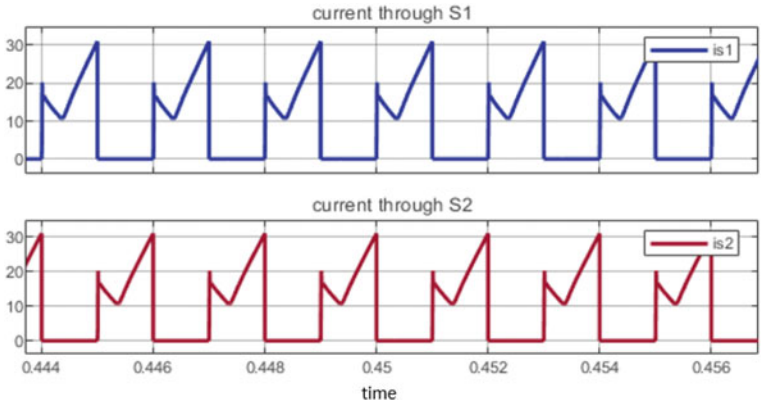

Fig. 4 Currents through the power switches of the converter

The proposed interleaved design calculation uses half the frequency, that is, 20 kHz and the ripple current is twice as that of the single-phase model. This scales down the inductance value by half, which can be verified from (15). Also, the total input inductor current of the single phase gets divided in the two-phase IBC. This reduces the inductor specifications such as current and power ratings that are mentioned in [6]. The losses occurred due to conduction are also substantially low compared to the conventional single-phase boost converter.

Discontinuous Conduction Mode (DCM) can be used in low-power applications when the energy requirement of the load is significantly less. Since the proposed model deals with high-power applications, Continuous Conduction Mode (CCM) is considered for the analysis and operation. The CCM design of proposed two-phase IBC is identical to the traditional single-phase boost converter. But the duty cycle

formula and inductance value to be chosen are different. DCM design is comparatively different from the CCM design. Also, the duty cycle changes according to the load in DCM, but duty cycle value is independent of load in CCM design as mentioned in [7].

In the proposed circuit, the inductor currents are out of phase by 180 degrees as observed from the graph in Fig. 3. Thus, it can be concluded that when input inductor L1 is charging, the other inductor L2 will get discharged and vice versa. The inductor currents have an average of 12A. The ripple observed in each inductor current is 2 A. The switching frequency of the inductor currents is observed to be twice as that of the single-phase design and the ripple is also significantly scaled down. The observed value of the input current ripple is 1.5 A which indicates that the input current ripple can be cancelled naturally by using interleaving technique.

4 Operation of the Converter

The analysis of operation of two-phase IBC with VM cell is done by using state-space averaging technique. The functioning of the converter is illustrated with the help of four switching stages of the converter. The equations for each stage can be put forth in the state-space representation of the form:

$$\dot{x} = Ax + Bu \tag{1}$$

$$y = Cx + Du \tag{2}$$

where

$$x = \begin{bmatrix} i_{L1} \\ i_{L2} \\ V_C \end{bmatrix} \text{ and } u = V_{in}$$

The functioning of the two-phase IBC with VM cell in CCM with k > 0.5 occurs in four stages as explained below.

4.1 First Stage: t_1-t_0

During this stage, both the power switches S_1 and S_2 conduct as shown in Fig. 5.

Since the switches act as a short circuit, the diodes will have no significance and will be in OFF state. The input inductors L_1 and L_2 store energy supplied from the FC system. Hence, the inductor current increases and reaches peak.

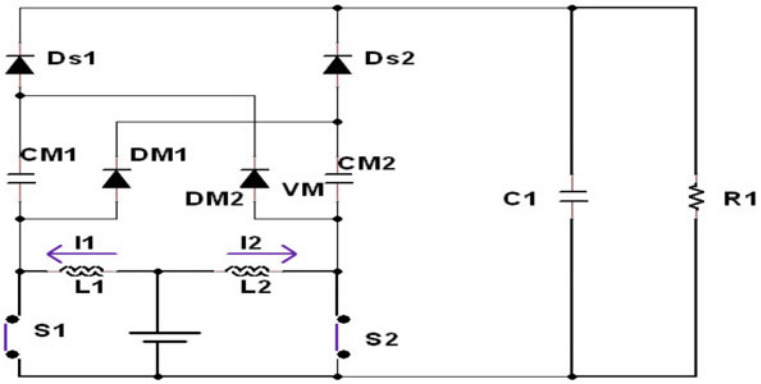

Fig. 5 Circuit operation during first stage with k > 0.5

Considering the inductor currents, i_{L1} and i_{L2}, and output capacitor voltage V_C as state variables, the equations for the state space can be written as

$$\frac{di_{L1}}{dt} = \frac{Vin}{L_1} \tag{3}$$

$$\frac{di_{L2}}{dt} = \frac{Vin}{L_2} \tag{4}$$

$$\frac{dv_c}{dt} = \frac{V_c}{C_1 * R_1} \tag{5}$$

$$A_1 = \begin{bmatrix} 0\,0 & 0 \\ 0\,0 & 0 \\ 0\,0 & \frac{-1}{R_1 C_1} \end{bmatrix} \; and \; B_1 = \begin{bmatrix} \frac{1}{L_1} \\ \frac{1}{L_2} \\ 0 \end{bmatrix}$$

4.2 Second Stage: t_2-t_1

Here, in this stage, the power switch S_2 is in OFF state. The power switch S_1 conducts. Diodes D_{S1} and D_{M2} conduct and corresponding topologies of the converter are designed as represented in Fig. 6. The output capacitor C_1 gets charged due to the energy dissipated from the input inductors through D_{S2} and also through C_{M1} and D_{M2}.

Figure 6 shows that the VM cell capacitors C_{M1} and C_{M2} are connected in series through the diode D_{M2}. Also, each capacitor in VM cell is connected in parallel with the output capacitor by the diode D_{S2}. Hence, the output capacitor voltage is double the multiplier capacitor voltage, i.e., ($V_C = 2V_{CM}$). Here, the node and loop equations

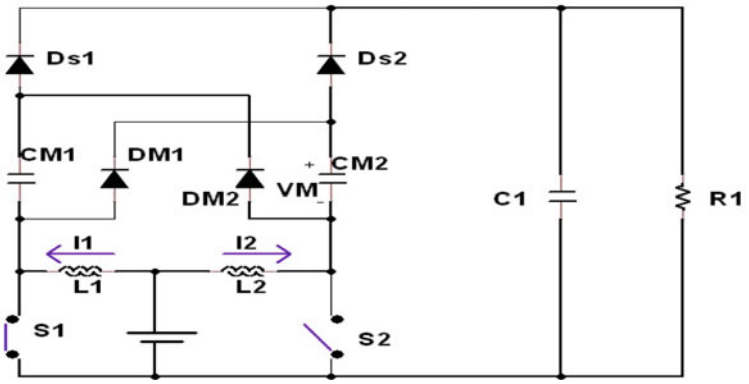

Fig. 6 Circuit operation during second stage with k > 0.5

can be written as

$$\frac{di_{L2}}{dt} = \frac{Vin - V_{CM1}}{L_2} \tag{6}$$

$$\frac{di_{L1}}{dt} = \frac{Vin}{L_1} \tag{7}$$

$$\frac{di_{L2}}{dt} = \frac{Vin - Vc - V_{CM2}}{L_2} \tag{8}$$

From (6) and (8),

$$V_{CM1} = V_C + V_{CM2} \tag{9}$$

With the help of these equations, A_2 and B_2 matrices can be obtained as

$$A_2 = \begin{bmatrix} 0 & 0 & 0 \\ 0 & 0 & \frac{-1}{L_2} \\ 0 & 0 & 0 \end{bmatrix} \; and \; B_2 = \begin{bmatrix} \frac{1}{L_1} \\ \frac{1}{L_2} - \frac{V_{CM2}}{L_2 * V_{in}} \\ 0 \end{bmatrix}$$

4.3 *Third Stage: t_3-t_2*

During the third stage, the power switches S_1 and S_2 will be in ON state as seen in Fig. 7.

The energy is stored in both the input inductors as in the first stage. Hence, the equations of first stage are applicable in this stage. Therefore, $A_3 = A_1$ *and* $B_3 = B_1$.

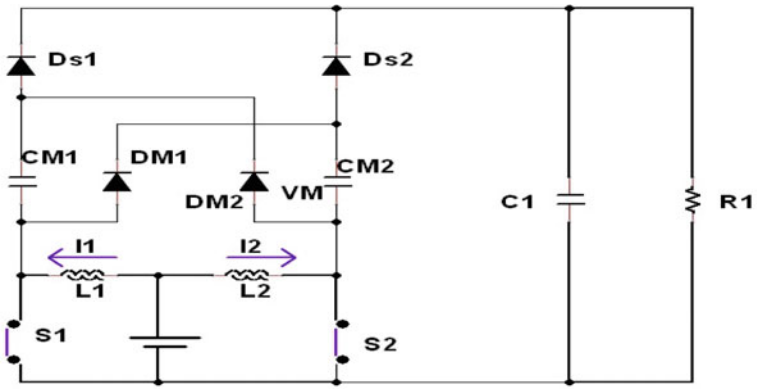

Fig. 7 Circuit operation during third stage with k > 0.5

4.4 Fourth Stage: t_4-t_3

Here, the switch S_1 is in OFF state as shown in Fig. 8.

The output capacitor C_1 and also the capacitor in the VM cell, i.e., C_{M2} gets charged due to the energy dissipated from the inductor L_1. The state-space equations of this stage and corresponding equations of the second stage are alike and can be obtained by swapping the subscripts 1 and 2. Thus the equations are

$$\frac{di_{L1}}{dt} = \frac{Vin - V_{CM2}}{L_1} \tag{10}$$

$$\frac{di_{L2}}{dt} = \frac{Vin}{L_2} \tag{11}$$

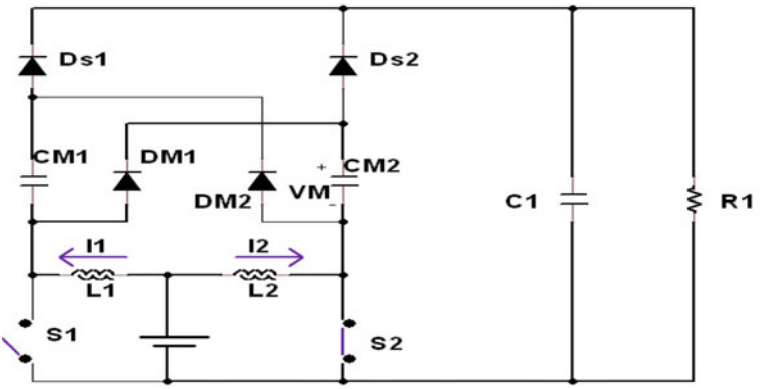

Fig. 8 Circuit operation during fourth stage with k > 0.5

$$\frac{di_{L1}}{dt} = \frac{Vin - Vc - V_{CM1}}{L_1} \tag{12}$$

$$V_{CM2} = V_C + V_{CM1} \tag{13}$$

With the help of these equations, A_4 and B_4 matrices can be obtained as

$$A_4 = \begin{bmatrix} 0 & 0 & 0 \\ 0 & 0 & \frac{-1}{L_1} \\ 0 & 0 & 0 \end{bmatrix} \; and \; B_4 = \begin{bmatrix} \frac{1}{L_2} \\ \frac{1}{L_1} - \frac{V_{CM1}}{L_1 * V_{in}} \\ 0 \end{bmatrix}$$

The operation in CCM with k < 0.5 is represented in Figs. 9, 10, 11 and 12. The duty cycle of both the switches is kept same.

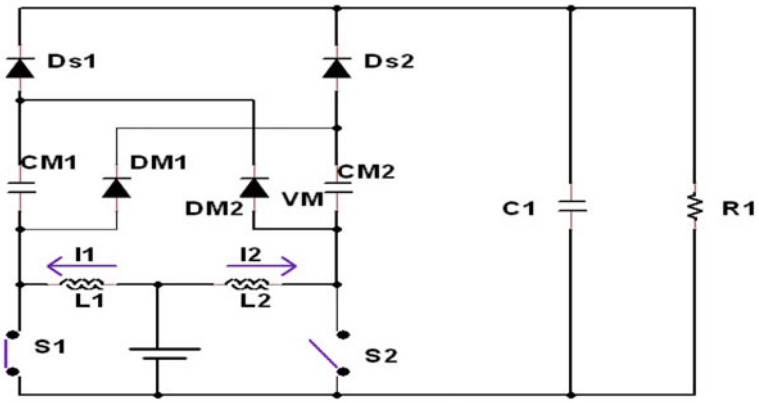

Fig. 9 Circuit operation during first stage with k < 0.5

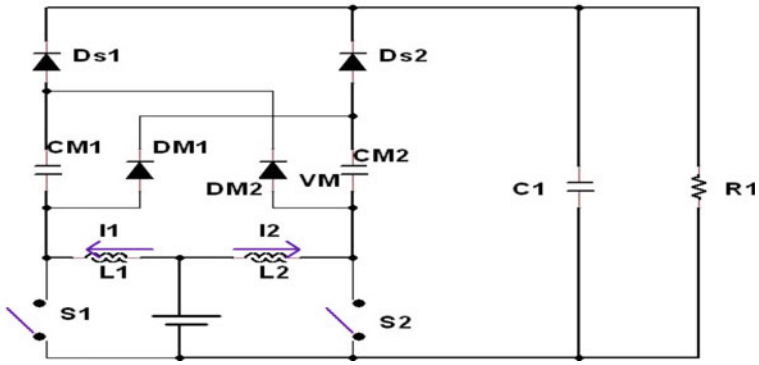

Fig. 10 Circuit operation during second stage with k < 0.5

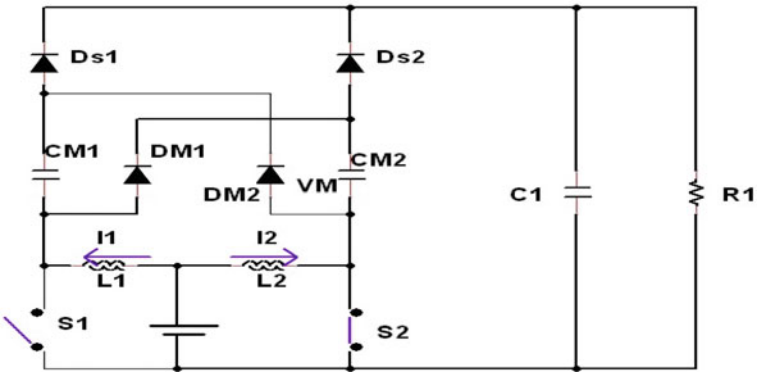

Fig. 11 Circuit operation during third stage with k < 0.5

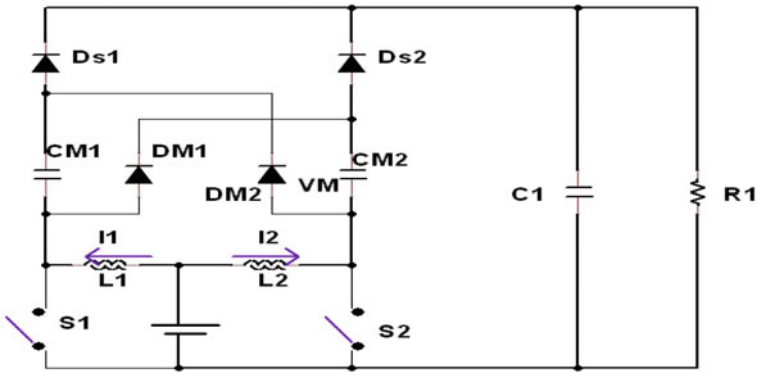

Fig. 12 Circuit operation during fourth stage with k < 0.5

4.5 First Stage: t_1-t_0

The switch S_1 is in ON state and inductor L_1 stores the energy supplied from the power source. The output capacitor gets charged due to the energy dissipated from the inductor L_2 through the diode $D_{S2.}$ Similarly, the capacitor in VM cell, C_{M1} gets charged through diode D_{M2}.

4.6 Second Stage: t_2-t_1

Here, all the switches will be in OFF state. Also, all the diodes in the VM cell will be in OFF state. Thus, the output capacitor C_1 gets charged due to the energy dissipated

from the input inductors L_1 and L_2 through the diode D_{S1}. The diode D_{S2} continues to be in ON state and conducts the current i_{L2}.

4.7 Third Stage: t_3-t_2

The switch S_2 is in ON state. The energy supplied from the power source gets stored in the input inductor L_2. The diode D_{M1} goes to ON state and starts conducting and also charges the capacitor in the VM cell, C_{M2}.

4.8 Third Stage: t_4-t_3

This stage is identical to the second stage.

5 Proposed Converter Design

5.1 Static Gain of the Boost Converter

As mentioned in [8], the static gain of the two-phase IBC with VM cell working in CCM can be represented as (14). This equation is also applicable for the functioning of the converter with $k < 0.5$.

$$G = \frac{Vo}{Vin} = \frac{(N+1)}{(1-k)} \tag{14}$$

where N is the number of VM cells and k is the duty cycle of the power switch.

5.2 Magnitude of the Passive Components

Determining the value of input inductance is similar to that of conventional boost converter as mentioned in [9]. Considering the peak input inductor current ripple as 15% of the average input inductor current, the inductance values can be evaluated from the equation

$$L_1 = L_2 = \frac{k * Vin}{f * S * \Delta i_L} \tag{15}$$

where Δi_L is the input inductor current ripple.

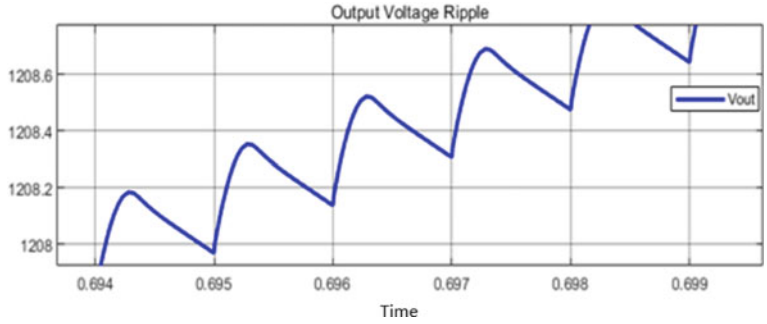

Fig. 13 Ripple in the output voltage

The equations for calculating the capacitance values of voltage multiplier stage and output capacitor are presented in (16) and (17), respectively.

$$C_{M1} = C_{M2} = \frac{(1-k) * Iin}{S * (N+1) * f * \Delta \mathrm{Vc}} \tag{16}$$

$$C_1 = \frac{k * Vc}{f * R_1 * \Delta \mathrm{Vc}} \tag{17}$$

where ΔV_c is the output voltage ripple.

Rearranging (17), the equation for output voltage ripple can be given as

$$\Delta \mathrm{Vc} = \frac{k * V_{in}}{C_1 * f * R_1} \tag{18}$$

Using this technique, the ripple frequency can be doubled. This results in scaling down of the output voltage ripple which is represented in Fig. 13.

6 Experimental Results

The experimental model of two-phase IBC with VM cell working in discontinuous conduction mode [10] designed using MATLAB-SIMULINK is depicted in Fig. 14 (Table 1).

It can be confirmed from Fig. 3 that the design works in DCM mode, since the value of inductor current reaches zero for a short time period during each cycle. The analysis is performed under open-loop condition. The output voltage is observed to be 1000 V for an input of 150 V as depicted in Fig. 15 and also reduces output voltage ripple from 200 to 180 mV. The experimental voltage gain ratio can be verified with the theoretical voltage gain G mentioned in (14).

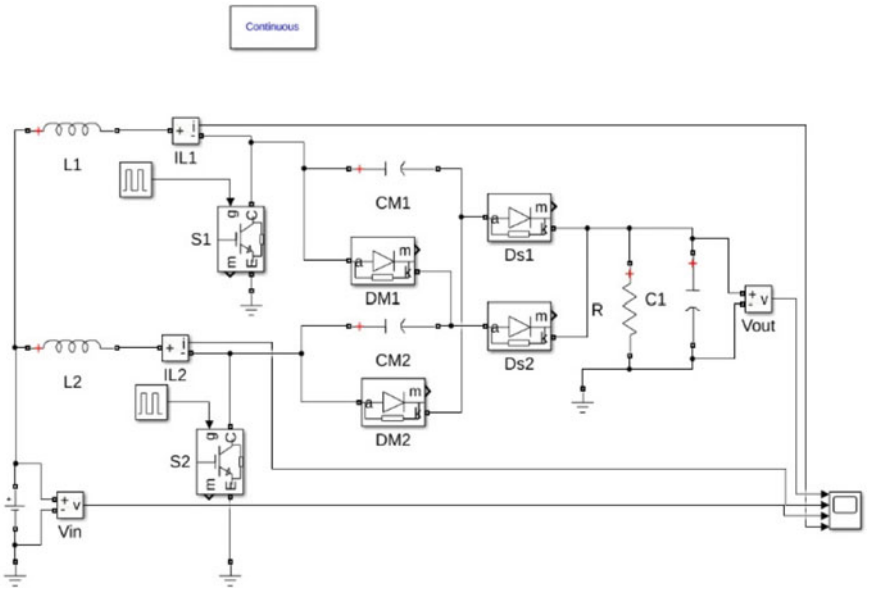

Fig. 14 Experimental circuit of IBC with VM cell

Table 1 Design metrics of the converter

Design metrics	Values
Input voltage	150 V
Output capacitor voltage	1000 V
Switching frequency	20 kHz
Output voltage ripple	180 mV
Multiplier capacitances	40 μF
Output capacitance	500 μF
Inductance	480 μH
Resistive load	850 Ω

7 Conclusion

In this paper, the functioning of two-phase IBC with VM cell in continuous conduction mode has been analyzed using state-space averaging technique. The proposed converter design is simulated in discontinuous conduction mode using MATLAB-SIMULINK and the behavior of the design like high voltage gain, reduction of ripples in current, and voltage values are verified. The input voltage can be boosted by a factor of 3.33 using interleaving technique. The addition of VM cell to the two-phase IBC doubles the output voltage by a factor of 6.66. The design significantly reduces the ripple in the output voltage from 200 to 180 mV. The design proves that the

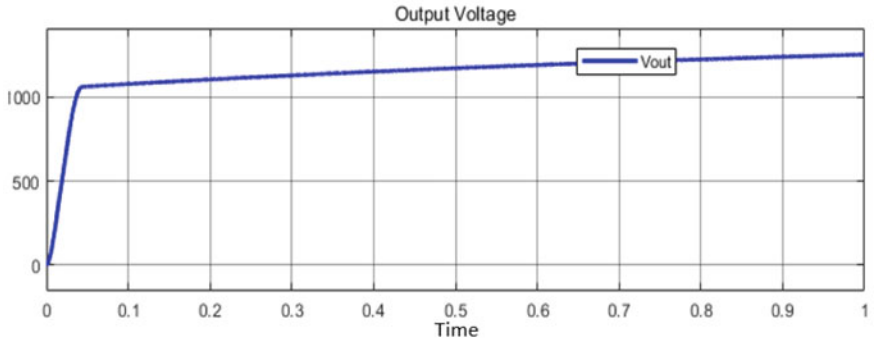

Fig. 15 Voltage across the output capacitor or the load

two-phase interleaving technique significantly reduces the inductance value than the single-phase design by dividing the input current into two inductor currents of the two-phase design.

References

1. Xu H, Wen X, Qiao E, Guo X, Kong L (2005) High power interleaved boost converter in fuel cell hybrid electric vehicle. In: 2005 IEEE international conference on electric machines and drives, pp 1814–1819, 15 May 2005
2. Wen J, Jin T, Smedley K (2006) A new interleaved isolated boost converter for high power applications. In: Applied power electronics conference and exposition, 2006. APEC '06. Twenty-First Annual IEEE, vol 6, pp 19–23, March 2006
3. Pietkiewicz A, Cuk S. A three-switch high-voltage converter. IEEE Trans Power Electron 14(1):177–183
4. Berkovich Y, Axelrod B (2012) High step-up DC-DC converter based on the switched-coupled-inductor boost converter and diode-capacitor multiplier. In: 6th IET international conference power electronics, machines and drives (PEMD 2012), pp P43–P43
5. Hegazy O, Mierlo JV, Lataire P (2012) Analysis, modeling, and implementation of a multidevice interleaved DC/DC converter for fuel cell hybrid electric vehicles. IEEE Trans Power Electron 27(11):4445–4458. https://doi.org/10.1109/TPEL.2012.2183148
6. Betten J, Kollman R. Interleaving DC-DC converters boost efficiency and voltage. Application report, Texas Instruments
7. Zhang L, Shen G, Chen M, Ioinovici A, Xu D (2012) Two-phase interleaved boost converter with voltage multiplier under APS control method for fuel cell power system. In: Proceedings of the 7th international power electronics and motion control conference, Harbin, 2012, pp 963–967. https://doi.org/10.1109/IPEMC.2012.6258925
8. Franco LC, Pfitscher LL, Gules R (2003) A new high static gain nonisolated DC-DC converter. In: IEEE 34th annual conference on power electronics specialist, 2003. PESC '03, Acapulco, Mexico, vol 3, pp 1367–1372. https://doi.org/10.1109/PESC.2003.1216786
9. Lloyd A, Dyer C (1999) The future of fuel cells. Sci Am 281:64–75
10. Altimania M, Nia MSS, Ferdowsi M, Shamsi P (2019) Analysis and modeling of a non-isolated two-phase interleaved boost converter with diode-capacitor cells in the DCM. In: 2019 North American power symposium (NAPS). https://doi.org/10.1109/naps46351.2019.9000260

A Unipolar Phase Disposition PWM Technique for Reduced Switch Count Symmetrical Nine-Level Multilevel DC Link Inverter Topology

Rajakumar Sakile, Marco Rivera, Kasoju Bharath Kumar, Bandela Supriya, and A. Bhanuchandar

1 Introduction

DC-AC power conversion plays a vital role in the area of generation, transmission, distribution, and utilization of the electrical energy such as power quality, HVDC transmission, flexible AC transmission (FACTS), and renewable energy applications (solar PV, fuel cell, wind) [1]. By nature of the output, DC-AC power converters (inverter) are classified as square wave inverter, quasi-square wave inverter, two-level PWM inverter, and multilevel inverters (MLIs) [2]. Due to the low power quality output, requirement of filters before the load, the two-level PWM inverter and quasi-square wave inverters are not suitable for the inversion operation [3]. The MLIs are introduced to overcome above-said drawbacks. MLIs are widely used in scientific communication and many industries, due to the output of MLIs which are imitating a sine wave [4]. The MLIs offer many advantages which are

(i) MLIs maintain power quality in high-power applications.
(ii) MLIs have high modularity.
(iii) MLIs has a capability of transformerless operation.
(iv) MLIs have high fault tolerance capability.

R. Sakile (✉)
Electrical Engineering Department, NIT Jamshedpur, Jamshedpur, Jharkhand, India
e-mail: 2018rsee006@nitjsr.ac.in

M. Rivera
Faculty of Engineering, Universidad de Talca, Maule, Chile

K. B. Kumar
EEE Department, Mahatma Gandhi Institute of Technology, Hyderabad, Telangana, India

B. Supriya
EEE Department, Chaitanya Bharathi Institute of Technology (A), Hyderabad, Telangana, India

A. Bhanuchandar
Electrical Engineering Department, NIT Warangal, Warangal, Telangana, India

S. Kumar et al. (eds.), *Recent Advances in Power Electronics and Drives*, Lecture Notes in Electrical Engineering 852, https://doi.org/10.1007/978-981-16-9239-0_8

(v) MLIs draw very low input current distortions.
(vi) Filter requirements have been greatly brought down or even eliminated for higher level of operations.
(vii) MLIs produce low or NO common mode voltages, and thus the over stress of multilevel motor drive can be eliminated.

Due to the above-said abilities, the MLIs have been impacted in several areas of industries, such as electric traction, electric vehicles, marine propulsion drives, high-power conveyors, and also power quality applications like FACTS, HVDC, and static var compensation [5]. Various basic MLIs topologies are present for the analysis, and out of all the basic or classical topologies which are used in many industries are

1. Diode clamped MLI (DCMLI).
2. Flying capacitor MLI (FCMLI).
3. Cascaded H-bridge MLI (CHB).

CHB and DCMLI required only one DC source in the operation, whereas FCMLI required multiple DC sources [6]. The most important property of MLI topology is modularity. The modularity of CHB structure is high compared to DCMLI and FCMLI. Practically, DCMLI, FCMLI generates up to five-level output beyond that the structure becomes complex and device count has been increased. So far CHB is best for the higher levels and same power rating [7]. When CHB is implemented for the MLIs topology many number of semiconductor devices are required and design of control strategies is more complex [8]. Therefore, the new MLI has proposed to eliminate or reduce semiconductor devices which is known as reduced switch count MLI or multilevel DC link inverter (MLDCL). For K level inverter, number of switches required for classical topologies are $2 \times (K - 1)$ and $(K + 3)$ switches are required for MLDCL topologies [9]. Therefore, the MLDCL topology is better than classical or existing topologies.

In this paper, Sect. 2 discusses about the description of MLDCL topology, Sect. 3 represents the proposed control scheme used in the circuit, and Sects. 4 and 5 discuss the simulation results and conclusion.

2 Description of MLDCL Topology

Generally, MLDCL inverters are operated with 100kw load for low inductance motor drives. MLDCL inverters reduce the capacitors, clamping diodes, and reduce the switch count [10]. For every switch, one protection circuit, gate driver circuit, heat sink, and control unit are required, and therefore the initial cost has been increased. By using MLDCL inverters the cost and volume of the system have drastically reduced. The single-phase MLDCL inverter with RL load is shown in Fig. 1. It consists of series connection of symmetrical DC sources and H-bridge [11]. In order to generate multilevel outputs, MLDCL inverters are separated with level generator and polarity generator. The level generator is used to generate the multilevel output and polarity generator is used to change the polarity of the output as per the control strategy.

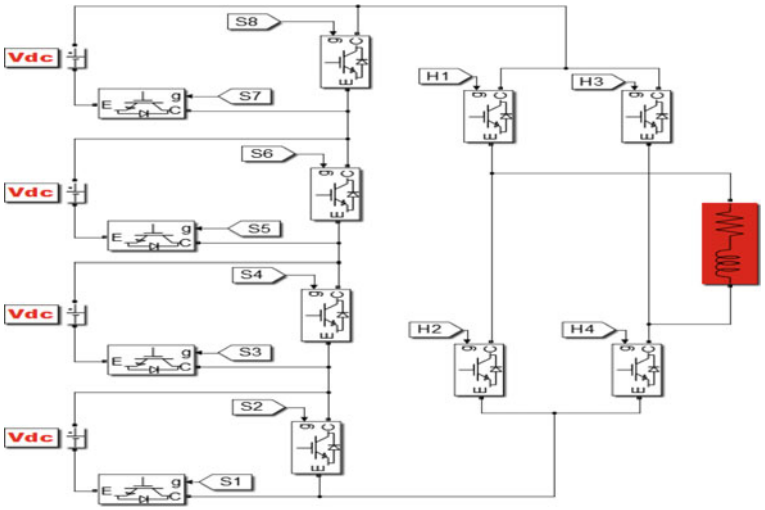

Fig. 1 Single-phase nine-level multilevel DC link inverter with RL load

In polarity generator side, one full H-bridge is required to decide the polarity, and it consists of four switches named as H1, H2, H3, and H4. In level generator side, four half-bridge circuits are connected in cascaded manner with eight switches [12, 13]. To get the 0Vdc output, the combination of conducted switches in level generator is S2, S4, S6, S8 and polarity generator is H1, H4. Similarly to get remaining outputs, switching sequence is discussed in Table 1. In level generator side, four switches are operated every time at high switching frequency, whereas in polarity generator side two switches are operated every time with low or fundamental frequency [14]. The MLDCL inverter produces required voltage levels with less switching and conduction losses [15–18]. Three-phase MLDCL inverter with RL load is shown in Fig. 2.

Table 1 Switching sequence for single-phase nine-level MLDCL inverter

Level number	Output voltage	ON state switches
1	4 Vdc	S1-S3-S5-S7-H1-H4
2	3 Vdc	S1-S3-S5-S8-H1-H4
3	2 Vdc	S1-S3-S6-S8-H1-H4
4	1 Vdc	S1-S4-S6-S8-H1-H4
5	0	S2-S4-S6-S8-H1-H4
6	−1 Vdc	S1-S4-S6-S8-H2-H3
7	−2 Vdc	S1-S3-S6-S8-H2-H3
8	−3 Vdc	S1-S3-S5-S8-H2-H3
9	−4 Vdc	S1-S3-S5-S7-H2-H3

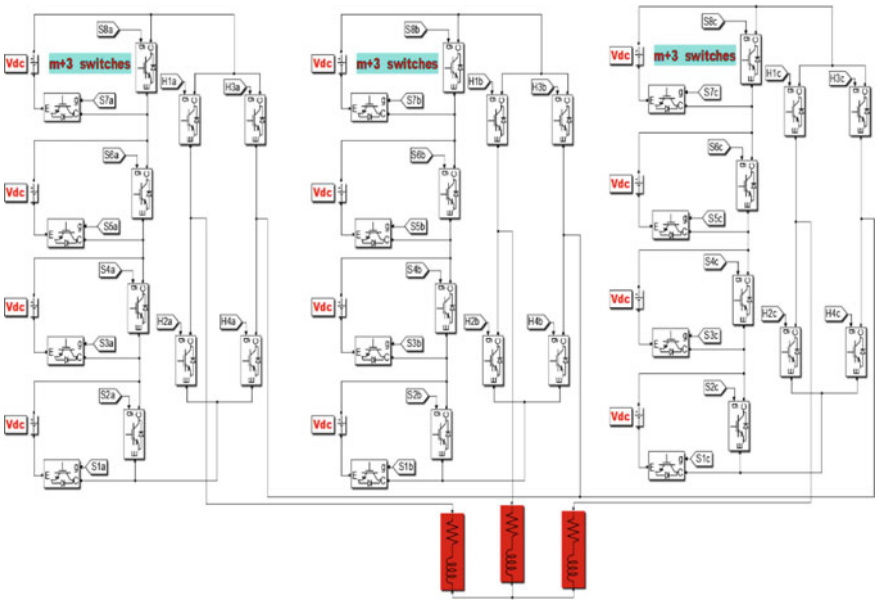

Fig. 2 Three-phase multilevel DC link inverter with RL load

3 Proposed Control Scheme

In order to generate valid gate pulses, control scheme development is very important. Generally, control schemes are broadly classified into Pulse Width Modulation (PWM) technique and stepped low-frequency technique. Among the traditional modulation schemes, the space vector method gives feasible solution with better DC bus utilization. However, this control technique can be easily applicable up to two- or three- or five-level inverter topologies according to number of switching states. As going to higher levels, the SVM technique becomes more complex. Therefore, the researchers or developers choose the carrier-based modulation technique. In carrier based, the most famous technique is Phase Disposition (PD), and it generates the level-shifted carriers within the same phase to generate K level output and it requires $(K - 1)$ carriers. In this paper, a Unipolar Phase Disposition (UPD) technique has been proposed. In order to generate K level output, UPD requires only $\mathbf{(K - 1)/2}$ carriers. Almost half of the carriers are reduced as compared with the conventional PD technique. The proposed control technique is well suitable for generalized structure of MLDCL topology to any level count. The proposed control scheme is shown in Fig. 3.

Modulating signal or reference signal is applied to both polarity and level generators. The modulating signal is compared with the zero, and then it will generate the gate pulses or switching pulses for the polarity generator from H1 to H4. In level generator case, the modulating signal is given to the absolute function and it

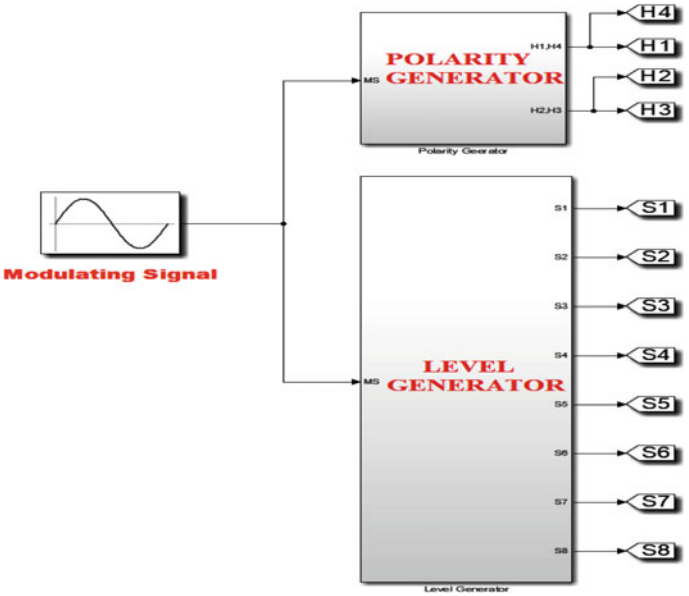

Fig. 3 Proposed control scheme

Table 2 Carrier count comparison

Control scheme name	Carrier level	Carrier count
PD	K − 1	8
Proposed UPD	(K − 1)/2	4

generates unipolar modulating signal. Due to absolute function, the number of carrier count can be reduced by half. Now the unipolar modulating signal is compared with the high switching frequency carriers and then it generates gate pulses from S1 to S8. Finally, this proposed control scheme gives the nine-level output for the inverter topology. If asymmetrical configurations are increased (1:2:3:4 and 1:2:4:8) with the same number of switches, the level count can be increased (Table 2).

4 Simulation Results and Discussion

In the proposed control scheme, the modulating signal is given to absolute function, and then unipolar modulating signal is generated with the reduced carrier count. The reduced carrier strategy PWM is shown in Fig. 4, and it is clearly observed that the carrier count has become reduced to four carriers.

From the proposed UPD control technique, nine-level output is generated, and the nine-level phase voltage is shown in Fig. 6. In level generator side, all the switches

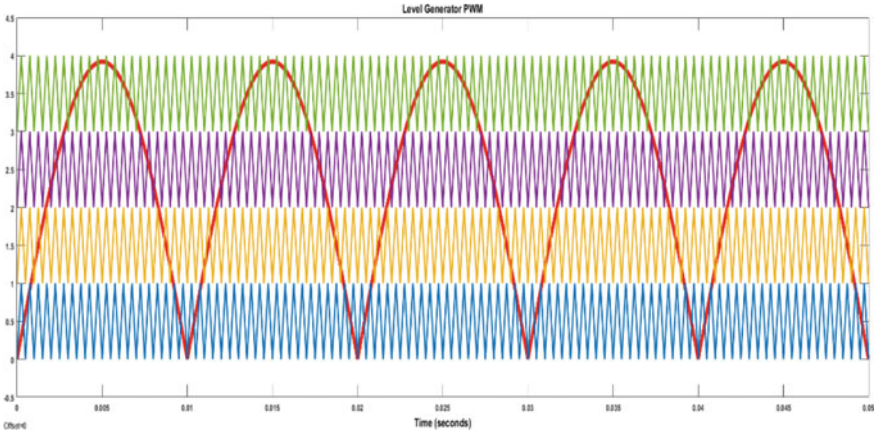

Fig. 4 Reduced carrier strategy PWM scheme level generator side

S1 to S8 are operated with high switching frequency, whereas in polarity generator side, the switches H1 to H4 are operated with low-frequency mode. The switching pulses of S1 to S8 and H1 to H4 are shown in Fig. 5. The load current depends on the RL load.

According to the Total Hormonic Distortion (THD), the phase voltage, line voltage, and load current have been analyzed. At fundamental frequency, the peak voltage of the phase voltage is 393.2 V and THD = 14.36% and line voltage at fundamental frequency is 679.7 V and THD = 12.76%. Similarly, the load current of the inverter peak current at fundamental frequency is 3.923A and THD = 4.18%. The phase, line voltages, and load currents are shown in Figs. 7, 8 and 9.

Simulation Parameters

See Table 3.

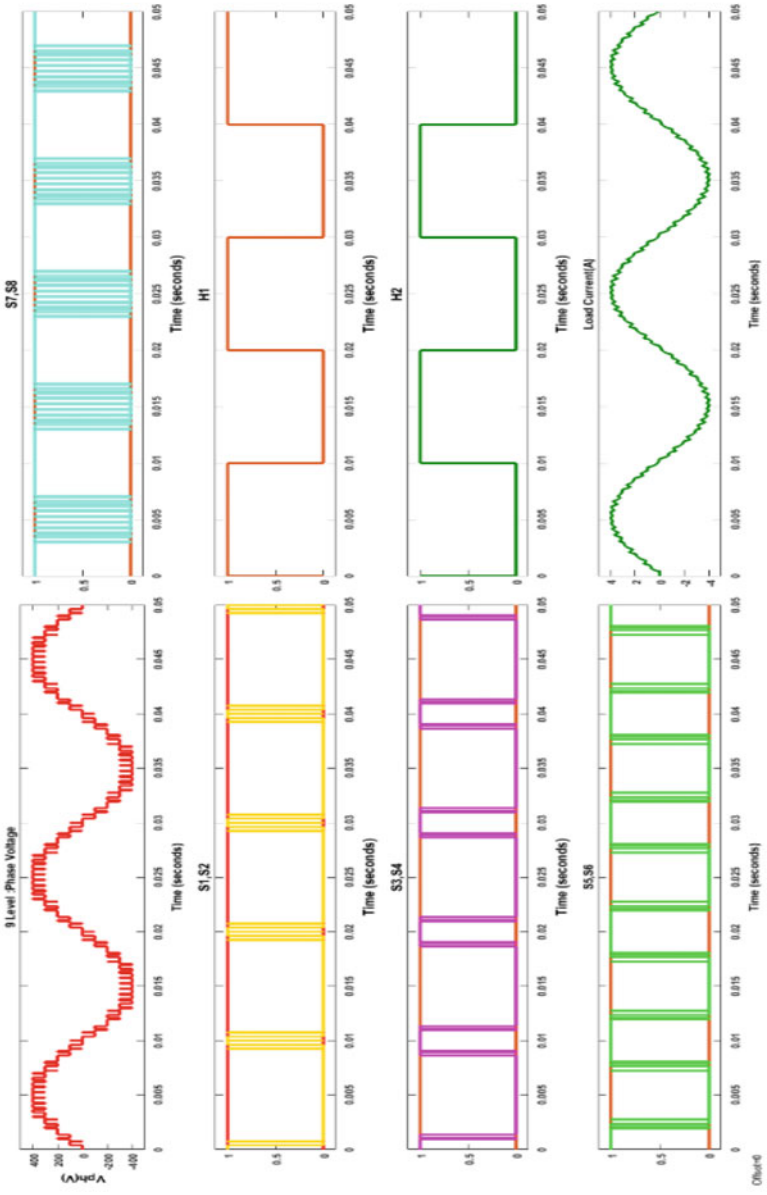

Fig. 5 Simulation waveforms for the single-phase RL load, both level and polarity generators

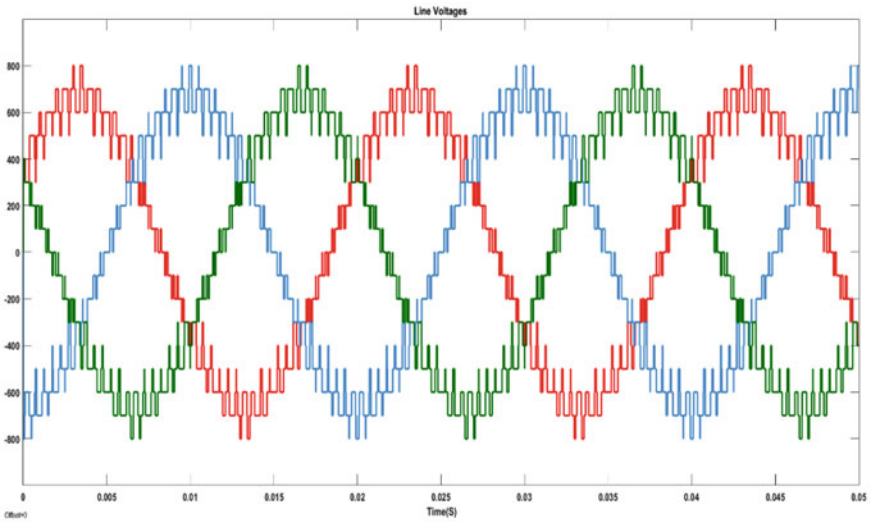

Fig. 6 Line voltage for three-phase RL load

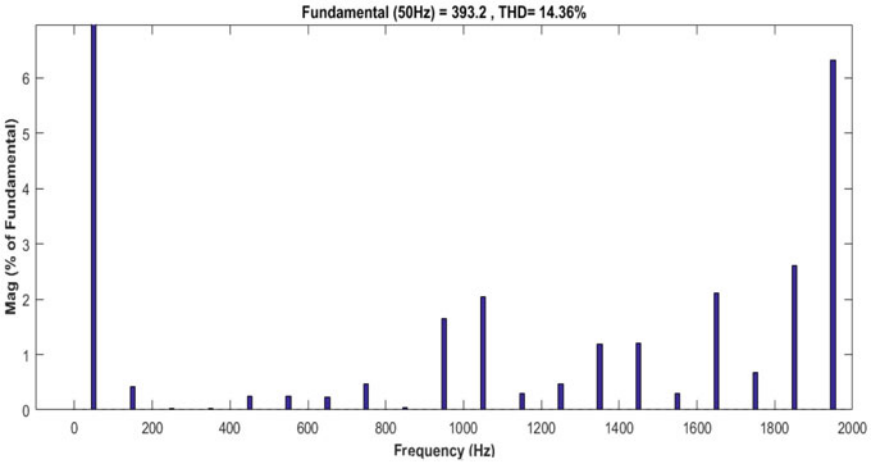

Fig. 7 FFT analysis of phase voltage

5 Conclusion

In this paper, the single-phase MLDCL inverter with UPD PWM control technique has been discussed. Basically this topology has the advantages like high modularity, redundant structure, even power distribution, equal utilization of the DC sources, great fault-tolerant capability, and equal device blocking voltages in level generator side. By taking asymmetrical configuration with the same number of switches, it is

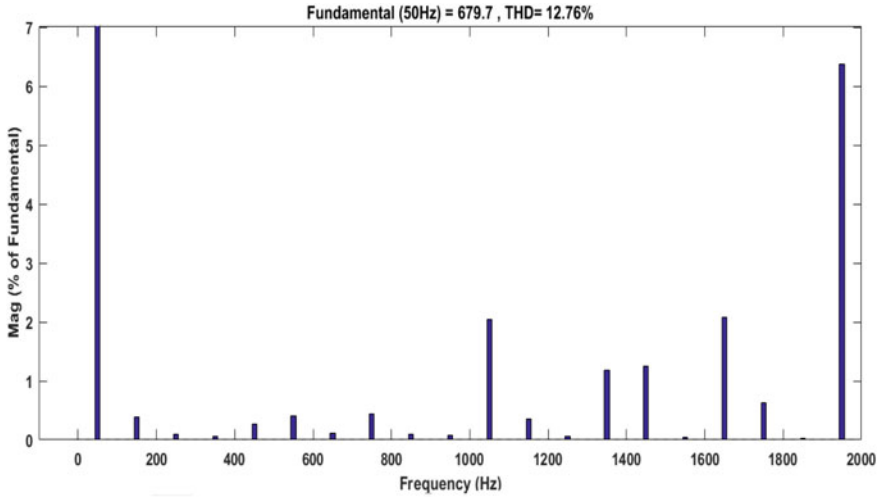

Fig. 8 FFT analysis of line voltage

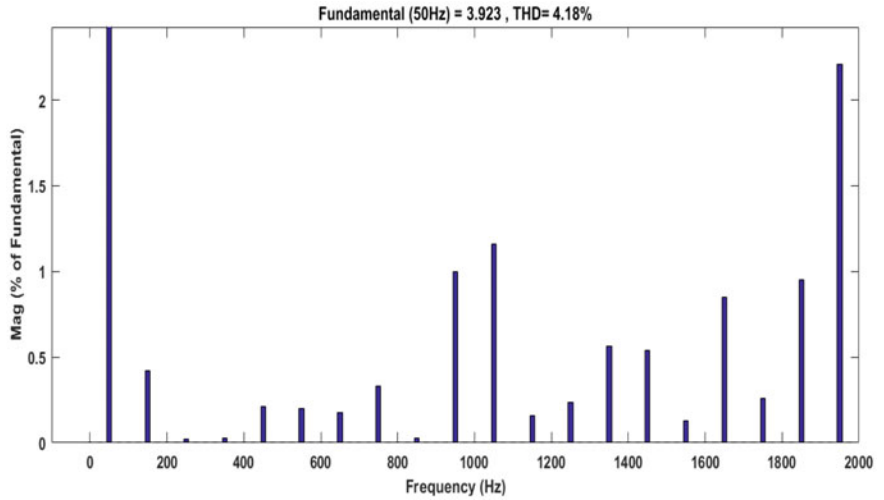

Fig. 9 FFT analysis of load current

possible to generate more number of levels. The proposed UPD control technique produces nine-level output voltage with reduced carrier strategy. Due to the reduction of carrier signals, the control complexity and burden on the processor can be reduced as compared with conventional PD technique. This control scheme is greatly applicable for any level count of MLDCL inverter topology and it is well suitable for photovoltaic-based grid-connected applications.

Table 3 Simulation parameters

Parameter	Parameter value
V_{dc}	100 V
R	100 Ω
L	22 mH
Switching frequency	2 kHz
Fundamental frequency	50 Hz
Modulation index	0.98
Total blocking voltage	6 p.u
Voltage gain	1

References

1. Omer P, Kumar J, Surjan BS (2020) A review on reduced switch count multilevel inverter topologies. IEEE Access 8:22281–22302. https://doi.org/10.1109/Access.2020.2969551
2. Kumawat RK, Palwalia DK (2018) A comprehensive analysis of reduced switch count multilevel inverter. Aust J Electr Electron Eng. https://doi.org/10.1080/1448837X.2019.1693884
3. Su G-J (2005) Multilevel DC-link inverter. IEEE Trans Ind Appl 41(3):848–854. https://doi.org/10.1109/TIA.2005.847306
4. Rao SN, Kumar DVA, Babu CS (2013) New multilevel inverter topology with reduced number of switches using advanced modulation strategies. In: 2013 international conference on power, energy and control (ICPEC), Sri Rangalatchum Dindigul, pp 693–699. https://doi.org/10.1109/ICPEC.2013.6527745
5. Zeb K, Khan I, Uddin W, Khan MA, Sathishkumar P, Busarello TDC, Ahmad I, Kim HJ (2018) A review on recent advances and future trends of transformer less inverter structures for single-phase grid-connected photovoltaic systems. Energies
6. Rodriguez J, Lai J, Peng FZ (2002) Multilevel inverters: a survey of topologies, controls, and applications. IEEE Trans Ind Electron 49(4):724–738. https://doi.org/10.1109/TIE.2002.801052
7. Belekar RA, Nakade RP et al (2013) Single phase 9 level MLDCL inverter with half bridge cell topology: performance analysis. In: 2013 international conference on power, energy and control (ICPEC)
8. Siddique MD, Rawa M et al (2021) A new cascaded asymmetrical multilevel inverter based on switched dc voltage sources. Int J Electr Power Energy Syst 128:106730
9. Selvakumar K, Patel PD (2021) Single phase five-level inverter topology with reduced number of switches for PV application. Mater Today Proc
10. Maheswari KT, Bharanikumar R et al (2020) A comprehensive review on cascaded H-bridge multilevel inverter for medium voltage high power applications. Mater Today Proc
11. Eguchi K, Shibata A et al (2020) An inductor-less step-up/step-down multilevel inverter with a single input source. Energy Rep 6(Supplement 2):146–152
12. Palle K, Bhanuchandar A (2020) A novel modified voltage oriented control of an active of an active front-end rectifier used for PMSG based wind turbine systems. IJITEE 9(8). ISSN-2278–3075
13. Su GJ, Adams DJ (2001) Multilevel DC link inverter for brushlesspermanent magnet motors with very low inductance. İn: Conference on REC 2001 IEEE-IAS annual meeting, vol 2, pp 829–834
14. Lai JS, Peng FZ (1995) Multilevel converters—a new breed of power converters. İn: Conference on REC 2001 IEEE-IAS annual meeting, pp 2348–2356

15. Nabae A, Takahashi I, Akagi H (1981) A new neutral-point-clamped PWM inverter. IEEE Trans Ind Appl 17(5):518–523
16. Kumar KB, Bhanuchandar A, Mahesh C (2021) A novel control scheme for symmetric seven level reduced device count multi-level DC link (MLDCL) inverter. In: 2021 international conference on sustainable energy and future electric transportation (SEFET), Hyderabad, India, 2021, pp 1–4. https://doi.org/10.1109/SeFet48154.2021.9375714
17. Bhanuchandar A, Murthy BK (2020) Single phase nine level switched capacitor based grid connected inverter with LCL filter. In: 2020 3rd international conference on energy, power and environment: towards clean energy technologies, 2021, pp 1–5. https://doi.org/10.1109/ICEPE50861.2021.9404491
18. Sathisha D (2021) A simplified control approach of AC-DC-TLBC for bi-polar DC microgrid applications. Turk J Comput Math Educ (TURCOMAT) 12(2):818–824. https://doi.org/10.17762/turcomat.v12i2.1090

A Novel Current Control Scheme for Three-Phase Three-Level Grid-Tied Neutral Point Clamped Inverter

Kowstubha Palle and Bandela Supriya

1 Introduction

The generation of clean energy is becoming a challenge due to shortage of the resources, geographical constraints along with the drastic increase in power demand by population [1]. Therefore, there is a need to explore alternative means for the generation of electricity like solar and wind energy systems [2, 3]. In modern power conversion systems, the grid converters (GC) play a vital role as they are much flexible in converting different renewable sources such as solar, wind energy into corresponding DC or AC systems [4, 5]. In comparison to the last decade, renewable resources-based electricity generation has increased nowadays.

Different innovative control methods are being constantly employed on photovoltaic panels and wind turbines so that they can perform fully as an energy source [6]. These control methods are employed on inverters, which are responsible for grid synchronization and energy conversion [7, 8]. The performance of these inverter topologies may vary from off-grid to grid connected and also with/without an isolation transformer along with its ability to operate in closed-loop configuration [9, 10].

These inverter topologies have different levels with an influence on the switching pattern and resolution of the inverter [10, 11]. In addition, these selected topologies determine the efficiency, utilization, size, weight, cost, etc. that affects the final product. In this paper, an emphasis on neutral point clamped (NPC) inverter is carried out and a simple and novel control scheme is proposed. In this scheme, PI controller and phase-locked loop (PLL) are not used unlike that of conventional space vector modulation (SVM) [12, 13]. Therefore, the computational burden on the processor reduces in comparison with the conventional SVM technique and is simple to execute.

NPC inverter topology is widely used among various types of multilevel inverter topologies [14, 15]. In NPC inverter, a combination of clamping diodes and cascaded

K. Palle (✉) · B. Supriya
EEE Department, Chaitanya Bharathi Institute of Technology (A), Hyderabad, Telangana, India

S. Kumar et al. (eds.), *Recent Advances in Power Electronics and Drives*, Lecture Notes in Electrical Engineering 852, https://doi.org/10.1007/978-981-16-9239-0_9

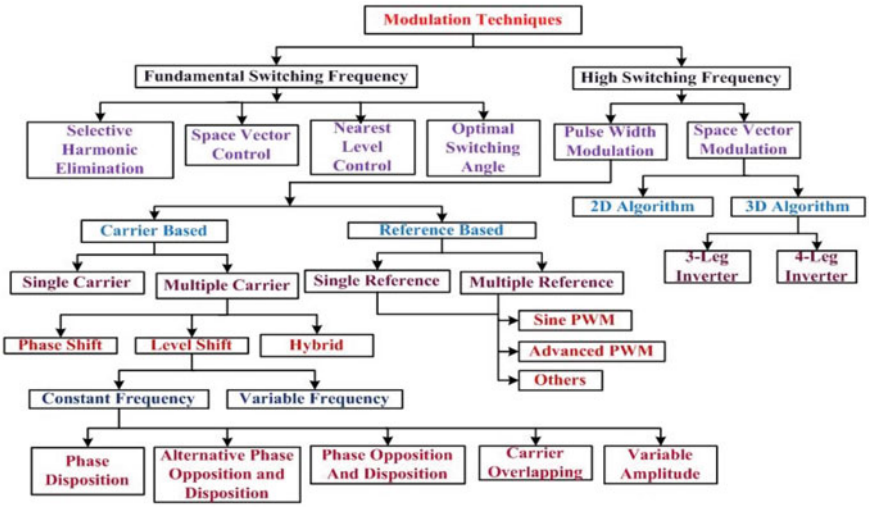

Fig. 1 Different modulation schemes—multilevel inverter topologies

DC capacitors is used to produce AC voltage waveforms with multiple levels [16, 17]. These inverters are used widely in large-power medium-voltage (MV) drives [18, 19] and grid-connected applications. In comparison with other multilevel inverters, NPC inverter will provide reduced dv/dt stress and total harmonic distortion (THD) in its AC output voltage. In this topology, the two cascaded DC link capacitors with midpoint as the neutral point makes the DC input voltage to split into two equal voltages.

In the field of power electronics, the development of control schemes for different power converters is a biggest thrust area for research. Summarized details of the most established control schemes for different power electronic converters are given in Fig. 1. Conventionally, different modulation schemes are available for multilevel inverter topologies and are depicted in Fig. 1.

Many pulse width modulation (PWM) techniques are developed for inverter circuits to control the fundamental component of output voltage with reduced THD [20, 21]. In the recent past, many topologies like a seven-level multilevel DC link inverter and a nine-level switched capacitor-based inverter were proposed as compared to grid-connected systems [22–24].

Among various PWM techniques, SVM is widely implemented for multilevel inverters. But in this technique, mathematical complexity for every switching state is predominant [25]. In this paper, a simple and novel current control scheme for three-phase three-level grid-connected NPC inverter is proposed. This proposed scheme is very much suitable for a renewable energy grid-connected system that is shown in Fig. 2.

In this paper, the main focus of work is carried out in the shaded portion of Fig. 2 where it is assumed that DC link capacitors are balanced by DC link chopper circuit.

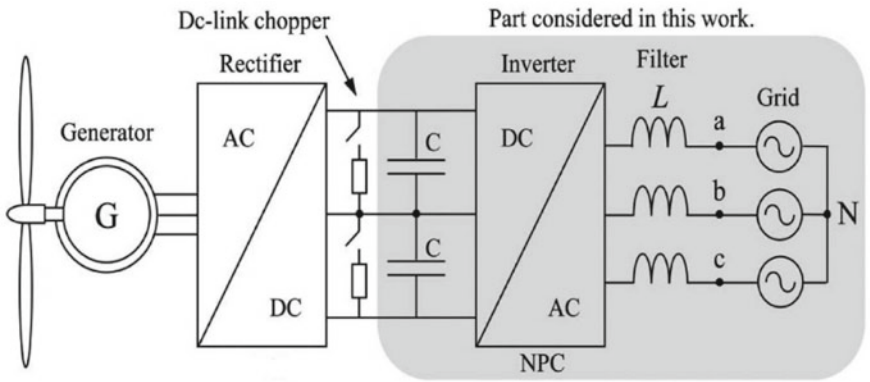

Fig. 2 Grid-connected wind energy conversion system

This paper is organized as follows, after the introduction, the description of the NPC inverter and its operation are explained in Sect. 2, the proposed control technique is presented in Sect. 3. Section 4 analyzes the simulation results which is followed by the conclusion in Sect. 5.

2 Description of NPC Inverter and Its Operation

Figure 3 represents a three-level three-phase NPC inverter circuit with 3-φ grid. In this diagram, leg A consists of four switching devices from ga_1 to ga_4 with diodes D_1 to D_4 connected in anti-parallel and clamping diodes D_{a1} and D_{a2} (Table 1).

The capacitors C_{d1} and C_{d2} are called as equalizing capacitors used to equalize the voltages as E or $V_{dc}/2$ taken from V_{dc}. The number of components used for

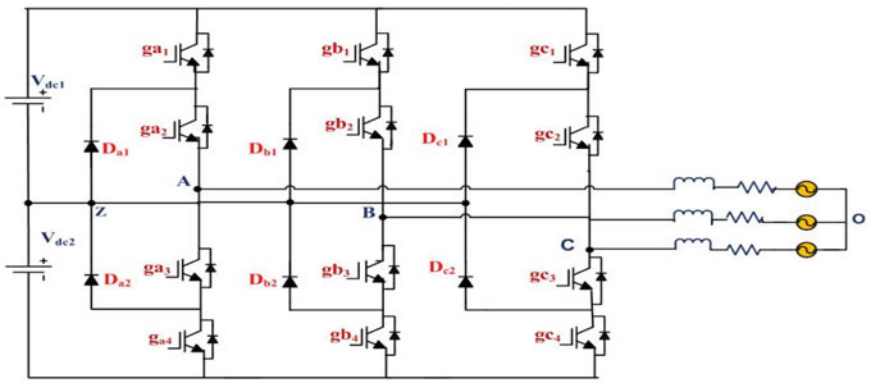

Fig. 3 Three-phase three-level NPC inverter circuit with 3-φ grid

Table 1 Generalized expressions for selecting the number of components used for one leg of three-phase k-level NPC inverter

Power component	NPC
Main switching devices	2 (k − 1)
Anti-parallel diodes	2 (k − 1)
Clamping diodes	(k – 1) (k − 2)
DC bus capacitors	(k − 1)
Flying capacitors	zero

Table 2 Switching pattern for three-phase three-level NPC inverter circuit

Switching state	Device switching status (Phase A)				Pole voltage, V_{AZ}
	ga_1/S_1	ga_2/S_2	ga_3/S_3	ga_4/S_4	
1 (or) +	On	On	Off	Off	E or $V_{dc}/2$
0 (or) 0	Off	On	On	Off	0
−1 (or) −	Off	Off	On	On	−E or $-V_{dc}/2$

three-phase p-level NPC inverter for one leg is given in Table 2 with generalized expressions. The switching pattern for three-level three-phase NPC inverter circuit with IGBTs as switches is given in Table 2.

From Table 2, it is understood that ga_1 and ga_3 are complementary and similarly ga_2 and ga_4 are complimentary. From Table 1, it is clear that the switching transition from "1" to "−1" makes inverter pole voltage V_{AZ} to go from +E, 0 to −E directly. This transition causes a high amount of dv/dt stress on switches, unequal dynamic voltage sharing on switches, and doubling of switching loss. Therefore, the switching transition from "1" to "−1" is always avoided for NPC inverter. Generally, switching transitions are taken as [1] to [0], [−1] to [0] or vice versa giving rise to equal dynamic voltage sharing during the commutation from each switching state. Three-level three-phase NPC inverter has reduced THD and dv/dt in comparison with two-level inverters for the same operating specifications. The static voltage equalization is obtained in NPC, only when the leakage current flow of switches ga_1 and ga_4 in a leg is lower than that of switches ga_2 and ga_3.

Space vector is a mathematical concept that is useful for visualizing the effect of three-phase variables in space. The division of sectors and the regions for three-phase three-level NPC inverter circuit is given in Fig. 4.

Depending on the magnitude of the voltage vectors, they are classified as four groups and have a total of $3^3 = 27$ switching states. Description of these switching states (stationary space vectors) along with their vector classification and magnitude is given in Table 3.

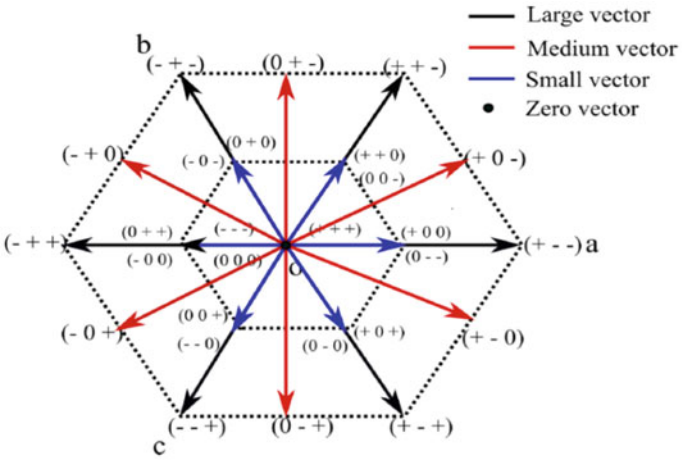

Fig. 4 Division of sectors and regions for three-phase three-level NPC inverter circuit

3 Proposed Control Technique

Figure 5 represents the block diagram of the proposed current and the control scheme of three-phase three-level grid-tied NPC inverter is given in Fig. 3.

In this block diagram of the control technique, SVM is basically reflected with a new digital switching approach. The entire explanation of block diagram is presented as two parts, namely, part A and part B. The working procedure of part A is given as follows. In this process, three-phase load currents and three-phase injected reference grid currents are initially converted into αβ frames. These converted αβ frame currents are compared and the errors so obtained will undergo a conversion process, resulting in two outputs, namely, magnitude and phase angle as given in Fig. 5. Magnitude output vector undergoes relational comparisons with a set of a simple error band signal (EB_1) or with the summation of two error band signals (EB_1 and EB_2). The outputs so obtained are multiplied with gains and finally added to obtain the control port signal—CP_1. This control port signal CP_1 can be interpreted with reference control vector of switching states of SVM.

The other output (angle) obtained from the conversion process is considered for the remaining operation. The angle gives the exact location of the reference vector of SVM with its presence in any one of the sector areas as given in Fig. 4. Therefore, this output is considered for different blocks with different sector areas as mentioned in Table 3 as small, medium, and large vectors and is used in the block diagram given in Fig. 5 Data port 2 (DP_2) is taken from the block consisting of small vector (V_1 to V_6) with multiplicities. The switching states [1 0 0], [1 0 −1] are automatically obtained from sector selection of medium and large by taking 4 A (peak current) of reference active current injecting to the grid. Data port 3 (DP_3) is taken from the

Table 3 Space vectors-27 switching states

Space vector		Switching state		Vector classification	Vector magnitude
V_0		[+ + +][0 0 0][− − −]		Zero vector	0
$\vec{v}_1$		+ Type	− Type	Small vector	$\frac{1}{3}V_d$
	$\vec{v}_{1+}$	[+ 0 0]			
	$\vec{v}_{1-}$		[0 − −]		
$\vec{v}_2$	$\vec{v}_{2+}$	[+ + 0]			
	$\vec{v}_{2-}$		[0 0 −]		
$\vec{v}_3$	$\vec{v}_{3+}$	[0 + 0]			
	$\vec{v}_{3-}$		[− 0 −]		
$\vec{v}_4$	$\vec{v}_{4+}$	[0 + +]			
	$\vec{v}_{4-}$		[− 0 0]		
$\vec{v}_5$	$\vec{v}_{5+}$	[0 0 +]			
	$\vec{v}_{5-}$		[− − 0]		
$\vec{v}_6$	$\vec{v}_{6+}$	[+ 0 +]			
	$\vec{v}_{6-}$		[0 − 0]		
$\vec{v}_7$		[+ 0 −]		Medium vector	$\frac{\sqrt{3}}{3}V_d$
$\vec{v}_8$		[0 + −]			
$\vec{v}_9$		[− + 0]			
$\vec{v}_{10}$		[− 0 +]			
$\vec{v}_{11}$		[0 − +]			
$\vec{v}_{12}$		[+ − 0]			
$\vec{v}_{13}$		[+ − −]		Large vector	$\frac{2}{3}V_d$
$\vec{v}_{14}$		[+ + −]			
$\vec{v}_{15}$		[− + −]			
$\vec{v}_{16}$		[− + +]			
$\vec{v}_{17}$		[− − +]			
$\vec{v}_{18}$		[+ − +]			

summation of sector area comprising of medium and large vectors (V_7-V_{12} and V_{13}-V_{18}). The explanation for part B is given as follows. The block truncated value (first input) which is given in part B just works like a digital multiple port digital switch. The generated CP_1, DP_2, DP_3, and additional zero vector V_{19} (DP_1) are given to truncated block and this block will select proper data port signal (DP_3) according to CP_1. The output of this block CP_1 is given with saturation limits and the obtained value CP_2 is once again given to truncated block along with all other input vectors (V_1 to V_{19}) as data ports. According to CP_2, the respective data port V_7 is selected [1 0 −1] automatically. To this value of V_7, a constant value k is added to generate desired CPs for abc phases labeled in the block diagram as CP_3, CP_4, and CP_5.In each phase, these control port values will undergo truncation once again with the

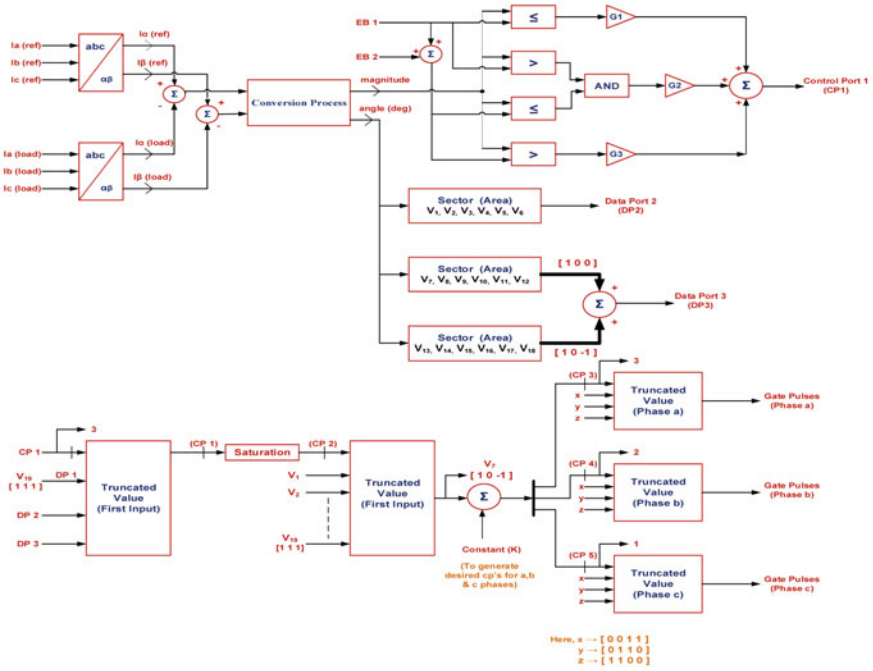

Fig. 5 Block diagram of proposed current control algorithm of three-phase three-level grid-tied NPC inverter

switching action x-[0 0 1 1], y-[0 1 1 0], z-[1 1 0 0] as data ports giving rise to gate pulses for three phases according to the injecting reference active grid current 4 A (peak).

The advantages of the proposed control technique are: there is no need of PI controller (tuning is not required), phase-locked loop (PLL), and calculation of dwell time. Finally, this technique reduces the computational burden on processor in comparison with conventional SVM technique and is simple to execute.

4 Simulation Results and Their Analysis

The specifications considered for current control technique of three-phase three-level grid-tied NPC inverter are given in Table 4.

For the given specifications, a simulation current control scheme is developed on MATLAB/Simulink platform. The simulation is run for a period of 5 s and the results are presented as follows.

The NPC inverter terminal/pole voltage on incorporating the proposed control scheme for three-phase three-level grid-tied NPC inverter is shown in Fig. 6. It is understood that three levels (+300 V, 0, −300 V) are obtained on each leg of the

Table 4 Specifications of three-phase three-level NPC grid-tied inverter

Parameter	Value
DC link voltage ($V_{dc1} = V_{dc2}$)	300 V
Injected grid current reference value ($i_{a\_ref} = i_{b\_ref} = i_{c\_ref}$) in amperes	4 A
Grid voltage (peak amplitude)	339 V
Grid frequency	50 Hz
Sampling time (T_s)	10e−6 s
Filter values (R, L)	0.031 Ω, 3.02 mH

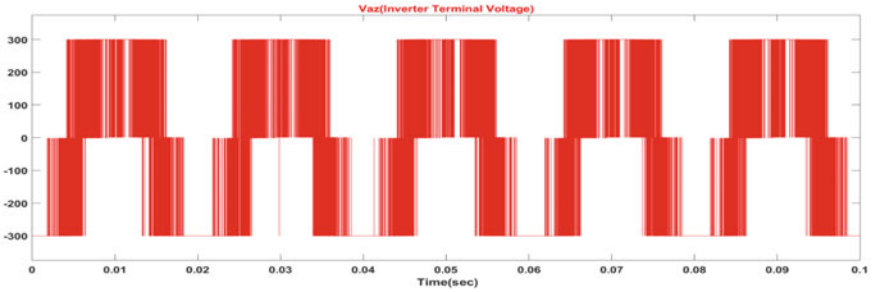

Fig. 6 Inverter terminal/pole voltage (V) for one phase

inverter. Figure 7 shows the NPC inverter terminal three-phase line-to-line voltages V_{ab}, V_{bc},V_{ca} with a maximum value of 600 V each. It is concluded that five levels of voltage are obtained at the output of the inverter from Fig. 7.

Figure 8 shows the three-phase grid currents in amperes for an injected maximum reference current of 4 A. It is understood from this figure that the maximum of 4 A is obtained for each phase.

Figure 9 shows injected reference phase-A current and grid current in amperes. In this figure, it is understood that the grid current follows the reference current.

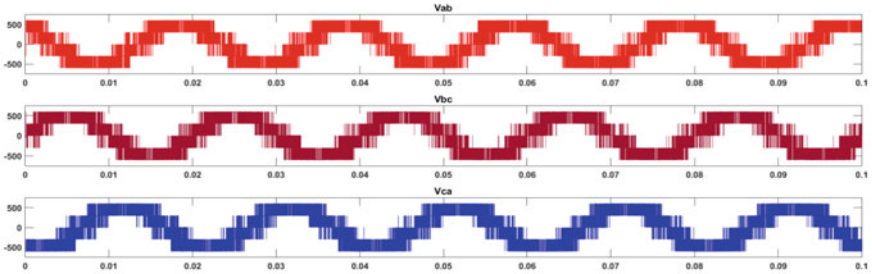

Fig. 7 Line voltage (five level) in volts

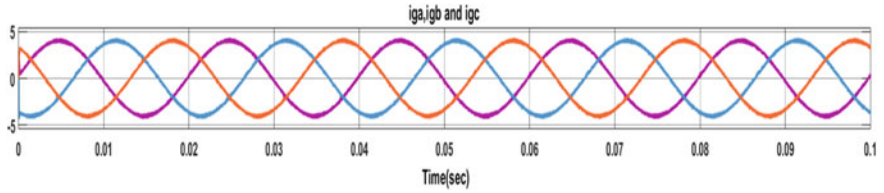

Fig. 8 Three-phase grid currents in amperes

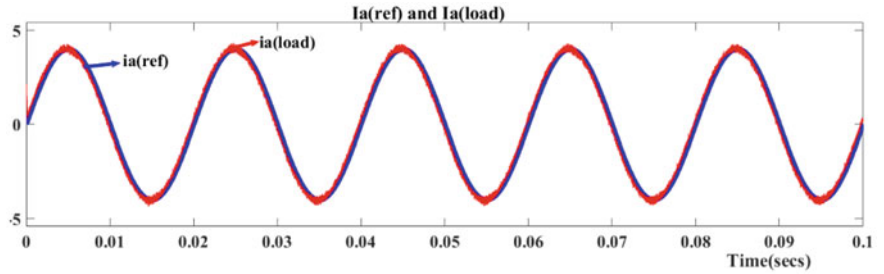

Fig. 9 Injected reference phase-A current and grid current in amperes

In this proposed control scheme, if the reference current changes, automatically the switching states will be changed for giving the gate pulses to the switches.

Figure 10 shows harmonic spectrum for grid current obtained through FFT analysis. From the figure, it is observed that the THD is 3.51% and this value is meeting the standards of IEEE-519. Figure 11 represents the three-phase grid line voltages with a peak value of 587.9 V at fundamental frequency.

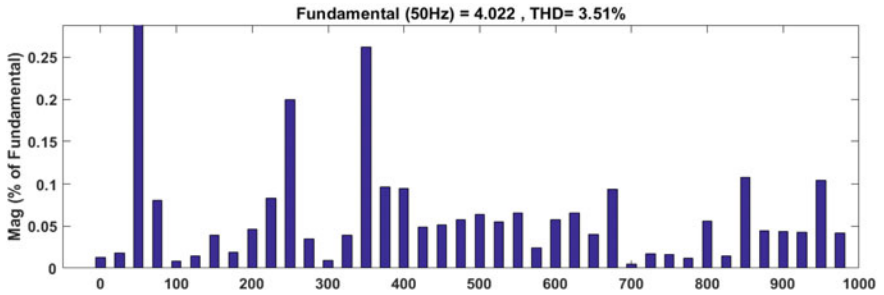

Fig. 10 Harmonic spectrum—grid current

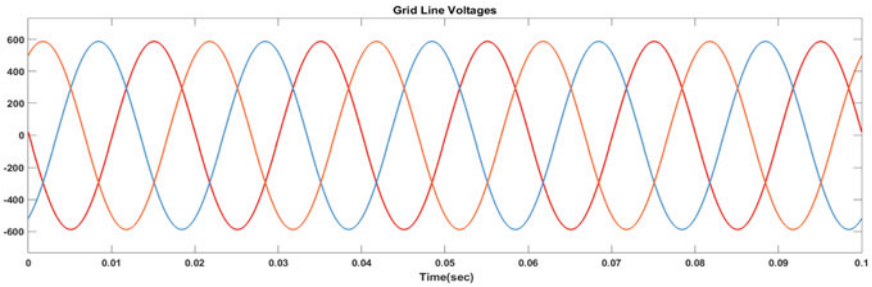

Fig. 11 Three-phase grid line voltages

5 Conclusion

In this paper, a simple and novel current control scheme for three-phase three-level grid-tied NPC inverter is proposed. This scheme is simple and intuitive because of the elimination of all dwell time calculations in comparison with the conventional modulation schemes. For a reference injected grid current with a maximum value of 4 A, it is understood that the grid current follows same as reference by the proposed control scheme and grid current THD is obtained as 3.51%. Based on the reference injected grid current, the region of switching states is automatically selected with this new digital switching control approach. This scheme reduces the control complexity and burden on the processor. The NPC with proposed current control scheme is well suitable to wind energy conversion and photovoltaic-based systems.

References

1. Nabae A, Takahashi I, Akagi H (1981) A new neutral-point-clamped PWM inverter. IEEE Trans Ind Appl IA-17(5):518–523. https://doi.org/10.1109/TIA.1981.4503992
2. Layate Z, Bahi T, Abadlia I, Bouzeria H, Lekhchine S (2015) Reactive power compensation control for three phase grid-connected photovoltaic generator. Int J Hydrog Energy 40
3. MCU SAE Team (2012) Center-aligned SVPWM realization for 3-phase, 3-level inverter. Texas Instruments
4. Palle K, Bhanuchandar A (2020) A novel modified voltage oriented control of an active front-end rectifier used for PMSG based wind turbine systems. Int J Innov Technol Explor Eng (IJITEE) 9(8)
5. Rodríguez P, Teodorescu R, Candela I, Timbus AV, Liserre M, Blaabjerg F (2006) New positive-sequence voltage detector for grid synchronization of power converters under faulty grid conditions. In: IEEE annual power electronics specialists conference
6. Ross D, Theys J, Bowling S (2004) Using the dsPIC30F for vector control of an ACIM. Microchip
7. Sharma A, Singh A, Yadav P (2015) Analysis of 3 level SVPWM based open loop and closed loop V/F control of induction motor. Int J Eng Res Technol 4(4)
8. Solar Choice Staff (2010) Conventional and transformerless inverters. Solar Choice
9. Teodorescu R, Liserre M, Rodríguez P (2011) Grid converters for photovoltaic and wind power systems, 1st edn. Wiley

10. Tolunay B (2012) Space vector pulse width modulation for three-level converters. Uppsala Universitet
11. Zhu R, Wu X, Tang Y (2015) Duty cycle-based three-level space vector pulse-width modulation with overmodulation and neutral-point balancing capabilities for 3-phase neutral-point clamped inverters. IET Power Electron 8(10)
12. Celanovic N, Boroyevich D (2001) A fast space-vector modulation algorithm for multilevel three-phase converters. IEEE Trans Ind Appl 37(2):637–641
13. Wu B (2006) High-power converters and AC drives, 1st edn. Wiley-IEEE Press. Wiley
14. Aneesh M, Gopinath A, Baiju MR (2009) A simple space vector PWM generation scheme for any general n – level inverter. IEEE Trans Ind Electron 56(5):1649–1656
15. Leon J, Vazquez S, Portillo R, Franquelo L, Carrasco J, Wheeler P, Watson A (2009) Three-dimensional feedforward space vector modulation applied to multilevel diode-clamped converters. IEEE Trans Ind Electron 56(1):101–109
16. Mekhilef S, Abdul Kadir M (2010) Voltage control of three-stage hybrid multilevel inverter using vector transformation. IEEE Trans. Power Electron 25(10):2599–2606
17. Gopinath A, Mohamed A, Baiju MR (2009) Fractal based space vector PWM for multilevel inverters—a novel approach. IEEE Trans Ind Electron 56(4):1230–1237
18. Saeedifard M, Bakhshai A, Joos G (2005) Low switching frequency space vector modulators for high power multimodule converters. IEEE Trans Power Electron 20(6):1310–1318
19. Fernando Silva J, Rodrigues N, Costa J (2000) Space vector alpha-beta sliding mode current controllers for three-phase multilevel inverters. In: EEE Power Electronics Specialists Conference (PESC), vol 1, pp 133–138
20. Kouro S, Rebolledo J, Rodriguez J (2007) Reduced switching-frequency-modulation algorithm for high-power multilevel inverters. IEEE Trans Ind Electron 54(5):2894–2901
21. Saeedifard M, Nikkhajoei H, Iravani R (2007) A space vector modulated STATCOM based on a three-level neutral point clamped converter. IEEE Trans Power Del 22(2):1029–1039
22. Kumar KB, Bhanuchandar A, Mahesh C (2021) A novel control scheme for symmetric seven level reduced device count multi-level DC link (MLDCL) inverter. In: 2021 international conference on sustainable energy and future electric transportation (SEFET), pp 1-4. https://doi.org/10.1109/SeFet48154.2021.9375714
23. Bhanuchandar A, Murthy BK (2021) Single phase nine level switched capacitor based grid connected inverter with LCL filter. In: 2020 3rd international conference on energy, power and environment: towards clean energy technologies, pp 1–5.https://doi.org/10.1109/ICEPE50861.2021.9404491
24. Sathisha D, Bhanuchandar A, Harshaa D, Srisailam C (2021) A simplified control approach of AC-DC-TLBC for bi-polar DC microgrid applications. Turk J Comput Math Educ 12(2):818–824
25. Rodriguez J, Bernet S, Steimer PK, Lizama IE (2010) A survey on neutral-point-clamped inverters. IEEE Trans Industr Electron 57(7):2219–2230

Active and Reactive Power Control of Grid-Tied Asymmetrical MLI-based PV System with Reduced Switching Frequency

Hareesh Myneni, A. Pranay Kumar, Somnath A. Mandale, and Ganjikunta Siva Kumar

1 Introduction

The use of renewable energy resources is growing rapidly in recent days. Renewable energy resources exist worldwide, in contrast to fossil fuels, which are insufficient for the present energy requirements. The rapid development of renewable energy resources plays a vital role in electricity generation. Solar, wind, geothermal, etc., are the abundant sources of renewable energy. Electricity production from renewable energy is free from pollution and its cost also less. The energy extraction from the sun is increasing, because of abundantly available solar energy. Multilevel inverter with solar PV system is widely used in applications like stand-alone systems and grid- connected system [1]. There are two types of inverters which are commonly used for solar application. One is a conventional two-level and three-level inverter used in a solar PV system for stand-alone and grid-tied mode. The drawback of the conventional inverter is having high Total Harmonic Distortion (THD) and excess voltage stress on the inverter switches. Hence, for the minimization of THD in the inverter current, required high switching frequency operated system [2, 3]. These higher switching frequencies further leads to higher switching losses.

In recent years, various MLI topologies are using grid-tied PV systems because of having numerous advantages over conventional inverters. The significant features of the MLI are low voltage stress on the inverter switching devices, lower THD,

H. Myneni (✉)
National Institute of Technology Srinagar (NITSRI), Srinagar, India

A. Pranay Kumar
KITS Warangal, Warangal, India

S. A. Mandale
Toshiba Mitsubishi-Electric Industrial Systems Corporation (TMEIC), Bengaluru, India

G. Siva Kumar
National Institute of Technology Warangal (NITW), Warangal, India

S. Kumar et al. (eds.), *Recent Advances in Power Electronics and Drives*, Lecture Notes in Electrical Engineering 852, https://doi.org/10.1007/978-981-16-9239-0_10

lesser Electro-Magnetic Interference (EMI), and reduce switching frequency [4]. The MLI name itself says that multiple number of voltage levels which is more than conventional (i.e., greater than three). The requirement of switching devices also increases to generate additional voltage levels. The increase in switching devices increases the size and complexity of the inverter. This drawback can be overcome by using reduced switching devices count MLI. There are numerous MLI topologies which are having reduced switching devices count [4, 5]. In this work, a grid-tied solar PV system is implemented with the reduced switching device count asymmetrical MLI [6, 7]. In the past decade, several MLI topologies with reduced switch count are used in power electronic applications [4, 5]. In the asymmetrical MLI configuration, both unidirectional and bidirectional switching devices are used. These switching devices increase the voltage levels of the seven-level inverter output voltage by giving proper switching pulses. More voltage levels will be generated at reduced switching device count using asymmetrical MLI configuration [6]. The asymmetrical MLI configuration also minimizes the systems' cost.

In literature, various PWM techniques are proposed to control current injection, reduce switching losses, and THD [8]. Among these techniques, the sinusoidal PWM technique is the most commonly used technique and further it is classified into level shifted PWM and phase shifted PWM techniques [9, 10]. In this paper, level shifted PWM (LS-PWM) technique for seven-level asymmetrical MLI is used. The grid current injection and maintaining power factor at unity is done with a proportional integral (PI) controller-based LS-PWM technique [6]. The comparative study of LS-PWM with PI controller and Model Predictive Control (MPC) algorithm is studied and simulation results are verified. The application of MPC techniques to control the power electronic applications is a versatile method [11]. In this technique, variables' future behavior will be predicted to analyze the control variable. Depending on the control variable, cost function is defined in MPC. In this method, MPC is basically used to control the injection of grid current and maintain the unity power factor with reduced switching frequency [12, 13]. The load current reactive component is also controlled by the MPC algorithm. Solar photovoltaic (PV) system with multilevel inverter is widely used in applications like grid-connected and stand-alone systems. The grid-connected multilevel inverter has the drawback of power quality, so for improving the power quality, the controlled reactive power injection is needed. The power quality issue is minimized by the proposed model predictive active and reactive power control method [14, 15].

In this paper, Sect. 2, describes the detailed analysis of asymmetrical MLI with LS-PWM technique and also an explanation of the PI controller-based closed-loop algorithm to control the required variables. In Sect. 3, the study of MPC and control algorithm for maintaining unity power factor and to control the injected grid current at the reduced switching frequency. Section 4 describes, the controlling of active and reactive power at reduced switching frequency. The simulation results of the proposed control algorithm are discussed in Sect. 5. At the end, the conclusion is presented in Sect. 6.

2 Grid-tied PV System with Asymmetrical Multi Level Inverter

An asymmetrical MLI topology with a reduced switching device count is shown in Fig. 1. It consists of four unidirectional switches (T_1, T_2, T_3, T_4) and two bidirectional switches (S_1, S_2) to produce seven-level waveform. This MLI topology having two DC-link voltage sources which are not equal in magnitude. The voltage magnitude of DC-link sources is in the proportion such as 1:2 (*i.e.*, $V_{dc1} : V_{dc2} = V_{dc} : 2V_{dc}$).

For achieving all possible combination of the voltage levels in an asymmetrical MLI, a proper switching of devices is mandatory. The switching status of each switch for the generation of seven voltage levels of magnitude $3V_{dc} = V_{dc1} + V_{dc2}$, $2V_{dc} = V_{dc2}$, $V_{dc} = V_{dc1}$, 0, $-V_{dc} = -V_{dc1}$, $-2V_{dc} = -V_{dc2}$, and $-3V_{dc} = -(V_{dc1} + V_{dc2})$ are shown in Table 1. The voltage level of $3V_{dc} = V_{dc1} + V_{dc2}$ will be achieved by an additive series combination of two dc-link voltage sources V_{dc1} and V_{dc2}. To attain these voltage level, switches T_1 and T_4 should be ON. Similarly, for the generation of the $2V_{dc}$ voltage level, switch T_1 and S_2 should be ON. In case if the switches T_4 and S_1 are ON, the V_{dc} voltage level will be obtained. Fundamental positive half cycle of the inverter output voltage is generated by conducting T_1 and T_4. Similarly, the switches T_2 and T_3 are responsible for the generation of the fundamental negative half cycle of the inverter output volatge. Application of LS-PWM technique to generate the switching states using LS-PWM is explained below.

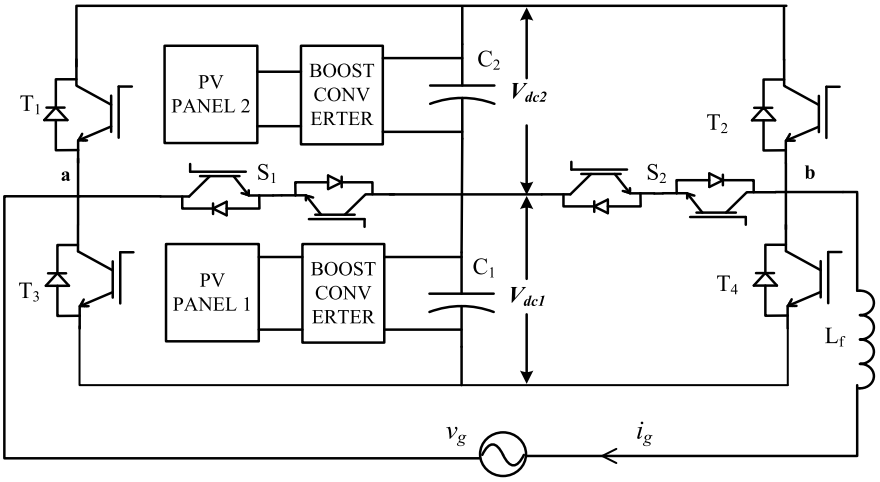

Fig. 1 Grid-tied PV system with seven-level asymmetrical MLI configuration

Table 1 Voltage levels corresponding to switching devices status in the inverter with '1' as ON, '0' as OFF

Voltage level	Switching status					
	T_1	T_2	T_3	T_4	S_1	S_2
$3V_{dc}$	1	0	0	1	0	0
$2V_{dc}$	1	0	0	0	0	1
V_{dc}	0	0	0	1	1	0
0	0	0	1	1	0	0
	1	1	0	0	0	0
	0	0	0	0	1	1
$-V_{dc}$	0	0	1	0	0	1
$-2V_{dc}$	0	1	0	0	1	0
$-3V_{dc}$	0	1	1	0	0	0

2.1 Carrier-Based LS-PWM Technique

Carrier-based LS-PWM technique has been implemented for the seven-level grid-tied asymmetrical MLI. In carrier-based LS-PWM technique, for the generation of n-level inverter, $(n-1)$ high-frequency triangular carriers will be required. Hence, six high-frequency triangular carrier signals should be required to generate the gale pulses for seven-level inverter. Each carrier is compared with a reference signal to produce the switching state pulses.

The amplitude modulation index of fixed magnitude of the carrier-based LS-PWM technique is defined as,

$$m_a = \frac{m_r}{m_c} \tag{1}$$

where, m_a is defined as the amplitude modulation index which is the ratio of the peak value of reference sinusoidal signal (m_r) to the peak value of high-frequency carrier signal (m_c).

2.2 Control Strategy for Grid-Tied Asymmetrical MLI Based Solar Photo Voltaic System

The grid current reference magnitude depends on the magnitude of available PV power. It is required to track the frequency of the grid voltage to maintain power factor as unity and to generate the grid current reference (i_g^*). To achieve this, the

proposed technique is incorporated with phase locked loop (PLL). The difference between reference (i_g^*) and actual measured grid current (i_g) is passed through a proportional integral (PI) controller. The gains of PI controller K_p, K_c are tuned to produce switching signals for MLI [16]. In this way, the unity power factor is maintained on the grid side and the PV power is injected to the grid. There are two types of control algorithms that are implemented and explained below.

3 Principle of Model Predictive Controller

There are so many control techniques that have been developed, among these control techniques, MPC is more efficient than the conventional techniques [17, 18]. The MPC has many advantages, such as being easy to understand, implement and multiple variables can be controlled. Future behavior of the control variables is predicted using model of the system. These are achieved by minimizing the cost function. The cost function basically consists of the difference between the predicted and reference control variable. A discrete state-space model is used in MPC, which is as follows:

$$\begin{aligned} X(K+1) &= AX(K) + BU(K) \\ Y(K+1) &= CX(K) + DU(K) \end{aligned} \tag{2}$$

For getting discrete time model, discretization methods are used. Euler forward method is used to approximate the derivative for first-order system

$$\frac{\mathrm{d}y}{\mathrm{d}x} = \frac{x(k+1) - x(k)}{T_s} \tag{3}$$

where, T_s is the sampling time. This Euler forward method to approximate the derivative. The desired behavior of system is expressed in cost function as follows:

$$J = f(x(k), u(k), ...u(k+N)) \tag{4}$$

The value of the weighing factor is decided according to the priority of each term in the cost function and it is used to control the variable. In MPC, the behavior of these control variables is predicted for all possible combination switching states and the value of cost function is calculated for all switching states, and finally optimal state is selected which minimizes the cost function. That switching state is called optimal switching state which is applied to the switches of MLI.

4 Proposed Control Algorithm

Figure 2 shows the control block diagram of the proposed MPC with an asymmetrical seven-level MLI. MPC consists of future value prediction block that will generate future behavior of controlled variables $i(k+1)$ signal using measured actual controlled variables $i(k)$ signal. The MPC will select optimal switching state from available states (S) by evaluating the minimized cost function (S). The optimal switching state (S) is applied to control the behavior of the controlled variables.

4.1 Predictive Grid Current Tracking and Maintain UPF

In the proposed predictive current control technique, the behavior of the control variables is predicted for seven switching states of inverter model of the system. Evaluation of the minimized cost function is done and the selected optimal switching state is applied to the inverter. The primary objective of the proposed current control is to track the reference grid current and maintaining power factor as unity. The cost function is defined for achieving this objective as follows:

$$g = |i_r^*(k+1) - i_p(k+1)|. \tag{5}$$

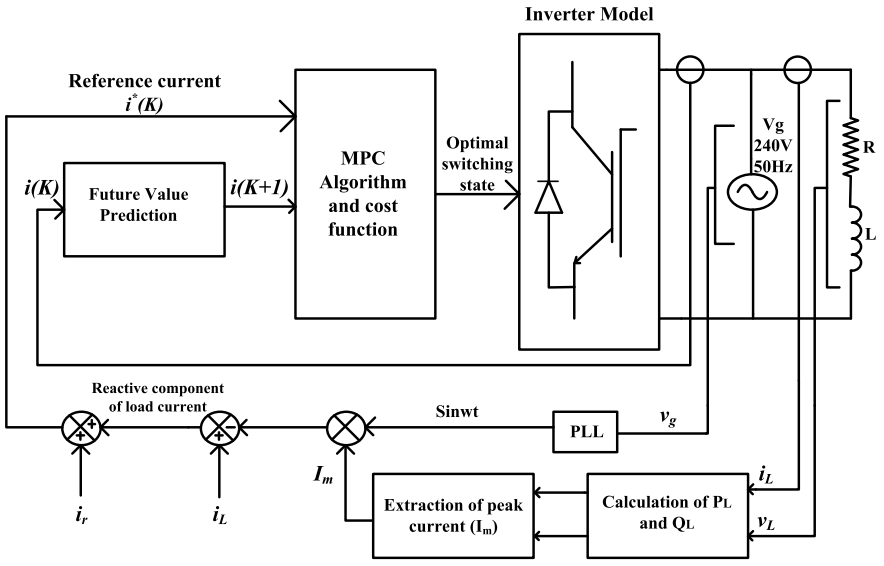

Fig. 2 Proposed model predictive control block diagram

where, $i_r^*(k+1)$ represents the grid current reference values and $i_p(k+1)$ is the predicted value of grid current. For the calculation of the $i_p(k+1)$ i.e., predicted value of grid current from the grid voltage and measured grid current, discrete time model will be used. Forward Euler approximation is used to approximate grid current derivative di_p/dt and is given as

$$\frac{\mathrm{d}i_p}{\mathrm{d}t} = \frac{i_p(k+1) - i_p(k)}{T_s}. \tag{6}$$

By applying KVL to the grid-connected inverter model

$$v(k) = L\frac{\mathrm{d}i_p}{\mathrm{d}t} + Ri_p(k) + e(k). \tag{7}$$

By solving, an expression for the prediction of future grid current for every seven switching states by considering the voltage vectors of the inverter $v(k)$ and grid $e(k)$ is

$$i_p(k+1) = \frac{(v(k) - e(k))T_s}{L} + i_p(k)\Big(1 - \frac{RT_s}{L}\Big). \tag{8}$$

From the above expression, prediction of future grid current is evaluated and which is used to evaluate the cost function consists of the difference between reference and predicted grid current vector for each seven switching states. From the available seven switching states, the optimal switching state gives the minimized cost function and it is applied to the inverter model.

4.2 Controlling of Active and Reactive Powers Using MPC

The flow of active and reactive powers in a PV supported grid-connected system is controlled in the proposed MPC. In MPC technique, the load currents are used to extract the reference current. In general, the load current $i_L(t)$ can be expressed as

$$\begin{aligned} i_L(t) = {} & I_{dc} + I_{m1}\sin(wt + \phi_1) + I_{m2}\sin(2wt + \phi_2) \\ & + I_{m3}\sin(3wt + \phi_3) + ...I_{mn}\sin(nwt + \phi_n). \end{aligned} \tag{9}$$

In the above equation 'mn' indicates the nth harmonics peak value and ϕ_n indicates phase angle of the load current $i_L(t)$. The power consumed is given below.

$$P_s = (V_{m1}I_{ms}\cos\phi_s)/2 \tag{10}$$

where, V_{m1} represents the fundamental peak value of the supply voltage and I_{ms} is the reference source currents peak value. The peak value of reference source current (I_{ms}) from (10) is given as

$$I_{ms} = 2P_s/(V_{m1}\cos\phi_s) \tag{11}$$

The time domain reference source current is expressed by

$$i_s^*(t) = I_{ms}\sin(wt - \phi_s) \tag{12}$$

Finally, from (9) and (12), for controlling the reactive component of load current the reference current is expressed as

$$i_f^*(t) = i_L(t) - i_s^*(t) \tag{13}$$

The injecting current equal to reference current (i_f^*) by MLI with model predictive control, unity power factor is achieved on grid side. In order to inject active power to the grid, first, calculate the reference current corresponding to PV power. Suppose, the reference current corresponding to PV power is i_{pv}^*, the resultant reference for MLI is $i_{pv}^* + i_f^*$. This resultant reference current controls active and reactive powers which are injected into the grid.

4.3 Switching Frequency Reduction

In this method, switching frequency reduction is one of the control variables along with current control and power control. In which, the error between present and previous switching state is considered as cost function to achieve reduced switching frequency. For all seven switching states (S), the cost function has been calculated and the switching state that gives minimal cost function value is called as optimal cost function. The optimal cost function is applied to the seven-level inverter model.

In this paper, the control technique is implemented to fulfill power quality enhancement and PV power injection into the grid. To achieve these aspects, a model predictive controller is implemented. This method gives the advantage of reduced switching frequency when compared to conventional methods. The simulation results of LS-PWM technique with PI type current controller performance are compared with the proposed MPC technique.

5 Simulation Results

The proposed reduced switching frequency model predictive control algorithm of asymmetrical MLI is simulated in MATLAB/Simulink and corresponding simulation parameters are mentioned in Table 2. In simulation analysis, an asymmetrical grid-

Table 2 Simulation parameters

Parameters	Values
Grid voltage	240 V rms
Grid frequency	50 Hz
Load resistance (R)	14 Ω
Load inductance (L)	22 mH
Interfacing inductance (L_f)	12 mH
dc-link capacitance (C_1, C_2)	3600 μF

connected MLI with RL load connected in parallel with the grid consisting of two DC voltage sources in the proportion of 1:2 is considered. In the simulation results, mainly focusing on two control algorithm, i.e., controlling of active and reactive powers using MPC technique and second is the reduction of switching frequency.

5.1 Only Reactive Power Control Technique

Reactive power control technique has been implemented to reduce the power quality issues. In this control technique, the main control variable is reactive power injected by the inverter into the load. In this case, the active component of load current is supplied by the grid. It implies that the grid current (i_g) is in phase with grid voltage (v_g), such that the unity power factor will be maintained.

The inverter voltage (v_{inv}), inverter current (i_{inv}), grid current (i_g), grid voltage (v_g), and load current (i_{load}) in case of only reactive power injection are shown in Fig. 3. It is observed that the inverter current (i_{inv}) supplied by the inverter is phase shifted by 90° to the inverter output voltage (v_{inv}). It implies that the reactive component of load current is injected by the inverter and the active component is injected by the grid.

Figure 4a shows the simulation results of current tracking of actual current and the reference sinusoidal current under only reactive power control. It is observed from zoomed part of Fig. 4a that, the tracking is perfect with the proposed method. Figure 4b shows the real and reactive powers injected by the inverter (P_{inv} and Q_{inv}), and the grid real and reactive powers (P_g and Q_g) to the load. The reactive power required for load is supplied by the inverter, that's why grid reactive power (Q_g) is zero. At the same time, the inverter is not injecting any real power. However, it draws a small amount of real power from the grid to supply losses in the inverter, that's why P_{inv} value is negative as shown in Fig. 4b.

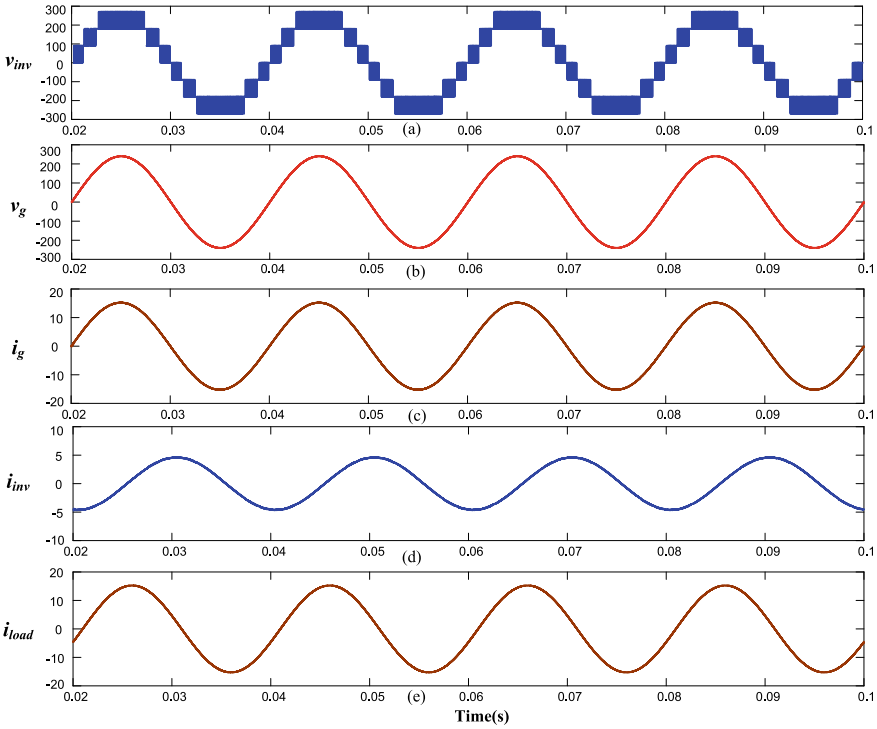

Fig. 3 During only reactive power control: seven-level inverter voltage (v_{inv}), grid voltage (v_g), grid current (i_g), injected current by the inverter (i_{inv}) and load current (i_{load}) under reactive power control; (scale: X-axis in seconds, Y-axis voltage in volts, current in ampere)

5.2 Real and Reactive Power Control Technique

A real-reactive power control means controlling of total power supplied by the inverter which is required for the load. In this control algorithm, the requirement of load power has been supplied by the inverter, which implies that the inverter is extracting maximum power. In this case, the power supplied by the grid will be zero or negligible. In case if the inverter is not capable to supply the total amount of required load power, the leftover power is supplied by the grid. In the model predictive direct power control algorithm, only the required amount of total load power will be extracted from the inverter.

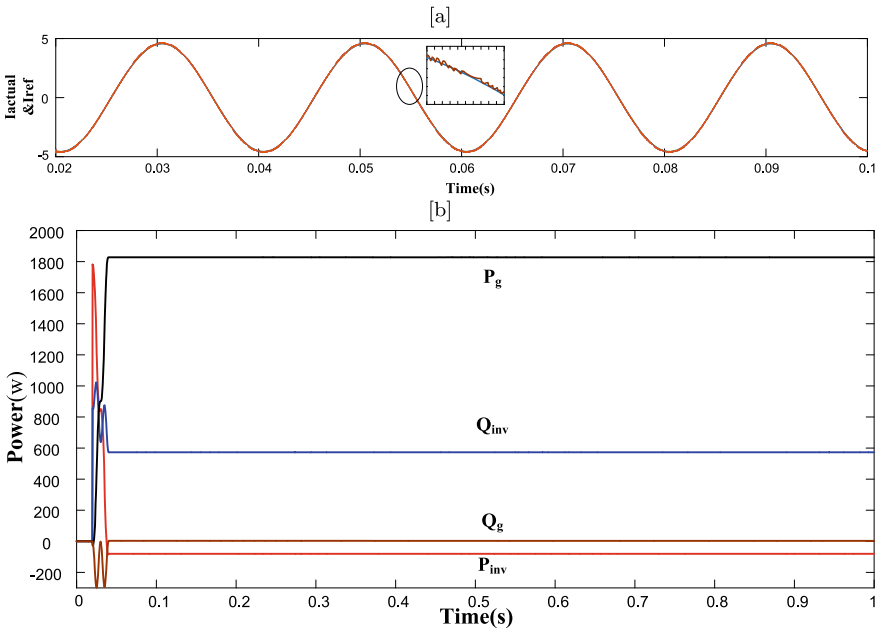

Fig. 4 **a** Current tracking under reactive power control only (scale: X-axis in seconds, Y-axis in Ampere); **b** real and reactive powers of grid and inverter

Figure 5 shows, the simulation results of the inverter voltage (v_{inv}), grid voltage (v_g), grid current (i_g), inverter current (i_{inv}) and load current (i_{load}), respectively.

It is observed from Fig. 5 that grid current is very small in magnitude, which implies that the power supplied by the grid to the load is also negligible. In this case, the total power required for the load is injected by the inverter only. Therefore, the inverter current (i_{inv}) and load current (i_{load}) are equal in magnitude, it can be observed from Fig. 5.

Figure 6a shows the simulation results of current tracking of actual current and the reference current under the real-reactive power control. It is observed from Fig. 6a that, the tracking of reference with the proposed method is well and good. Figure 6b shows the power injected by the inverter and grid to the load. In this case, the active and reactive power injected by the inverter (P_{inv}) and (Q_{inv}) is equal to the required load power. Therefore, real power (P_g) and reactive power (Q_g) supplied by the grid to the load is zero as shown in Fig. 6b.

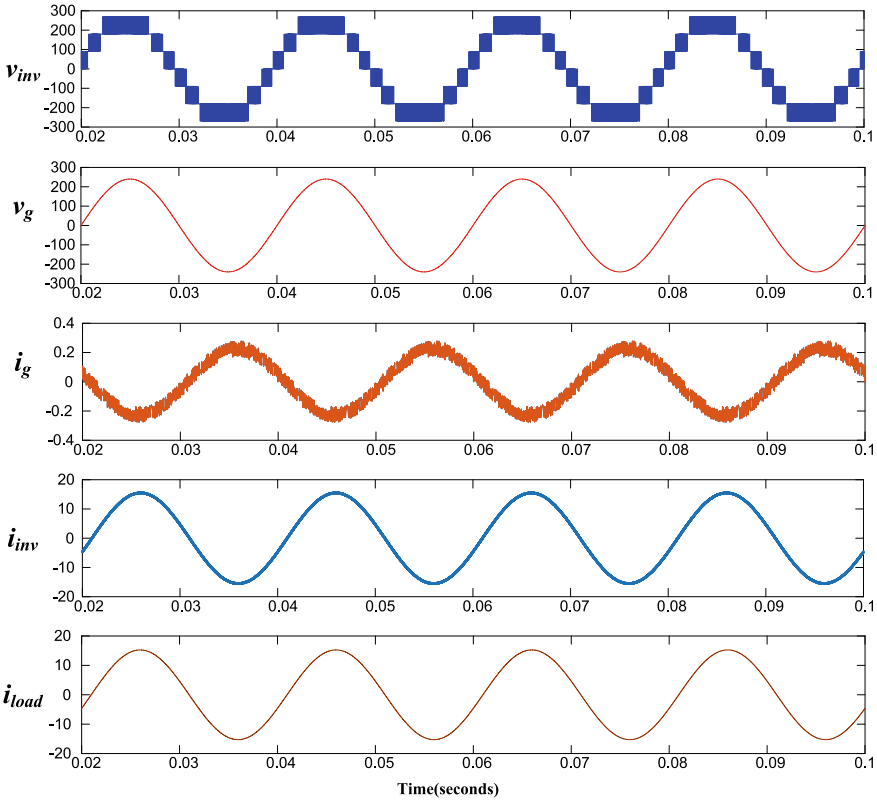

Fig. 5 During real and reactive power control: sevel-level inverter voltage (v_{inv}), grid voltage (v_g), grid current (i_g), injected current by the inverter (i_{inv}) and load current (i_{load}) under real-reactive power control; (scale: X-axis in seconds, Y-axis voltage in volts, current in ampere)

5.3 *Load Variation*

The main motivation of load variation is to analyze the dynamic performance of the proposed model predictive control under different powers injection. The proposed model predictive control requires less time to get stable when compared to conventional methods. Figure 7 shows the simulation results under load variation at t = 1 s and t = 1.05 s. It is observed that for both the instants of load variation within one and a half cycle, the grid current and inverter current reaches a steady state.

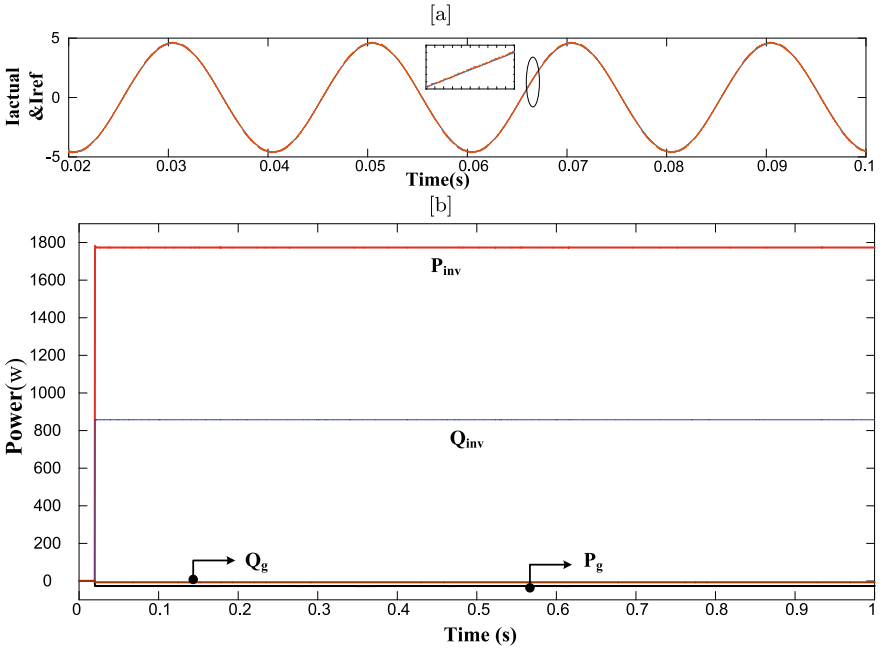

Fig. 6 **a** Current tracking under real-reactive power control (scale: X-axis in seconds, Y-axis in Ampere); **b** real and reactive powers of grid and inverter

Under the variable of load condition, the reference current (i_{ref}) and actual current (i_{actual}) of inverter are shown in Fig. 8a. It is observed that the current tracking capability of the proposed control technique is excellent, which implies the faster dynamics response of the proposed predictive control algorithm. The real and reactive powers of inverter and grid under variable load conditions are shown in Fig. 8b.

5.4 Reduction of Switching Frequency

The proposed reduced switching frequency model predictive control algorithm of asymmetrical MLI is simulated. Table 3 presents the reduced switching frequencies (Hz) for each switching device. Table 3 shows the switching frequency in Hz for all six switching devices with and without switching frequency constraints. The switching frequency is reduced with adding frequency constraint when compared to without constraint. Even though, the THD of the grid current increases, it is less than the specified limit of 5% (IEEE-519 standard).

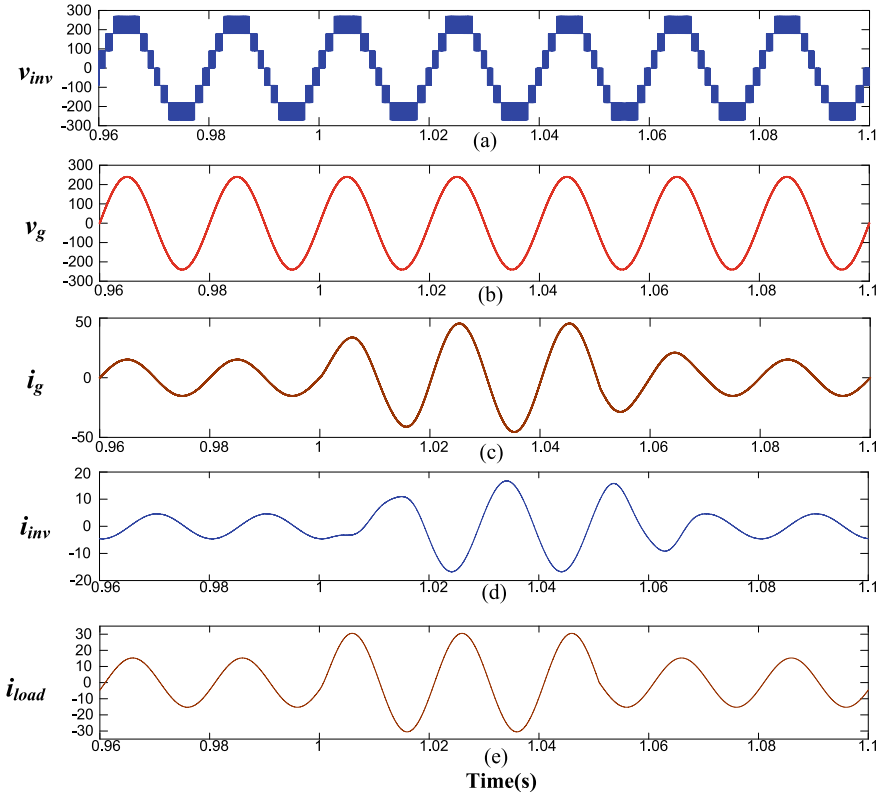

Fig. 7 Simulation results under load variation: seven-level inverter voltage (v_{inv}), grid voltage (v_g), grid current (i_g), injected current by the inverter (i_{inv}), and load current (i_{load}); (scale: X-axis in seconds, Y-axis voltage in volts, current in ampere)

6 Conclusion

In the proposed work, the performance of seven-level asymmetrical Multi-Level Inverter (MLI) under the controlled injection of the grid current with accurate tracking capability is analyzed. Also, the control of active power and reactive power by using a model predictive controller is discussed at reduced switching frequency. The performance of the proposed model predictive control (MPC) is analyzed under the variable weighting factor. The controlled active and reactive power injection at reduced switching frequency to maintain the Unity Power Factor (UPF) on the grid side is analyzed and the discussion on simulation results is done in this paper. It has been concluded that the variation of the weighting factor leads to the weightage of

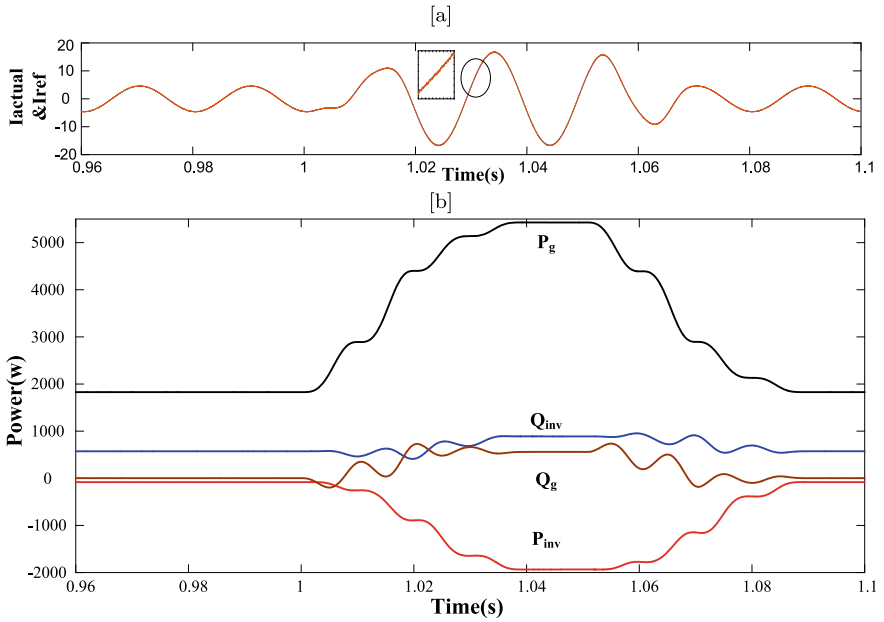

Fig. 8 **a** Current tracking under load variation (scale: X-axis in seconds, Y-axis in Ampere); **b** real and reactive powers of grid and inverter

Table 3 Switching frequency (Hz) and grid current THD (%) without and with adding switching frequency constraint

Number of constraints	Switching frequency (Hz)						Grid current THD
	T_1	T_2	T_3	T_4	S_1	S_2	
Without switching frequency constraint	3050	3050	10900	11050	13093	14100	0.34%
With adding switching frequency constraint	1411	1383	3397	3478	4156	4205	2.63%

the controlled variable implies the reduction of switching frequency with accurate current tracking capability. The proposed model predictive control was also tested under the variable load condition to analyze the dynamic performance of the MPC.

References

1. El-Hawary ME (2014) The smart grid-state-of-the-art and future trends. Electr Power Compon Syst 42(3–4):239–250
2. Alepuz S, Busquets-Monge S, Bordonau J, Gago J, González D, Balcells J (2006) Interfacing renewable energy sources to the utility grid using a three-level inverter. IEEE Trans Ind Electron 53(5):1504–1511
3. Patrao I, Garcerá G, Figueres E, González-Medina R (2014) Grid-tie inverter topology with maximum power extraction from two photovoltaic arrays. IET Renew Power Gener 8(6):638–648
4. Gupta KK, Ranjan A, Bhatnagar P, Sahu LK, Jain S (2015) Multilevel inverter topologies with reduced device count: a review. IEEE Trans Power Electron 31(1):135–151
5. Babaei E (2008) A cascade multilevel converter topology with reduced number of switches. IEEE Trans Power Electron 23(6):2657–2664
6. Das MK, Jana KC, Sinha A (2017) Performance evaluation of an asymmetrical reduced switched multi-level inverter for a grid-connected PV system. IET Renew Power Gener 12(2):252–263
7. Rahim NA, Chaniago K, Selvaraj J (2010) Single-phase seven-level grid-connected inverter for photovoltaic system. IEEE Trans Ind Electron 58(6):2435–2443
8. Bhavsar T, Narayanan G (2009) Harmonic analysis of advanced bus-clamping PWM techniques. IEEE Trans Power Electron 24(10):2347–2352
9. McGrath BP, Holmes DG (2002) Multicarrier PWM strategies for multilevel inverters. IEEE Trans Ind Electron 49(4):858–867
10. Chavarria J, Biel D, Guinjoan F, Meza C, Negroni JJ (2012) Energy-balance control of PV cascaded multilevel grid-connected inverters under level-shifted and phase-shifted PWMs. IEEE Trans Ind Electron 60(1):98–111
11. Kouro S, Cortés P, Vargas R, Ammann U, Rodríguez J (2008) Model predictive control—a simple and powerful method to control power converters. IEEE Trans Ind Electron 56(6):1826–1838
12. Kwak S, Kim SE, Park JC (2015) Predictive current control methods with reduced current errors and ripples for single-phase voltage source inverters. IEEE Trans Ind Electron 11(5):1006–1016
13. Mathew D, Shukla A, Bandyopadhyay S (2016) Modified predictive current control of neutral-point clamped converter with reduced switching frequency. In: IEEE applied power electronics conference and exposition (APEC) 2016, pp 3286–3290. IEEE
14. Bozorgi AM, Gholami-Khesht H, Farasat M, Mehraeen S, Monfared M (2018) Model predictive direct power control of three-phase grid-connected converters with fuzzy-based duty cycle modulation. IEEE Trans Ind Appl 54(5):4875–4885
15. Latifi M, Sabzehgar R, Rasouli M, Fajri P (2019) Active and reactive power compensation using a PEV-based three-level capacitor clamped inverter. In: IEEE Texas power and energy conference (TPEC) 2019, pp 1–6
16. Myneni H, Ganjikunta SK (2021) Design, analysis, and switching losses reduction of hybrid shunt compensator with adaptive control scheme. Int Trans Electr Energ Syst 31
17. Garcia CE, Prett DM, Morari M (1989) Model predictive control: theory and practice-a survey. Automatica 25(3):335–348
18. Kumar AP, Kumar GS, Sreenivasarao D, Myneni H (2019) Model predictive current control of DSTATCOM with simplified weighting factor selection using VIKOR method for power quality improvement. IET Gener, Transm Distrib 13(16):3649–3660

Modelling and Control Aspects of STATCOM Connected to a Grid-Integrated PV System

Koneti Varalakshmi, R. L. Narasimham, and G. Tulasi Ramdas

1 Introduction

In an AC microgrid system, different reactive as well as nonlinear loads consume reactive power. Adequate control of reactive power can solve many different problems which arise in an AC power system. Very good review articles on reactive power compensation system can be found in [1–4]. Reactive power compensation has two different aspects such as (a) load compensation and (b) voltage support. STATCOM is a shunt-connected CPD which is capable of providing compensating effect to current associated with power quality events. STATCOM is generally a voltage source inverter (VSI) which comprises of DC source and different power electronic switches (IGBT). The inclusion of STATCOM has numerous benefits in microgrid system [5]. Nowadays a lot of research is carried out to design efficient topology and control mechanism for STATCOM. Integration of distributed energy resources (DERs) provide a significant benefit to the existing power system in terms of voltage profile. Grid-connected PV system provides significant benefit, but grid-connected PV system is only operational at day time and remains idle at night time which reduces the efficiency and utilization aspect of the system. STATCOM is combined with PV system to increase the utilization and efficiency of the system as well as provide reactive power compensation to the grid. Generally, classical 2-level inverter is used as STATCOM and coupling transformer or inductor is used for connecting the

K. Varalakshmi (✉)
Department of Electrical and Electronics Engineering, Aditya College of Engineering and Technology, Surampalem, Andhra Pradesh, India

R. L. Narasimham
Department of Electrical Engineering, Andhra University, Visakhapatnam, India

G. Tulasi Ramdas
Department of Electrical and Electronics Engineering, Jawaharlal Nehru Technological University Hyderabad, Hyderabad, Telangana, India

S. Kumar et al. (eds.), *Recent Advances in Power Electronics and Drives*, Lecture Notes in Electrical Engineering 852, https://doi.org/10.1007/978-981-16-9239-0_11

grid with STATCOM. There are different topologies, as well as control schemes, for STATCOM. The DC-link voltage of STATCOM is controlled using different control scheme such as PID controller, vector controller, model predictive controller, fractional controller and intelligent controller.

This paper provides the mathematical modelling and analysis of grid-integrated PV system along with STATCOM. Different modes of STATCOM and the operation of STATCOM in an AC microgrid have been discussed in this paper. Detailed mathematical modelling and controller design has been done for the system where the current control scheme is used for the control of STATCOM and the MPPT scheme is used to extract maximum power from PV panel. Simulation analyses have been provided to validate the theoretical explanation.

The paper is organized as follows. Section 2 provides the operation of STATCOM in a microgrid. Section 3 presents the overall system description of grid-integrated PV system along with STATCOM. Section 4 presents the control scheme for PV-fed boost converter as well as STATCOM. Section 5 presents the simulation results and Sect. 6 provides the concluding remarks.

2 STATCOM Operations in Microgrid

The different operating modes of STATCOM are as follows [6]:

- **Partial STATCOM mode**: This mode is used during the daytime when the inverter provides reactive power to the grid. The most priority is given to the real power during partial STATCOM mode.
- **Full STATCOM mode**: Full STATCOM mode is required when there is some sort of faults, disturbances, etc., and there is an urgent need for reactive power support. In this mode, the PV system discontinues the generation and real power and provides reactive power via the inverter. Full STATCOM mode is completely used during nighttime. The discontinuation of real power during daytime via STATCOM is done by a solid state relay that disconnects the PV panel.
- **Full PV mode**: Solar system generates real power without the requirement of reactive power.

3 System Description

The complete circuit diagram and control scheme of grid-integrated PV system along with STATCOM has been shown in Fig. 1. Figure 1 comprises of an array of PV cells, DC-DC boost converter. As PV voltage is variable to change in solar irradiance and ambient temperature, maximum power point tracking (MPPT) unit along with a voltage regulation unit is placed to extract maximum power from the PV module. Boost converter is used to step-up the voltage of PV module and switching signal to

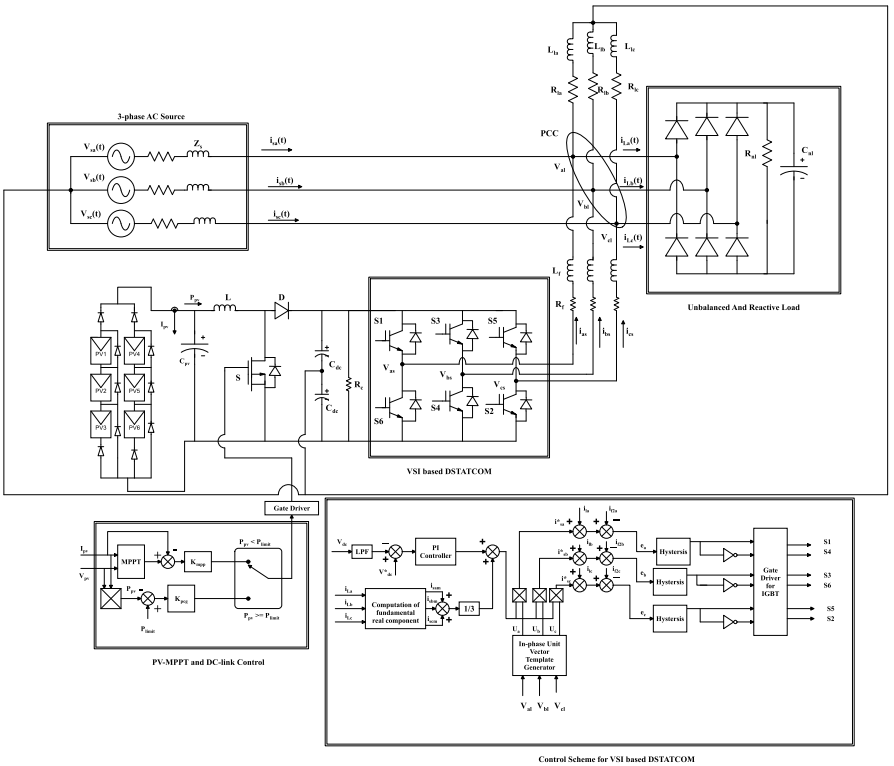

Fig. 1 Circuit diagram and control scheme of PV-STATCOM

boost converter is provided by the MPPT unit. DC-link capacitors (split capacitors) are connected in the output terminal of the boost converter to maintain the constant DC-link voltage. STATCOM is modelled as 3-ϕ-2-level,2-leg, six-pulse IGBT power semiconductors with antiparallel freewheeling diode based DC-AC voltage source inverter operating at a switching frequency f_{sw}. Output current of STATCOM is represented as i_{as}, i_{bs} and i_{cs}. STATCOM is connected to the middle point of transmission line at point of common coupling (PCC) via interfacing filter L_f. To suppress any additional ripple of STATCOM, ripple filters can also be placed. The gate-pulse of the STATCOM is provided by the control unit of STATCOM. 3-ϕ-4-wire AC source represented as V_{sa}, V_{sb} and V_{sc} having an impedance of Z is connected to linear as well as nonlinear load via PCC. AC-DC bridge rectifier with capacitive filter is considered as the nonlinear load. The voltage at PCC is represented as V_{al}, V_{bl} and V_{cl}.

3.1 PV Array

The dynamics of a practical PV cell can be represented as

$$I = I_{pv} - I_o \left[\exp\left(\frac{V + R_s I}{V_t a} \right) - 1 \right] - \frac{V + R_s I}{R_p} \tag{1}$$

where PV current is represented by I_{pv}, saturation current is represented by I_o, parallel resistance of PV cell is R_p, series resistance of PV cell is R_s and thermal voltage of PV cell is V_t

3.2 VSI Based STATCOM

The 3-ϕ dynamic model of STATCOM can be represented as

$$\begin{aligned} L_f \tfrac{di_{La}}{dt} &= -R_f i_{sta} + V_{as} - V_{al} \\ L_f \tfrac{di_{Lc}}{dt} &= -R_f i_{stb} + V_{bs} - V_{bl} \\ L_f \tfrac{di_{Lc}}{dt} &= -R_f i_{stc} + V_{cs} - V_{cl} \end{aligned} \tag{2}$$

$$\frac{d}{dt}\left(\frac{1}{2} C_{dc} V_{dc}^2 (t) \right) = -\left(V_{as} i_{as} + V_{bs} i_{bs} + V_{cs} i_{cs} \right) - \frac{V_{dc}^2}{R_c} \tag{3}$$

Using *abc* to *dq* transformation

$$\frac{d}{dt} \begin{bmatrix} i_{ds} \\ i_{qs} \\ V_{dc} \end{bmatrix} = \begin{bmatrix} -\frac{R_f}{L_f} & \omega & \frac{K}{L_f} \cos\alpha \\ -\omega & -\frac{R_f}{L_f} & \frac{K}{L_f} \sin\alpha \\ -\frac{3K}{2C_{dc}} \cos\alpha & -\frac{3K}{2C_{dc}} \sin\alpha & -\frac{1}{R_c C_{dc}} \end{bmatrix} \begin{bmatrix} i_{ds} \\ i_{qs} \\ V_{dc} \end{bmatrix} \tag{4}$$

The design of AC interfacing inductor L_f is as follows:

$$L_f = \frac{\sqrt{3} m V_{dc}}{12 a f_{sw} i_{cr(p-p)}} \tag{5}$$

where m is the modulation index, a is the overloading factor, V_{dc} is the DC-link voltage, $i_{cr(p-p)}$ is 15%, f_{sw} is the switching frequency.

4 Control Scheme for PV-Integrated STATCOM

4.1 MPPT and DC-Link Control

Based on voltage and current measurement at each step, power is computed. The P&O MPPT steps the panel voltage along the P–V curve such that voltage at MPP can be reached. The step-size of P&O MPPT is large enough due to settling issues of converter dynamics. P&O MPPT with PID controller is one of the widely used technique which provides a relatively stable results for power point tracking of PV module [7, 8].

At MPP

$$\frac{dP_{pv}}{dV_{pv}} = 0 \Rightarrow V_{pv}\frac{dI_{pv}}{dt} + I_{pv}\frac{dV_{pv}}{dt} = 0 \tag{6}$$

Equation 6 can be re-written as

$$V_{pv}\frac{dI_{pv}}{dt} + I_{pv} = 0 \tag{7}$$

At any point other than MPP

$$V_{pv}\frac{dI_{pv}}{dt} + I_{pv} = \psi; \psi \neq 0 \tag{8}$$

Dynamic resistance of PV panel can be represented as

$$r_{pv} = -\frac{dV_{pv}}{dI_{pv}} \tag{9}$$

Using dynamic resistance of PV panel, we get

$$I_{pv} - \frac{V_{pv}}{r_{pv}} = \psi \tag{10}$$

Figure 2 provides the control scheme of STATCOM connected to a grid-integrated PV system.

4.2 Generation of Reference Current Source

The reference compensating current are calculated by subtracting load current from reference source current

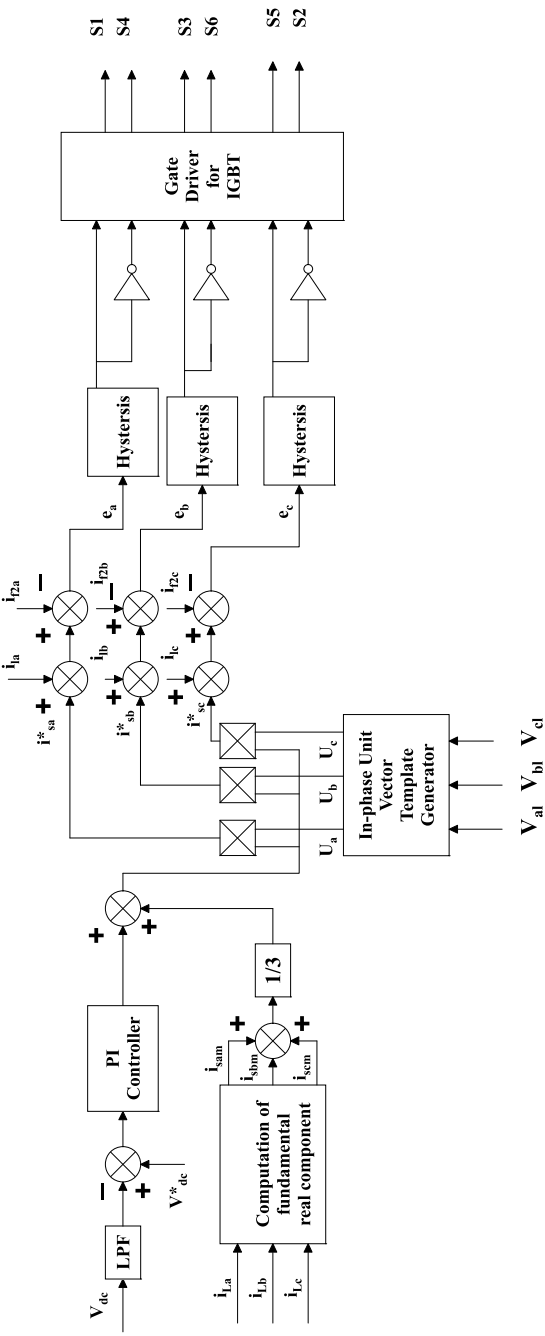

Fig. 2 Control scheme of STATCOM connected to a grid-integrated PV system

$$
\begin{aligned}
i_{L_a} &= I_{La1} \sin(\omega t - \phi_{a1}) + \sum_{n=2}^{\infty} I_{Lan} \sin(n\omega t - \phi_{an}) \\
i_{L_b} &= I_{Lb1} \sin(\omega t - \phi_{b1}) + \sum_{n=2}^{\infty} I_{Lbn} \sin(n\omega t - \phi_{bn}) \\
i_{L_c} &= I_{Lc1} \sin(\omega t - \phi_{c1}) + \sum_{n=2}^{\infty} I_{Lcn} \sin(n\omega t - \phi_{cn})
\end{aligned} \tag{11}
$$

The active component of load current are

$$
\begin{aligned}
I_{sam} &= |I_{La1}| \cos \phi_1 \\
I_{sbm} &= |I_{Lb1}| \cos \phi_1 \\
I_{scm} &= |I_{Lc1}| \cos \phi_1
\end{aligned} \tag{12}
$$

DC-link voltage is measured and passed through a low pass filter with transfer function $\left(G(s) = \frac{1}{1+\tau_f s}\right)$ is used. Error detector is used to get the error signal which is then provided to the proportional-integral (PI) controller which can be represented as

$$
G_c(s) = \frac{u(s)}{e(s)} = K_p + \frac{K_i}{s} \tag{13}
$$

The output of PI controller is added to the calculation of peak magnitude of the reference source current. For unity power factor, the reference source current should be in phase with source voltage. Therefore, reference source current supplied by compensator is to be multiplied by unit sinusoidal template which are in phase with source voltage.

5 Simulation Results

The simulation parameters of grid-tied PV system with STATCOM are summarized in Table 1. MATLAB-Simulink has been used for simulation purpose.

Figure 3a presents the PV module characteristics with varying solar irradiance. Figure 3b illustrates the PV array characteristics (including 5 series modules and 66 parallel strings) with varying solar irradiance.

As the voltage of solar array is variable with respect to solar irradiance and temperature, to extract maximum power from the solar array, voltage-based MPPT scheme is used. Classical P&O MPPT is used for extracting maximum power from array. Figure 4a illustrates the DC-link voltage with uniform solar irradiance. Figure 4b illustrates the DC-link voltage with ramp increase in solar irradiance and Fig. 4c presents the DC-link voltage with non-uniform solar irradiance.

Table 1 Simulation parameters for grid-tied PV system with STATCOM

PV module	Power at standard test condiion	P_{STC}	305 W
	Voltage at MPP	V_{mp}	54.7 V
	Current at MPP	I_{mp}	5.58 A
	Short circuit current	I_{sc}	5.98 A
	Open circuit voltage	V_{oc}	64.2 V
PV array	Number of series connected module	N_s	5
	Number of parallel connected module	N_p	66
DC–DC converter	Input capacitor	C_{in}	100 µF
	Peak value of capacitor	V_{peak}	100 V
	Inductor	L	5 mH
	RMS value of current	I_{rms}	3 A
	DC-link capacitor	C_{dc}	24 mF
	Peak value of capacitor	V_{peak}	500 V
	Switching frequency	f_{sw}	5 kHz
	Peak voltage of diode	V_{peak}	500 V
	RMS current of diode	I_{rms}	5 A
	Peak voltage of MOSFET	V_{peak}	500 V
	RMS current of MOSFET	I_{rms}	5 A
3-ϕ DC–AC inverter	Switching frequency	f_{sw}	20 kHz
L_f	Filter inductance	L_f	3 mH
	RMS current of inductance	I_{rms}	3 A
Source voltage			3-ϕ 230 V, 50 Hz
Source impedance			$R_s = 0.1$, $L_s = 0.1$ mH
Nonlinear load			$R_L = 100$, $L = 10$ mH

Figure 5a provides the graph for 3-ϕ–4-wire source voltage and source current. Figure 5b illustrates the load voltage and load current due to different nonlinear load. In this work, the nonlinear load is modelled as a 3-ϕ rectifier with passive load. Figure 5c presents the voltage and current at PCC. Figure 5d illustrates the inverter current injected to PCC. In this work, the inverter is modelled as STATCOM.

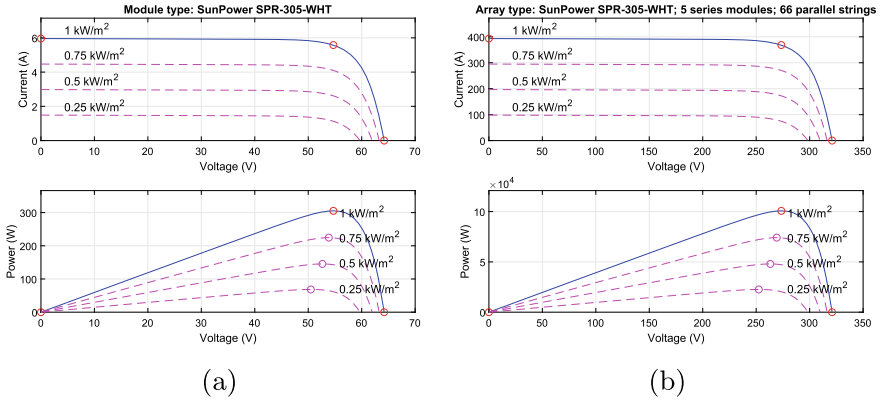

Fig. 3 Characteristics of PV panel with varying solar irradiance **a** PV module, **b** PV array

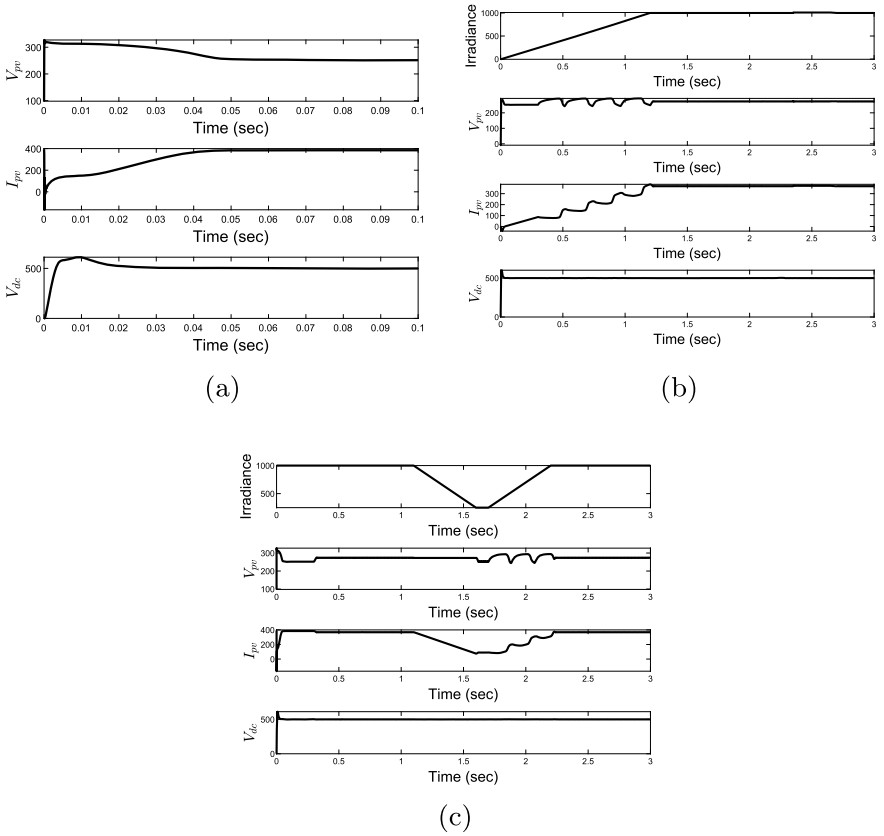

Fig. 4 Simulation results of DC-link voltage at different solar irradiance **a** uniform irradiance, **b** ramp increase in solar irradiance, **c** non-uniform solar irradiance

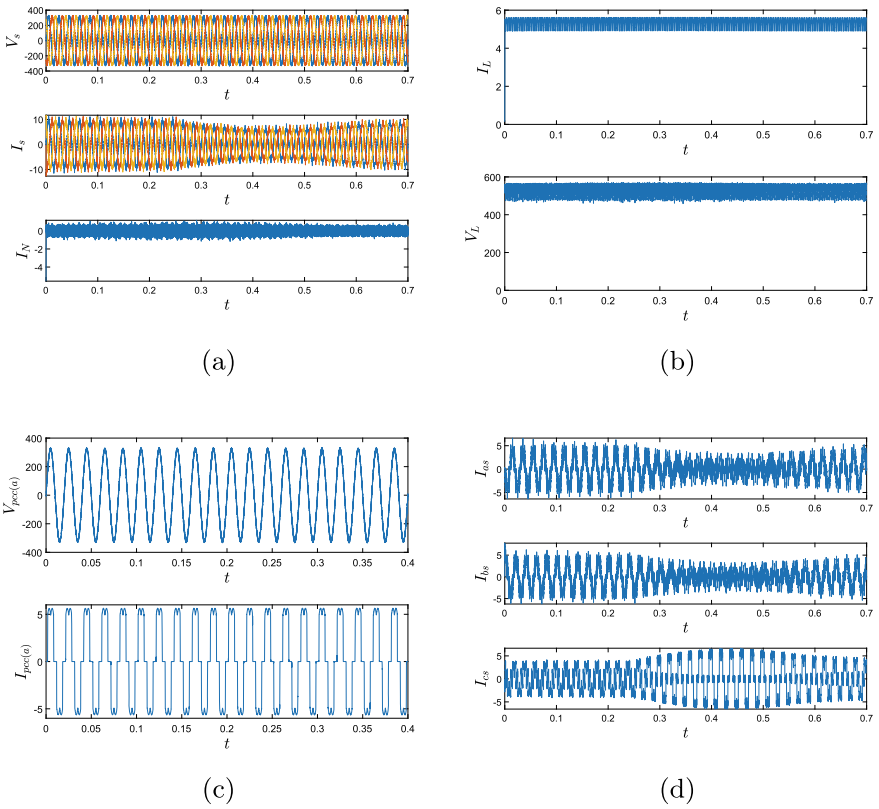

Fig. 5 Simulation results **a** 3-ϕ–4-wire source voltage and source current, **b** load voltage and load current due to nonlinear loads, **c** voltage and current at PCC, **d** output inverter current to be injected to PCC

6 Conclusion

This paper provides mathematical modelling and control of grid-integrated PV system with STATCOM, where STATCOM is used for reactive power compensation. Mathematical modelling and control structure of different converter and STATCOM has been discussed. MPPT scheme is used for PV-fed boost converter and current control scheme is used for controlling the STATCOM. Simulation analyses have been presented for the AC microgrid.

References

1. Ismail B, Wahab NIA, Othman ML, Radzi MAM, Vijyakumar KN, Naain MNM (2020) A comprehensive review on optimal location and sizing of reactive power compensation using hybrid-based approaches for power loss reduction, voltage stability improvement, voltage profile enhancement and loadability enhancement. IEEE Access 8:222733–222765
2. Dixon J, Moran L, Rodriguez J, Domke R (2005) Reactive power compensation technologies: state-of-the-art review. Proc IEEE 93(12):2144–2164
3. Majumder R (2012) Reactive power compensation in single-phase operation of microgrid. IEEE Trans Ind Electron 60(4):1403–1416
4. Barr J, Majumder R (2014) Integration of distributed generation in the volt/var management system for active distribution networks. IEEE Trans Smart Grid 6(2):576–586
5. Singh B, Jayaprakash P, Kothari DP, Chandra A, Haddad KA (2014) Comprehensive study of DSTATCOM configurations. IEEE Trans Ind Inform 10(2):854–870
6. Varma RK, Siavashi EM (2018) PV-STATCOM: a new smart inverter for voltage control in distribution systems. IEEE Trans Sustain Energy 9(4):1681–1691
7. Subudhi B, Pradhan R (2018) A new adaptive maximum power point controller for a photovoltaic system. IEEE Trans Sustain Energy 10(4):1625–1632
8. De Brito MAG, Galotto L, Sampaio LP, de Azevedo e Melo G, Canesin CA (2012) Evaluation of the main MPPT techniques for photovoltaic applications. IEEE Trans Ind Electron 60(3):1156–1167

Comparative Analysis Between Single Diode and Double Diode Solar Topologies of Solar PV Cell

Sriparna Das and Kumari Namrata

1 Introduction

The demand of using renewable energy has improved significantly. Nowadays, a greater number of solar-, hydro-, wind-, etc., based plants are being set up for increasing in power production [1]. Out of all these existing plants, solar or sun's rays is easily available in most of the places throughout the year. So, solar-based generation is more preferred than other ones. About 40.4% of the total energy comes from solar generation [2]. Thus, the designing and performance analysis is important for solar photovoltaic cell [3, 4]. In this paper, two topologies of solar modelling are considered, i.e., single and double diode schemes. A photovoltaic cell named Solarex: MSX60 is considered as test parameters for making the comparison between the schemes. The modeling is first shown followed by their circuit diagrams and the inputs are taken from the parameters of the existing solar cells and the outputs of the various schemes are compared. The yearly production of power for single and double diode schemes [5, 6] is plotted to get how the variation of generated power occurs. The variation of power is compared w.r.t single cell used. To obtain desired power, a greater number of cells can be connected either in series or parallel fashion.

2 Modeling of Single Diode Scheme

The ideal circuital representation of photovoltaic cell is shown in Fig. 1. From Fig. 1, applying Kirchhoff's current division rule, we can get [4]

S. Das (✉) · K. Namrata
Department of Electrical Engineering, NIT Jamshedpur, Jamshedpur, Jharkhand 831014, India

K. Namrata
e-mail: namrata.ee@nitjsr.ac.in

S. Kumar et al. (eds.), *Recent Advances in Power Electronics and Drives*, Lecture Notes in Electrical Engineering 852, https://doi.org/10.1007/978-981-16-9239-0_12

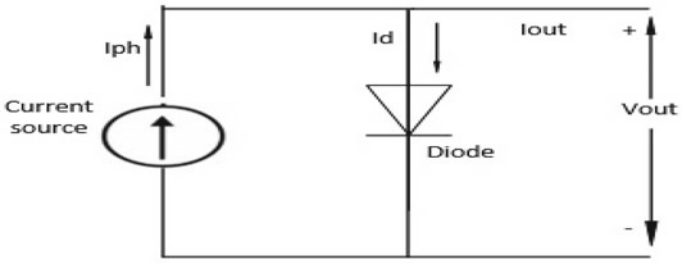

Fig. 1 Representation of ideal solar cell

$$I_{out} = I_{ph1-Id1} \tag{1}$$

The general diode equation can be expressed as

$$I_{d1} = I_{s1}\left[\exp\left(\frac{q_1 V_{oc1}}{N_{s1} K_1 A_1 T_0}\right) - 1\right] \tag{2}$$

Placing the value of diode current from Eqs. (2) to (1), the final output current can be expressed as

$$I_{out} = I_{ph1} - I_{s1}\left[\exp\left(\frac{q_1 v_{oc1}}{N_{s1} K_1 A_1 T_o}\right) - 1\right] \tag{3}$$

These above equations are valid for an ideal system. But in practical scenario, there are some losses [5] that will take place into the system. So, the Fig. 1 [7] is modified into Fig. 2 with the addition of some series and parallel resistances [8]. The loss that happens due to flowing of current in metal grid, semiconductor material, collecting bus, and terminal is denoted by adding some series drop into the circuit. The parallel drop is due to current flowing through cell thickness and surface effect. So, the diode current and output current expression gets changed and are represented as

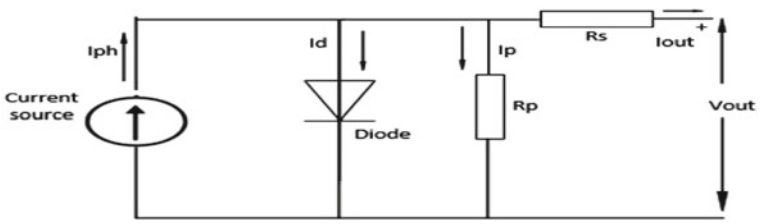

Fig. 2 Single diode scheme solar cell representation

$$I_{d1} = I_{s1}\left[\exp\left(\frac{q_1(V_1 + I_1 R_{s1})}{N_{s1} K_1 A_1 T_0}\right) - 1\right] \tag{4}$$

$$I_{out} = I_{ph1} - I_{s1}\left[\exp\left(\frac{q_1(V_1 + I_1 R_{s1})}{N_{s1} K_1 A_1 T_0}\right) - 1\right] \tag{5}$$

There are certain parameters those are needed to calculate the output current of the system. But they are not described in the above equations. They are photo current (I_{ph1}), reverse saturation current (I_{rs1}), and the saturation current (I_{s1}), which are expressed as follows:

$$I_{ph1} = [I_{sc1} + K_{i1}(T_{01} - T_{r1})] * \frac{G_1}{G_{ref1}} \tag{6}$$

$$I_{rs1} = \frac{I_{sc1}}{\left[\exp\left(\frac{q_1 V_{oc1}}{N_{s1} K_1 A_1 T_0}\right) - 1\right]} \tag{7}$$

$$I_{s1} = I_{rs1}[\frac{T_{01}}{T_{r1}}]^3 \exp\left[\left(\frac{q_1 E_{g1}}{A_1 K_1}\right)\left(\frac{1}{T_{r1}} - \frac{1}{T_{01}}\right)\right] \tag{8}$$

This is the entire process of designing a solar photovoltaic cell according to the single diode configuration.

3 Modeling of Double Diode Scheme

The double diode scheme is slightly different than single diode representation. Here, the use of more than one diode takes place. The circuit representation is shown in Fig. 3. The modeling is same as that of single diode, only the output current will vary. The output current is expressed as

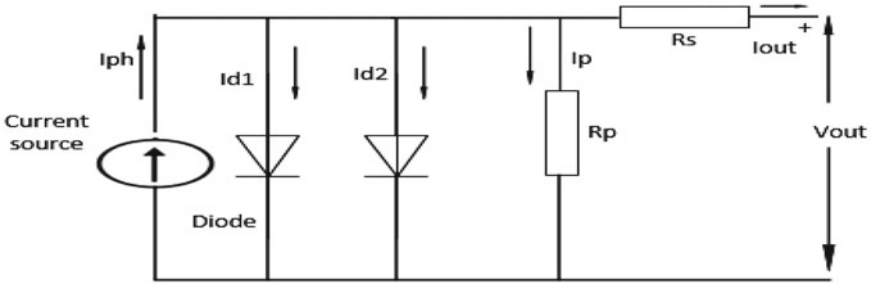

Fig. 3 Double diode scheme solar cell representaion

Table 1 Paramerets of Solarex: MSX 60 Solar cell [9]

S. L. no	Parameters	Denoted name	Values used
1	Max. power	P_{m1}	60 W
2	Max. voltage	V_{m1}	17.1 V
3	Max power current	I_{m1}	3.5 A
4	O.C. voltage	V_{oc1}	21.1 V
5	S.C. current	I_{sc1}	3.8 A
6	No. of series cells	N_{s1}	36
7	No. of parallel cell	N_{p1}	1
8	Ideality factor of diode	A_1	1.3
9	Temp. coefficient of cell	K_{i1}	0.003/°C
10	Ref. temp	T_{ref1}	25 °C
11	Solar irradiance	G_{ref1}	1000 at STC

$$I_{out} = N_{p1} * I_{ph1} - N_{p1} * I_{s1}\left[\exp\left(\frac{q_1(V_{out1} + I_{out1}R_{s1}}{N_{s1}K_1A_1T_0}\right) - 1\right] - N_{p2} * I_{s2}\left[\exp\left(\frac{q_2(V_{out1} + I_{out1}R_{s1}}{N_{s1}K_1A_1T_0}\right) - 1\right] \quad (9)$$

The advantage of this model is in case of failure of a diode it can behave as single diode approach, so the power generation will not get stopped. Due to connection of critical loads that need to get supply throughout the time, stopping of generation is not a proper solution thus this model can be considered.

The parameters of solar cell that has been used to test the performance of the models are shown in Table 1. Basically, the temperature and solar irradiance are obtained for the place of New Delhi and these along with the parameters of Solarex: MSX 60 are fed as an input to the model of single and double diode topologies and their performance are being compared throughout the year. In the table, the parameters to design the solar cell such as O.C. current, S.C. voltage, and other various constants are described that will help to design the cell easily.

4 Simulation and Comparative Analysis

The simulated model of single diode modeling of solar cell is shown in Fig. 4 and the double diode representation is shown in Fig. 5.

The above models are designed in Simulink and the inputs to this model are temperature and irradiance that are taken for the place of New Delhi. The other input is system voltage that is taken from the datasheet of the practical existing solar cell [10, 11]. The output is power generated calculated for entire year by varying the

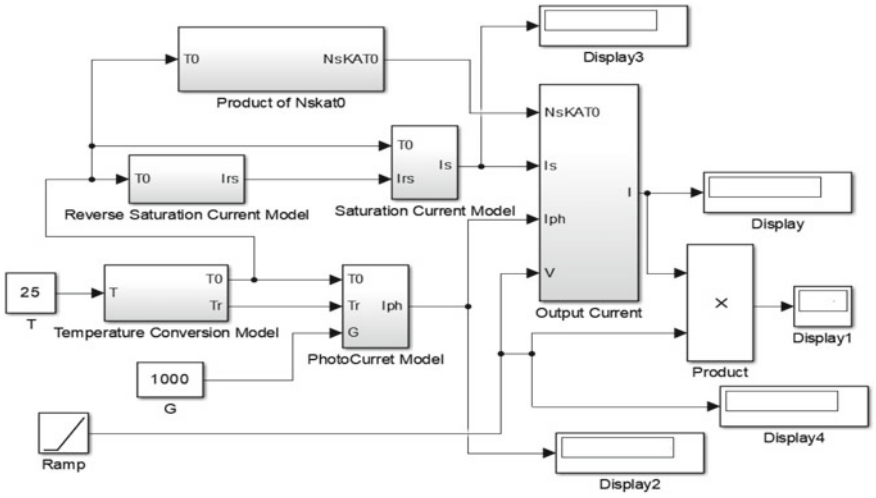

Fig. 4 Single diode simulated model

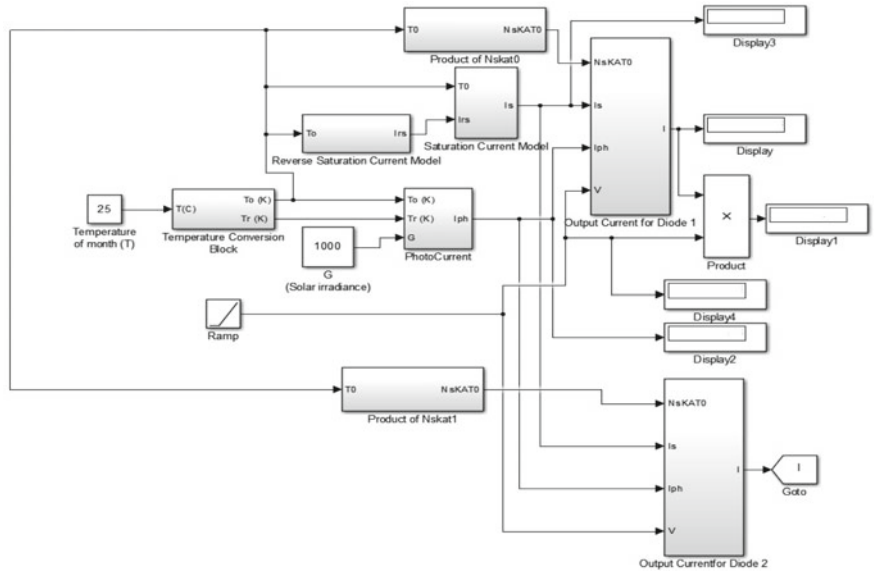

Fig. 5 Double diode simulated model

temperature and irradiance as they vary with change in months for a certain place. The variation in power by using both the topologies are shown in Table 2.

From the above Table 2, the variation of monthly power can be seen. The maximum power that can be produced while using Solarex: MSX 60 is 60 W. So, to get the

Table 2 Power and current variation for single and double diode schemes in case of Solarex: MSX 60 solar cell for the place New Delhi

S. L. No	Month	Temp (°C)	G (MJ/m^{2}month)	S.D P_{mp} (W)	S.D I_{mp}(A)	D.D P_{mp}(W)	D.D I_{mp}(A)
1	Jan	14.11	412.92	24.80	1.37	23.80	1.39
2	Feb	17.05	459.76	27.34	1.51	26.59	1.56
3	Mar	22.59	639.84	37.31	2.06	37.26	2.18
4	Apr	29.66	722.10	36.29	2.01	39.63	2.32
5	May	33.38	757.33	32.22	1.78	38.87	2.27
6	Jun	33.50	676.20	26.66	1.47	33.71	1.97
7	Jul	31.01	591.17	25.60	1.41	30.49	1.78
8	Aug	29.86	551.49	24.65	1.36	28.75	1.68
9	Sept	29.40	567.00	26.30	1.45	30.00	1.75
10	Oct	26.24	520.80	26.64	1.47	28.57	1.67
11	Nov	20.77	423.90	23.62	1.31	23.83	1.39
12	Dec	15.26	369.83	21.66	1.20	20.98	1.23

desired amount of power, more number of solar cell can be connected in various fashion as required. The variation of monthly power is represented in Fig. 6.

From Fig. 5, clear comparison of power production between the two schemes can be observed. With the change in temperature and solar radiation, the power production get effected. With the increase in solar radiation the power production will gets increased while keeping temperature constant. But in case of vice versa, while keeping solar radiation constant and the temperature increase, it is observed the power production gets decreased slightly.

In case of single diode scheme, the maximum power is generated, i.e., 36.29 W in the month of April due to maximum deviation in the figure as seen and high amount of radiation occurs whereas lowest power production of 21.66 W takes place in month of December as minimum amount of solar radiation, i.e., 369.83 MJ/m^{2}month takes place. The yearly production when the solar cell is acting as single diode scheme is 333.09 W, whereas the monthly average production is 27.75 W. This is the production from a single solar cell. By adding more cells in number, the production can be done as per requirements. The maximum production of solar cell takes place when the solar irradiance is 1000 MJ/m^{2}month and the temperature is 25 °C. Thus, the error of production is 0.1% that is quite less.

In case of double diode scheme, the maximum power is generated, i.e., 39.63 W in the month of April due to increase in solar radiation of 722.10 MJ/m^{2}month and the lowest production takes place for the month of December, i.e., 20.98 W due to less radiation of 369.83 MJ/m^{2}month. The yearly production when the solar cell is acting as double diode scheme is 362.48 W, whereas the monthly average production is 30.21 W which is high enough than single diode scheme. Here, the maximum production takes place when the solar irradiance is 1000 MJ/m^{2}month

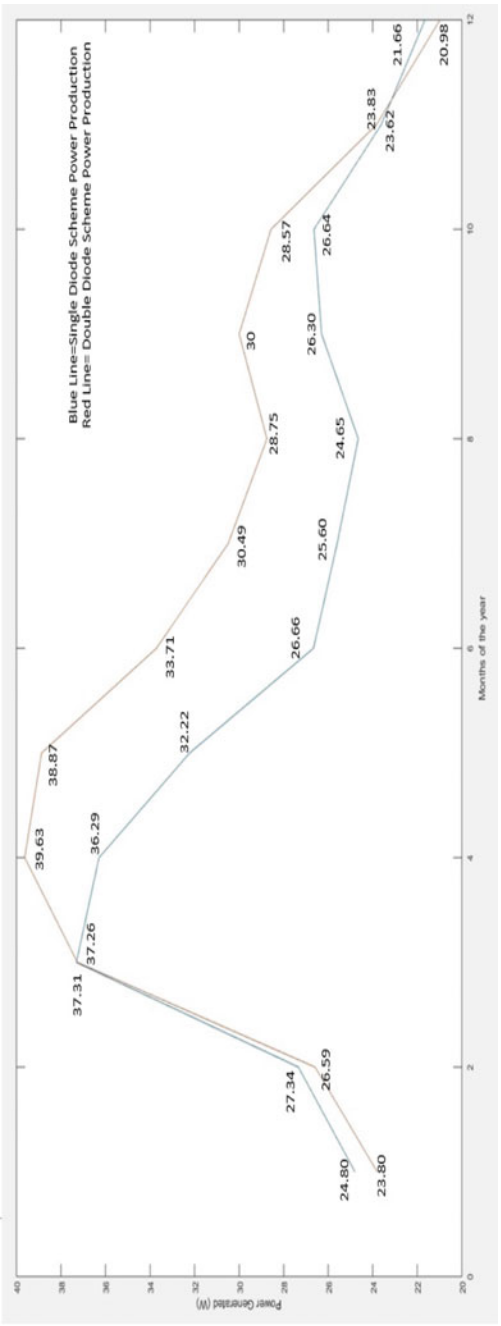

Fig. 6 Schematic representation of power variation throughout the year for various schemes

and temperature is 25 °C which is 59.50 W having an error of 0.83%. Thus, the increase in production proves better result for double diode topology than single diode scheme. The system errors are also within limits thus this model can represent a solar PV cell.

5 Conclusion

A clear comparison is presented between the various approaches of modeling [12–14] of solar PV cell. Due to higher demand of energy production from renewable energy sources, the designing of PV cell is an important aspect of production purpose. Double diode scheme produces higher amount of production than single diode scheme. Due to higher production and more advantage this modeling can be preferred than single diode scheme. Here, for the place New Delhi double diode modeling suits with better production. As the Government of India is giving more emphasis on the use of renewable energy sources [15], this paper will give a clear view of designing and production of solar rays for a certain area.

References

1. Valencia-Calvo J, Oliver Tost G, Garcia Ortega M (2020) Model and simulation of a renewable energy market: integration of renewable energy sources with the conventional generation system. In: IEEE 2020, 15th Iberian conference on information system and technologies (CISTI), pp 1–7
2. Ministry of New and Renewable Energy, Government of India, Physical Progress (Achievements), Retrieved 18th July, 2018
3. Perara PU, He L (2018) A simplified mathematical model of PV cell simulation. In: IEEE 2018, 7th world conference on photovltaic energy conversion (WCPEC), pp 3204–3207
4. Morsy KA, Abouelatta MA, El-Banna MM, Elsaid MK (2018) Modelling and simulation of photovoltaic module for space applications using simulink/MATLAB. In: 2018 first ınternational workshop on deep and representation learning (IWDRL), pp 55–61
5. Nascimento AJ, Cavalcanti MC, Bradaschia F, Silva EA, Michels L, Pietta LP (2017) Parameter estimation technique for double diode model of photovoltaic module. In: 2017 Brazilian power electronics conference (COBEP), pp 978–984
6. Vinod RK, Singh SK (2018) Solar photovoltaic modelling and simulation: as a renewable energy solution. Energy report, Research Paper in Elsevier, Available in ScienceDirect, pp-710–712
7. Selmi T, Abdul-Niby M, Devis L, Devis A (2014) P&O MPPT ımplementation using MATLAB/simulink. In: 2014 9th ınternational conference on ecological vehicles and renewable energies (EVER), pp 1–8
8. Ahmad T, Sobhan S, Faysal Nayan Md (2016) Comparative analysis between single diode and double diode method of PV cell: concentrate different parameters effect on its efficiency. J Power Energy Eng 31–46
9. Bana S, Saini RP (2016) A mathematical modelling framework to evaluate the performance of single diode and double diode based SPV systems. Energy report. Research Paper in Elsevier, Available in ScienceDirect, pp 171–187
10. Rodrigues EMG, Godina R, Pouresmaeil E, Porto JPS (2017) Simulation study of a photovoltaic cell with ıncreasing level of model complexity. In: 2017 IEEE ınternational conference on

environmental and electrical engineering and 2017 IEEE ındustrial and commercial power systems europe (EEEIC/I&CPS Europe), pp 1–4
11. Louzazni M, Khouya A, Amechnoue K, Gandelli A, Mussetta M, Craciunescu A (2018) Meta-heuristic algorithm for photovoltaic parameters: comparative study and prediction with a firefly algorithm. MDPI Appl Sci 1–22
12. Ibharim MM, Jiya JJ, Idakwo HO (2016) Characterization of PV-cell using real data. Int J Eng Dev Res 4(2):1696–1703
13. Chandel TA, Yasin MY, Mallick A (2019) Modelling and simulation of photovoltaic cell using single diode solar cell and double diode solar cell model. Int J Innov Technol Explor Eng 8(10):558–565.
14. abed-Ali RA, Yasin NM (2019) Simulation of solar cell and sinusoidal pulse width modulation inverter using MATLAB and proteus. In 4th Scientific International Conference-Najaf-IRAQ-2019, pp 86–91
15. Sahu P, Verma D, Nema S (2016) Physical design and modelling of boost converter for maximum power point tracking in solar PV systems. İn: 2016 ınternational conference on electrical power and energy systems (ICEPES), pp 10–15

Control of Three-Phase Grid-Connected Inverter Using dq Axis Theory

Deepak Kumar Singh, Saibal Manna, and Ashok Kumar Akella

1 Introduction

Energy demand is rising every day as urban development and population increase. This increased energy demand contributes to a rapid decrease of fossil fuels and thus promotes the distributed generations (DG) like wind power, hydro power, and PV system, etc. All these are clean sources of energy. DG sources are connected to the grid for the reliability of the system [1]. Energy is transferred from DG to the utility grid using power electronic converters. Various power electronic converters are used for DG, depending on the energy source. DC/DC converter is used to transform DC energy provided by the PV panels to constant DC voltage, which provides the inverter's DC-link. An additional DC/DC converter for boosting DC voltage is used in some applications. At last, an inverter is used for transferring energy to the grid from DC-link [2, 3]. The main concern with inverter connected to grid system is THD of grid current and the system's power factor. The grid current has a THD value of less than 5% and power factor should be nearly unity. 3-ϕ voltages and currents must be synchronized with each other [4].

Different methods, including dq theory, power balance control theory and pq theory are mentioned in the literature for control of the grid converters. The dq axis theory is used here as it is easy to implement, active and reactive current can be controlled separately. One more reason to use this theory is all control variable are in DC frame, so by using simple PI controller, the complete control algorithm can be implemented [5]. SPWM technique is used to provide the gate signal to the 3-ϕ GCI. It is a conventional switching scheme. The carrier wave, which is the required frequency, is compared with the reference wave (Sine wave). Further, SPWM has two switching schemes such as bipolar and unipolar switching. Unipolar switching has complex control, less fluctuation, and high switching frequency from bipolar scheme [6]. Use of power converters causes a slew of power quality issues like poor

D. K. Singh (✉) · S. Manna · A. K. Akella
National Institute of Technology, Jamshedpur 831014, Jharkhand, India

S. Kumar et al. (eds.), *Recent Advances in Power Electronics and Drives*, Lecture Notes in Electrical Engineering 852, https://doi.org/10.1007/978-981-16-9239-0_13

power factor, interruptions, flickers, and noise. The use of filters resolves this issue [7].

Synchronization is essential for the inverter connected to grid. Here, synchronization means same frequency, phase angle, and voltage level. If it does not meet then circulating current will flow in the system and which leads to the damage of the system. A reference current must be found to achieve synchronization, which will be injected into the system through inverter. Various synchronization techniques exist, including zero crossing, Atan function, and PLL [8, 9]. The simplest technique for grid synchronization is zero crossing. Each half cycle, grid voltage zero crossing points are detected and grid frequency is defined. This technique, on the other hand, does not have a quick dynamic response to changes in frequency [10]. Grid voltages are calculated then converted into a reference frame and filtered using the Atan function technique to eliminate voltage notches effect. To increase performance, delay cancellation methods are employed as signal delays result from filters [11].

PLL is most popular synchronization technique and it is widely used. To send active power in the grid, first mark the grid side voltage. Now, the current which has to be sent should be in phase with this voltage. To send this current, a reference signal must be produced, which must be in phase with the actual voltage and have a magnitude between −1 and 1. The signal is thus produced using PLL and used as a reference signal in an inverter linked to the grid to execute current controller. In the same way, PLL is used to produce a signal 90 degree out of phase with the actual voltage to transfer reactive power to the grid [12, 13]. The control and simulation of 3-ϕ GCI is presented. Section 2 describes the operation of 3-ϕ GCI and dq control scheme is explained in Sect. 3. Section 4 explains the detail implementation of proposed control strategy. Simulation outputs are placed in Sects. 5 and 6 summarizes conclusion of the article.

2 Operation of 3-ϕ GCI

Figure 1 shows the basic block representation of 3-ϕ GCI. DC source is connected at the input with the bus capacitance across it. It is then connected to the inverter bridge, which can be MOSFET/IGBT. The inverter output is then plugged into the LCL filter.

The current produced by the inverter contains lots of harmonics. When this current is directly inserted to the grid, then it deteriorates grid voltage and hence causes lots of power qualities issue. In order to avoid all these issues, filter is used at the inverter

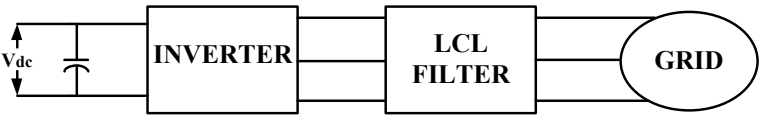

Fig. 1 Block representation of 3-ϕ GCI

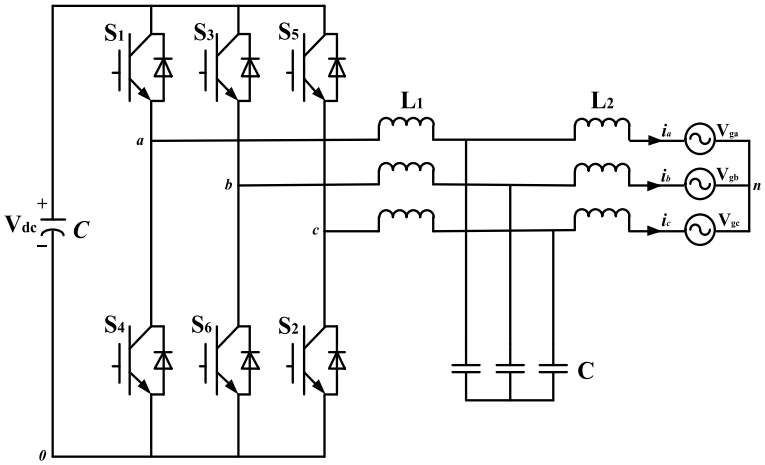

Fig. 2 Internal structure of 3-ϕ GCI

output. After connecting the filter, smooth sinusoidal current is obtained without any harmonics.

Figure 2 shows basic schematic of the 3-ϕ GCI. V_{dc} is DC voltage source at the input. S_1–S_6 are the power electronics switches (MOSFET/IGBT) which form the inverter bridge. Inductors (L_1, L_2) and capacitors (C) form LCL filter. Finally, inverter is connected to the grid. V_{ga}, $V_{gb,}$ and V_{gc} are grid voltage of a, b, and c phases, respectively. Similarly, i_a, $i_{b,}$ and i_c are grid current.

3 dq Axis Theory

Direct-quadrature theory or dq is a transformation principle in which AC sinusoidal signals are converted into DC signal and then operate upon the DC values and then back again transform it into the AC signals. So, this process of transformation from AC domain to DC domain, DC domain to AC domain is popularly known as dq axis theory. This theory is generally used to design controller and analysis of 3-ϕ grid connected system. There are two transformations in the dq axis theory, i.e., forward and reverse transformation. Forward transformation is AC to DC transformation while reverse transformation is DC to AC transformation.

Figure 3 shows abc–αβ–dq coordinate system phasor representation, where ρ is the angle between αβ and dq coordinates system. Clarke and Park transform are used in abc–αβ–dq transformation. The abc to αβ transformation, i.e., three phase system in time domain to orthogonal stationary frame is done using Clarke transform. The αβ to dq (orthogonal rotating reference frame) transformation is done using Park transform. The consecutive implementation of these two transforms simplifies

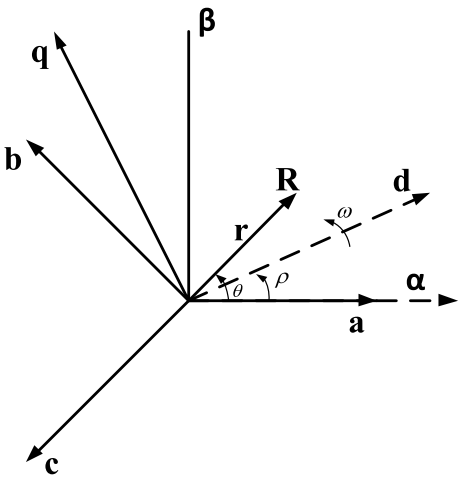

Fig. 3 abc–αβ–dq coordinate axis [15]

calculations with AC current and voltage waveform transformation into DC signal [14]. Consider a space vector R having amplitude r at an angle θ.

3.1 AC to DC Transformation

This is also called forward transformation. abc to αβ transformation

$$\begin{bmatrix} r_\alpha \\ r_\beta \end{bmatrix} = \begin{bmatrix} 1 & -\frac{1}{2} & -\frac{1}{2} \\ 0 & \frac{\sqrt{3}}{2} & -\frac{\sqrt{3}}{2} \end{bmatrix} \begin{bmatrix} r_a \\ r_b \\ r_c \end{bmatrix} \tag{1}$$

αβ to dq transformation

$$\begin{bmatrix} r_d \\ r_q \end{bmatrix} = \begin{bmatrix} \mathrm{Cos}\rho & \mathrm{Sin}\rho \\ -\mathrm{Sin}\rho & \mathrm{Cos}\rho \end{bmatrix} \begin{bmatrix} r_\alpha \\ r_\beta \end{bmatrix} \tag{2}$$

3.2 DC to AC Transformation

This is also called reverse transformation. dq to αβ transformation

$$\begin{bmatrix} r_\alpha \\ r_\beta \end{bmatrix} = \begin{bmatrix} \mathrm{Cos}\rho & -\mathrm{Sin}\rho \\ \mathrm{Sin}\rho & \mathrm{Cos}\rho \end{bmatrix} \begin{bmatrix} r_d \\ r_q \end{bmatrix} \tag{3}$$

αβ to abc transformation

$$\begin{bmatrix} r_a \\ r_b \\ r_c \end{bmatrix} = \begin{bmatrix} \frac{2}{3} & 0 \\ -\frac{1}{3} & \frac{1}{\sqrt{3}} \\ -\frac{1}{3} & -\frac{1}{\sqrt{3}} \end{bmatrix} \begin{bmatrix} r_\alpha \\ r_\beta \end{bmatrix} \tag{4}$$

The same procedure is applied to transform current or voltage.

4 Control Strategy

Figure 4 demonstrates the control strategy of 3-ϕ GCI. To set up the controller, first voltages need to be sensed. These 3-ϕ abc voltages are then transformed to 2-phase αβ voltages. Using these αβ voltages, PLL is implemented. The αβ voltages are then converted to dq voltages. Now, currents need to be sensed for controller implementation. Either grid current or inverter side current is used for the implementation. Here, inverter side current is being sensed. These currents are then transformed to αβ domain and then it is transformed into dq domain.

I_d and I_q correspond to active and reactive currents, respectively. To find the error, I_d and I_q are subtracted from the reference current. Error is being given to the PI

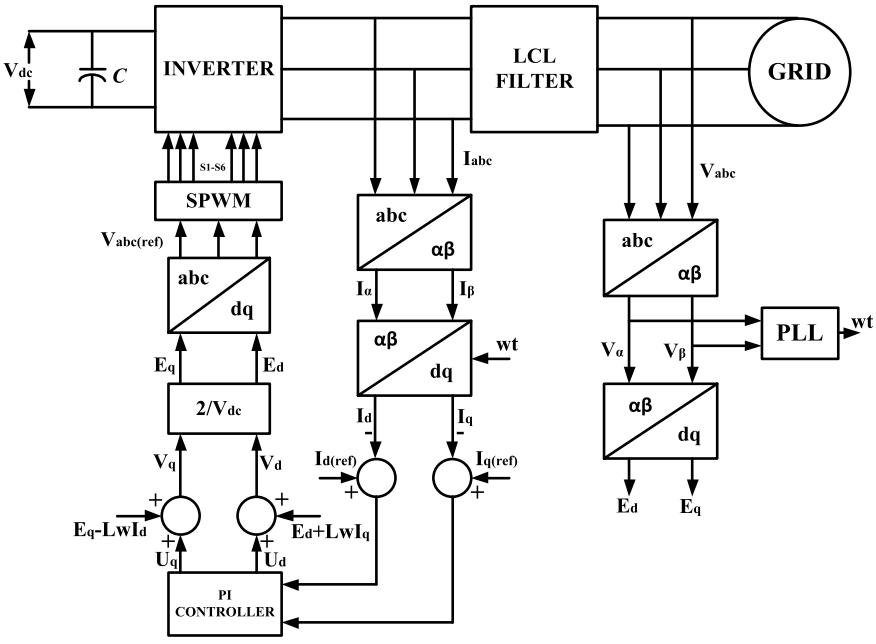

Fig. 4 Control block of 3-ϕ GCI

controller to find out the voltages U_d and U_q.

$$V_d = U_d + E_d + LwI_q \tag{5}$$

$$V_q = U_q + E_q - LwI_d \tag{6}$$

Here, w and L are grid frequency and inductance of the filter, respectively. For SPWM, the relation between modulation index and inverter voltage is given by

$$V_d = M_d * \frac{V_{dc}}{2} \tag{7}$$

$$V_q = M_q * \frac{V_{dc}}{2} \tag{8}$$

Therefore, V_d and V_q are multiplied with $(2/V_{dc})$ to obtain E_d and E_q. Finally, it is transformed to abc voltages to get the reference for PWM generation.

5 Simulation Result

MATLAB/SIMULINK is used to simulate the system. The circuit's parameters are described in Table 1. The complete topology can be analyzed by varying the circuit parameter. The results are taken into consideration for verification of the model.

Set active current reference ($I_{d(\text{ref})}$) to 200A and $I_{q(\text{ref})}$ to zero to pass only active power to the utility grid. 3-ϕ grid voltages and currents are displayed in Fig. 5 and Fig. 6, respectively. It is clearly recognized that the actual current is same as the reference current. Figure 7 exhibits that grid current and voltage are in phase. Figure 8 depicts the grid current harmonic spectrum. The grid current's THD is 2.55%. The system has nearly UPF.

To check the effectiveness of the controller, set new reference current value ($I_{d(\text{ref})}$ = 150 A). It is clearly acknowledged that the grid current has changed to new

Table 1 Parameters of the circuit

Parameters	Values
DC input voltage	800 V
Switching frequency	10 kHz
Grid frequency	50 Hz
Grid voltage	415 V
Filter inductance	0.5 mH
Filter capacitance	0.1 mF

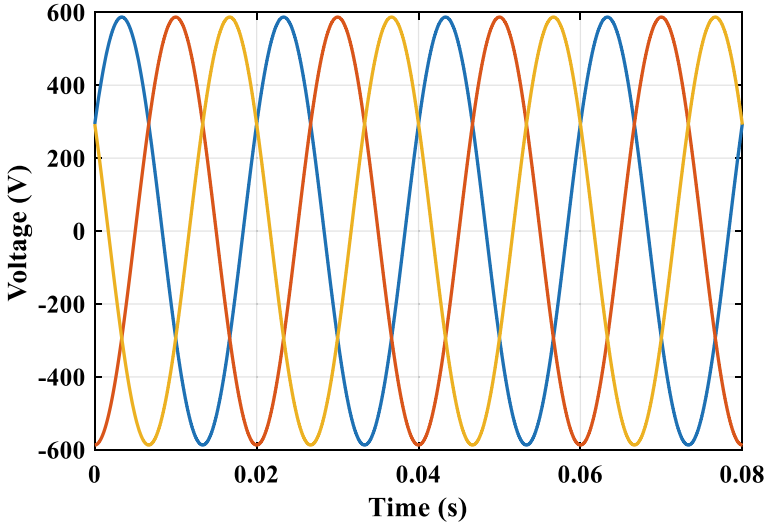

Fig. 5 3-ϕ grid voltages

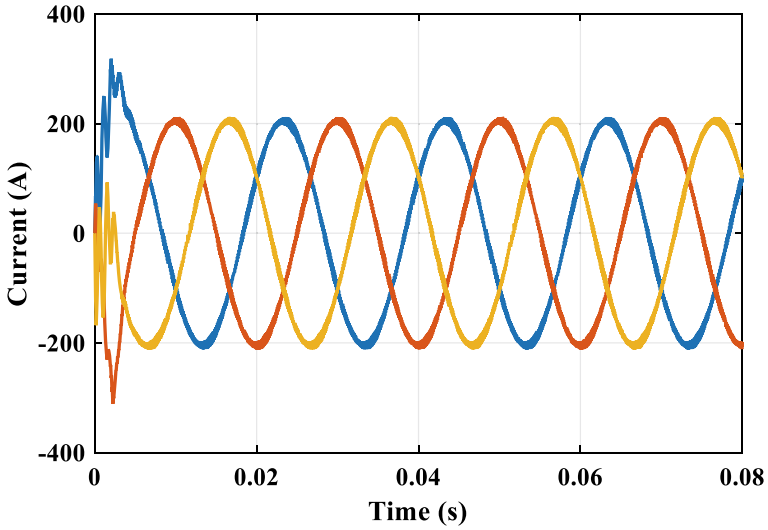

Fig. 6 3-ϕ grid currents at $I_{d(\text{ref})} = 200$ A

reference value, i.e., 150 A as shown in Fig. 9. 1-ϕ current and voltage are still in phase as illustrated in Fig. 10.

To transfer only reactive power to the grid, set $I_{q(\text{ref})} = 200$ A and $I_{d(\text{ref})} = 0$ A. It is clearly validated that current is same as reference current. Since, only reactive

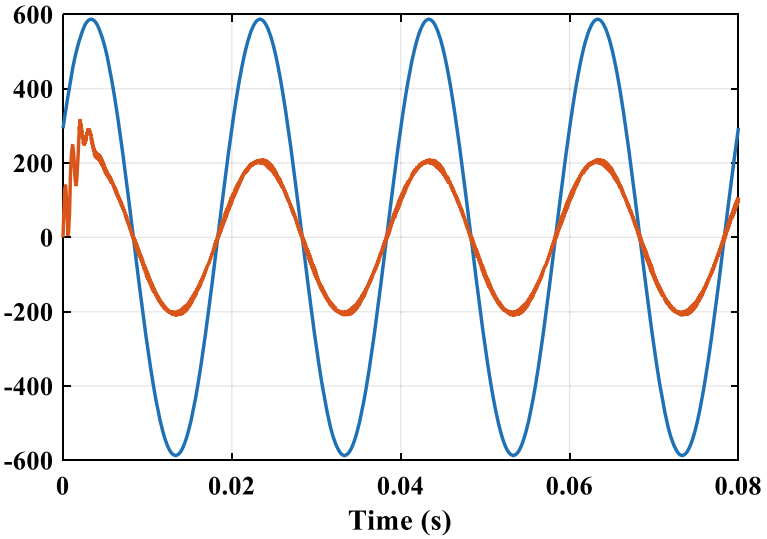

Fig. 7 1-ϕ grid voltage and current at $I_{d(\text{ref})} = 200$ A

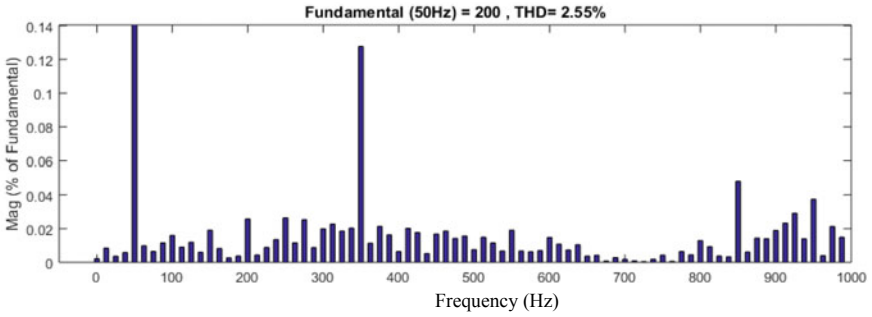

Fig. 8 Grid current harmonic spectrum

current is being sent to the grid, then there is 90° phase difference between voltage and current as depicted in Fig. 11.

6 Conclusion

In this study, control of 3-ϕ GCI using dq axis theory is presented. LCL filter is employed as it has superior filtering performance. 3-ϕ inverter is regulated with SPWM switching scheme at switching frequency 10 kHz. It has been seen that active and reactive current are easily controlled and output is followed the reference value.

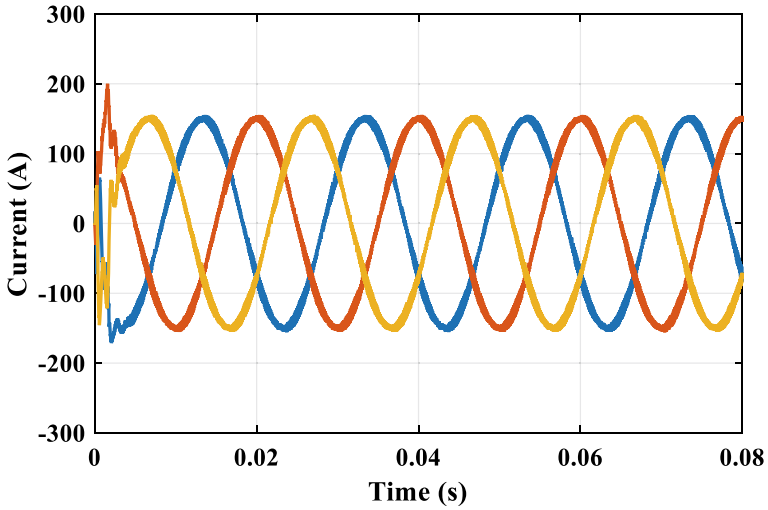

Fig. 9 3-ϕ grid currents at $I_{d(\text{ref})} = 150$ A

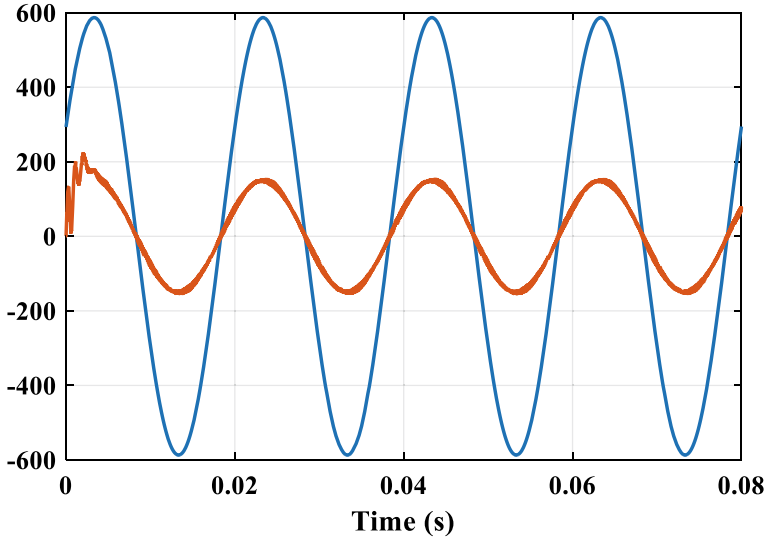

Fig. 10 1-ϕ grid voltage and current at $I_{d(\text{ref})} = 150$ A

The output frequency and voltage magnitude of the inverter has been regulated to track the grid frequency and voltage in such a way that nearly UPF is always maintained. The grid current THD is 2.55%, which is less than 5%. The simulation output exhibits that the proposed control scheme is effective. All the analysis, controller design, and simulation results are verified.

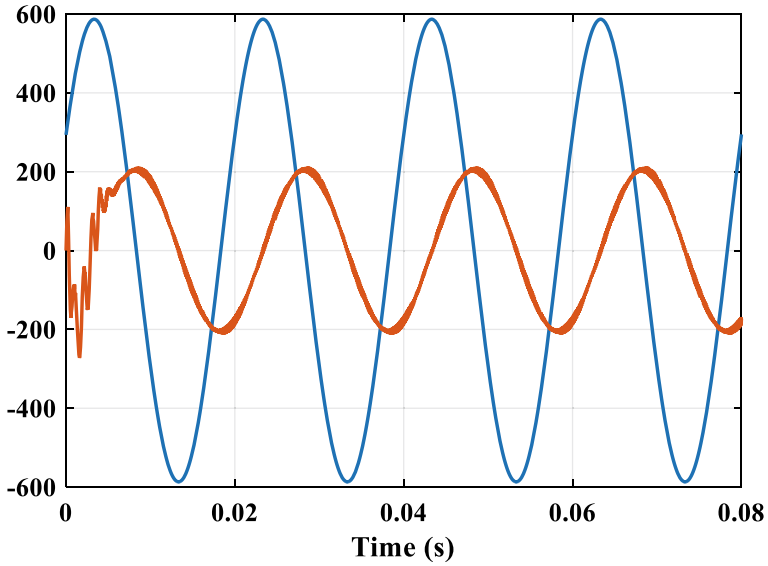

Fig. 11 1-ϕ grid voltage and current at $I_{q(\text{ref})} = 200$ A

References

1. Khanna A, Garg A, Singh A (2019) Maintenance of DC link voltage using synchronous reference frame theory. In: 2019 3rd international conference on recent developments in control, automation & power engineering (RDCAPE), Noida, India, pp 17–21. https://doi.org/10.1109/RDCAPE47089.2019.8979040
2. Isen E, Bakan AF (2016) Development of 10 kW three-phase grid connected inverter. Automatika 57(2):319–328. https://doi.org/10.7305/automatika.2016.10.1081
3. Isen E, Bakan AF (2012) 10 kW grid-connected three-phase inverter system: control, simulation and experimental results. In: 2012 3rd IEEE international symposium on power electronics for distributed generation systems (PEDG), Aalborg, Denmark, pp 836–840. https://doi.org/10.1109/PEDG.2012.6254098
4. Mejía-Ruiz GE, Rodríguez JR, Paternina MRA, Muñoz-Galeano N, Zamora A (2019) Grid-connected three-phase inverter system with LCL filter: model, control and experimental results. In: 2019 IEEE PES innovative smart grid technologies conference—Latin America (ISGT Latin America), Gramado, Brazil, pp 1–6. https://doi.org/10.1109/ISGT-LA.2019.8895017
5. Yazdani A, Iravani R (2012) Voltage-sourced converters in power systems: modeling, control, and applications. IEEE Press, Piscataway, NJ, USA
6. Bahrami A, Narimani M (2019) A sinusoidal pulsewidth modulation (SPWM) technique for capacitor voltage balancing of a nested T-type four-level inverter. IEEE Trans Power Electron 34(2):1008–1012. https://doi.org/10.1109/TPEL.2018.2846618
7. Handoko S, Hadi SP, Suharyanto, Firmansyah E (2014) The performance of three-phase four-wire grid-connected inverter with enhanced power quality. In: 2014 6th international conference on information technology and electrical engineering (ICITEE), Yogyakarta, Indonesia, pp 1–5. https://doi.org/10.1109/ICITEED.2014.7007956
8. Blaabjerg F, Teodorescu R, Liserre M, Timbus AV (2006) Overview of control and grid synchronization for distributed power generation systems. IEEE Trans Ind Electron 53(5):1398–1409

9. Shaikh F, Joseph B (2017) Simulation of synchronous reference frame PLL for grid synchronization using Simulink. In: 2017 international conference on advances in computing, communication and control (ICAC3), Mumbai, India, pp 1–6. https://doi.org/10.1109/ICAC3.2017.8318790
10. Trinh Q, Choo FH, Wang P (2017) Control strategy to eliminate impact of voltage measurement errors on grid current performance of three-phase grid-connected inverters. IEEE Trans Ind Electron 64(9):7508–7519. https://doi.org/10.1109/TIE.2017.2682029
11. Klumpner C, Liserre M, Blaabjerg F (2004) Improved control of an active-front-end adjustable speed drive with a small DC-link capacitor under real grid conditions. In: Proceedings of IEEE 35th annual power electronics specialists conference, Aachen, Germany, pp 1156–1162
12. Guo XQ, Wu WY (2013) Simple synchronisation technique for three-phase grid-connected distributed generation systems. IET Renew Power Gener 7:55–62
13. Chung SK (2000) A phase tracking system for three phase utility interface inverters. IEEE Trans Power Electron 15:431–438
14. https://in.mathworks.com/solutions/power-electronics-control/clarke-and-park-transforms.html?s_tid=srchtitle
15. https://in.mathworks.com/help/physmod/sps/ref/clarketoparkangletransform.html?s_tid=srchtitle

Active–Reactive Power Support with Optimal Allocation of DG and DSTATCOM in Distribution System Using Flower Pollination and Artificial Bee Colony Algorithm with Load Growth

Nandola Maitrey Bharatbhai and Atma Ram Gupta

1 Introduction

The power grid network is made up of generation, transmission, and distribution. Power is given from generation station to the transmission network with higher voltage and transmission network transfers power to very long distance at load center with lower voltage. So power reaches to load center via transmission and DN. Transmission network requires large land space as compared to DN and also they differ to each other via voltage ratings. It is also fact that power received at load station is always lower than supplied by generation station due to various losses in power system network. Losses are also dependent on equipment efficiency, aging of the network, and rating of the network. Generally, power system losses are majorly considering as T&D losses (transmission and distribution losses) because as compared to other losses in the network, T&D losses are dominant. Due to high R/X ratio in DN, high losses have been seen as compared to transmission system.

As per the report by Government of India in 2019, T&D losses in India are 21.04% which is almost double than average T&D losses of the world [1]. As of August 2020, with a gross installed capacity of 372,693 MW, India is the world's third largest producer and third largest consumer of electricity [2]. Mode wise installed capacity is shown in Fig. 1, and mode wise gross generation is shown in Fig. 2. India is the third largest country in consumption of electricity in this 41.16% of total electricity consumed by industrial consumer, 24.76% by residential consumer, and 17.69% by agricultural consumer. This consumption rate is gradually increasing year by year. Per capita consumption in India is increased from 16 KWh in 1947 to 1181 KWh in 2019 as shown in Fig. 3.

N. M. Bharatbhai (✉) · A. R. Gupta
Department of Electrical Engineering, National Institute of Technology Kurukshetra, Kurukshetra, Haryana, India
e-mail: nandola_31904219@nitkkr.ac.in

S. Kumar et al. (eds.), *Recent Advances in Power Electronics and Drives*, Lecture Notes in Electrical Engineering 852, https://doi.org/10.1007/978-981-16-9239-0_14

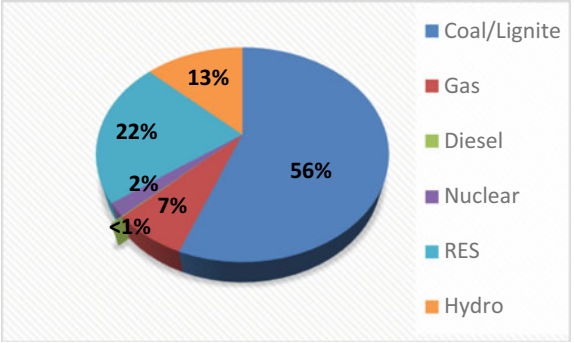

Fig. 1 All India installed capacity as on 31–03–2019 [2]

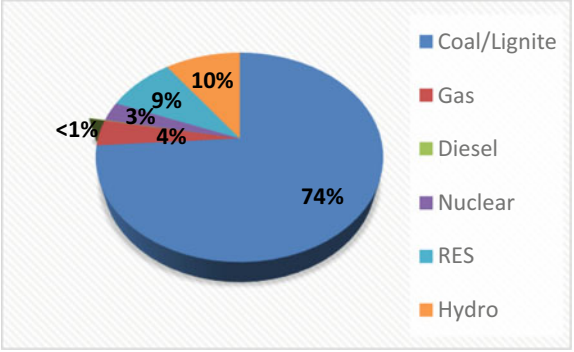

Fig. 2 Mode wise gross electricity generation (2018–19) [2]

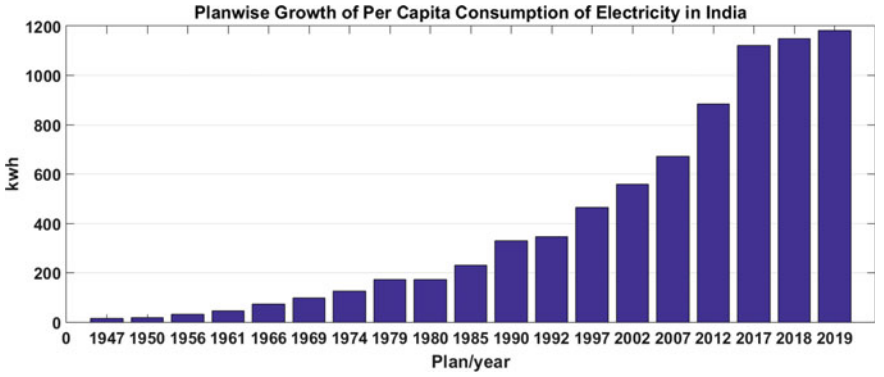

Fig. 3 Per capita electricity consumption in India [2]

If we compare the growth in generation and growth in demand, then load growth dominates and it is sensitive factor. For reliable operation, generation and demand should equal and it is also true that if generation is increasing and if generated power cannot be transferred through transmission and distribution network due to its lower power rating, then power utility takes some steps like, transmission and distribution network restructuring, substation expansion or new substation installation, and their associated new feeders or both [3]. Study in [4] presented that many countries in the world has almost 40-year-old power system network, so at this load, growth condition power system network may not capable to operate in reliable manner. Also cost of restructuring is too high and lack of investment in transmission network makes very hard to operate power system in healthy manner. In the operation of the power grid, the distribution system plays an important role since it is directly linked to the load center. After deregulation of power system these problems becomes larger. Due to limited reactive power sources, distribution system faces unwanted issues in voltage like, voltage fluctuation in voltage, and voltage decay. Due to these problems, some other power quality issues like increased power loss and decreased power flow limits. The reason of limited reactive power sources is many power utilities work under stress because of strict economic constraints and are as regards to the regulatory limits [5]. In order to earn benefit rather than pay a penalty, distribution firms typically aim to keep the real power losses as low as possible.

The requirement of extra active and reactive power or increment in demand can be fulfilled by DG and DSTATCOM, respectively. We can get benefits like reduction in power loss, improved voltage profile, load balancing, and many more by using DG and DSTATCOM.

There are serval definitions of DG based on voltage level (kV), DG scale (MW), technology based on renewable and hybrid. According to CIGRE, DG is a system which does not organized centrally and not dispatched centrally, and smaller than 50–100 MW and connected to the distribution grid [6].

The reasons for implementing DGs are shorter construction time, lower cost, modular generation site, lower space requirement, diversification of energy sources, energy efficiency, competition policy, etc. [3]. DG are often broadly classified in two types renewable and non-renewable. Solar energy plants, wind generation plants, power plants with fuel cells, power plants with biogas, etc., are counted in renewable DG and non-renewable DG contains, duel-fed induction generator, ICE, etc. DG will be graded on the idea of the active/reactive power supplied/absorbed as follows [7].

- Type-1: If DG supplies real and reactive power to the network at unity power factor (pf) then it is known as type 1 DG. Wind, tidal, and wave energy sources are the examples.
- Type-2: If DG supplies only real power to the network with leading pf of 0.8–0.99 then it is known as type 2 DG like solar energy plants, photovoltaic systems, fuel cell, etc.
- Type-3: If DG supplies only reactive power to the network with zero pf, then it is defined as type 3 DG, at zero power factor. Like, synchronous motor in overexcited mode, synchronous condenser.

- Type-4: If DG provides real power and absorb reactive power from the system at lagging pf of 0.8–0.99 then it is known as type 4 DG like duel-fed induction generator.

In recent years, the energy sector has undergone many changes following the implementation of smart grids. It affects not only utilities but consumers too. India also moves faster towards smart grid and electric vehicles. With introduction of electrical vehicles, electricity demand increases in remarkable way. To archive this, government also promotes DG. GOI promotes DG via various policies and subsidies like Rajiv Gandhi Grameen Vidhyutikaran Yojna (RGGVY) [8]. Since distribution generation installed at the consumer side, consumer becomes prosumer (producer + consumer).

Another device known as STATCOM which is power electronics-based voltage–source converter. STATCOM may be operate as either source or sink of reactive power. In some operations, it also supplies active power if connected as a source. This device initially developed for transmission systems for operations like faster and continuous inductive or capacitive compensation. Similarly, for distribution system, a tool D-STATCOM is employed. D-STATCOM can inject leading or lagging current as per the requirement of compensation. Here, the benefit is the total demand of specified load meets utility connection specification because DSTATCOM is related to a specified load [9, 10].

In actual scenario, loads are mixtures of varied load types like combination of residential, industrial, and commercial loads. So, looking on the character of the realm being supplied, each bus of the system includes a various type of load connected thereto. Distribution system planners normally provide their various customer groups with dedicated feeders, each of which have its distinctive load pattern that varies hourly and seasonally [11]. As we have seen, there are four types of DG based on active/reactive power supplied/absorbed, so as per the requirement DG couples with a specific node which helps to fulfil some percentage of active/reactive power demand at that node. Similarly, D-STATCOM couples with a particular load, which controls bus voltage for controlling the power component. DG changes voltage at that bus and branch current to get minimum power loss. There are many techniques for finding optimal location and size of DG and DSTATCOM with objective of reducing power loss in the system, (i) methods based on analysis, (ii) numerical methods, and (iii) intelligence based methods [12]. Sandeep Kaur et al. [12] used mixed integer liner programming-based numerical to find optimal placement of multiple DG. Shukla T. N. et al. [3] used genetic algorithm. Ke-Yan Liu [14] used tie sequence characteristics of loads and DGs to find optimal siting and sizing of DG. Yuvraj T. et al. [15] proposed Cuckoo search method. S. Devi et al. [15] used particle swarm optimization algorithm.

A review of DG planning and various optimization techniques have been carried out in [16] and changing in power system load flow after DG implementation is carried out in [17]. In this article, we compare two separate approaches, FPA and ABC algorithm, to decide the best size and position of DG and DSTATCOM for reducing losses and optimizing voltage profiles. Yang and Deb [18] suggested a

metaheuristic search algorithm called FPA. Alyasseri et al. [19] offers a description of FPA varieties. The FPA is focused on flower pollination methods used by birds, insects, bats, and other species. In [20], Levy flights are used to characterize the behavior of birds and insects. ABC algorithm is also a metaheuristic approach which is proposed by Karaboga for solving multidimensional optimization problems [21]. Honey bee swarms' intelligent foraging behavior motivated the ABC algorithm. Seker and Hocaoglu [22] finds the optimum size and position of DG using the ABC algorithm. IEEE 33 bus RDS is used to compare the two approaches by evaluating the decrease in power loss and improvements in voltage profile after DG and DSTATCOM are applied in the device. Load and bus data for IEEE 33 are taken from [24].

In this analysis, type 2 DG is taken which can deliver only active power to the system and DSTATCOM which can only deliver reactive power to the system. The formulation of this paper is as follows, Sect. 2 covers problem formulation, Sects. 3 and 4 cover FPA and ABC algorithm, respectively, Sect. 5 includes results, and, finally, conclusion is covered in Sect. 6.

2 Problem Formulation

2.1 Load Flow Analysis

In this paper, the direct approach based load flow analysis method is used. This method first proposed by J. H. Teng [25]. By this, voltage profile at each node and power loss at each branch are calculated. To understand this algorithm, here let's take small example of six bus distribution system (radial) as shown in Fig. 4.

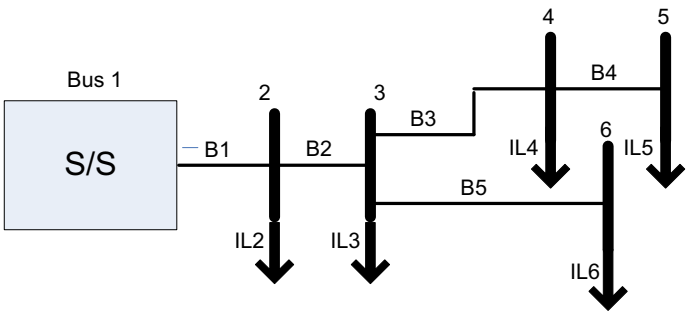

Fig. 4 Six bus RDS

2.1.1 Computation of BCBV (Branch Current to Bus Voltage Matrix) and BIBC (Bus Injection to Branch Current Matrix) Matrix

For node voltages,

$V_2 = V_1 - Z_{12}*I_{12}$.
$V_3 = V_2 - Z_{23}*I_{23} = V_1 - Z_{12}*I_{12} - Z_{23}*I_{23}$.
$V_4 = V_3 - Z_{34}*I_{34} = V_1 - Z_{12}*I_{12} - Z_{23}*I_{23} - Z_{34}*I_{34}$.
$V_5 = V_4 - Z_{45}*I_{45} = V_1 - Z_{12}*I_{12} - Z_{23}*I_{23} - Z_{34}*I_{34} - Z_{45}*I_{45}$.
$V_6 = V_3 - Z_{36}*I_{36} = V_1 - Z_{12}*I_{12} - Z_{23}*I_{23} - Z_{36}*I_{36}$

$$\begin{bmatrix} V1-V2 \\ V1-V3 \\ V1-V4 \\ V1-V5 \\ V1-V6 \end{bmatrix} = \begin{bmatrix} Z12 & 0 & 0 & 0 & 0 \\ Z12 & Z23 & 0 & 0 & 0 \\ Z12 & Z23 & Z34 & 0 & 0 \\ Z12 & Z23 & Z34 & Z45 & 0 \\ Z12 & Z23 & 0 & 0 & Z36 \end{bmatrix} \begin{bmatrix} I12 \\ I23 \\ I34 \\ I45 \\ I36 \end{bmatrix}$$

$$[dV] = [BCBV][Ibranch] \tag{1}$$

From the above figure,

$I_{45} = I_5$.
$I_{34} = I_{45} + I_4 = I_5 + I_4$.
$I_{23} = I_{34} + I_{36} + I_3 = I_6 + I_5 + I_4 + I_3$.
$I_{12} = I_{23} + I_2 = I_6 + I_5 + I_4 + I_3 + I_2$, $I_{36} = I_6$.

So,
$$\begin{bmatrix} I12 \\ I23 \\ I34 \\ I45 \\ I36 \end{bmatrix} = \begin{bmatrix} 1 & 1 & 1 & 1 & 1 \\ 0 & 1 & 1 & 1 & 1 \\ 0 & 0 & 1 & 1 & 0 \\ 0 & 0 & 0 & 1 & 0 \\ 0 & 0 & 0 & 0 & 1 \end{bmatrix} \begin{bmatrix} I2 \\ I3 \\ I4 \\ I5 \\ I6 \end{bmatrix}$$

$$[Ibranch] = [BIBC][Ibus] \tag{2}$$

2.1.2 Computation of Bus Voltage and Branch Currents

From Eqs. (1) and (2),

$$[Ibranch] = [BIBC][Ibus]$$

$$[dV] = [BIBC][Ibranch]$$

$$[dV] = [BIBC][BIBC][Ibus]$$

$$\text{So, [dV]} = \text{[DLF][Ibus]} \tag{3}$$

where DLF is direct load flow matrix.

2.1.3 The Active and Reactive Power Loss for Branch J Can Be Found by

$$\text{P(j)} = \text{I}^2\text{(j)} * \text{r(j)} \tag{4}$$

$$\text{Q(j)} = \text{I}^2\text{(j)} * \text{x(j)} \tag{5}$$

To perform this method in any number of bus system, general steps are given here, for this consider Fig. 5.

Step-1 In this step, we have to initialize all bus voltages as 1 p.u. Initialization of voltages, $V(i) = 1\text{p.u.}$ for $i = 1, 2, 3, \ldots, N$

Step-2 In this step, we have to read load data and bus data.

Step-3 Compute BCBV and BIBC matrices.

Step-4 Now initialize iteration count $k = 0$

Step-5 Calculate load current at all buses except slack bus which is generally numbered bus 1.

$\text{IL(i)} = \frac{\text{PL(I)} - \text{jQL(i)}}{\text{V(i)}*}$ for $i = 2, 3, \ldots, N$

Step-6 Now calculate current through each branch,

$$\text{[Ibranch]} = \text{[BIBC][Ibus]}$$

Step-7 Find DLF matrix and compute bus voltages

$$\text{[dV]} = \text{[DLF][Ibus]}$$

Step-8 Calculate difference between new voltages and previous voltage values and update voltages

$\text{ei}^{\text{k}} = \left|\text{Vi}^{\text{k}} - \text{Vi}^{\text{k}-1}\right|$ for $i = 2, 3, \ldots, N. Vi = Vi^k$

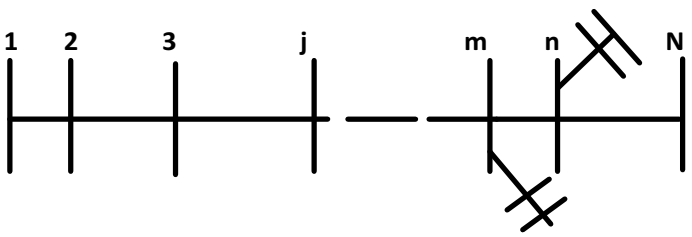

Fig. 5 N bus distribution system

Step-9 Check the tolerance condition, $emax^k = \max(e1^k, e2^k, \ldots, eN^k)$

If emax <tol, then move to nest step otherwise update the iteration count k = k+1 and go to step 5.

Step-10 Calculate line losses and line flows.
Step-11 Print the results.
Step-12 Stop

2.2 Objective Function (oF)

OF is helpful to find best solution of any problem using mathematical approaches. In our analysis, we have used OF which contains only one component which is Total Active Power Loss (TPL).

$$OF = \text{minimum}(TPL) \tag{6}$$

$$TPL = \sum_{j=1}^{N} I^2(j) * r(j)$$

where N is the total number of branches.

The best position for DG and DSTATCOM based on the constraints mentioned below.

2.2.1 Active Power Constraint

$$P_{DGi}^{min} < P_{DGi} < P_{DGi}^{max} \tag{7}$$

where $P_{DGi}{}^{max}$ and $P_{DGi}{}^{min}$ are the maximum and minimum sizes of DG at bus i.

2.2.2 Reactive Power Constraint

$$Q_{DSi}^{min} < Q_{DSi} < Q_{DSi}^{max} \tag{8}$$

where $Q_{DSi}{}^{min}$ and $Q_{DSi}{}^{max}$ are the minimum and maximum sizes of DSTATCOM at bus.

2.3 Investment Cost (IC)

For the cost analysis of our solution, we have to consider investment cost. For calculating investment expense of DG, consider cost characteristics of DG given in Eq. (9) [26], DSTATCOM's annual investment expense can be estimated using Eq. (10) [26].

$$\text{Cost of DG} = (\text{aPdg}^2 + \text{bPdg} + \text{c})\$/\text{MWh} \tag{9}$$

where Pdg is the active power supplied by DG in MW. In this paper, values of confidents are taken as, a = 0, b = 20, c = 0.25

$$\text{C(DSTATCOM)per year} = \text{C(DSTATCOM)}\frac{(1+\text{B})^{\text{n}} * \text{B}}{(1+\text{B})^{\text{n}} - 1} \tag{10}$$

where C(DSTATCOM)/year is the DSTATCOM annual cost in $ and C(DSTATCOM) is the DSTATCOM investment cost in dollars per kVAr at the time of installation. DSTATCOM's asset rate of return and durability are B and n, respectively. Here, C(DSTATCOM) = 50 $/kVAr, B = 0.1, and n = 30 used in this article.

2.4 Cost of Energy Saving (CE)

Energy saving (ES) is difference between energy loss before installation of DG and DSTATCOM and energy loss after installation of DG and DSTATCOM [26]. It can be formulated as (11)

$$\text{ES} = (\text{EL})\text{TkWh} \tag{11}$$

where EL is the difference between TPL in kW before installation and TPL' in kW after installation. T is the time duration in hours.

2.5 Annual Cost Saving (ACS)

ACS is the difference between cost of energy saving and cost of investment. It can be calculated using (12).

$$\text{ACS} = \text{Ke(ES)} - \text{IC\$} \tag{12}$$

where Ke is the energy rate in per kWh. In this paper, we have used Ke = 0.06 /KWh, T = 8760 (hours),

3 Flower Pollination Algorithm (FPA)

The FPA is focused on flower pollination methods used by birds, insects, bats, and other species. Yang and Deb [18] suggested a metaheuristic search algorithm called FPA. FPA is metaheuristic search algorithm. Pollination are often divided in two forms, organic and inorganic. Generally, 90% pollination is finished by pollens, so it's called as organic, and 10% pollination is inorganic means no pollen required. Wind and water diffusion in this inorganic pollination allows the pollination of certain plants. Organic pollination is done in two ways, pollination by self and cross-pollination.

Organic and cross-pollination may have counted in global pollination because in this, pollination can be done by long distance traveling of bees, birds, and other animals. Study in [20] says that jump or distance covered by pollinators can be formulated as Levy distribution. Hence, birds, bees may behave as Levy flight behavior. Steps in this distribution can be found using similarity or difference of two flowers. Based on this, global pollination can be mathematically as [18]

$$\mathrm{Pi}^{t+1} = \mathrm{Pi}^{t} + \lambda \mathrm{L}(\gamma)(\mathrm{G} - \mathrm{Pi}^{t}) \tag{13}$$

where the solution vector of Pi at iteration t + 1 is Pit + 1. At iteration t + 1, G is the best solution, λ is a scaling factor, L(λ) is the pollination power, which is effectively a step size since pollinators travel in steps over a long distance. From [19], to imitate these functions, we can use Levy travel (L), which is L > 0 from the Levy distribution.

$$\mathrm{L}(\gamma) = \frac{\lambda \Gamma(\gamma) \sin\left(\mathrm{pi} * \frac{\lambda}{2}\right)}{\mathrm{pi}} * \left(\frac{1}{\mathrm{s}^{1+\gamma}}\right) \mathrm{s} \gg \mathrm{s0} > 0 \tag{14}$$

This distribution is used for larger steps s > 0 and Γ(γ) is the standard gamma function. Here, Γ(γ) = 1.5 is used based on review in [20].

For the local pollination,

$$\mathrm{Pi}^{t+1} = \mathrm{Pi}^{t} + \varepsilon(\mathrm{Pj}^{t} - \mathrm{Pk}^{t}) \tag{15}$$

where Pjt and Pkt are pollen produced from separate flowers of the same genus of plants. ε is uniformly distributed in [0, 1]. A detailed review of variants of FPA is given in [19]. In Fig. 6, flow chart of FPA is shown.

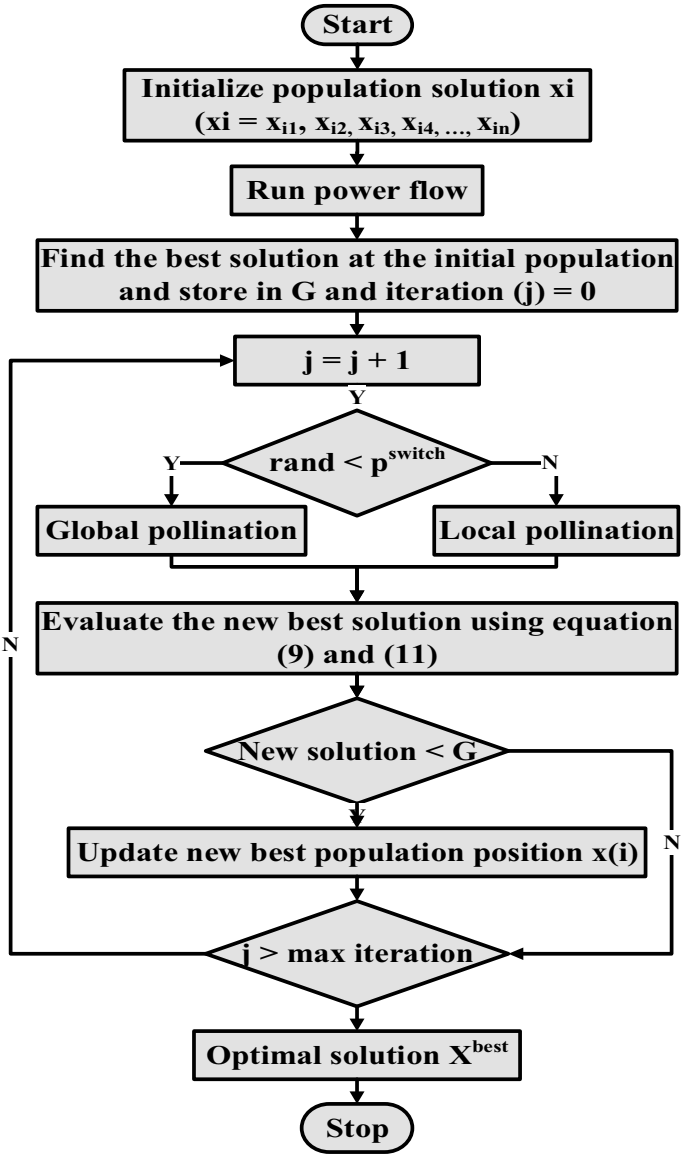

Fig. 6 Flow chart for FPA [19]

4 Artificial Bee Colony (ABC) Algorithm

The behavior of real honey bees looking for food influenced the ABC algorithm. The introduction of ABC is first given by Karaboga in 2005 [21]. ABC is an optimization technique that offers a population-based search procedure in which artificial bees

change individual food locations over time, with the aim of the bees being to locate the places of food supply with the most nectar and recognize it as the one with the greatest nectar. Employed bees, onlooker bees, and scout bees are the three groups of bees that make up a honey bee swarm [23].

- **Employed bees**: During this, randomly searching for food source locations (solutions) as per number of communities such that the information is exchanged is done. The dance cycle depends on the amount of honey from the food supply (fitness value).
- **Onlooker bees**: in step with the standard of food source from searching by assorted employed bees, best food source position could even be found.
- **Scout bees**: An overlooked employed bee source turns into a scout and continues to fly in search of a specific food source [23].

Phase 1: Initialization

The initial food source or populations can be found by the expression,

$$\text{xi} = \text{Lb} + \text{rand}(-1, 1)(\text{Ub} - \text{Lb}) \tag{16}$$

where Ub and Lb are the upper and lower bounds of the solution X.

Phase 2: Employed phase

The following expression is used to calculate the location of the nearest food source:

$$\text{vi, j} = \text{xi, j} + \text{u}(\text{xi, j} - \text{xk, j}) \tag{17}$$

where j is the randomly selected parameters index. U is the random choice that exists among [−1, 1] xk, j is a randomly selected food source. This formula is used to measure fitness, after which greedy selection is added between xi and vi,j,

$$Fitm(Xm) = \frac{1}{1 + Fm(Xm)} if\, Fm(Xm) > 0 \tag{18}$$

$$Fitm(Xm) = 1 + Fm(Xm) if\, Fm(Xm) < 0 \tag{19}$$

where Fm(Xm) is the objective function value of Xm.

Phase 3: Onlooker phase

The profitability of a food source influences its quality, and profitability is measured by expression.

$$Pi = \frac{fitnessi}{\sum_{i=0}^{N} fitnessi} \tag{20}$$

where fitnessi denotes the solution's fitness value and N denotes the number of food source positions (populations). Onlooker bees use the following expression to find a local food source:

$$\mathrm{vi,j} = \mathrm{xi,j} + \mathrm{u(xi,j} - \mathrm{xk,j}) \tag{21}$$

Phase 4: Scout phase

When the location of food is discarded, employed bees become scouts. As follows, Scout generates new food positions:

$$\mathrm{xi,j} = \mathrm{Lb,j} + \mathrm{rand}(-1, 1)(\mathrm{Ubj} - \mathrm{Lb,j}) \tag{22}$$

At initialization step random sources is generated using Eq. (12). After phase 1 completed, phase 2 to phase 4 proceed, this cycle repeats till it reaches maximum cycle limit. In every cycle, new fitness value is computed and new fitness value is greater than previous one then bee replace this new fitness value with old one. In every cycle, employed bees first finds nectar information and its location then shares information with onlooker bees. Onlooker bees utilize this information and try to find best location of source which gives highest nectar quantity. Figure 7 Illustrates the ABC algorithm flow chart.

As quantity of nectar increases, onlooker bees trying to prefer that location. The location of highest nectar is found by onlooker bees using Eq. (16). Scout bees are the pioneers but haven't any direction when trying to find food, so it generates probability of sources which has the lowest and the highest nectar quantity. The selection in scout bee (phase 4) is regulated by the parameter "limit". When the number of trails reaches the limit, the employed bee abandons the source and becomes a scout [28].

5 Results and Discussions

In this section, we will see results obtain by ABC and FPA optimization methods. As we have seen FPA relies on flower pollination process. Number of populations N, and switch probability p, are the sole parameters that makes FPA simple, and when N is fixed, the values of p controls the pollinators. For the calculation, values of $n = 20$ and $p = 0.8$ are taken here, and DG and DSTATCOM range and position are found for IEEE 33 bus RDS. The ABC algorithm solution depends on the digestive tracts of actual honey bees. This algorithm has three control parameters, the colony size (CS) (which is summation of employed bees and onlooker bees), limit value, and maximum cycle number MAXCYCLE. Table 1 lists the parameters required for the ABC and FPA optimization methods.

FPA and ABC algorithms are coded in MATLAB R2015a and simulation results for the IEEE 33 bus RDS are performed in Asus laptop with Intel core i5 @3.4 GHz. The following are the results for IEEE 33 bus test systems.

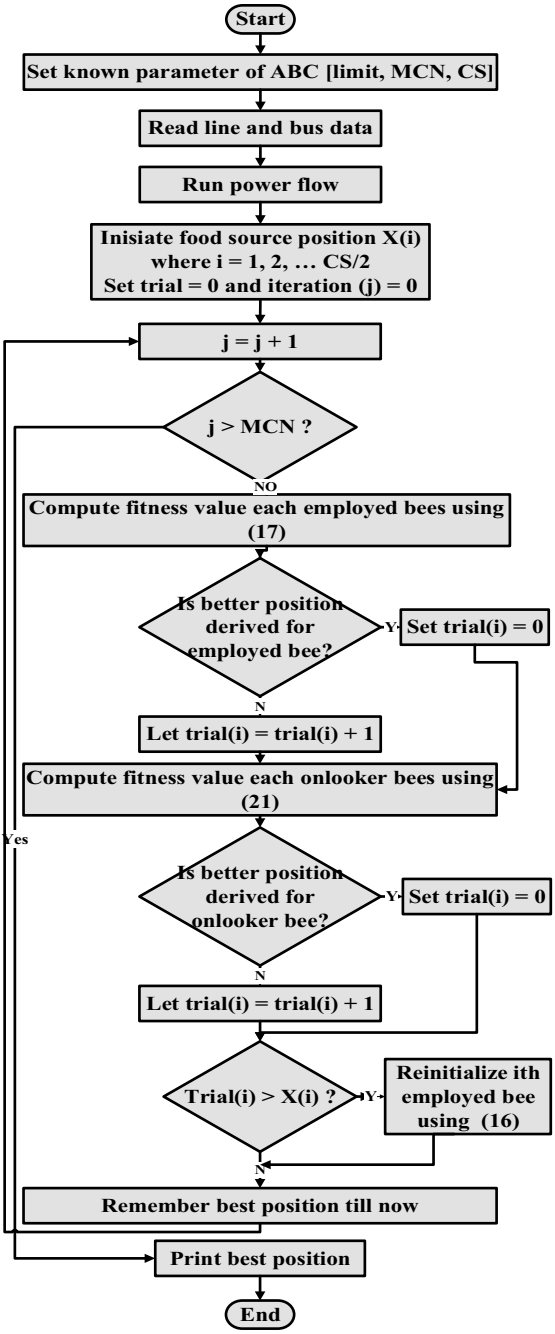

Fig. 7 Flow chart for ABC algorithm [22]

Table 1 Parameters of FPA and ABC

FPA	ABC
No. of populations = 20 Probability = 0.8 Max. iterations = 1500	CS = 40 MAXCYCLE(MCN) = 30 Failure limit = 3

Here, optimal locations of DG and DSTATCOM are searched between bus numbers 2 and 33. Results separated based on various cases like ***case 1 is base case, case 2 is for only DG installation, case 3 is for only DSTATCOM installation, and in case 4, both DG and DSTATCOM*** have implemented in the system. To find best solution of various cases, we have used two metaheuristic methods named ABC and FPA. Initial parameters for the calculation of both methods as shown in Table 1. For the load flow parameters, 100 MVA as a base power and 12.66 kV as a base voltage are taken. For the base load scenario, the total active and reactive power demand is 3.715 MW and 2.30 MVAr, respectively. Results for the optimization problem is shown in Tables 2 and 3.

Table 2 DG and DSTATCOM optimum positioning and sizing using ABC

Parameters	Case 1	Case 2		Case 3	Case 4
		0.8 PF lagging	UPF		
Location	–	8	7	30	7, 30
Size	–	2000 kW	2000 kW	1258.8 kVAr	2000, 1258.8
TPL kW	210.98	119.09	115.19	151.37	61.69
Vmin in p.u	0.9038	0.9405	0.9364	0.9165	0.9486
EL in KWh	1,848,205.8	1,043,228.4	1,009,064.4	1,326,026.6	540,447.3
ES in KWh	–	796,371.6	839,141.4	522,179.2	1,307,758.5
EC in $	–	47,782.29	50,348.48	31,330.75	78,465.51
ACS in $	–	7782.05	10,098.48	9227.70	16,109.98

Table 3 DG and DSTATCOM optimum positioning and sizing using FPA

Parameters	Case 1	Case 2		Case 3	Case 4
		0.8 PF lagging	UPF		
Location	–	8	7	30	7, 30
Size	–	2000 KW	2000	1258.00	2000,1258.00
TPL kW	210.98	119.09	115.98	151.37	61.69
Vmin in p.u	0.9038	0.9405	0.9364	0.9165	0.9486
EL in KWh	1,848,205.8	1,043,228.4	1,016,070.6	1,326,026.6	540,447.3
ES in KWh	–	796,371.6	832,135.2	522,179.2	1,307,758.5
EC in $	–	47,782.296	49,928.11	31,330.75	78,465.51
ACS in $	–	7782.05	9678.11	9225.22	16,109.98

Table 2 shows results obtain using ABC algorithm. Without DG and DSTATCOM, active power loss is 210.98 kW, for case 2, it is 119.09 kW (for 0.8 pf lagging), and 115.19 kW (for Upf), for case 3, it is 151.37 kW, and, for case 4, it becomes 61.69 kW which is lowest among all other cases.

Loss reduction in case 2 is 45%, for case 3 is 28.3%, and for case 4, it is 70.7%. Also the annual cost saving for case 2 is 9678 $, for case 3, it is 9225$, and, for case 4, it is 16109.98 $. In case 4, loss reduction is highest and cost saving is also highest (Tables 4 and 5).

Minimum bus voltage in p.u. before installation of DG and DSTATCOM is 0.9038 p.u. which is lower than permissible limit 9.5 p.u. Now as we install DG and DSTATCOM, it improves and, for case 4, it becomes 0.9486 p.u. for DG size of 2000 kW and for DSTATCOM size of 1258 kVAr. If size of DG and DSTATCOM increases, then voltage profile also improves. Here, we find results for maximum

Table 4 Comparison with existing methods for case 2

Parameters	MINLP [12]	CPLSM [28]	IVM [28]	VSI [29]	ABC	FPA
location, size (KW)	6, 2590	8, 1800	30, 1550	16, 1000	7, 2000	7, 2000
TPL without DG (KW)	211.176	210.976	210.976	210.976	210.982	210.982
TPL with DG (KW)	111.10	118.13	125.16	136.75	115.19	115.98
Loss reduction %	47.39	44.01	40.68	35.18	45.40	45.03
Vmin in p.u	–	0.9433	0.9275	0.9318	0.9364	0.9364
EC in $	–	48,800.3	45,109.4	39,011.5	50,348.5	49,928.1
Cost of Pdg $/MWh	–	36.25	31.25	20.25	40.25	40.25
ACS in $	–	12,550.3	13,859.4	18,761.5	10,098.5	9678.1

Table 5 Comparison with existing methods for case 3

Parameters	VSI [30]	PSI [30]	BA [31]	ABC	FPA
location, size (KVAr)	30, 1250	29, 1300	30, 1150	30, 1258.78	30, 1258.00
TPL without DG (KW)	210.98	210.98	202.67	210.98	210.98
TPL with DG (KW)	151.37	153.07	143.97	151.37	151.37
Loss reduction %	28.25	27.44	28.97	28.25	28.25
ES KWh	522,183.6	507,291.6	514,212.0	522,179.2	522,179.2
Vmin in p.u	–	–	0.9244	0.9165	0.9165
EC in $	–	–	24,768.00	31,330.75	31,330.75

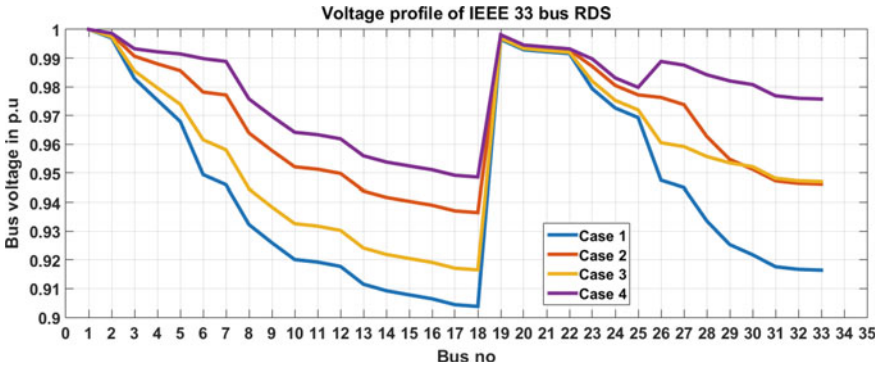

Fig. 8 Voltage in p.u. at each bus for different cases

DG rating as 2000 kW and maximum DSTATCOM rating as 2000 kVAr. Voltage changes at each node in every cases and it is shown in Fig. 8.

Results in Tables 2 and 3 are only for constant loading. Tables 6 and 7 shows optimization results for 20% under loading, 20% overloading, and 7% load growth for 5 years. The active power demand at base loading is 3.715 MW, while the reactive power demand is 2.30 MVAr. For 20% under loading, it becomes 2.972 MW and 1.84 MVAr, for 20% overloading, it becomes 4.458 MW and 2.76 MVAr. If the load increases by 7% per year for 5 years, the power rises to 5.210 MW and 3.23 MVAr. Tables 4 and 5 demonstrate how the results correspond to all other methods for deciding the best size and position of DG and DSTATCOM.

The value of branch currents changes as DG and DSTATCOM are installed in the device and, as a result, active power loss (Ibr2 * r) decreases. Figure 9 shows reduction in branch currents for all cases. From the graph, we can see the reduction in branch currents as we install DG and DSTATCOM in the system.

Figure 10 illustrates voltage profile changes for different loading conditions, while Fig. 11 illustrates active power loss for various loading conditions and cases. As the load on each node increases, the voltage drops below the minimum permissible voltage limit, and the load on each node decreases, the voltage attempts to reach the maximum permissible voltage limit.

Annual Energy loss cost and annual cost savings for different cases are shown in Fig. 12. Annual energy loss cost for case 1 is 110892.3 $ and it is decreased to 32,426.84 $ in case 4. Annual cost savings is also highest in case 4 by 16,109.98 $.

Table 6 Results for IEEE 33 bus RDS using ABC

Parameters	Case 1	Case 2	Case 3	Case 4
With constant load				
Location	–	7	30	7, 30
Size	–	2000 kW	1258.8 kVAr	2000, 1258.8
TPL in kW	210.98	115.19	151.37	61.69
Vmin in p.u	0.9038	0.9364	0.9165	0.9486
EL in KWh	1,848,205.8	1,009,064.4	1,326,026.6	540,447.3
ES in KWh	–	839,141.42	522,179.22	1,307,758.50
EC in $	–	50,348.48	31,330.75	78,465.51
ACS in $	–	10,098.48	9227.7	16,109.98
20% load decrease at each bus				
Location	–	6	30	6, 30
Size	–	2000 kW	1002.31 kVAr	2000, 1002.31
TPL in kW	130.72	69.85	94.55	36.97
Vmin in p.u	0.9244	0.9536	0.9342	0.9630
20% load increase at each bus				
Location	–	8	30	8, 30
Size	–	2000 kW	1519.76 kVAr	2000, 1519.76
TPL in kW	314.49	174.36	223.59	394.20
Vmin in p.u	0.8822	0.9287	0.8982	0.9542
7% load growth for 5 years				
Location	–	8	30	8, 30
Size	–	2000 kW	1791.2 kVAr	2000, 1791.2
TPL in kW	445.94	250.96	313.87	136.59

Table 7 Results for IEEE 33 bus RDS using FPA

Parameters	Case 1	Case 2	Case 3	Case 4
With constant load				
Location	–	7	30	7, 30
Size	–	2000 kW	1258.00 kVAr	2000, 1258.00
TPL in kW	210.98	115.98	151.38	61.69
Vmin in p.u	0.9038	0.9364	0.9165	0.9486
EL in KWh	1,848,205.8	1,016,070.6	1,326,026.6	540,447.3
ES in KWh	–	832,135.18	522,179.22	1,307,758.50
EC in $	–	49,928.11	31,330.75	78,465.51
ACS in $	–	9678.11	9225.22	16,109.98
20% load decrease at each bus				
Location	–	6	30	6, 30
Size	–	2000 kW	1000.41 kVAr	2000, 1000.41
TPL in kW	130.72	69.85	94.55	36.97
Vmin in p.u	0.9244	0.9536	0.9342	0.9630
20% load increase at each bus				
Location	–	8	30	8, 30
Size	–	2000 kW	1519.22 kVAr	2000, 1519.22
TPL in kW	314.49	174.36	223.59	94.20
Vmin in p.u	0.8822	0.9287	0.8962	0.9542
7% load growth for 5 years				
Location	–	8	30	6, 30
Size	–	2000 kW	1787.88 kVAr	2000, 1787.88
TPL in kW	445.94	250.96	313.88	136.58

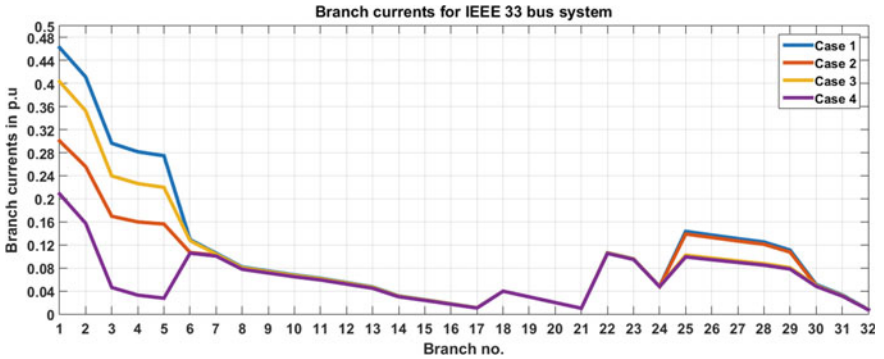

Fig. 9 Branch currents in p.u. for each branch

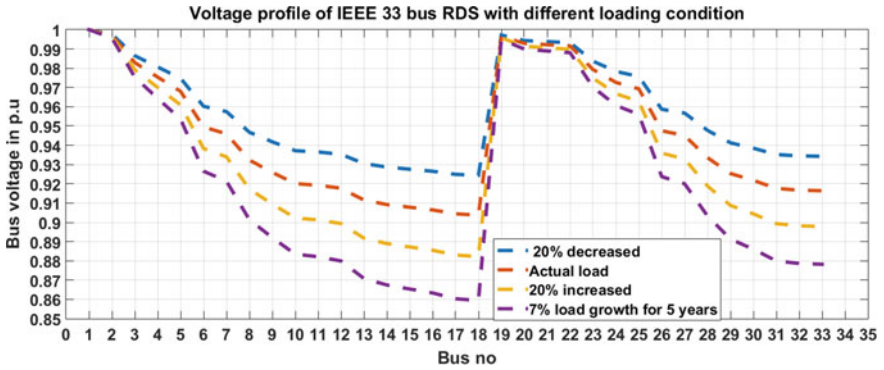

Fig. 10 Voltage in p.u. at each bus for different cases

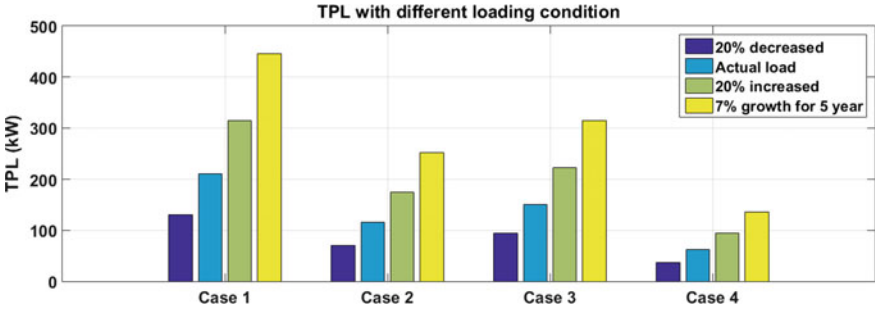

Fig. 11 Total active power loss for different cases and different loadings

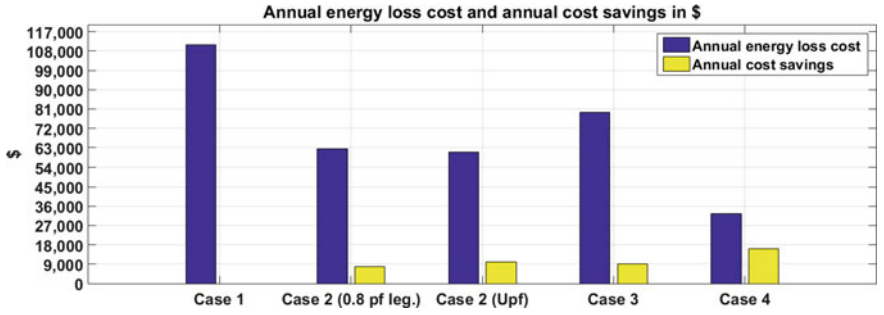

Fig. 12 Annual energy loss cost and annual cost savings for different cases

6 Conclusions

In different cases, the FPA and ABC algorithms are used to determine the best size and position of the DG and DSTATCOM in order to improve the voltage profile and minimize active power loss and of the system. The comparison of the results for IEEE 33 bus RDS with existing methods is shown. ABC algorithm requires very less computation time as compared to FPA for solving these kind of optimization problem. Solution using ABC requires 1.2–2 s, while FPA requires 27–30 s. Comparison of base load results with various load growth cases is done. From the results, we can conclude that,

- After installing DG and DSTATCOM, voltage profile of system improves. Results with both DG and DSTATCOM is better as compared to alone DG or DSTATCOM. For case 2, voltage improvement in case 2 is 3.6%, in case 3 is 1.4%, and in case 4 is 4.5%.
- The annual cost savings and loss reduction are greatest when both DG and DSTATCOM are installed. Annual cost saving in case 2 is 9678.11 $, for case 3 is 9225.22 $, and in case 4 is 16109.98 $.
- As the load increases, the system's minimum bus voltage changes. For base case, minimum bus voltage is 0.9038 p.u., for 20% decrease in load, it becomes 0.9244 p.u., for 20% load increment, minimum bus voltage falls to 0.8822 p.u.
- As system loading changes, voltage profile of the system changes and, for over-loading condition, it goes below the minimum voltage limit and for under loading, it goes above maximum voltage limit.

Improved voltage profile of the system, reduced active power loss, and cost savings are all advantages of using a network with both DG and DSTATCOM.

References

1. https://En.Wikipedia.Org/Wiki/Electricity_Sector_In_India
2. Growth of Electricity Sector In India From 1947–2019, Central Electricity Authority. August 2019
3. Shukla TN, Singh SP, Naik KB (2008) Allocation of optimal distributed generation using GA for minimum system losses. NPSC, Dec 2008
4. Root CE (2006) The future beckons [Electric Power Industry]. IEEE Power Energy Mag 4:24–31
5. Joscow P (2006) Patterns of transmission investments in competitive electricity markets and sustainability. 131
6. Acharya N, Mahat P, Mithulananthan N (2006) An analytical approach for DG allocation in primary distribution network. Int J Electr Power Energy Syst 28:669–678
7. Singh B, Mishra DK (2018) A survey on power performance by optimally placed DG in distribution network. Energy Rep 4:129–132
8. https://Powermin.Nic.In/En/Content/Decentralized-Distributed-Generation-Ddg
9. Chen B-S, Hsu Y-Y (2008) A minimal harmonic controller for a STATCOM. IEEE Trans Ind Electron 55(2):655–664

10. Devabalaji KR, Ravi K (2014) Power quality improvement in wind farm connected to grid using STATCOM. In: Proceedings of the international conference on advances in electrical engineering (ICAEE'14), pp 1–5, Unnao, India, Jan 2014
11. Kanwar N, Gupta N, Niazi KR, Swarnkar A (2015) Optimal distributed generation allocation in radial distribution systems considering customer-wise dedicated feeders and load patterns. J Mod Power Syst Clean Energy 3(4):475–484
12. Kaur S, Kumbhar G, Sharma J (2014) A MINLP technique for optimal placement of multiple DG units in distribution systems. Electr Power Energy Syst 63:609–617
13. Yuvaraj T, Devabalaji KR, Ravi K (2015) Optimal allocation of DG and DSTATCOM in radial distribution system using cuckoo search optimization algorithm. Hindawi, 2017
14. Liu K-Y, Sheng W, Liu Y, Meng X, Liu Y (2015) Optimal sitting and sizing of DGs in distribution system considering time sequence characteristics of loads and DGs. Electr Power Energy Syst 69:430–440
15. Devi S, Geethanjali M (2014) Optimal location and sizing determination of distributed generation and DSTATCOM using particle swarm optimization algorithm. Electr Power Energy Syst
16. Theo WL, Lim JS, Ho WS, Hashim H, Lee CT (2017) Review of distributed generation (DG) system planning and optimisation techniques: comparison of numerical and mathematical modelling methods. Renew Sustain Energy Rev 67:531–573
17. Singh B, Mishra DK (2018) A survey on enhancement of power system performances by optimally placed DG in distribution networks. Energy Rep 4:129–158
18. Yang X-S (2012) Flower pollination algorithm for global optimization. Unconventional computation and natural computation, vol 9. Springer, p 240
19. Alyasseri ZAA, Khader AT, Al-Betar MA, Awadallah MA, Yang X-S (2018) Variants of the flower pollination algorithm: a review. Springer
20. Pavlyukevich I (2007) L´Evy flights, non-local search and simulated annealing. J Comput Phys 226:1830–1844
21. Karaboga D (2005) An idea based on honey bee swarm for numerical optimization. Technical report TR06. Computer Engineering Department, Erciyes University, Turkey
22. Seker AA, Hocaoglu MH (2013) Artificial bee colony algorithm for optimal placement and sizing of distributed generation. IEEE ELECO 2013
23. D. Karaboga, B. Akay: A Modified Artificial Bee Colony (ABC) Algorithm For Constrained Optimization Problems. Applied Soft Computing, Volume 11, Issue 3, April 2011, Pages 3021–3031, ISSN 1568–4946.
24. Kashem MA, Ganapathy V, Jasmon GB, Buhari MI (2000) A novel method for loss minimization in distribution networks. In: International conference on electric utility deregulation and restructuring and power technologies 2000. IEEE
25. Teng JH (2000) A network-topology based three-phase load flow for distribution systems. Proc Natl Sci Council ROC (A) 24(4):259–264
26. Kumar A, Vijay Babu1 P, Murty VVSN (2017) Distributed generators allocation in radial distribution systems with load growth using loss sensitivity approach. J Inst Eng India Ser B 98(3):275–287
27. Gupta AR, Kumar A (2019) Reactive power deployment and cost benefit analysis in DNO operated distribution electricity markets with D-STATCOM. Front Energy 13:86–98
28. Murty VVSN, Kumar A (2013) Comparison of optimal DG allocation methods in radial distribution systems based on sensitivity approaches. Electr Power Energy Syst 53:450–467
29. Kejun Q, Chengke Z, Malcolm A, Yue Y (2011) Effect of load models on assessment of energy losses in distribution generation planning. Electr Power Res 2:1243–1250
30. Guptaa AR, Kumar A (2015) Energy savings using D-STATCOM placement in radial distribution system. Proc Comput Sci 70:558–564
31. Yuvaraj T, Ravi K, Devabalaji KR (2015) DSTATCOM allocation in distribution networks considering load variations using bat algorithm. Ain Shams Eng J

Analysis and Design Optimization of Six-Phase Induction Motor by Metaheuristic Methods

Pratyush Prasanna Das and S. N. Mahato

1 Introduction

Induction motor is the most popular machine because of its low cost, little maintenance, easy availability, and robust construction. Nowadays, multi-phase induction machines find many applications in high-power drives as these machines reduce the torque pulsation frequency and amplitude. Also, it reduces harmonic currents that flow in rotor circuits. The DC link current harmonics are reduced and reliability is increased with the increase of power. These multi-phase machines have applications in electric hybrid vehicles, in aerospace applications and ship propulsion [1]. The modeling of six-phase induction motor under open-phase fault condition has been performed in [2]. The genetic algorithm-based design optimization has been reported by Fazlipour et al. [3] and the results have been compared with that of traditional design method.

Digital synchronous frame current regulation for six-phase induction motor has been reported by Bojoi et al. [4]. The high phase order induction motor theory has been presented in [5]. Nanoty and Chudasama presented the control and design of six-phase induction motor [6]. The testing of six-phase induction motor has been discussed by Gregor et al. [7]. Using third harmonic current injection for the increase in torque density in case of six-phase induction motor has been reported in [8]. Modi and Chaturvedi [9] discussed the theory of six-phase induction motor design. Mondal [10] analyzed the performance of a six-phase induction motor.

In case of Novel Bat Algorithm (NBA) with habitat selection and Doppler effect in echos, a self-adaptive local search has been proposed by Meng et al. [11]. The authors have developed the way of habitat selection based on quantum and mechanical behavior of a bat. Cuckoo search algorithm facilitates both local and global search capabilities and uses Levy flights as a way to reach the global optima [12].

P. P. Das (✉) · S. N. Mahato
Department of Electrical Engineering, NIT Durgapur, Durgapur, India
e-mail: ppd.16EE1503@phd.nitdgp.ac.in

S. Kumar et al. (eds.), *Recent Advances in Power Electronics and Drives*, Lecture Notes in Electrical Engineering 852, https://doi.org/10.1007/978-981-16-9239-0_15

The Levy flight is the straight line trajectory flight with sudden twist of 90° within the flight [13]. In Cuckoo search algorithm, each pattern is attributed to both a nest and to an egg [14]. Many complex multi-objective engineering problems like spring design optimization and welded beam design have been solved with Cuckoo search algorithm [15]. Optimal design of PID controller for speed control of BLDC motor have been done by Flower Pollination Algorithm [16].

The main contributions of this paper are:

- Modification of Flower Pollination optimization algorithm.
- Use of modified Flower Pollination optimization algorithm (mFPA), NBA, Cuckoo Search Algorithm, and traditional design method for optimized design of a six-phase induction motor.
- Study and comparison of the performances of the motor using these optimized parameters of different algorithms in MATLAB/SIMULINK simulation environment.

2 Optimization Algorithms

2.1 Modified Flower Pollination Algorithm

In case of flower pollination algorithm (FPA), pollens are pollinated to the flowers by insects or any living being. This type of pollination is done by selecting the best pollen and making the desired flower pollinated. This concept has the Levy flight involved with the movement of the insects.

The modification is done in this mFPA by incorporating a matrix manipulation that leads to more closure to the best-valued matrix or the position of the flower having best pollen. The Levy step size is also applied each time of matrix management. The updated position of the flower is as follows:

$$x_i(t+1) = x_i(t) + L \times \{x_i(t) - gbest\}$$

Here, the evolutionary matrix manipulation has been done in order to get much more convergent position of the optimal best flower, associated with globally best position of the pollen. The matrices added here for convergence are as follows:

$$\lambda_1 = L \times (x_i(t)/best)$$

$$\lambda_2 = L \times \sqrt{\left|best/1.414^2\right|}/best$$

$$\lambda_3 = L \times ((1/best) \times ((1 - x_i(t))/(1 + x_i(t))))$$

$$\lambda_4 = L \times ((x_i(t) - best)/2 + (best - x_i(t))/2)$$

$$\lambda_5 = L \times (x_i(t)/2) + L \times (x_i(t)/2)$$

$$\lambda_6 = L \times (|(x_i(t) - best)/best|)$$

$$\lambda_7 = L \times (|(x_i(t) - best)/(x_i(t) + best)|)$$

$$\lambda_8 = L \times (best - x_i(t)) \times 1.414$$

$$\lambda_9 = L \times (x_i(t) - best)$$

$$\lambda_{10} = x_i(t)$$

The correction vector is the function of aforesaid vectors, i.e., equals to f (λ_1, $\lambda_2 \ldots. \lambda_{10}$).

The equation for updated flower position for biotic pollination is given as

$$x_i(t+1) = x_i(t) + f(\lambda_1, \lambda_2 \ldots..\lambda_{10})$$

2.2 Novel Bat Algorithm

A short-waved modulated frequency called echolocation is used by each bat to avoid obstacles, which controls the velocity of the bat in the Bat algorithm. An inertia weight factor, contraction and expansion coefficients, and a compensation rate of Doppler effect involved for echoes are incorporated in positional and velocity equations in order to increase the convergence of the optimization algorithm and thus called NBA. In this paper, taking losses of six-phase induction motor as objective function, the optimized design of the SPIM is obtained.

2.3 Cuckoo Search Algorithm

In Cuckoo search algorithm, cuckoos lay eggs to a nest selected by the cuckoos. The host bird finds the best nest with eggs or could throw the egg away to build a new nest instead, with a probability of 0–1. In this paper, both the rotor and stator copper losses are minimized to get the optimized design of six-phase induction motor.

3 Design Problem Formulation of Six-Phase Induction Motor

In order to formulate the design problem for optimization of the six-phase induction motor, some design parameters are used as design variables to be optimized. The objective functions involved here for optimization are stator and rotor copper losses.

If $f_1(x_i)$ and $f_2(x_i)$ are two objective functions, where x_i are the design variables to be optimized, then minimization of $f_1(x_i)$ and $f_2(x_i)$ gives optimized values of x_i.

4 Objective Functions and Design Equations

The rating of six-phase induction motor used in traction application in Indian scenario, which is intended to be optimally designed, is given as follows:

1150 kW, 50 Hz, 2180 V, 6 Pole, Delta-connected six-phase induction motor, number of stator slots = 72, and number of rotor slots = 54.

The control parameters for mFPA, NBA, and Cuckoo search algorithm, respectively, are given as follows:

Control parameters for Modified Flower Pollination Algorithm:

$$\begin{aligned}&\text{Size of population } = 20\\ &\text{Value of switch probability } = 0.8\\ &\text{Iteration number in total } = 2000\end{aligned}$$

$$\begin{aligned}\text{Search variables dimension } &= 3 \text{ in case of rotor copper loss}\\ &= 1 \text{ in case of stator copper loss}\end{aligned}$$

Control parameters in Novel Bat Algorithm (NBA):

$$\begin{aligned}&\text{Rate of pulse emission and loudness updating frequency } = 10\\ &\text{Selection ofhabitatprobability, maximum } = 0.9\\ &\text{Selection ofhabitatprobability, minimum } = 0.6\\ &\text{Co - efficient of expansion, maximum } = 1\\ &\text{Co - efficient of contraction, minimum } = 0.5\\ &\text{Weight of inertia, maximum } = 0.9\\ &\text{Weight of inertia, maximum } = 0.5\\ &\text{Doppler effect echos compensation rate, maximum } = 0.9\\ &\text{Doppler effect echos compensation rate, minimum } = 0.1\end{aligned}$$

$$\text{Search variables dimension} = 3 \text{ in case of rotor copper loss}$$

$= 1$ in case of stator copper loss

Control parameters for Cuckoo Search Algorithm:

Number of nests or solutions $= 3$
Rate of discovery of alienated eggs or solutions $= 0.25$
Iteration Number time $= 4$

Dimension of search variables $= 3$ in case of rotor copper loss
$= 1$ in case of stator copper loss

The design variables and the design constraints are given as follows:

There are seven design variables for six-phase induction motor intended to be designed optimally. They are as follows:

Core length which is equal to rotor and stator $= x_1$
Stator inner diameter $= x_2$
Depth of stator slot $= x_3$
Width of stator teeth $= x_4$
Depth of stator core $= x_5$
Efficiency, $\eta = x_6$
Power factor $= x_7$

Design Constraints are as follows:

Current density in the rotor bar is between 4 and 7 A/mm^2
Ratio of pole length to pole face length, $L/\tau = 1.5$
Average flux density, $B_{av} = 0.45$ Wb/m^2
$K_w = 0.955$
Space factor $= 0.4$
Maximum allowable flux density in the stator slot $= 1.7$ Wb/m^2.
Flux density in the stator core $= 0.8$ Wb/m^2

The maximum and minimum values design variables for mFPA, NBA, and Cuckoo search algorithm are given as follows:

For Novel Bat algorithm:

$0.3 <$ Core length, $x_1 < 0.54$
$0.68 <$ Stator inner diameter < 0.8
$0.8 <$ Efficiency < 0.99

0.8 < Power factor < 0.99.

For modified Flower Pollination Algorithm:

0.3 < Core length, x_1 < 0.54
0.68 < Stator inner diameter < 0.8
0.99 < Efficiency < 1
0.97 < Power factor < 0.98.

For cuckoo search algorithm:

0.3 < Core length, x_1 < 0.54
0.68 < Stator inner diameter < 0.8
0.8 < Efficiency < 0.99
0.8 < Power factor < 0.99.

Rotor copper loss in six-phase cage rotor induction motor, in terms of bar current, diameter of end ring can be written as

$$P_{rcl} = \left(r_r s_r I_b^2/a_b\right) \times ((L_r + 2D_e)/P) = 6.8 I_b (x_1 + D_e/3)$$

In case of six-phase induction motor, power = $6V_{ph}I_{ph}\cos\emptyset$ and therefore
$I_s = 87.9/(p.f \times \eta)$ A.
and the rotor bar current is given as

$$((2m_s k_{ws} T_s)/S_r) \times (87.9/(\cos\varnothing \times \eta)) \times \cos\varnothing$$

Putting the value of ms, this expression becomes as

$$1057.8 \times k_{ws}(T_s/(S_r \times \eta))$$

The expression for maximum flux density is $(B_{av}L_2)/1.5$ and in terms of the design variables, it becomes as $0.29 \times x_1^2$.

The stator turns per phase = $2180/\left(4.44 \times 50 \times 0.29 \times x_1^2 \times 0.955\right) = 35.46/x_1^2$

Bar current = $4.8 k_{ws}(T_s/(S_r\eta)) = 2.9/\left(x_1^2 \times \eta\right)$

The end ring current becomes $(S_r I_b)/\pi p$ and, after putting the values of variables, the expression becomes as $8.41/\left(x_1^2 \times \eta\right)$ A. Considering the value of current density as 6 A/mm^2, the area of end ring will be $1.4/\left(x_1^2 \times \eta\right)$ mm^2. Now from the table of recommended sizes of copper strip IS 1897–1962, the value of t is taken as 0.47w.

The outside and inside diameters of the end ring in terms of the design variables are given as $\left(x_2^2 - 0.006\right)$ m and $x_2^2 - 0.006 - 0.1/\left(x_1 \times \eta^{(1/2)}\right)$ m, respectively. Therefore, the mean diameter of ring becomes $x_2 - 0.0006 - 0.1/\left(x_1 \times \eta^{(1/2)}\right)$ m.

The rotor copper loss = $6.8 I_b (x_1 + 0.33 D_e)$
$= \left(19.72/\left(x_1^2 \times x_6\right)\right) \times \left(x_1 + 0.33x_2 - 0.0002 - 0.033/\left(x_1 \times x_6^{1/2}\right)\right)$ watts.

4.1 Novel Bat Algorithm

The rotor copper loss $= \left(19.72/\left(x_1^2 \times x_6\right)\right) \times \left(x_1 + 0.33x_2 - 0.0002 - 0.033/\left(x_1 \times x_6^{1/2}\right)\right)$ watts.

As the stator current is $88.8/x_7$, the area of stator conductor will be $14.8/x_7$. The length of mean turn is taken as $(2L + 2.3\Gamma + 0.24) = 5x_1 + 0.24$.

The stator resistance $= x_7(0.18x_1 + 1.2)/x_1^2 \times 0.001\ \Omega = x_7(0.18x_1 + 1.2)/x_1^2 \times 0.001\ \Omega$ and the stator copper loss becomes as $210.473/x_7$ watts.

4.2 Modified Flower Pollination Algorithm

Similarly, as per above calculation, the rotor copper loss for mFPA is.

$\left(19.72/\left(x_1^2 \times x_6\right)\right) \times \left(x_1 + 0.33x_2 - 0.0002 - 0.033/\left(x_1 \times x_6^{1/2}\right)\right)$ watts.

The stator copper loss $= 659.223/x_7$ watts.

4.3 Cuckoo Search Algorithm

The rotor copper loss $= \left(19.72/\left(x_1^2 \times x_6\right)\right) \times \left(x_1 + 0.33x_2 - 0.0002 - 0.033/\left(x_1 \times x_6^{1/2}\right)\right)$ watts and the stator copper loss $= 298.899/x_7$ watts.

5 Results and Discussions

The optimization of the parameters of the six-phase induction machine has been carried out using the above-mentioned algorithms and also by traditional design method. The results obtained have been presented in Table 1. It is observed from this table that the new mFPA algorithm gives better efficiency of 82.828% and the optimized value of power factor is 0.98, in comparison to the other optimization algorithms and the traditional method of design. The modified version of FPA is the most energy efficient method. It is also found that, in case of the mFPA algorithm of optimization, the size of the motor is highly reduced as compared to the other optimization methods, as stator stack length is reduced to 0.3 m. Hence, the cost of material also gets reduced. As the flux density in the stator core and the maximum flux density in the stator teeth are reduced in case of modified FPA, the specific iron loss is reduced and in turn, the stator iron loss gets reduced.

In the same way, the rotor-specific iron loss and thus the rotor iron loss are also reduced. As the magnetizing reactance, in case of mFPA, is increased to a value of 151.0655 Ω than the other design methods, the short-circuit current is minimum in this case. The mFPA provides reduced stator and rotor resistances, hence the stator and rotor copper losses are also lowered. As the iron loss is proportional to the weight of the stator and rotor, the weight of the motor gets reduced in case of mFPA. As the stator and rotor losses, which are the main sources of temperature rise, are decreased in case mFPA method, the temperature rise of the motor is also reduced. As the maximum flux density of the rotor core, stator teeth, rotor teeth are lowest in value in case of mFPA design method than other design methods, so the iron loss also gets reduced in case of mFPA design method (Table 1).

Figure 1 shows the efficiency curve of different design methods. It is seen that the efficiency of mFPA is the highest among all the design methods. The total losses as obtained using different design methods are presented in Fig. 2, which shows that the total loss in mFPA method is the lowest among the different methods of design. Also, it is observed from Figure 3 that the stator stack length is the minimum in case of mFPA method of design.

From Table 2, it is found that the time taken to reach steady operating condition in case of mFPA design method is very much less and it is only 0.4 secs, whereas in traditional design method it is 3.3 secs and other methods had not reached the steady operating condition. The time taken to reach 500 RPM on 28 Nm traction load is 0.4 secs in case of mFPA design method but other methods had produced more time. The mFPA design method yields less time taken to reach 500 RPM on no load and that is 0.6 secs. Reduced times in both the cases contribute to reduced heating and reduced power loss for mFPA design method. Also, results of Table 2 show mFPA design method produces more stable motor than others.

Table 3 shows comparison of mFPA design method of this paper with that of GA-based design method which is done by Fazlipur et al. and is referenced hereby at [3]. From the Table-3, it is found that mFPA design method yields much more improved power factor, increased efficiency, reduced total loss, and reduced stator stack length. Although, motor rating for mFPA-based design and GA-based design (under paper in Ref. [3]) are different but the mFPA design method is much more good results.

5.1 Validation of Proposed Algorithm

From Table 4, it is found that the proposed mFPA design method is a confident method of design as for both the cases of design, viz., for 1150 KW motor which have been done here and for 0.26 KW motor which have been done but not shown here, yields 12.4 and 4% increase in full-load efficiency, total loss decreased 41.94 and 19.3%, as well as stator stack length decreased 44.44 and 6.67% for 1150 and 0.26 KW motors, respectively. Other methods of designs like NBA and Cuckoo search produces infidel results as in those cases efficiency at full load, total loss, and stator

Table 1 Parametric values of different design methods

Design parameters	Novel Bat algorithm	Modified FPA	Cuckoo search	Traditional design
Power factor	0.99	0.98	0.9548	0.86
Efficiency at FL (%)	78.4711	82.828	70.3965	73.685
Total loss (W)	3.1551×10^5	2.3842×10^5	4.836×10^5	4.107×10^5
No-load power factor	0.1	0.1	0.1	0.1
Stator resistance (Ω)	0.4	0.3	0.4	0.4
Rotor resistance (Ω)	6	8	6	6
Equivalent resistance (Ω)	150	138	150	150
Equivalent Reactance (Ω)	3	5.7	5.2	5.2
Magnetizing Reactance (Ω)	120.5096	151.0665	117.1576	120.5096
Stator stack length (m)	0.54	0.3	0.4955	0.54
Stator inner diameter (m)	0.68	0.68	0.7887	0.68
Rotor inner diameter (m)	0.399	0.499	0.5268	0.3996
Width of stator teeth (m)	0.006	0.0049	0.008	0.0088
Depth of stator slot (m)	0.015	0.015	0.015	0.015
Stator slot width (m)	0.0869	0.0869	0.0869	0.0869
Depth of stator core (m)	0.112	0.0625	0.103	0.0057
Flux density of stator core (T)	0.8	0.8	0.8	0.8
Flux density of rotor core (T)	0.7397	0.4109	0.5501	0.7397
Maximum stator teeth flux density (T)	3.4	1.8889	3.1198	3.4
Maximum rotor teeth flux density (T)	0.8551	0.4751	0.6359	0.8551

stack length decreased, increased, and increased, respectively, in case designing 0.26 KW motor. Those characteristics has been shown in bar chart Fig. 4a–c.

6 Development of Simulink Model

The electromagnetic torque developed by the six-phase induction motor is given as (Eq. 1)

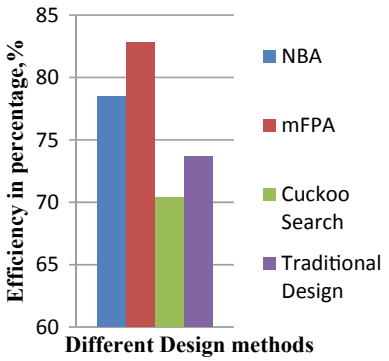

Fig. 1 Efficiency bar chart of different design methods

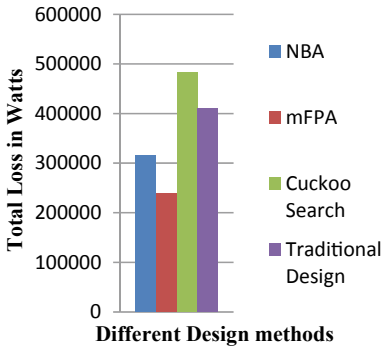

Fig. 2 Total loss bar chart of different design methods

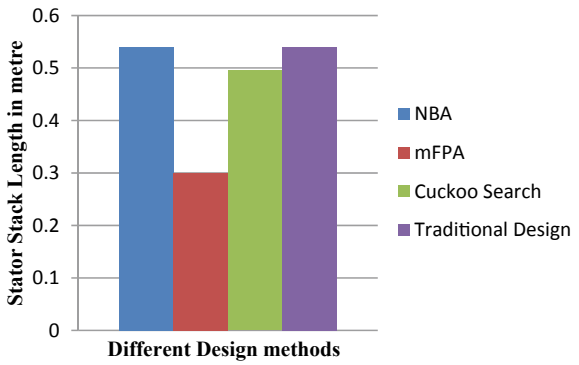

Fig. 3 Stator stack length bar chart of different design methods

$$T_e = (3/2)(P/2)(L_m/L_{lr}) \left\{(i_{dr}L_{lr} + i_{dr}L_m + i_{ds}L_m + i_{dso}L_m) - \left(i_{qr}L_{lr} + i_{qr}L_m + i_{qs}L_m + i_{dso}L_m\right)\right\} \quad (1)$$

and the expression of speed can be written as (Eq. 2).

Table 2 Comparison of different design method's parametric values

Design parameters	Novel Bat algorithm	Modified FPA	Cuckoo search	Traditional design
Maximum torque on 28 Nm traction load (Nm)	510	420	600	600
Time taken to reach maximum torque on 28 Nm traction load (s)	0.01	0.01	0.01	0.01
Time taken to reach steady operating condition on 28 Nm traction load (s)	Not reached	0.4	Not reached	3.3
Maximum torque on no load (Nm)	510	330	600	600
Time taken to reach maximum torque on no load (s)	0.01	0.01	0.01	0.01
Time taken to reach 500 RPM on 28 Nm traction load (s)	15.4	0.4	20	11.1
Time taken to reach 500 RPM on no load (s)	13.3	0.6	19.2	10

Table 3 Comparison of mFPA design method with that of GA-based design method

Design parameters	Percentage increase or decrease (%) for GA-based design to traditional design (for paper in Ref. [3])	Percentage increase or decrease (%) for mFPA design to traditional design	Remarks
Power factor	Same	13.95 (increase)	Power factor improved much more in case of mFPA design
Efficiency at FL	7.5 (increase)	12.4 (increase)	Efficiency increased much more in case of mFPA design
Total loss	22.3 (decrease)	41.94 (decrease)	Total loss decreased much more in case of mFPA design
No-load power factor	18.8 (increase)	Same	No-load Power factor remains same in of mFPA design
Stator resistance	71.45 (decrease)	25 (decrease)	Stator resistance decreased in case of mFPA design
Magnetizing Reactance	18.2 (increase)	24.79 (increase)	Magnetic reactance increased in case of mFPA design
Stator stack length	36 (increase)	44.44 (decrease)	Stator stack length decreased much more in case of mFPA design

Table 4 Validation data for different algorithms

Motor ratings	1150 KW			0.26 KW		
Design parameters	Percentage increase or decrease (%) for mFPA design to traditional design	Percentage increase or decrease (%) for NBA design to traditional design	Percentage increase or decrease (%) for Cuckoo search design to traditional design	Percentage increase or decrease (%) for mFPA design to traditional design	Percentage increase or decrease (%) for NBA design to traditional design	Percentage increase or decrease (%) for Cuckoo search design to traditional design
Efficiency at FL	12.4 (increase)	6.5 (increase)	4.46 (increase)	4 (increase)	6.5 (decrease)	14 (decrease)
Total loss	41.94 (decrease)	23.2 (decrease)	17.75 (increase)	19.3 (decrease)	36 (increase)	84 (increase)
Stator stack length	44.44 (decrease)	No Change	8.24 (decrease)	6.67 (decrease)	85.2 (increase)	67 (increase)

$$\omega_r = \int (P/2J)(T_e - T_L)\, dt. \tag{2}$$

The zero sequence current does contribute to the torque and hence for the speed. Accordingly, it is taken into consideration.

The direct and quadrature axes voltage equations of stator and rotor in terms of currents and flux linkages and stator and rotor resistances, are as follows (from Eqs. 3–6):

$$v_{ds} = R_s i_{ds} + \frac{d\psi_{ds}}{dt} - \omega_e \psi_{qs} \tag{3}$$

$$v_{qs} = R_s i_{qs} + \frac{d\psi_{qs}}{dt} + \omega_e \psi_{ds} \tag{4}$$

$$v_{dr} = R_r i_{dr} + \frac{d\psi_{dr}}{dt} + (\omega_e - \omega_r)\psi_{qr} \tag{5}$$

$$v_{qr} = R_r i_{dr} + \frac{d\psi_{qr}}{dt} + (\omega_e - \omega_r)\psi_{dr} \tag{6}$$

The stator and rotor flux linkage equations in terms of magnetizing inductances, stator and rotor inductances are as follows (from Eqs. 7–8):

$$\psi_{ds} = L_{ls} i_{ds} + L_m (i_{ds} + i_{dr}) \tag{7}$$

$$\psi_{dr} = L_{lr} i_{dr} + L_m (i_{ds} + i_{dr}) \tag{8}$$

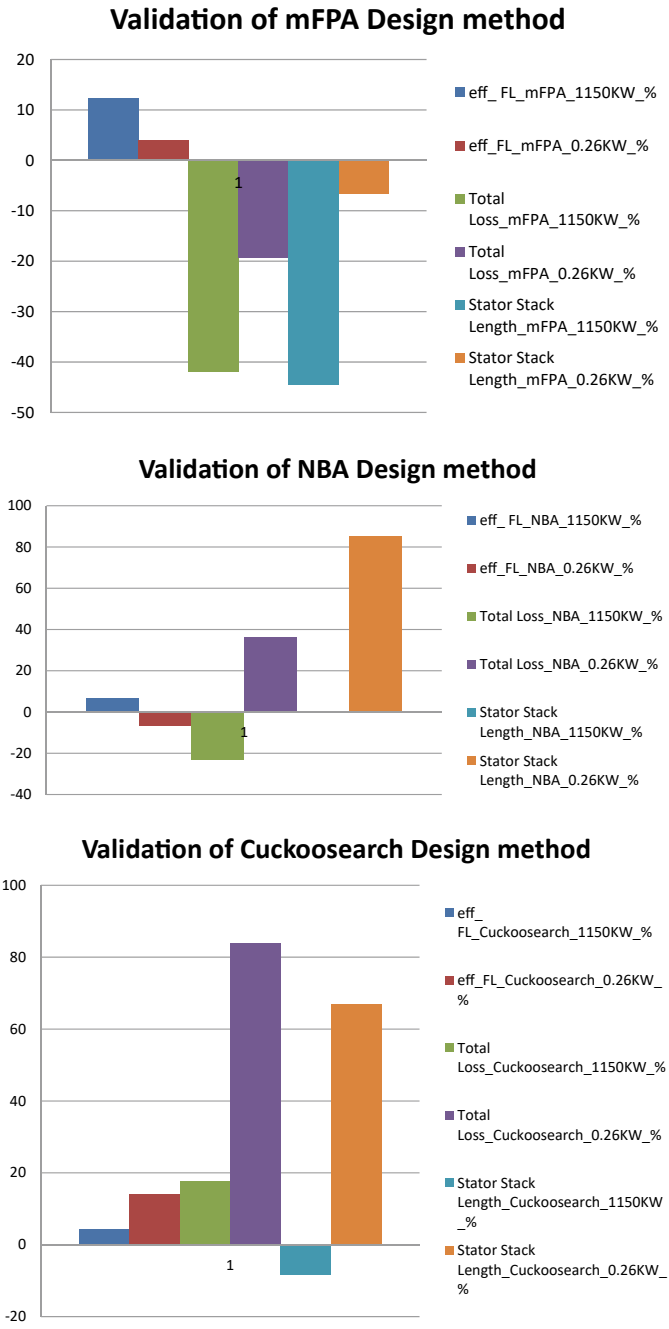

Fig. 4 **a** Validation bar chart of mFPA design method. **b** Validation bar chart of NBA design method. **c** Validation bar chart of Cuckoo search design method

$$\psi_{qs} = L_{ls} i_{ds} + L_m \left(i_{qs} - i_{qr} \right) \tag{9}$$

$$\psi_{qr} = L_{lr} i_{dr} + L_m \left(i_{qs} + i_{qr} \right) \tag{10}$$

An arbitrary reference frame with a rotating speed w_e is considered here, to which the machine equations are transformed. With the equations of voltage of stator and rotor sides in terms of flux linkages and currents, the SIMULINK/MATLAB model has been prepared for simulation.

7 Performance Analysis of the SPIM for Different Design Methods

Simulation has been carried out in arbitrary reference frame (Figs. 5, 6, 7, 8, 9, 10, 11, 12, 13, 14). The parameters, as obtained from different optimization algorithms and traditional method of design, have been incorporated in simulation. Simulation has been done for 28 Nm traction load and no-load condition. Traction speed has been taken as 500 RPM. From Fig. 15, it is found that, in case of mFPA design no-load current is 2.4 A and, from Fig. 16, it is found that the full load current is

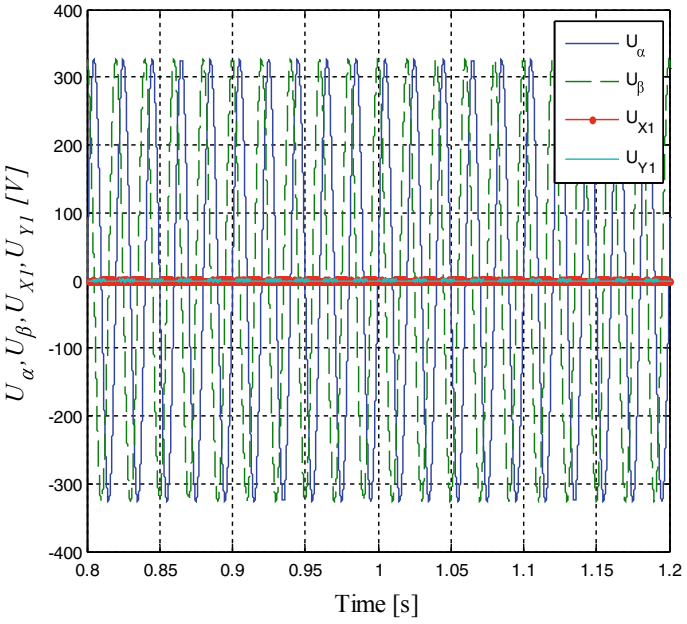

Fig. 5 Alpha, beta, x, y component voltage curve of Cuckoo search design method

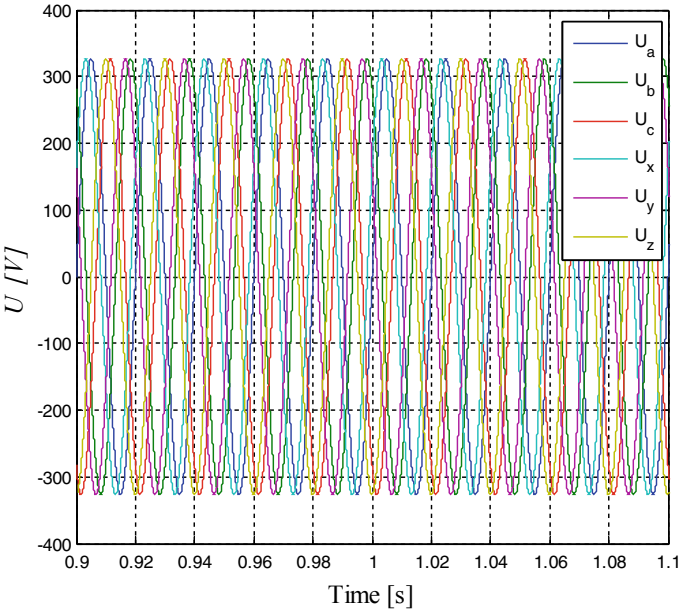

Fig. 6 Six-phase input voltage curve of Cuckoo search design method

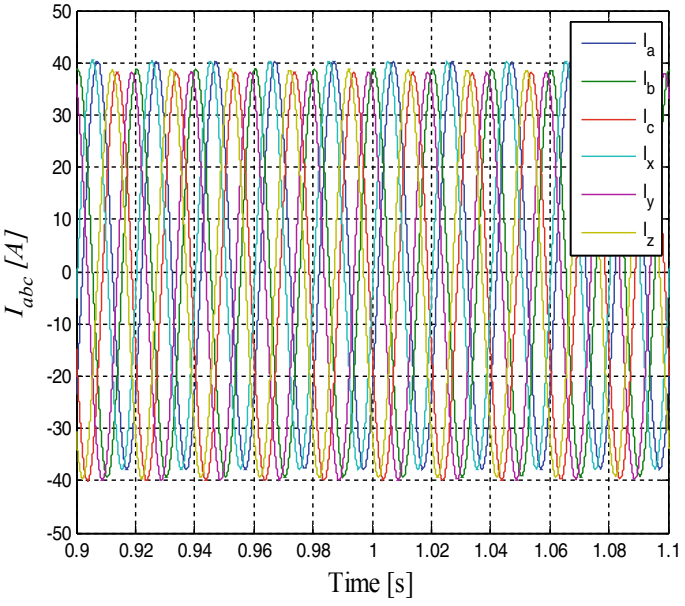

Fig. 7 Six-phase input current curve of Cuckoo search design method on no-load

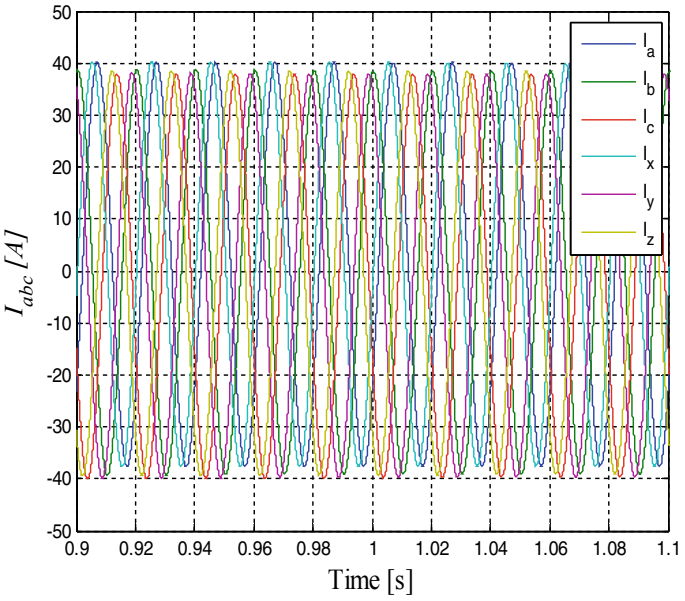

Fig. 8 Six-phase input current waveform of Cuckoo search design method on 28 Nm traction load

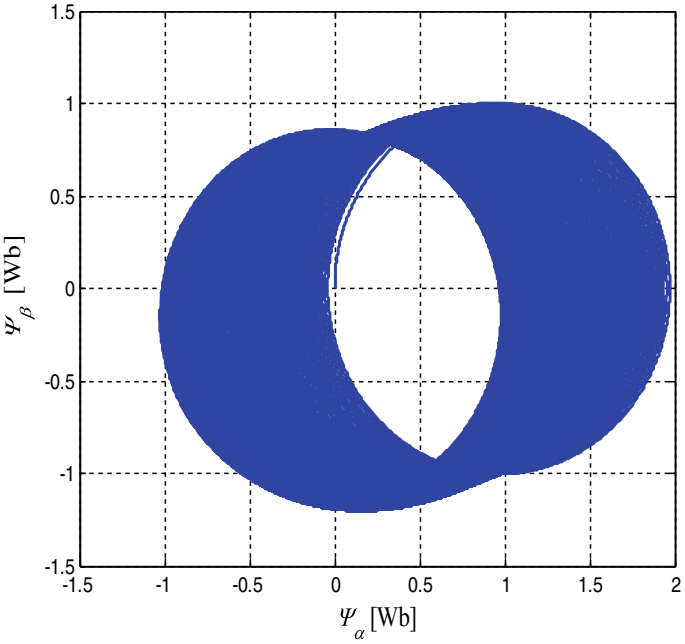

Fig. 9 Flux distribution curve of alpha–beta axes of Cuckoo search design method on no-load

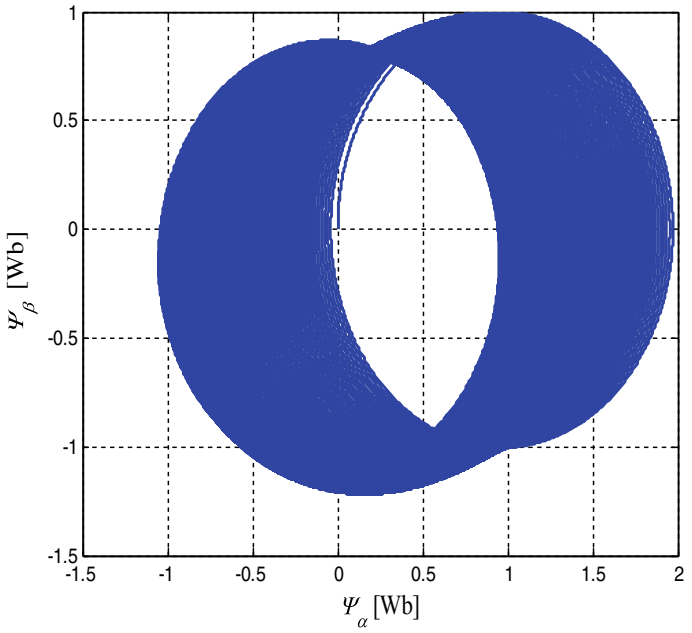

Fig. 10 Flux distribution curve of alpha–beta axes of Cuckoo search design method on 28 Nm traction load

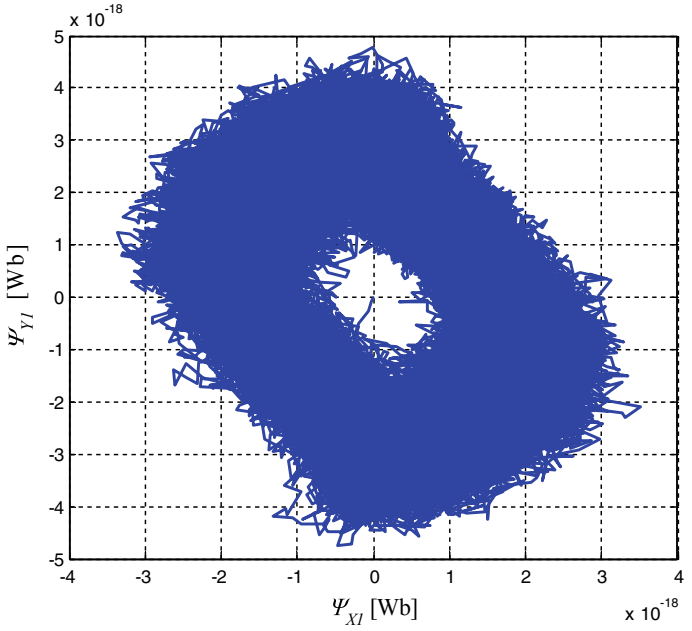

Fig. 11 Flux distribution curve of X–Y component of Cuckoo search design method on no load

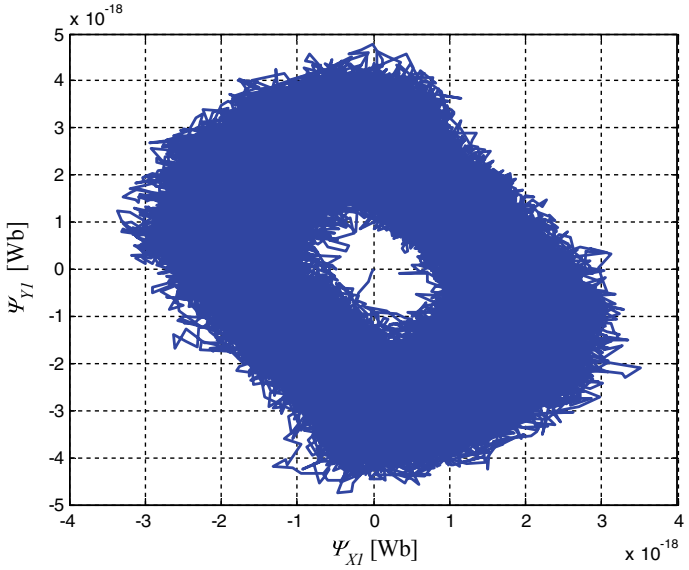

Fig. 12 Flux distribution curve of X–Y component of Cuckoo search design method on 28 Nm traction load

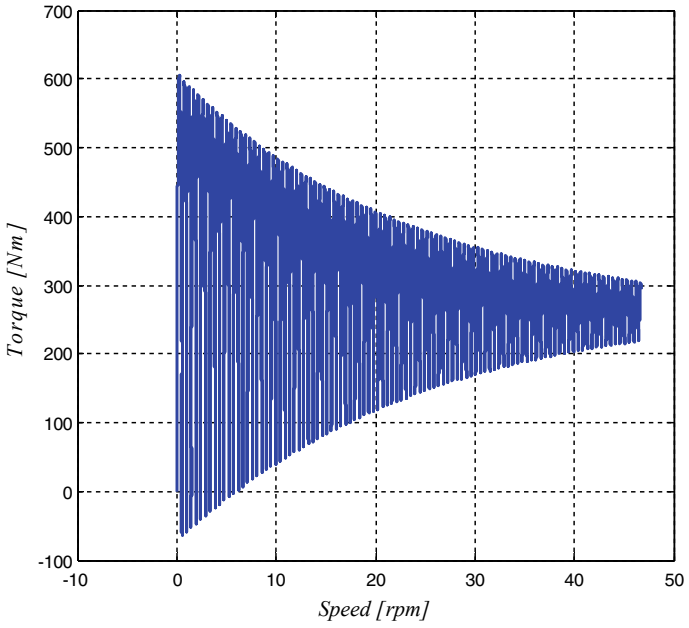

Fig. 13 Torque versus speed curve of Cuckoo search design method at no load

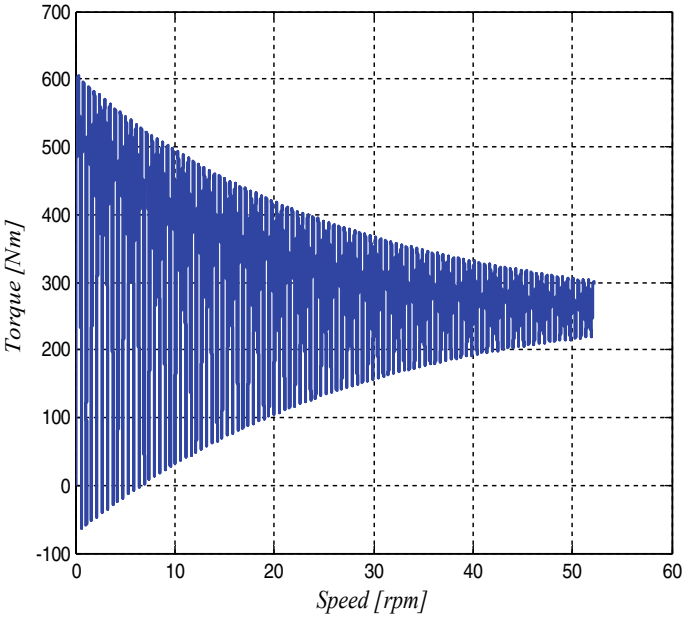

Fig. 14 Torque versus speed curve of Cuckoo search design method on 28 Nm traction load

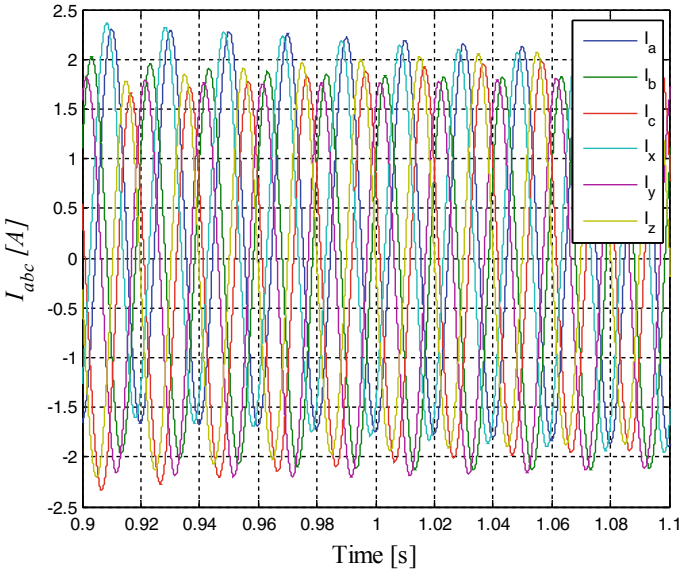

Fig. 15 Six-phase input current curve of mFPA design method on no load

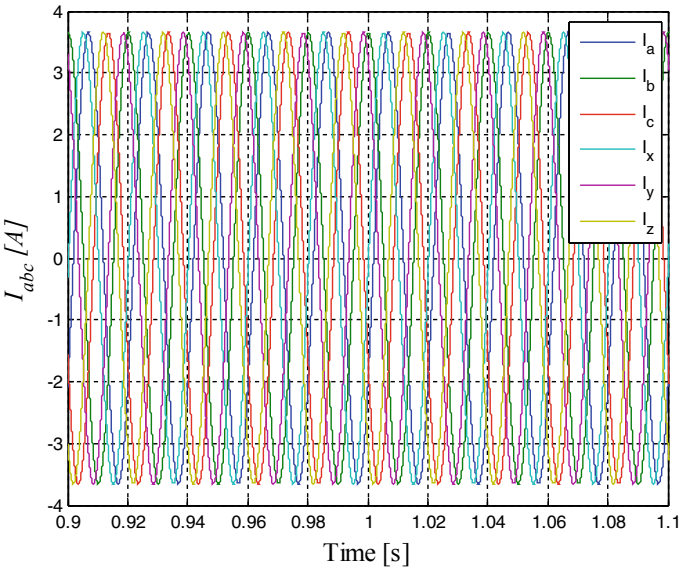

Fig. 16 Six-phase input current waveform of mFPA design method on 28 Nm traction load

3.8 A. So, change of current from no load to full load of 28 Nm is small. Figures 7, 8, 23, 24, 27, and 28 are the current curves of Cuckoo search, NBA, and traditional design methods, respectively, and these curves show that no change of current from no load to full load. Figures 17, 18 of mFPA design method show flux distribution curve of alpha–beta components and Figs. 19, 20 show flux distribution curve of X–Y components and those curves show that the flux distributions are uniformly rotating for Alpha–Beta components, flux linkages are intense for X–Y components. Flux distribution curves of other design methods of Alpha–Beta and X–Y components are as in figures of Cuckoo search design method, which show that this method produces less uniformly rotating and less intense flux distribution. Other design methods like NBA and traditional method produce same magnetic properties like Cuckoo search design method, so only Cuckoo search methods' magnetic behavior regarding Alpha–Beta and X–Y axes at no load and full load have been given in Figs. 9, 10, 11, and 12, respectively. Voltage curves of Alpha, Beta, X, Y components are at Fig. 5, input six-phase voltage curves are at Fig. 5. These curves are for Cuckoo search design method. The voltage curves are similar in nature for other design methods, so only one design method of Cuckoo search is shown (Figs. 21, 22, 23, 24, 25, 26, 27 and 28). Figures 13, 14, 21, 22, 25, 26, 29, and 30 are the Torque–speed characteristics curves on 28 Nm Traction load and on no load of Cuckoo search, mFPA, NBA, and traditional design methods, respectively. From these curves, it is found that only mFPA design method has stable operating region.

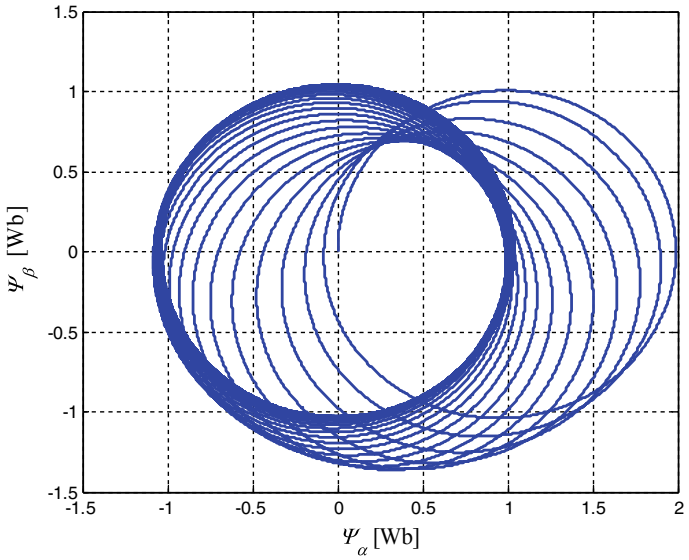

Fig. 17 Flux distribution curve of alpha–beta component of mFPA design method on no load

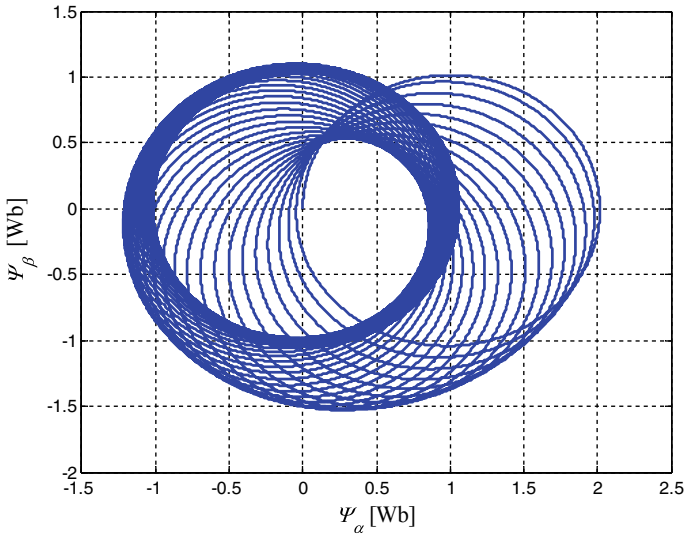

Fig. 18 Flux distribution curve of alpha–beta component of mFPA design method on 28 Nm traction load

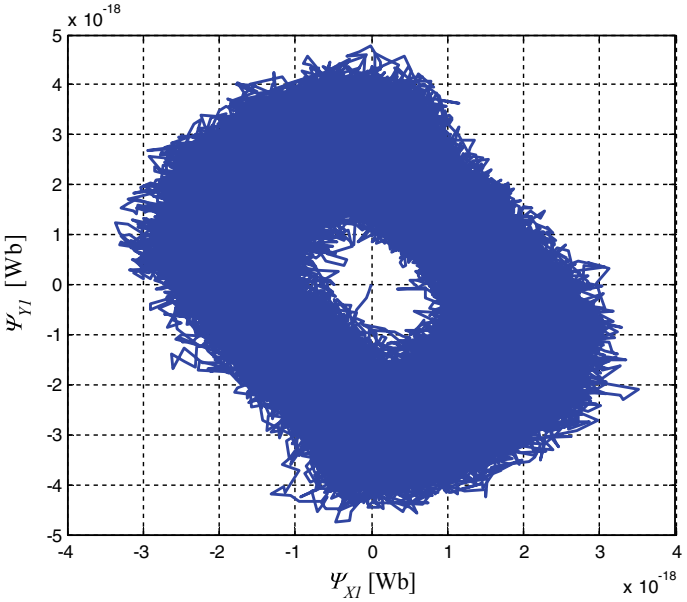

Fig. 19 Flux distribution curve of X–Y component of mFPA design method on No load

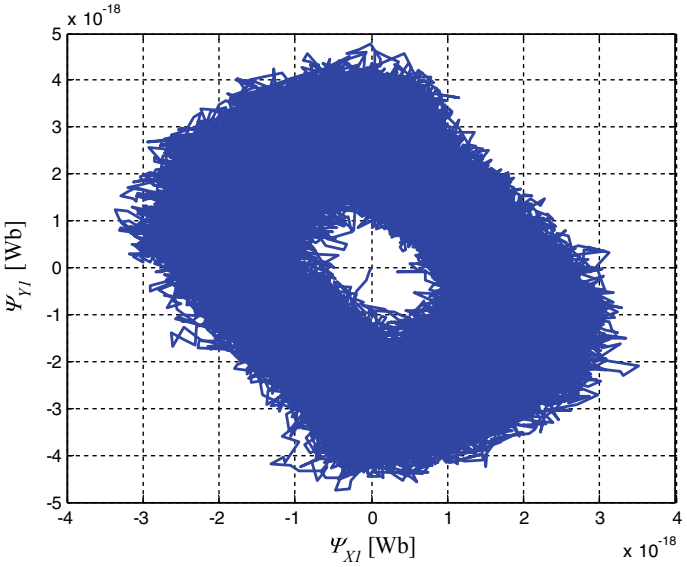

Fig. 20 Flux distribution curve of X–Y component of mFPA design method on 28 Nm traction load

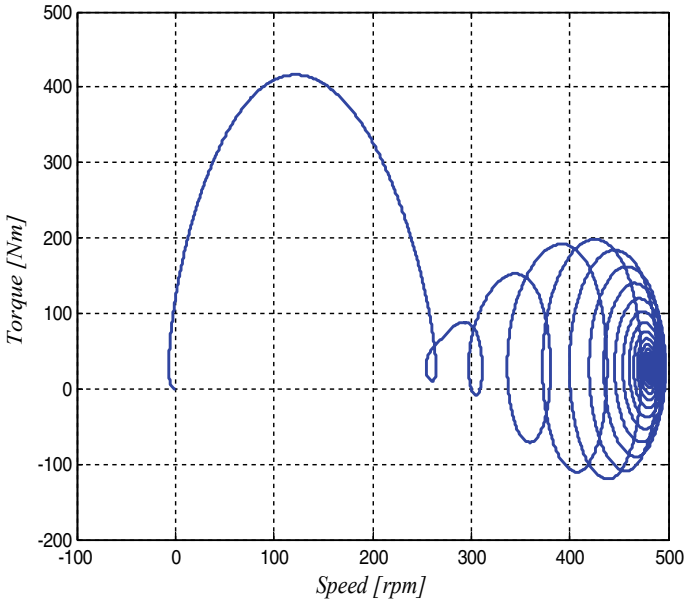

Fig. 21 Torque versus speed curve of mFPA design method on 28 Nm traction load

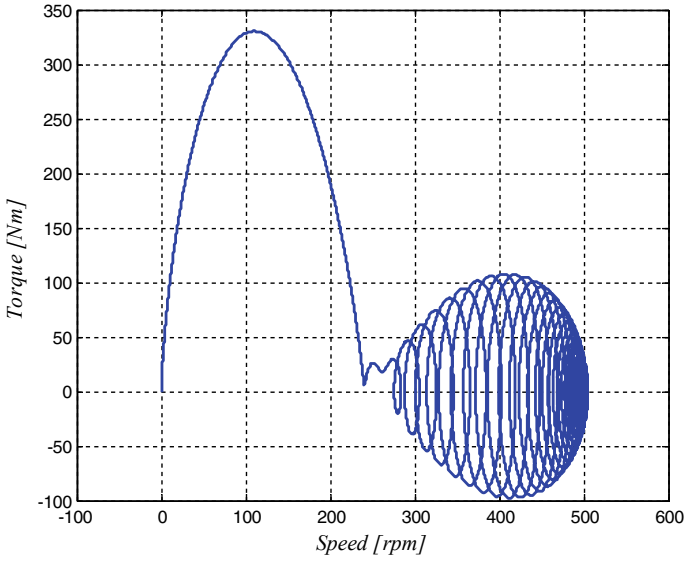

Fig. 22 Torque versus speed curve of mFPA design method on no load

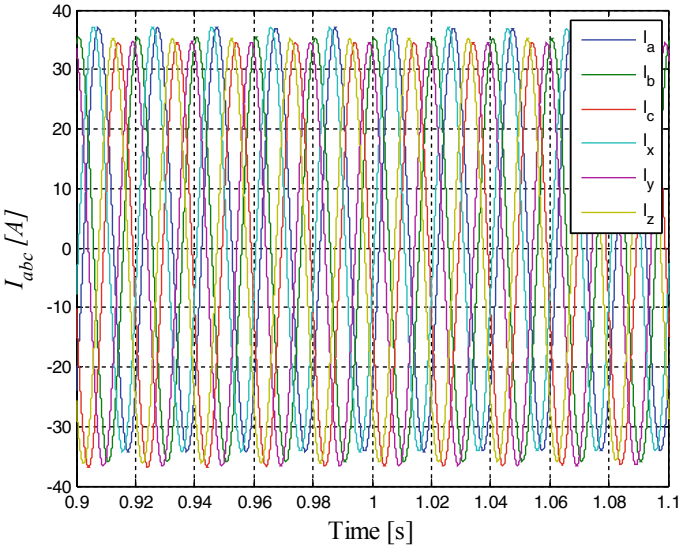

Fig. 23 Six-phase input current waveform of NBA design method on 28 Nm load

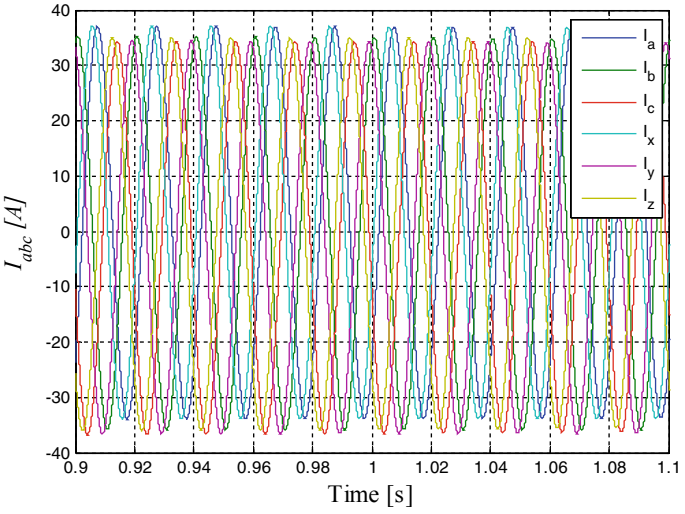

Fig. 24 Six-phase input current waveform of NBA design method on no load

8 Conclusions

A new modified version of Flower Pollination algorithm, NBA with habitat selection and Doppler effect in echos, Cuckoo search algorithm, and also traditional method of

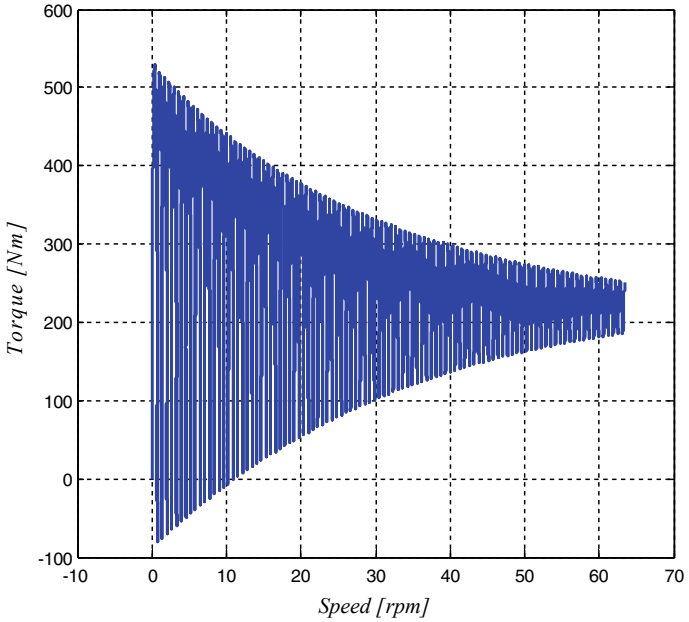

Fig. 25 Torque–speed characteristics curve of NBA design method on 28 Nm traction load

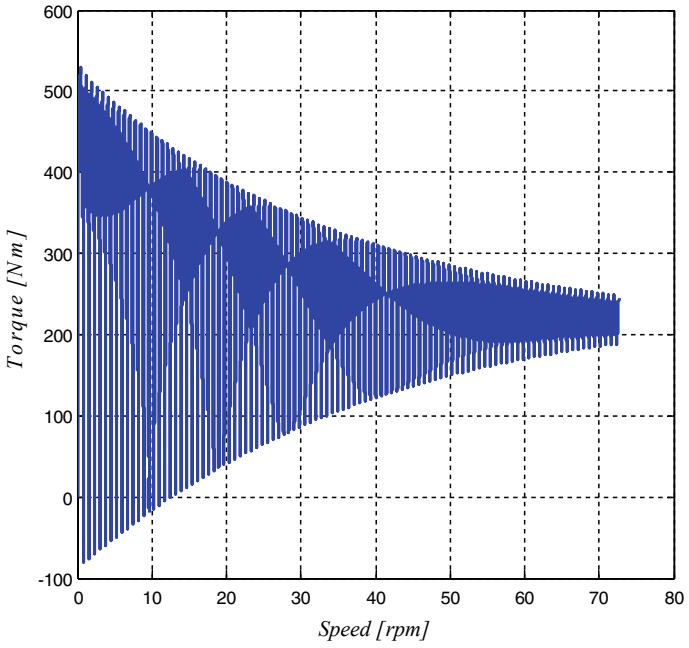

Fig. 26 Torque–speed characteristics curve of NBA design method on no load

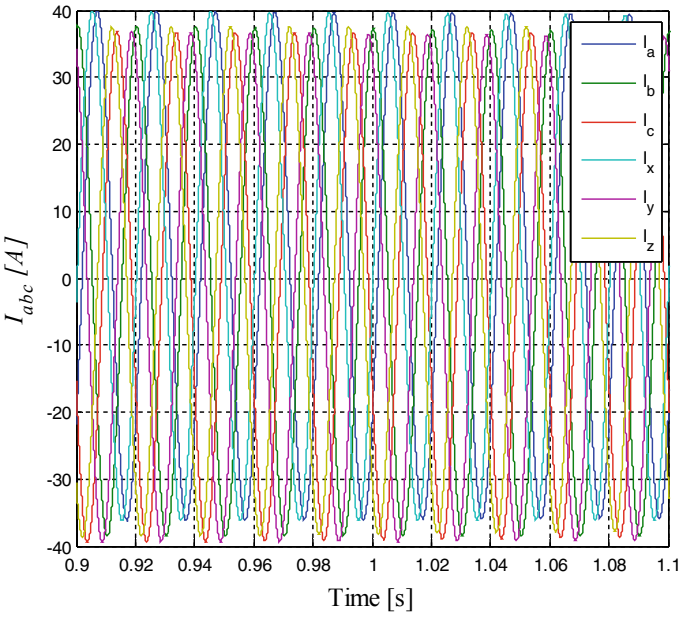

Fig. 27 Input current waveform of traditional design method on 28 Nm traction load

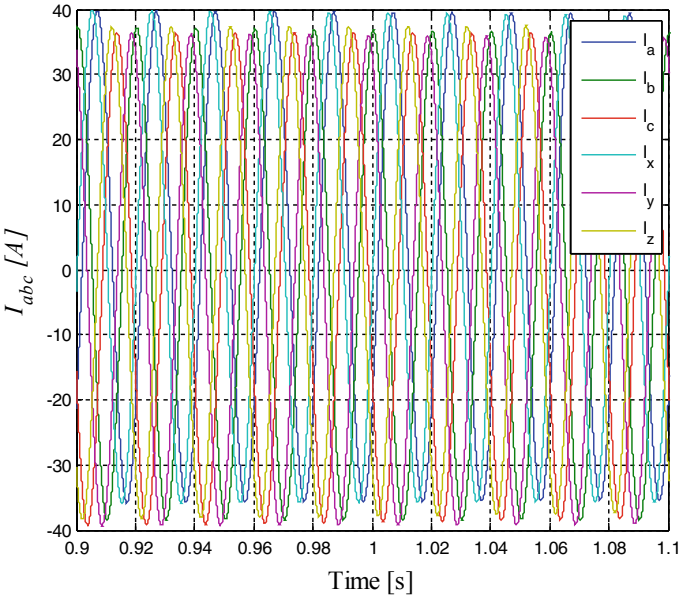

Fig. 28 Input current waveform of traditional design method on no load

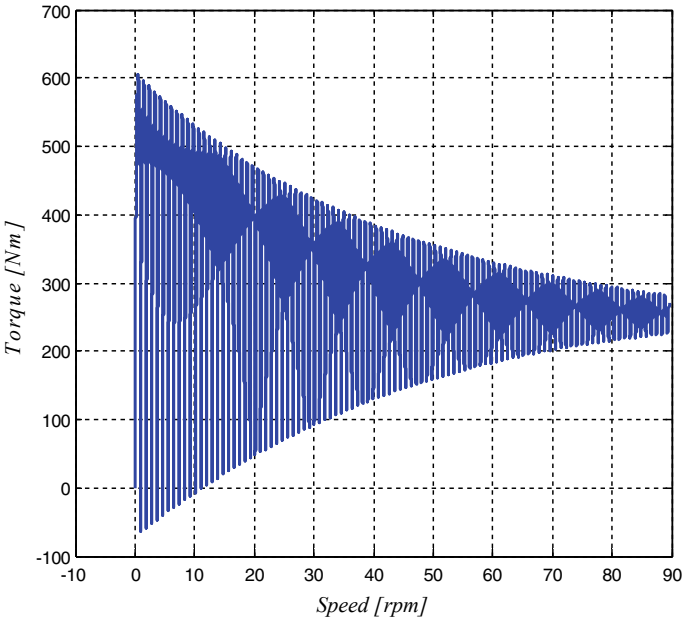

Fig. 29 Torque versus speed curve of traditional design method on 28 Nm traction load

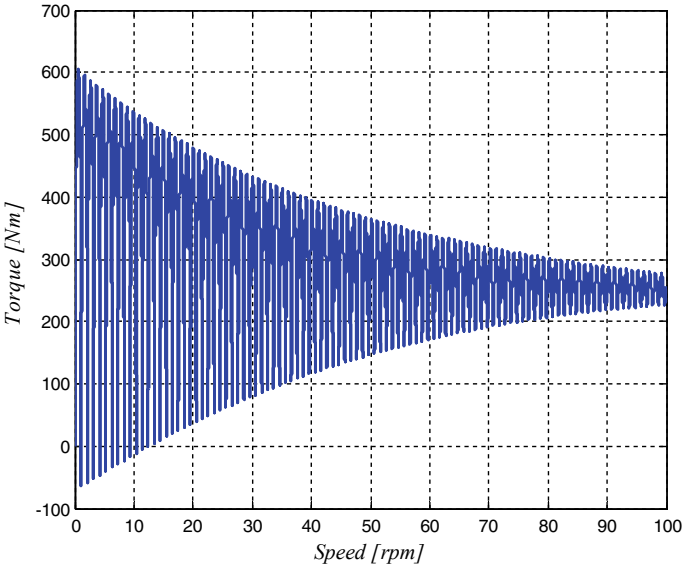

Fig. 29 Torque versus speed curve of traditional design method on no load

design have been presented for design of a six-phase induction motor. Simulation has been carried out using the optimized parameters obtained from the different methods in MATLAB/SIMULINK environment. It is observed that the mFPA method of optimization gives the better performance as given below:

- The full-load efficiency of the six-phase induction motor is increased under mFPA design method.
- The size of the six-phase induction motor is reduced under mFPA design method.
- The cost of material is reduced as the size of the motor is reduced.
- The maximum torque generated is the highest in case of mFPA design.

The total losses are greatly reduced in case of mFPA design and it is the most energy-efficient among these methods.

9 List of Symbols Used

The list of symbols used here for different equations and expressions are as follows:

$x_i(t + 1)$ = the updated position of a pollen or an insect carrying pollen.
$x_i(t)$ = any initial position of a pollen or insect carrying pollen.
gbest = It is the position of best flower within a different plant having that flower.
L = Levy flight or essentially a step size.
best = position of the best flower of different plant situated elsewhere.
av = $(x_i\ (t) + \text{best})/2$.
r_r = 0.021 Ω/m = resistivity of copper conductor at 75 °C.
s_r = No. of rotor slots.
m_s = No. of phases.
P = No. of poles.
I_b = Rotor bar current.
a_b = Rotor bar x-sectional area.
D_e = Mean end ring diameter.
L_r = Length of the core.
$I_{ph} = I_s$ = Stator current per phase.
$V_{ph} = V_s$ = Stator voltage per phase.
p.f. = cos Ø = power factor.
η = efficiency.
t = Thickness of copper strip.
w = width of copper strip.
J = Moment of inertia of SPIM.
T_e = Electromagnetic torque developed by six-phase induction motor.
T_L = Load torque.
K_{ws} = Space factor.
dt = A very small amount of time.
i_{qs} = Quadrature axis component of stator current.
i_{dr} = Direct axis component of rotor current.

i_{ds} = Direct axis component of stator current.
i_{qr} = Quadrature axis component of rotor current.
L_m = Magnetizing inductance.
R_s, R_r = Resistances of stator and rotor.
L_{ls}, L_{lr} = Inductances of stator and rotor.
i_{qs0} = Zero sequence component of quadrature axis component of stator current.
i_{ds0} = Zero sequence component of direct axis component of stator current.
v_{ds}, v_{dr} = Direct axis voltages of stator and rotor, respectively.
v_{qs}, v_{qr} = Quadrature axis voltages of stator and rotor.
Ψ_{ds}, Ψ_{dr} = Direct axis flux linkages of stator and rotor.
Ψ_{qs}, Ψ_{qr} = Quadrature axis flux linkages of stator and rotor.

References

1. Nanoty A (2012) Control of designed developed six phase induction motor. Int J Electromagn Appl 2(5):77–84
2. Miranda RS, Gomes EC (2012) Analysis and modeling of six-phase induction motor under open phase fault. Anais do XIX Congresso Brasileiro de Automática, CBA
3. Fazlipour Z, Kianinezhad R, Razaz M (2015) Genetic algorithm based design optimization of a six phase induction motor. J Electr Eng Technol 10(3):1007–1014
4. Bojoi R, Profumo F, Tenconi A (2003) Digital synchronous frame current regulation for dual three-phase induction motor drives. In: Conf. Rec. IEEE-PESC'03, Acapulco (Mexico), pp 1475–1480
5. Klingshirn EA (1983) High phase order induction motors part-1, Description and theoretical consideration. IEEE Trans PAS 102(1):47–54
6. Nanoty A, Chudasama AR (2012) Control of designed developed six phase induction motor. Int J Electromagn Appl 2(5):77–84
7. Gregor R, Barrero F, Toral S, Durán MJ (2008) Realization of an asynchronous six-phase induction motor drive test-rig, RE&PQJ 1(6)
8. Lyra ROC, Lipo TA (2002) Torque density improvement in a six-phase induction motor with third harmonic current injection. In: IEEE Trans Ind Appl 38(5)
9. Modi SC, Chaturvedi RK (2015) Theory & manage of designed developed prototype six phase induction motor. Int J Eng Res Manag Technol 2(Issue-6)
10. Mandal S (2015) Performance analysis of six-phase induction motor. Int J Eng Res Technol (IJERT) 4(Issue 02)
11. Meng X-S, Gao XZ, Liu Y, Zhang H (2015) A novel bat algorithm with habitat selection and Doppler effect in echoes for optimization. Expert Syst Appl 42(Issues 17–18):6350–6364
12. Fister I Jr, Fister D, Fister I (2013) A comprehensive review of cuckoo search: variants and hybrids. Int J Math Model Numer Optim 4(4):2013
13. Yang X-S, Deb S (2009) Cuckoo search via Levy flights. In: 2009 world congress on nature & biologically inspired computing (NaBIC 2009)
14. Civicioglu P, Besdok E (2011) 'A conceptual comparison of the Cuckoo-search, particle swarm optimization', differential evolution and artificial bee colony algorithms. Springer Science + Business Media B.V.
15. Yang X-S, Deb S (2010) Engineering optimization by Cuckoo search. Int J Math Model Numer Optim 1(4):330–343
16. Potnurua D, Mary KA, Babuc ChS (2019) Experimental implementation of flower pollination algorithm for speed controller of a BLDC motor. Ain Shams Eng J 10(Issue 2):287–295

Implementation of Complete Vector Control for DFIG Based Wind Turbine

Rajesh Kumar, Ch. Sekhar, Saibal Manna, and A. K. Akella

1 Introduction

The need of wind turbines is nothing less than the demand of solar energy. With recent developments and technologies, the off shore wind turbines are getting more interest because of the percentage of availability of wind in offshore is more when compared to onshore [1]. The challenging we can see in the off shore wind energy conversion system are cost of installation, corrosion, erosion, frequent lightning strikes, and others [2, 3]. By considering the measures of design or manufactures, the effect of corrosion or lightnings can be minimized but the cost will be increased further. After the installation the maintenance and transmission costs can be minimized by the introduction of power electronic converters in the wind energy conversion. In 1990, 16 countries cumulatively generated electric power from wind around 3.58 billion kWh and in 2017, electric power of 1.2 trillion kWh was generated from wind in a whole by 129 countries. By recent report by power technology.com as on March 20, 2019, India ranks fourth position in the record of top countries from world in the area of wind power capacity and India ranks second in Asian region with a total capacity of 34.6 GW. In recent generation we can observe the preference of variable wind speed turbines over the fixed speed wind turbines due to higher inertia of rotating structure in the variable wind turbines and that helps to smoothen the output power fluctuations [3, 4]. Furthermore, it also helps to reduce the mechanical stresses over the drive train. The presence of power electronic converter systems is usually placed between the generator system and the utility grid system. Power electronic converters can be defined as the brain system for the wind turbine system because the control of the system is carried by the designed power electronic converters in the system [5, 6]. It enables variant speed operation and sustained behavior of the turbine. For high voltage transmission systems where large ocean-going wind farms are linked to each other, there is a high need for FACTs devices like SVC, STATCOM for ensuring better

R. Kumar (✉) · Ch. Sekhar · S. Manna · A. K. Akella
NIT Jamshedpur, Jamshedpur 831014, India

S. Kumar et al. (eds.), *Recent Advances in Power Electronics and Drives*, Lecture Notes in Electrical Engineering 852, https://doi.org/10.1007/978-981-16-9239-0_16

reliability and better power quality. For more dynamic compensation in modern large turbines, thyristor switched capacitor (TSC) is used [7]. Not only for higher energy yield but also for remote controllability and adjustability of power quality, power electronics are used widely. This availability feature of remote controllability provides feasibility for offshore applications and the adjustability feature also provides fine tuning for superior grid connections. The role of power electronic converters are to match the wind turbine features with the grid featured requirements [6, 7]. The characteristics are such as frequency, reactive power, voltage, power factor, active power, and harmonics, etc. the wind turbine design system includes the components like turbine rotor, generator, gearbox, power electronic system along with a transformer for connecting with the utility grid. In brief the rotor blades of the turbine get rotated by the flow of wind and convert the effect into mechanical power, the generator convert the mechanical power to electrical power, the gearbox maintains the synchronism of turbine speed with the generator speed by some internal mechanism, the power electronic system takes care the process of power fed to the grid from the wind power system, and the transformer along with circuit breakers ensures the connection and power flow from wind system to grid [8]. In the context of wind turbine design, power electronic devices play a crucial role in integrating the variable speed (or fixed speed) wind power generation units with the main utility grid for continuous power supply with better reliability and efficient performance.

The knowledge of simulating the mathematical models of wind energy, converter systems, and their implementation with grid is well learned and designed in MATLAB software tool. Simulation of controller related to both rotor side and grid side is carried by the PI controllers and transformation blocks [9]. We correlate the theoretical results with the obtained results from the designed model and analyze the practical considerations to be taken care in the context of wind turbine design. A schematic diagram of designed model is drawn in Fig. 1.

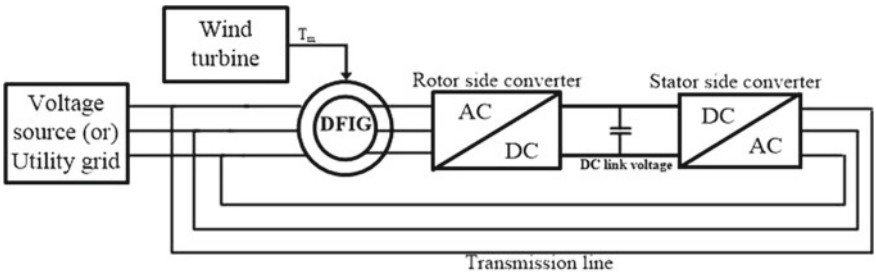

Fig. 1 Schematic diagram of DFIG linked wind turbine system implemented to grid

2 Wind Turbine

In general wind turbine consists of a group of blades (basically 3 blades) attached to a hub. The hub is placed over a tower with a nacelle in which a gear box and a generator is fixed as shown in Fig. 2. The wind movement on the blades produces a force on the surface of blades and generate a rotational energy which is a form of kinetic energy and is then transferred to the generator via gear box in the form of mechanical energy and after that generator transforms the mechanical energy input into an output form of electrical energy [10]. The gear box function is adjusting the rotation of wind turbine with the rotation of the shaft of the generator. The general equation for the wind power is expressed in Eq. 1.

$$P = \frac{1}{2}\rho A C_p v^3 \tag{1}$$

where P is the power in the wing when the blowing direction of wind is perpendicular, ρ is the density of air flow, v is the speed of the wind flow, and C_p is the coefficient of power extracted whose maximum value is 0.597 known as Betz limit. There are two kinds of wind turbine designs, and they are vertical axis wind turbine and horizontal axis wind turbine. In vertical axis wind turbine, the blades are connected in vertical manner so that the wind will be facing the surface of the blades. In horizontal axis

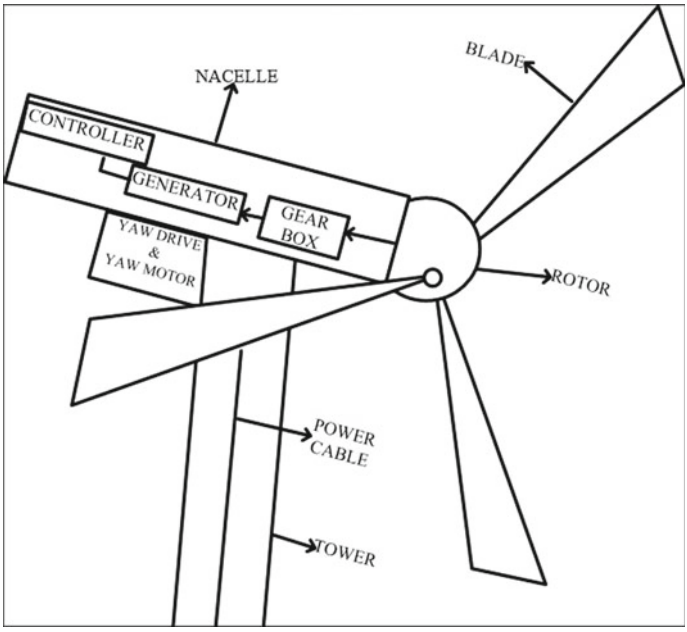

Fig. 2 Block representation of components of wind turbine

wind turbine, the blades are connected in horizontal manner such that the wind falls perpendicularly to the surface of the blade. The construction related to vertical axis type is simpler and less expensive compared to horizontal axis type. The horizontal type demands for a tower to mount the turbine in higher altitudes [10, 11]. Large wind turbines are manufactured for rotation with a reference to the speed of wind. The range of speed of wind is limited within the range of cut-in speed (lowest wind speed required for given power generation in the name plate of the generator) and cut-off speed (highest wind speed at which power flow from the generator stops transferring to utility grid) [11].

3 Doubly Fed Induction Machine

Depending on the kind of energy form given to the machine, the machine is categorized as generator and motor. If mechanical energy is given as input to the machine and electrical energy is obtained as output energy then the machine can be named as generator and if electrical energy is fed as input and mechanical energy is obtained as output then the machine can be denoted as motor [12]. Depending on the type of electrical supply, there are two types of generators viz. DC generator and AC generator. With respect to the output speed, the AC generators are characterized into two types which are synchronous generators and asynchronous generators. The asynchronous generator is again categorized as squirrel cage induction generator (SIG) and wound rotor induction generator (WIG). The WIG which converts the variable mechanical energy to electrical energy with fixed frequency is termed as doubly fed induction generator (DFIG). A DFIG is an induction generator with three phases where the windings of stator and that of rotor are being fed with AC three phase signals [12, 13]. The construction of DFIG includes the multiphase windings and multi-phase ring assembly for transferring power to the rotor. In DFIG rotor speed is controlled by the means of back to back controllers which are named as rotor side controller and grid side controller [13]. For electrical power generation using wind turbine, the DFIG and permanent magnet synchronous generator (PMSG) are preferred mostly. In this paper wind turbine linked with DFIG is simulated and the results are obtained.

The reasons for selecting DFIG are stated as follows:

a. Irrespective of variable wind speed, the supply of output signal with constant frequency to the utility grid.
b. The rating of required power electronic devices in the system is of low power rating and hence the cost of control system is low.
c. Almost unity power factor is maintained or controlled.
d. Even at low speed of wind, electrical power generation is possible.
e. The handle capacity of total load is partial i.e. 20–30% by the power electronic converter [14].

4 Vector Control for Implemented DFIM

The aim of the control loop is to make the system respond to the requirement of electrical energy and for that role sequential PWM converters are connected for providing excitation to the rotor of the DFIG [15]. Many control methods exist as current control methods from rotor side of DFIG but here vector control is considered because of its extended version in large areas and appropriately the most stable one. The space vector representation of DFIG is shown in Fig. 3 with respect to different frames such as dq frame with reference to synchronous speed ω_s, DQ with respect to mechanical speed ω_m and $\alpha\beta$ with reference to plane [16].

The vector control for DFIG is simulated by taking the reference of the control loops and is drawn for the rotor side and stator side controller for DFIG, and the generated pulse signal is given as input to the universal bridges simulated for interlinking DFIG with the utility grid or main voltage source. The active output power and reactive output power from the grid or source connected can be controlled up to some extent by the voltage of the rotor controlled by the rotor side converter [16]. For extraction of maximum output energy in wind turbine design system with variable speed, the maximum power versus rotor speed plot is used widely. Two loops, viz. control loop of rotor side and control loop of stator side (or referred as grid side), are used to control the flow of active power and reactive power and to regulate the shared voltage which is in DC type among the two converters. The vector control for the DFIG is framed in a synchronously rotating dq plane reference to stator flux space vector, where d represents direct axis and q represents quadrature axis. With reference to the alignment, the direct axis component of current flowing in rotor components (I_{dr}) is seen as proportional to the reactive power of stator (Q_s) and the quadrature axis component of current in rotor (I_{qr}), is seen as proportional to the active power obtained from stator. Necessary transformation matrices are simulated in the SIMULINK diagram and the angle is estimated for the reference plane transformation. The required (dq to abc) transformation matrices and (abc to dq) transformation matrices are expressed in the following equations.

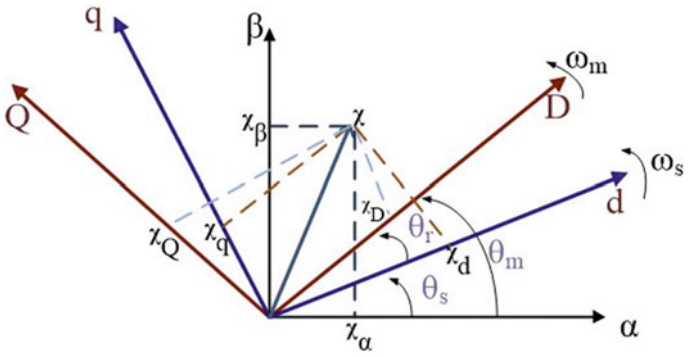

Fig. 3 Space vector representation of DFIG with reference to different frames

$$\begin{bmatrix} V_\alpha \\ V_\beta \end{bmatrix} = \begin{bmatrix} \cos\theta & -\sin\theta \\ \sin\theta & \cos\theta \end{bmatrix} \begin{bmatrix} V_d \\ V_q \end{bmatrix} \tag{2}$$

$$\begin{bmatrix} V_a \\ V_b \\ V_c \end{bmatrix} = \begin{bmatrix} 1 & 0 \\ -1/2 & \sqrt{3}/2 \\ -1/2 & -\sqrt{3}/2 \end{bmatrix} \begin{bmatrix} V_\alpha \\ V_\beta \end{bmatrix} \tag{3}$$

$$\begin{bmatrix} V_\alpha \\ V_\beta \end{bmatrix} = \frac{2}{3} \begin{bmatrix} 1 & -1/2 & -1/2 \\ 0 & \sqrt{3}/2 & -\sqrt{3}/2 \end{bmatrix} \begin{bmatrix} V_a \\ V_b \\ V_c \end{bmatrix} \tag{4}$$

$$\begin{bmatrix} V_\alpha \\ V_\beta \end{bmatrix} = \begin{bmatrix} \cos\theta & -\sin\theta \\ \sin\theta & \cos\theta \end{bmatrix}^T \begin{bmatrix} V_\alpha \\ V_\beta \end{bmatrix} \tag{5}$$

where V_d and V_q are the dq frame space vectors of vector V, V_α, and V_β are the $\alpha\beta$ references of vector V and V_a, V_b, V_c are phasor voltage representations of vector V. If the DFIG used in the system provides different turns ratio at the side of rotor and stator, then the effect must be considered at the control loop. Therefore, the stator side referred rotor currents are taken as input for the control loop. A complete vector control for DFIG is drawn in Fig. 4.

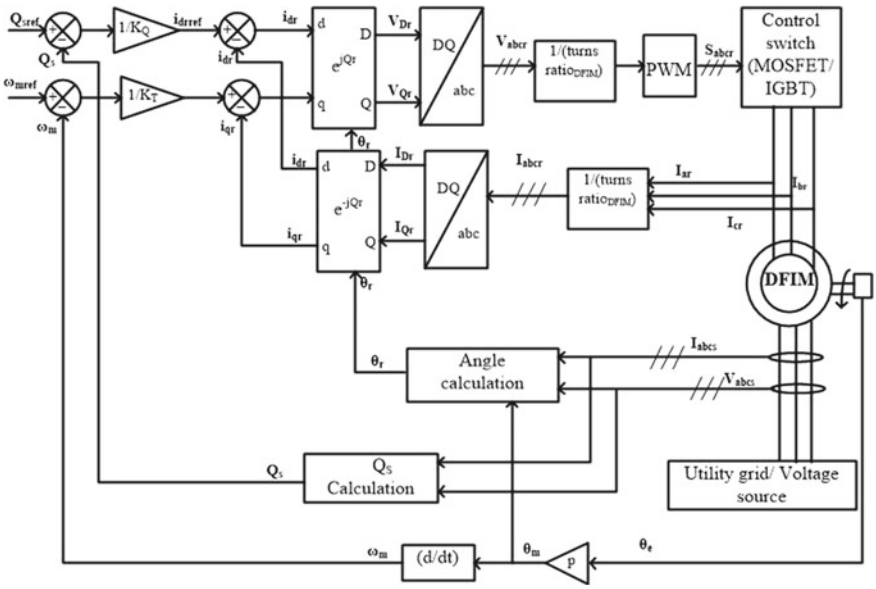

Fig. 4 Block diagram of complete vector control loop for DFIG

5 MATLAB Simulation

The MATLAB Simulink diagram for the block diagram shown in Fig. 1 is modeled in Fig. 5. The subsystems of controller on rotor side and on stator side are shown in Figs. 6 and 7 respectively to emphasis the input given to the controllers and the output obtained from them. The parameter specifications of the DFIG and the grid along with transmission lines are specified in Table 1.

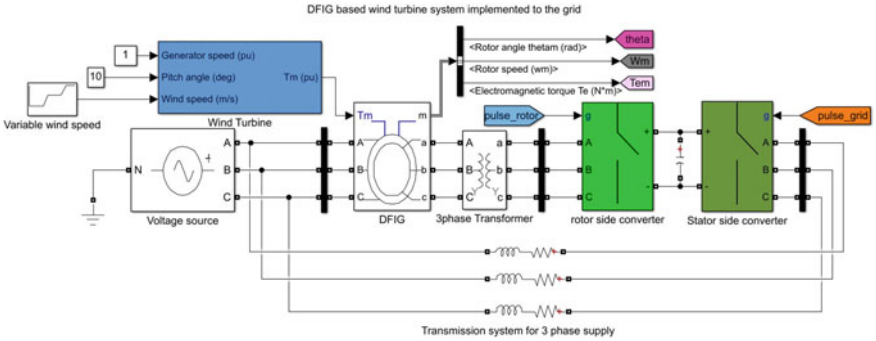

Fig. 5 MATLAB block diagram of modeled wind turbine system

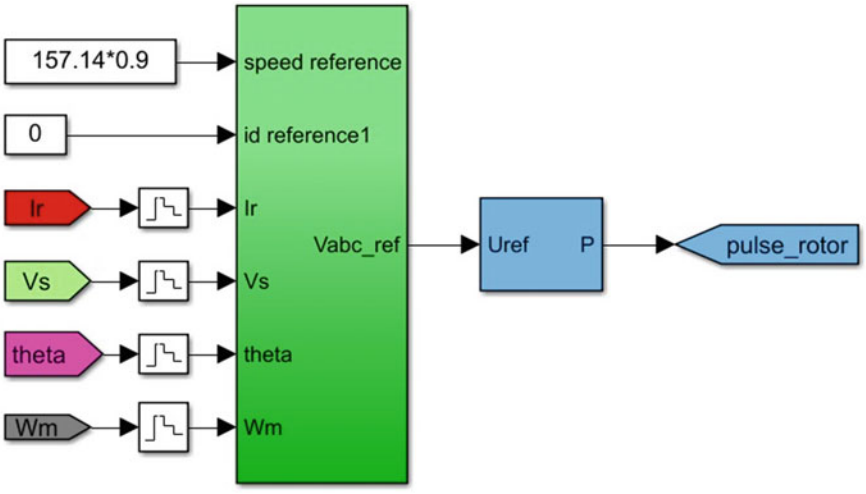

Fig. 6 Rotor side controller for the control of DFIG linked to wind turbine system

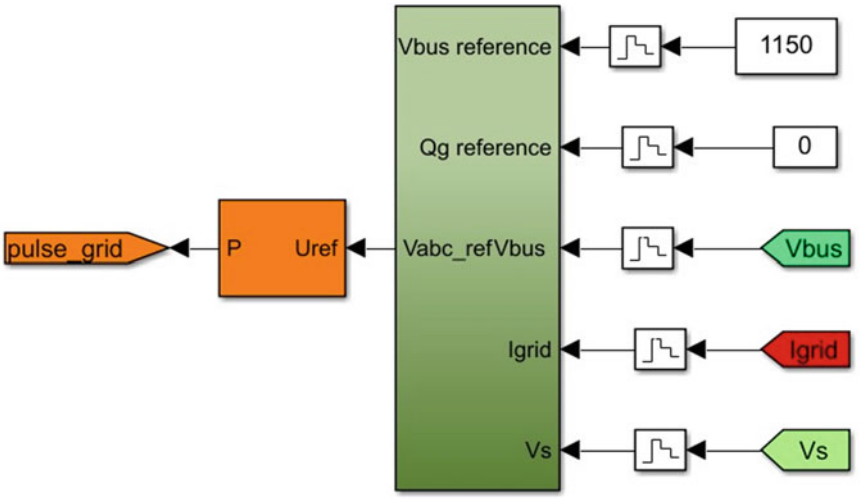

Fig. 7 Stator side controller for the control of DFIG linked to wind turbine system

Table 1 Parameter specifications

DFIG parameters referred to stator side and grid parameters	
Nominal power	2 MW
Supply frequency	50 Hz
Speed of synchronous	1500 rpm
V_s line to line	690 V
Stator current	1760 A
No of poles	2
R_{stator}	2.59 Mω
L_{stator}	2.577 Mh
R_{rotor}	2.9 Mω
L_{rotor}	2.587 mH
Maximum slip	0.33
Turns ratio	1/3
Electromagnetic torque	12,732 Nm
Switching frequency	4000 Hz
Bus voltage	$230\sqrt{2}$
Grid resistance per meter	20 μΩ
Grid inductance per meter	400 μH
Bus capacitance	80 mF
Gear box ratio	100

6 Results and Discussions

The Simulink model is examined for the runtime of 0.4 s or 20 cycles by applying different wind speeds for different intervals of time. The results are auto scaled from 0 to 0.4 s for better understandings of results and wind speed available in this interval is 10 m/s (Figs. 8, 9, 10 and 11).

The necessary output results are presented in this paper to show the function of the vector control loop implemented to the DFIG which is linked to wind turbine system. The stator current is not similar as voltage source due to the given values of

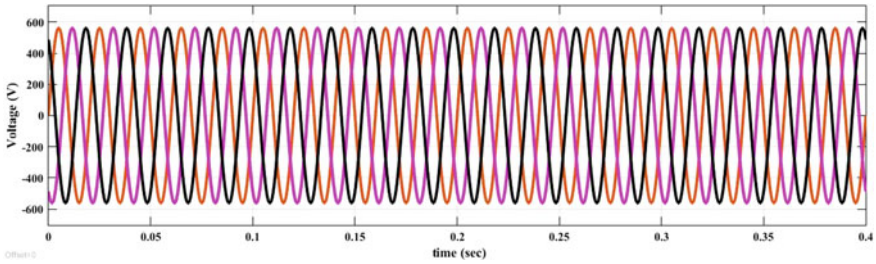

Fig. 8 Voltage source versus time for wind flow of 10 m/s

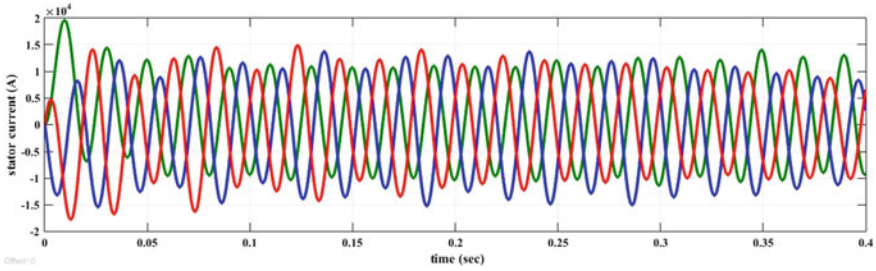

Fig. 9 I_{stator} of DFIG versus time

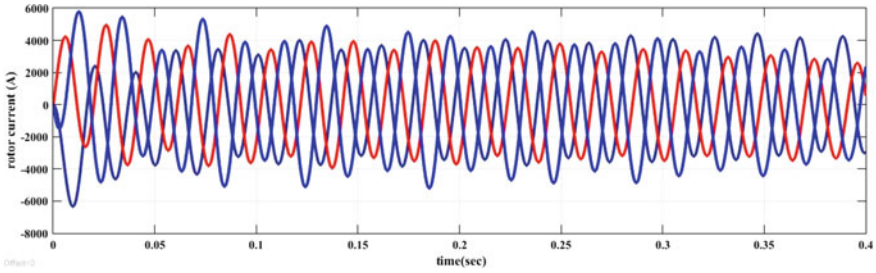

Fig. 10 Rotor current of DFIG versus time

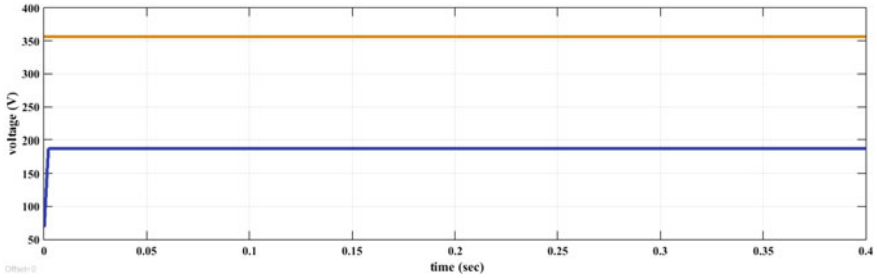

Fig. 11 D component reference of voltage versus time

speed reference, d-axis reference and q-axis reference. The control loop inputs are the Q_s available from the system and the speed of the machine implemented. We can observe the symmetrical behavior in the system and the control loop takes care of the changes in the measured values and input values. The rotor current in Fig. 10 and bus voltage in Fig. 12 will be found to be satisfactory if compared with the ideal cases of the system. The speed reference and speed waveform of the DFIG is simulated for 4 s as for the first 2 s, the speed of DFIG tends towards the reference value (Fig. 13).

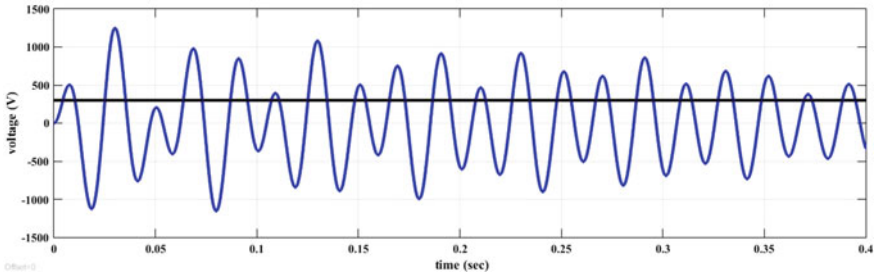

Fig. 12 Voltage of the bus system and reference bus voltage versus time

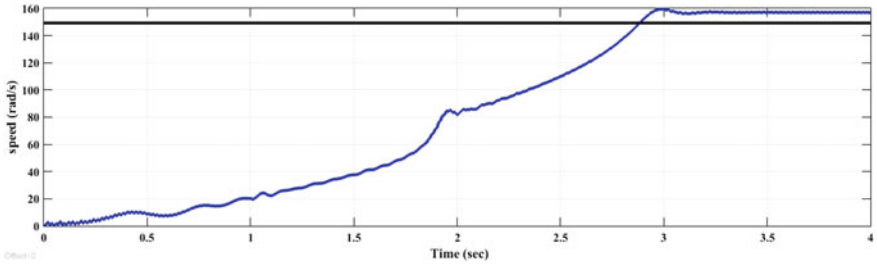

Fig. 13 Speed of DFIG versus time

7 Conclusion

In this paper we can conclude that the vector control of DFIG gives appreciated results when it is implemented with the wind turbine system and grid system. We attempted to bring minor changes in the system but still the system acquires its stability within a small interval of time. To the existing vector control concept, we attempted some changes such as taking the reference value of q-axis as zero and changing the speed reference with respect to percentage output. It helps to reduce the power loss in the system when implemented practically. A lot of future scope is available for the system discussed here because we have not implemented the pitch control of the wind turbine system and assumed it as constant. Even with low speed we can expect for stable power supply which is understood from the results. Further hybrid system can also be designed by integrating a battery system or solar system with the above system, then it will create a stable microgrid with continuous supply of power.

References

1. Djeghloud H, Bentounsi A, Benalla H (2010) Simulation of a DFIG-based wind turbine with active filtering function using MATLAB/Simulink. In: The XIX international conference on electrical machines - ICEM 2010, Rome, Italy, pp 1–7. https://doi.org/10.1109/ICELMACH.2010.5607885.
2. Puchalapalli S, Singh B (2020) A novel control scheme for wind turbine driven DFIG interfaced to utility grid. IEEE Trans Indus Appl 56(3):2925–2937. https://doi.org/10.1109/TIA.2020.2969400
3. Tang W, Hu J, Chang Y, Liu F (2018) Modeling of DFIG-based wind turbine for power system transient response analysis in rotor speed control timescale. IEEE Trans Power Syst 33(6):6795–6805. https://doi.org/10.1109/TPWRS.2018.2827402
4. Ouyang J, Tang T, Yao J, Li M (2019) Active voltage control for DFIG-based wind farm integrated power system by coordinating active and reactive powers under wind speed variations. IEEE Trans Energy Convers 34(3):1504–1511. https://doi.org/10.1109/TEC.2019.2905673
5. Ekanayake J, Jenkins N (2004) Comparison of the response of doubly fed and fixed-speed induction generator wind turbines to changes in network frequency. IEEE Trans Energy Convers 19(4):800–802. https://doi.org/10.1109/TEC.2004.827712
6. Arani MFM, Mohamed YAI (2015) Analysis and impacts of implementing droop control in DFIG-based wind turbines on microgrid/weak-grid stability. IEEE Trans Power Syst 30(1):385–396. https://doi.org/10.1109/TPWRS.2014.2321287
7. Li Y, Xu Z, Meng K (2017) Optimal power sharing control of wind turbines. IEEE Trans Power Syst 32(1):824–825. https://doi.org/10.1109/TPWRS.2016.2549741
8. Li S, Haskew TA, Williams KA, Swatloski RP (2012) Control of DFIG wind turbine with direct-current vector control configuration. IEEE Trans Sustain Energy 3(1):1–11. https://doi.org/10.1109/TSTE.2011.2167001
9. Qiao W, Zhou W, Aller JM, Harley RG (2008) Wind speed estimation based sensor less output maximization control for a wind turbine driving a DFIG. IEEE Trans Power Electron 23(3):1156–1169. https://doi.org/10.1109/TPEL.2008.921185
10. Mohammadi J, VaezZadeh S, Afsharnia S, Daryabeigi E (2014) A combined vector and direct power control for DFIG-based wind turbines. IEEE Trans Sustain Energy 5(3):767–775. https://doi.org/10.1109/TSTE.2014.2301675

11. Ghosh S, Kamalasadan S, Senroy N, Enslin J (2016) Doubly fed induction generator (DFIG)-based wind farm control framework for primary frequency and inertial response application. IEEE Trans Power Syst 31(3):1861–1871. https://doi.org/10.1109/TPWRS.2015.2438861
12. Saruwatari M et al (2016) Design study of 15-MW fully superconducting generators for offshore wind turbine. IEEE Trans Appl Supercond 26(4):1–5, Art no. 5206805. https://doi.org/10.1109/TASC.2016.2535315
13. Nguyen N, Almasabi S, Mitra J (2018) Impact of correlation between wind speed and turbine availability on wind farm reliability. In: 2018 IEEE industry applications society annual meeting (IAS). Portland, OR, USA, pp 1–7. https://doi.org/10.1109/IAS.2018.8544643
14. Fischer K (2019) Reliability of power converters in wind turbines: exploratory analysis of failure and operating data from a worldwide turbine fleet. IEEE Trans Power Electron 34(7):6332–6344 https://doi.org/10.1109/TPEL.2018.2875005
15. Abad G, López J, Rodríguez M, Marroyo L, Iwanski G (2011) Vector control strategies for grid-connected DFIM wind turbines. In: Doubly fed induction machine: modeling and control for wind energy generation applications. IEEE, pp 303–361. https://doi.org/10.1002/9781118104965.ch7
16. Ma L, Zheng Y, Ma H (2011) Research and simulation of double-fed wind power generation rotor side control technology. In: 2011 International conference on electrical and control engineering. Yichang, China, pp 2472–2475. https://doi.org/10.1109/ICECENG.2011.6058038

TLO Based OPF with FACTS Devices for DC Link Placement Problem

B. Suresh Babu

Nomenclature

A_i B_i C_i	Fuel cost coefficients
D_i E_i	Coefficients of valve point effects of the generator
TFC	Total fuel cost
TRPL	Total real power loss
NVSI	Net voltage stability index
LVSI	Largest voltage stability index
FACTS	Flexible AC transmission systems
$Type_f$	Integer number in the range of (1–3) denoting the type of fth FACTS device, 1 represents SVC, 2 denote TCSC and 3 indicates UPFC

1 Introduction

The optimal power flow (OPF) has been widely used in power system operation and planning since its introduction by Carpentier [1]. The existence of nonlinear power flow constraints and the DC link equations make the problem non-convex even in the absence of discrete control variables [2–5]. Over the years, numerous mathematical programming techniques such as linear programming, nonlinear programming [6–8]. The difficulties in solving OPF can be overcome by modern stochastic algorithms such as particle swarm optimization (PSO), evolutionary programming (EP), harmony search optimization (HSO) [9–14], Recently, teaching learning based optimization (TLO) has been suggested for solving optimization problems [15].

B. S. Babu (✉)
Electrical and Electronics Engineering, Shri Vishnu Engineering College for Women, West Godavari District, Vishnupur, Bhimavaram, Andhra Pradesh 534202, India

S. Kumar et al. (eds.), *Recent Advances in Power Electronics and Drives*, Lecture Notes in Electrical Engineering 852, https://doi.org/10.1007/978-981-16-9239-0_17

The recent progress in power electronics have introduced Flexible AC Transmission Systems (FACTS) [16]. TLO with a view of obtaining the global best solution and demonstrates its performance through simulation results on IEEE 14 and 30 bus test systems.

2 Problem Statement with FACTS Devices

Three FACTS devices, SVC, TCSC and UPFC, each with different characteristics are chosen for placement in order to control reactive power injections and active power flows in the proposed strategy.

Repair the i-th student, replace the transmission lines by DC links, place FACTS devices and set the control parameters according to i-th student grade points and Run AC/DC load flow.

Test 1: TFC

Minimize

$$\Phi_1(x,u) = \sum_{j\in\Pi} A_j\, P_j^{G2} + B_j\, P_j^{G} + C_j + \left|D_j \sin\left(E_j\left(P_j^{G}(\min) - P_j^{G}\right)\right)\right| \tag{1}$$

$$\text{FACTS device constraints } -0.8 \le \eta_k \le 0.2 \text{ for TCSC and UPFC} \tag{2}$$

$$-100\,MVAR \le Q_i^F \le +100\,MVAR \text{ for SVC and UPFC} \tag{3}$$

Test 2: TRPL
Test 3: Enhancement of VS
Test 4: TFC + TRPL
Test 5: TFC + VS
Test 6: TRPL + VS
Test 7: TFC + TRPL + VS

Evaluate the AOF and performance function, select the best student with highest F_i in the population as the optimal solution

$$\text{Maximize } f = \frac{1}{1+AOF} \tag{4}$$

2.1 Representation of Decision Variables

The control variable in vector representation in TLO method as follows

Table 1 TLBO parameter

Parameter	Value
No. of students	30
Max. iteration	300

Table 2 Number of devices to be placed

Test system	14 bus	30 bus
Number of DC links	1	2
Number of FACTS devices	2	3

$$S = \left[Type_f,\ Loc_f,\ \eta_f,\ Q_f^F,\ P_k^G,\ V_j^G,\ T_v,\ L_p^{dc},\ I_p^{dc}\right] \tag{5}$$

3 Results and Discussions

The TLO is tested on IEEE 14 and 30 bus test systems, and the data have been taken from Ref. [17] (Tables 1, 2, 3, 4, 5 and 6).

It is observed from Tables 3 and 5 that TLO in this Test 1, Test 2 and Test 3 is the reduce of the TFC,TRPL and LVSI for IEEE 14 and 30 bus test system. It is seen from the results of Test 4, Test 5, Test 6 and Test 7 that the TLO and as well as the PSO and HSO offer a compromised solution. The % savings of TFC, TRPL and VS Enhancement for IEEE 14 and 30 bus test systems in Figs. 1 and 2.

4 Conclusion and Future Research

In this paper TLBO solution technique for OPFDC with FACTS placement are developed and tested on three IEEE14 and 30 bus test systems. The algorithms use sequential AC/DC load flow involving NR technique for computing the objective function during search and are able to offer the global best solution. It can also be observed that the proposed methods perform better with FACTS devices. The scope for future research the other FACTS devices such as SSSC and IPFC may be considered in the formulation of the problem.

Table 3 Results of IEEE 14 for Test 1–Test 7

Test		Base Test	IEEE 14		
			TLO	PSO	HSO
1	TFC	834.6716	814.8536	817.5147	815.7954
	TRPL	8.9737	6.0321	7.0616	6.4411
	NVSI	0.3724	0.3388	0.3265	0.3553
	LVSI	0.0750	0.0718	0.0673	0.0727
2	TFC	834.6716	1020.7136	1021.2605	1015.0630
	TRPL	8.9737	2.0437	2.3207	2.2245
	NVSI	0.3724	0.3158	0.3451	0.3875
	LVSI	0.0750	0.0600	0.0720	0.0780
3	TFC	834.6716	860.6775	874.4455	838.4990
	TRPL	8.9737	8.5319	7.0419	8.6873
	NVSI	0.3724	0.2157	0.2168	0.2177
	LVSI	0.0750	0.0326	0.0379	0.0364
4	TFC		900.4238	954.0228	963.7662
	TRPL		3.4375	2.7358	2.7435
	NVSI		0.3305	0.3595	0.3492
	LVSI		0.0674	0.0721	0.0738
5	TFC		842.5334	857.5641	834.3707
	TRPL		8.7328	9.0501	10.1520
	NVSI		0.2460	0.2827	0.3046
	LVSI		0.0407	0.0542	0.0503
6	TFC		1003.7122	1001.2078	1005.2532
	TRPL		2.3690	2.8254	2.4856
	NVSI		0.2882	0.2757	0.3207
	LVSI		0.0529	0.0593	0.0676
7	TFC		926.3375	943.0159	920.3096
	TRPL		3.1284	3.3853	3.1100
	NVSI		0.3129	0.2607	0.2994
	LVSI		0.0570	0.0564	0.0665

Table 4 Solution of TLO for IEEE 14

	Base Test	Test 1 TFC	Test 2 TRPL	Test 3 VS	Test 6 TRPL + VS	Test 4 TFC + TRPL	Test 5 TFC + VS	Test 7 TFC + TRPL + VS
P^G	188.974 35.000 20.000 12.000 12.000	208.901758 20.000000 16.130359 10.000000 10.000000	66.103032 80.000000 50.000000 35.000000 29.940624	162.465763 39.293198 18.018575 28.489782 19.264631	77.985842 80.000000 50.000000 23.824707 29.558413	127.562486 55.003782 36.083444 13.787810 30.000000	185.767811 26.093413 18.317468 18.240963 19.313102	112.111149 52.387035 40.330989 28.616944 28.682266
V^G	1.060 1.045 1.010 1.070 1.090	1.091626 1.071827 1.047213 1.010819 1.013973	1.046741 1.038227 1.022883 1.006294 1.033028	1.044781 0.992240 0.950728 1.007576 1.018693	1.024141 1.008369 0.999669 1.038515 1.064612	1.038874 1.036558 1.019790 1.023449 1.044612	1.051549 1.040252 1.028669 1.067179 1.079894	1.016353 1.013070 0.992228 0.989859 1.037511
T	0.978 0.969 0.932	1.036260 1.089908 0.919960	1.035949 1.048395 1.022987	1.001334 1.046936 0.900000	0.973753 0.975872 0.977289	0.989459 0.981519 1.068977	0.977035 1.007912 0.984713	1.036637 1.006847 0.956953
L_p^{dc}	–	4	3	3	3	4	11	4
I_p^{dc}	–	0.995070	0.525269	1.000000	0.613878	0.798408	0.334221	0.666732
Facts type		3 2	2 2	2 2	2 2	2 2	1 2	2 2
Facts location		7 12	17 11	11 17	12 17	11 12	12 17	11 17
VAR support		60.329 –	– –	– –	– –	– –	55.346 –	– –
Line com fact		−0.138 0.176	−0.747 −0.507	−0.800 −0.797	−0.624 −0.690	−0.260 −0.468	– −0.599	−0.712 −0.638

Table 5 Results of IEEE 30 for Test 1–Test 7

Test		Base test	IEEE 30		
			TLO	PSO	HSO
1	TFC	813.6941	789.0199	793.9881	791.9971
	TRPL	7.0990	5.7185	5.9928	6.7249
	NVSI	1.6705	1.7005	1.5685	1.7032
	LVSI	0.1336	0.1373	0.1295	0.1310
2	TFC	813.6941	964.8873	964.9062	964.9016
	TRPL	7.0990	1.9381	1.9428	1.9412
	NVSI	1.6705	1.4524	1.4538	1.4535
	LVSI	0.1336	0.1068	0.1070	0.1069
3	TFC	813.6941	885.2828	863.1441	855.1094
	TRPL	7.0990	11.5340	8.7832	8.8625
	NVSI	1.6705	0.8189	0.9406	0.9125
	LVSI	0.1336	0.0499	0.0625	0.0621
4	TFC		937.3572	944.7096	894.2697
	TRPL		2.0710	2.0401	2.3679
	NVSI		1.4344	1.4606	1.5078
	LVSI		0.1049	0.1069	0.1226
5	TFC		794.7903	800.8039	806.0572
	TRPL		7.6315	5.9798	9.8711
	NVSI		1.2688	1.4024	1.2666
	LVSI		0.0748	0.0878	0.0761
6	TFC		964.8502	964.8313	964.8999
	TRPL		1.9419	1.9437	1.9424
	NVSI		1.4515	1.4533	1.4523
	LVSI		0.1065	0.1066	0.1068
7	TFC		922.3340	924.3042	894.9846
	TRPL		2.1289	2.1326	2.3328
	NVSI		1.4062	1.4180	1.4935
	LVSI		0.1007	0.1025	0.1215

Table 6 Solution of TLO for IEEE 30

	Base Test	Test 1 TFC	Test 2 TRPL	Test 3 VS	Test 6 TRPL + VS	Test 4 TFC + TRPL	Test 5 TFC + VS	Test 7 TFC + TRPL + VS
P^G	138.539 57.560 24.560 35.000 17.930 16.910	176.158866 48.197453 19.652961 20.299167 12.810086 12.000000	50.340844 79.999982 49.999677 34.999930 30.000000 39.997704	163.245678 20.163249 48.437909 26.593007 10.599845 25.894290	50.367124 80.000000 50.000000 35.000000 29.974730 40.000000	58.973346 77.643720 46.348710 34.944779 29.561586 37.998846	180.653083 48.486956 19.479194 17.725836 12.005007 12.681471	63.245366 76.867933 43.419597 34.997792 30.000000 36.998175
V^G	1.050 1.0338 1.0058 1.0230 1.0913 1.0883	1.038428 1.019645 0.999386 1.003538 1.043440 1.047130	1.045526 1.039370 1.034382 1.037476 1.067559 1.090400	1.054416 1.041288 1.013316 1.053726 1.054044 1.081825	1.044582 1.038140 1.034043 1.036359 1.065253 1.089889	1.047897 1.040368 1.034132 1.039421 1.068494 1.091342	1.078516 1.061678 1.024740 1.035812 1.045030 1.083279	1.049988 1.041765 1.034853 1.039318 1.071041 1.092072
T	1.0155 0.9629 1.0129 0.9581	1.082984 0.947624 1.034320 0.965501	0.972115 1.001305 1.011821 0.964632	1.050706 0.997420 0.900044 1.020328	0.970561 1.002034 1.013126 0.965851	0.968194 0.999104 1.010996 0.964933	0.964225 0.924463 0.935517 0.933096	0.963403 0.994426 1.002060 0.962257
L_p^{dc}	–	5 2	6 5	40 3	6 5	6 5	11 5	6 5
I_p^{dc}	–	0.681020 0.662481	0.287488 0.401750	0.569400 0.998841	0.291466 0.407965	0.306704 0.415457	0.212152 0.609589	0.296228 0.449165
Facts type		2 2 2	2 2 2	2 3 3	2 2 2	2 2 2	2 2 2	2 2 2

(continued)

Table 6 (continued)

	Base Test	Test 1 TFC	Test 2 TRPL	Test 3 VS	Test 6 TRPL + VS	Test 4 TFC + TRPL	Test 5 TFC + VS	Test 7 TFC + TRPL + VS
Facts Location		21 39 28	36 25 31	22 36 12	36 25 31	36 25 31	36 38 25	36 25 31
VAR support		– – –	– – –	– 60.722 84.990	– – –	– – –	– – –	– – –
Line com fact		−0.100 0.169 0.078	−0.384 −0.312 −0.381	−0.788 −0.409 −0.579	−0.396 −0.309 −0.368	−0.404 −0.293 −0.420	−0.799 −0.580 −0.754	−0.467 −0.328 −0.411

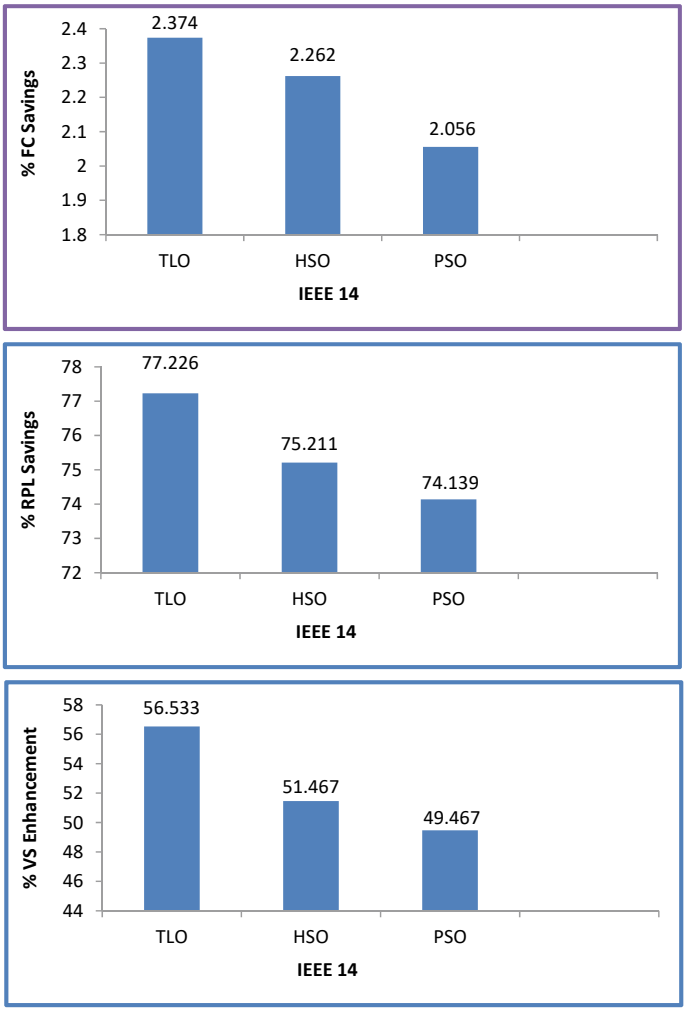

Fig. 1 Percentage of savings TFC, TRPL and VS enhancement for IEEE 14

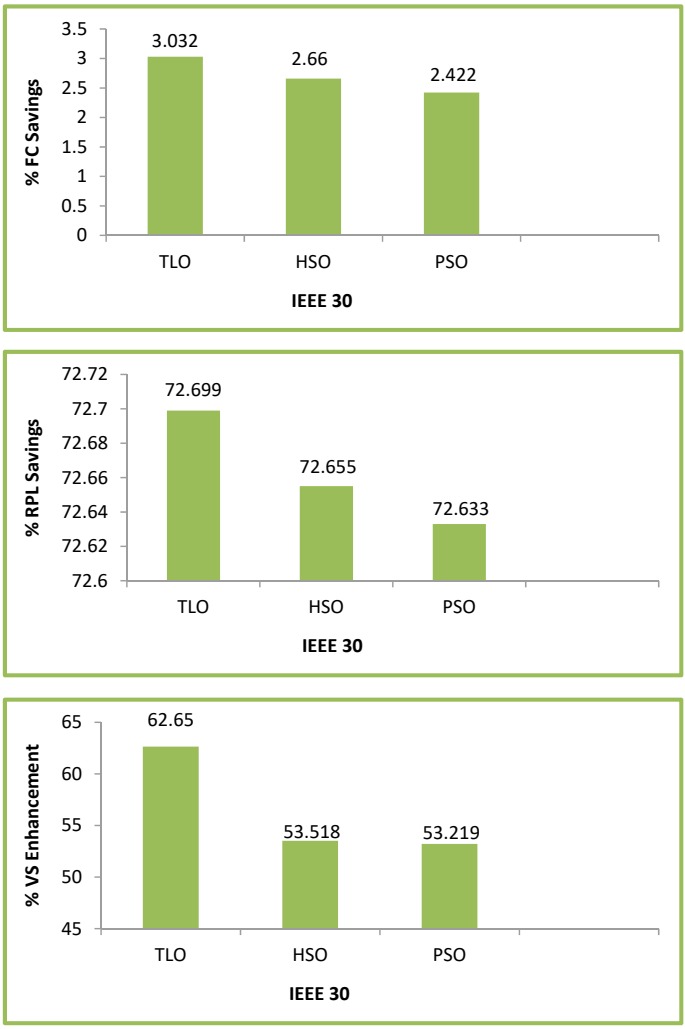

Fig. 2 Percentage of savings TFC, TRPL and VS enhancement for IEEE 30

Acknowledgements The author gratefully acknowledge the authorities of Department of Electrical and Electronics Engineering, Shri Vishnu Engineering College for Women for their continued support, encouragement and the facilities provided to carry out this work.

References

1. Carpentier J (1962) Contribution a l'Etude du Dispatching Economique'. Bulletin de la Societe

Francaise des Electriciens 3:431–474
2. Momoh JA, El-Hawary ME, Adapa R (1999) A review of selected optimal power flow literature to 1993 Part I: nonlinear and quadratic programming approaches. IEEE Trans Power Syst 14:96–104
3. Momoh JA, El-Hawary ME, Adapa R (1999) A review of selected optimal power flow literature to 1993 Part II: Newton, linear programming and interior point methods. IEEE Trans Power Syst 14:105–111
4. Nagsarkar TK, Sukhija MS (2007) Power system analysis. Oxford University Press
5. Arrillaga J, Watson NR (2013) Computer modelling of Electrical power systems. Wiley
6. Arrillaga J, Arnold C, Harker BJ (1983) Computer modelling of Electrical power systems. Wiley
7. Lee KY, Park YM, Oritz JL (1984) Fuel-cost minimization for both real and reactive power dispatches. IEE Proc C 131(3):85–93
8. Alsac O, Scott B (1974) Optimal load flow with steady state security. IEEE Trans Power Apparatus Syst PAS 745–751
9. Abido MA (2002) Optimal power flow using particle swarm optimization'. Proc Int J Electr Power Energy Syst 24(7):563–571
10. Abido MA, Al-Ali NA (2009) Multi-objective differential evolution for optimal power flow. In: International conference on power engineering, energy and electrical drives, POWERENG 2009. Lisbon, Portugal, pp 101–106
11. Abou El Ela AA, Abido MA (2010) Optimal power flow using differential evolution algorithm. Electr Power Syst Res 80(7):878–885
12. Naresh babu AV, Ramana T, Sivanagaraju S (2014) Analysis of optimal power flow problem based on two stage initialization algorithm. Int J Electr Power Energy Syst 55:91–99
13. Niknam T, Narimani MR, Jabbari M, Malekpour AR (2011) A modified shuffle frog leaping algorithm for multi-objective optimal power flow. Energy 36:6420–6432
14. Sivasubramani S, Swarup KS (2011) Multi-objective harmony search algorithm for optimal power flow problem. Int J Electr Power Energy Syst 33(3):745–752
15. Rao RV, Savsani VJ, Vakharia DP (2012) Teaching-learning-based optimization: a novel optimization method for continuous non-linear large scale problems. Inf Sci 183(1):1–15
16. Hingorani NG, Gyugy L (2001) Understanding FACTS concepts and technology of flexible AC transmission systems. Standard Publishers Distributors, New Delhi
17. Test Archive, Systems. http://www.ee.washington.edu/research/pstca/. Accessed Dec 2012

Performance Comparison Analysis of Energy Management Strategies for Hybrid Electric Vehicles

Jai Kumar Maherchandani, R. R. Joshi, Ritesh Tirole, Raju Kumar Swami, and Bibhu Prasad Ganthia

1 Introduction

Increasing pollution and the fast depletion of fossil fuels are the two major problems of today's world. Convention fuel-based transportation sector is one of the main contributors to the pollution problem. The transport sector in the U.S. contributes about 28% of the total greenhouse gas (CHG) emission and continuously increases with a rapid growth rate [1]. In India, this sector is at third place in CHG emission and growing exponentially. Approximately 70% of the total diesel and 95% of the petrol consumption are caused by this sector in India [2].

Worldwide, continuous efforts are being made to shift from conventional fuel-based vehicles to environmentally friendly electric vehicles (EV) or HEV. EV consisting of a battery as a single source of power has a limited range with a single charge. Combining two or more sources in HEV has many advantages, such as increased range, reliability, and lifetime, in comparison to EV using a single source of energy. HEV may consist of a combination of different types of energy sources such as a battery, internal combustion engine (ICE), fuel cell (FC), and supercapacitor (SC), in a hybrid manner.

Because of its various advantages, such as high performance, low operating temperature, and almost zero-emission, the proton exchange membrane fuel cell (PEMFC) is now commonly used as a primary energy source in electric vehicle

J. K. Maherchandani (✉) · R. R. Joshi
College of Technology and Engineering, MPUAT, Udaipur, India

R. Tirole
Sir Padampat Singhania University, Udaipur, India
e-mail: ritesh.tirole@spsu.ac.in

R. K. Swami
Pacific University, Udaipur, Rajasthan, India

B. P. Ganthia
IGIT, Sarang, Dhenkanal, Odisha, India

S. Kumar et al. (eds.), *Recent Advances in Power Electronics and Drives*, Lecture Notes in Electrical Engineering 852, https://doi.org/10.1007/978-981-16-9239-0_18

(EV) applications [3, 4]. However, PEMFC's sluggish dynamic is a major downside that prevents it from meeting fast-changing load demand. It is possible to solve this problem by using additional energy sources with various characteristics. The high dynamic efficiency of HEV is ensured by a combination of high energy density sources such as battery and high-power density sources such as supercapacitor with PEMFC [5–8].

A proper energy management strategy (EMS) is always needed to exploit the full benefit of the hybridization of an HEV. Designing an effective EMS for an HEV consisting of different energy sources is a difficult challenge [9, 10]. The main goal of EMS is to break the instantaneous load demand among source components in such a way that one or more performance objectives can be met, such as minimizing fuel consumption, maximizing overall efficiency, putting the least amount of stress on individual source components, reducing pollution, and achieving optimal vehicle performance. Various methods for achieving optimum efficiency have been proposed in the literature [11–15].

EMS's may be classified into two broad categories, i.e., rule-based EMS and optimization-based EMS. RB EMS is computationally efficient, easy to implement, and can be applied in real-time. Designing rule-based EMS depends on experience, engineering intuition, and characteristics of power train [16]. These types of strategies do not involve any optimization techniques directly during the implementation of EMS. Optimization-based EMS's may be designed to meet one or more objectives. They may be further classified as real-time and off-time EMS. Equivalent consumption minimization (ECMS), model predictive control (MPC), and intelligent control system are the example of few real-time EMS.

The present work focuses on the performance comparison of three popular EMS, i.e., conventional PI, ECMS, and RB. HEV used in this work consists of FC, battery, and SC. The performance comparison of all three strategies is carried out in terms of efficiency, fuel consumption, and battery SOC. All three strategies are simulated for identical conditions.

2 System Architecture

The system architecture of HEV used in this work is shown in Fig. 1. FC acts as a primary source and is connected to the DC bus via a unidirectional DC-DC converter. The battery may supply or absorb the power with the help of a bidirectional dc-dc converter, depending on the mode of operation. SC being a high-power density source helps in meeting high dynamic load demand or absorb the excess power instantaneously.

The energy management controller decides power-sharing by the respective source. It may have one or more objectives: ensure the operation of the respective source at an optimal level, maintain a high SOC level of the battery, achieve high overall efficiency, minimize the fuel consumption, etc.

Dynamic modelling of the proposed HEV system components is presented below.

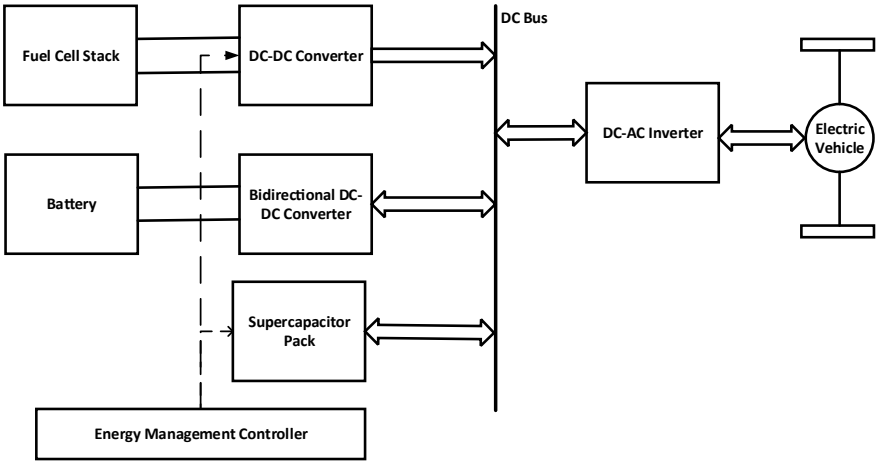

Fig. 1 System architecture

Modelling of fuel cell

FC stack voltage (V_{fc}) and Nernst voltage (V_{NV}) relationship can be represented as [17, 18]:

$$V_{fc} = n_{cs} V_{NV} - V_{IVL} \tag{1}$$

where n_{cs}, V_{IVL} are series-connected cell and irreversible voltage loss, respectively.

The output power of FC is given as

$$P_{fc} = V_{fc} I_{fc} \tag{2}$$

where I_{fc} is FC output current.

Modelling of Battery Storage System

The lithium-ion battery model comprises a voltage source V_B and its internal series resistance R_i considering both are the function of battery SOC can be given by [19]:

$$I_B = \frac{V_B(SOC) - \sqrt{V_B^2(SOC) - 4 \cdot R_i(SOC) \cdot P_B}}{2 \cdot R_i(SOC)} \tag{3}$$

where P_B and I_B are the power supplied or absorbed by the battery and battery current, respectively.

Table 1 Rating of HEV Components

HEV component	Rating
FC power	11 kW
Battery power	4 kW
Allowable battery SOC level	55–90%
DC bus voltage	V

Supercapacitor Modelling

Here, the Stern model combines both the "Gouy–Chapman and Helmholtz models" [20, 21] is considered. The capacitance may be expressed as

$$C_{SC} = \left[\frac{1}{C_{GC}} + \frac{1}{C_H}\right]^{-1} \tag{4}$$

where C_{GC}, C_H are "Gouy–Chapman" and "Helmholtz" capacitance (in farads), respectively.

Hybridization of FC with SC is done to enhance the dynamics of such a system to efficiently meet the fast-varying load demand put on the electric vehicle. Bidirectional DC-DC battery converter regulates the DC bus voltage as well as SC SOC level. The value of different HEV components has been shown in Table 1.

3 Energy Management Strategies

This section briefly discusses widely used classical PI, optimization-based ECMS, and RB EMS for the HEV system shown in Fig. 1.

3.1 Classical PI Control Strategy

This type of strategy relies on PI controllers to control key performance parameters like battery SOC, SC voltage, and dc-bus voltage. The distribution of load power is done in such a way that FC provides the steady-state load demand. In this type of strategy, the PI controller may regulate the battery power depending upon the battery current SOC level. Fuel cell reference power is decided after subtracting battery share from load demand. Battery SOC level plays the main role in such a type of strategy. Depending upon the battery SOC level above or below the reference value, the battery power share increases or decreases, which in turn varies the fuel cell power share in meeting the load demand. Conventional PI EMS is easier to implement, and the PI gains may be tuned online for a better response.

3.2 Optimization Based ECMS

ECMS is the most widely used real-time EMS. ECMS is a cost function optimization strategy to ensure FC optimal operation with maximum fuel economy [22, 23]. The power distribution is determined by minimizing an instantaneous cost function that includes the fuel consumption of the FC and the equivalent fuel consumption of the battery's electrical energy. The method proposed in [24] is used in this study, where the battery SOC is regulated by the battery energy penalty coefficient. The optimization problem is defined as follows.

Find FC power P_{fc}, equivalence factor α and battery power P_{batt} which minimizes equivalent fuel cost

$$F = [P_{fc} + \alpha P_{batt}] \cdot \Delta T \tag{5}$$

under the equality constraints

$$P_{load} = P_{fc} + P_{batt} \tag{6}$$

Within the boundary conditions

$$\begin{aligned} &P_{fc\_\min} \leq P_{fc} \leq P_{fc\_\max} \\ &P_{batt\_\min} \leq P_{batt} \leq P_{batt\_\max} \\ &0 \leq \propto \leq 100 \end{aligned} \tag{8}$$

where, P_{fc}, P_{batt}, P_{load} are the FC, battery, and load power, respectively. α is the equivalence factor, μ is a constant, ΔT is the sampling time. $P_{fc\_\min}$, $P_{fc\_\max}$, $P_{batt\_\min}$, $P_{batt\_\max}$ are the FC minimum, FC maximum power, battery maximum and battery minimum power, respectively. $SOC_{\min}$ and $SOC_{\max}$ are the minimum and maximum battery SOCs respectively.

Only FC and battery power are considered in optimization problems as SC is connected to the DC bus and recharged from the battery directly.

3.3 RB Energy Management Strategy

RB control strategies are computationally efficient and can be applied in real-time. Such a strategy is designed considering the characteristics of different sources, experience, driving cycle requirements, etc. This type of strategy may be further classified broadly as a deterministic or fuzzy rule-based strategy. Here, a simple RB strategy consisting of eight rules is taken for comparison purposes [25]. The RB strategy implemented is shown in Table 2.

Table 2 Rule-based energy management strategy

Rule	Operating conditions	Fuel cell power
I	If SOC High and $P_{load} < P_{fc\_min}$	$P^*_{fc} = P_{fc\_min}$
II	If SOC high and $P_{load} \in [P_{fc\_min}, P_{fc\_max}]$	$P^*_{fc} = P_{load}$
III	If SOC high and $P_{load} \geq P_{fc\_max}$	$P^*_{fc} = P_{fc\_max}$
IV	If SOC normal and $P_{load} < P_{fc\_opt}$	$P^*_{fc} = P_{fc\_opt}$
V	If SOC normal and $P_{load} \in [P_{fc\_opt}, P_{fc\_max}]$	$P^*_{fc} = P_{load}$
VI	If SOC normal and $P_{load} \geq P_{fc\_max}$	$P^*_{fc} = P_{fc\_max}$
VII	If SOC low and $P_{load} < P_{fc\_max}$	$P^*_{fc} = P_{load} + P_{char}$
VIII	If SOC low and $P_{load} \geq P_{fc\_max}$	P_{fc_max}

Here SOC High means $OC > SOC_{\max}$, SOC Normal means SOC is between 65 and 85%, and SOC Low means $SOC < SOC_{\min}$.

The FC power is decided based on the battery SOC range and load power P_{load}. The comparison among EMSs is made using MATLAB software. Results are presented and discussed in the next section.

4 Results and Discussion

This section presents a comparative analysis of the above discussed conventional PI, ECMS, and RB EMS. Performance comparison in overall efficiency, battery SOC, and hydrogen consumption is presented for these strategies. The same initial conditions are used for all three EMS's. The comparative results are given below. Figure 2 shows the variable load demand of HEV.

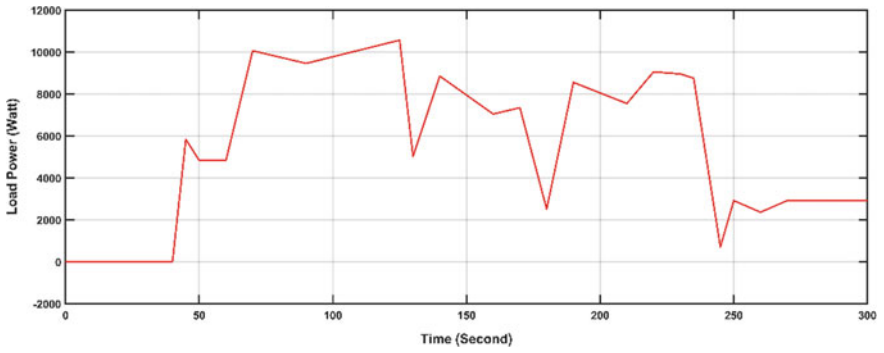

Fig. 2 Load profile

Table 3 Comparative energy contribution (Wh)

S. No.	Source name	PI strategy	ECFM strategy	RB strategy
1	Fuel cell output	420.89	484.64	439.61
2	Battery output	82.45	18.62	56.07
3	Super-capacitor output	−6.93	−6.85	0.750

4.1 Comparative Energy Contribution by Individual Power Source

Table 3 show the energy contributed by individual energy source in the simulation periods under different control strategy.

It is clear that FC energy contribution is maximum and minimum in the ECMS and PI control strategy, respectively, and the reverse is true for battery energy contribution. Rule-based control strategy shares the power in a more optimum way between the fuel cell and battery.

4.2 Performance Comparison Among RB, PI and ECMS Strategy

Overall Efficiency

Figure 3 shows overall efficiency comparison among RB, PI, and ECMS control strategies. It can be concluded that the RB control strategy (83.01%) provide better average efficiency in comparison with the ECMS control strategy (79.46%) and PI control strategy (82.11%).

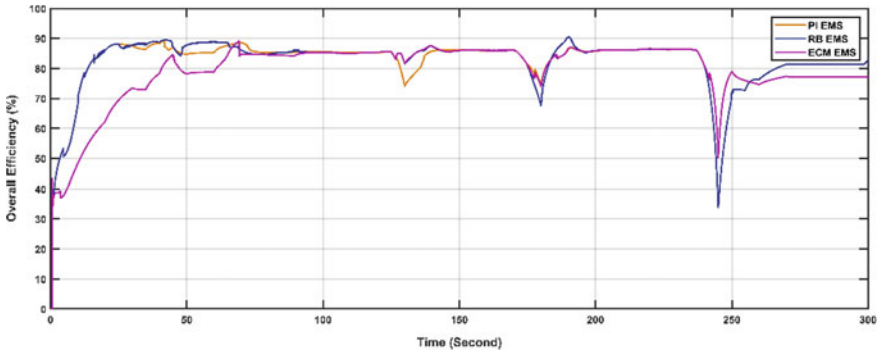

Fig. 3 Efficiency comparison of PI, ECMS and RB strategy

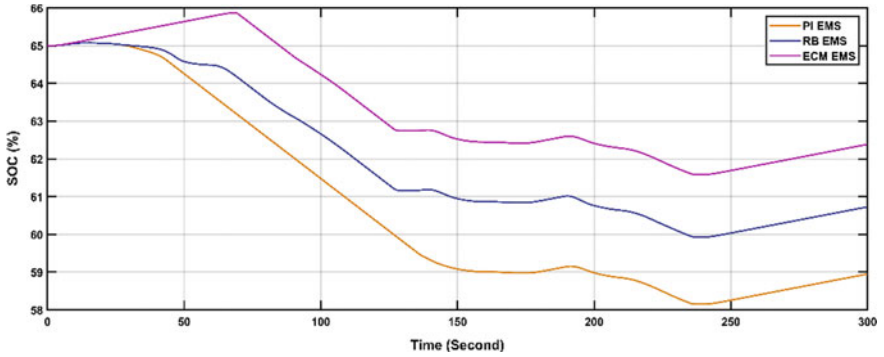

Fig. 4 Battery SOC comparison of PI, ECMS and RB strategy

Table 4 Performance comparison of proposed, PI, and EFCM strategies

	PI strategy	RB strategy	ECMS strategy
Overall efficiency (%)	82.11	83.01	79.46
State of charge (SOC)	58.15–65.07	59.93–65.07	61.59–65.87
H_2 consumption (gm)	12.82	14.43	16.74

Battery SOC

Figure 4 shows the comparative use of battery storage for RB, PI, and ECMS control strategies. It can be revealed that the ECMS strategy uses the lesser battery power and maintains a slightly higher SOC level compared to RB and PI control strategy, as shown in Table 4.

Hydrogen Consumption

Figure 5 gives a comparison of hydrogen consumption for RB, PI, and ECMS control strategies. ECMS has higher average fuel consumption compared to RB and PI control strategies. The fuel consumption during the simulation period is given in Table 4.

5 Conclusion

Performance comparison of commonly used PI, ECMS, and RB energy management schemes for a fuel-cell hybrid energy vehicle has been presented. The same initial conditions are used for all the schemes. Comparison among EMS's the PI EMS causes the lowest hydrogen consumption, ECMS causes the highest battery SOC, and the RB EMS provided slightly better efficiency. It may be concluded that the

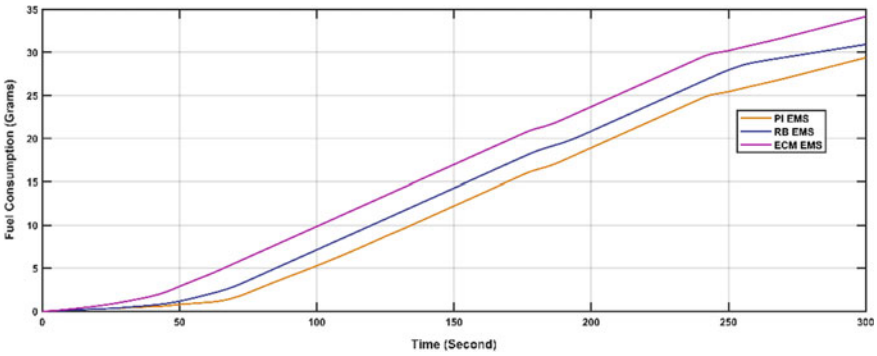

Fig. 5 Fuel consumption comparison of PI, ECMS and RB strategy

EMS suitable for different applications is selected based on a particular criterion to prioritize. Proper tuning of PI controller for PI EMS, more expertise in designing RB EMS rules, and efficient optimization algorithms for ECMS play a very important role.

References

1. United States Environmental Protection Agency Department of Transportation and Air Quality (2020) Fast FastFacts: U.S. transportation sector greenhouse gas emissions 1990–2018, p. EPA-420-F-20-037
2. Singh N, Mishra T, Banerjee R (2019) Greenhouse gas emissions in India's road transport sector. Clim Chang Signals Response 197–209. https://doi.org/10.1007/978-981-13-0280-0_12
3. Geng B, Mills JK, Sun D (2012) Two-stage energy management control of fuel cell plug-in hybrid electric vehicles considering fuel cell longevity. IEEE Trans Veh Technol 61(2):498–508. https://doi.org/10.1109/TVT.2011.2177483
4. Erdinc O, Uzunoglu M (2010) Recent trends in PEM fuel cell-powered hybrid systems: investigation of application areas, design architectures and energy management approaches. Renew Sustain Energy Rev 14(9):2874–2884. https://doi.org/10.1016/j.rser.2010.07.060
5. Emadi A, Rajashekara K, Williamson SS, Lukic SM (2005) Topological overview of hybrid electric and fuel cell vehicular power system architectures and configurations. IEEE Trans Veh Technol 54(3):763–770. https://doi.org/10.1109/TVT.2005.847445
6. Fadel A, Zhou B (2011) An experimental and analytical comparison study of power management methodologies of fuel cell-battery hybrid vehicles. J Power Sources 196(6):3271–3279. https://doi.org/10.1016/j.jpowsour.2010.11.114
7. Uzunoglu M, Onar OC, Alam MS (2009) Modeling, control and simulation of a PV/FC/UC based hybrid power generation system for stand-alone applications. Renew Energy 34(3):509–520. https://doi.org/10.1016/j.renene.2008.06.009
8. Erdinc O, Vural B, Uzunoglu M (2009) A wavelet-fuzzy logic based energy management strategy for a fuel cell/battery/ultra-capacitor hybrid vehicular power system. J Power Sources 194(1):369–380. https://doi.org/10.1016/j.jpowsour.2009.04.072
9. Panday A, Bansal HO (2014) A review of optimal energy management strategies for hybrid electric vehicle. Int J Veh Technol 2014. https://doi.org/10.1155/2014/160510

10. Wang Y et al (2019) A comprehensive analysis of energy management strategies for hybrid electric vehicles based on bibliometrics. J Energy Storage 26(February):57–66. https://doi.org/10.1109/TVT.2017.2660764
11. Lü X, et al (2020) Energy management of hybrid electric vehicles: a review of energy optimization of fuel cell hybrid power system based on genetic algorithm. Energy Convers Manag 205. https://doi.org/10.1016/j.enconman.2020.112474
12. Zhou B, Burl JB, Rezaei A (2020) Equivalent consumption minimization strategy with consideration of battery aging for parallel hybrid electric vehicles. IEEE Access 8. https://doi.org/10.1109/ACCESS.2020.3036033
13. Wang Y, Wang W, Zhao Y, Yang L, Chen W (2016) A fuzzy-logic power management strategy based on Markov random prediction for hybrid energy storage systems. Energies. https://doi.org/10.3390/en9010025
14. Liu X, Qin D, Wang S (2019) Minimum energy management strategy of equivalent fuel consumption of hybrid electric vehicle based on improved global optimization equivalent factor. Energies 12(11). https://doi.org/10.3390/en12112076
15. Schmid R, Buerger J, Bajcinca N (2021) Energy management strategy for plug-in-hybrid electric vehicles based on predictive PMP. IEEE Trans Control Syst Technol. https://doi.org/10.1109/TCST.2020.3048129
16. Zhang P, Yan F, Du C (2015) A comprehensive analysis of energy management strategies for hybrid electric vehicles based on bibliometrics. Renew Sustain Energy Rev 48(205):88–104. https://doi.org/10.1016/j.rser.2015.03.093
17. Hajizadeh A, Golkar MA, Feliachi A (2010) Voltage control and active power management of hybrid fuel-cell/energy-storage power conversion system under unbalanced voltage sag conditions. IEEE Trans Energy Convers 25(4):1195–1208. https://doi.org/10.1109/TEC.2010.2062516
18. Wang C, Nehrir MH, Shaw SR (2005) Dynamic models and model validation for PEM fuel cells using electrical circuits. IEEE Trans Energy Convers. https://doi.org/10.1109/TEC.2004.842357
19. Tang L, Rizzoni G, Onori S (2015) Energy management strategy for HEVs including battery life optimization. IEEE Trans Transp Electrif. https://doi.org/10.1109/TTE.2015.2471180
20. Musolino V, Piegari L, Tironi E (2013) New full-frequency-range supercapacitor model with easy identification procedure. IEEE Trans Ind Electron. https://doi.org/10.1109/TIE.2012.2187412
21. Oldham KB (2008) A Gouy-Chapman-Stern model of the double layer at a (metal)/(ionic liquid) interface. J Electroanal Chem 613(2):131–138. https://doi.org/10.1016/j.jelechem.2007.10.017
22. Rodatz P, Paganelli G, Sciarretta A, Guzzella L (2005) Optimal power management of an experimental fuel cell/supercapacitor- powered hybrid vehicle. Control Eng Pract 13(1):41–53. https://doi.org/10.1016/j.conengprac.2003.12.016
23. Xu L, Li J, Hua J, Li X, Ouyang M (2009) Optimal vehicle control strategy of a fuel cell/battery hybrid city bus. Int J Hydrog Energy. https://doi.org/10.1016/j.ijhydene.2009.06.021
24. Garcia P, Fernandez LM, Garcia CA, Jurado F (2010) Energy management system of fuel-cell-battery hybrid tramway. IEEE Trans Ind Electron 57(12):4013–4023. https://doi.org/10.1109/TIE.2009.2034173
25. Njoya Motapon S, Dessaint LA, Al-Haddad K (2014) A comparative study of energy management schemes for a fuel-cell hybrid emergency power system of more-electric aircraft. IEEE Trans Ind Electron 61(3):1320–1334. https://doi.org/10.1109/TIE.2013.2257152

Evaluative Study of Cascaded Multilevel Inverter Topologies

Hemant Gupta, Arvind Yadav, and Sanjay Kumar Maurya

1 Introduction

In all the high power applications of industry, multilevel inverter is more preferable because it is tremendously advantageous due to its high quality of output voltage, higher efficiency, less component of harmonics and its dynamic performance with different loading conditions [1–4]. Multilevel inverters are very much capable to synthesize approximated pure ac sinusoidal waveform by using separate dc input sources [2]. In the classical structure of multilevel inverter it has many of topologies out of which there are three basic and popular topologies named as flying capacitor MI, neutral point clamped MI and cascaded H bridge MI [2, 5–7]. Among them cascade H bridge based multilevel inverter is more preferable because of its configurable framework and minimized count number of switches in contrast with other topologies [8]. The use of differing magnitudes in DC sources enables symmetric and asymmetric configurations of cascaded multilevel inverter topologies. Asymmetrical topologies can produce higher voltage levels by using the same number of power semiconductor devices including DC sources of unequal magnitude, whereas a symmetrical multilevel inverter needs DC sources of the same magnitude [9]. Hybrid modulation, Selective Harmonic Elimination (SHE), Nearest Level Modulation (NLM), and Multicarrier PWM are few of the typical modulation methods used in cascade multilevel inverters. Full-bridge inverter comprises switches that are purposely designed to withstand voltage levels than other switches in some topologies [10].

H. Gupta (✉) · A. Yadav · S. K. Maurya
GLA University, Mathura, India
e-mail: hemant.gupta@gla.ac.in

A. Yadav
e-mail: arvind.yadav@gla.ac.in

S. K. Maurya
e-mail: sanjay.maurya@gla.ac.in

S. Kumar et al. (eds.), *Recent Advances in Power Electronics and Drives*, Lecture Notes in Electrical Engineering 852, https://doi.org/10.1007/978-981-16-9239-0_19

Literature reveals that first MLI was created at the beginning of 1975 and that several forms and variations in multilevel converter topologies were documented in literature with research and development. In recent decades, a good much of the literature have shown a strong interest in the study of diode clamped, flying capacitor and cascaded H-bridge topologies with regard to their respective pros and cons. The main drawback with conventionally used multilevel inverter topologies is that the quantity of power electronic components used increases as the levels increase [11]. In recent years, research on CHB inverters has been more focused due to the modularity of the circuit, balanced DC voltage, and more levels of inverter output voltage with a smaller number of components without needing high ratings for each unit [12]. New structures have been developed to ensure the multilevel inverter's excellent performance. Recently the research work that has been done on multilevel inverter relies on the required level count at the output side and dc source used at input. And at the same time its switching losses and switching stress need to be considered. Another study's topology demonstrates the creation of output voltage having multiple levels by configuring series and parallel connection of DC voltage sources. Besides the conventional topologies of multilevel inverter, some advanced modular structure of multilevel inverter also designed in which more attention has been paid towards the number of switches count and dc source used [13].

2 Classical 11-Level CHB

Figure 1 presents the classical 11-level cascade multilevel inverter which comprises five modules of H bridge, and each module is capable to provide three level of output 0 and $\pm V_{dc}$ [10]. Each H bridge contains one dc source and four switches S1, S2, S3, S4 of low voltage rating, two switches in each leg of H bridge. A series-connected H bridge string is used in a multilevel inverter to provide stepped output from multiple dc sources. The numbers of levels achieved at the output side of inverter with the number of H bridges used are related with equation as

$$N_{level} = 2N + 1 \tag{1}$$

where N is the number of H bridges used. Here the output level and dc source required has same count of number. On the basis of magnitude of dc voltage sources, two types of configuration are available for multilevel inverter symmetrical and asymmetrical [14]. If the magnitude of all dc sources is equal then it is called symmetrical otherwise unsymmetrical. Here the used configuration is of symmetrical multilevel inverter and the maximum voltage achieved ate the output is the sum of several the dc sources of each H bridge as

$$Vo = Vdc1 + Vdc2 + Vdc3 + Vdc4 + Vdc5 \tag{2}$$

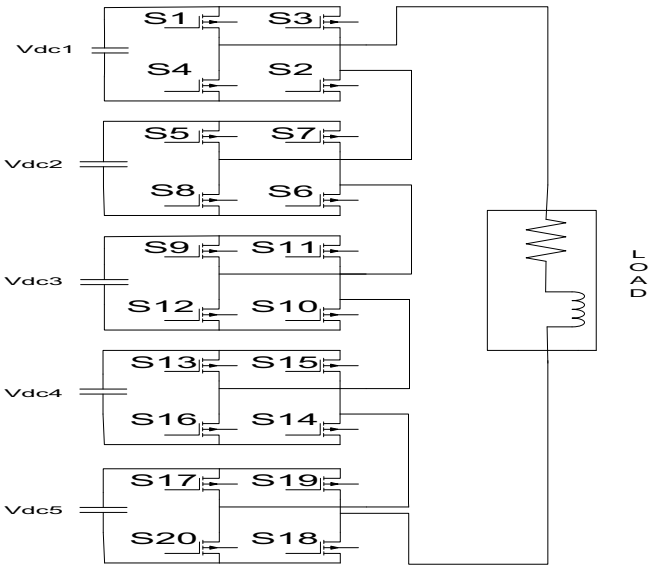

Fig. 1 Classical 11-level CHB

The biggest advantage of using symmetrical configuration is that it is even power distribution and modular structure because of which its modulation technique can be designed easily for getting the switched output voltage of the multilevel inverter [15].

3 Modulation Strategy for Classical CHB

There are several modulation techniques for cascaded H bridge multilevel inverter which is based upon the number of output level and amount of THD [16]. Among the many recent modulation techniques multicarrier PWM technique has been most commonly used because of its improved harmonic performance [17].

Here the carrier-based phase shifted PWM strategy is used for the 11-level cascaded multilevel inverter in which $N - 1$ triangular carriers are used of same magnitude and frequency where output voltage level count of inverter is typified as N. The switched output voltage for the multilevel inverter is calculated by comparing the reference sinusoidal signal with each carrier signal for each cell. In the midst of the two neighbouring carrier waves the phase shift occurs of angle

$$\Phi \text{cr} = \frac{360}{N-1} \tag{3}$$

where N is typified as output voltage level count of inverter is typified. In this paper ten carriers are used with a phase shift of 36° between two adjacent carrier signals for the 11-level cascade multilevel inverter and there is an 180° phase shift between the carrier-based gate triggered signals for upper and lower switch of cells of multilevel inverter as shown in Fig. 2. All switching combination for getting the 11-level output voltage for cascaded multilevel inverter of Fig. 1 is tabulated in Table 1.

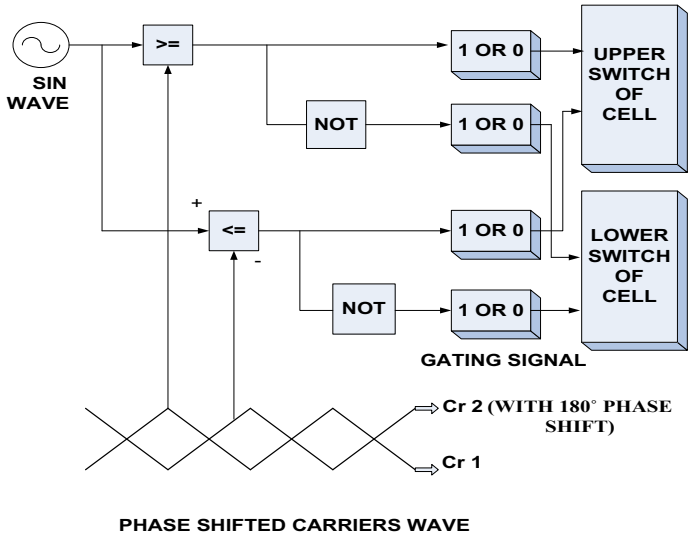

Fig. 2 Phase shifted modulation pattern

Table 1 Switching table for classical 11-level CHB

S. No.	Vo(t)	Switches in on state
1	5Vdc	S1, S2, S5, S6, S9, S10, S13, S14, S17, S18
2	4Vdc	S1, S2, S5, S6, S9, S10, S13, S14, S18, S20
3	3Vdc	S1, S2, S5, S6, S9, S10, S14, S16, S18, S20
4	2Vdc	S1, S2, S5, S6, S10, S12, S14, S16, S18, S20
5	Vdc	S1, S2, S6, S8, S10, S12, S14, S16, S18, S20
6	0	S1, S2, S6, S8, S10, S12, S14, S16, S18, S20
7	−Vdc	S3, S4, S6, S8, S10, S12, S14, S16, S18, S20
8	−2Vdc	S3, S4, S7, S8, S10, S12, S14, S16, S18, S20
9	−3Vdc	S3, S4, S7, S8, S11, S12, S14, S16, S18, S20
10	−4Vdc	S3, S4, S7, S8, S11, S12, S15, S16, S18, S20
11	−5Vdc	S3, S4, S7, S8, S11, S12, S15, S16, S19, S20

4 Modulated 11-Level CHB

The modified structure of 11-level multilevel inverter is shown in Fig. 4 in which ten semiconductor switches are used out of which six switches A, B, C, D, E, F are unidirectional while other four switches G, H, I, J are bidirectional. The entire model of this structure consists of two modules, each module contains two switches and two dc sources. In this paper the symmetrical configuration is used for modulated multilevel inverter in which magnitude of all the dc sources are equal [13]. Each module of this inverter is capable to produce three voltage levels as 0, Vdc and 2Vdc as shown in given Table 2 and the process of these voltage labels arrivals shown in Fig. 3b–d.

Number of voltage level produced by the modified topology of MI can be decided by the magnitude of external dc source as shown in Fig. 3. For N level of output voltage, the number of dc sources required is

$$\mathrm{m} = \frac{N-1}{2} \tag{4}$$

Table 2 Voltage levels of each module

Voltage level	S1	S2
2Vdc	1	0
Vdc	0	1
0	0	0

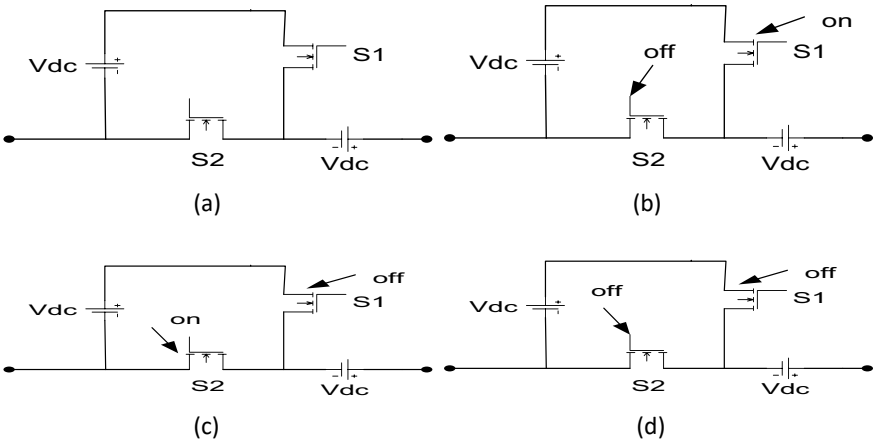

Fig. 3 **a** Module configuration **b** Equivalent circuit for the voltage 2Vdc **c** Equivalent circuit for the voltage Vdc **d** Equivalent circuit for the voltage 0

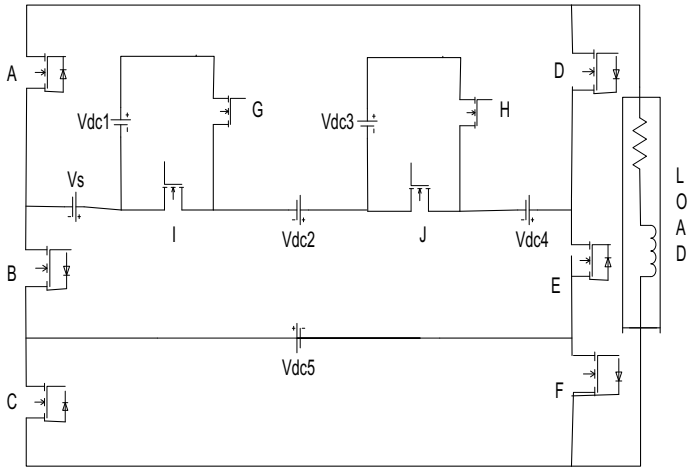

Fig. 4 Modulated 11-level CHB

where N is the number of output voltage levels. In this paper for 11-level of output voltage five dc sources are required because of which the value of Vs voltage source in the proposed topology is zero. The number of modules used with respect to count of dc source used is defined by the equation as

$$\mathrm{K} = \frac{m-1}{2} \tag{5}$$

where m typifies the dc sources used in proposed topology. The number of output voltage level with the maximum magnitude of output voltage and the magnitude of dc source are related with the equation as

$$\mathrm{N} = \frac{2\mathrm{Vo\ max}}{\mathrm{Vdc}} + 1 \tag{6}$$

Where Vo max is the maximum magnitude of output voltage and Vdc is the magnitude of each dc source. In this configuration, the polarity of voltage can be easily changed in both the direction by providing a suitable current path with the help of unidirectional switches A, B, C, D, E and F where D, E, F switches working in complimentary manner with respect to switches A, B and C respectively. In this paper the modulation strategy has been designed for the modulated model of 11-level CHB which is based upon the switching state for each voltage level as shown in Table 3 in which 0 indicates the off position of switch while 1 indicates on position of switch (Fig. 4).

Table 3 Switching table for modulated 11-level CHB

Vo	A	B	C	G	H	I	J	D	E	F
5Vdc	0	1	1	1	1	0	0	1	0	1
−5Vdc	1	0	1	1	1	0	0	0	1	0
4Vdc	0	1	0	0	1	1	0	1	0	1
−4Vdc	1	0	0	0	1	1	0	0	1	0
3Vdc	0	1	0	0	0	1	1	1	0	1
−3Vdc	1	0	0	0	0	1	1	0	1	0
2Vdc	0	1	0	0	0	1	1	1	0	0
−2Vdc	1	0	0	0	0	1	1	0	1	1
Vdc	1	1	0	0	0	0	0	0	0	1
−Vdc	0	0	0	0	0	0	0	1	1	0
0	0	1	0	1	1	0	0	0	1	0

5 Comparative Assessment Between Classical and Modified CHB

In this paper both the classical cascaded H bridge and modified topology of multilevel inverter have been compared on the basis of their advantages and limitations out of which the modularity in structure and reduced switch count number in the modified topology of MI for the same level of output voltage is a main consideration. The overall performance for both topologies of multilevel inverter can be evaluated on the basis of some desirable features that have to be always kept in mind such as their modularity in structure, harmonic performance, switch count number, dc source number and so on. In this paper all the comparisons are shown in Table 4 and also the comparative graphs for voltage stress and number of switches are also shown in Fig. 5.

Table 4 Comparative table between classical and modified CHB

Topology	Output voltage levels (N)	Switch count number	DC source required	Modularity	Configuration	Voltage harmonic content (%)
Classical CHB	11	20	5	Possible	Symmetrical or unsymmetrical	11.8
Modulated CHB	11	10	5	Possible	Symmetrical	18.7

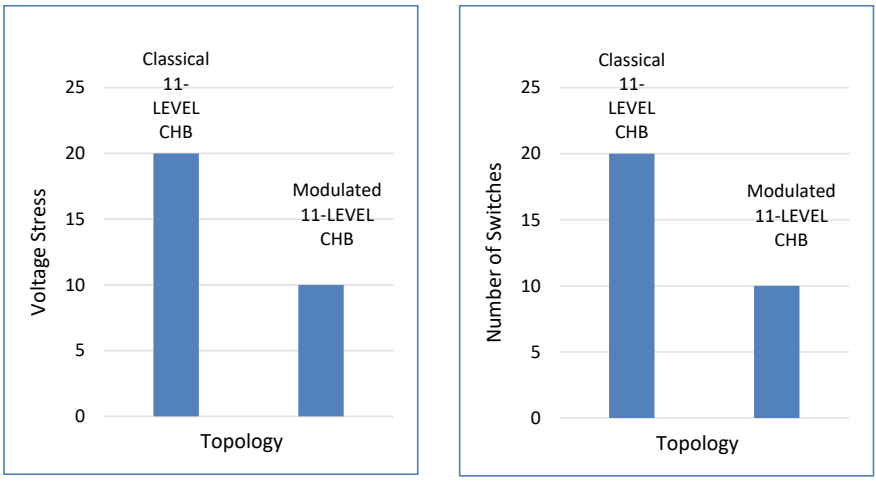

Fig. 5 Comparative graphs between classical 11-level CHB and modulated 11-level CHB

6 Simulation Result

To vindicate the effectiveness of modified topology of MI over the classical cascaded H bridge, the Simulink results are shown in Figs. 6 and 7 for modified and classical CHB respectively. The FFT analyses of these two topologies are also shown in Figs. 8 and 9 which shows its voltage harmonic content. Both topologies of modulated multilevel inverter and classical multilevel inverter are simulated for the same number of voltage level that is eleven in which the switching frequency and load parameters are also taken of same rating. Table 4 compares the modified and classical topologies of multilevel inverters based on switch count number and essential parameters, in addition to the simulation results.

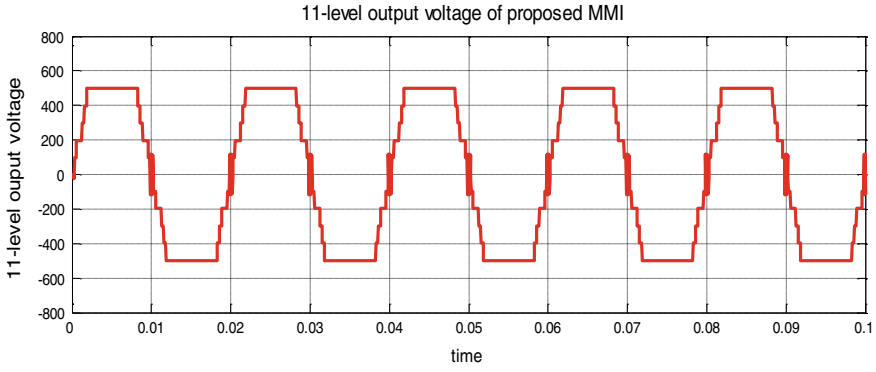

Fig. 6 Output voltage waveform of modulated 11-level CHB

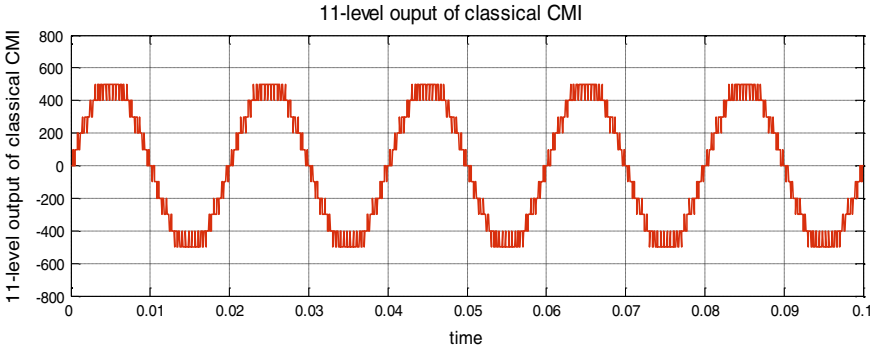

Fig. 7 Output voltage waveform of classical 11-level CHB

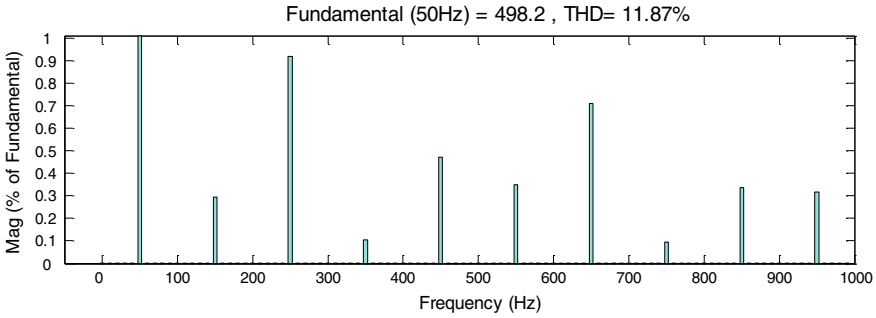

Fig. 8 THD spectra of classical 11-level CHB

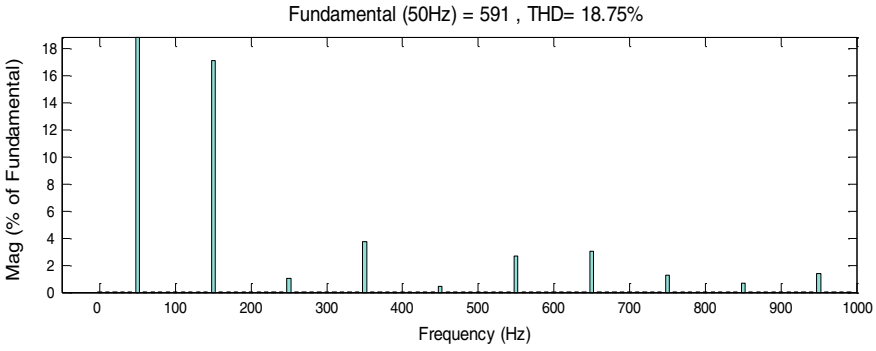

Fig. 9 THD spectra of modulated 11-level CHB

7 Conclusion

In this paper comparative assessment has been done between the modified topology of multilevel inverter and classical topology of CHB on the basis of switch count number, modularity in structure, harmonic performance for the same output voltage levels. The modified multilevel inverter topology decreases the switch count that is necessary to achieve output voltage of 11 levels thereby, the size and cost of the equipment reduced. In this paper the multicarrier PWM technique are used for classical topology of CHB and it is to be found that this technique is best suitable in terms of simplicity and harmonic performance. The switched output for the changed topology of the multilevel inverter is accomplished using a modulation strategy based on the switching states listed in Table 3. The whole comparison has been shown in Table 4 between two topologies. In future research, a range of more multilevel inverter topologies can be developed for industrial high-power applications where the number of switches, voltage level and stress can be given importance.

References

1. Gupta H, Yadav A, Maurya S (2016) Dynamic performance of cascade multilevel inverter based STATCOM. In: 2016 IEEE 1st international conference on power electronics, intelligent control and energy systems (ICPEICES), Delhi, India, pp 1–4. https://doi.org/10.1109/ICPEICES.2016.7853479
2. Lai J-S, Peng FZ (1996) Multilevel converters-a new breed of power converters. IEEE Trans Ind Appl 32(3):509–517. https://doi.org/10.1109/28.502161
3. Rodriguez J, Lai J-S, Peng FZ (2002) Multilevel inverters: a survey of topologies, controls, and applications. IEEE Trans Ind Electron 49(4):724–738.https://doi.org/10.1109/TIE.2002.801052
4. Dahidah MSA, Konstantinou G, Agelidis VG (2015) A review of multilevel selective harmonic elimination PWM: formulations, solving algorithms, implementation and applications. IEEE Trans Power Electron 30(8):4091–4106. https://doi.org/10.1109/TPEL.2014.2355226
5. McGrath BP, Holmes DG (2002) Multicarrier PWM strategies for multilevel inverters. IEEE Trans Ind Electron 49(4):858–867. https://doi.org/10.1109/TIE.2002.801073
6. Perez MA, Bernet S, Rodriguez J, Kouro S, Lizana R (2015) Circuit topologies, modeling, control schemes, and applications of modular multilevel converters. IEEE Trans Power Electron 30(1):4–17. https://doi.org/10.1109/TPEL.2014.2310127
7. Rohner S, Bernet S, Hiller M, Sommer R (2010) Modelling, simulation and analysis of a Modular Multilevel Converter for medium voltage applications. In: 2010 IEEE international conference on industrial technology, Via del Mar, Chile, pp 775–782. https://doi.org/10.1109/ICIT.2010.5472634
8. Rao BN, Suresh Y, Panda AK, Naik BS, Jammala V (2020) Development of cascaded multilevel inverter based active power filter with reduced transformers. CPSS Trans Power Electron Appl 5(2):147–157. https://doi.org/10.24295/CPSSTPEA.2020.00013
9. Dhanamjayulu C, Meikandasivam S (2018) Implementation and comparison of symmetric and asymmetric multilevel inverters for dynamic loads. IEEE Access 6:738–746. https://doi.org/10.1109/ACCESS.2017.2775203

10. Gupta H, Yadav A, Maurya S (2020) Multi carrier PWM for cascade topology of multilevel inverter. In: 2020 international conference on recent trends on electronics, information, communication & technology (RTEICT), Bangalore, India, pp 328–332. https://doi.org/10.1109/RTEICT49044.2020.9315586
11. Hasan MM, Abu-Siada A, Dahidah MSA (2018) A three-phase symmetrical DC-link multilevel inverter with reduced number of DC sources. IEEE Trans Power Electron 33(10):8331–8340. https://doi.org/10.1109/TPEL.2017.2780849
12. Goel V, Kumar J, Gambhir J (2015) Different multilevel inverter topologies with reduced number of devices. In: 2015 2nd international conference on recent advances in engineering & computational sciences (RAECS), pp 1–6. https://doi.org/10.1109/RAECS.2015.7453375
13. Ebrahimi J, Babaei E, Gharehpetian GB (2012) A new multilevel converter topology with reduced number of power electronic components. IEEE Trans Ind Electron 59(2):655–667. https://doi.org/10.1109/TIE.2011.2151813
14. Zaid MM, Ro J (2019) Switch ladder modified H-Bridge multilevel inverter with novel pulse width modulation technique. IEEE Access 7:102073–102086. https://doi.org/10.1109/ACCESS.2019.2930720
15. Lee SS, Sidorov M, Lim CS, Idris NRN, Heng YE (2018) Hybrid cascaded multilevel inverter (HCMLI) with improved symmetrical 4-level submodule. IEEE Trans Power Electron 33(2):932–935. https://doi.org/10.1109/TPEL.2017.2726087
16. Cho Y, LaBella T, Lai J, Senesky MK (2014) A carrier-based neutral voltage modulation strategy for multilevel cascaded inverters under unbalanced DC sources. IEEE Trans Ind Electron 61(2):625–636. https://doi.org/10.1109/TIE.2013.2254091
17. Napoles J, Leon JI, Franquelo LG, Portillo R, Aguirre MA (2009) Selective harmonic mitigation technique for multilevel cascaded H-bridge converters. In: 2009 35th annual conference of ieee industrial electronics, Porto, Portugal, pp 806–811. https://doi.org/10.1109/IECON.2009.5415023

Low Speed Performance Improvement of Dual VSI Fed Direct Torque Controlled Five Phase Open-End Winding Induction Motor

C. Venkata Subba Reddy and Swati Devabhaktuni

1 Introduction

With the great development of power electronic converters and modern Digital signal processors, interest on Multi-phase machines tremendously increased in the beginning of twenty-first century [1]. Multi-phase induction motors have many features when compared with conventional three phase induction motor such as reduced per phase current or per phase power without increase in per phase voltage, Higher torque density, lower Torque pulsations, high fault tolerant capability for loss of any one or more phases, Higher efficiency, reduced current ripples, reduced noise which makes drive reliable, compact and smooth operation [1]. Due to these additional features, multi-phase induction machine can be used in ship propulsion, space craft, and electric vehicles. Recently many researchers focused on implementation innovative advanced control methods such as direct torque control, flux-orientation control, predictive control for five leg voltage source inverter-fed five-phase induction motor, making drive performance faster and efficient [2, 3]. DTC of Induction Motor drive is implemented in the stationary reference frame ($\alpha - \beta$), and the advantages of DTC compared with FOC are less sensitivity to motor parameter variation, simplicity, better dynamic performance, easy implementation, and no complex coordinate transformation required makes preferred control technique in industrial Drive applications [2, 3]. However the Traditional DTC scheme suffers from the large torque ripples and variable switching frequency. DTC method implemented with hysteresis controller based torque and flux comparators with a lookup table for appropriate voltage vector selection of the inverter to control of stator flux and developed torque separately. Multi-phase inverter gives higher number voltage vectors,

C. V. S. Reddy (✉) · S. Devabhaktuni
Department of Electrical Engineering, National Institute of Technology, Warangal, India
e-mail: cvsreddy@student.nitw.ac.in

S. Devabhaktuni
e-mail: swatikjm@nitw.ac.in

S. Kumar et al. (eds.), *Recent Advances in Power Electronics and Drives*, Lecture Notes in Electrical Engineering 852, https://doi.org/10.1007/978-981-16-9239-0_20

which will facilitate finer torque and flux control in Direct Torque Controlled Induction motor. Nowadays, many research works are in progress for improvements in Direct Torque Control schemes in conventional Three Phase as well as multi-phase drives.

Nowadays, PTC became popular and competitive with DTC for improving dynamic performance. In PTC, the required switching voltage vector selection is based on evaluation of cost function. However, it has some limitations such as sensitive to model parameter change, more calculation time, require cost function weighting factor tuning [2, 4, 5]. The available literature on various Direct Torque Control schemes of multi-phase drives are as follows: In [6, 7], voltage space vector-based DTC is proposed, which require additional PI controllers and carrier based, maintains constant switching frequency; however, it does not guarantee stable operation under low speeds. In [8–12], Modified DTC schemes proposed to improve performance of 2-level inverter fed five phase induction motor drive, where mainly focused on xy components reduction, low speed performance improvement, and common mode voltage reduction. Normal 2-level multi-leg inverter generates higher THD voltages.

MLI topologies in multi-phase systems are implemented for improving the THD of voltage waveforms. Furthermore, DTC approach can be applied for multilevel VSI (MLI) fed multi-phase IM drives for precise flux and torque response in medium and high power applications. Recently in [13–15], various DTC schemes of 3-level neutral point clamped inverter (NPC) driven five phase Induction Motor are performed for torque ripple reduction and low speed performance improvement, where it requires clamping diodes and capacitor neutral point balancing issue is addressed. Also it is not feasible for going to beyond three-level by NPC, cascade H-bridge, flying capacitor topologies due to hardware complexity and cost for multi-phase drives. Apart from above investigated multi-level inverter topologies for multi-phase motor drive applications, the dual VSI configuration fed open-end winding five-phase induction motor (FP-OEWIM) attains important features. They are simple configuration, clamping diodes not required, and neutral point voltage balancing issues avoided. Multilevel inversion is possible with the usage of two independent dc voltage sources with different ratios in dual inverter configuration. Due to these features, dual-inverter configuration fed FP-OEWIM attains important role in the field of multilevel inverter topologies of electrical drives. Many researchers focused on dual inverter fed three phase open end winding induction motor (TP-OEWIM), where TP-OEWIM excited from two isolated DC sources. And very few researchers recently focused on multi-phase Open end winding induction motor drives are as follows: In [16], FP-OEWIM drive with dual inverters configuration with isolated dc link voltage sources is discussed, where the SVM-DTC method is applied which suffers from above stated issues same as DTC-SVM control of normal multi-phase machine. In [17], A Modified DTC is implemented for OEWIM, which uses 20 adjacent and non-adjacent voltage vectors for eliminating common mode voltage and suffers from higher torque ripples; demagnetization under low speed and small xy components appears. In [18], Hysteresis band based DTC implemented for OEWIM, which uses 10 virtual non-adjacent voltage vectors and improves the DC bus utilization, xy components zero,

CMV elimination and suffers from high torque ripple and demagnetization under low speed region.

This paper concentrates on three-level dual voltage source Inverter fed FP-OEWIM drive using the modified DTC scheme. The major objectives of this paper are to suppress higher torque ripples under low speed operation, and avoiding flux demagnetizing problem at zero/low speed due frequent selection of zero vectors in dual-inverter fed FP-OEWIM drive. The conventional method of DTC generates higher torque ripple under low speed operation in dual-inverter fed FP-OEWIM drive due to selection of large voltage vectors. Besides this, flux demagnetization occurs under zero speed condition for conventional method [17, 18]. All these above stated problems in conventional Direct Torque Control of FP-OEWIM are overcome in the proposed DTC technique with modified lookup table. This paper configured as follows: In Sect. 2, Mathematical modelling of dual inverter fed FP-OEWIM; in Sect. 3, theoretical analysis and method of implementation of Proposed DTC method for five-phase OEWIM; in Sect. 4, comparative analysis of Proposed DTC with Conventional DTC method along with simulation results; Sect. 5 discusses about conclusions.

2 Mathematical Modelling of Dual VSI Fed Five Phase OEW Induction Motor

The 3-level dual inverter configuration of five phase open end winding induction motor (FP-OEWIM) can be modelled mathematically with 1:1 DC link voltage ($V_{dc}/2$) by using individual pole voltages as shown below.

Each inverter pole voltages of dual inverter fed FP-OEWIM are expressed by (1) and (2) as given below

$$\begin{pmatrix} V_{a0} \\ V_{b0} \\ V_{c0} \\ V_{d0} \\ V_{e0} \end{pmatrix} = \begin{pmatrix} S_a^+ \\ S_b^+ \\ S_c^+ \\ S_d^+ \\ S_e^+ \end{pmatrix} * \frac{V_{dc}}{2} \tag{1}$$

$$\begin{pmatrix} V_{a'0} \\ V_{b'0} \\ V_{c'0} \\ V_{d'0} \\ V_{e'0} \end{pmatrix} = \begin{pmatrix} S_{a'}^+ \\ S_{b'}^+ \\ S_{c'}^+ \\ S_{d'}^+ \\ S_{e'}^+ \end{pmatrix} * \frac{V_{dc}}{2} \tag{2}$$

where S_a^+, S_b^+ …. and $S_{a'}^+$, $S_{b'}^+$…. are upper switches of inverter 1 and 2 legs of dual inverter.

The resultant pole voltage of dual inverter configuration exhibits three-level and can be represented by (3) as shown below

$$\begin{pmatrix} \Delta V_{aa'} \\ \Delta V_{bb'} \\ \Delta V_{cc'} \\ \Delta V_{dd'} \\ \Delta V_{ee'} \end{pmatrix} = \begin{pmatrix} V_{a0} - V_{a'0} \\ V_{b0} - V_{b'0} \\ V_{c0} - V_{c'0} \\ V_{d0} - V_{d'0} \\ V_{e0} - V_{e'0} \end{pmatrix} \tag{3}$$

The common mode voltage (CMV) and phase voltage of dual inverter configuration can be obtained from (1), (2), (3) and shown by (4) and (5) as below.

$$V_{cm} = \frac{1}{5} * (\Delta V_{aa'} + \Delta V_{bb'} \Delta V_{cc'} + \Delta V_{dd'} + \Delta V_{ee'}) \tag{4}$$

$$\begin{pmatrix} V_{aa'} \\ V_{bb'} \\ V_{cc'} \\ V_{dd'} \\ V_{ee'} \end{pmatrix} = \begin{pmatrix} \Delta V_{aa'} \\ \Delta V_{bb'} \\ \Delta V_{cc'} \\ \Delta V_{dd'} \\ \Delta V_{ee'} \end{pmatrix} - (V_{cm}) \tag{5}$$

Time varying mutual inductances in motor torque and voltage equations makes induction motor dynamic behavior analysis complex. For simple analysis, five phase induction motor is modelled as two-phase machine by transforming five phase quantities to two phase quantities [19]

The block diagram representation of Direct Torque Controlled (DTC) dual inverter fed FP-OEWIM is shown in Fig. 1, which contains 5-ph OEWIM, two 2-level inverters, speed sensor, torque and flux estimation block, torque and flux hysteresis controllers.

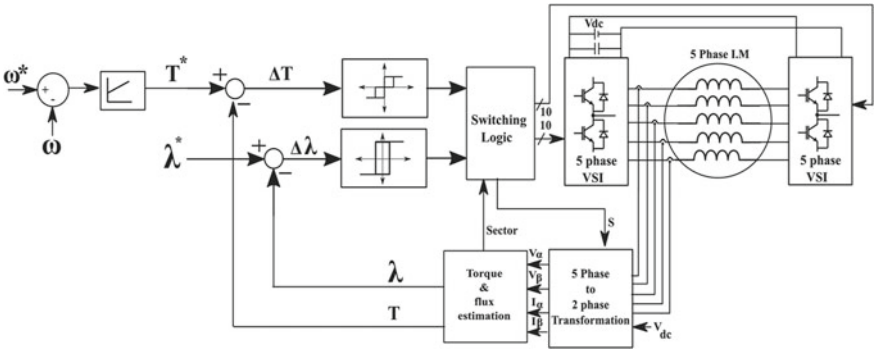

Fig. 1 Schematic diagram of DTC controlled dual inverter fed 5-ph open end winding induction motor

The dynamic behavior of induction motor can be observed by dynamic modelling of five phase induction which can be done by following equations under stationary reference frame. Electrical quantities represented in space vector form.

Stator voltage equations in space vector form fixed reference frame are:

$$V_s = R_s I_s + \frac{d}{dt}\varphi_s \tag{6}$$

Rotor voltage equations:

$$0 = R_s I_r + \frac{d}{dt}\varphi_r - \omega_r \varphi_r \tag{7}$$

By using above voltage equations stator flux linkages are found as follows:

$$\varphi_s = \int (V_s - I_s R_s) dt \tag{8}$$

Flux linkages of stator conductors and rotor conductors can be written as

$$\varphi_s = L_s i_s + L_m i_r \tag{9}$$

$$\varphi_r = L_r i_r + L_m i_s \tag{10}$$

Electromagnetic torque developed in two axis machine stationary reference frame can be written as

$$T_e = \frac{5}{2}\frac{P}{2} imag(\varphi_s * I_s) \tag{11}$$

From machine mechanical dynamics, torque balancing equation can be written as

$$T_e = T_l + j\frac{d\omega_r}{dt}$$

And

$$\omega_r = \int \frac{T_e - T_l}{J} dt \tag{12}$$

where

p—no. of poles of machine
J—Moment of inertia
T_l—Load torque
T_e—developed Torque
ω_r—Rotor mechanical speed.

Five phase induction can be modeled by using Eqs. (6)–(12) in stationary reference frame.

3 Proposed DTC Operation for Dual Inverter Configuration

The DTC schematic block diagram for 3-level dual VSI fed FP-OEWIM is shown in Fig. 1. The speed of the motor is compared with set speed, and the speed error is processed passed through speed PI controller, which gives the ref. torque command (Tm*). The actual electromagnetic torque (Tm) and flux (Ψs) are estimated from motor voltages and currents as in Eqs. (8)–(11). Estimated torque compared with commanded torque and estimated flux compared with reference flux (Ψ*s). Based on Torque error, flux error and stator flux sector information appropriate switching vector is selected from lookup table through five level torque and two level flux hysteresis controllers. In DTC, Switching states directly influences the stator flux and torque.

The effective voltage space vector V_s of dual inverter configuration can expressed from voltage space vectors V_{s1}, V_{s2} of individual VSIs as in (13), which are represented in αβ plane in stationary reference frame. Null voltage vectors are obtained during inv1 and inv2 have same switching states or all upper or lower switches of either inverter ON simultaneously.

$$V_{s1} = \frac{2}{5}\left(\frac{V_{dc}}{2}\right)\left(S_a^+ + S_b^+ e^{-\frac{i2\pi}{5}} + S_c^+ e^{-\frac{i4\pi}{5}} + S_d^+ e^{-\frac{i6\pi}{5}} + S_e^+ e^{-\frac{i8\pi}{5}}\right)$$

$$V_{s2} = \frac{2}{5}\left(\frac{V_{dc}}{2}\right)\left(S_{a'}^+ + S_{b'}^+ e^{-\frac{i2\pi}{5}} + S_{c'}^+ e^{-\frac{i4\pi}{5}} + S_{d'}^+ e^{-\frac{i6\pi}{5}} + S_{e'}^+ e^{-\frac{i8\pi}{5}}\right)$$

$$V_s = V_{s1} - V_{s2} \tag{13}$$

The 5-leg 2-level VSI consists of fundamental plane (αβ) and harmonic x–y plane. Fundamental plane consist torque producing components whereas x–y plane consists of harmonic components which are not responsible for torque production. A 2-level VSI consists of 32 switching vectors with 30 active voltage vectors and 2 zero voltage vectors and categorized as large voltage vectors (10), medium voltage vectors (10) and small vectors (10). The large voltage vectors in αβ-plane are appeared as to small voltage vectors in xy harmonic plane or vice versa with opposite direction. Medium voltage vectors in αβ plane mapped as medium vectors in xy harmonic plane.

For proposed dual inverter configuration, fundamental space vector plane αβ is divided as 20 sectors, with 18° angle span. Dual inverter configuration generates 40 active space vectors and two null voltage vectors which are obtained from *inv*1 and *inv*2 large vector switching states which gives small xy components as shown in

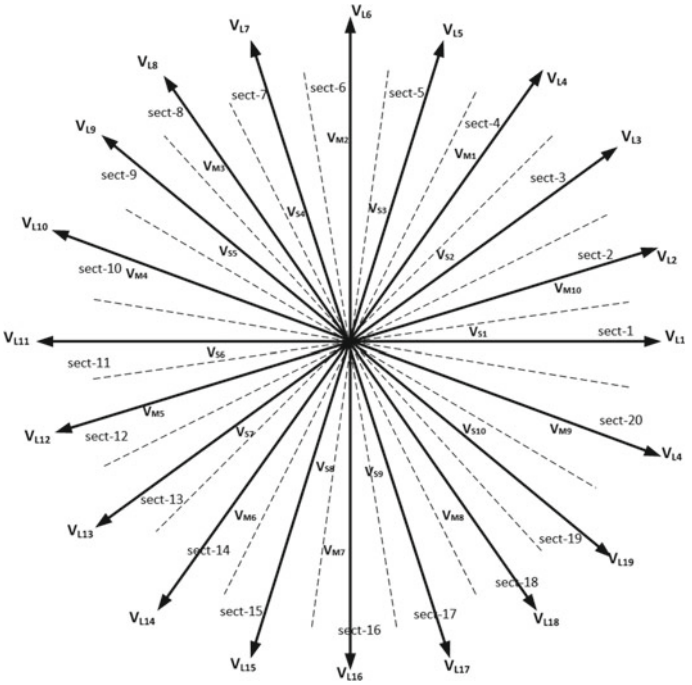

Fig. 2 Switching voltage vector diagram of dual inverter in αβ plane

Fig. 2 and are divided into four groups as: Large vectors (20), Medium vectors (10), small vectors (10) and Null voltage vectors (2) as follows.

Small voltage vector (10) is

$$\begin{aligned} V_{s1} &= V_{3inv1} - V_{4inv2} = 0.647V_{dc}\angle 2\pi/5 - 0.647V_{dc}\angle(3\pi/5) \\ &= 0.618V_{dc}\angle(0) \end{aligned} \tag{14}$$

Medium voltage vectors (10) is

$$\begin{aligned} V_{m1} &= V_{1inv1} - V_{9inv2} = 0.647V_{dc}\angle 0 - 0.647V_{dc}\angle(9\pi/5) \\ &= 0.757V_{dc}\angle(3\pi/10) \end{aligned} \tag{15}$$

Large voltage vector (10 + 10)

$$\begin{aligned} V_{l1} &= V_{1inv1} - V_{6inv2} = 0.647V_{dc}\angle 0 - 0.647V_{dc}\angle(\pi) \\ &= 1.29V_{dc}\angle 0 \\ V_{l2} &= V_{1inv1} - V_{7inv2} = 0.647V_{dc}\angle 0 - 0.647V_{dc}\angle(6\pi/5) \\ &= 1.23V_{dc}\angle(\pi/10) \end{aligned} \tag{16}$$

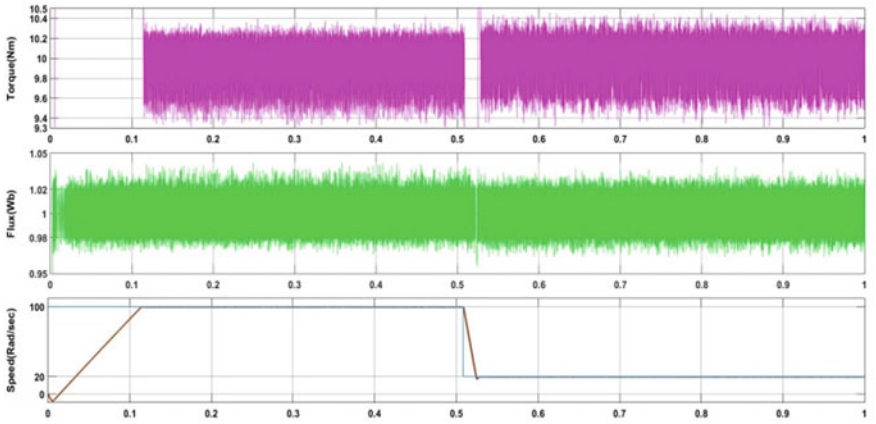

Fig. 3 Torque, flux, speed response under high speed (100 rad/sec) and low speed (20 rad/sec) for conventional method

Conventional DTC [17, 18] uses only 10 medium and 10 large vectors along with null voltage vectors as in Fig. 3 for all possible speed as shown which causes higher torque ripples and flux instability at lower/zero speeds under flux error +1 and torque error 0. In conventional DTC, under flux error +1 and torque error 0, null voltage vectors applied for long duration which causes flux drooping. But really it needs increased stator flux under flux error +1 and consequently flux becomes unstable especially under low speed. Whereas in case of high speed operation application of null vectors are acceptable under flux error +1 and torque error 0 and flux is maintained as constant due to short interval of null vectors.

In proposed lookup table based DTC, more no. of voltage vectors generated which facilitates finer torque and flux variation. Use of small voltage vectors under low speed or zero speed gives lower torque ripple. Modified lookup table uses large and medium vectors for higher speeds along with null voltage vectors shown in Table 1 unshaded form and uses small vectors for small speeds as shown in Table 1. Flux instability or flux drooping problem under low speeds overcome by replacing null vectors with small vectors which gives higher flux component which really needed and little influence on torque component under flux error +1 and torque error 0 which are shown in modified lookup Table 1 with shaded format. In sector 1, for case $d\Psi = +1$ and $dT = 0$ condition small vector S_2 selected which have large flux component and little torque component. Similarly small voltage vectors selected for other sectors under $d\Psi = 1$, $dT = 0$.

Table 1 Proposed DTC lookup table (unshaded-high speed, shaded-low speed)

dΨ	dT	Sector																			
		1	2	3	4	5	6	7	8	9	10	11	12	13	14	15	16	17	18	19	20
1	2	L4	L5	L6	L7	L8	L9	L10	L11	L12	L13	L14	L15	L16	L17	L18	L19	L20	L1	L2	L3
	1	S3	S3	S4	S4	S5	S5	S6	S6	S7	S7	S8	S8	S9	S9	S10	S10	S1	S1	S2	S2
	1	M1	M2	M2	M3	M3	M4	M4	M5	M5	M6	M6	M7	M7	M8	M8	M9	M9	M10	M10	M1
		S2	S2	S3	S3	S4	S4	S5	S5	S6	S6	S7	S7	S8	S8	S9	S9	S10	S10	S1	S1
	0	Null																			
	2	S2	S2	S3	S3	S4	S4	S5	S5	S6	S6	S7	S7	S8	S8	S9	S9	S10	S10	S1	S1
	-1	M8	M9	M9	M10	M10	M1	M1	M2	M2	M3	M3	M4	M4	M5	M5	M6	M6	M7	M8	M8
	0	S10	S10	S1	S1	S2	S2	S3	S3	S4	S4	S5	S5	S6	S6	S7	S7	S8	S8	S9	S9
	-	L18	L19	L20	L1	L2	L3	L4	L5	L6	L7	L8	L9	L10	L11	L12	L13	L14	L15	L16	L17
	-2	S9	S9	S10	S10	S1	S1	S2	S2	S3	S3	S4	S4	S5	S5	S6	S6	S7	S7	S8	S8
	2	L8	L9	L10	L11	L12	L13	L14	L15	L16	L17	L18	L19	L20	L1	L2	L3	L4	L5	L6	L7
		S4	S4	S5	S5	S6	S6	S7	S7	S8	S8	S9	S9	S10	S10	S1	S1	S2	S2	S3	S3
	1	M3	M3	M4	M4	M5	M5	M6	M6	M7	M7	M8	M8	M9	M9	M10	M10	M1	M1	M2	M2
		S5	S5	S6	S6	S7	S7	S8	S8	S9	S9	S10	S10	S1	S1	S2	S2	S3	S3	S4	S4
	0	Null																			
		Null																			
	-1	M6	M6	M7	M7	M8	M8	M9	M9	M10	M10	M1	M1	M2	M2	M3	M3	M4	M4	M5	M5
		S7	S7	S8	S8	S9	S9	S10	S10	S1	S1	S2	S2	S3	S3	S4	S4	S5	S5	S6	S6
	-2	L14	L15	L16	L17	L18	L19	L20	L1	L2	L3	L4	L5	L6	L7	L8	L9	L10	L11	L12	L13
		S8	S9	S9	S10	S10	S1	S1	S2	S2	S3	S3	S4	S4	S5	S5	S6	S6	S7	S7	S8

4 Results and Discussion

The Dual inverter fed FP-OEWIM drive operation with proposed lookup table DTC method is verified through MATLAB/Simulink software. Results obtained in the proposed method are compared with conventional DTC approaches [17, 18]. All the Direct Torque control methods are developed with same sampling frequency with same torque and flux hysteresis bands for comparison purpose. The 5-level torque and 2-level flux hysteresis bands are set at 0.2Nm and 0.02Wb for comparing both proposed and conventional DTC methods. The 5-ph induction motor speeds below 20 rad/sec is treated as low speed and above that treated as high speed. The simulated results for conventional method [17] and proposed method are shown in below figures and discussed for comparison (Table 3).

4.1 Simulation Results

For the 5-ph induction motor set speeds of 100 rad/sec and 20 rad/sec, steady-state speed, torque, and flux responses for conventional method [17] are given in Fig. 3 under low speed and high speed conditions. Similarly, speed, torque, flux responses for the same reference speeds of 100 rad/sec and 20 rad/sec of a proposed DTC schemes shown in Fig. 4. From Figs. 3 and 4, it can be concluded that proposed DTC scheme produces appreciable torque ripple reduction under low speed with small

Table 2 Five-Ph induction motor parameters

5-Ph OEW induction motor parameters	
Stator resistance (Rs)	6.03 Ω
Stator inductance (Ls)	0.4893 H
Rotor resistance (Rr)	6.085 Ω
Rotor inductance (Lr)	0.4893 H
Mutual inductance (Lm)	0.45 H
No. of poles (P)	4
Rated speed	1440 rpm
Inertia constant (J)	0.0048
Inverter DC voltage (Vdc/2)	

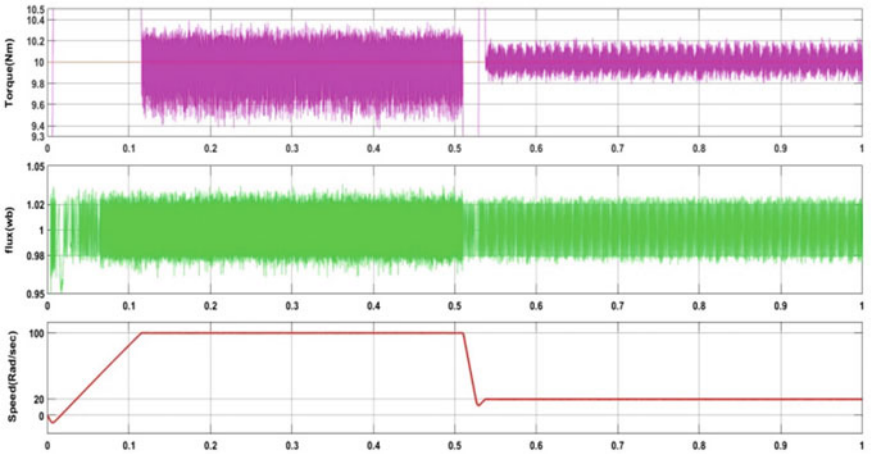

Fig. 4 Torque, flux, speed response under high speed (100 rad/sec) and low speed (20 rad/sec) for proposed DTC method

decrement flux ripples due to selection of small voltage vectors when compared with conventional DTC method.

Figures 5 and 6 show the switching pattern of S_a switch of inv1 and inv2 for both conventional and proposed DTC, which concludes that proposed DTC scheme gives lower switching frequency operation under low speeds when compared with conventional method even though switching frequency almost same for higher speed operation which facilitates greater reduction in switching losses under low speed operation. Switching loss reduction occurs due to avoiding of frequent zero switching under lower speed operation with replacement of small voltage vectors.

Figures 7 and 8 show the phase current of convention DTC and Proposed DTC schemes under high speed and low speed conditions. It can observe that current waveforms almost similar for both conventional and proposed methods under high

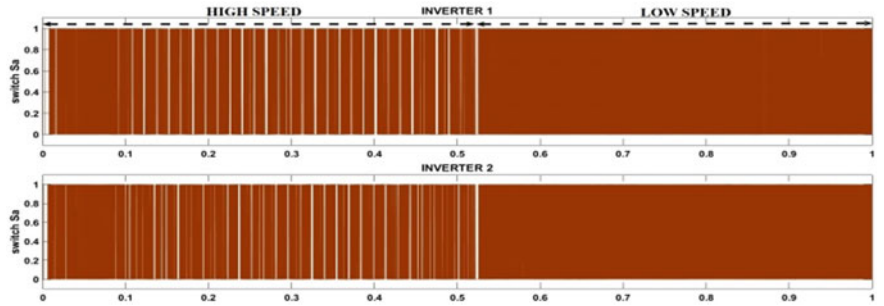

Fig. 5 Switching of S_a of inverter 1 and 2 under high speed and low speed for conventional DTC method

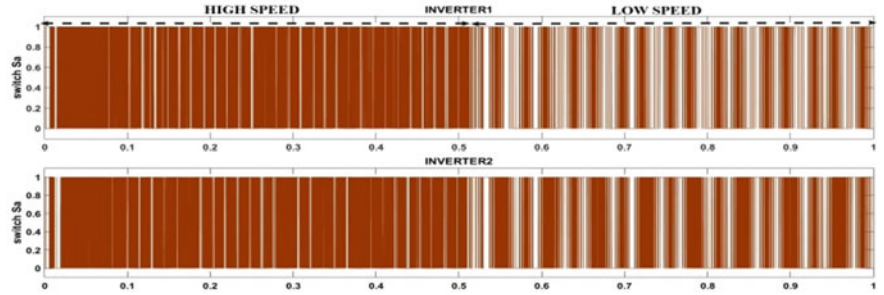

Fig. 6 Switching of S_a of inverter 1 and 2 under high speed and low speed for proposed DTC method

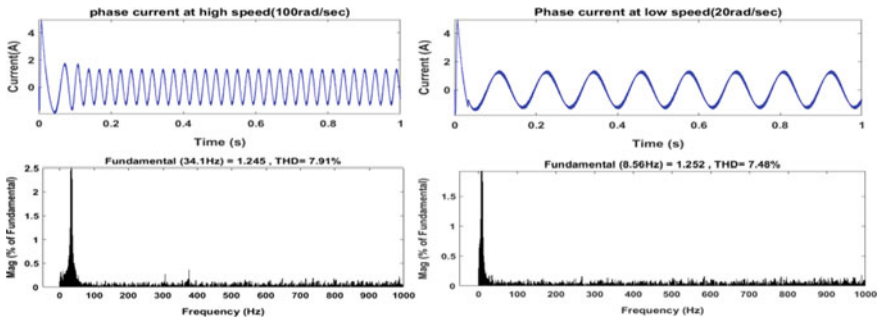

Fig. 7 Current response under high speed and low for conventional DTC method

speeds, but with little THD improvement of current under low speed operation of proposed DTC.

Figure 9 shows the developed torque, stator flux, speed response of conventional method of DTC under low/zero speed under no load condition. From Fig. 9 flux instability occurs at zero speed i.e. unable to maintain rated flux due to frequent

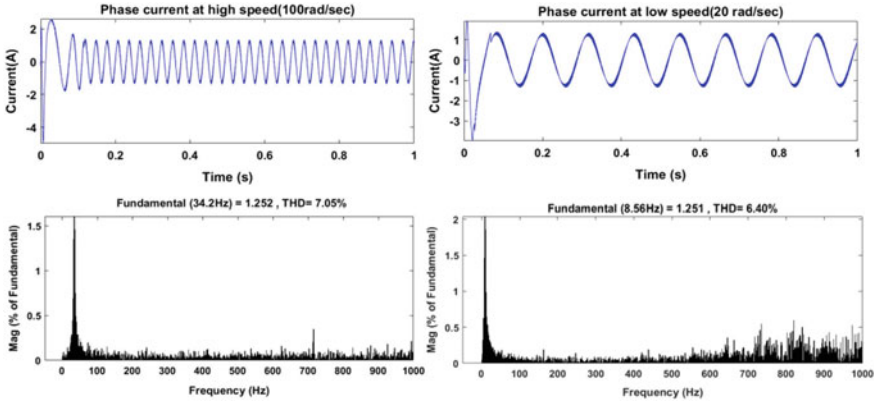

Fig. 8 Current response under high speed and low for Proposed DTC method

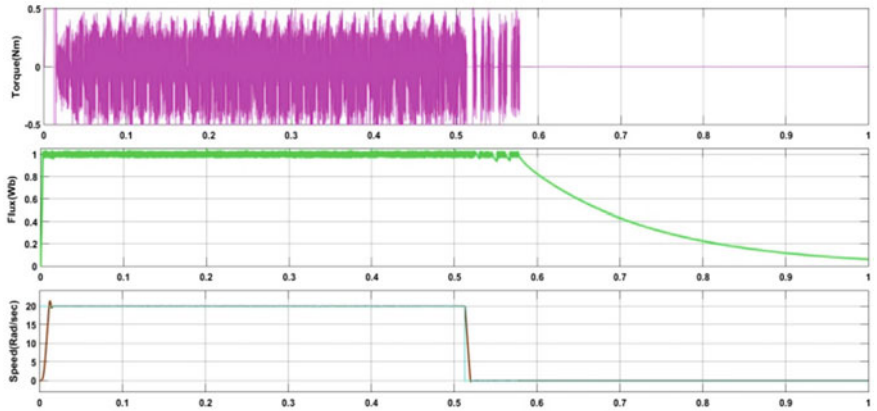

Fig. 9 Torque, flux, speed response under low speeds (20 rad/sec, 0 rad/sec) for conventional DTC method

selection of zero voltage vectors and after some time no active vectors switched on and becomes zero flux.

Figure 10 shows the torque, speed and flux response under low speed operating conditions. From Fig. 10, this can be stated that rated flux maintained i.e. demagnetization problem eliminated under zero speed with no load due to selection small voltage vectors in place of zero vectors. Torque ripples also less under low speed operation due to selection small vectors.

Finally, from Table 3 it can be stated that the overall changes to conventional lookup table in the proposed DTC scheme results in improvement of torque response, switching frequency reduction, elimination of demagnetizing effect under low speed, improvement of current THD under low speed operation.

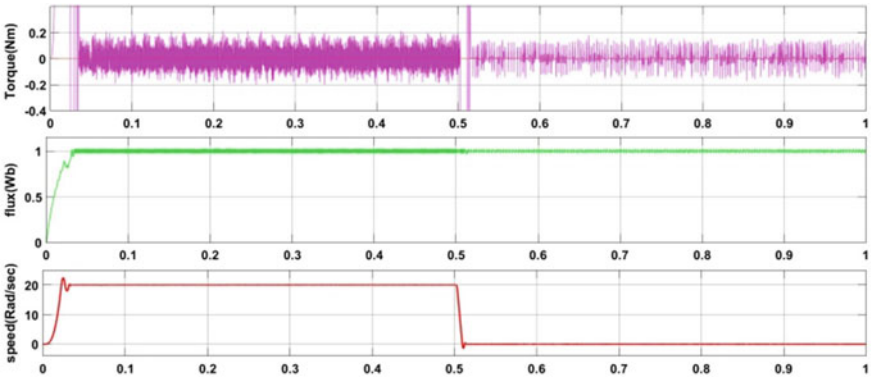

Fig. 10 Torque, flux, speed response under low speeds (20 rad/sec, 0 rad/sec) for proposed DTC method

Table 3 Results comparison table

	Conv method	Proposed method	Conv method	Proposed method	Conv method	Proposed method
	Torque ripple (p-p)		Switching frequency		Current %THD	
High speeds (100 rad/sec)	8%	6%	3.26 kHz	3.16 kHz	7.91	7.05
Low speeds (20 rad/sec)	8%	3.5%	5 kHz	2.2 kHz	7.48	6.4

5 Conclusions

The proposed DTC scheme which uses 40 active vectors with modified lookup table improves drive performance under low speed operation with dual inverter model. Modified lookup tables for both high and low speeds gives following benefits under low speed operation: torque ripple reduction under both high and low speeds particularly at low speeds, low switching frequency under low speed over conventional method, stable flux operation possible under zero/low speeds under no load, less current THD under low speed. Hence it is suggested that proposed DTC scheme exhibits better performance results for dual inverter fed OEWIM under low speed operations without degrading high speed performance. These benefits in proposed DTC scheme verified with MATLAB/Simulink software.

References

1. Levi E, Bojoi R, Profumo F, Toliyat HA, Williamson S (2007) Multiphase induction motor drives—a technology status review. IET Electr Power Appl 1(4):489–516

2. Wang F, Zhang Z, Mei X, Rodriguez J, Kennel R (2018) Advanced control strategies of induction machine: field oriented control, direct torque control and model predictive control.Energies 11.https://doi.org/10.3390/en11010120
3. Abu-Rub H, Iqbal A, Guzinski J (2021) High performance control of AC drives with Matlab/Simulink models (pp 298–356)
4. Riveros J, Prieto Corvalán J, Barrero F, Toral SL, Levi E (2010) Predictive torque control for five-phase induction motor drives. In: IECON proceedings (Industrial Electronics Conference), pp 2467–2472.https://doi.org/10.1109/IECON.2010.5675341
5. Bhowate A, Aware MV, Sharma S (2020) Predictive torque control algorithm for a five-phase induction motor drive for reduced torque ripple with switching frequency control. IEEE Trans Power Electron 35(7):7282–7294. https://doi.org/10.1109/TPEL.2019.2954991
6. Lai Y-S, Chen J-H (2001) A new approach to direct torque control of induction motor drives for constant inverter switching frequency and torque ripple reduction. IEEE Trans Energy Convers 16(3):220–227. https://doi.org/10.1109/60.937200
7. Mahanta U, Patnaik D, Panigrahi B, Panda A (2015) Dynamic modeling and simulation of switching table based DTC of five phase induction motor. 1–6. https://doi.org/10.1109/EESCO.2015.7253740
8. Khaldi BS, Abu-Rub H, Iqbal A, Kennel R, Mahmoudi MO, Boukhetala D (2011) Sensorless direct torque control of five-phase induction motor drives. In: IECON 2011 - 37th annual conference of the IEEE industrial electronics society, Melbourne, VIC, pp 3501–3506. https://doi.org/10.1109/IECON.2011.6119875
9. Zheng L, Fletcher JE, Williams BW, He X (2011) A novel direct torque control scheme for a sensorless five-phase induction motor drive. IEEE Trans Ind Electron 58(2):503–513. https://doi.org/10.1109/TIE.2010.2047830
10. Gao L, Fletcher JE, Zheng L (2011) Low-speed control improvements for a two-level five-phase inverter-fed induction machine using classic direct torque control. IEEE Trans Ind Electron 58(7):2744–2754. https://doi.org/10.1109/TIE.2010.2070775
11. Riveros JA, Durán MJ, Barrero F, Toral S (2012) Direct torque control for five-phase induction motor drives with reduced common-mode voltage. In: IECON 2012 - 38th annual conference on IEEE industrial electronics society, Montreal, QC, pp 3616–3621. https://doi.org/10.1109/IECON.2012.6389317
12. Payami S, Behera RK (2017) An improved DTC technique for low-speed operation of a five-phase induction motor. IEEE Trans Ind Electron 64(5):3513–3523. https://doi.org/10.1109/TIE.2017.2652397
13. Tatte YN, Aware MV (2015) Torque ripple minimization in five-phase three-level inverter fed direct torque control induction motor drive. In: 2015 17th European conference on power electronics and applications (EPE'15 ECCE-Europe), Geneva, pp 1–6. https://doi.org/10.1109/EPE.2015.7309400
14. Tatte YN, Aware MV (2017) Direct torque control of five-phase induction motor with common-mode voltage and current harmonics reduction. IEEE Trans Power Electron 32(11):8644–8654. https://doi.org/10.1109/TPEL.2016.2644988
15. Chikondra B, Muduli UR, Behera RK (2020) Performance comparison of five-phase three-level NPC to five-phase two-level VSI. IEEE Trans Ind Appl 56(4):3767–3775. https://doi.org/10.1109/TIA.2020.2988014
16. Karampuri R, Jain S, Somasekhar VT (2016) Phase displaced SVPWM technique for five-phase open-end winding induction motor drive. In: 2016 IEEE students' conference on electrical, electronics and computer science (SCEECS), Bhopal, pp 1–6. https://doi.org/10.1109/SCEECS.2016.7509283
17. Mavila PC, Rajeevan PP (2019) A five level DTC scheme for dual inverter-fed five phase open-end winding induction motor drives with single DC source. In: 2019 IEEE industry applications society annual meeting, Baltimore, MD, USA, pp 1–6. https://doi.org/10.1109/IAS.2019.8912445

18. Mavila PC, Rajeevan PP (2020) A new direct torque control scheme for five phase open-end winding induction motor drives with reduced DC voltage requirement. In: 2020 IEEE international conference on power electronics, smart grid and renewable energy (PESGRE2020), Cochin, India, p 16. https://doi.org/10.1109/PESGRE45664.2020.9070665
19. Levi E (2008) Multiphase electric machines for variable-speed applications. IEEE Trans Ind Electron 55(5):1893–1909

Self-balanced Symmetric Source Configuration of Nine Level Switched Capacitor-Based Grid Connected Inverter with LCL Filter

Aratipamula Bhanuchandar and Bhagwan K. Murthy

1 Introduction

In DC to AC power conversion applications, Multilevel Inverters (MLIs) play a very important role to generate staircase waveform with imitation of sine wave [1]. As compared with traditional two level inverters, MLIs give curtailed voltage stress, less electromagnetic interference, higher efficiency, small size filters and less Total Harmonic Distortion (THD) [2]. Mainly there are three conventional MLI topologies are available in the literature, viz., Neutral Point Clamped (NPC) [3], Flying Capacitor (FC) [4] and Cascaded H-Bridge (CHB) [5]. In these, CHB MLI has higher modularity but requires more number of isolated DC sources [6]. For generating 9-level output, the aforementioned topologies take more number of switches, gate driver circuits and protection circuits. To curtail the voluminous of above conventional topologies, Reduced Device Count (RDC) MLIs have been reported in [7]. In RDC MLI topologies, one of the popular topologies is Multilevel DC Link Inverter (MLDCL) topology and for generating nine level output, it takes 12 switches, 3 DC sources and separate backend H-Bridge is required [8]. The nine level [9] MLI has the disadvantages like control uncertainty and diversity of voltage factors have been rapidly increasing because of high switching frequency devices. For generating nine level output, the topology [10] requires 4 DC sources, ten switches and TSV/TBV of 16.5Vdc. In [11], the topology comprises 2 DC sources, 12 switches, 3 capacitors and TSV of 14Vdc have been reported. Similarly, the topologies [12, 13] take more standing voltage for generating nine level output. Generally, TSV is the one of the key parameters to analyze the cost requirement of devices.

To alleviate aforementioned problems, a new nine level symmetric source (1:1) configuration of grid connected MLI topology has been introduced with less per unit TSV. By taking asymmetric source configuration (1:2 and 1:3) that is binary and trinary modes, it is possible to generate 13 level and 17 levels, respectively. Generally,

A. Bhanuchandar (✉) · B. K. Murthy
Electrical Engineering Department, NIT Warangal, Warangal, Telangana, India

S. Kumar et al. (eds.), *Recent Advances in Power Electronics and Drives*, Lecture Notes in Electrical Engineering 852, https://doi.org/10.1007/978-981-16-9239-0_21

for any MLI topology, the PWM technique has been placed a very important role for making self-balancing of capacitors and to generate the required level output. For 1:1, 1:2 and 1:3 source configurations with RL load, the modified version of Nearest Level Control (NLC) technique [14, 16] that is URCS has been applied for getting required level output. In grid connection, a ULSPD-PWM scheme has been applied for making successful operation of an inverter.

The rest of the work is summarized as follows: The operation and control schemes of the proposed topology have been presented in Sect. 2. In Sect. 3, the comparative study has been described. Section 4 gives the simulation results for both RL load and grid connected cases. Finally, the conclusion has been presented in Sect. 5.

2 Operation of Proposed Topology and Control Schemes

A. *Operation of Proposed Inverter Topology with LCL filter*

The schematic of RSC inverter topology with LCL filter is depicted in Fig. 1. It comprises 2 DC sources, 2 Switched capacitors and 10 unidirectional switches. For generating 9 levels, 13 levels and 17 levels, the 1:1 (symmetric), 1:2 (binary) and 1:3 (trinary) source configurations have been considered respectively. And the operation of respective switching arrangements for all configurations has been depicted in Tables 1, 2 and 3, respectively. For 1:1, 1:2 and 1:3 source configurations, the voltage peak values have been obtained as 2Vdc, 3Vdc and 4Vdc, respectively. In this paper, for grid connection, the symmetric source configuration has been considered. The

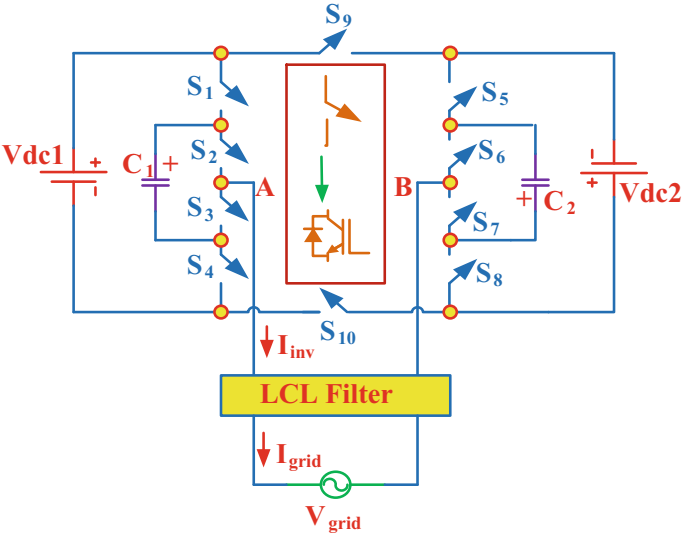

Fig. 1 Proposed RSC inverter topology with LCL filter

Table 1 Switching arrangement-1:1 source configuration (9-level)

State	S_1	S_2	S_3	S_4	S_5	S_6	S_7	S_8	S_9	S_{10}	C_1	C_2
$2V_{DC}$	1	1	0	0	1	1	0	0	0	1	–	–
$1.5V_{DC}$	0	1	0	1	1	1	0	0	0	1	D	–
V_{DC}	0	0	1	1	1	1	0	0	0	1	–	–
$0.5V_{DC}$	0	0	1	1	1	0	1	0	0	1	–	C
0	0	0	1	1	0	0	1	1	0	1	–	–

Table 2 Switching arrangement-1:2 source configuration (13-level)

State	S_1	S_2	S_3	S_4	S_5	S_6	S_7	S_8	S_9	S_{10}	C_1	C_2
$3V_{DC}$	1	1	0	0	1	1	0	0	0	1	–	–
$\frac{5V_{DC}}{2}$	1	0	1	0	1	1	0	0	0	1	C	–
$2V_{DC}$	0	0	1	1	1	1	0	0	0	1	–	–
$\frac{3V_{DC}}{2}$	1	0	1	0	0	1	0	1	0	1	C	D
V_{DC}	1	1	0	0	0	0	1	1	0	1	–	–
$\frac{V_{DC}}{2}$	1	0	1	0	0	0	1	1	0	1	C	–
0	0	0	1	1	0	0	1	1	0	1	–	–

Table 3 Switching arrangement-1:3 source configuration (17-level)

State	S_1	S_2	S_3	S_4	S_5	S_6	S_7	S_8	S_9	S_{10}	C_1	C_2
$4V_{DC}$	1	1	0	0	1	1	0	0	0	1	–	–
$\frac{7V_{DC}}{2}$	1	0	1	0	1	1	0	0	0	1	C	–
$3V_{DC}$	0	0	1	1	1	1	0	0	0	1	–	–
$\frac{5V_{DC}}{2}$	1	1	0	0	1	0	1	0	0	1	–	C
$2V_{DC}$	1	0	1	0	1	0	1	0	0	1	C	C
$\frac{3V_{DC}}{2}$	0	0	1	1	1	0	1	0	0	1	–	C
V_{DC}	1	1	0	0	0	0	1	1	0	1	–	–
$\frac{V_{DC}}{2}$	1	0	1	0	0	0	1	1	0	1	C	–
0	0	0	1	1	0	0	1	1	0	1	–	–

Table 4 gives the TSV/TBV calculation of all switches with 1:1 source configuration. And Table 5 gives generalized equations for different source configurations.

Generally, for calculating SC values, the longest/maximum discharge period method has been preferred. For better operation, the capacitance values have to be taken little more than the actual calculated values. For finding switching and conduction losses, the PLECS/PSIM software have been used in the literature and according to datasheet values, it is possible to get easily the final efficiency of the power converter. The proposed topology actually looks like three-level FC with two

Table 4 Per-unit TSV of the proposed topology-1:1

S. No.	Switches	Blocking voltage
1	S_1 to S_8	$(0.5V_{DC})8$
2	S_9 and S_{10}	$(2V_{DC})2$
Total standing voltage (TSV) in per unit		$8V_{DC}/2V_{DC} = 4$ p.u

Table 5 Generalized equations for different source configurations for the proposed topology

S. No.	Description	1:1 source configuration	1:2 source configuration	1:3 source configuration
	U = Number of basic units/cells			
1	Total number of levels	8U + 1	12U + 1	16U + 1
2	Total number of DC sources	2U	2U	2U

legs and in between it consists additionally S9 and S10 switches. For this topology, there is no need of bidirectional switches requirement for generating nine, thirteen and seventeen levels.

After getting particular level output, the design of filter is very much important for the grid connection. As compared with L, LC filters, LCL filter gives better ripple attenuation. However, it suffers from resonance problem and finally the system becomes unstable. To tackle these resonance problems, generally active damping method has been preferred. Because of this method, no additional power losses are present as compared with passive damping method. The values of inverter side inductance, grid side inductance and filter capacitances have been calculated from [15].

B. ***Proposed Control Schemes***

(i) ***URCS-RL load case***

For all source configurations with RL load, the URCS has been applied and its strategy as depicted in Fig. 2. The proposed control scheme is the modified version of NLC technique. The URCS provides less computation time as compared with NLC scheme and SHE PWM technique.

Fig. 2 Unified rounding control scheme—URCS

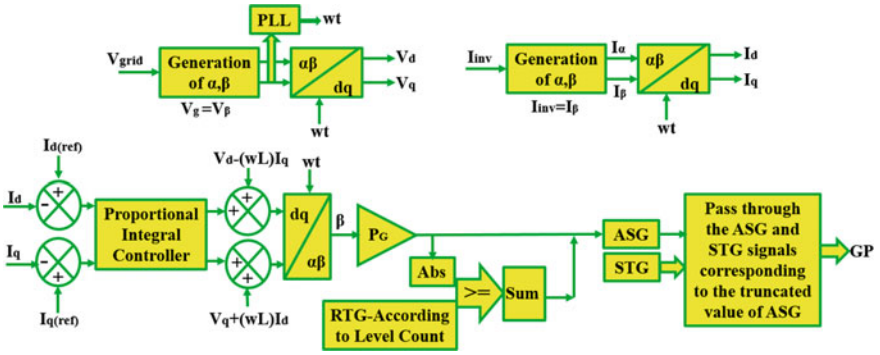

Fig. 3 Proposed dq frame current control scheme-1:1 source configuration

In this scheme, modulating signal is given to rounding function and it generates Aggregated Signal (ASG). The Switching Table Generation (STG) has been penetrated from Tables 1, 2 and 3 for the respective source configurations. Because of truncation, there is no need of logic gate requirement for generating Gate Pulses (GP). This control scheme is basically a fundamental switching frequency technique thereby switching losses greatly reduce and it also provides self-balancing of capacitors. It is universally applicable for any MLI topology with valid switching table.

(ii) ***dq Frame Current Control Strategy-Grid Connected Case***

The control strategy for symmetric source configuration in grid connected case has been depicted in Fig. 3. Firstly, sense the grid voltage (let, $V_{grid} = V_{\beta}$) and through proper PLL, the V_d and V_q components have been generated. Here, PLL has been used to generate reference variable for grid synchronization. Similarly, the I_d and I_q components have been generated by sensing inverter current (let, $I_{inv} = I_{\beta}$). To inject active and reactive power into the grid, $I_{d(ref)}$ and $I_{q(ref)}$ have been used. From decoupling control strategy, the modulating β-component signal has been generated. By using Proper Gain (P_G) value, it is possible to generate desired modulating signal. By taking absolute function, it is possible to curtail the number of high frequency carriers present in Repeating Table Generation (RTG) block. After truncation of ASG and STG, the required switching pulses/Gate Pulses (GP) have been generated. If by taking $I_{q(ref)}$ is equal to zero then it is possible to get UPF operation at grid side.

3 Comparative Analysis

Table 6 represents generalized comparison of symmetrical MLI topologies and Table 7 represents the comparison of nine level symmetrical inverters topologies. From this

Table 6 Comparison of conventional and proposed topologies

Components (L = number of voltage levels)	NPC	FC	CHB	Proposed
Number of switches	$2(L-1)$	$2(L-1)$	$2(L-1)$	$\frac{5(L-1)}{4}$
Number of DC sources/DC bus capacitors	$\frac{(L-1)}{3}$	$\frac{(L-1)}{3}$	$\frac{(L-1)}{2}$	$\frac{(L-1)}{4}$
FC	0	$\frac{(L-1)(L-2)}{2}$	0	$\frac{(L-1)}{4}$
Number of main diodes	$2(L-1)$	$2(L-1)$	$2(L-1)$	$\frac{5(L-1)}{4}$
Number of clamping diodes	$(L-1)(L-2)$	0	0	0
TBV/TSV	$(L-1)$Vdc	$(L-1)$Vdc	$(L-1)$Vdc	$(L-1)$Vdc

Table.7 Comparison of nine level symmetrical inverter topologies

References	DC sources	Switches	Capacitors	Diodes	TBV ($*V_{DC}$)
NPC	01	16	00	56	08
FC	01	16	28	00	08
CHB	04	16	00	00	08
[9]	02	12	03	00	14
[10]	04	10	00	03	16.5
[11]	02	12	03	00	14
[12]	02	12	03	00	12
[6]	02	14	02	00	18
[13]	02	14	02	00	15
Proposed	02	10	02	00	08

table, it is concluded that the proposed topology has less number of switches and less Total Blocking Voltage (TBV).

4 Simulation Results

A. *RL Load Case*

Figures 4, 5 and 6 show inverter output voltage waveforms with 1:1, 1:2 and 1:3 source configurations, respectively. For generating 9, 13 and 17 levels, the URCS has been applied. At t = 0.05 s, step changes in Modulation Indexes (MI) from 1 to 0.5 have been applied to all configurations. Table 8 shows simulation parameters with RL load.

From all source configurations, the number of levels has been varied with respect to change in MI values. Finally, from simulation results, it is concluded that the applied URCS provides self-balancing of capacitors even if step changes in MIs.

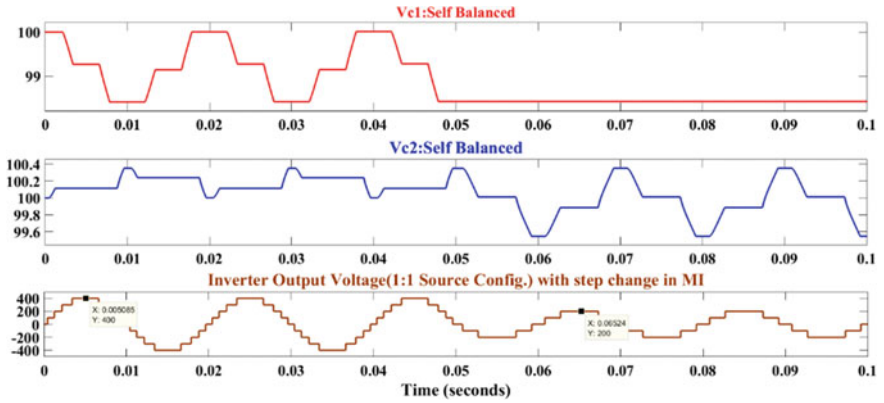

Fig. 4 Inverter output voltage with 1:1 source configuration using URCS

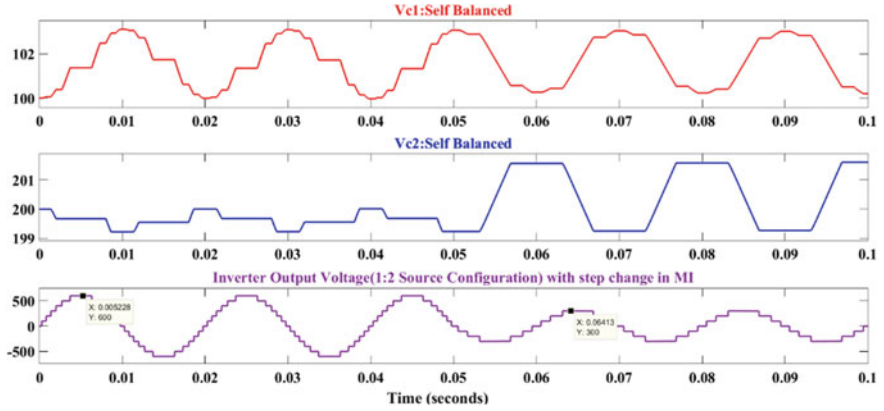

Fig. 5 Inverter output voltage with 1:2 source configuration using URCS

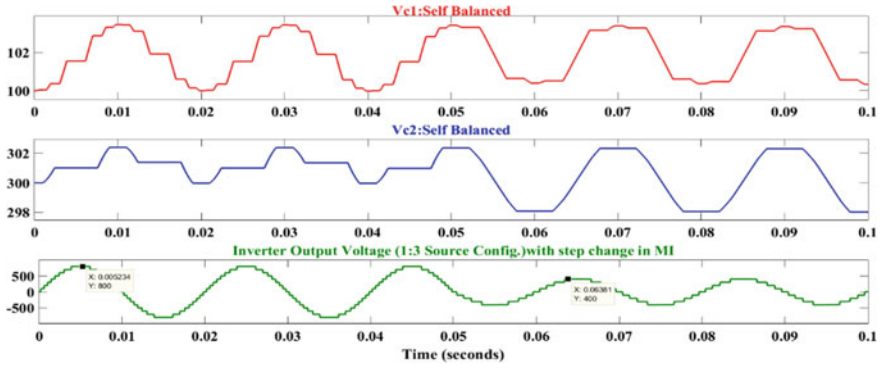

Fig. 6 Inverter output voltage with 1:3 source configuration using URCS

Table 8 Simulation parameters-RL load case

S. No.	Parameters	1:1 source configuration (9-level)	1:2 source configuration (13-level)	1:3 source configuration (17-level)
1	DC sources	Vdc1 = Vdc2 = 200 V	Vdc1 = 200 V; Vdc2 = 400 V	Vdc1 = 200 V; Vdc2 = 600 V
2	Load-RL	R = 100 Ω, L = 30 mH		
3	SC	C1 = C2 = 3300μF		
4	f_0	50 Hz		
5	Control scheme	URCS/ULSFCS		

Table 9 Simulation parameters-grid connected case

S. No.	Parameters	Value
1	Grid voltage	230 V(RMS)
2	Switching frequency	10 kHz
3	Grid frequency	50 Hz
4	Resonance frequency	1416 Hz
5	Rated power (S)	2 kVA
6	Vdc1 = Vdc2	200 V
7	Inverter side inductance	4 mH
8	Grid side inductance	4.3 mH
9	Filter capacitance	6 μF
10	Switched capacitors (C1 = C2)	4700 μF

B. *Grid Connected Case-1:1 Source Configuration*

The control strategy of Fig. 3 has been applied with the simulation parameters mentioned in Table 9. For generating grid voltage 230 V (RMS), the peak value of 400 V with nine level output has been considered and for that Vdc1 and Vdc2 values have been selected as 200 V. Figure 7 shows simulation results for UPF operation mode with step change in $I_{d(ref)}$ from 10 to 5 A at 0.05 s. From this, firstly, the capacitors are self-balanced within permissible limits of voltage ripple then nine level output is obtained with peak value of 400 V. Lastly, the grid voltage and grid current maintain UPF operation even if step changes in $I_{d(ref)}$. Generally, $I_{d(ref)}$ is used to inject active power into the grid. Figures 8 and 9 show the harmonic spectrums of nine level output voltage and grid current.

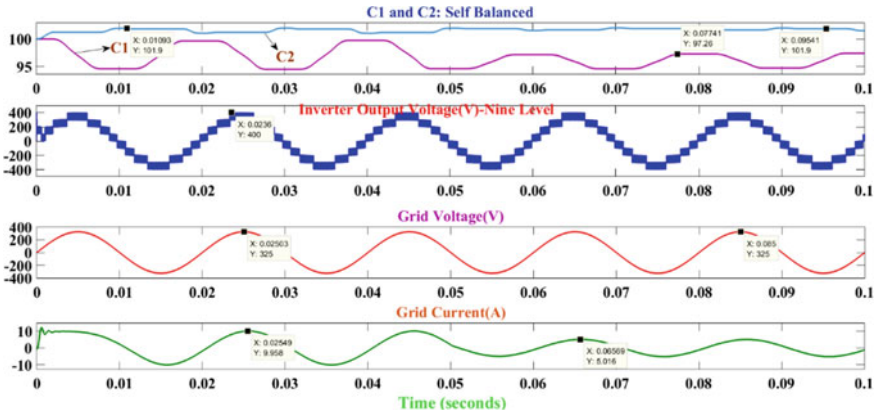

Fig. 7 Step changes in $i_{d(ref)}$ with 1:1 source configuration: UPF operation mode

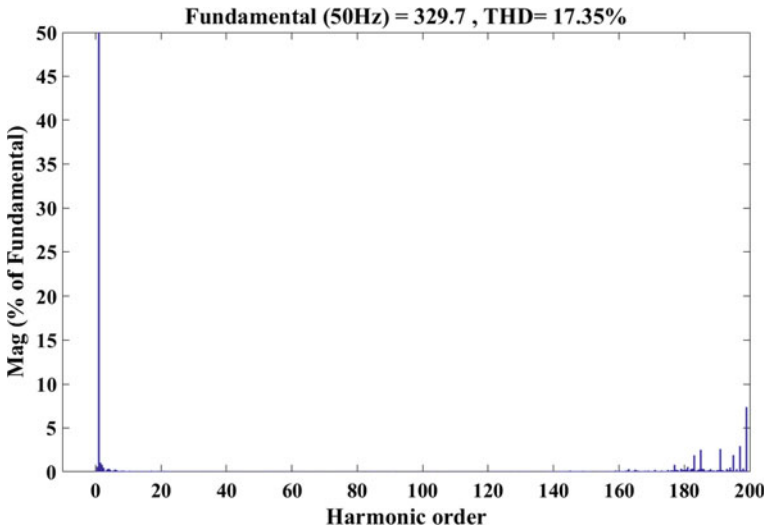

Fig. 8 Harmonic spectrum-nine level output voltage

5 Conclusion

With less number of switches, DC sources and capacitors, a new nine level symmetric source configuration of SC-based MLI topology has been implemented. This topology also provides binary and trinary source configurations for generating more number of levels. For all source configurations, the URCS gives good results to obtain desired output even if step changes in MI values. In this topology, the capacitors are self-balanced without the need of auxiliary circuits and no backend H-Bridge is required for generating negative voltage levels. A comparative study is

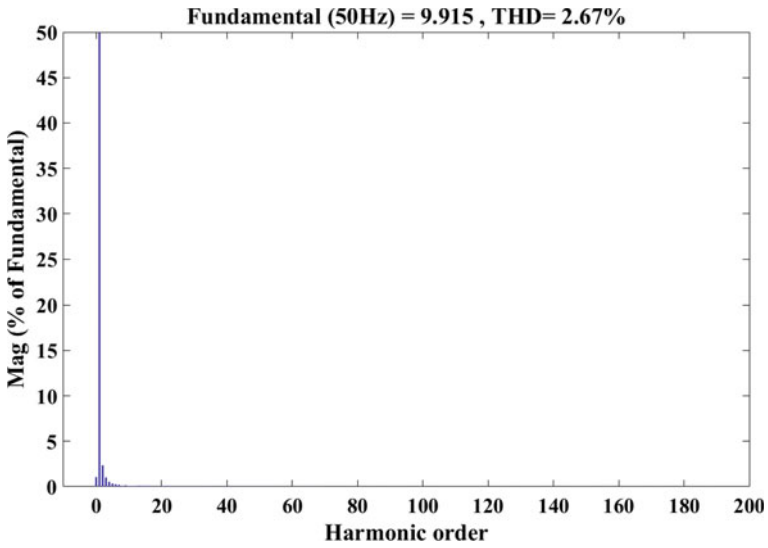

Fig. 9 Harmonic spectrum-grid current with $i_{d(ref)} = 10$ A

also done with other conventional topologies and finally it provides very less per unit TSV. With dq frame current control strategy and ULSPD-PWM scheme, the UPF operation has been obtained at grid side. The drawback of this topology is that it has only unity voltage gain that means there is no boosting factor ability. This topology is well suitable for photovoltaic and fuel cell-based grid-connected applications.

References

1. Rodriguez J, Bernet S, Wu B, Pontt JO, Kouro S (2007) Multilevel voltage-source-inverter topologies for industrial medium-voltage drives. IEEE Trans Ind Electron 54(6):2930–2945
2. Abu-Rub H, Holtz J, Rodriguez J, Baoming G (2010) Medium-voltage multilevel converters—state of the art, challenges, and requirements in industrial applications. IEEE Trans Ind Electron 57(8):2581–2596
3. Zhang L, Waite MJ, Chong B (2013) Three-phase four-leg flying capacitor multi-level inverter-based active power filter for unbalanced current operation. IET Power Electron 6(1):153–163
4. Nabae A, Takahashi I, Akagi H (1981) A new neutral-point-clamped PWM inverter. IEEE Trans Ind Appl IA-17(5):518–523
5. Kersten A, Theliander O, Grunditz EA, Thiringer T, Bongiorno M (2019) Battery loss and stress mitigation in a cascaded H-bridge multilevel inverter for vehicle traction applications by filter capacitors. IEEE Trans Transp Electrific 5(3):659–671
6. Veenstra M, Rufer A (2005) Control of a hybrid asymmetric multilevel inverter for competitive medium-voltage industrial drives. IEEE Trans Ind Appl 41(2):655–664
7. Vemuganti HP, Sreenivasarao D, Siva Kumar G, Sai Spandana A (2018) Reduced carrier PWM scheme with unified logical expressions for reduced switch count multilevel inverters. IET Power Electron 11(5):912–921. https://doi.org/10.1049/iet-pel.2017.0586

8. Su G-J (2005) Multilevel DC-link inverter. IEEE Trans Ind Appl 41(3):848–854. https://doi.org/10.1109/TIA.2005.847306
9. Rajeevan PP, Sivakumar K, Gopakumar K, Patel C, Abu-Rub H (2013) A nine-level inverter topology for medium-voltage induction motor drive with open-end stator winding. IEEE Trans Ind Electron 60(9):3627–3636
10. Ali AIM, Sayed MA, Mohamed EEM, Azmy AM (2019) Advanced single-phase nine-level converter for the integration of multi terminal DC supplies. IEEE J Emerg Sel Topics Power Electron 7(3):1949–1958. https://doi.org/10.1109/JESTPE.2018.2868734
11. Li J, Bhattacharya S, Huang AQ (2011) A new nine-level active NPC (ANPC) converter for grid connection of large wind turbines for distributed generation. IEEE Trans Power Electron 26(3):961–972
12. Barbosa P, Steimer P, Steinke J, Winkelnkemper M, Celanovic N (2005) Active-neutral-point-clamped (ANPC) multilevel converter technology. In: Proceedings of European conference on power electronics and applications, Dresden, Germany, p 10
13. Chaudhuri T, Barbosa P, Steimer P, Rufer A (2007) Cross-connected intermediate level (CCIL) voltage source inverter. In: Proceedings IEEE power electronics specialists conference, Orlando, FL, USA, pp 490–496
14. Rodriguez J et al (2009) Multilevel converters: an enabling technology for high-power applications. Proc IEEE 97(11):1786–1817. https://doi.org/10.1109/JPROC.2009.2030235
15. Ali A, Shanmugham P, Somkun S (2017) Single-phase grid-connected voltage source converter for LCL filter with grid-current feedback. In: 2017 international electrical engineering congress (iEECON), Pattaya, Thailand, pp 1–6.https://doi.org/10.1109/IEECON.2017.8075720
16. Bhanuchandar A, Murthy BK (2021) Single phase nine level switched capacitor based grid connected inverter with LCL filter. In: 2020 3rd international conference on energy, power and environment: towards clean energy technologies, pp 1–5. https://doi.org/10.1109/ICEPE50861.2021.9404491

Priority-Based Charging of Electric Vehicles to Prevent Distribution Transformer Overloading

Arjun Visakh, T. Sornavel, and M. P. Selvan

1 Introduction

Today, electric vehicles (EVs) are considered to be one of the most popular solutions to the degrading air quality in cities across the world. The use of efficient electric motors that produce zero tailpipe emissions makes EVs ideal for the urban commute. As the popularity and penetration of EVs continue to grow, so does the challenge of meeting their battery energy requirement. Meeting the chage requirement of a fleet of EVs can overstress the power distribution system.

Allowing EVs to recharge as and when they are plugged in could lead to overloads, low efficiency, and voltage sags in the distribution system [1]. To overcome these challenges and minimize the impact of EV charging, several charge scheduling schemes have been developed in the past [2]. Some of these seek to prevent equipment overloads by minimizing the contribution of EVs to the peak load [3]. Shifting the charging of EVs from peak load to off-peak hours can lead to load leveling and a higher load factor. This can be achieved by minimizing the variance of system demand from a reference loading level [4]. A few authors have attempted to improve the efficiency of power delivery by minimizing the power lost in distribution lines [5]. Research on improving the voltage profile using dynamic programming [6] has also been undertaken. Dynamic pricing-based charge scheduling schemes that minimize the charging cost borne by EV users [7] are also available in the literature. Thus, optimization of EV charging may be motivated by a variety of objectives.

A situation in which several EV owners return home from work around the same time and immediately plug in their EVs can result in the addition of a substantial charging load on the system when the system demand is already quite high [8]. In this scenario, as EV loads spread across the network, the total load on the system will eventually exceed the transformer capacity. Avoiding prolonged overloads on

A. Visakh (✉) · T. Sornavel · M. P. Selvan
National Institute of Technology, Tiruchirappalli, Tiruchirappalli, Tamil Nadu, India
e-mail: selvanmp@nitt.edu

S. Kumar et al. (eds.), *Recent Advances in Power Electronics and Drives*, Lecture Notes in Electrical Engineering 852, https://doi.org/10.1007/978-981-16-9239-0_22

transformers, an essential and costly equipment for power distribution, should be given a top priority. By preventing overloads and reducing the risk of transformer failure, the distribution network's reliability can be improved considerably.

In this paper, the charging of EVs is scheduled with the objective of preventing overloads on the distribution transformer. To prevent overloading, the EV loads should be scheduled in a manner that reduces their concurrence with the peak load hours of the system. One such EV management system that delays charging until sufficient capacity becomes available was trialed in the UK [9]. During those intervals when the transformer can accommodate some but not all of the EV loads, the EVs are charged cyclically to distribute the available capacity evenly.

However, sharing the available energy equally among all the plugged-in EVs may result in failure to meet the charging demand of some users, e.g., those planning long trips or those plugged-in for a short duration. To avoid this and improve overall customer satisfaction, this paper introduces a priority-based charging scheme. Priorities are assigned to plugged-in EVs based on their initial SOC, desired SOC, arrival time, and departure time. The priority values, being dependent on the amount of energy required, and the charging time available reflect the vehicle user's urgency of charge requirement.

2 System Modeling

2.1 Network Topology

The test system on which the scheduling algorithm's performance is assessed is based on the IEEE 4-node test feeder. The system voltage is lowered from 24.9 kV to 400 V to represent an Indian distribution system. Fifteen domestic customers are assumed to be connected at bus 4, the terminal load bus (Fig. 1).

Each residence is supplied by a single-phase 230V connection rated at 3 kW. The maximum load on the distribution transformer is thus 45 kW. Considering a 25% margin for future loads, the transformer should be capable of supplying a load up to 56.25 kW. The nearest standard transformer rating is 63 kVA [10]. Thus, the distribution transformer is rated at 11kV/400V and 63 kVA.

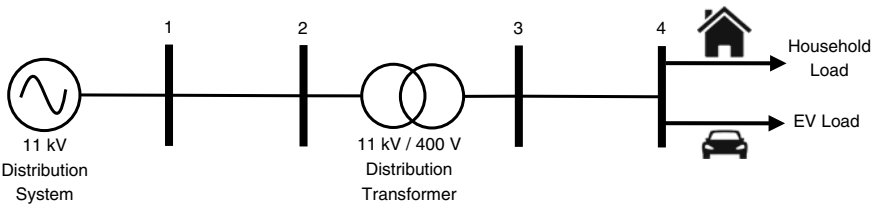

Fig. 1 Test system

2.2 Base (Non-EV) Load on the System

The fifteen residential connections are uniformly distributed among the three phases, i.e., five customers in each phase. Daily load profiles [11] that give the power demand over 15-min intervals are randomly assigned to each consumer. A power factor of 0.90 lagging is assigned to all the residential loads. The resulting kVA load on the transformer over a day can be seen in Fig. 2.

2.3 EV Charging Load

The level of EV penetration determines the number of consumers who own EVs. In this paper, a 100% penetration level is considered, i.e., all the residences have EV loads. The maximum power limit for EV chargers is taken as 3 kW [12]. The EVs plugged into the network are modeled as constant power loads operating at unity power factor for the load flow analysis [12]. All the EVs are assumed to have their battery capacity equal to 20 kWh.

All the EVs are assumed to recharge their batteries overnight by slow AC charging. Each EV's energy demand is decided by the initial battery state of charge (SOC) upon arrival and the desired SOC at departure. The random nature of EV mobility is replicated by assigning a normal probability distribution to the EV arrival time. The probability distribution for arrival time is defined with $\mu = 6$ p.m. and $\sigma = 2$ h [13]. The initial SOC values upon arrival are uniformly distributed between 0.15 and 0.4 p.u. All the EVs are expected to be fully charged at departure, which is assumed to be at 8 a.m. here.

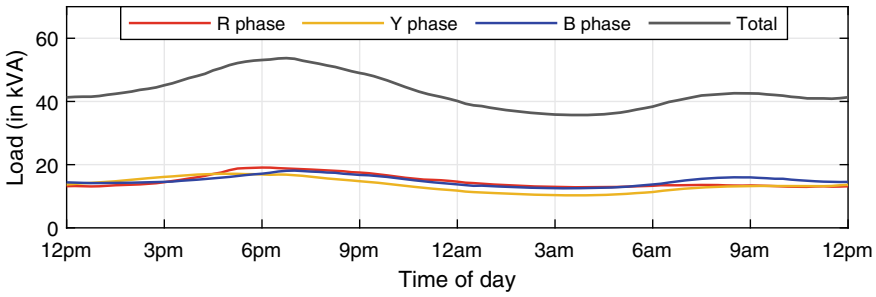

Fig. 2 Base load on the transformer

2.4 Load Flow Analysis

The transformer loading can be monitored throughout the day by performing load flow analysis on the unbalanced three-phase network. In this work, OpenDSS software was used to solve the test system's load flow equations. The 'time-series solution' method was employed to run the load flow at the beginning of each 15-min interval.

3 Priority-Based Charging

3.1 Motivation

Uncoordinated charging represents a situation in which the batteries start recharging as soon as the EVs are plugged in. Most EV users plug in their cars for charging upon returning home from work around 6 p.m. [13]. As this coincides with the system's peak load hours, the transformer is very likely to get overloaded. Such an uncontrolled charging scenario was simulated with the parameters specified in Sect. 2 using MATLAB and OpenDSS. Its impact on transformer loading is shown in Fig. 3.

A considerable portion of EV charging overlaps with the peak base-load hours. As a result, the transformer's peak load is significantly higher than its rated capacity of 63 kVA. It is evident that during peak load hours, it is not feasible for the transformer to support the charging of all EVs. Thus, there is a need to coordinate and schedule the charging of EVs so as to stagger their aggregate load on the transformer.

One approach is to share the available transformer capacity cyclically among all the plugged-in EVs. However, by giving equal preference to all EVs without giving adequate weightage to the amount of energy required and plug-in duration, the urgency of charge requirement may get overlooked. Thus, in order to improve cus-

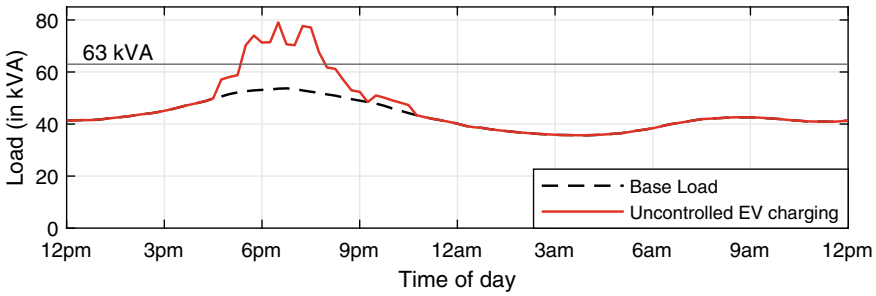

Fig. 3 Impact of uncontrolled charging on transformer loading

tomer satisfaction without overloading the transformer, a priority-based scheduling algorithm is required.

3.2 Methodology

Let $\mathbf{T}$ denote the set of all 15-min intervals in a day, starting at 12 noon. Let $\mathbf{N^t_{conn}}$ denote the set of plugged-in EVs at time slot $t (\forall t \in \mathbf{T})$. Let N^t be the maximum number of EVs that can be connected to the system without overloading the transformer at time slot t. The values of N^t calculated over a day to avoid the transformer loading from exceeding its rated capacity of 63 kVA are shown in Fig. 4. It is clear the actual number of EVs connected to the system exceeds the acceptable value during the peak load hours.

The value of N^t is then compared with the number of EVs plugged-in at that interval, i.e., the size or cardinality of the set $\mathbf{N^t_{conn}}$. If the number of plugged-in EVs, i.e., $n(\mathbf{N^t_{conn}})$ is lower than N^t, then the scheduling algorithm does not intervene, and the EVs may be charged normally. However, if $n(\mathbf{N^t_{conn}}) > N^t$, then each EV is assigned a priority value based on its energy requirement and plug-in time. The EVs in the set $\mathbf{N^t_{conn}}$ are then sorted based on their priority values, and the first N^t EVs are allowed to charge during that interval. The remaining $[n(\mathbf{N^t_{conn}}) - N^t]$ EVs have to wait for their turn. At the next interval $(t + 1)$, the priority-based sorting and charging of EVs is repeated. Such a scheduling algorithm ensures that the transformer does not get overloaded at any interval and prioritizes urgent charging requests.

3.3 Calculation of Priority

During each time slot t $(\forall t \in \mathbf{T})$, the priority values of all EVs in the set $\mathbf{N^t_{conn}}$ are calculated to determine their charging status. The formula for calculating priority comprises three parts. The first part is based on the battery's current SOC, represented

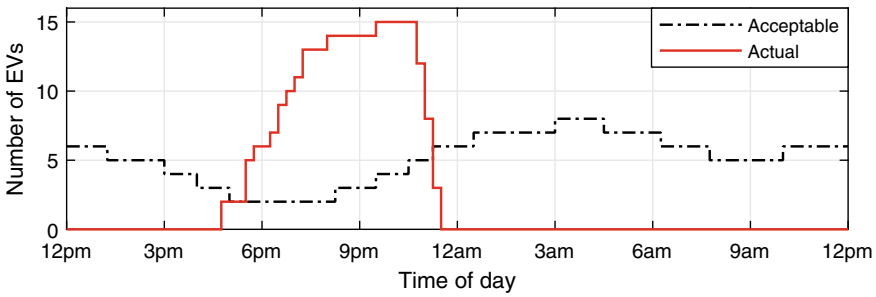

Fig. 4 Number of EVs plugged-in to the distribution system

as SOC_c. It is given by the formula

$$p_1 = 1 - SOC_c \tag{1}$$

The second part is based on the percentage of charge completed and is given by

$$p_2 = 1 - \frac{SOC_c - SOC_i}{SOC_d - SOC_i} \tag{2}$$

where the subscripts i, c, and d depict the initial, current, and desired values, respectively. The third part is determined by the slack time. It is evaluated as

$$p_3 = 1 - \left(\frac{t_{av} - t_{req}}{t_{total}}\right) \tag{3}$$

where t_{av} represents the available time left for charging, t_{req} represents the time required to meet the desired charge, and t_{total} denotes the total plug-in time of the EV. The final priority of each EV is then calculated as

$$p = p_1 + p_2 + p_3. \tag{4}$$

4 Results and Analysis

In this section, the impact of uncoordinated charging on the distribution system is compared with that of priority-based charging. The aggregate EV load on the system for both cases is compared in Fig. 5. It can be seen that the bulk of the EV load has been delayed from the peak load hours to the off-peak hours around midnight. The impact of this staggering on transformer loading is shown in Fig. 6.

The transformer loading during each 15-min interval has now been reduced to a value below its rated capacity. Furthermore, by charging the EVs according to their priorities, every owner's demand for a fully charged battery has been met, as evident in Fig. 7. It can be observed that the SOC of all the EVs reaches 1 p.u. (full charge) by 8 a.m., the hour of departure.

Under the prioritized-charging scenario, although the charging start time was delayed for a few low-priority EVs, the energy requirement of all the vehicles was met well before their departure time. As all the EVs are charged up to the SOC desired by their users, customer satisfaction is guaranteed. The SOC profiles in both scenarios have a constant slope as the charging rate is never altered from the nominal value of 3 kW.

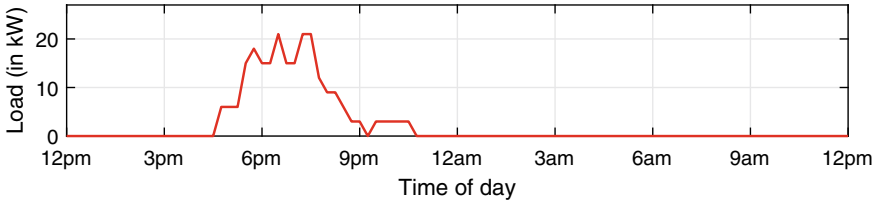

(a) Uncontrolled EV charging

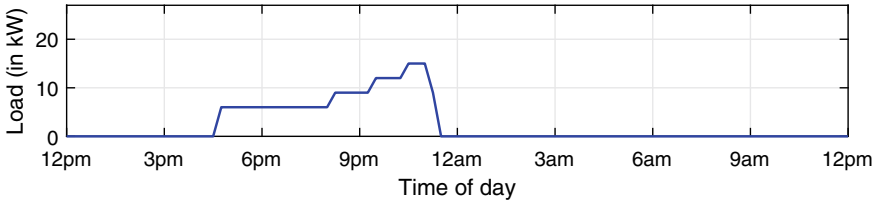

(b) Prioritized EV charging

Fig. 5 Comparison of aggregate EV load on the system

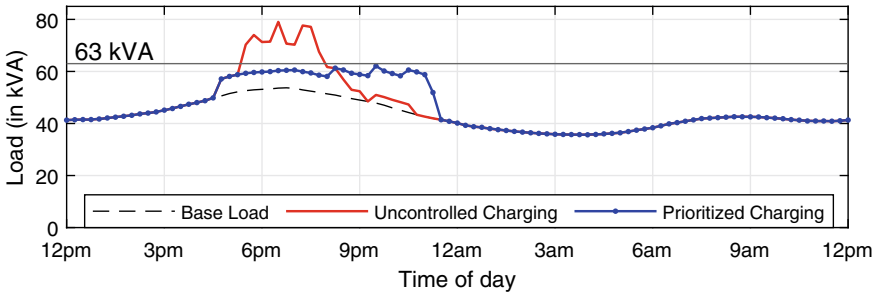

Fig. 6 Comparison of transformer loading

5 Conclusion

An EV charge scheduling system that prevents distribution transformers from getting overloaded is presented in this paper. The EV user's urgency to charge the battery is also taken into account while scheduling the charging. The urgency is represented by EV charging priority, formulated as a function of energy requirement and plug-in duration. During peak load hours, the scheduling algorithm postpones the charging of low-priority EVs. Thus, a portion of the EV load gets shifted from on-peak to off-peak hours without defaulting on any high-priority charging deadline. Although delayed from the time of plug-in, the charging of low-priority EVs is completed before the departure time deadline. As a result, the aggregated load on the distribution transformer does not exceed its capacity at any time, and the charge requirements of all the EV users are satisfied.

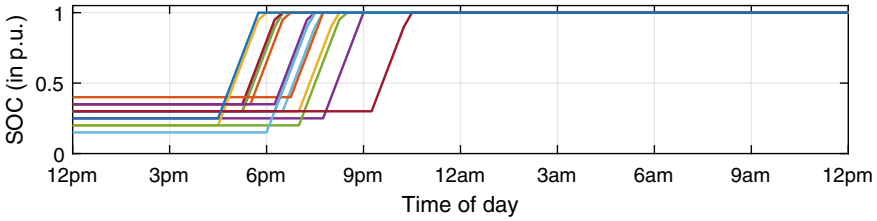

(a) Uncontrolled EV charging

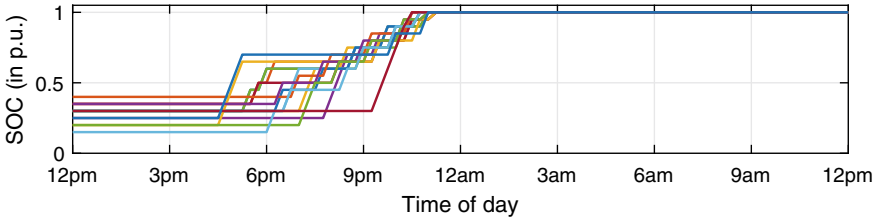

(b) Prioritized EV charging

Fig. 7 Comparison of SOC profile of EVs

References

1. García-Villalobos J, Zamora I, San Martín JI, Asensio FJ, Aperribay V (2014) Plug-in electric vehicles in electric distribution networks: a review of smart charging approaches. Renew Sustain Energy Rev 38:717–731
2. Solanke TU, Ramachandaramurthy VK, Yong JY, Pasupuleti J, Kasinathan P, Rajagopalan A (2020) A review of strategic charging-discharging control of grid-connected electric vehicles. J. Energy Storage 28:101193
3. Erdogan N, Erden F, Kisacikoglu M (2018) A fast and efficient coordinated vehicle-to-grid discharging control scheme for peak shaving in power distribution system. J Mod Power Sys Clean Energy 6(3):555–566
4. Kisacikoglu MC, Erden F, Erdogan N (2018) Distributed control of PEV charging based on energy demand forecast. IEEE Trans Ind Inf 14(1):332–341
5. Suyono H, Rahman MT, Mokhlis H, Othman M, Illias HA, Mohamad H (2019) Optimal scheduling of plug-in electric vehicle charging including time-of-use tariff to minimize cost and system stress. Energies 12(8):1500
6. Dubey A, Santoso S (2015) Electric vehicle charging on residential distribution systems: impacts and mitigations. IEEE Access 3:1871–1893
7. He Y, Venkatesh B, Guan L (2012) Optimal scheduling for charging and discharging of electric vehicles. IEEE Trans Smart Grid 3(3):1095–1105
8. Deilami S, Masoum AS, Moses PS, Masoum MA (2011) Real-time coordination of plug-in electric vehicle charging in smart grids to minimize power losses and improve voltage profile. IEEE Trans Smart Grid 2(3):456–467
9. Saunders E, Butler T, Quiros-Tortos J, Ochoa LF, Hartshorn R (2015) Direct control of EV charging on feeders with EV clusters. In: 23rd international conference on electricity distribution, pp 1–5
10. Power transformers—Part 1: General. Standard, International Electrotechnical Commission, Geneva, CH (2000)
11. California ISO: Today's outlook—demand trend (2021). http://www.caiso.com/TodaysOutlook/Pages/default.aspx

12. Veldman E, Verzijlbergh RA (2014) Distribution grid impacts of smart electric vehicle charging from different perspectives. IEEE Trans Smart Grid 6(1):333–342
13. Jin C, Tang J, Ghosh P (2013) Optimizing electric vehicle charging: a customer's perspective. IEEE Trans Vehicular Technol 62(7):2919–2927

Implementation of Three-Phase Hybrid Energy System Integrated with UPQC

Shravan Kumar Yadav and Krishna Bihari Yadav

1 Introduction

Many power electronic-based systems are evolved in recent years, and when linked to power system, such systems cause power quality issues and even decrease system efficiency [1, 2]. The issue of drawing non-sinusoidal current and reactive electricity from origin plagues power electronic devices, which are being most commonly used during automotive, consumer, and residential areas. Some modules attached at the same point of common coupling (PCC) suffer from voltage variations as a result of this action [3]. The widespread usage of non-linear flows today has resulted in a slew of power quality problems, including elevated current harmonics, voltage distortion, and poor efficiency in the electrical grid [4, 5]. As a result, as a non-linear load increases, discrete currents are injected into the device. This twisted supply voltage and current triggers critical equipment to overload, as well as the breakdown of certain safety features, transmission lines, and engines, as well as wire overloading. As a result, it is much more important to install compensating equipment that compensate for harmonic currents and voltages produced by uneven loads [6]. Active power filters (APFs) have been investigated and established method of resolving this issue in grid-connected renewable sources [7]. An addition of a green electricity supply to the grid has a significant impact on the system efficiency. Harmonic frequencies are pumped into the system mostly as a result of non-linear loads being associated, and green technology necessitates the usage of reactive electricity upon its system. With the use of non-linear forces, power requirements may impact utility and consumer devices. It emphasizes the importance of power efficiency at different stages of electricity use. Such power quality issues should be addressed in order to have stable and high-quality power when combining renewable resources (RSs) [8–10]. To fix

S. K. Yadav (✉) · K. B. Yadav
Department of EE, NIT, Jamshedpur, Jamshedpur 831014, Jharkhand, India

K. B. Yadav
e-mail: kbyadav.ee@nitjsr.ac.in

S. Kumar et al. (eds.), *Recent Advances in Power Electronics and Drives*, Lecture Notes in Electrical Engineering 852, https://doi.org/10.1007/978-981-16-9239-0_23

the significant electric power quality problems in indoor and outdoor, The hybrid series active filter (The THSeAF) is built on the voltage source form converters. This electricity quality compensator offers a cost-effective way to address existing challenges while still incorporating solar energy to provide a long-term flow to the load. To derive voltage and current harmonics and also voltage disrupts, the controller uses a creative mixture of the p-q theory and Synchronous Reference Frame (SRF) [11]. Results in the combining of voltage spikes with a short term voltage fluctuation behind a dynamical load level can be defined as a distribution system which is mainly affected by complicated voltage fluctuations. As a result, the dynamic voltage restorer (DVR) integrated with battery would have sufficient storage to resolve large and dense complicated voltage fluctuations exist in a supply chain with a PV device [12]. The DVR is a sequence filter which prevents sensitive loads from the electric power quality issues including voltage swell, sag, harmonics and distortions. This indicates that DVR will handle power quality problems at the output terminals. Harmonic has become a significant power quality issue that pollutes the supply chain, allowing end-user devices to refuse to operate due to voltage, current, or frequency fluctuations [13].

The architecture and analysis study of a three-phase Hybrid energy system UPQC is discussed in this article. To increase the variable output during load active current extraction, a frequency-dependent d-q theory-based regulation is used. The below are the key benefits of the proposed model:

- Coordination of renewable energy supply and improved power efficiency.
- Output voltage and output current improved at same time.
- Load current compensation has been improved.

The output of proposed devices is thoroughly examined using MATLAB-Simulink tools.

The following is the general structure of the work: The literature work is depicted in Sect. 2. Section 3 outlines the proposed control structure, while Sect. 4 defines the device architecture and setup. In comparison, Sect. 5 addresses the observations, and Sect. 6 takes the article to an end.

2 Literature Survey

Initially, that Shunt active power filter (SAPF) paradigm was touted as the ideal method for reducing harmonic pollution [14], but its control algorithms can operate harmonic removal, DC-link capacitance manipulation, current power, and command signal strategies are both looked at and discussed. During non-ideal grid voltage environments, an inverter of 3-level neutral-point clamped diode (NPC)-based filter offers effective harmonic distortion stabilization and power factor correction [15]. The recommended model is called the dual fundamental component extraction (DFCE) method. The suggested process derives fundamental voltage and current elements that are needed at the very same time in order to generate reference current and

synchronization stages, accordingly. This literature includes a detailed analysis of efficiency in [16] power systems, including DC and green energy systems. Technologies for measuring power condition and potential solutions to power quality problems are thoroughly investigated. Then, we look at how customized energy devices like D-STATCOM, UPQC, UPS, TVSS, and DVR can be used to mitigate these issues for microgrid systems. STATCOM can be a viable option for renewable energy systems due to its numerous benefits, while spinning reserve may improve power efficiency in conventional systems. [16, 17] Introduces a 3ϕ UPQC with efficient architecture. The sequence compensator employs a basic DVR with PLL. Applying the d-q principle to the controller portion of the shunt compensator, on the other side, improves the efficiency of the UPQC. A series compensator based on a basic hysteresis controller is often used. The suggested system's key features are that (a) the voltage and current are sustained concurrently, and (b) under a variety of harmonics, sags/swells, and unstable situations, reliability is guaranteed. Fuel Cell Integrated UPQC (FCI-UPQC) is used to improve the power quality in [18] 3ϕ four-wire distribution grid. On the shunt line, the planned FCI-UPQC with 4-leg converter, and on the sequence side, it has 3-leg converter. Enhanced integration of renewable energy sources [19] into the electricity network, as well as the spreading of uneven loads in the home and industry, have exacerbated power quality problems and rendered coordination more difficult than before. Extended renewable energy sources into the electricity network, as well as the spreading of industrial and domestic critical loads, have exacerbated electric power quality problems and rendered coordination more difficult than before. To address this issue, a number of advanced PLLs with improved disturbance rejection capabilities were developed by various researchers. Almost all of these PLLs may be thought of traditional SRF-PLL with additional filters that can be added within or before the SRF-PLL control loop. As the DG device is positioned between the grid and either generic load, UPQC acts as a symmetric device. The DG device conducts active power-line condition when delivering the energy provided by the PV into the grid in [20, 21] grid-connected mode. To gain a complete function of the system function and properly build the electrical power, a comprehensive power analysis through the PV-UPQC is needed.

3 System Design and Configuration

Figure 1 depicts the HES-structure. UPQC's three-phase framework is needed for the HES-UPQC. Shunt and series compensators are attached to a standard DC-bus in the HES-UPQC. At the load side, the shunt compensator is associated. The photovoltaic, BESS, and wind energy systems are all linked to the UPQC through a standard dc bus.

Via a dc-dc converter, the solar PV array, wind, and BESS are connected directly to UPQC's DC-link. The grid electric voltage sags/swells are compensated by the series compensator when voltage is in regulation mode. The series and shunt compensators

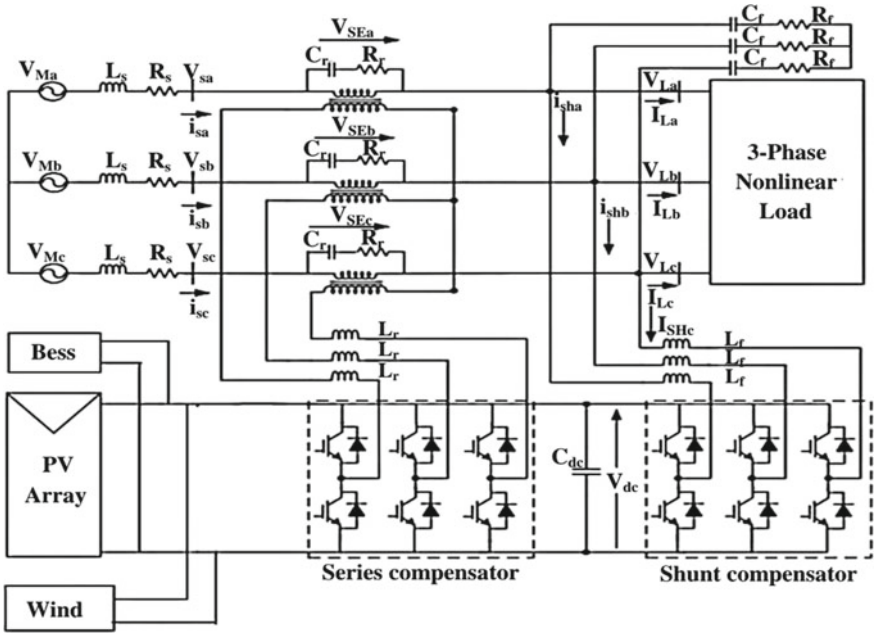

Fig. 1 System configuration HES-UPQC

are connected to grid by integrating inductance. Through the series injection transformer, the voltage created by series compensator is injected into the grid. Harmonics produced by the switching operation of converters are filtered with ripple filters.

Both a series and shunt compensator may be called a voltage source inverter (VSI) with a balanced voltage source. Insulated gate bipolar transistors (IGBTs) with the DC capacitors make up the circuit. The extreme dynamic energy required in DC connection the voltage is a significant factor in VSI-based hybrid filter mitigation.

4 PV-UPQC Control

The series compensator and shunt compensator are the two primary modules of HES-UPQC. Shunt compensator corrects issues with load control efficiency including the load current harmonics and the reactive power. In the situation planned, the shunt compensator in UPQC also acts as the power source for the solar PV collection. To derive the power of PV collection, the algorithm used is maximum power point tracking (MPPT) by shunt compensator. Supplying sufficient voltage in phase prevents the module from power quality issues.

4.1 Shunt Compensator Control

Through running the solar at its extreme energy point, shunt compensator draws the extreme power from it. Figure 2 shows the overall layout of the SOGI-FLL dependent control algorithm. The algorithm of MPPT is used to run the Photovoltaic array in such a manner that the full electric power is provided. The technique SOGI-FLL is used to remove the quadrature portion of basic load present. MPPT power and compensator switching control are part of the control method. To produce reference DC connection voltage, the MPPT control is used.

MPPT Control Approach

Full Power Point is discovered using the steepest descent method (MPP). The steep descent path is used in the different phase size than traditional approach, which are the key benefits which improves convergence significantly. P&O algorithm is known as the gradient descent process, because it is optimization technique. MPP is calculated as follows [22]:

$$V_{DC}(k+1) = V_{DC} + \frac{(dP_{PV}/dV_{DC})_{V=V_{DC}(k)}}{k_{\varepsilon}} \tag{1}$$

where k_{ε} is the phase volume corrector, which defines how steep is each step which is in the direction of gradient and the inverter's DC connection voltage. (dp/dv) represents the MPP variance in each phase. The dp/dv ratio is determined as follows:

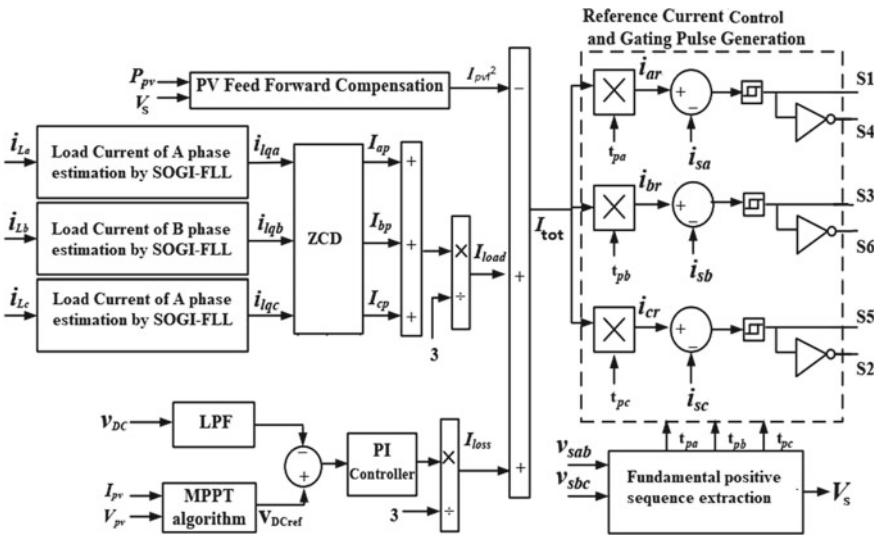

Fig. 2 Architecture of shunt compensator control

$$\frac{dP_{pv}}{dV_{DC}} = f(V_{DC}(k), P_{pv}(k)) \tag{2}$$

Inverter Switching Control

The switching process involves calculating the magnitude of PCC voltages, computer models, collecting process reference currents, a leakage element, and feed-forward part of PV electricity.

Fundamental positive sequence extraction

Compensation would not be sufficient if residual voltages are used explicitly to measure reference filter currents. To produce comparison filter currents, the basic positive sequence components of three-phase voltages are collected.

Component Loss and Photovoltaic Feed Forward

In control system, the Photovoltaic (PV) feed-forward component can be used to account for differences in solar generation and voltage magnitude. PV feed-forward unit is calculated using PV power and PCC voltage [23].

$$I_{pvf}^2 = \frac{2P_{pv}}{3V_s} \tag{3}$$

The loss component (I_{loss}) is obtained by Proportional Integral (PI) controller with the feedback of a imbalance signal between V_{DCref} and V_{DC}. The loss factor is assessed as follows:

$$I_{loss} = (K_p + \frac{k_1}{s})(V_{DCref} - V_{DC}) \tag{4}$$

Fundamental Load Current Estimation

Figure 3 demonstrates the arrangement of SOGI-FLL. SOGI-FLL contains two blocks the updated SOGI and the frequency locked loop (FLL). The controller FLL calculates grid operator frequency (i_q) by an in-phase component (i_d) and a quadrature element. The feature of the input electric current i_L (with the offset DC of "A" and magnitude I_{pa}) is as follows [3]:

$$I_L(s) = \frac{I_{ap}\omega'}{s^2 + \omega'^2} + \frac{A}{s} \tag{5}$$

The transition parameters for I_d and I_q are shown in Fig. 3.

$$I_d(s) = \frac{k\omega' s}{s^2 + k\omega' s + \omega'^2} I_L(s) \tag{6}$$

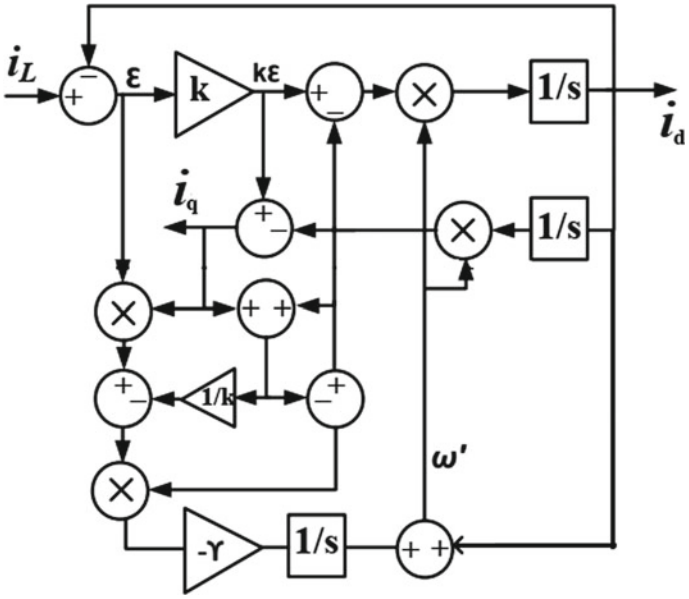

Fig. 3 SOGI-FLL

$$I_q(s) = \frac{ks^2}{s^2 + k\omega' s + \omega'^2} I_L(s) \tag{7}$$

Basic load terms are derived from these I_d and I_q coefficients, as seen in Fig. 3.

The in-phase of fundamental load portion has no impact on control algorithm's output, in the case of the offset DC. The load current is orthogonal to the quadrature portion (i_q). The FLL controller takes a quadrature portion (i_q) of the basic load component and the error (between i_L and i_d), for grid frequency estimation. Furthermore, in steady-state operating conditions, FLL output is unaffected by the existence of a DC offset in the load portion. As a consequence, the framework that adapts to frequency of SOGI-FLL is efficient and accurate for estimating grid frequency. Zero crossing detectors estimate the magnitude of three basic load currents processes (I_{ap}, I_{bp}, and I_{cp}). Load currents' net load portion (I_{load}) is measured as follows:

$$I_{load} = \frac{I_{ap+}I_{bp+}I_{cp}}{3} \tag{8}$$

The feed-forward, load, and loss components are used to calculate the net weight of the reference grid present. The cumulative weight present in the reference grid is calculated as follows [23]:

$$I_{tot} = I_{load} - I_{pvf^2} - I_{loss} \tag{9}$$

Reference Current Control

$$i_{ar} = t_{pa} * I_{tot} \tag{10}$$

$$i_{br} = t_{pb} * I_{tot} \tag{11}$$

$$i_{cr} = t_{pc} * I_{tot} \tag{12}$$

The error current is measured from the reference and the sensed grid electric currents and provided to hysteresis current controller, which regulates the VSI switching pulses.

4.2 Series Compensator Control

Compensation of in-phase, pre-sag, and energy-optimal compensation which are the three management strategies of series compensator [19, 20] includes a comprehensive overview of the multiple compensation mechanisms used for sequence compensator power. The voltage is injected by the series compensator in the same step as the grid voltage in this job, resulting in the series compensator injecting the least amount of voltage necessary.

Figure 4 depicts the sequence compensator's control system. The quantization of the PCC voltage obtained by PLL is used to produce the zero axis in the dq-0 domain.

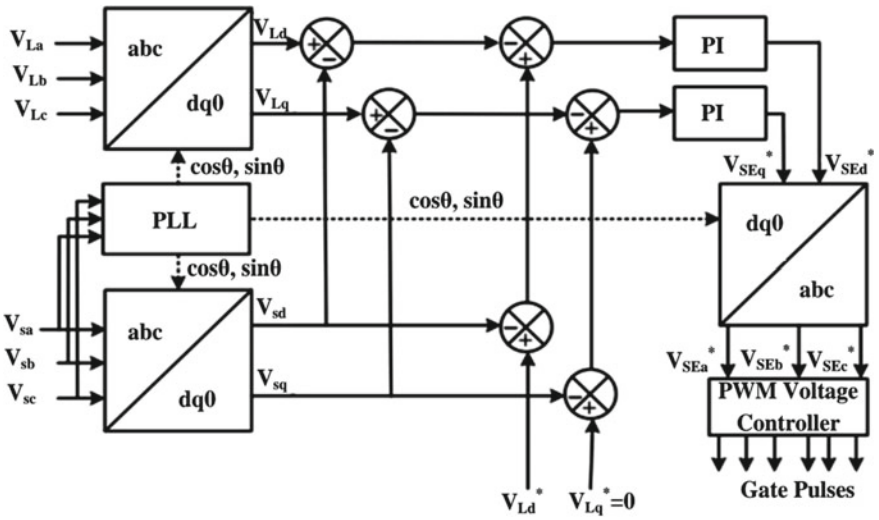

Fig. 4 Control architecture of series compensator

The voltage and load from the PCC are translated to the d-q-0 domain. At zero, a part of the q-axis is held. Series compensator reference voltage is defined by discrepancy between PCC voltage and the load reference voltage. The real voltages of series compensator are determined by the discrepancy between the load voltage and the PCC voltage. PI controllers use the disparity between reference and real voltage of series compensator to produce acceptable reference signals. To produce sufficient gating signals for inverter, such reference signals are translated in abc-domain and it is passed via a PWM controller.

5 Simulation Results

The HES-UPQC framework in the MATLAB-Simulink software is used to test its effects and performance. The non-linear load used is made up of a 3ϕ diode rectifier bridge connected with the R-L load. The simulation was run with a 50e−6 s solver phase scale. The machine is exposed to a number of complex situations, including PCC voltage sags and swells.

Figure 5 depicts the complex output of PV-UPQC in the presence of PCC voltage swells/sags. Irradiation level (G) is maintained at 1000 W/m2. DC-link voltage (Vdc), PCC voltages (Vs), load voltages (VL), grid currents (is), load currents in each line (iLa, iLb, iLc), and load currents (iL) are shown in Fig. 5.

6 Conclusion

The configuration and output of three-phase HES-UPQC have been examined under grid voltage sags/swells. The system's accuracy has been checked using MATLAB/Simulink. It has been discovered that HES-UPQC mitigates the harmonics caused by non-linear- loads. The use of control techniques has improved the efficiency of d-q control, especially in load unbalanced conditions. It can be shown that HES-UPQC, by combining distributed generation with power quality enhancement, is a successful option for current delivery systems.

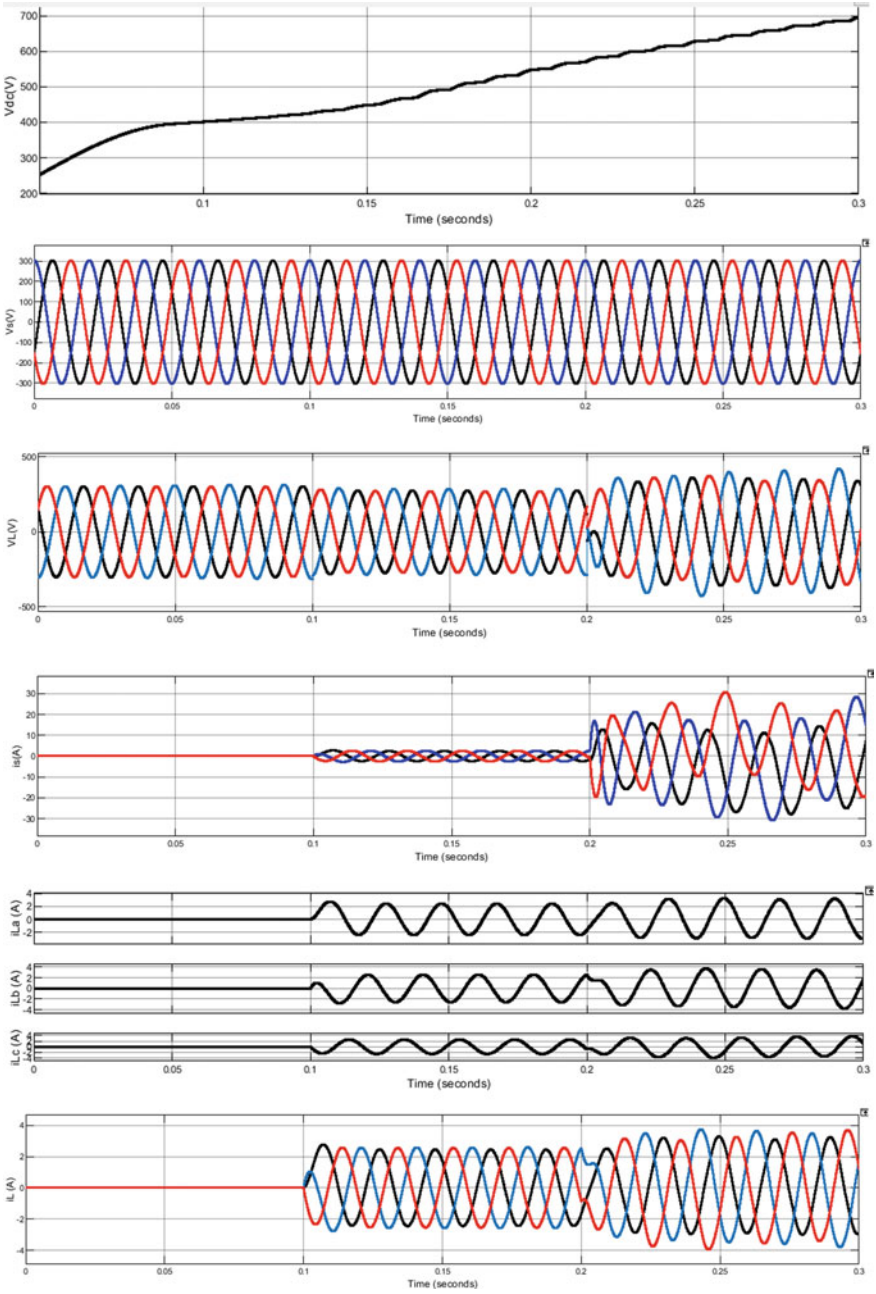

Fig. 5 Performance of HES-UPQC

References

1. De Yong D, Bhowmik S, Magnago F (2017) Optimized complex power quality classifier using one vs. rest support vector machines. Energy Power Eng 09(10):568–587
2. Li D, Yang K, Zhu ZQ, Qin Y (2017) A novel series power quality controller with reduced passive power filter. IEEE Trans Ind Electron 64(1):773–784
3. Modesto RA, da Silva SAO, de Oliveira Junior AA (2015) Power quality improvement using a dual unified power quality conditioner/uninterruptible power supply in three-phase four-wire systems. IET Power Electron 8(9):1595–1605
4. Swain SD, Ray PK, Mohanty KB (2017) Improvement of power quality using a robust hybrid series active power filter. IEEE Trans Power Electron 32(5):3490–3498
5. Javadi A, Hamadi A, Woodward L, Al-Haddad K (2016) Experimental investigation on a hybrid series active power compensator to improve power quality of typical households. IEEE Trans Ind Electron 63(8):4849–4859
6. Li S, Qi W, Tan SC, Hui SR (2016) Integration of an active filter and a single-phase AC/DC converter with reduced capacitance requirement and component count. IEEE Trans Power Electron 31(6):4121–4137
7. Tareen WU, Mekhilef S, Seyedmahmoudian M, Horan B (2017) Active power filter (APF) for mitigation of power quality issues in grid integration of wind and photovoltaic energy conversion system. Renew Sustain Energy Rev 70:635–655
8. Kasa S, Ramanathan P, Ramasamy S, Kothari DP (2016) Effective grid interfaced renewable sources with power quality improvement using dynamic active power filter. Int J Electr Power Energy Syst 82:150–160
9. Eltigani D, Masri S (2015) Challenges of integrating renewable energy sources to smart grids: a review. Renew Sustain Energy Rev 52:770–780
10. Mira MC, Zhang Z, Knott A, Andersen MA (2017) Analysis, design, modeling, and control of an interleaved-boost full-bridge three-port converter for hybrid renewable energy systems. IEEE Trans Power Electron 32(2):1138–1155
11. Javadi A, Woodward L, Al-Haddad K (2018) Real-time implementation of a three-phase THSeAF based on a VSC and a P+R controller to improve the power quality of weak distribution systems. IEEE Trans Power Electron 33(3):2073–2082
12. Mansor MA, Othman MM, Musirin I, Noor SZM (2019) Dynamic voltage restorer (DVR) in a complex voltage disturbance compensation. Int J Power Electron Drive Syst 10(4):2222–2230
13. Farooqi A, Othman MM, Abidin AF, Sulaiman SI, Radzi MAM (2019) Mitigation of power quality problems using series active filter in a microgrid system. Int J Power Electron Drive Syst 10(4):2245–2253
14. Hoon Y, Radzi MAM, Hassan MK, Mailah NF (2017) Control algorithms of shunt active power filter for harmonics mitigation: a review. Energies 10(12)
15. Hoon Y, Radzi MAM, Hassan MK, Mailah NF (2018) Operation of three-level in-verter-based shunt active power filter under non ideal grid voltage conditions with dual fundamental component extraction. IEEE Trans Power Electron 33(9):7558–7570
16. Hossain E, Tur MR, Padmanaban S, Ay S, Khan I (2018) Analysis and mitigation of power quality issues in distributed generation systems using custom power devices. IEEE Access 6(c):16816–16833
17. Rohouma W, Balog RS, Peerzada AA, Begovic MM (2020) D-STATCOM for harmonic mitigation in low voltage distribution network with high penetration of nonlinear loads, Renew Energy 145:1449–1464
18. Hasan K, Othman MM, Rahman NFA, Hannan MA, Musirin I (2019) Significant implication of unified power quality conditioner in power quality problems mitigation. Int J Power Electron Drive Syst 10(4):2231
19. Sundarabalan CK, Puttagunta Y, Vignesh V (2019) Fuel cell integrated unified power quality conditioner for voltage and current reparation in four-wire distribution grid. IET Smart Grid 2(1):60–68

20. Golestan S, Guerrero JM, Vasquez JC (2017) Three-phase PLLs: a review of recent advances. IEEE Trans Power Electron 32(3):1897–1907
21. Chen J et al (2021) Distributed control of multi-functional grid-tied inverters for power quality improvement. IEEE Trans Circuits Syst I Regul Pap 68(2):918–928
22. Yadav SK, Raj S, Suman S, Madhuri M (2014) Design of low power Mppt with digital control for thermo PV generator. IOSR J Electr Electron Eng 9:17–26
23. Devassy S, Singh B (2016) Design and performance analysis of three-phase solar PV integrated UPQC. In: 2016 IEEE 6th international conference on power systems (ICPS), pp 1–6

Design of Permanent Magnet Brushless DC Motor for Electric Vehicle Traction Application

Sandeep Vuddanti, Sharankumar Shastri, and Surender Reddy Salkuti

1 Introduction

Nowadays many technologies have been developed to replace conventional internal combustion (IC) engines, which are among the primary producers of greenhouse gas emissions. Environmentally safer technologies are being researched and developed and the most prominent advancements have been in electric vehicles in the past 10–15 years. Electric vehicles (EVs) could play a major role in the development of vehicles to replace IC engines, leading to a reduction of greenhouse gas emissions [1]. The increased demand for electric vehicles brings in the need to improve their operation to the maximum by employing proper parts like batteries, motors, transmission, etc. Due to the everlasting need for higher efficiency, the utilities look to implement compact motors with higher power density and efficiency. This brings in a need to design high-efficiency motors specifically for this application, considering design requirements and constraints. The introduction of newer materials, faster electronic switches, and processors made it possible to develop and improve efficient special electrical machines such as PM synchronous machines (PMSMs) [2]. PMSMs possess high torque density, high efficiency, less maintenance, and simplicity of structure. These features make the PM synchronous motors suitable for traction purposes, and they are also in the renewable energy sector, e.g., wind turbines [3].

S. Vuddanti
Department of Electrical Engineering, National Institute of Technology Andhra Pradesh (NITAP), Tadepalligudem, India

S. Shastri
Department of Electrical Engineering, Indian Institute of Technology Delhi (IITD), New Delhi, India

S. R. Salkuti (✉)
Department of Railroad and Electrical Engineering, Woosong University (WSU), Daejeon, Republic of Korea
e-mail: surender@wsu.ac.kr

S. Kumar et al. (eds.), *Recent Advances in Power Electronics and Drives*, Lecture Notes in Electrical Engineering 852, https://doi.org/10.1007/978-981-16-9239-0_24

PMSMs can be classified based on the wave shape of the back-electromotive force [4]. They are further classified into permanent magnet brushless DC (PMBLDC) motors and permanent magnet synchronous machines (PMSMs). PMSMs generate a sinusoidal BEMF, while PMBLDC motors produce a trapezoidal one.

PMBLDC motors are synchronous motors that are fed DC input from an inverter to produce AC to drive each phase of motor. These controllers help provide pulses of current to motor windings, hence controlling the torque and speed of the motor. PMBLDC motors have gained popularity since their inception in 1975, and are being used in a wide number of applications due to factors like high efficiency and simple structure [5]. Permanent magnet machines have recently been used for more demanding applications, mainly due to the extensive use of low-cost power electronics switches [6].

Reference [7] describes the applications, principles and topologies, materials, electric circuit parameter computations, equivalent circuits, specifications and design principles (above and below 100 kW), design optimization and performance analysis for Induction motors, from which the stator design of the PM motor is mainly based on. Reference [8] presents the methods to design permanent magnet motors. The sizing procedure and main dimension calculations along with performance calculations of the designed motor are mentioned. Drive topologies for the permanent magnet motors are also described. The rotor analysis, calculation of maximum magnet thickness, width, etc., have been adapted from here. The magnetic flux accumulated in this type of internal PM configuration is higher than a surface permanent magnet of the same dimensions. Simulations are compared to the hardware of the motor.

An approach for the design of AC PM motors for EV traction is proposed in [9]. Reference [10] presents the modeling of a 10 kW BLDC Motor controller by using the PSIM software. Reference [11] reviews the relevant literature on the vehicle dynamics and analyzes the same for a three-wheeler *auto-rickshaw*, and its behavior under varying drive cycle load. Extensive simulation is done on the auto-rickshaw replacing its drivetrain with that of a parallel hybrid drivetrain. A detailed insight into the design parameters and performance analysis for the permanent magnet motors is one of the main references for the design formulae taken into account in Ref. [12].

The major contributions of this paper are as follows:

- A study on the current types of powertrains utilized in electric vehicles is presented in this paper. Powertrain study includes the study on batteries and motor drives. A brief insight about PMBLDC motors and their comparison with other motors is also described.
- The dynamics of the vehicle based on a standard vehicle model are presented based on the amount of power required for the motor.
- Dynamics of an electric vehicle over simulation is proposed to design and assess the performance of a PMBLDC motor for the EV application.
- Calculation of motor dimensions using analytical calculations using references is presented. The structure and the design procedure of the required PMBLDC motor are addressed.

- Simulations of the analytically designed motor using ANSYS's Maxwell package are presented and compared with the simulation results obtained using RMXprt (analytical) and Maxwell 2D (FEM-based). The design is optimized by varying parameters.
- Compared the simulation of the assessed motor with FEM simulation to obtain a model with the least error.

The organization of this paper is as follows. Section 2 presents the description of brushless DC motors and the analysis of vehicle dynamics. Motor design using analytical calculations is presented in Sect. 3. Section 4 describes the motor design using ANSYS Maxwell software. Simulation results using RMxprt and ANSYS 2D software are included in Sect. 5. Conclusion is drawn in the last section.

2 Brushless DC Motors and Analysis of Vehicle Dynamics

In this section, different motors used in EVs are compared and the focus is made on BLDC motors. The efficiency and the reason for the choice of BLDC motors due to their advantages are also covered. This section also estimates the power required by the motor to run the EV at the speeds given in the Indian Driving Cycle and takes into account all the forces acting on the vehicle [13].

2.1 Brushless DC Motors

Here the primary focus is on the application of BLDC motors in EVs, the following part explains the construction and operating principle of brushless DC motors. The advantages of using BLDCs include high operating speeds, low maintenance, compact size, 90+% efficiency, no brush sparking, quick response, rotor made of permanent magnets, less rotor inertia, linear speed/torque curve produces a predictable speed regulation, brush inspection is eliminated, quieter operation, therefore, reduced electromagnetic interference, regenerative braking has good efficiency [14]. As one can notice, the benefits of using BLDC motors are higher, especially from its brushed counterparts and Induction motors, making it more suitable for EV applications.

2.2 Analysis of Vehicle Dynamics

With all EVs, it is very important to predict the performance and range before it is manufactured. Several types of models exist to predict vehicle performance through simple calculations. Vehicle performance modeling includes the prediction of several

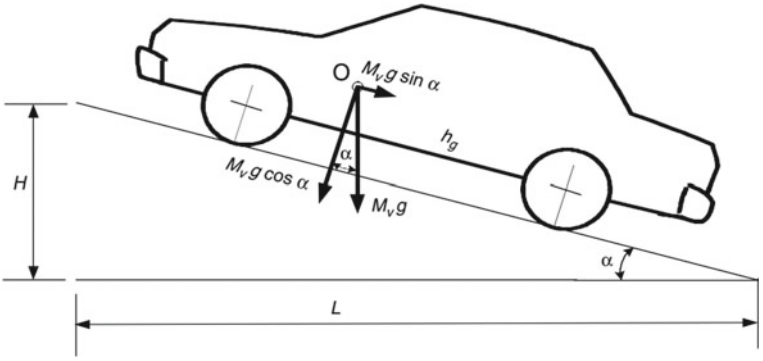

Fig. 1 Vehicle dynamics

parameters like acceleration, top speed, range, power, etc. It becomes essential to necessitate the electric vehicle with enough performance to properly blend in with general traffic. It is also essential to model the EV before manufacturing individual parts to avoid over-powering or under-powering the system. This becomes a very important method to cut the costs of the EV [15]. The performance parameter we need for the motor is the 'power required', to predict what the power of the designed motor should be. This helps to avoid costs in production and allows the motor to run at rated power to give maximum efficiency. Figure 1 depicts the vehicle dynamics.

The model used here to evaluate performance is called the force model/tractive effort model [16, 17]. The propelling force of vehicle forward, the tractive effort should be able to accomplish greater than the aerodynamic drag, greater than the rolling resistance, accelerate the vehicle, and provides the force needed to overcome the vehicle's weight component along the slope. It depends mainly on the frontal area and how wind opposes this area [18]. The mathematical equation for the aerodynamic drag is given by,

$$F_w = \frac{1}{2}\rho A_f C_d (V + V_w)^2 \tag{1}$$

where V_w is a component of the wind speed in the vehicle's moving direction, which has a positive sign when the wind is against the vehicle motion, and negative when the wind is along the vehicle direction [19]. ρ is the air density, A_f is the vehicle frontal area, V is the vehicle speed, C_d is the aerodynamic drag coefficient. When the tire is rolling, the tire causes the asymmetric distribution of ground reaction forces, which leads to a resistance in the wheels opposing the rolling of the wheel. The mathematical equation for the rolling resistance is given by [20],

$$F_r = \mu_{rr} M_V g \tag{2}$$

where μ_{rr} is rolling resistance coefficient, g is the acceleration due to gravity and M_V is the mass of the vehicle. The typical value of μ_{rr} is 0.015 for a radial-ply tire [21]. The force required by the vehicle when it is accelerating, i.e., when its velocity is changing. The linear acceleration of the vehicle is given by,

$$F_a = M_V a \tag{3}$$

where a is the acceleration of the vehicle (m/s^2). The grading resistance can be expressed as [22],

$$F_g = M_V g \sin \alpha \tag{4}$$

where α is the road slope angle.

2.3 Net Tractive Effort and Power Required

Net tractive effort (F_{TE}) now becomes the sum of all the forces acting on vehicle [23], and it is expressed as,

$$F_{TE} = F_w + F_r + F_a + F_g \tag{5}$$

where F_r is rolling resistance force, F_a is acceleration force, F_w is the aerodynamic drag force, F_g is grading resistance force**.** The total power required to overcome the net tractive effort is equal to the force times the velocity of the vehicle at each recorded instant of time [24]. The average power can be calculated and the power of the motor can be estimated.

$$P = F_{TE} V \tag{6}$$

where F_{TE} (N) is the total tractive effort required to overcome the net resistance by the vehicle, and V (m/s) is the velocity of the vehicle.

2.4 Vehicle (E-Rickshaw) Model and Specifications

In this section, the amount of power required by the motor to run the electric vehicle at the speeds given is estimated in the Indian Driving Cycle and takes into account all the forces acting on the vehicle. The reference for the rickshaw has been taken from the Bajaj RE 2S model [25, 26] manufactured by Bajaj Auto Limited®, and it is depicted in Fig. 2. The vehicle is equipped with a 145.5 cc single-cylinder (2-stroke)

Fig. 2 Bajaj RE 2S rickshaw as a reference model

engine. The transmission consists of a manual gearbox (4-speed) with reverse gear and a wet-plate clutch. The curb weight of the vehicle is 284 kg and the maximum weight (gross) is about 610 kg [27]. Different parameters of Bajaj RE 2S rickshaw are presented in Table 1.

The analysis can be done through basic calculations, either by using software like MATLAB or even Excel. The obtained aerodynamic drag force (F_w) is 106.33 $_N$, rolling resistance (F_r) is 60.329 $_N$, and grading resistance (F_g) is 0 N. Driving cycles are plots of the speed of the vehicle versus time, i.e., helps us visualize the speed of the vehicle at every second. The driving cycles provide us with a more realistic and practical test for vehicle testing than analyzing the slope or the distance covered by the vehicle which could provide a wrong result during simulation [28, 29]. The drive cycle adopted is called the modern Indian driving cycle which is developed by

Table 1 Different parameters of Bajaj RE 2S rickshaw

Component/Parameter	Values
Engine	Single cylinder, 2 strokes, 145.5 cc
Tires (Front-rear, R)	4.00-8, 4PR
Dimensions (W × L × H)	1300 mm × 2625 mm × 1710 mm
Drag coefficient (C_d)	0.45
Rolling resistance (μ_{rr})	0.01
Frontal area (A_f)	2 m^2

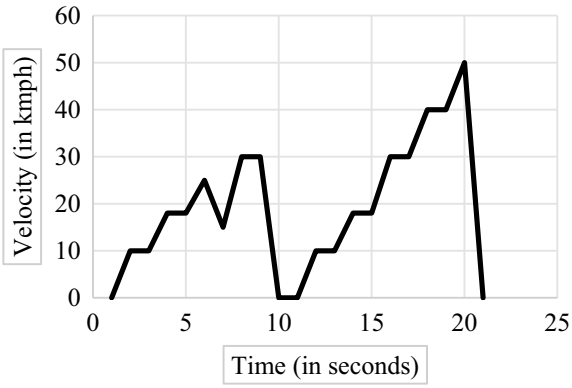

Fig. 3 Modified Indian driving cycle

ARAI, India to simulate the realistic driving models for the Indian roads. Figure 3 depicts the modified Indian Driving Cycle.

The values are then added in an Excel worksheet (or a MATLAB code or Simulink model) [30]. The calculations were done and added to excel to calculate the solutions at once. The final power values were obtained and the average was taken to be 1530 W or 1.5 kW.

3 Motor Design Using Analytical Calculations

In this section, the design of a surface PMBLDC motor for e-rickshaw application is discussed. Motor design is a rigorous process and needs many parameters to be generally assumed due to their validity due to industry usage. Also, generally, several iterations run to obtain the correct parameters and their desired values [31]. This continuous re-evaluation is what makes motor design rigorous and the whole process can be semi-automated using scripting, motor simulations in software like ANSYS Maxwell®, FEMM®, MotorSolve®, etc.

The quarter motor cross-section showing all the dimensions depicted in Fig. 4. In this figure, D_{in} is the stator inner diameter, D_{out} is the stator outer diameter, D_r is the rotor outer diameter, h_m is the magnet thickness, g is an air gap, b_{s2} is the slot width top, b_{s1} is the slot width bottom, w_t is the tooth width, h_{cs} is the back iron length, $(h_{os} + h_w + h_s)$ is the slot depth [32].

Initial parameters were assumed and the calculations were carried out by using the standard Refs. [33, 34]. The predicted results using analytical calculations for the design of brushless DC machines are shaft torque (T), which is equal to 4.77 Nm; the predicted power, which is equal to 1500 W; the predicted current, which is equal to 6.57A; RMS armature current, which is equal to 5.36 A; the applied voltage to the motor, which is equal to 120 V; the resistance obtained per phase, which is equal to 0.25 ohms/phase; and the maximum back emf, which is expected to be 120 V. These values can now be added to simulation results and checked for the validity of

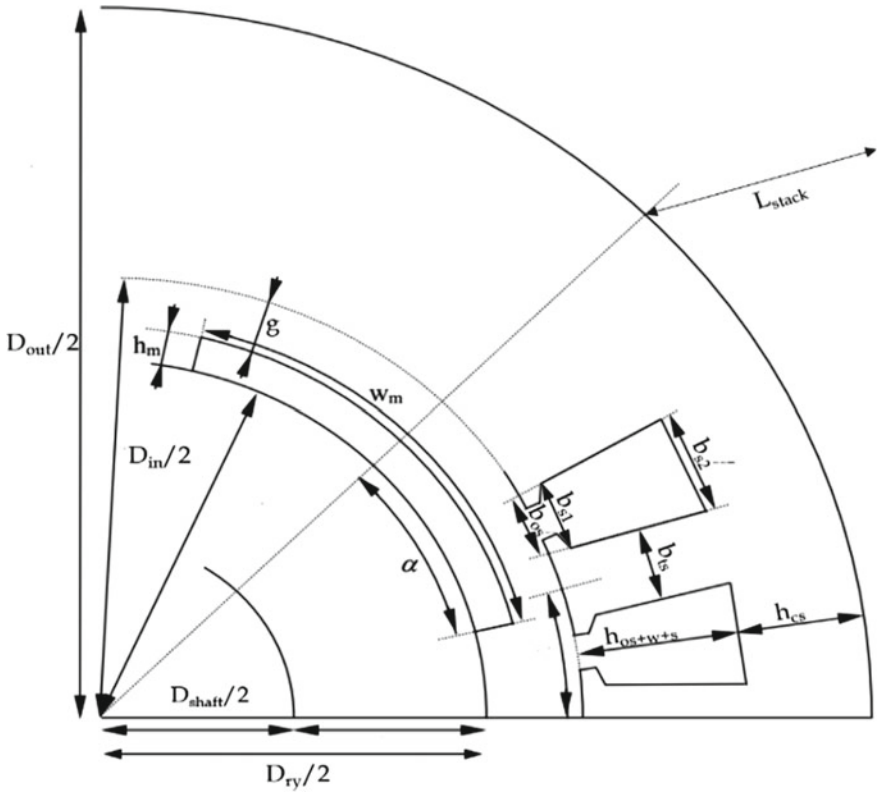

Fig. 4 Quarter motor cross-section showing all the dimensions

the analytical method [35]. In this paper, the motor is designed using the ANSYS Maxwell software [36, 37].

4 Results and Discussion

This section presents the obtained simulated results for the analytically designed motor, using FEA software, ANSYS Maxwell. Its modules RMxprt and 2D are used to simulate the motor and obtain more accurate outputs than the ones obtained from analytical calculations.

4.1 Simulation Results Using RMxprt

The design sheet for RMxprt output for PMBLDC motor design is presented next. The general data for motor design is: rated output power is 1.5 kW, rated voltage is 120 V. The stator data is as follows: the number of stator slots is 24, the outer diameter of the stator is 120 mm, the inner diameter of the stator is 69 mm, type of stator slot is 3. The stator slot having hs0 is 1 mm, hs1 is 2 mm, hs2 is 11.77 mm, bs0 is 2 mm, bs1 is 4 mm, bs2 is 5 mm, rs is 1 mm, top tooth width is 5.8199 mm, bottom tooth width is 7.90104 mm, skew width (number of slots) is 0, length of the stator core is 50 mm, stacking factor of the stator core is 0.95, and type of steel is steel_1010. The slot insulation thickness is 0.5 mm, layer insulation thickness is 0 mm, end length adjustment is 0 mm, the number of parallel branches is 1, the number of conductors per slot is 16, the number of coils is 11, average coil pitch is 5, the number of wires per conductor is 2, wire diameter is 0.912 mm, wire wrap thickness is 0 mm, slot area is 65.5358 mm^2, net slot area is 38.6844 mm^2, limited slot fill factor is 75%, stator slot fill factor is 68.8025%, and coil half-turn length is 125.28 mm.

The rotor data is as follows: minimum air gap is 0.75 mm, inner diameter is 30 mm, length of rotor is 50 mm, stacking factor of the iron core is 0.95, the material is steel-1010, polar arc radius is 33.75 mm, mechanical pole embrace is 1, electrical pole embrace is 0.968883, the maximum thickness of magnet is 2.5 mm, the width of the magnet is 51.0509 mm, type of magnet is NdFe35, and there is no magnetic shaft. Permanent magnet data is as follows: residual flux density is 1.23 T, coercive force is 890 kA/m, maximum energy density is 273.675 kJ/m^3, relative recoil permeability is 1.09981, the demagnetized flux density is 7.50732e-005 T, recoil residual flux density is 1.23 T, and recoil coercive force is 890 kA/m.

Full-load data is as follows: average input current is 13.4992 A, root mean square armature current is 12.4873 A, armature thermal load is 211.426 A^2/mm^3, specific electric loading is 22.1208 A/mm, armature current density is 9.55781 A/mm^2, frictional and windage loss is 0 W, an iron-core loss is 0.00215665 W, armature copper loss is 118.566 W, the total loss is 119.89 W, the output power is 1500.02 W, input power is 1619.91 W, efficiency is 92.5989%, rated speed is 2737.67 rpm, rated torque is 5.23223 Nm, locked-rotor torque is 35.4585 Nm, and locked-rotor current is 236.321 A. The RMxprt modeled figure is depicted in Fig. 5.

When all the above-obtained parameters are added into the Ansys RMxprt simulation module, the simulation results from RMxprt for 1500 W, 120 V, 24 slot BLDC motor are presented next.

The efficiency versus speed curve is presented in Fig. 6. From this figure, it can be noticed that the efficiency of the system at rated speed is quite high (95% +).

Figure 7 depicts the output torque versus speed curve. From this figure, it can be noticed that the starting torque of the motor is quite high due to large starting currents in BLDC (due to low BEMF), but at rated speed, the torque is about 5 Nm, which is the desired value.

Cogging torque is caused due to the interactions between the stator and magnet poles. This is more prominent at lower speeds due to the longer time of interaction

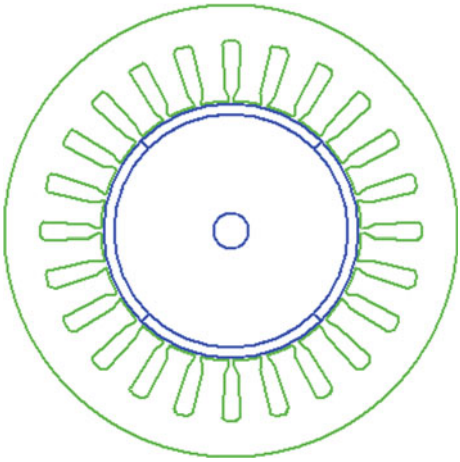

Fig. 5 RMxprt modeled figure

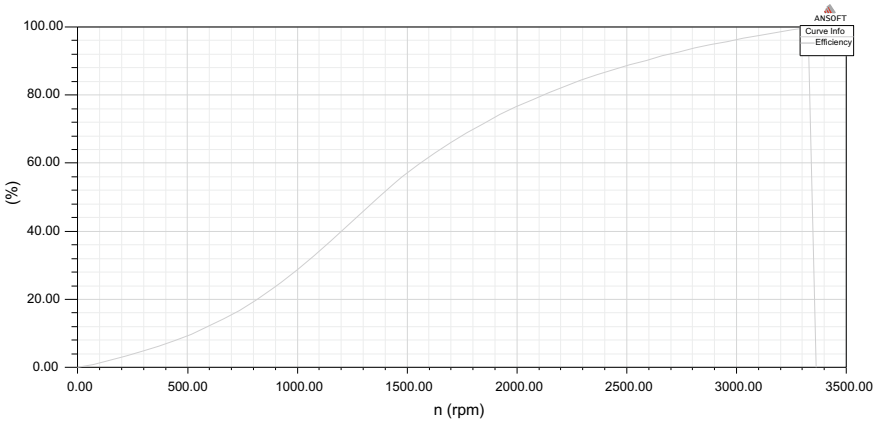

Fig. 6 Efficiency versus speed characteristics

between the stator and rotor. Cogging torque output in two teeth is depicted in Fig. 8. The cogging torque here is quite high and can be efficiently reduced/optimized by using fractional slot/pole ratio, skewing of rotor magnets, skewing of stator teeth, and optimum rotor arc width.

Figure 9 depicts the air gap flux density. From this figure, it can be observed that an air gap flux density of about 0.75 T, which is lesser than the 0.9 T assumed in the calculations.

Figure 10 depicts the induced voltages at rated speed. Induced back emf waveforms, which are exactly equal to 99.6 V as estimated ($\varepsilon = 0.83$), after the losses are considered.

Figure 11 depicts the winding currents at full load. The peak value of winding currents at full load is about 18 A, which is normal.

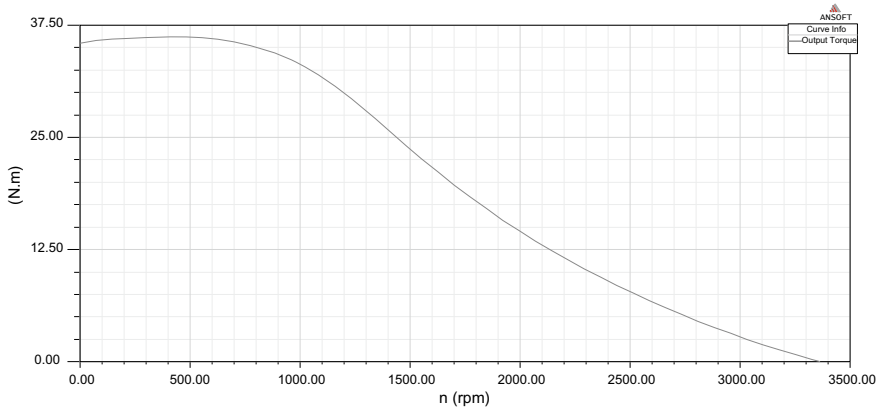

Fig. 7 Output torque versus speed

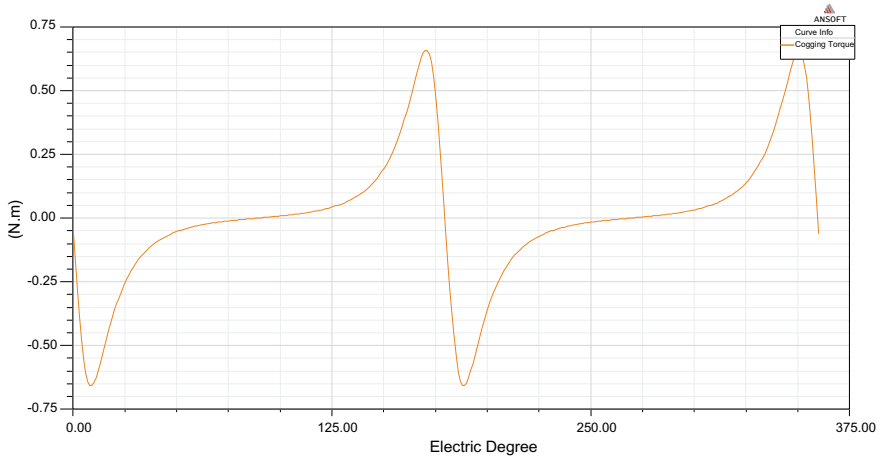

Fig. 8 Cogging torque output

The winding voltages under load conditions are depicted in Fig. 12. The winding voltages are not purely square waves, this waveform has to be enhanced by properly adjusting the lead angle and the drive configuration in the Maxwell circuit editor.

A 2D design is created from the same RMxprt module and the outputs are analyzed. Due to FEA, 2D and 3D analyses provide more accurate results due to meshing.

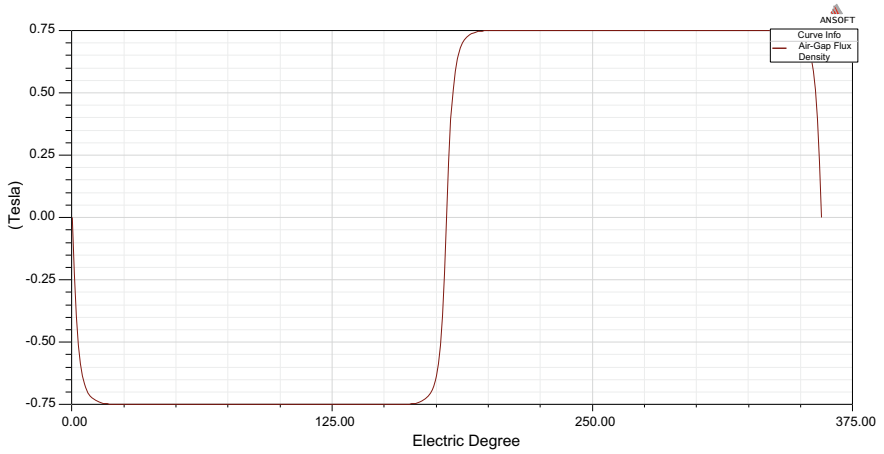

Fig. 9 Air gap flux density

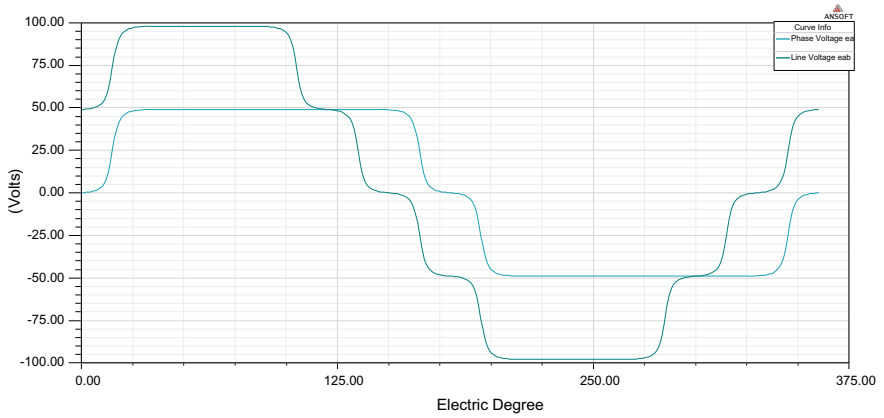

Fig. 10 Induced voltages at rated speed

4.2 Simulation Results Using ANSYS 2D

2D cross-section of the designed motor is depicted in Fig. 13. When the RMxprt module is exported to 2D simulation, then the obtained results are presented next.

The torque output of the designed motor is depicted in Fig. 14. From this figure, it can be observed that the torque output is about 5 Nm as estimated (average), but due to high cogging torque, there is a high rippling that takes place. This is undesirable 72 torque and needs to be reduced. Torque ripple can be reduced by efficient driving methods and skewing.

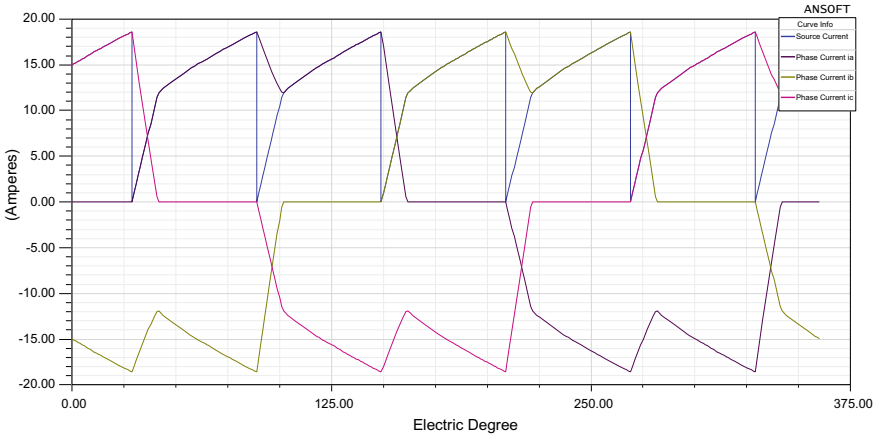

Fig. 11 Winding currents at full load

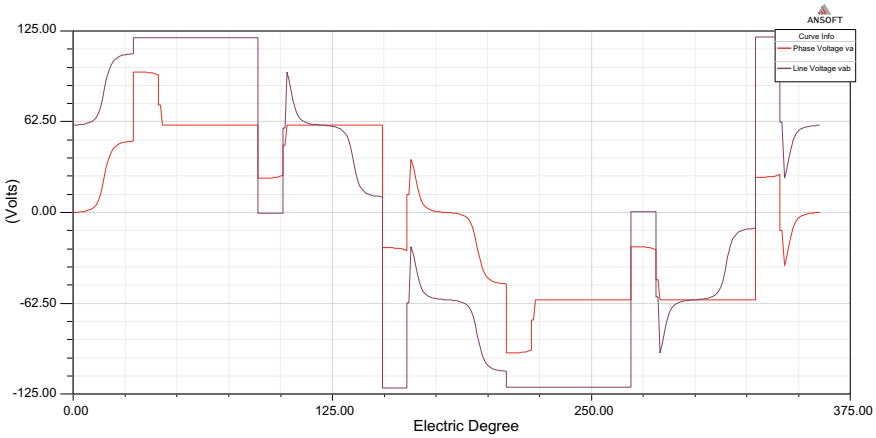

Fig. 12 Winding voltages at full load

Figure 15 depicts the winding currents under load. From this figure, it can be observed that the currents at rated speed, under load, about 13 A average and 12 A rms current.

Here, the simulated results are obtained for the analytically designed motor using FEA software, ANSYS Maxwell. Its modules RMxprt and 2D are used to simulate the motor and obtain more accurate outputs than the ones obtained from analytical calculations.

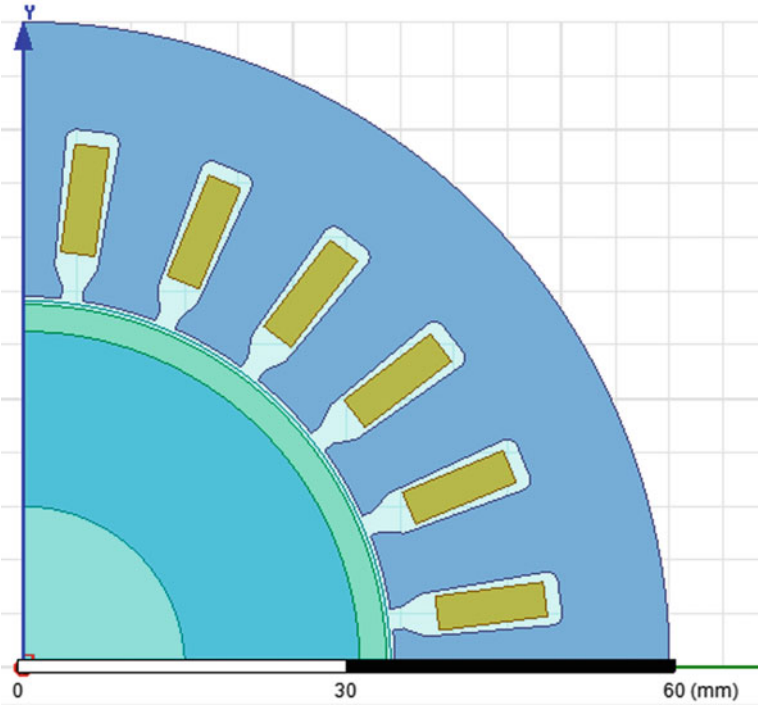

Fig. 13. 2D cross-section of the designed motor

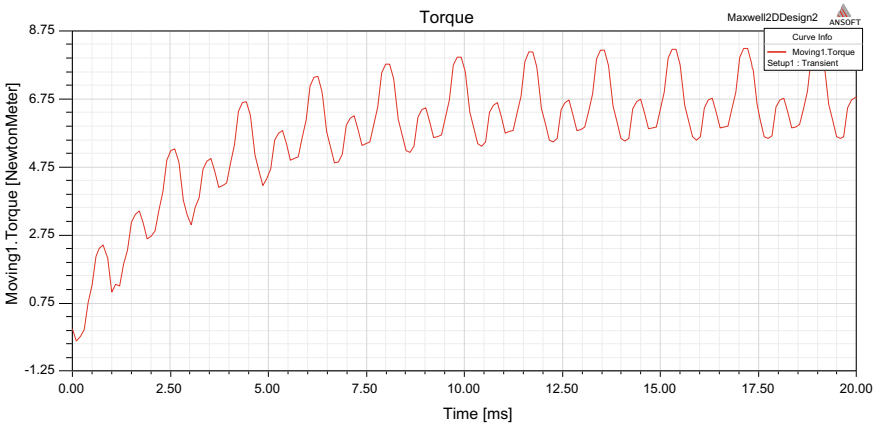

Fig. 14 Torque output

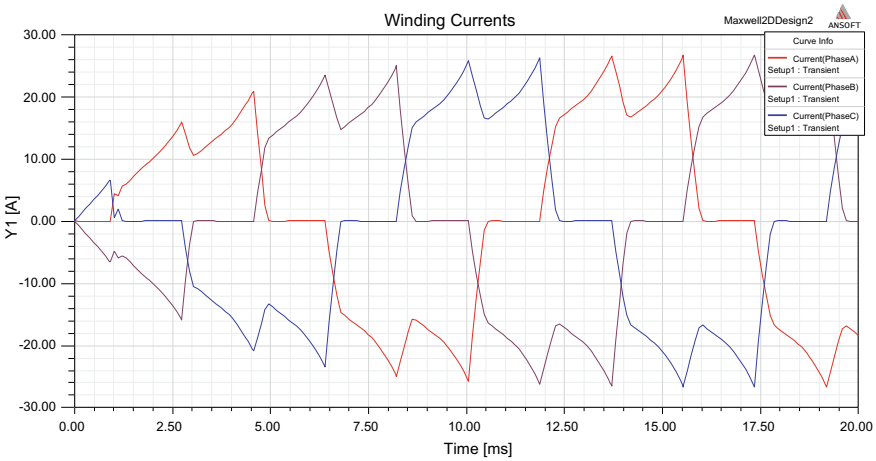

Fig. 15 Winding currents under load

5 Conclusions

This paper has discussed various types of electric vehicles, their powertrains, and the importance of considering the brushless DC motors for traction applications. Based on comparison with other motors, a permanent magnet brushless DC (PMBLDC) motor is set to be designed for traction application, and the power is estimated using a tractive force model in vehicle dynamics. Based on the required parameters, the motor was designed using analytical calculations and the outputs were estimated. The calculations are stopped at the point where the industry gets sufficient data to design and fabricate a motor. The obtained parameters were input into design software like ANSYS Maxwell and the analytical, and 2D parameters were obtained, which gave us an idea of how some variables are varied, making analytical hand calculations inaccurate at certain aspects on how they don't consider a lot of factors such as load. This again proves how simulation software can be more efficient to design a motor. Using a parametric optimization toolbox in ANSYS to optimize the parameters to extract better outputs and testing new magnetic arrangement configurations like Halbach Array to enhance flux density in the air gap is the scope for future research work. This future work can be done to enhance efficiency, reduce losses, and cogging torque.

Acknowledgements This research work was funded by "Woosong University's Academic Research Funding—2022".

References

1. Department of Heavy Industry, Ministry of Heavy Industries & Public Enterprises, Government of India
2. Kumar BVR, Kumar KS (2016) Design of a new dual rotor radial flux Halbach array for an electric vehicle. In: IEEE international conference on power electronics, drives and energy systems, pp 1–5
3. Hsieh M, Lin I, Hsu Y, McMahon RA (2012) Design of brushless doubly-fed machines based on magnetic circuit modeling. IEEE Trans Magn 48(11):3017–3020
4. Krishnan R (2001) Electric motor drives: modeling, analysis and control. Pearson
5. Lee KH, Cha HR, Kim YB (2016) Development of an interior permanent magnet motor through rotor cooling for electric vehicles. Appl Therm Eng 95:348–356
6. Nguyen PH, Hoang E, Gabsi M (2013) Bi-criteria optimization design of an interior permanent magnet synchronous machine for a hybrid electric vehicle application. Math Comput Simul 90:178–191
7. Boldea I, Nasar SA (2002) The induction machine handbook. CRC Press
8. Gieras JF (2010) Permanent magnet motor technology: design and applications, 3rd edn. CRC Press
9. Goss J, Wrobel R, Mellor P, Staton D (2013) The design of AC permanent magnet motors for electric vehicles: a design methodology. In: International electric machines & drives conference, Chicago, IL, pp 871–878
10. Satria A, Farisi V, Rizqiawan A, Heryana N, Purwadi A, Haroen Y (2014) Synthesis modeling of 10 kW BLDC controller for city electric car based on PSIM. In: 2nd IEEE conference on power engineering and renewable energy, Bali, pp 251–256
11. Tatimapula S (2013) Study of a parallel electric hybrid three-wheeled motor taxi. Int J Comput Appl 38–41
12. Hendershot JR, Miller TJE (2010) Design of brushless permanent-magnet motors. Motor Design Books LLC
13. Zhu ZQ, Howe D (2007) Electrical machines and drives for electric, hybrid and fuel cell vehicles. Proc IEEE 95:746–765
14. Raines GB (2009) Electric motor drives for battery, hybrid and fuel cell vehicles. In: Electric vehicles: technology, research and development, Nova Science, New York, pp 1–40
15. Ehsani M, Gao Y, Longo S, Ebrahimi K (2018) Modern electric, hybrid electric, and fuel cell vehicles, 3rd edn. CRC Press
16. Larminie J, Lowry J (2012) Electric vehicle technology explained, 2nd edn. Wiley
17. Buyukdegirmenci VT, Bazzi AM, Krein PT (2014) Evaluation of induction and permanent magnet synchronous machines using drive-cycle energy and loss minimization in traction applications. IEEE Trans Ind Appl 50:395–403
18. Cheng M, Sun L, Buja G, Song L (2015) Advanced electrical machines and machine-based systems for electric and hybrid vehicles. Energies 8:9541–9564
19. Kreuawan S, Gillon F, Brochet P (2008) Comparative study of design approach for electric machine in traction application. Int Rev Electr Eng 3(3):455–465
20. Wang J, Xia ZP, Howe D (2005) Three-phase modular permanent magnet brushless machines for torque boosting on a downsized ICE vehicles. IEEE Trans Veh Technol 54:809–816
21. Gu W, Zhu X, Quan L, Du Y (2015) Design and optimization of permanent magnet brushless machines for electric vehicle applications. Energies 8:13996–14008
22. Sandeep V, Shastri S (2019) Analysis and design of PMBLDC motor for three wheeler electric vehicle application. In: E3S web of conferences, vol 87, pp 1–7
23. [Online] https://www.bajajauto.com/intracityvehicles/bajajre/our-range-compact.html. Last accessed 26 Mar 2021
24. Sheikh MB, Manware PS (2016) Brushless DC motor design for electric traction system. J Res 2(4):18–22

25. Vuddanti S, Karknalli V, Salkuti SR (2021) Design and comparative analysis of three phase, four phase and six phase switched reluctance motor topologies for electrical vehicle propulsion. Bull Electr Eng Inf 10(3):1495–1504
26. Dalcali A (2018) Optimal design of high-performance interior PM motor for electric vehicle. Int J Energy Eng Sci 3(2):26–35
27. Mahmoudi A, Rahim NA, Ping HW (2012) Axial-flux permanent-magnet motor design for electric vehicle direct drive using sizing equation and finite element analysis. Prog Electromagn Res 122:467–496
28. Bhatt P, Mehar H, Sahajwani M (2019) Electrical motors for electric vehicle—a comparative study. In: Proceedings of recent advances in interdisciplinary trends in engineering & applications, pp 1–10
29. Huang C, Lei F, Han X, Zhang Z (2019) Determination of modeling parameters for a brushless DC motor that satisfies the power performance of an electric vehicle. Measure Control 52(7–8):765–774
30. Sandeep V, Shastri S, Sardar A, Salkuti SR (2020) Modeling of battery pack sizing for electric vehicles. Int J Power Electr Drive Syst 11(4):1987–1994
31. Niapour SAKHM, Garjan GHS, Shafiei M, Feyzi MR, Danyali S, Kouhshahi MB (2014) Review of permanent-magnet brushless DC motor basic drives based on analysis and simulation study. Int Rev Electr Eng 9(5)
32. Nugraha YU, Cahyadi A, Yuniarto MN, Sidharta I (2019) Design optimization for torque density in brushless DC motor with IPM V-type using PSO Method. IOP Conf Ser Mater Sci Eng 694:1–8
33. Salkuti SR (2019) Optimal operation of microgrid considering renewable energy sources, electric vehicles and demand response. In: E3S web of conferences, vol 87, pp 1–6
34. Ludois DC (2017) Brushless and permanent magnet free wound field synchronous motors for EV traction, Technical report
35. Guerra AL, Icaza LA, Torres L (2018) Brushless DC motor control with unknown and variable torque load. IFAC-PapersOnLine 51(13):644–649
36. Wang W, Fu R, Fan Y (2018) Electromagnetic parameters matching of permanent magnet synchronous motor for hybrid electric vehicles. IFAC-PapersOnLine 51(31):407–414
37. Ebadpour M, Bagher M, Sharifian B, Babaei E (2018) Modeling and synchronized control of dual parallel brushless direct current motors with single inverter. Comput Electr Eng 70:229–242

D-FACTS-Based Power Quality Enhancement Using Power Balance Theory

Vikash Anand and S. K. Mallik

1 Introduction

Electric users must be provided good quality signal, voltage/current, means great promising power factors, viz., harmonizing with 3-ϕ standards regular system, voltage/current magnitude, harmonic contents, voltage steadiness grade, and system frequency on stated significance. Every so often, users are delivered with deprived power class which leads to harmless, consistent, and proficient equipment operation. Whereas, reduced quality harms result since a range of complaints, for example, voltage/current—sags/swells, glimmer, altered harmonic, disruptions and transitory disturbances because of existence of prominent cause.

European Communities stated that sags (dips) are some decreased voltage below a manipulator termed bounds—flanked in cycle and 2.55 s. Swells (surges) are similar sags, apart from voltage go beyond a manipulator expressed higher edge. Even though innumerable meanings of sag/swell relation toward breadth too period quiet overcome, IEEE 1159-1995 commended run-through continuously observing electric power fineness outlines "*Sag (dip) as a decrease to between 0.1pu and 0.9pu in rms voltage or current at the power frequency for durations of 0.5 cycle to 1 min and Swell as an increase to between 1.1pu and 1.8pu in rms voltage or current at the power frequency for durations from 0.5 cycle to 1 min*" [1–3]. Research framework has discussed that sags/swells may be diminished through various approaches. Usage of tradition power electronics expedient alike FACTS device stays stared as best adept technique [4–6].

V. Anand (✉)
Department of Electrical & Electronics Engineering, SRM Institute of Science & Technology NCR Campus, Ghaziabad, India
e-mail: vikasa@srmist.edu.in

S. K. Mallik
Department of Electrical Engineering, National Institute of Technology Patna, Patna, India
e-mail: skmallik@nitp.ac.in

S. Kumar et al. (eds.), *Recent Advances in Power Electronics and Drives*, Lecture Notes in Electrical Engineering 852, https://doi.org/10.1007/978-981-16-9239-0_25

In late 1980s, Electric Power Research Institute (EPRI) familiarized Flexible AC Transmission Systems (FACTS) by means of innovative methodology for resolving problematic like planning, governing, and functioning power system. Along with improving ability of existing as well as innovative lines, it compromises new possibilities to control power with growing transmission volume, improving voltage regulator, and enhancing system strength. At first in April 19, 1988, FACTS idea was presented by N. G. Hingorani. Continually several FACTS devices such as SVC, STATCOM, DVR, and Static Synchronous Series Compensator have been announced. UPFC leads to best adjustable, proficient, and favorable kind of FACTS device, and it was introduced in 1991. It functions to regulate concurrently all three constraints, viz., voltage, impedance, and phase angle. Research recommends that UPFC efficiently control drift in active/reactive power and progresses voltage contour inside power system [7–10].

Well along, a new FACTS device, DPFC was familiarized to moderate current/voltage aberration and enrich superiority of power. Its configuration is originated from organization of UPFC and comprises a shunt converter and several little self-governing series converters. It works on principle of power theory of non-sinusoidal components. Like UPFC, DPFC is capable to control concurrently, viz., bus voltage, line impedance, and transmission angle. Because of having capability to remove vast dc link between shunt-series converter and establish real power interchange through 3rd harmonic current, it can lead above UPFC [1, 11].

Underneath this framework, this paper validates DPFC operation in single machine of power network comprising two parallel lines in SIMULINK environs. With/without DPFC, performance of voltage/current is analyzed on strife taking place at load side. It observes effervescent operation of system encompassing DPFC control scheme centered d-q axis theory, and PI control is very supportive in forming steady formal.

2 Distributed Power Flow Controller (DPFC)

DPFC has been consequent as of UPFC through eliminating dc linked capacitor amidst UPFCs series-shunt converters, through employing disseminated series converters of numerous elements in succession along line conductor. Power give-and-take way in DPFC is done on power model of non-sinusoidal modules. At altered frequencies active power remains confiscated as of one another, and current/voltage at one frequency haven't been impacted on real power by another frequency. Self-governing real power at altered frequencies offers chance where converter without any power cause is able to produce real power at particular frequency and absorbs it at a different frequency. At fundamental frequency shunt converter is able to captivate real power from line and at harmonic frequency it can inject current into line. Likewise, at fundamental frequency, series converter can insert voltage into line and at the harmonic frequency it captivates active power from line [12]. Figure 1 depicts DPFC positioned in power network of two-bus system.

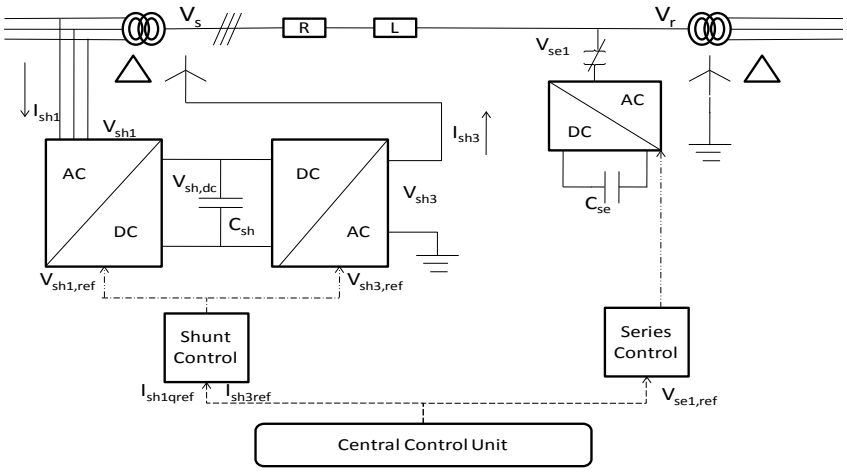

Fig. 1 Simple control circuit diagram of DPFC

Due to change in active power inside DPFC, third harmonic is nominated for the reason that it remains zero-sequence harmonic that may be effortlessly stuck in Δ-winding of transformer. Supplementary, there is a need for a high-pass filter in order to create closed-loop for harmonic current and chunk 1st harmonic current. High-pass filter can remain substituted by cable linked between Δ winding of transformer and ground by using 3rd harmonic. Harmonic present can be routed to pounded through this cable as depicted in Fig. 2 [13].

Shunt converter captivates generated power at fundamental frequency. 3rd harmonic current remains stuck in Y-Δ transformer and are inserted into neutral of Δ-Y transformer by yield point of shunt converter resulting in harmonic current flow through transmission line. Series capacitors' DC voltage is controlled by this harmonic current.

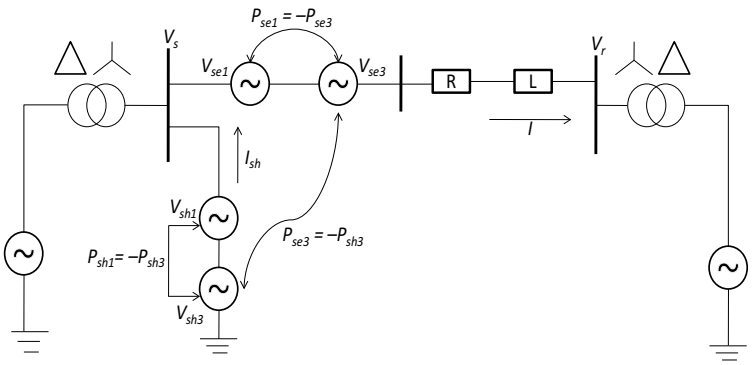

Fig. 2 Single line diagram of DPFC

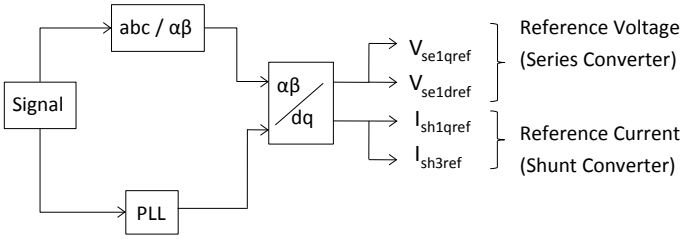

Fig. 3 Simple structure of DPFC central controller

2.1 DPFC Control Mechanism

The three governor schemes of DPFC are Central, Shunt, and Series Control. Each has been discussed below [13, 14].

2.1.1 Central Control

Central controller produces locus pointers for shunt and series converters of DPFC focusing on DPFC functions at level of power system, viz., short frequency power oscillation damping, power flow control, and asymmetrical components toning (Fig. 3).

As per scheme requirements, voltage-reference and reactive current signals for series and shunt converters correspondingly stand given by central controller. All locus pointers are produced by central controller stand by fundamental frequency.

2.1.2 Shunt Control

Shunt controller purposes imparting continual 3rd harmonic current in route for providing real power for series converters. At fundamental frequency, 3rd harmonic current remains sealed along with bus voltage.

PLL is secondhand to seizure bus voltage frequency in directive to generate a simulated spin locus casing for 3rd harmonic constituent, and multiplies this one yield phase signal by 3. Fundamental frequency control of shunt converter purposes to impart manageable reactive current into line and to retain capacitor DC voltage at persistent level. Two flowed controllers are existing to control constituents of 1st frequency. Current control modulating shunt current at fundamental frequency is inner control loop. Components q and d of shunt converters' reference signal stays got from central controller and DC control, respectively [13] (Fig. 4).

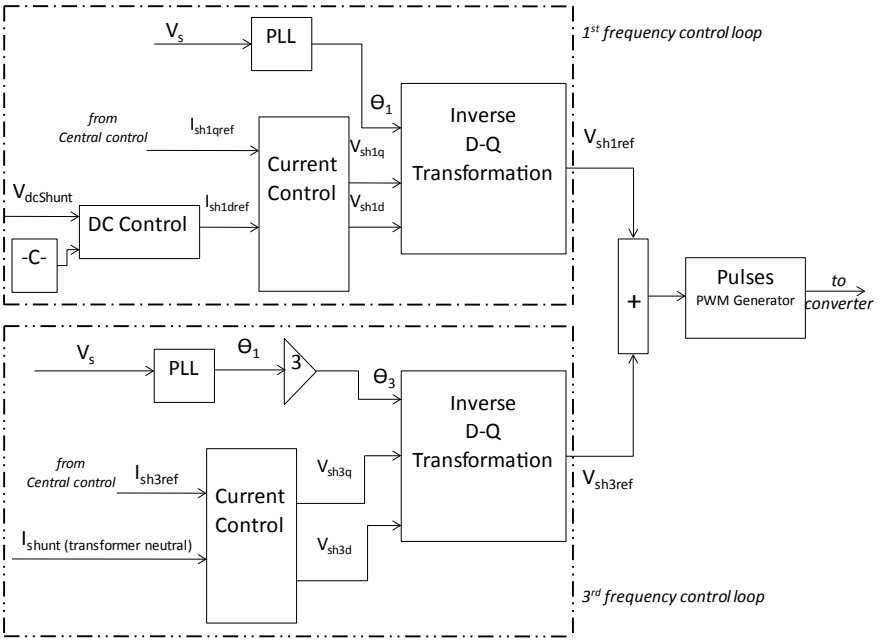

Fig. 4 Simple structure of DPFC shunt controller

2.1.3 Series Control

Separately 1-ϕ converter takes its particular series control over route. Series capacitor voltages, line current, and series voltage reference are positioned controller inputs in d-q frame [14] (Fig. 5).

In series control within DPFC, 3rd harmonic frequency control is prime control loop. Vector control principle is adopted to control dc-voltage. For 1-ϕ park transformation, 3rd harmonic current is designated as spin locus casing. It can stand straight forwardly seized over phase-locked loop (PLL) in series-converter.

3 Performance Study of Demonstrated Results in MATLAB

Non-linear load linked system depicted in Fig. 1 is simulated in SIMULINK block set environment through 3-ϕ source. Load remains linked source via parallel lines I and II of equal length. D-FACTS are integrated in line II independently. Simulink block parameters are enumerated in Appendix. Simulation studies are carried out in imperative to investigate working of DPFC with PI controller for compensation of voltage sag, current swell, and drop in load voltage harmonics at 3-ϕ fault near load side.

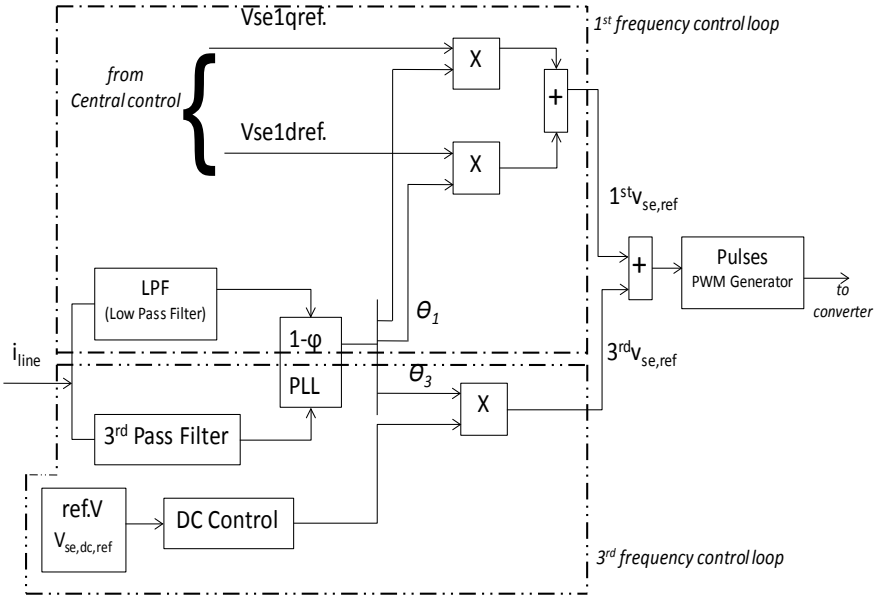

Fig. 5 Simple outline of DPFC's series controller

From simulated results, effect of voltage sag is observed through generating 3-ϕ fault in short of compensator. Time length in lieu of fault stands 0.06 s. (0.06–0.12 s.). Feeder power determines sternness of let fall to 0.5-unit voltage as depicted in Fig. 6.

On employed DPFC, voltage sag mitigation is operative with pintsize transitory spike in fault occurring-diminishing instant. Figure 7 depicts compensated voltage sag waveform.

Due to 3-ϕ fault in power arrangement, current swell is depicted for duration of 0.06 s in Fig. 8.

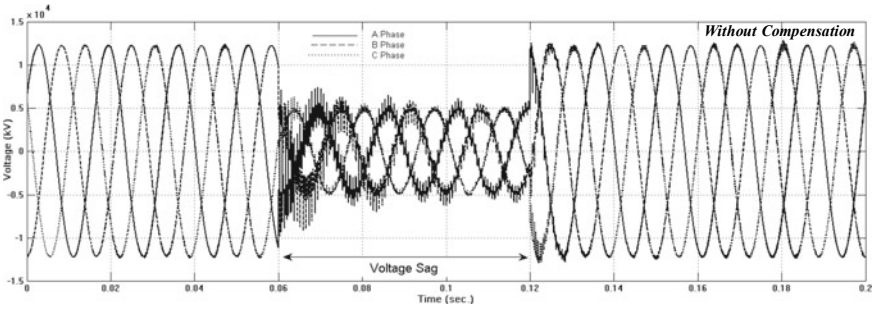

Fig. 6 Load voltage sag in short of compensation

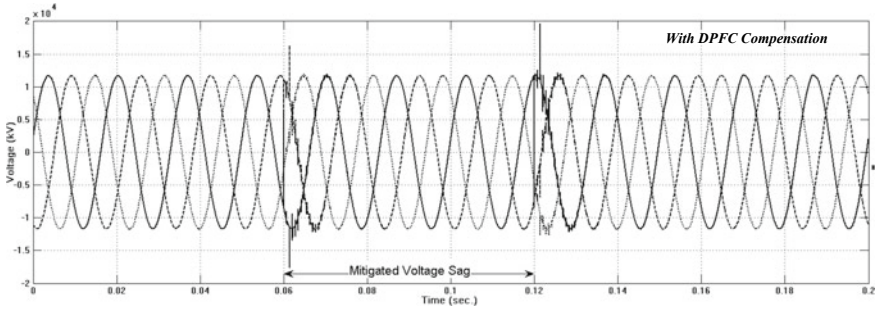

Fig. 7 Mitigated load voltage dip with DPFC

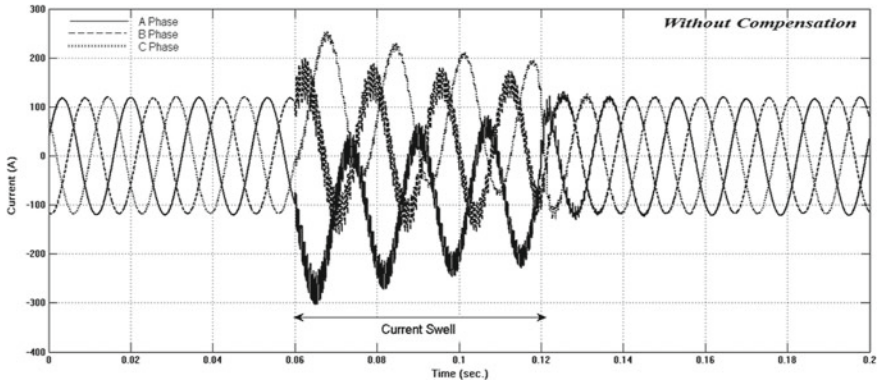

Fig. 8 Load current swell without compensation

It is noticeable point that with DPFC compensator line current swell is diminished with spikes at beginning-ending of fault duration. It is depicted in Fig. 9. Mitigated current swell is found in better quality with DPFC compensator.

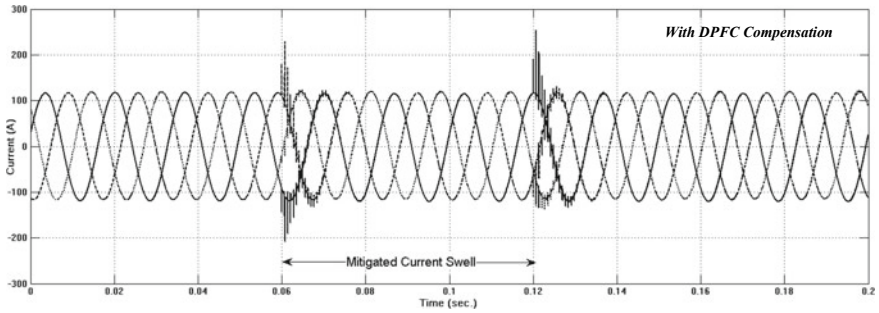

Fig. 9 Mitigated load current swell with DPFC

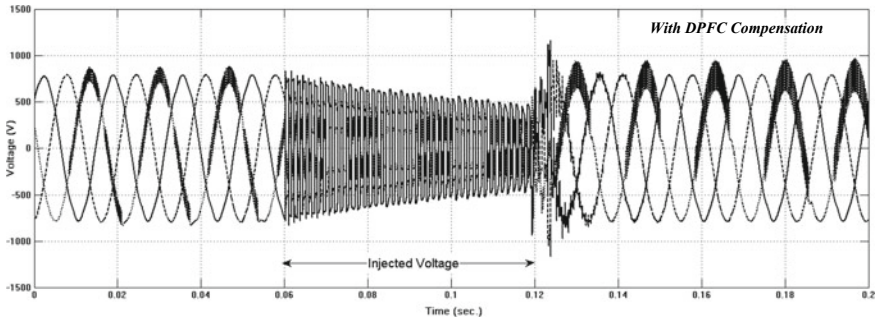

Fig. 10 Injected voltage of series converters in fault line2 for duration of 0.06 s

Fig. 11 Load voltage's THD (total harmonic distortion) deprived of compensation

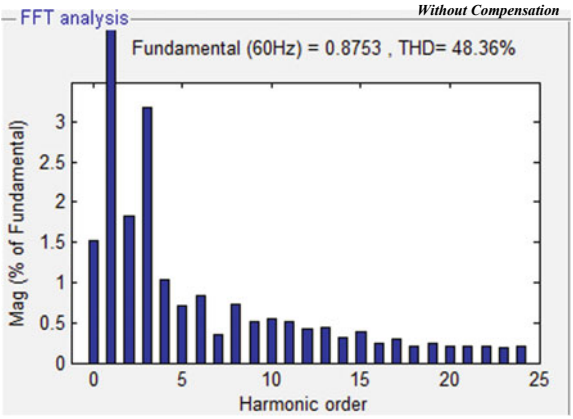

At fault occurring instant, line2's series converters inject voltage in fault line to maintain the required bus voltage and stops after clearing the fault, which has been depicted in Fig. 10.

Load voltage harmonics study, Fast Fourier Transform (FFT) is validated through figures. Figure 11 illustrates load voltage harmonics short of compensator.

On unification D-FACTS compensator, even harmonics stay eradicated while odd harmonics are abridged to adequate edge specified in THD of IEEE standards, i.e., below 5% [15]. It is shown in Fig. 12.

The respective THD ethics of load voltage are specified in Table 1.

From Table 1, load voltage THD is decreased to large extent on employment of DPFC compensator. Therefore, simulation outcomes authenticate DPFC capability to recover power excellence in better extent with wild vigorous reaction.

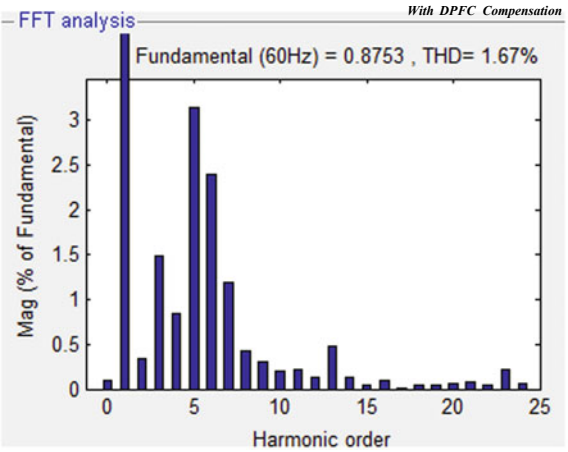

Fig. 12 Load voltages' total harmonic distortion (THD) using DPFC compensation

Table 1 Total harmonic distortion (THD) of load voltage

THD of load voltage	Without compensation	With DPFC
Value in percentage	48.36%	1.67%

4 Conclusion

The results clearly show that at 3rd harmonic frequency, real power can be swapped via line through shunt-series converters in DPFC. Controllable active-reactive power may also stay filled by series converters at fundamental frequency. Redundancy of series converter and non-requisite of the high-voltage segregation with low rating of components clue to better reliability and lower cost of DPFC. Simulation results—mitigated voltage sag, mitigated current swell and reduced harmonic distortion, confirmations efficacy of DPFC in power quality enhancement. It tips to improvement in stability and quality of power system encompassing DPFC with D-Q axis mechanism.

Appendix

The investigation system in use aimed at simulation study of mounted DPFC in solitary machine of power arrangement. This arrangement is comprised of two parallel transmission line with load in MATLAB. Structure facts considered for validation in simulation exist like this in Table 2 [2, 16].

Table 2 System figures in simulink

System components	Parameter	Ratings
Three-phase source	Transmission voltage	220 kV
	Power/Frequency	110 MW/60 Hz
	X/R	3
	Short circuit capacity	11 GW
Transmission line	Resistance	1/100 pu/km
	Inductive and capacitive Reactance	12/100 pu/km
	Line length	100 km
Unsymmetrical fault	Fault type	ABC- G
	Ground resistance	0.05 Ω
DPFC		
Shunt converter 3-φ	Nominal power	60 MVAR
	DC linked capacitor	600 μF
Coupling transformer (shunt)	Nominal power	100 MVA
	Voltage rating	220 kV/11 kV
Series converter 1-φ	Nominal power	6 MVAR
	Voltage rating	6 kV

References

1. Omar R, Rahim NA, Sulariman M (2009) Modelling and simulation for voltage sag/swell mitigation using dynamic voltage restore (DVR). J Theoret Appl Inf Technol 5(4):464–470
2. Barakati SM, Sadigh AK, Mokhtarpour E (2011) Voltage sag and swell compensation with DVR based on asymmetrical cascade multicell converter. In: North American Power Symposium (NAPS), pp 1–7
3. Jamshidi A, Barakati SM, Ghahderijani MM, Power quality improvement and mitigation case study using distributed power flow controller. Case 978-1-4673-0158-9/12/$31.00. IEEE pp 464–468
4. Round SD, Yu Q, Norum LE, Underland TM (1996) "Performance of unified power flow controller using a d-q control system", conference publication No. 423 of the IEE sixth international conference on AC and DC power transmission, London, pp 357–362, April–May
5. Edris A-A (1997) Proposed terms and definitions for flexible AC transmission system (FACTS). IEEE Trans Power Delivery 12(4):1848–1853
6. Nita I, Patne R, Thakre KL (2008) Factor affecting characteristics of voltage sag due to fault in the power system. Serbian J Electr Eng 5(1):171–182
7. Gyugui L, Schauder CD, Williams SL, Rietman TR, Torgerson DR, Edris A (1995) The unified power flow controller: a new approach to power transmission control. IEEE Trans Power Delivery 10(2):1085–1097
8. Papic I, Zunko P, Pouh D, Weinhold M (1997) Basic control of unified power flow controller. IEEE Trans Power Syst 12(4):1734–1739
9. Padiyar KR, Kulkarni AM (1997) Control design and simulation of a unified power flow controller. IEEE Trans Power Delivery 13(4):1346–1354
10. Hingorani NG, Gyugyi L (2000) Understanding FACTS, concepts and technology of flexible AC transmission system. Institute of Electrical and Electronics Engineers

11. Singh P, Tiwari R (2017) Amalgam power flow controller: a novel flexible, reliable and cost effective solution to control power flow. IEEE Trans Power Syst. https://doi.org/10.1109/TPWRS.2017.2764954
12. Yuan Z, Sjoerd WHDH, Braham F, Dalibar C (2010) A FACTS device: distributed power flow controller (DPFC). IEEE Trans Power Electron 25(10):1085–1097
13. Anand V, Mallik SK (2018) Power flow analysis and control of distributed FACTS devices in power system. AEE 67(3):545–561
14. Anand V, Mallik SK (2019) Introducing supplementary control scheme to DPFC during series converter failure. JEAS 14(7):2124–2134
15. http://www.schneider-electric.com.tw/documents/Event/2016_electrical_engineering_seminar/IEEE_STD_519_1992vs2014.pdf. Accessed Nov 2020
16. Dwivedi OP, Singh JG, Singh SN (2004) Simulation and analysis of unified power flow controller using SIMULINK. In: National power systems conference, NPSC 2004, IIT, Madras, Dec. 27–30, pp 1048–1054
17. Zhang R, Cardinal M, Szczesny P, Dame M (2002) A grid simulator with control of single-phase power convertors in D-Q rotating frame. In: Power electronics specialists conference (PESC), IEEE, Australia, pp 1431–1436

Design and Implementation of Electrical Dynamic Braking System in Electric Car Using Buck Converter

Walid Alqaisi and Claude Ziad El-Bayeh

1 Introduction

Conventional vehicles that run on fossil fuels contribute to the global warming phenomenon, as a result, they have negative environmental impacts. The electric vehicle is gaining popularity as a promising alternative.

As a conventional system, the hydraulic car braking drives the static brake pad against the brake drum. A friction force, which retards the vehicle movement, is produced between them. Recently, Electrical Brake (EB) systems in electric vehicles (EVs) have drawn the attention of researchers for their advantages in real applications. The development of power converters nowadays plays a big part in improving the controllability of EBs. EB systems are eco-friendly because they don't contain copper, mercury, lead, cadmium, and chromium, unlike hydraulic brake pads which are harmful materials. Fine particles these metals flake off on our roadways, then flow into our rivers and lakes when it rains [1]. The EB system is able to provide a low-cost large braking force using only a relatively small electrical energy. Pulse-Width Modulation (PWM) provides control and regulation of the total output DC voltage. Compared to traditional hydraulic braking components, EBs have a compact design and better braking performance. Furthermore, the torque developed from an EB is faster than a hydraulic braking system by 10–100 times [2].

An EB is an electro-mechanical system that requires a precise control system in order to develop a safe and reliable braking force. In [3], a gain-scheduled nonlinear PI controller is designed to regulate a tire slip in an EB system. In [4], monitoring the behavior of the rear wheels is utilized to estimate tire slips in an antilock brake system (ABS). In [5], an adaptive EB which is changing with driving and road conditions is designed. The three-phase AC output of the inverter is used to drive and stop

W. Alqaisi (✉)
School of Engineering Technology, College of the North Atlantic - Qatar, Doha, Qatar

C. Z. El-Bayeh
Canada Excellence Research Chairs Team, Concordia University, Montreal, Canada

S. Kumar et al. (eds.), *Recent Advances in Power Electronics and Drives*, Lecture Notes in Electrical Engineering 852, https://doi.org/10.1007/978-981-16-9239-0_26

the motor [6]. Although the good performance of the mentioned system, simpler approaches can be used with similar results.

In [7], the braking of an induction motor is analyzed for different values of electronics parts. A Braking scheme for a Six-phase induction motor is used in [8]. A braking approach for squirrel-cage induction motors is demonstrated using a three-phase rectifier [9]. A Regeneration during deceleration is designed for an electric vehicle [10]. Generative energy storage using bidirectional power conversion is used in [11], where the converter's output is fixed and it is not a variable, which makes the selection of fast or smooth braking not possible for an operator to choose.

In electric vehicle braking operation, induction motor braking is mainly of three types [12]: Regenerative braking, Plugging Braking, and Dynamic braking. Regenerative braking of an induction motor is possible if the motor's speed is higher than the synchronous speed. The first method is suitable for other applications, while the second method generates a very high current. It is found that DC dynamic braking is the most suitable method for electrical braking. Figure 1 shows the structure of the overall system.

The main highlighted points in this paper are:

- The proposed system uses a buck controller for its simplicity.
- An induction motor braking is selected because it produces less heat than other braking types.
- Motor braking voltage is variable as desired and controlled by a PID controller.
- It is not required to know the exact dynamic model and the application can be applied to other satiations and applications.
- The entire system's advantages are high precision, low cost, and high reliability.

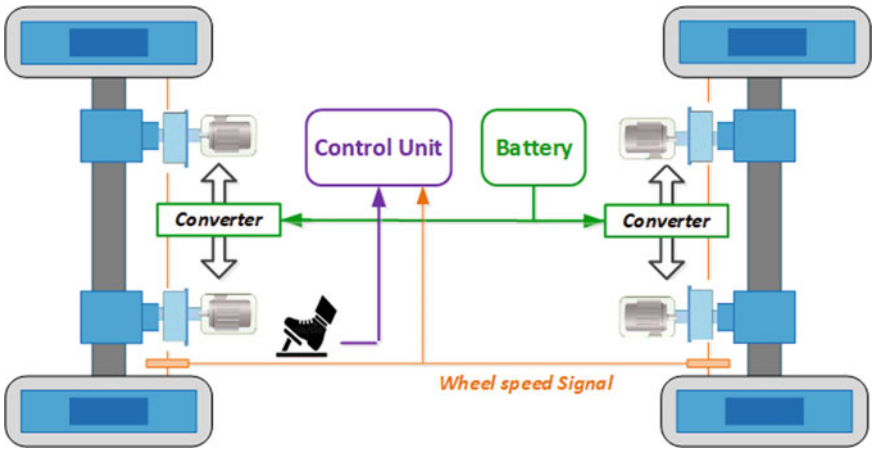

Fig. 1 Electric braking system

This paper is presented as follows. Section 2 demonstrates the buck converter design. Section 3 clarifies control design formulation. Section 4 describes the calculation of braking design and braking travel time. Section 5 explains the electric braking system. Section 6 presents Matlab/Simulink simulation and Sect. 7 concludes the paper.

2 Proposed Design of the DC to DC Buck Converter

The structure of the used converter is shown in Fig. 2. The designed converter is built to provide stable regulated output. Voltage value, PWM width, and frequency are the controller parameters, while the speed of the vehicle and the time to stop are the braking parameters. The Buck converter is a step-down converter consisting of a low-pass LC filter. The capacitor is in parallel with the load. The inductance prevents high current spikes. The free-wheeling diode is added to absorb the inductor's current momentum. Correct design of the components allows high-frequency switching.

The operation of the circuit involves open and closed conditions of the insulated-gate bipolar transistor (IGBT). During the charging period, the capacitor voltage moves from the minimum to the maximum. The function of the capacitor is to regulate the output voltage ripples, noting that large capacitance causes spikes in the source current when the transistor opens. Capacitor selection is given as [13]

$$C = \frac{LI_{L,max}^2}{(V_{out} + \Delta V_{out,overshoot})^2 - V_{out}^2} \tag{1}$$

where L is the inductor value, V_{out} is the output voltage, $\Delta V_{out,overshoot}$ is the peak overshoot voltage allowed on the output, $I_{L,max}^2$ is the peak inductor current.

The inductance prevents a high current spike in addition to providing current at the off-state of the IGBT. Inductor current never reaches zero, it is ranging from I_{min}

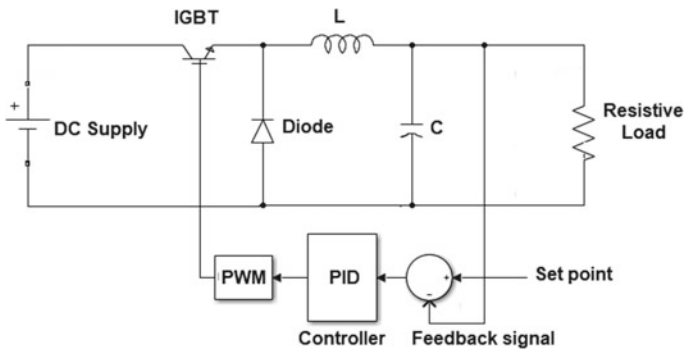

Fig. 2 System block diagram

to I_{max}. Peak to peak current is $\Delta I_L = I_{max} - I_{min}$ and I_{Avg} is the average current. The value of the capacitance is selected as [14]

$$L = \frac{(V_{in} - V_{out})V_{out}}{V_{in} F_{sw} \Delta I_L} \tag{2}$$

where V_{in} is the input voltage, V_{out} is the output voltage, F_{sw} is the switching frequency (Hz), L is the inductance in Henry (H).

3 Control Design

Circuit analysis is based on the two switching states of the circuit, on-state and off-state as shown in Fig. 3.

During the on-state condition, Fig. 3a, the circuit is analyzed as follows:

$$L\frac{di_L}{dt} = v_g(t) - v_c(t) \tag{3}$$

In the same way, for the capacitor current

$$C\frac{dv_c}{dt} = i_l(t) - i_o(t) \tag{4}$$

Then we can write

$$\frac{dv_c}{dt} = \frac{i_l(t)}{C} - \frac{i_o(t)}{C} \tag{5}$$

$$\frac{dv_c}{dt} = \frac{i_l(t)}{C} - \frac{v_o(t)}{RC} \tag{6}$$

Equations (3) and (6) can be written in state space form as

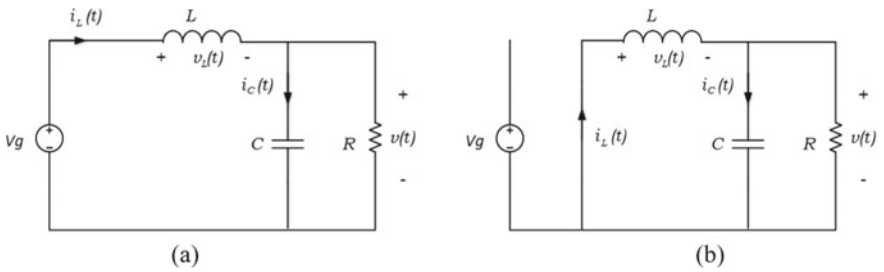

Fig. 3 On-state **a** and off-state **b** of the DC power converter

$$\begin{bmatrix} \frac{di_l}{dt} \\ \frac{dv_c}{dt} \end{bmatrix} = \begin{bmatrix} 0 & \frac{-1}{L} \\ \frac{-1}{C} & \frac{-1}{RC} \end{bmatrix} \begin{bmatrix} i_l(t) \\ v_c(t) \end{bmatrix} + \begin{bmatrix} \frac{-1}{L} \\ 0 \end{bmatrix} [v_g] \tag{7}$$

Then it can be written in the state space form as

$$\dot{x} = A_{on} + B_{on}u \tag{8}$$

where

$$x = \begin{bmatrix} i_l(t) \\ v_c(t) \end{bmatrix}, A_{on} = \begin{bmatrix} 0 & \frac{-1}{L} \\ \frac{-1}{C} & \frac{-1}{RC} \end{bmatrix}, B_{on} = \begin{bmatrix} \frac{-1}{L} \\ 0 \end{bmatrix}, u = v_g$$

During the off-state condition, Fig. 3b, the transistor is open, and the load current is supplied by the stored energy in the inductor, with the circuit completed by the diode. The circuit can be analyzed as follows:

During this time, inductor voltage is

$$v_l(t) = -v_c(t) \tag{9}$$

$$\frac{di_l}{dt} = \frac{-v_c(t)}{L} \tag{10}$$

In the same way, for capacitor current

$$i_c(t) = i_l(t) - i_o(t) \tag{11}$$

Then, we can write

$$\frac{dv_c}{dt} = \frac{i_l(t)}{C} - \frac{v_o(t)}{RC} \tag{12}$$

Equations (10) and (12) can be written in the state space form as follows:

$$\begin{bmatrix} \frac{di_l}{dt} \\ \frac{dv_c}{dt} \end{bmatrix} = \begin{bmatrix} 0 & \frac{-1}{L} \\ \frac{-1}{C} & \frac{-1}{RC} \end{bmatrix} \begin{bmatrix} i_l(t) \\ v_c(t) \end{bmatrix} + \begin{bmatrix} 0 \\ 0 \end{bmatrix} [v_g] \tag{13}$$

Then, it can be written in the state space form as given below

$$\dot{x} = A_{off}x + B_{off}u \tag{14}$$

where

$$x = \begin{bmatrix} i_l(t) \\ v_c(t) \end{bmatrix}, A_{off} = \begin{bmatrix} 0 & \frac{-1}{L} \\ \frac{-1}{C} & \frac{-1}{RC} \end{bmatrix}, B_{off} = \begin{bmatrix} 0 \\ 0 \end{bmatrix}, u = v_g$$

The converter is controlled by the pulse width modulator (PWM) signal. The converter on-time is in the time interval $t_{on} = Td_n$ and the converter off-time $t_{off} = T(1 - d_n)$. The state space form is given as follows:

$$\dot{x} = \big(A_{on}d(t) + A_{off}(1 - d_n)\big)x + \big(B_{on}d(t) + B_{off}(1 - d_n)\big)u \tag{15}$$

The widely used controller, PID, is utilized where the tracking error is fed to the PID controller which computes the proportional, derivative, and integral error signal. The output of the PID controller $u(t)$ applied to the plant is given as

$$u(t) = K_p e(t) + K_i \int e(t)dt + K_d \frac{de(t)}{dt} \tag{16}$$

where K_p, K_i, and K_d are the integral, proportional, and derivative gains, respectively.

4 Calculation of Braking Travel Time

The function of the proposed system is to provide the three-phase winding with a stationary magnetic field ϕ to set up in the stator bore. This magnetic field causes a voltage charge to be induced in the cage-rotor bars as long as the motor rotor is moving. When motor speed is reduced, induced voltage frequency, as well as the inductive impedance, falls. Braking torque is approximately equal to the rated motor torque on average. Braking current I_{DC} is nearly 2–2.5 times of the rated motor current I_N, i.e.

$$I_{DC} = 2.5I_N \tag{17}$$

Higher I_{DC} values produce harder dynamic braking as in Fig. 4, where $I_{DC1} > I_{DC2} > I_{DC3}$, while softer braking occurs for lower current values. Lowering the controlled voltage is required if harsh braking is experienced during practical implementation. It is complicated to calculate braking time because of the nonlinearity of involved parameters such as the changes of the mechanical load, inertia, motor r.p.m, rated current, and pulses. Velocity to current curve is shown in Fig. 4. The kinetic energy of the rotating parts is equal to the dissipated rotor losses, and the braking torque is proportional to the square of the dc braking current. The electrical resistance of motor windings is very low. Thus, a small injected voltage creates a high current. Such current generates a solid braking effect on motor bars and the rotor. Figure 5 shows that the reverse torque falls to zero as speed reduces to stand still. Braking torque is shown in Fig. 5 [15], where M is the instantaneous braking torque, M_{av} is the average value of the braking torque, n is motor speed, n_{sy} is the synchronous speed. As velocity dropped down, the motor ohmic resistance turned

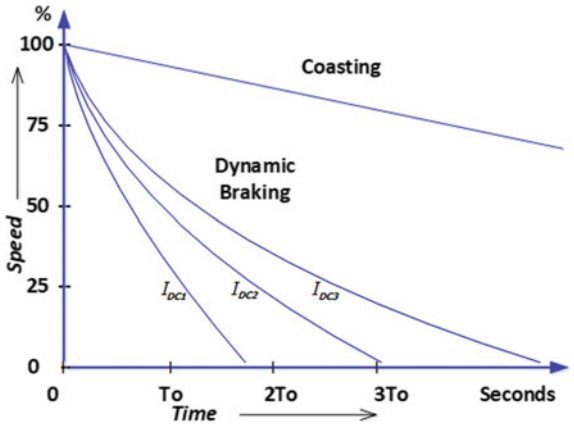

Fig. 4 Current—r.p.m curve for a fixed load

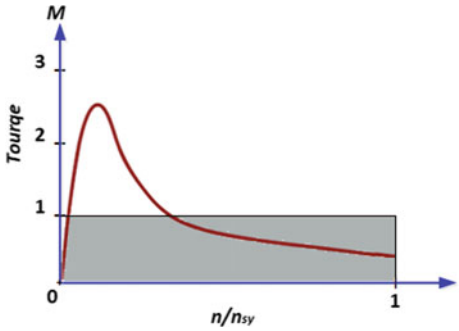

Fig. 5 Current—r.p.m curve for a fixed load

to be more dominant which will strengthen the braking force. This braking torque falls away and finishes when there is no further movement.

5 Electric Brake Systems

Electric braking (EB) systems are environment-friendly because they do not use hydraulic parts or any mechanical disks. Brake pads in cars contain copper, mercury, lead, cadmium, and chromium which are harmful materials that flow into our rivers and lakes when it rains [1]. An EB is able to provide a safe and large braking force. To generate a proper braking force, induction motors are used due to their efficiency and durability. In addition, induction motors have high efficiency-to-size characteristics when compared to other types of motors which must be larger for the same efficiency. They are connected to each wheel and controlled by a PID closed-loop controller where the desired braking force is proportional to the output of the converter. The

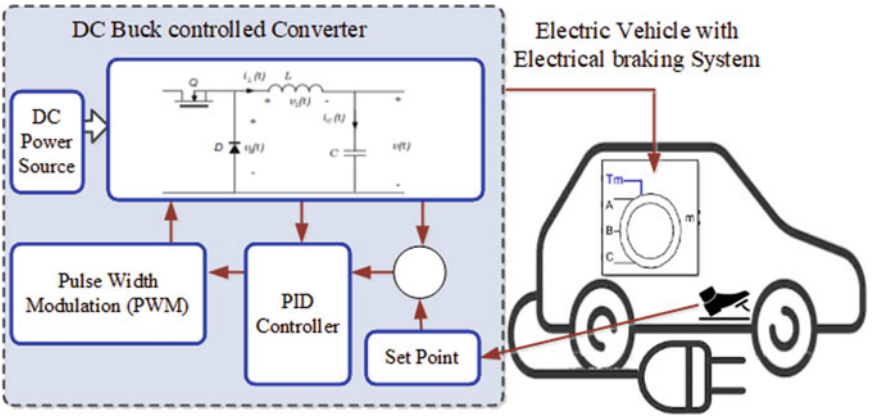

Fig. 6 The block diagram of the system

value of the setpoint is proportional to the vehicle speed in order to have smooth braking as the speed is being reduced.

The structure requires velocity continuous measurement. The block diagram of the control system is shown in Fig. 6, while the overall system is shown in Fig. 1.

6 Simulation

The simulation was performed using Matlab/Simulink in three parts built as shown in Figs. 7 and 10. A variable desired voltage is expected to enter the controller, thus the buck converter in Fig. 7 was tested for a voltage changing from ten to zero volts as in Fig. 8 and for a fixed voltage as in Fig. 9. The desired voltage in the system is a function of the tire's r.p.m.

The second part was simulated by using an induction motor model provided by the Simscape tool in Matlab Simulink as in Fig. 10. Testing was performed on three time sequences, at first, the motor is driven to the nominal speed ω_n, then the power is disconnected letting the speed decrease gradually. At the third stage, DC braking is applied at $V_{DC} = 14, 10, 6.3$ V, as a result, different baking forces are obtained which led to a complete stop at different times as in Fig. 11. The first stage ends at $t_1 = 0.5$ second, the second stage ends at $t_2 = 1$ second, while the third stage ends when the speed reached zero at t_3.

The stator current is an important factor to consider, a higher value of stator current for a long time can damage the windings. Figures 12, 13, 14 show the stator currents for $V_{DC} = 14, 10, 6.3$, respectively. Braking currents peak at $t_2 = 1$, but they remain within the acceptable range. Note that I_1, I_2, and I_3 are the stator winding currents.

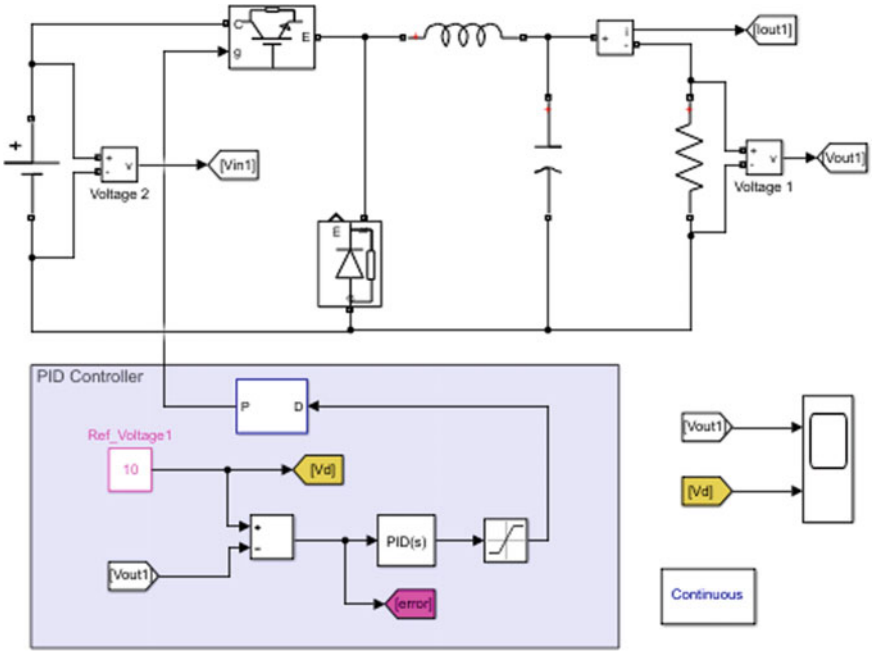

Fig. 7 The buck DC converter in simulink

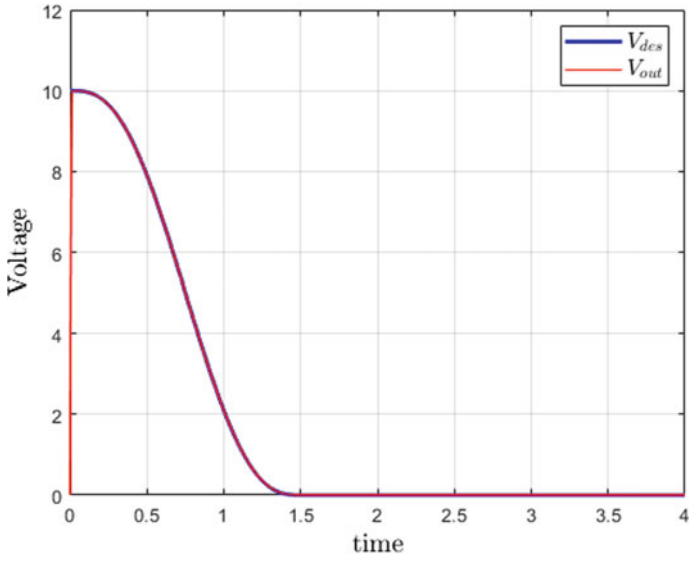

Fig. 8 Testing the converter for a variable desired voltage

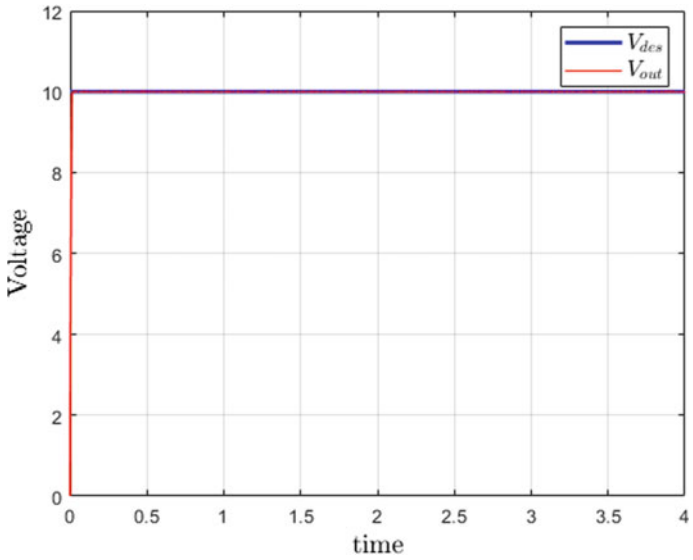

Fig. 9 Testing the converter for a fixed desired voltage

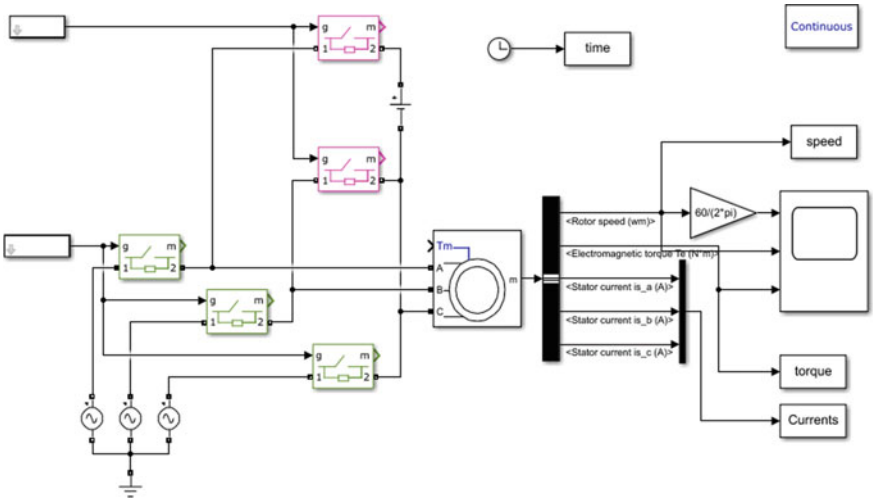

Fig. 10 Induction motor braking simulink model

The Proposed Scheme

Simulation results show braking travel time achieved at $t = [1 - 3.5]$ seconds, which means that 2.5 s to come to a complete stop (Fig. 15). The buck converter controls the voltage as in Fig. 16, where a high shock happens when braking starts at $t = 1$ second, and then it returns to stability quickly. Then the controller reduces the voltage

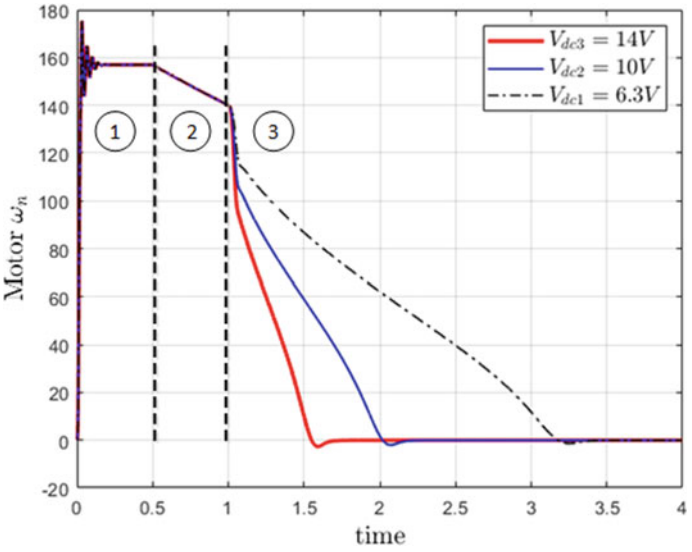

Fig. 11 Testing was performed on three time sequences

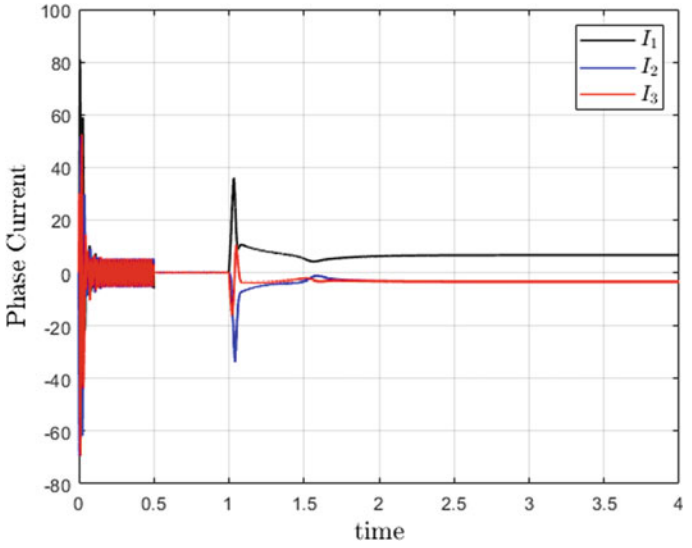

Fig. 12 Induction motor winding currents for $V_{DC} = 14$

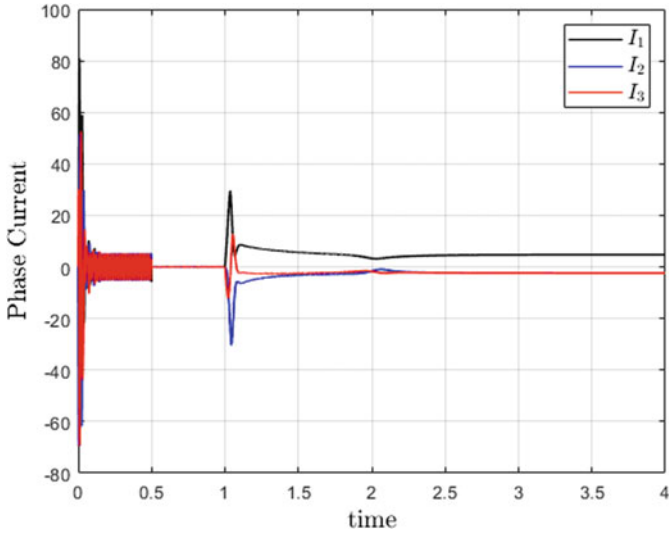

Fig. 13 Induction motor winding currents for $V_{DC} = 10$

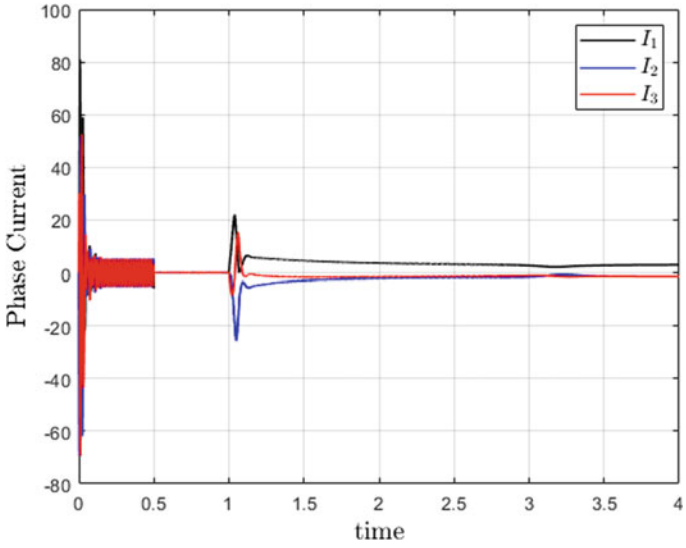

Fig. 14 Induction motor winding currents for $V_{DC} = 6.3$

to zero in order to prevent unnecessary stator current. The stator currents are shown in Fig. 17, it can be seen that the condition in Fig. 16 is met where the braking current remains in the acceptable limit.

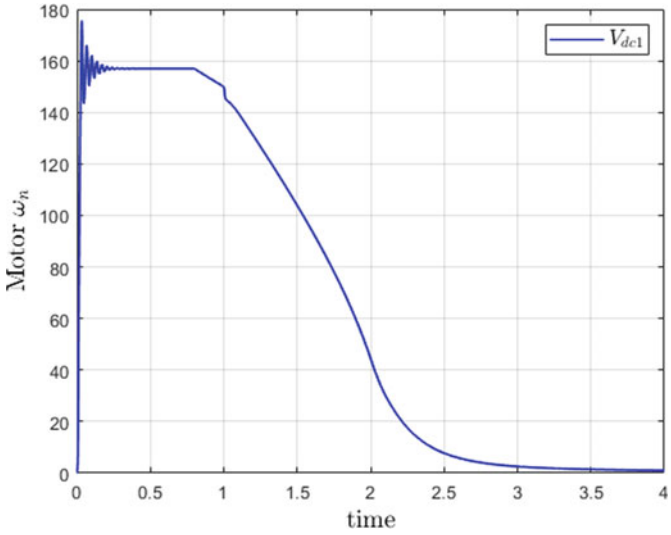

Fig. 15 Braking travel time

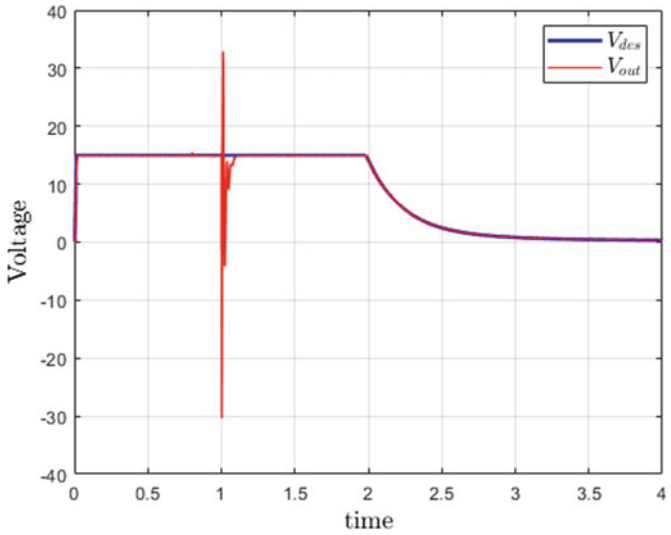

Fig. 16 Buck converter regulated voltage

7 Conclusion

In this paper, we proposed a design of closed-loop control of pulse width modulated DC Buck converter with a PID controller for an electrical braking system in an electric car. This system is the future development of braking moving vehicles for its

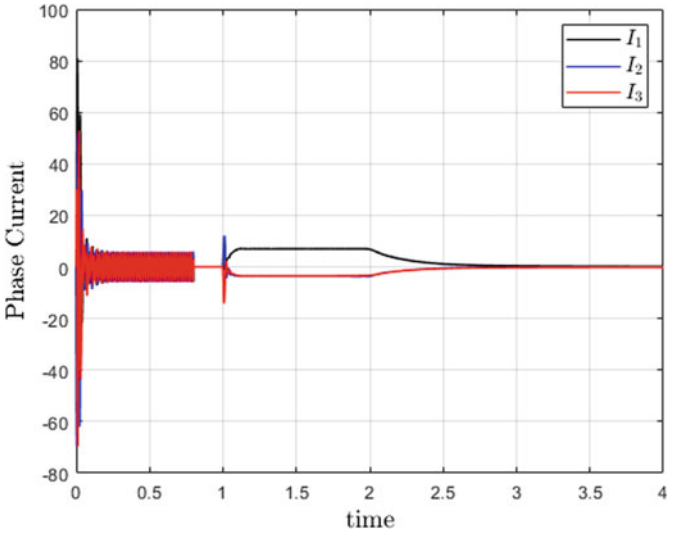

Fig. 17 Stator current in the three windings

advantages, i.e., the designed system provides a strong braking force and it is environmentally friendly, unlike conventional systems. On the other hand, the strong brake force allowed controlling the stop time. The system was analyzed mathematically and simulated by Matlab/Simulink in order to prove its efficiency.

References

1. The hidden pollutant in our brake pads|Environment Canterbury. https://www.ecan.govt.nz/get-involved/news-and-events/2018/the-hidden-pollutant-in-our-brake-pads/. Accessed 31 Jan 2021
2. Solyom S, Rantzer A (2014) Synthesis of a model-based tire slip controller. Taylor Fr 41(6):475–499. https://doi.org/10.1080/004231105123313868
3. Zhang L, Li L, Lin C, Wang C, Qi B, Song J (2014) Coaxial-coupling traction control for a four-wheel-independent-drive electric vehicle on a complex road. Proc Inst Mech Eng Part D J Automob Eng 228(12):1398–1414
4. Choi SB (2008) Antilock brake system with a continuous wheel slip control to maximize the braking performance and the ride quality. IEEE Trans Control Syst Technol 16(5):996–1003
5. Dousti M, Baslamısli SC, Onder ET, Solmaz S (2015) Design of a multiple-model switching controller for ABS braking dynamics. Trans Inst Meas Control 37(5):582–595
6. Awari P, Sawarkar P, Agarwal R, Khergade A, Bodkhe S (2017) Speed control and electrical braking of axial flux BLDC motor. In: 2017 6th international conference on computer applications in electrical engineering—recent advances, CERA 2017, Apr. 2018, vol. 2018-January, pp 297–302. https://doi.org/10.1109/CERA.2017.8343344
7. Singh R, Umashankar S, Vijaykumar D, Kothari DP (2013) Dynamic braking of induction motor-Analysis of conventional methods and an efficient multistage braking model. In: 2013 international conference on energy efficient technologies for sustainability, pp 197–206

8. Duran MJ, Gonzalez-Prieto I, Barrero F, Mengoni M, Zarri L, Levi E (2015) A simple braking method for six-phase induction motor drives with diode front-end rectifier. In: IECON 2015–41st annual conference of the IEEE industrial electronics society, pp 1542–1547
9. Rata M, Rata G (2016) Study solution of induction motor dynamic braking. In: 2016 international conference on development and application systems (DAS), pp 33–37
10. Mahapatra AA, Gopalakrishna S (2014) Regenerative braking in induction motor drives in applications to Electric Vehicles. In: 2014 IEEE students' conference on electrical, electronics and computer science, pp 1–5
11. Agrawal SK, Kumar V, Alam A, Thakura P (2014) Regenerative braking for induction motor drive. In: 2014 6th IEEE power India international conference (PIICON), pp 1–6
12. Induction motor braking regenerative plugging dynamic braking of induction motor|Electrical4U. https://www.electrical4u.com/induction-motor-braking/. Accessed 11 Mar 2021
13. Maimone G (2010) Selecting l and c components in the power stage of the mc34700 switching regulators. Free. Semicond. Appl. Note AN4067
14. Mondal A (2014) Digital PID controller design for DC-DC buck converter
15. Gear T, Specialist M, Starting, braking and positioning with three-phase cage induction motors

A Reduced Device Count of Self Balancing Five-Level Switched Capacitor-Based Grid-Connected Inverter

Aratipamula Bhanuchandar and Bhagwan K. Murthy

1 Introduction

In Renewable Energy Source (RES) applications, the Multilevel Inverters (MLIs) are very popular and produce staircase waveform with imitation of sinusoidal wave [1]. Conventionally, three types of MLIs have been reported, viz., Neutral Point Clamped (NPC), Flying Capacitor (FC), and Cascaded H-Bridge (CHB). Generally, for any MLI, the number of switch count, input DC sources, gate drivers, discrete diodes, capacitors, and Total Blocking Voltage (TBV/TSV) are important to decide the size of the inverter and requirement of filter size in grid connection. For generating five-level output, the NPC inverter takes more number of diodes, more number of capacitors, and voltage gain becomes unity. Additionally, to balance the capacitors, separate auxiliary circuits or complex control schemes are required [2]. The number of requirements is more as compared with NPC, and in this, for better operation, the capacitors must be precharged [3]. As compared with NPC and FC, CHB MLI has higher modularity but requires more number of isolated DC sources [4]. The TBV is more in [5] for generating five-level output with a single DC source. Generally, in most of MLIs, less TSV has been preferred for reducing the cost. The topology [6] provides five-level output with a single DC source and single capacitor, but TBV becomes more. For generating five-level output with a single DC source, it takes TSV of $11V_{dc}$ [7]. The topologies [8, 9] produce TBV of 12Vdc with the same number of component count for generating five-level output and a separate backend H-Bridge, which is required in [9] for generating negative voltage levels. The topology [10] requires two DC sources with TSV of $10V_{dc}$ for generating five-level output, but the drawback of this topology is unity voltage gain, which means there is no boosting ability. For generating five-level output, the topologies [11, 12] require two capacitors and a single DC source. Here, both topologies give TSV of 14Vdc. The topology [13] gives less TBV, but requires two DC sources and there is no boosting ability. To

A. Bhanuchandar (✉) · B. K. Murthy
Electrical Engineering Department, NIT Warangal, Warangal, Telangana, India

S. Kumar et al. (eds.), *Recent Advances in Power Electronics and Drives*, Lecture Notes in Electrical Engineering 852, https://doi.org/10.1007/978-981-16-9239-0_27

alleviate the aforementioned problems, a new RDC five-level output inverter topology has been introduced in this paper and it provides self-balancing of capacitors and boosting ability with a single DC source. Conventionally, there are different types of modulation techniques [14, 15] that are available and, in this paper, a new ULSFCS has been reported in the RL load case by taking reference of Nearest Level Control (NLC) technique. For higher ripple attenuation purpose, the LCL filter has been integrated with the grid [16, 17].

The rest of the paperwork is categorized as follows. The operation and control schemes of the proposed topology have been presented in Sect. 2. In Sect. 3, the comparative study has been described. The Sect. 4 gives the simulation results for both RL load and grid-connected cases. Finally, the conclusion has been presented in Sect. 5.

2 Operation of Proposed Topology and Control Schemes

2.1 Operation of Proposed Inverter Topology with LCL Filter

The schematic of RDC inverter topology with LCL filter is depicted in Fig. 1. It comprises eight unidirectional switches, one bidirectional switch and one SC with a single DC source supply. Here, the switches (S1, S2), (S3, S4), (S6, S7), and (S8, S9) are in complementary mode and the bidirectional switch S5 is connected in common emitter configuration mode for reducing the gate driver circuit by one as compared with common collector configuration mode. The operation of the proposed topology is depicted in Table 1. Generally, the capacitors are charged in parallel and discharged in series, then finally with proper switching action, the capacitor has been self-balanced. From Table 1, it is concluded that this topology provides voltage boosting of two with respect to a single DC source. Generally, the voltage stress of each switch is indexed with TBV/TSV. In this topology, all switches face an equal

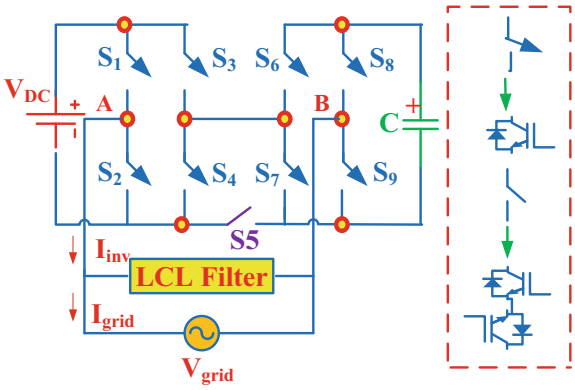

Fig. 1 Proposed five-level RDC inverter topology with LCL filter

Table 1 Switching arrangement—five-level SC inverter

Switches	0Vdc	1Vdc	2Vdc	−1Vdc	−2Vdc
S1	0	1	1	0	0
S2	1	0	0	1	1
S3	1	1	0	1	1
S4	0	0	1	0	0
S5	1	1	0	1	0
S6	1	1	1	1	0
S7	0	0	0	0	1
S8	0	0	0	1	1
S9	1	1	1	0	0

Table 2 Standing voltage of all switches

S. No.	Switches	Standing voltage
1	S1	V_{dc}
2	S2	V_{dc}
3	S3	V_{dc}
4	S4	V_{dc}
5	S5	$V_{dc} + V_{dc}$
6	S6	V_{dc}
7	S7	V_{dc}
8	S8	V_{dc}
9	S9	V_{dc}
Total standing voltage in per unit		$10\ V_{dc}/2\ V_{dc} = 5$ pu

amount of voltage stress Vdc individually, then per unit value of TBV becomes five and it is depicted in Table 2. Based on the maximum discharging period (MDP) method, it is possible to get proper switched capacitance value within permissible limits of voltage ripple. However, in this paper, little more capacitance value has been considered for making successful operation of the grid.

As compared with L and LC filters; the LCL filter provides higher ripple attenuation, but it suffers from resonance problem and finally the system becomes unstable. To alleviate the resonance problem, the active damping method has been preferred, and in this method, there are no additional power losses as compared with the passive damping method. The PLECS/PSIM software are very helpful for finding switching, conduction losses of any MLI topology. Lastly, the advantages of proposed topology is that it has less TBV, boosting ability and self-balanced capacitor with single dc source supply. This DC source supply can be considered PV with boost converter or fuel cell with boost converter with proper MPPT algorithms or suppose if PV panels are more then it is possible to integrate with single stage grid connected systems also.

2.2 *Proposed Control Schemes*

(i) *ULSFCS-RL load case*

The new ULSFCS has been applied to the proposed topology and its strategy as depicted in Fig. 2. The proposed control scheme is the modified version of the NLC technique and it is also called as Unified Rounding Control Scheme (URCS). The URCS provides less computation time as compared with conventional NLC and SHE PWM techniques.

In this scheme, modulating signal is given to rounding function and it generates an aggregated signal (AS). The Switching Table Generation (STG) is taken from Table 1. Because of truncation, there is no need for a logic gate requirement for generating gate pulses (GP). This control scheme is basically a fundamental switching frequency technique, where switching losses greatly reduce and it also provides self-balancing of capacitors. It is universally applicable for any MLI topology with a valid switching table.

(ii) *dq frame current control strategy-Grid Connected Case*

The control strategy for five-level SC inverter in grid-connected case has been depicted in Fig. 3. Firstly, sense the grid voltage (let, $V_{grid} = V_{\beta}$) and through proper

Fig. 2 Unified rounding control scheme-URCS/ULSFCS

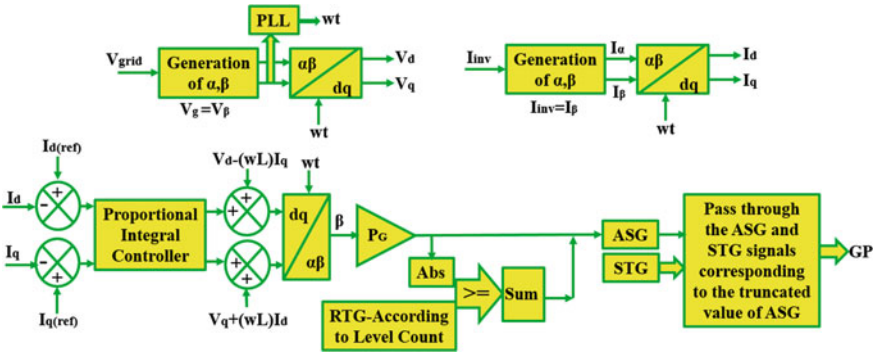

Fig. 3 Proposed dq frame current control scheme

Table 3 Comparative analysis with different conventional five-level inverter topologies

S. No.	Description	[5]	[6]	[7]	[8]	[9]	[10]	[11]	[12]	[13]	P
1	N_{Levels}	5	5	5	5	5	5	5	5	5	5
2	$N_{Switches}$	12	6	6	8	6	8	8	8	10	10
3	$N_{Drivers}$	12	6	6	8	5	8	8	8	9	9
4	N_{Diodes}	12	8	7	8	6	10	8	10	10	10
5	$N_{Sources}$	1	1	1	2	2	1	2	2	1	1
6	$N_{Capacitors}$	2	1	1	0	0	2	0	0	2	1
7	TSV	20	12	11	12	10	14	12	10	14	10

PLL, the V_d and V_q components have been generated. Here, PLL has been used to generate reference variable for grid synchronization. Similarly, the I_d and I_q components have been generated by sensing inverter current (let, $I_{inv} = I_\beta$). To inject active and reactive power into the grid, $I_{d(ref)}$ and $I_{q(ref)}$ have been used. From the decoupling control strategy, the modulating β-component signal has been generated. By using Proper Gain (P_G) value, it is possible to generate desired modulating signal. By taking absolute function, it is possible to curtail the number of high-frequency carriers present in the Repeating Table Generation (RTG) block. After truncation of ASG and STG, the required switching pulses/gate pulses (GP) have been generated. By taking $I_{q(ref)}$ equal to zero, it is possible to get UPF operation on the grid side.

3 Comparative Study

Table 3 shows the comparative analysis with different conventional five-level inverter topologies. From this table, it is concluded that the proposed topology gives less TBV with a single DC source supply, thereby decreasing the cost requirement of switches.. Generally, switch requirement reduces means; respective protection circuit, gate driver circuit, and heat sink also reduces thereby decreasing the size of the inverter.

4 Simulation Results

4.1 RL Load Case

Table 4 shows simulation parameters-RL load case. In this, for getting peak value of voltage 400 V, the input DC supply $V_{dc} = 200$ V has been considered. The ULSFCS has been applied to the proposed topology with step change (at $t = 0.05$ s) in Modulation Index (MI) values 1 and 0.5. Figure 4 shows simulation results for five-level SC inverter with RL load. From this, the capacitor is self-balanced at 200

Table 4 Simulation parameters—RL load case

S. No.	Parameters	Value
1	Vdc	200 V
2	Voltage gain	2
3	TSV (pu)	5
4	R	100 Ω
5	L	30 mH
6	SC	3300 μF
7	MI	1 and 0.5

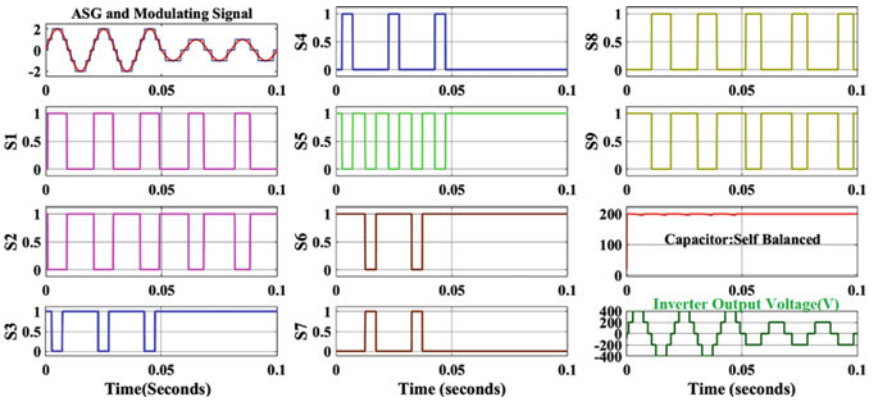

Fig. 4 Simulation results for five-level SC inverter with RL load: ULSFCS/URCS

volts even if the step changes in MIs. With MI = 1 and 0.5, the inverter generates five-level and three-level outputs, respectively.

4.2 Grid-Connected Case

Table 5 shows the simulation parameters of the grid-connected case. The LCL filter values have been calculated from [16, 17]. Figure 5 shows simulation results for step changes in $I_{d(ref)}$ from 20 to 10 A: UPF operation mode. From Fig. 5, the capacitor is self-balanced at 200 V and generates five-level output then grid voltage and grid current are maintains UPF operation even step changes in $I_{d(ref).}$ By the proposed control strategy of Fig. 3, the grid current exactly reaches the peak value according to $I_{d(ref).}$ Generally, $I_{d(ref)}$ is used to inject active power into the grid. Figures 6 and 7 shows harmonic spectrums of inverter output voltage and grid current with respect to $I_{d(ref)} = 20A$.

Table 5 Simulation parameters—grid-connected case

S. No.	Parameters	Value
1	Grid voltage	230 V (RMS)
2	Switching Frequency	10 kHz
3	Grid frequency	50 Hz
4	Resonance frequency	1405 Hz
5	Rated power(S)	2 kVA
6	Vdc	200 V
7	Inverter side inductance	3.98 mH
8	Grid side inductance	4 mH
9	Filter capacitance	5.95 μF
10	Switched capacitor	4700 μF

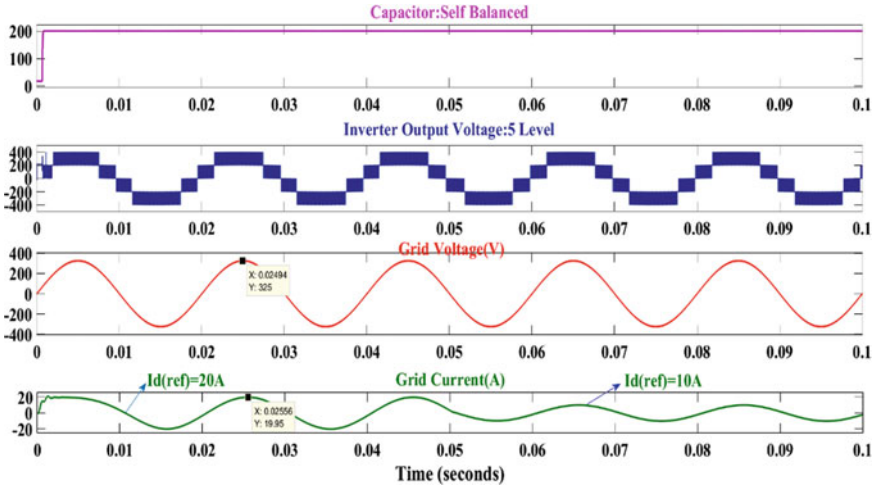

Fig. 5 Step changes in $I_{d(ref)}$. UPF operation mode

5 Conclusion

The proposed topology provides less per unit TSV and voltage boosting ability with less number of devices. In this, the capacitor is self-balanced without the need for auxiliary circuits and separate complex control schemes. The voltage stress of each switch does not exceed the input DC supply. A comparative study is also done with other conventional five-level inverter topologies. With RL load and grid-connected cases, the proposed control schemes give good results in the output. Even if step changes in direct axis reference current values, the grid voltage and grid current still maintain UPF operation. This topology is well suitable for photovoltaic and fuel cell-based grid-connected applications.

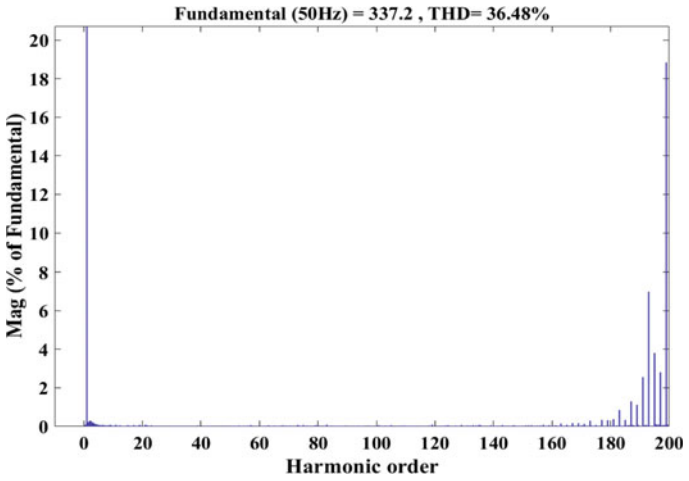

Fig. 6 Harmonic spectrum—five-level output voltage

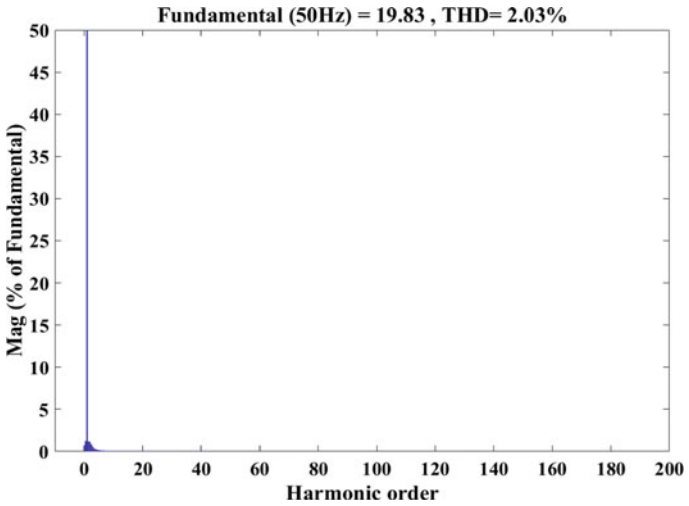

Fig. 7 Harmonic spectrum—grid current with $I_{d(ref)} = 20A$

References

1. Rodriguez J, Lai J-S, Peng FZ (2002) Multilevel inverters: a survey of topologies, controls, and applications. IEEE Trans Ind Electron 49(4):724–738. https://doi.org/10.1109/TIE.2002.801052
2. Nabae A, Takahashi I, Akagi H (1981) A new neutral-point-clamped PWM inverter. IEEE Trans Ind Appl IA-17(5):518–523. https://doi.org/10.1109/TIA.1981.4503992
3. Shukla A, Ghosh A, Joshi A (2007) Capacitor voltage balancing schemes in flying capacitor multilevel inverters. In: 2007 IEEE power electronics specialists conference, Orlando, FL,

USA, pp 2367–2372. https://doi.org/10.1109/PESC.2007.4342381
4. Peng FZ, Lai J-S, McKeever J, VanCoevering J (1995) A multilevel voltage-source inverter with separate DC sources for static VAr generation. In: IAS '95. Conference record of the 1995 IEEE industry applications conference thirtieth IAS annual meeting, Orlando, FL, USA, vol 3, pp. 2541–2548. https://doi.org/10.1109/IAS.1995.530626
5. Cheng C, He L (2016) Flying-capacitor-clamped five-level inverter based on switched-capacitor topology. In: 2016 IEEE energy conversion congress and exposition (ECCE), Milwaukee, WI, USA, pp 1–5. https://doi.org/10.1109/ECCE.2016.785512
6. Ye Y, Cheng KWE, Liu J, Ding K (2014) A step-up switched-capacitor multilevel inverter with self-voltage balancing. IEEE Trans Industr Electron 61(12):6672–6680. https://doi.org/10.1109/TIE.2014.2314052
7. Barzegarkhoo R, Kojabadi HM, Zamiry E, Vosoughi N, Chang L (2016) Generalized structure for a single phase switched-capacitor multilevel inverter using a new multiple DC link producer with reduced number of switches. IEEE Trans Power Electron 31(8):5604–5617. https://doi.org/10.1109/TPEL.2015.2492555
8. Ruiz-Caballero DA, Ramos-Astudillo RM, Mussa SA, Heldwein ML (2010) Symmetrical hybrid multilevel DC–AC converters with reduced number of insulated DC supplies. IEEE Trans Industr Electron 57(7):2307–2314. https://doi.org/10.1109/TIE.2009.2036636
9. Su G-J (2005) Multilevel DC-link inverter. IEEE Trans Ind Appl 41(3):848–854. https://doi.org/10.1109/TIA.2005.847306
10. Hari Priya V, Sreenivasarao D, Siva Kumar G (2017) Improved pulse-width modulation scheme for T-type multilevel inverter. IET Power Electron 10(8):968–976. https://doi.org/10.1049/iet-pel.2016.0729
11. Niu D et al (2019) A novel switched-capacitor five-level T-type inverter. In: 2019 2nd international conference on smart grid and renewable energy (SGRE), Doha, Qatar, pp 1–6. https://doi.org/10.1109/SGRE46976.2019.9021066
12. Ranjan A, Gupta KK, Kumar L, Jain S (2012) A switched-capacitors based multilevel boost inverter with single input source. In: 2012 IEEE 5th India international conference on power electronics (IICPE), Delhi, India, pp 1–6. https://doi.org/10.1109/IICPE.2012.6450373
13. Sivakumar K (2015) A fault-tolerant single-phase five-level inverter for grid-independent PV systems. IEEE Trans Ind Electron 62(12):7569–7577. https://doi.org/10.1109/TIE.2015.2455523
14. Rodriguez J et al (2009) Multilevel converters: an enabling technology for high-power applications. Proc IEEE 97(11):1786–1817. https://doi.org/10.1109/JPROC.2009.2030235
15. Bhanuchandar A, Murthy BK (2021) Single phase nine level switched capacitor based grid connected inverter with LCL filter. In: 2020 3rd international conference on energy, power and environment: towards clean energy technologies, pp 1–5. https://doi.org/10.1109/ICEPE50861.2021.9404491
16. Ali A, Shanmugham P, Somkun S (2017) Single-phase grid-connected voltage source converter for LCL filter with grid-current feedback. In: 2017 international electrical engineering congress (iEECON), Pattaya, Thailand, pp 1–6. https://doi.org/10.1109/IEECON.2017.8075720
17. Zhang N, Tang H, Yao C (2014) A systematic method for designing a PR controller and active damping of the LCL filter for single-phase grid-connected PV inverters. Energies 7:3934–3954. https://doi.org/10.3390/en7063934

Pitch Angle Control Using Fuzzy Logic for DFIG-Based WECS

Kirti Kaharwar and Bhavnesh Kumar

1 Introduction

Electrical energy has a vital crucial role in our everyday life. The world's progress is greatly dependent upon this energy as the industrialization process and economic developments are closely associated with it. However, with decreasing fossil fuels and increasing environmental issues like global warming and air pollution, the use of renewable and cleaner energy generation processes is growing. Thus, there is an acute need for green energy resources like solar, wind, hydro, tidal, and geothermal [1, 2].

Wind and solar energy harnessing systems are more attractive among all the available renewable energy sources as they are free, abundant, and available all over the globe. Among the two, wind energy is mostly popular because of its availability at night also. However, wind patterns show many deviations from the regular pattern leading to output power fluctuations. Hence, output power leveling is very much required in these systems [3].

For maintaining constant output power in WECS (Wind energy conversion system), an effective control mechanism is required to regulate the pitch angle. Conventionally, PI controllers are used for leveling output power by twisting the blades by a certain angle in case the wind speed is higher than the rated flows [4]. Some researchers have also explored the system's performance with PID controllers [5]. Although, simple to implement, these controllers are impotent in handling nonlinearities effectively. In [6], the H-infinity controller was proposed to provide reliable performance to the system even if there are deviations in wind and turbine parameters. However, it was a quite complex strategy to implement. The technique Sliding mode control (SMC) was also investigated to control pitch angle [7]. Prominent

K. Kaharwar (✉) · B. Kumar
Instrumentation and Control Engineering Department, Netaji Subhas University of Technology, New Delhi, India

S. Kumar et al. (eds.), *Recent Advances in Power Electronics and Drives*, Lecture Notes in Electrical Engineering 852, https://doi.org/10.1007/978-981-16-9239-0_28

results were presented for effectively handling all the nonlinearities and uncertainties present in the system. But the disadvantage of this method is that it requires wind data and the chattering effect is also there. To counter these drawbacks, IMC-PID (Internal Model Control-PID)-based controllers were implemented to regulate the pitch angle [8]. It provides the finest performance only at some specific operating conditions, but the demerit is that it is unable to account for all operating conditions, which change according to wind speed. For regulating and maintaining the extracted output power constant, a neural network-based SMC was designed [9]. This method was able to cater to all the uncertainties present in the aerodynamic model and continuous function was used instead of sign function to reduce the chattering phenomenon. Control of pitch angle using General predictive control (GPC) has also been introduced [10]. In this method, the error is directly proportional to GPC (General predictive control) law, so if there is a large error, then the controller will become unstable. Some authors also proposed Model Predictive Control (MPC). In [11], MPC (Model Predictive Control) provides an optimized solution despite considering all uncertainties and system constraints. It can predict future behavior using the system's model. But the problem with MPC (Model Predictive Control) is to solve quadratic programming online. Therefore, an intelligent controller named fuzzy logic is designed that can handle nonlinear functions of the system [12]. Mathematical data of wind turbines is not required and it is simple to implement and very effective than the above controllers. There are several pieces of kinds of literature about this fuzzy controller. The controller Linear Active Disturbance Rejection Control (LADRC) was proposed in [13]. LADRC can estimate the external as well as internal disturbances and can compensate for them in real time. Its purpose is to modulate the output power and the speed of the generator and to overcome safety issues. In [14, 15], the fuzzy logic controller was introduced for MPPT (Maximum power point tracking). In [16], a fuzzy logic-based pitch angle controller was designed in which the pitch angle was dependent on wind speed and the error voltage. In [17], the input to a fuzzy controller is wind speed, which will make the system costlier because of the anemometer required to compute the wind speed. In [18], a pitch angle controller based on fuzzy logic is implemented for the stabilization of the power system. In [19], mechanical power variations are given as input to the FLC (fuzzy logic controller) and if a sudden variation occurs in the wind speed, then the controller was not effective and fluctuations are observed and MPPT (Maximum power point Tracking) was also not there as compared to conventional PI controllers. Some researchers integrated the neural network, fuzzy logic, and PID and proposed a new scheme called Adaptive Fuzzy PID [20]. This method was designed to control the disturbances that can harm the system's efficiency. This method is capable of self-tuning the parameters under various conditions.

Hence, this paper outlines the leveling of output power, which is done by regulating the pitch angle using the fuzzy logic controller. The inputs applied to the controller are Error (change in power), variation in error, rotor speed, and the pitch angle, which is the output of the controller [21]. This approach is applied to the nine MW wind farm and can sustain constant power output for speeds exceeding the rated wind speeds.

Section 2 outlines the DFIG modeling and wind turbine modeling. Section 3 represents the implementation of leveling of output power, i.e., control of pitch angle with the help of a fuzzy-based controller, and Results and simulation studies are depicted in Sect. 4. The conclusion is drawn in Sect. 5 and references follow thereafter.

2 System Modeling and Description

2.1 A DFIG Model

Figure 1 illustrates the schematic of WECS (Wind energy conversion system) under investigation with pitch angle control mechanism. The complete system comprises a wind turbine, gear train, shaft, doubly fed induction generator (DFIG), three-phase transformer, transmission line, grid, converters of Rotor, and Grid side connected through a DC link capacitor to regulate DC voltage. The DFIG modeling can be explained through the following equations.

The voltages equations in a d-q reference frame are as follows:

$$v_{ds} = r_s i_{ds} + \frac{d\Phi_{ds}}{dt} - \omega_s \Phi_{qs} \tag{1}$$

$$v_{qs} = r_s i_{qs} + \frac{d\Phi_{qs}}{dt} + \omega_s \Phi_{ds} \tag{2}$$

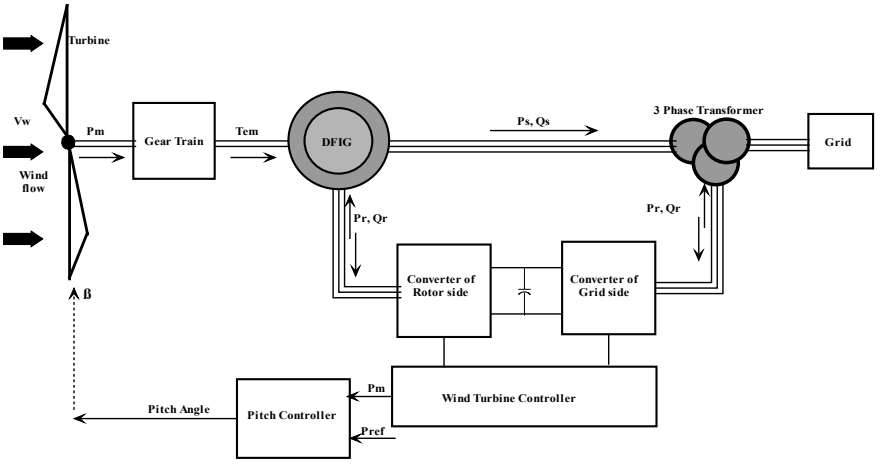

Fig. 1 Description of DFIG-based wind turbine model

$$v_{dr} = r_r i_{dr} + \frac{d\Phi_{dr}}{dt} - \omega_r \Phi_{qr} \tag{3}$$

$$v_{qr} = r_r i_{qr} + \frac{d\Phi_{qr}}{dt} + \omega_r \Phi_{dr} \tag{4}$$

where r_s and r_r is defined as the stator and rotor windings resistance, respectively, ω_s and ω_r is defined as the rotational speed of stator and rotor, respectively.

The flux linkages are given by the below equations

$$\Phi_{ds} = L_s i_{ds} + M i_{dr} \tag{5}$$

$$\Phi_{qs} = L_s i_{qs} + M i_{qr} \tag{6}$$

$$\Phi_{dr} = L_s i_{dr} + M i_{ds} \tag{7}$$

$$\Phi_{qr} = L_s i_{qr} + M i_{qr} \tag{8}$$

where L_s is defined as the stator inductance and L_r is defined as the rotor inductance and M is mutual inductance.

By using the above Eqs. 1–8, the DFIG (Doubly fed Induction Generator) model can be expressed as

$$\frac{d\Phi_{ds}}{dt} = -\frac{r_s}{L_s} i_{ds} + \omega_s \Phi_{qs} + \frac{r_s}{L_s} M i_{dr} + v_{ds} \tag{9}$$

$$\frac{d\Phi_{ds}}{dt} = -\frac{r_s}{L_s} i_{qs} - \omega_s \Phi_{ds} + \frac{r_s}{L_s} M i_{qr} + v_{qs} \tag{10}$$

$$\frac{di_{dr}}{dt} = -\frac{r_r}{\sigma} i_{dr} + \omega_r \sigma i_{qr} - \frac{M}{L_s}\frac{d\Phi_{ds}}{dt} + \omega_r \frac{M}{L_s}\Phi_{qs} + v_{dr} \tag{11}$$

$$\frac{di_{qr}}{dt} = -\frac{r_r}{\sigma} i_{qr} - \omega_r \sigma i_{dr} - \frac{M}{L_s}\frac{d\Phi_{qs}}{dt} - \omega_r \frac{M}{L_s}\Phi_{ds} + v_{qr} \tag{12}$$

where $\sigma = L_r - \frac{M^2}{L_s}$ is known as the dispersion factor.

The electromagnetic torque expression for the DFIG (Doubly fed Induction Generator) system is described below

$$T_{em} = P\frac{3}{2}\frac{M}{L_s}\left(\Phi_{ds} i_{qr} - \Phi_{qs} i_{dr}\right) \tag{13}$$

The useful and reactive power are defined below and the power losses are considered negligible:

$$P_s = \frac{3}{2}\left(v_{ds} i_{ds} + v_{qs} i_{qs}\right) \tag{14}$$

$$Q_s = \frac{3}{2}\left(v_{qs} i_{ds} - v_{ds} i_{qs}\right) \tag{15}$$

2.2 Wind Turbine Modeling

The aerodynamic power P_m is expressed as

$$P_m = \frac{1}{2}\rho A C_p(\lambda, \beta) v_w^3 \tag{16}$$

And wind turbine torque is expressed as

$$T_m = \frac{P_m}{\omega_r} \tag{17}$$

$$T_m = \frac{1}{2}\rho \pi R^3 C_p(\lambda, \beta)\frac{v_w^2}{\lambda} \tag{18}$$

where ρ is the density of air in kg/m^3, $A = \pi r^2$ denotes turbine blade area in m^2 and R denotes blade radius in m and ω_r represents the generator rotational speed in rad/sec.

The expression for Cp (power coefficient) is obtained by the relation given below, which is derived by turbine characteristics

$$C_p(\lambda, \beta) = a_1\left(\frac{a_2}{\lambda_i} - a_3\beta - a_4\right)e^{-\frac{a_5}{\lambda_i}} + a_6\lambda \tag{19}$$

$$\frac{1}{\lambda_i} = \frac{1}{\lambda + 0.08\beta} - \frac{1}{\beta^3 + 1} \tag{20}$$

C_p is the coefficient of power, and from the Eqs. (19) and (20), it can be stated that C_p is a function of both blade tip speed ratio λ and the pitch angle of the blade β. The coefficients a_1 to a_6 are defined as: $a_1 = 0.5176$, $a_2 = 116$, $a_3 = 0.4$, $a_4 = 5$, $a_5 = 21$, and $a_6 = 0.0068$. Figure 2 depicts the deviation of C_p (power coefficient) with respect to λ (tip speed ratio) for distinct values of the pitch angle β and also given that Cpmax = 0.5 is obtained at $\beta = 0$ degrees and for $\lambda = 10$.

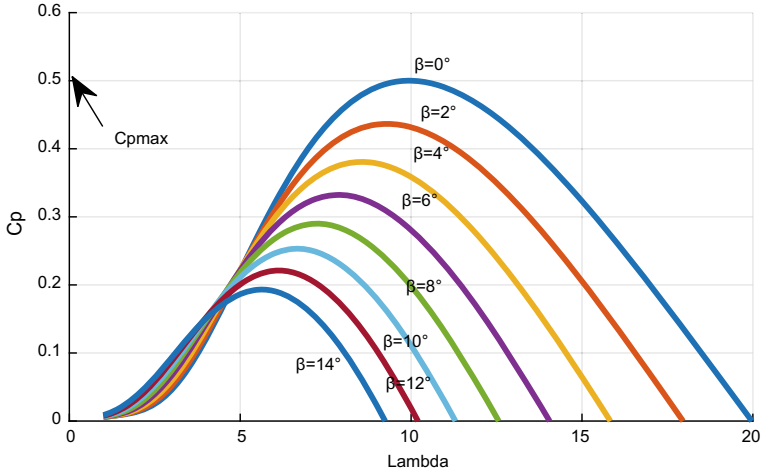

Fig. 2 Characteristics of Cp (λ, β)

For each pitch angle β, there exists a single λ_{opt}, which gives the coefficient Cp for the maximal value of power.

The tip speed ratio (TSR) is expressed as

$$\lambda = \frac{\omega_r R}{v_w}$$

At any given wind speed v_w, there will be the optimal rotational speed ω_{ropt} at which power will be maximum and from this optimal rotational speed, the optimal tip speed ratio can be calculated, which then gives maximum Cp (power coefficient).

The optimal value of tip speed ratio can be calculated by knowing the optimized rotational speed

$$\lambda_{opt} = \frac{\omega_{ropt} R}{v_w}$$

The wind turbine operation can be studied into four regions (Fig. 3). The region where the wind speed is smaller than the cut-in speed (the speed at which power generation starts) is denoted by region 1 and the power generation is zero in this region. Region 2 corresponds to the region between the cut-in and rated wind speed at which power generation starts growing. And for the winds having speeds greater than rated speed and below cut out speed is region 3 where power is to be sustained at the rated value. Above cut-out wind speed, the turbine is taken out of operation to safeguard the generator parts, and the generated power is zero in this region. Pitch control action will be taken in region 3 to sustain the output power.

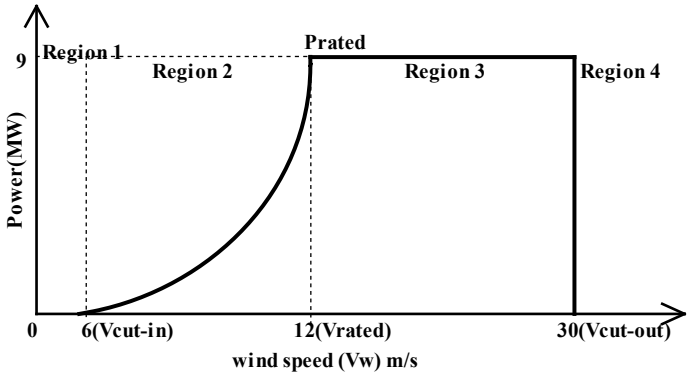

Fig. 3 Mechanical power versus wind speed curve

3 Proposed Control Strategy: FLC (Fuzzy Logic Controller)

Figure 4 represents the schematic of the proposed FLC. It comprises a fuzzifier, knowledge rule base, inference engine, and a defuzzifier. The role of the fuzzifier is to convert crisp inputs into fuzzifier inputs. The knowledge rule base defines the relationship between the input and the output membership functions. The inference engine is the core of the fuzzy logic controller, which can simulate the fuzzified inputs with the help of a knowledge rule base developed by humans to accomplish the desired control action. Defuzzifier converts the fuzzified quantities obtained from the inference engine into crisp quantities.

Mamdani type of inference technique is used and the defuzzification method used is center of gravity (COG). Three inputs are applied to the fuzzy controller and the controller as shown in Fig. 5 produces one output.

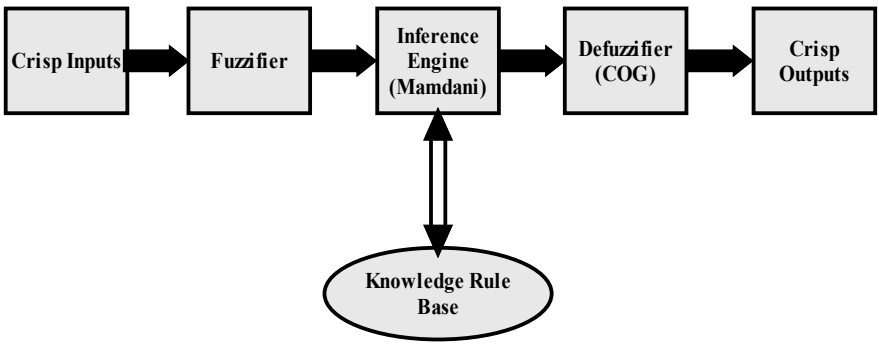

Fig. 4 Block diagram of FLC

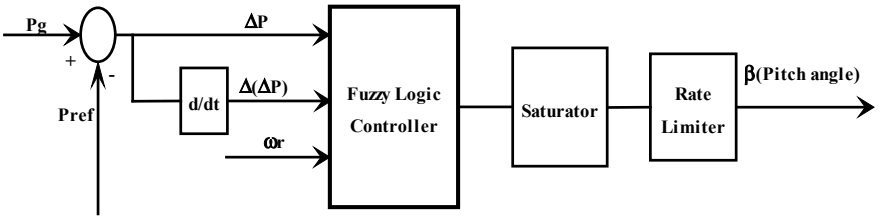

Fig. 5 Proposed fuzzy logic control strategy

Three inputs applied are:

(a) Change in power (△P)
(b) Variation in the change in power (△(△P))
(c) Rotor speed (ωr).

One output, i.e., Pitch angle (β) is there.

$$\Delta P = P_m - P_{ref}$$

$$\delta(\Delta P) = \Delta P(i) - \Delta P(i-1)$$

In fuzzy, linguistic variables are defined and are expressed as small (S), Medium (M), Big (B), Large Negative (LN), Small Negative (SN), Zero (Z), Small Positive (PS), Large Positive (LP). The fuzzy rules are formulated as given in the table. These rules can be interpreted as if the rotor speed.

(Δ_r) is B (Big) and △P is SP (Small Positive) and δ (△P) is LP (Large Positive) then pitch angle is LP (Large Positive). The fuzzy rule base, inputs, and output's membership functions are given in Table 1 and Fig. 6, respectively.

Table 1 Rule Base for FLC

Δ_r		S					M					B				
△P		LN	SN	Z	SP	LP	LN	SN	Z	SP	LP	LN	SN	Z	SP	LP
δ(△P)	LN	LN	LN	LN	LN	N	SN	SN	SN	P	P	SP	SP	P	P	LP
	SN	LN	LN	LN	N	N	SN	SN	Z	P	P	SP	SP	P	P	LP
	Z	LN	LN	N	SN	SN	SN	Z	Z	P	P	SP	P	P	LP	LP
	SP	LN	N	N	SN	SN	SN	Z	Z	P	SP	P	P	LP	LP	LP
	LP	N	N	SN	N	SN	Z	Z	SP	SP	SP	P	P	LP	LP	LP

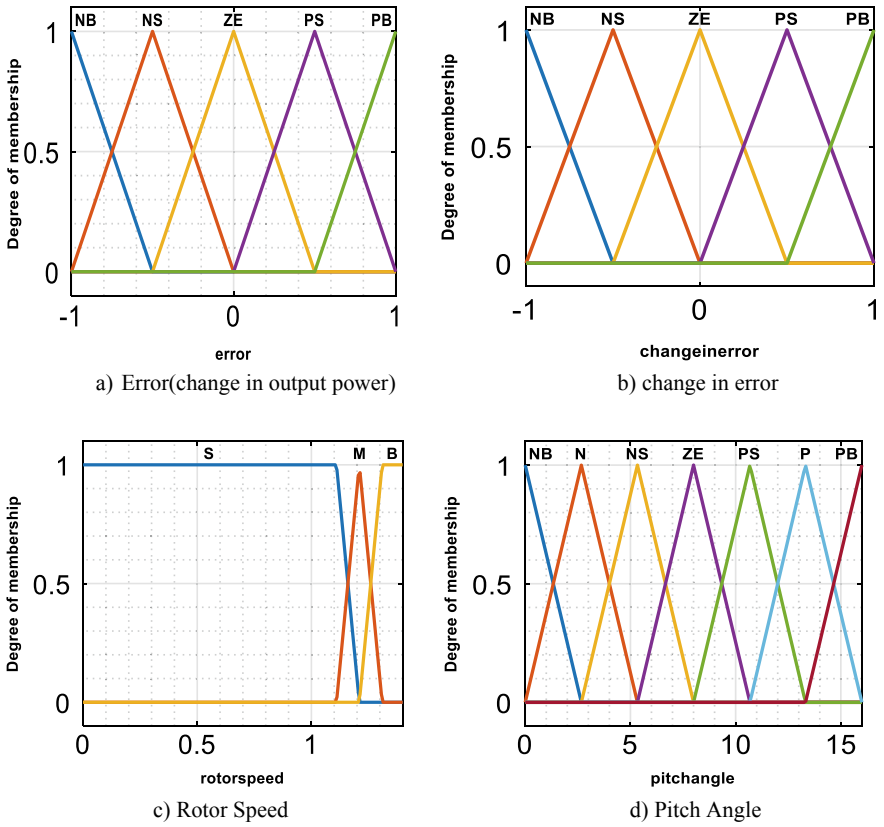

a) Error(change in output power)

b) change in error

c) Rotor Speed

d) Pitch Angle

Fig. 6 FLC membership functions

4 Simulation Results and Analysis

To examine the potency of the WECS on the presented FLC, simulation is performed on a DFIG-based wind turbine having a capacity of 9 MW. The simulation is performed on both the controllers, i.e., the PI controller and the fuzzy logic controller. In the PI controller, the values of Kp and Ki were varied until the desired tuned response is obtained [22] and were found to be 50 and 50, respectively.

First, the results of both the controllers are compared for a particular wind speed of 15 m/s as given in Fig. 7. In Fig. 7a, the output power is maintained constant, i.e., 9 MW, but oscillations are present in PI controllers as compared to the FLC. There is a sudden overshoot initially for PI controller, whereas in FLC, overshoot is minimal and the constant power and pitch angle is maintained constant for particular wind speed (Fig. 7b). Similarly, for the coefficient of power in Fig. 7c, respectively, oscillations are sustained for the PI controller, whereas in FLC oscillations die out after a few seconds. In Figs. 7d, e, the FLC is maintaining tip speed ratio and rotor

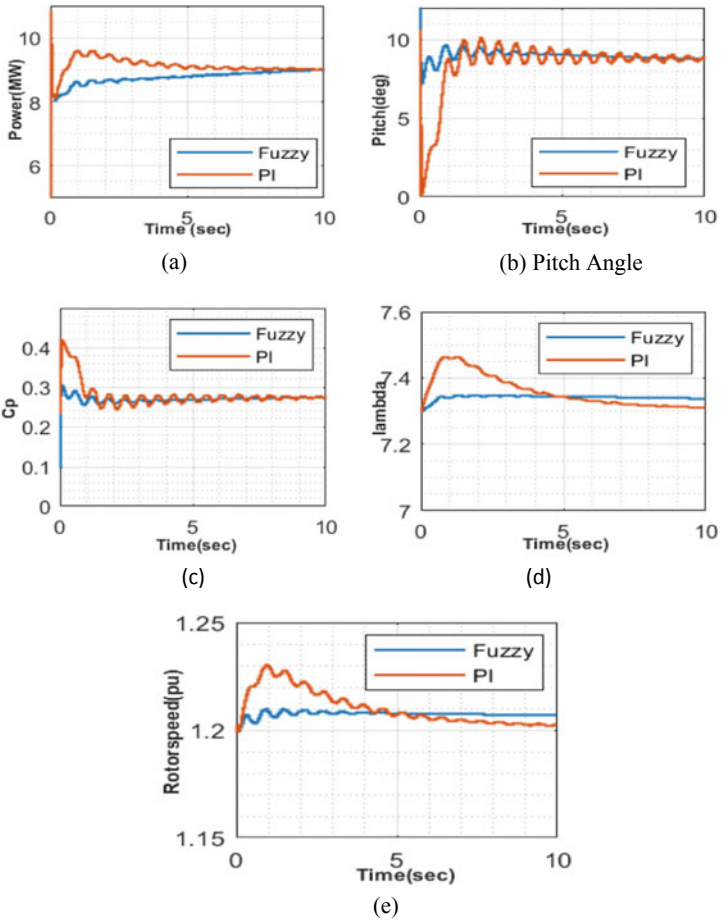

Fig. 7 Responses for PI controller and FLC at a particular wind speed of 15 m/s: **a** generated output power, **b** pitch angle, **c** coefficient of power, **d** tip speed ratio, **e** rotor speed

speed constant for particular wind speed, whereas the controller PI is unable to perform so. These parameters are continuously decreasing. Therefore, overall FLC performs better rather than the PI controller.

For realizing the effective implementation of the given FLC, the system has been examined on the wind profile illustrated in Fig. 8.

Responses recorded for case-II are shown in Fig. 9. In Fig. 9b, FLC is maintaining the power constant and reducing the oscillations also but the controller PI is unable to perform well and sustain oscillations. In Fig. 9c, FLC is maintaining the fixed pitch angle for fixed wind speed, instantly responding to step-change in wind speed, but PI is incompetent to do so. There are so many variations in the PI controller for pitch angle as well as for all the other parameters like Cp, lambda (tip speed ratio), and

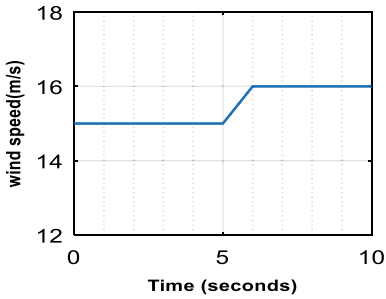

Fig. 8 Wind profile for case-II

rotor speed. Overall FLC is a very effective controller in maintaining the constant output power and regulating other parameters.

5 Conclusion

A 9 MW wind farm is examined for its operation on wind speed higher than rated. The absolute system model is created in MATLAB/Simulink environment for examination. The control strategy based on fuzzy logic is described and developed to manage the pitch angle. It is evident from the results that the system with FLC outperforms the PI controller in maintaining the constant output power for wind speeds exceeding the rated wind speeds. It also helps in reducing the oscillations that occur in output power in comparison to the PI controller. FLC (Fuzzy logic controller) can also regulate other parameters like rotor speed, coefficient of power, tip speed ratio, and pitch angle. Overall, FLC outperforms the PI controller in regulating the power output and other parameters and gives a stable response to all the deviations, which occur in wind speed for a particular time.

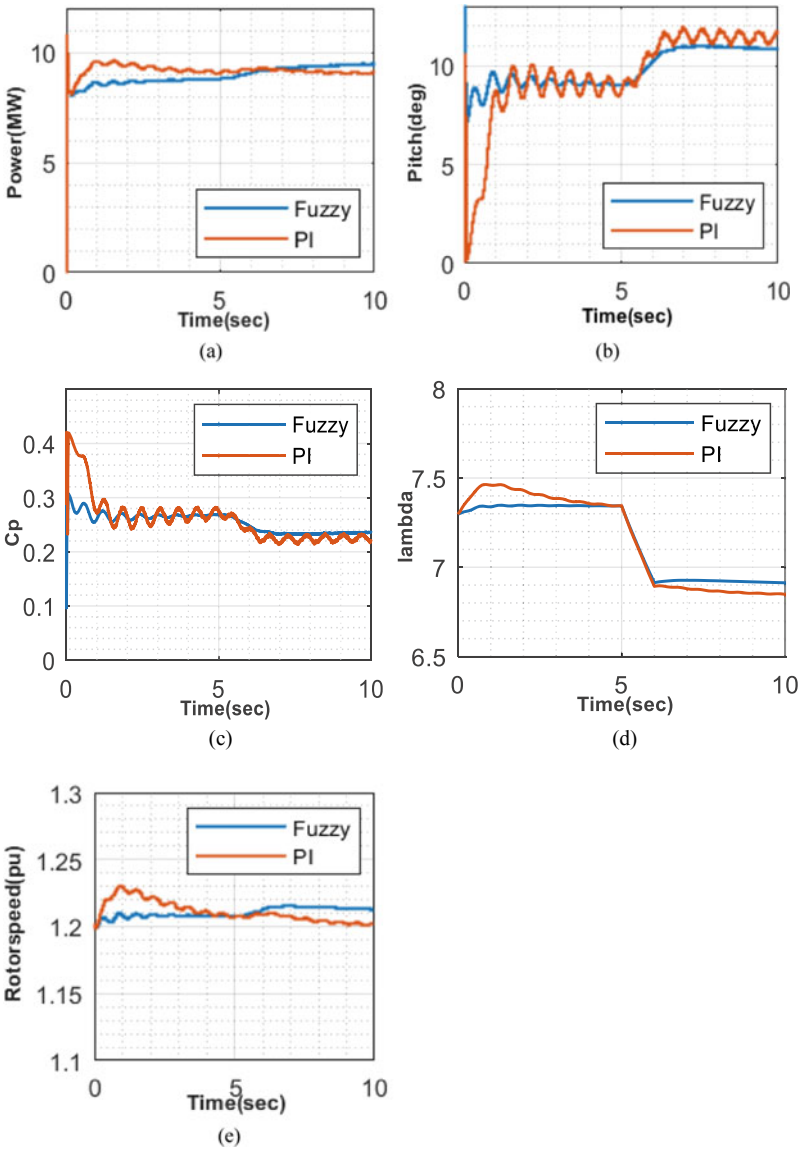

Fig. 9 Responses for PI controller and FLC at a constant variation in wind speed: **a** generated output power, **b** pitch angle, **c** coefficient of power, **d** tip speed ratio, **e** rotor speed

References

1. Committee on Environmental Impacts of Wind Energy Projects, "Environmental Impacts of Wind Energy Projects", Washington, The National Academies Press (2007)
2. Report of New and Renewable Energy Authority. http://www.nrea.gov.eg. Last access 20 Oct 2014
3. Mi Y, Bao X, Jiang E, Deng W, Li J, Ren L, Wang P (2014) The pitch angle control of squirrel-cage induction generator wind power generation system using sliding mode control. In: 16th European conference on power electronics and applications, Lappeenranta, pp 1–10
4. Hansen H, Larsen L (2005) Control design for a pitch-regulated, variable speed wind turbine. Riso, National Laboratory Roskilde, Denmark
5. Vidal Y, Acho L, Luo N, Zapateiro M, Pozo F (2012) Power control design for variable-speed wind turbines. Energies 5:3033–3050
6. Gaur P, Pathak D, Kumar B, Chauhan YK (2016) PI and fuzzy logic controller based tip speed ratio control for smoothening of output power fluctuation in a wind energy conversion system. In: 2016 7th India international conference on power electronics (IICPE), Patiala, India, pp 1–6. https://doi.org/10.1109/IICPE.2016.8079480
7. Shahgholian G, Karimi H, Mahmoodian H (2012) Design a power system stabilizer based on fuzzy sliding mode control theory. Int Rev Model Simul. 5(5):2191–2196
8. Naik KA, Gupta CP (2016) Improved oscillatory behavior of a grid-connected wind farm using IMC-PID based pitch angle controller. In: 2016 IEEE 6th International Conference on Power Systems (ICPS), New Delhi, pp 1–6
9. Dastres H, Mohammadi A Shamekhi M (2020) A neural network based adaptive sliding mode controller for pitch angle control of a wind turbine. In: 2020 11th power electronics, drive systems, and technologies conference (PEDSTC), pp 1–6. https://doi.org/10.1109/PEDSTC49159.2020.9088373
10. Senjyu T, Sakamoto R, Urasaki N, Funabashi T, Fujita H, Sekine (2006) Output power leveling of wind turbine generator for all operating regions by pitch angle control. IEEE Trans Energy Convers 21(2):467–475
11. Spencer MD, Stol KA, Unsworth CP, Carter JE, Norris SE (2013) Model predictive control of a wind turbine using short-term wind field predictions. Wind Energy 16(3):417–434
12. Chowdhury M, Hosseinzadeh N, Shen W (2012) Smoothing wind power fluctuations by fuzzy logic pitch angle controller. Renew Energy 38(1):224–233
13. Ullah F, Ali S, Ying D, Saeed A (2019) Linear active disturbance rejection control approach base pitch angle control of variable speed wind turbine. In: 2019 IEEE 2nd international conference on electronics technology (ICET), pp 614–618. https://doi.org/10.1109/ELTECH.2019.8839443
14. Chen Z, Gomez SA, McCormick M (2000) A fuzzy logic controlled power electronic system for variable speed wind energy conversion systems. In: Eighth international conference on power electronics and variable speed drives, Publication No. 475
15. Abo-Khalil AG, Lee D, Seok J (2004) Variable speed wind power generation system based on fuzzy logic control for maximum output power tracking. In: 35th annual IEEE power electronics specialists conference, Achen, Germany
16. Demata JV, Dimazana JNM, Fausto RS, Magwili GV, Chua EE, Pacis MC (2019) Utilization of fuzzy logic controller for pitch control of a small scale wind energy conversion system (WECS). In: 2019 IEEE 11th international conference on humanoid, nanotechnology, information technology, communication and control, environment, and management (HNICEM), pp 1–6. https://doi.org/10.1109/HNICEM48295.2019.9073448
17. Zhang J, Cheng M, Chen Z, Fu X (2008) Pitch angle control for variable speed wind turbines. In: Proceedings of the 3rd international conference on DRPT, pp 2691–2696
18. Jauch C, Cronin T, Sørensen P, Jensen BB (2007) A fuzzy logic pitch angle controller for power system stabilization. Wind Energy 19–30
19. Macedo AVA, Mota WS (2012) Wind turbine pitch angle control using fuzzy logic. In: Proceeding of the IEEE/TDC-LA, Montevideo, Uruguay, Sep, pp 1–6

20. Ali MMM, Youssef A, Abdel-Gaber G, Ali AS (2018) Adaptive fuzzy-PID based pitch angle control of wind turbine. In: 2018 twentieth international Middle East power systems conference (MEPCON), pp 1110–1114. https://doi.org/10.1109/MEPCON.2018.8635229
21. Hosseini E, Shahgholian G (2017) Output power leveling for DFIG wind turbine system using intelligent pitch angle control. Automatika 58(4):363–374. https://doi.org/10.1080/00051144.2018.1455017
22. Reynoso-Meza G, Sanchis J, Herrero JM, Ramos C (2012) Evolutionary auto-tuning algorithm for PID controllers. IFAC Proc 45(3):631–636. https://doi.org/10.3182/20120328-3-IT-3014.00107

Class-E Power Amplifier-Based Wireless Power Transfer System

Jay Prakash Narayan, Anamika Das, and Ananyo Bhattacharya

1 Introduction

Wireless power transmission (WPT) is a means of transmitting electrical power with help of transmitter and receiver over a large distance in the absence of conducting wires or cables. There are three techniques to transfer the power wirelessly, magnetic couplings, capacitive coupling, and electromagnetic radiation. Through the electromagnetic wave, power can be transferred over a very large distance, but it has lower efficiency and it has greater detrimental effect on the surroundings in which we are living. Due to loose coupling, the magnetic field energy and coupling coefficient quickly attenuate with increasing distance in electromagnetic induction. Due to this problem, the power can transferred only for few centimeters or sometimes even in millimeters by using the electromagnetic induction. In the electromagnetic radiation mode, the transfer efficiency declines as the wavelength of power transmission rises. Magnetic coupling method combines the benefits of both of the above technologies. It can transfer power over a large distance almost 2–4 times of the diameter of the resonating coils. In the recent, year the demand of the wireless Power Transfer (WPT) is increased tremendously. The WPT system finds its application in electric vehicles, charging cables, transportation security, medical implants, pacemaker, etc.

J. P. Narayan (✉) · A. Das · A. Bhattacharya
Department of Electrical Engineering, National institute of technology, Jamshedpur, Jharkhand, India

A. Das
e-mail: 2019rsee002@nitjsr.ac.in

A. Bhattacharya
e-mail: ananyo.ee@nitjsr.ac.in

S. Kumar et al. (eds.), *Recent Advances in Power Electronics and Drives*, Lecture Notes in Electrical Engineering 852, https://doi.org/10.1007/978-981-16-9239-0_29

2 System Model

Figure 1 illustrates the WPT System model block diagram. The system consists of an AC source which is used as an input source, with a diode rectifier rectifying the input voltage. Using class E power amplifiers, the high voltage is transformed to high frequency AC. After that, the transmitter is supplied with the oscillating signals. Power is transmitted wirelessly by maintaining sufficient resonant coupling between the transmitter and receiver stages.

The proposed scheme of WPT system is illustrated in Fig. 2. At first, the diode rectifier converts the input AC voltage to DC.

The DC inputs from the rectifier is collected by the class-E amplifier and transforms it to high frequency AC. In switched mode resonant converter, the class E amplification is very effective. Generally, transistor is used as a switch in the power amplifier, which have high efficiency due to low power losses in the switch.

The Class-E amplifier is made up of a parallel RF choke (L_2) and a Resonant circuit. The output coming from the class-E amplifier is directly interconnected with tank circuit, which are made up off transmitting coils and capacitor C_2 as shown in

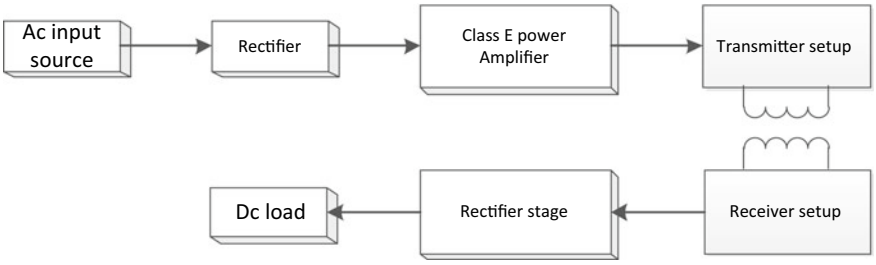

Fig. 1 Schematic diagram of (WPT)

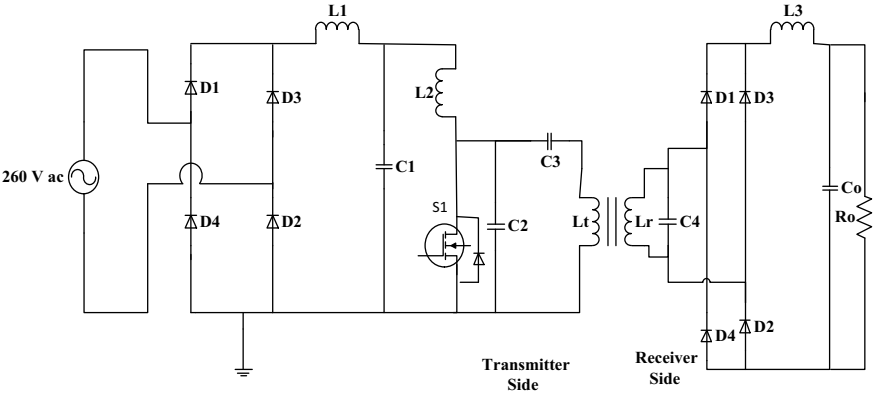

Fig. 2 Circuit configuration of proposed WPT

Fig. 2. The receiver is made up of the transmitting coils and a tank circuit consisting of capacitor C_4, as well as a full wave rectifier that transforms the AC into DC. A filter C_o eliminates harmonics before being fed to the load R0. Power is transmitted between the transmitter and receiver at the resonant condition.

3 Design of Parameters of WPT System

The assumption made in this WPT system are as follows:

(1) It is assumed that the component used in the WPT system is ideal.
(2) The switch resistance during the On state, as well as their parasitic capacitance, are not taken into account.
(3) The drop of voltage across the diodes are not taken into account.
(4) The value of capacitor is considered to be very large.

According to the requirements of power, the value of load can be calculated by the given equation

$$R_L = \frac{(v_{in})^2}{P_0} 0 \cdot 576 \left(1 - \frac{0 \cdot 45}{Q_L} - \frac{0 \cdot 40}{Q_L^2}\right) \tag{1}$$

where Q_L is a constant which is taken by the designer, generally Q_L value is between 0.5 to 2. Here Q_L value is taken approximately 0.90.

Then, using the equation below, you can determine the value of shunt capacitance (C_1 and C_2) that is connected through the switch.

$$C_1 = \frac{1}{2\pi f_o R_L \left(\frac{\pi^2}{4} + 1\right) \frac{\pi}{2}} + \left(1 + \frac{0.91}{Q_L} - \frac{1}{Q_L^2}\right) + \frac{0.6}{(2\pi f_o)^2 L_1} \tag{2}$$

$$C_2 = \frac{1}{2\pi f_o R_L} + \left(\frac{1}{Q_L - 0.104}\right) + \left(1 + \frac{1.014}{Q_L - 1.78}\right) - \frac{0 \cdot 2}{\left(2\pi f_o\right)^2 L_1} \tag{3}$$

The value of L_1 is randomly selected, which is taken as 1.465 μ_h and L_2 value is calculated as;

$$L_2 = Q_L \left(\frac{R_L}{2\Pi f_o}\right) \tag{4}$$

4 Simulation Analysis

The proposed WPT model was simulated with the help of MATLAB/SIMULINK. The theoretical model has been checked with a 260 V input voltage (Fig. 3).

The output of the system is calculated across the load R_o. The various parameters used in this WPT system to get the maximum efficiency are shown in Table 1.

The rectifier stage's output voltage is determined to be 234.2 V DC, which is then fed to the class-E power amplifier which converts it into high frequency AC and a 300 V output is obtained. Figure 6 displays the waveform of the WPT system output voltage at the receiving end. Because of the inclusion of an output capacitor, which acts as a filter, the system's output voltage becomes stable across time (Fig. 4).

As seen in Fig. 5, the output current of the designed wireless transmission system flows through the secondary side. The current flowing at the output of proposed WPT model is 60 mA.

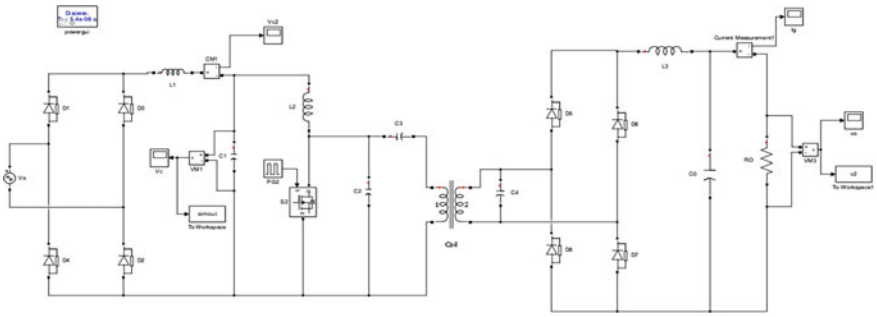

Fig. 3 Implementation of proposed WPT system using MATLAB\SIMULINK

Table 1 Parameters values

Parameter	Value
Input voltage	260 V
Switching frequency	100 kHz
L_1	1.465 µh
L_2	70 µh
L_3	1.07 mh
C_1	187 nf
C_2	187 nf
C_3	165 nf
C_4	65.8 pf
C_0	0.5 mf
R_0	500 Ω

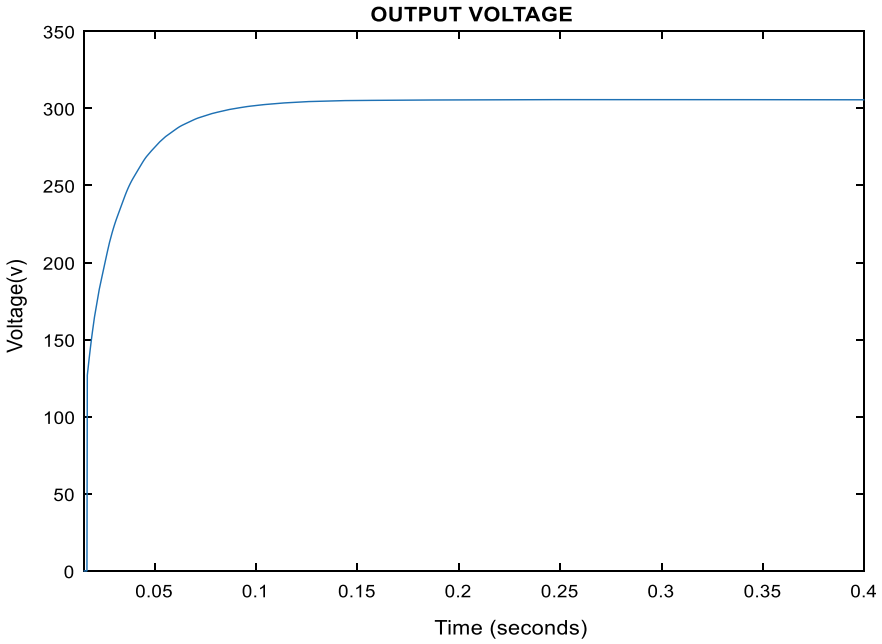

Fig. 4 Waveform of WPT system's output voltage

The WPT system has an output power of approximately 183.36 W. which is shown in the Fig. 6 (Table 2).

5 Conclusion

This paper describes a model of WPT system for power transfer in the medium range. The above system is suitable for the appliances whose output power is within the 300W. The model takes a 260 v AC input, which is then converted into high frequency AC. The above proposed WPT models give an output of 300 V across the output resistor. Generally, two coil WPT systems have efficiency within the range of 45–60%. In this WPT system, an efficiency of 59.4% is observed which indicates a highly efficient system. The WPT system with full wave bridge rectifier outperforms the WPT system without full wave rectifier in terms of voltage, power, efficiency, and other factors.

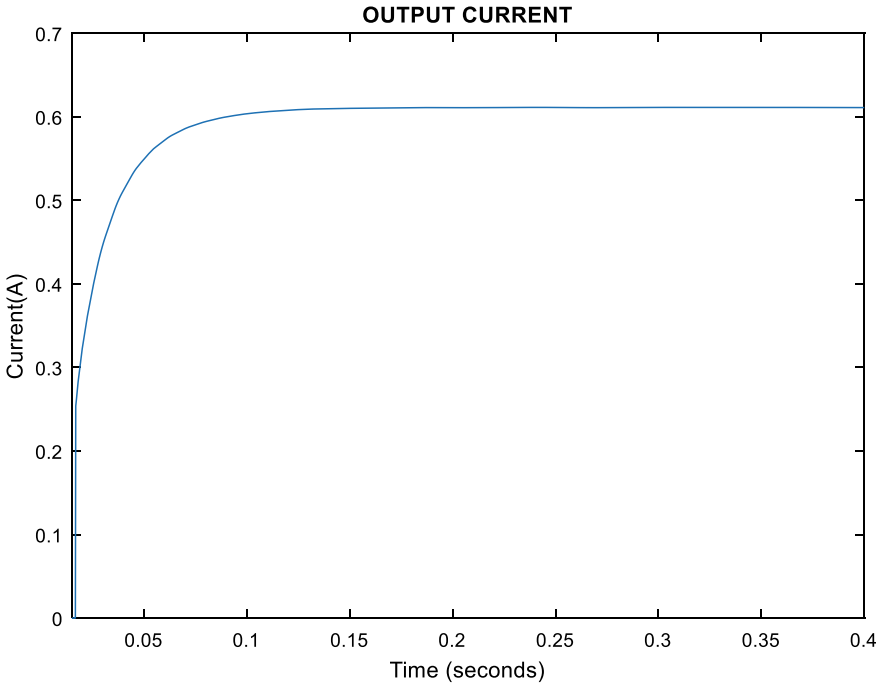

Fig. 5 Waveform of WPT system's output current

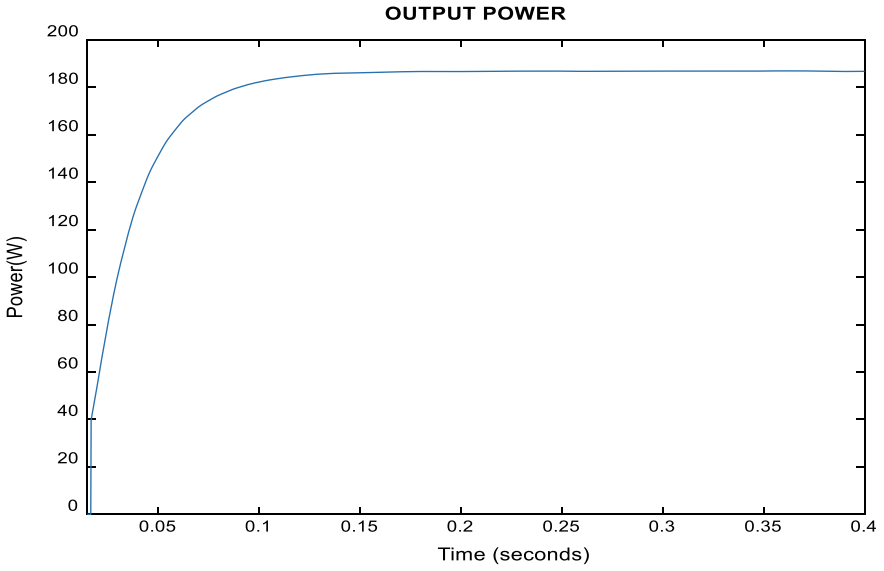

Fig. 6 Output Power waveform of WPT system

Table 2 Below is a comparison of the outputs of a wireless power transmission system with and without a full wave bridge rectifier

WPT model	Input source	Input voltage (V)	Output voltage (V)	Output current (Amp)	Output Power (W)	Ƞ in percentage
Without full wave rectifier	DC source	12	45	0.25	28	54.6
With full wave rectifier	AC source	260	300	0.60	183.36	59.4

References

1. Kursk A, Karalis A, Moffatt R, Joannopoulos JD, Fisher P, Soljacic M (2007) Wireless power transfer via strongly coupled magnetic resonances. Science 317(5834):83–86
2. Hu AP (2009) Wireless/contactless power supply: inductively coupled resonant converter solutions. Saarbrucken, Germany: VDM
3. Lee S-H, Lorenz RD (2011) Development and validation of model for 95%-efficiency 220-W wireless power transfer over a 30 cm air gap. IEEE Trans Appl Ind 47(6):2495–2504
4. Pinuela M, Yates DC, Lucyszyn S, Mitcheson PD (2013) Maximizing DC-to-load efficiency for inductive power transfer. IEEE Trans Power Electron 28(5):2437–2447
5. Sample A, Waters B, Wisdom S, Smith J (2013) Enabling seamless wireless power delivery in dynamic environments. Proc IEEE 101(6):1343–1358
6. Florian C, Mastri F, Paganelli R, Masotti D, Costanzo A (2014) Theoretical and numerical design of a wireless power transmission link withgan-based transmitter and adaptive receiver. IEEE Trans Microw Theory Tech 62(4):931–946
7. Ahn D, Hong S (2014) Wireless power transmission with self-regulated output voltage for biomedical implant. IEEE Trans Ind Electron 61(5):2225–2235
8. Aldhaher S, Luk P-K, Bati A, Whidborne J (2014) Wireless power transfer using Class E inverter with saturable DC-feed inductor. IEEE Trans Ind Appl 50(4):2710–2718
9. Hui S, Zhong W, Lee C (2014) A critical review of recent progress inmid-range wireless power transfer. IEEE Trans Power Electron 29(9):4500–4511
10. Prasanth V, Bauer P (2014) Distributed ipt systems for dynamic powering: misalignment analysis. IEEE Trans Ind Electron 61(11):6013–6021
11. Aldhaher S, Luk P-K, Whidborne JF (2014) Electronic tuning of misaligned coils in wireless power transfer systems. IEEE Trans Power Electron 29(11):5975–5982
12. Huang S-J, Lee T-S, Huang T-H (2014) Inductive power transfer systems for PT-based ozone-driven circuit with flexible capacity operation and frequency-tracking mechanism. IEEE Trans Ind Electron 61(12):6691–6699
13. Raval P, Kacprzak D, Hu A (2015) Multiphase inductive power transfer box based on a rotating magnetic field. IEEE Trans Ind Electron 62(2):795–802
14. Ahn D, Hong S (2015) Wireless power transfer resonance coupling amplification by load-modulation switching controller. IEEE Trans Ind Electron 62(2):898–909
15. Zhong W, Zhang C, Liu X, Hui S (2015) A methodology for makinga three-coil wireless power transfer system more energy efficient than atwo-coil counterpart for extended transfer distance. IEEE Trans Power Electron 30(2):933–942

16. Fu M, Zhang T, Ma C, Zhu X (2015) Efficiency and optimal loads analysis for multiple-receiver wireless power transfer systems. IEEE Trans Microw Theory Tech 63(3):801–812
17. Fu M, Tang Z, Liu M, Ma C, Zhu X (2015) Full-bridge rectifier input reactance compensation in megahertz wireless power transfer systems. In: Presented at the IEEE PELS workshop emerging technologies, wireless power, Daejeon, Korea
18. Ahn D, Mercier P (2016) Wireless power transfer with concurrent 200kHz and 6.78 MHz operation in a single transmitter device. IEEE Trans Power Electron 31(7):5018–5029

Enhancement of Power Factor and DC-Link Voltage Stabilization Using Multiple Techniques of HPFC

Satya Venkata Kishore Pulavarthi, Jami Rajesh, Nakka Jayaram, and Sukanta Halder

1 Introduction

Rectifiers are basically two types. The first one is line commutated rectifiers which use diodes and thyristors. The second one is Power Factor Correction (PFC) rectifiers which use MOSFET and IGBT. So, they need force commutation. PFC rectifiers are also classified as non-regenerative and regenerative PWM rectifiers. Boost and Vienna rectifiers [1] are non-regenerative PWM rectifiers in which the power flow is only in one direction from AC source to DC load. Voltage source rectifier and current source rectifier are regenerative PWM rectifiers in which the power flow is bidirectional [2]. Regenerative PWM voltage source rectifier is called High-Power Factor Converters (HPFCs).

Multi-pulse rectifiers [3, 4] are used to reduce the harmonics in the source side but the use of phase-shifting transformers restricted the use of these multi-pulse rectifiers.

One can use passive filters to reduce the harmonics. Different types of commonly used passive filters [5] are bandpass, high-pass, double bandpass, and composite filters. The main limitation of the passive filters is that they are not suitable for changing system conditions. The size of the filter and the tuned frequency can't be changed so easily.

Next active filters [6] came with power electronic equipment to reduce the harmonics seen by the source. The disadvantages of active filters include their large size, rating, control sophistication, and cost.

HPFCs are introduced to overcome these drawbacks and meet the above standards [7]. This lead HPFCs to be an essential segment of any AC–DC conversion system due to their well-regulated DC output, reduced size, and higher efficiency. There are

S. V. K. Pulavarthi (✉) · J. Rajesh · N. Jayaram · S. Halder
National Institute of Technology Andhra Pradesh, Tadepalligudem, India
e-mail: kishorepulavarthi.sclr@nitandhra.ac.in

S. Kumar et al. (eds.), *Recent Advances in Power Electronics and Drives*, Lecture Notes in Electrical Engineering 852, https://doi.org/10.1007/978-981-16-9239-0_30

variants of HPFCs, which are widely inherited for their characteristics such as sinusoidal input currents, negligible THD of input currents, good supply pf, controlled DC output voltage, fewer ripples in the DC output voltage, low switching stresses, and low Electro-Magnetic Interference (EMI) emissions.

Predictive reasoning-based adaptive hysteresis band control for the three-phase PWM rectifier is presented in [8]. But the authors have not shown the basic characteristics of PWM rectifier such as unity power factor and DC-link voltage stabilization. Model predictive control based on two vectors [9] is applied to the PWM rectifier to control the power flow. A novel low complexity model predictive direct power control (LC-MPDPC) for the PWM rectifier is presented in [10] to realize the active and reactive power control. This control has the advantage of eliminating the AC voltage sensor but the control involves complexity. A power predictive control for a three-phase PWM rectifier is proposed in [11]. This method has the advantage of eliminating the PI controller. A vector control method without an input voltage sensor for the PWM rectifier was proposed in [12]. The steady-state model of the filter inductor and the output of the current controller estimate the input voltage information required by the PLL. Authors in [13] proposed a new backstepping control system for the Three-phase PWM rectifier to control the active and reactive powers instantaneously. This method gave better results compared to the PI controller and PR (proportional resonant) controller.

In this paper, different control techniques used for three-phase HPFC are discussed and simulated [14, 15].

The remaining paper is structured as follows. Section 2 discusses the operation of the HPFC. Control schemes are discussed in Sect. 3. Simulation results of the HPFC controlled by the above schemes are presented in Sects. 4 and 5 represents the conclusion.

2 High-Power Factor Converter

Figure 1 shows the circuit diagram of the three-phase HPFC. A feedback control loop is used in it to make the output voltage/DC-link voltage constant at the desired value. The DC-link voltage (V_o) is measured and compared with the desired reference voltage of V_{oref}. The resultant error signal is routed through the control block, which turns on and off the converter's switching devices. HPFC is a bidirectional power flow converter, the power flow between the load and the source can be regulated based on the DC-link requirements. Controlling the DC-link voltage allows the current flow at the DC link to be reversed, allowing power reversal to be regulated [6]. The waveforms and phasor diagrams of the HPFC in both rectifier and regenerative mode are shown in Fig. 2.

The current flowing to the load (Io) is positive in the rectifier mode of operation, and the capacitor (CD) is discharged via the DC load. In this case, the control circuit requests more power from the AC supply due to the error signal. For producing the necessary PWM signals for the switching devices, the control circuit draws power

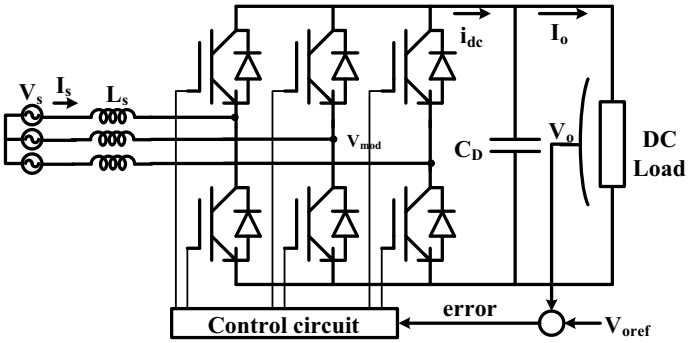

Fig. 1 High-power factor converter

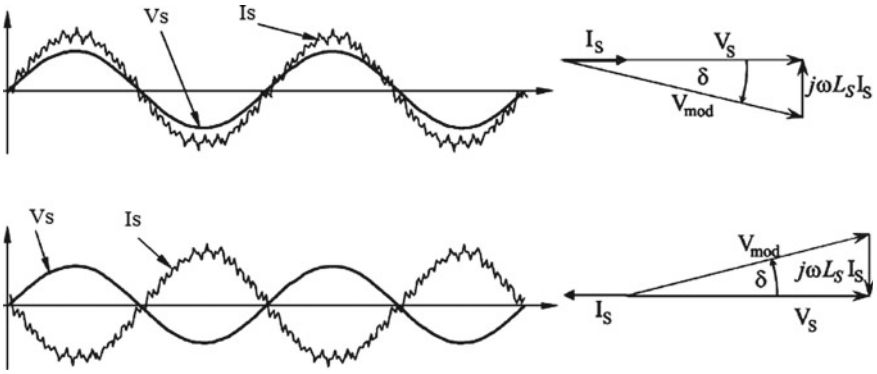

Fig. 2 Rectifier (top) and inverter (bottom) modes of operation

from the supply. The capacitor voltage is restored as more current flows from the AC to the DC side.

Io becomes negative in the inverter or regenerative mode of operation, and the capacitor CD is overcharged. The control circuit is commanded by the error signal to discharge the capacitor, allowing power to flow to the AC mains.

Both the active and reactive powers can be regulated by the PWM. Thus, power factor correction can be done by using this type of rectifiers. The current waveforms at the AC side can also be maintained almost sinusoidal, thus reducing the harmonic contamination to the mains supply.

3 Control Techniques

Three control schemes for the control of three-phase High-Power Factor Converter are discussed. They are (a) Current control technique, (b) Vector control technique, and (c) Voltage control technique.

3.1 Current Control Technique

The generalized control block diagram is shown in Fig. 3. The output voltage (V_o) is compared with the desired reference voltage (V_{oref}) and the error signal is obtained as given in Eq. (1).

$$\text{Error, } e = V_{oref} - V_o \tag{1}$$

This error passed through the PI controller will give the current reference template I which is shown in Eq. (2) as follows.

$$I = K_p e + K_I \int_0^t e dt \tag{2}$$

Here, K_p and K_I are the proportional gain and integral gain, respectively. This current template I is multiplied with a unit template V_{xu} (a sinusoidal signal with the same phase and frequency of the AC source voltage) to obtain the AC input current reference I_{xref} given by Eq. (3).

$$I_{xref} = I * V_{xu} \tag{3}$$

This I_{xref} is compared with the actual line current (I_x) and the error is again passed through the P controller to get modulating signal(m) given in Eq. (4), which has the desired phase and frequency.

$$m = K_{pi} * (I_{xref} - I_x) \tag{4}$$

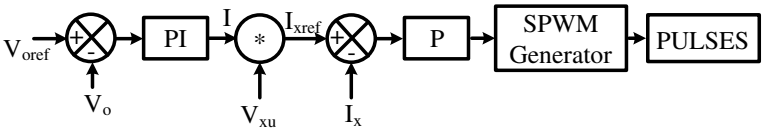

Fig. 3 Block diagram of current control technique

where K_{pi} is the proportional gain used to control the converter current. To produce the necessary pulses to the converter switches, this modulating signal is compared to the triangular carrier.

3.2 *Vector Control Technique*

Another method to control the HPFC is in d-q vector space. The control block diagram for the vector control technique is shown in Fig. 4.

The input source currents (i_a, i_b, and i_c) can be represented by using the vector notation such as $i_s = i_d + ji_q$, which is defined by Eq. (5).

$$\begin{bmatrix} i_d \\ i_q \end{bmatrix} = \frac{2}{3}\begin{bmatrix} \cos\theta & \sin\theta \\ -\sin\theta & \cos\theta \end{bmatrix}\begin{bmatrix} 1 & -\frac{1}{2} & -\frac{1}{2} \\ 0 & \frac{\sqrt{3}}{2} & -\frac{\sqrt{3}}{2} \end{bmatrix}\begin{bmatrix} i_a \\ i_b \\ i_c \end{bmatrix} \tag{5}$$

The actual DC-link voltage/output voltage (V_o) is compared with the desired reference voltage (V_{oref}) and the error is passed through the PI (proportional + integral) controller, which gives the value of i_{dref} and, the i_{qref} is set to zero in order to maintain the pf nearly unity. These references are compared with the input currents which are in d-q coordinates given in Eq. (5). Typically, two proportional controllers are used to pass these current errors to generate the values of Vmod_d and V mod_q. By applying the complete inverse transformation given by Eq. (6), the modulation signals in the abc reference frame can be generated. The SPWM technique can be used to generate gate drive pulses for the regulated power switches in the HPFC.

$$\begin{bmatrix} V_{a\,mod} \\ V_{b\,mod} \\ V_{c\,mod} \end{bmatrix} = \begin{bmatrix} 1 & 0 \\ -\frac{1}{2} & \frac{\sqrt{3}}{2} \\ \frac{1}{2} & -\frac{\sqrt{3}}{2} \end{bmatrix}\begin{bmatrix} \cos\theta & -\sin\theta \\ \sin\theta & \cos\theta \end{bmatrix}\begin{bmatrix} V_{mod\_d} \\ V_{mod\_q} \end{bmatrix} \tag{6}$$

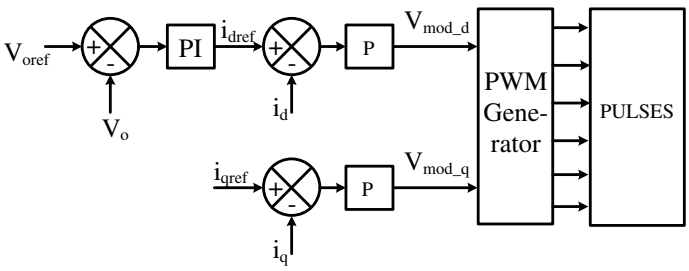

Fig. 4 Block diagram of vector control technique

3.3 Voltage Control Technique

Voltage V_{xmod} is generated using the differential equations that govern the HPFC circuit. The following differential Eq. (7) can be derived from Fig. 1

$$V_x(t) = L_s \frac{di_x}{dt} + Ri_x + V_{x\,mod}\,(t) \tag{7}$$

Assume that, $V_x(t) = V_m \sin(\omega t + \phi)$, and the solution for Eq. (7) to make the converter work at constant power factor should be of the form given in Eq. (8)

$$i_x(t) = I(t)\sin(\omega t + \phi) \tag{8}$$

Solving the Eqs. (7), (8), and $V_x(t)$ will yield the expression $V_{x\,mod}$ shown in Eq. (9), which will make the converter work at a fixed power factor.

$$\begin{aligned} V_{x\,mod} &= \left[X_s I \sin\phi + \left(V_m - RI - L_s \frac{dI}{dt}\right)\cos\phi\right]\sin\omega t \\ &- \left[X_s I \cos\phi + \left(RI + L_s \frac{dI}{dt} - V_m\right)\sin\phi\right]\cos\omega t \end{aligned} \tag{9}$$

For unity power factor operation,$\cos\phi = 1$ and $\sin\phi = 0$.
With these values, the above Eq. (10) can be reduced as Eq. (6) shown below.

$$V_{x\,mod} = \left(V_m - RI - L_s \frac{dI}{dt}\right)\sin\omega t - X_s I \cos\omega t \tag{10}$$

The block diagram of this technique implemented for unity pf is shown in Fig. 5. The advantage of this technique is that no input current sensing is needed. Here, sin ωt and cos ωt are obtained from the AC source.

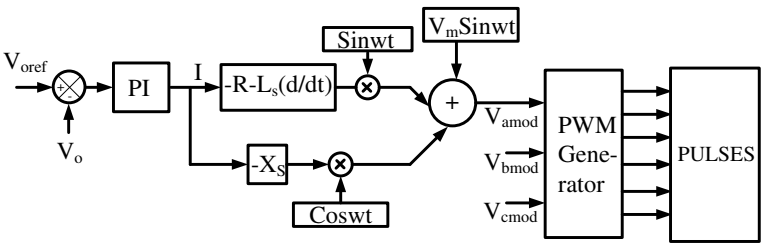

Fig. 5 Block diagram of voltage control technique for one leg of a converter

4 Simulation Results

The three-phase HPFC is simulated in MATLAB/SIMULINK with all the control techniques described above. The parameters taken for the simulation are shown in Table 1.

4.1 Current Control Technique

The circuit of three-phase HPFC with the current control technique is implemented in MATLAB/SIMULINK. Figure 6 shows that the DC-link voltage is tracking the reference value of 600 V. The voltage and current waveforms at the AC side under steady state which are in phase with each other are shown in Fig. 7. The harmonic spectrum of the input current wave is shown in Fig. 8 and THD is found to be 1.22% which is less than the IEEE519 standards [16].

Another 25 Ω load is connected from time 0.1 to 0.2 s, therefore current increases during this time. We can observe the same thing in Fig. 9. To work the circuit in inverter mode, a voltage source more than the reference voltage is connected across the DC bus from 0.3 to 0.4 s so that the current and voltages are in opposition to each other that can be observed in Fig. 10. From time 0.5 to 0.6 s, the source voltage

Table 1 Parameters used for simulation

Parameter	Value
AC source peak value	$230\sqrt{(2)}$
Source inductance	4.5 mH
Load resistance	25 Ω
Load side capacitance	3300 μF
V_{ref}	600 V
Switching frequency	10 kHz
Sampling time	10 μs

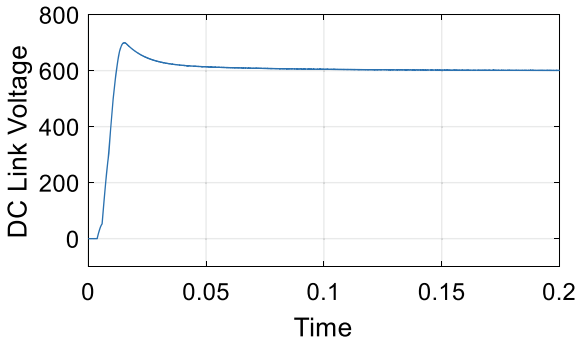

Fig. 6 DC-link voltage

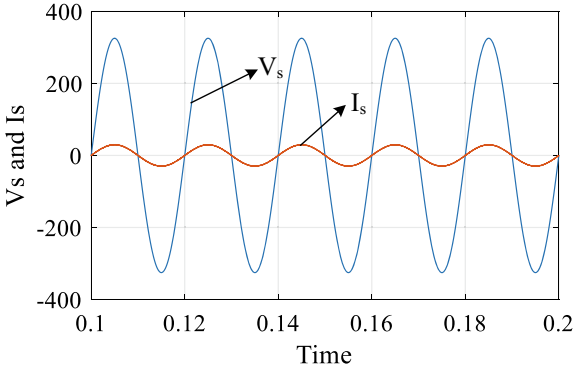

Fig. 7 Voltage and current waveforms at the AC side

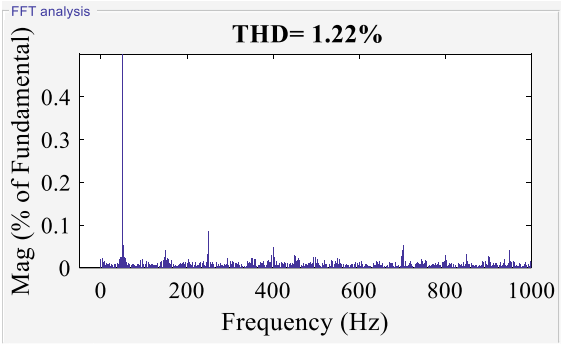

Fig. 8 AC side current harmonics

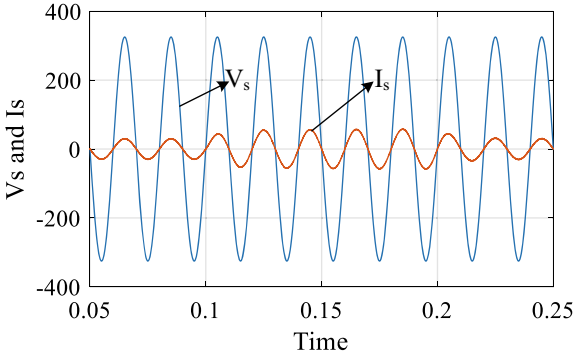

Fig. 9 Waveforms during load change

is reduced by 20%, therefore the source current increases to maintain the DC-link voltage back to its reference voltage, and both voltage and current waveforms still maintain the near unity power factor. The corresponding waveforms are shown in Fig. 11. Figure 12 represents the DC-link voltage which is regulated by maintaining the reference voltage at all load conditions and disturbances.

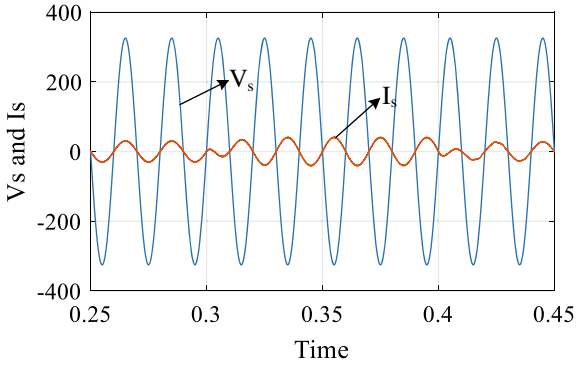

Fig. 10 Waveforms during inverter (Regenerative) mode

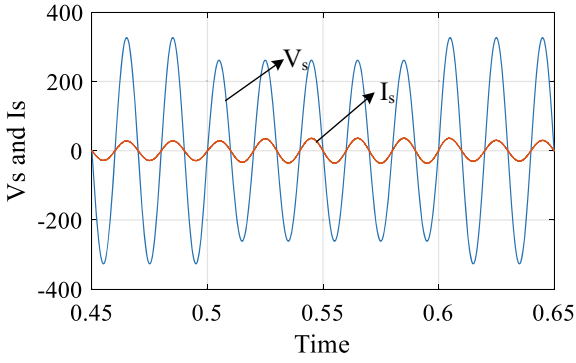

Fig. 11 Voltage and current waveforms during source perturbation

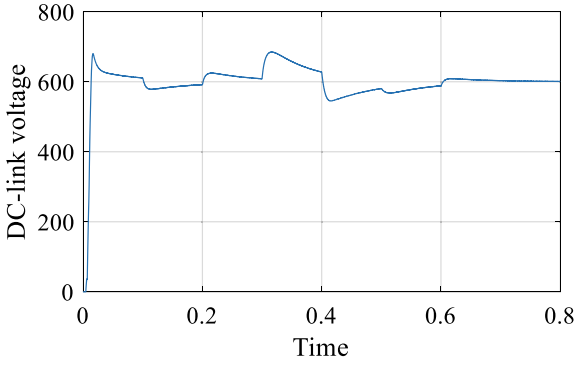

Fig. 12 DC-link voltage during disturbances

4.2 Vector Control Technique

The HPFC circuit with the vector control technique is also implemented in MATLAB/SIMULINK. The DC-link voltage is maintained constant which is shown in Fig. 13. The voltage and current waveforms at the AC side are shown in Fig. 14

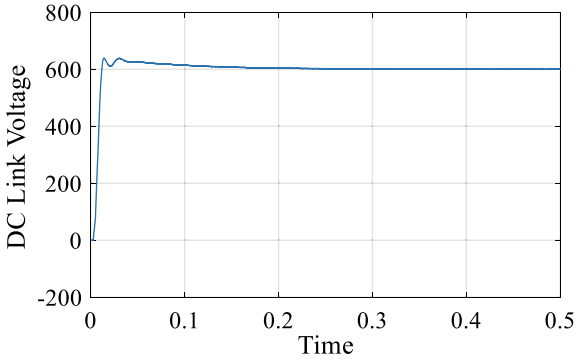

Fig. 13 DC-link voltage

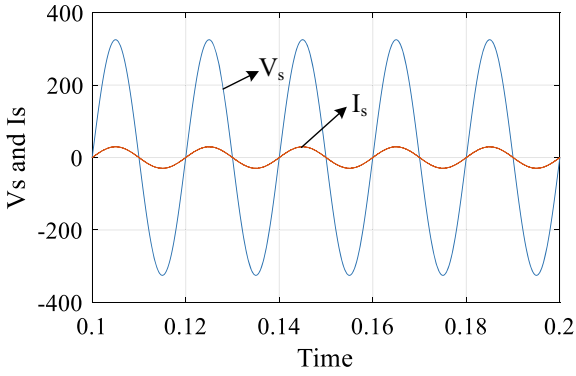

Fig. 14 Voltage and current waveforms

and the harmonic spectrum of the input current wave is shown in Fig. 15 and the THD is observed to be 2.14%.

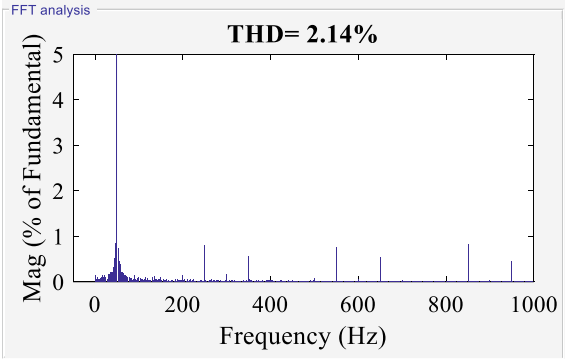

Fig. 15 AC side current harmonics

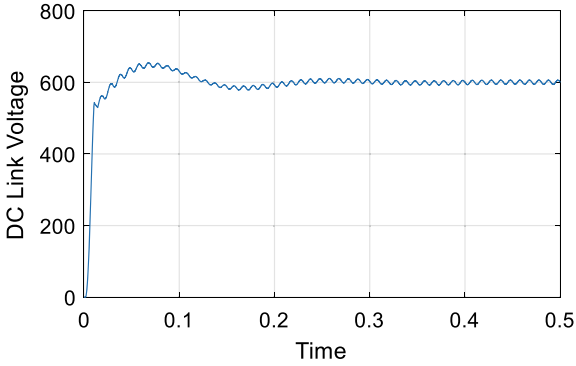

Fig. 16 DC-link voltage

4.3 Voltage Control Technique

The Three-phase HPFC is also simulated using the voltage control method described above. Figure 16 shows the DC bus voltage waveform which is made constant at 600 V. AC side voltage and current waveforms shown in Fig. 17 are in phase with each other. The harmonic spectrum of the AC side current is shown in Fig. 18. and the THD is observed to be 2.58%. Table 2 shows the comparison of THD for the above three methods.

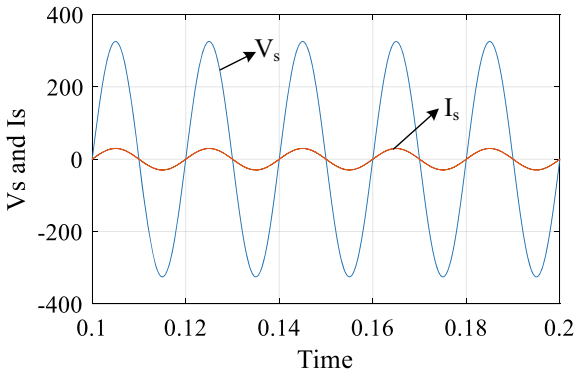

Fig. 17 Voltage and current waveforms

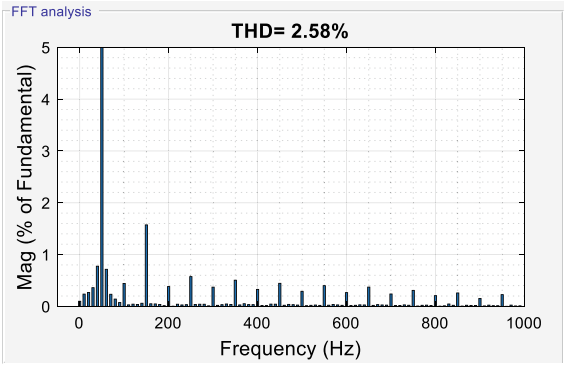

Fig. 18 AC side current harmonics

Table 2 Comparison of AC side current THD

Method	%THD
Current control	1.22
Vector control	2.14
Voltage control	2.58

5 Conclusion

Three methods to control the HPFC are discussed. The circuits are simulated in MATLAB/SIMULINK with parameters given in the above Table 1. The DC-link voltage is maintained constant during disturbances also and at the same time, the power factor at the AC side maintained nearly unity. THD is compared and tabulated for all the control techniques. The results show that the current-control technique gave the better THD compared with the other two techniques. This HPFC can be used in the integration of renewable energy sources to the grid.

References

1. Uddin MN, Abedin AH, Bashar KL, Islam S, Choudhury MA (2017) Three phase one switch modular-boost/vienna power factor corrected (PFC) rectifier. In: 2017 IEEE international conference on industrial technology (ICIT), pp 230–235
2. Rodriguez JR, Dixon JW, Espinoza JR, Pontt J, Lezana P (2005) PWM regenerative rectifiers: state of the art. IEEE Trans Ind Electron 52(1):5–22
3. Bin Wu (2006) High power converters and ac drives. IEEE PRESS. A John Wiley & Sons Inc., Publication
4. Kocman S, Kolar V, Trung Vo T (2010) Elimination of harmonics using multi-pulse rectifiers. In: Proceedings of 14th international conference on harmonics and quality of power—ICHQP
5. Das JC (2004) Passive filters-potentialities and limitations. IEEE Trans Ind Appl 40(1)
6. Singh B, Haddad KA, Chandra A (1999) A review of active filters for power quality improvement. IEEE Trans Ind Electron 46:960–971
7. Rashid MH (2001) Power electronics handbook. Academic Press. ISBN 0-12-581650-2

8. Begag S, Belhaouchet N, Rahmani L (2009) Three phase PWM rectifier with constant switching frequency. J Electr Syst 01:7–12
9. Zhang Y, Peng Y, Yang H (2016) Performance improvement of two-vectors-based model predictive control of PWM rectifier. IEEE Trans Power Electron 31(8):6016–6030
10. Li H, Lin M, Yin M, Ai J, Le W (2019) Three-vector based low complexity model predictive direct power control strategy for PWM rectifier without voltage sensors. IEEE J Emerg Select Top Power Electron 7(1):240–251
11. Cho Y, Lee K-B (2016) Virtual flux based predictive direct power control of three-phase PWM rectifiers, with fast dynamic response. IEEE Trans Power Electron 31(4):3348–3359
12. Upamanyu K, Ameta C, Narayanan G (2020) Simplified input voltage sensorless vector control for PWM rectifiers. IEEE Trans Ind Appl 56(4):4051–4060
13. Wai R, Yang Y, Wang Y (2018) Design of backstepping control for direct power control of three-phase PWM rectifier. In: 2018 3rd international conference on intelligent green building and smart grid (IGBSG), pp 1–4
14. Jungreis A (2012) High power factor isolated buck-type power factor correction converter. U.S. Patent 8,102,678, issued January 24
15. Vaideeswaran V, Sankar N (2018) Control techniques of three phase PWM rectifier. Int J Eng Adv Technol (IJEAT) 8(2S). ISSN: 2249-8958
16. EEE recommended practices and requirements for harmonics control in electric power systems. IEEE Std 519 (1992)

Design and Modeling of 3.3 kW GaN-Based HPFC Converter for Onboard EV Charger

Piyush Kumar, Amit Singh Tandon, Naveen Yalla, and A. V. J. S. Praneeth

1 Introduction

Power factor correction (PFC) converters are broadly used in EV applications for unity power factor [1]. Due to the use of rectifier and passive elements (inductor and capacitors), the power factor of the converter is less than desired. Hence to improve PF we use the PFC method. In the conventional PFC converter because of the bridge rectifier diode, there is high conduction loss which reduces the efficiency of the overall circuit. Researchers have been done research on bridgeless PFC boost converters to increase the overall efficiency. HPFC converter has low conduction loss, but when it operates in the CCM there is high reverse recovery loss of the MOSFET body diode [2, 3]. So, GaN HEMT is used in converter with less switching loss, less conduction loss and zero reverse recovery charge which overall increases its efficiency [4, 5]. GaN HEMT switches offer significantly better performance than MOSFETs. GaN reduces the physical size and improves the power density. High power density is desirable, especially for EV applications.

In this paper, we discuss two switching operations: high-frequency switching scheme and reduced switching control scheme. In a high-frequency switching scheme, all the four switches are operating at high frequency, but in this switching, we have high dv/dt and high distortion. The above problem is overcome by a reduced frequency switching scheme. In this, two switches (GaN switches) are operating at high frequency, whereas the other two switches (MOSFETs switches) are operating at power frequency. The reduced switching reduces the dv/dt stress on the switches and it also reduces the distortion which overall reduces the THD of input current.

Voltage control and current control controller are used in the converter circuit. A small-signal averaging model is done and the transfer function will be determined

P. Kumar · A. S. Tandon (✉) · N. Yalla
Department of EEE, NIT Tiruchirappalli, Tiruchirappalli, India

A. V. J. S. Praneeth
R&D Electrical, Borg Warner Inc-Luxembourg, Luxembourg, Germany

S. Kumar et al. (eds.), *Recent Advances in Power Electronics and Drives*, Lecture Notes in Electrical Engineering 852, https://doi.org/10.1007/978-981-16-9239-0_31

using the state-space averaging method. Inductor and capacitor values are calculated based on the circuit parameter of the HPFC converter. HPFC converter-based GaN HEMT is analyzed and the results are discussed in this paper.

2 HPFC Configuration

Figure 1a presents the onboard EV charger and Fig. 1b shows the PFC topology which is our area of research. In Fig. 1b we have two switches S_1 and S_2 as GaN HEMT which we are operating at high frequency and the switches S_3 and S_4 are Si switches that operate at power frequency.

2.1 Operating Modes

Interval 1: Positive line cycle inductor charging mode

Using Fig. 2a, S_2 is the principal switch during the positive half line cycle (line > neutral), and S_1 is driven by a complementary PWM signal. The boost DC/DC stage is made up of $\frac{S_1}{S_2}$ and L_1. Half-bridge leg S_4 is turned on during this positive half-cycle, when S_3 is still dormant. Current flows from $L_1 \rightarrow S_2 \rightarrow S_4$ and then back to N when the primary switch S_2 is switched on. During this time, the inductor L_1 charges current and the output capacitor C_L discharges to keep the output voltage in control.

Interval 2: Positive line cycle inductor discharging mode

In Fig. 2b, while still in the positive half line cycle, when S_2 is switched off, S_1 is turned on, and current flows via S_1 and back to N through S_4 throughout the time (1 − D). The inductor L_1 is discharging current to the output during this time when the output capacitor, C_L, is charging voltage.

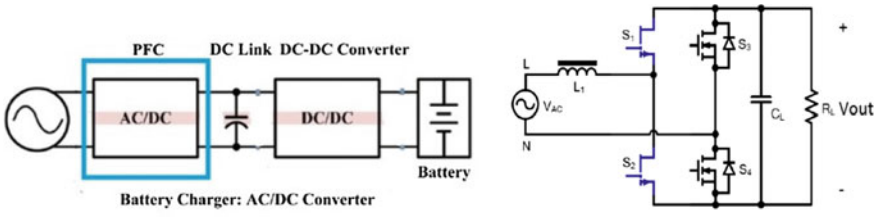

Fig. 1 **a** Onboard charger, **b** HPFC topology

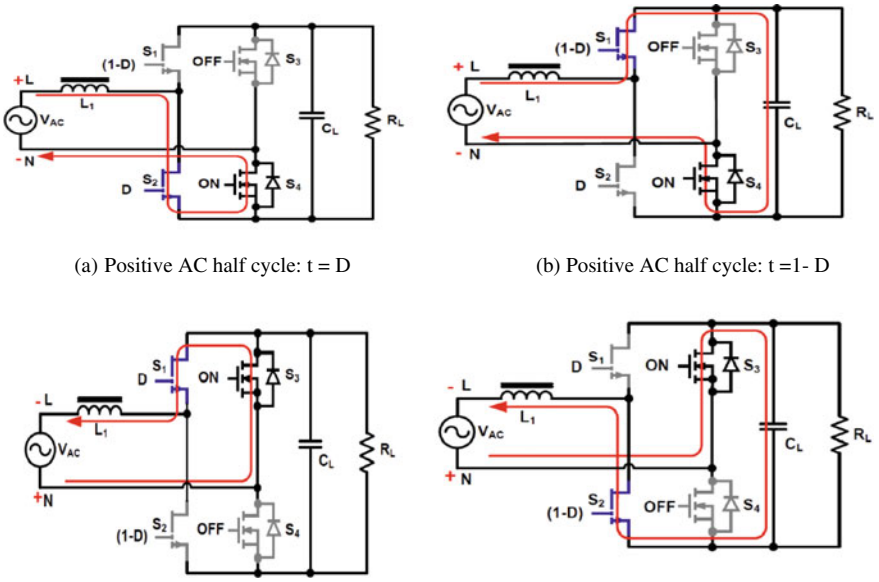

Fig. 2 Current flow in the circuit

As S_4 is performing all of the time in positive half line cycle operation (intervals 1 and 2), the DC bus ground V_{dc} is tied to N potential. For the duration of the positive half cycle, intervals 1 and 2 loop repeatedly.

Interval 3: Negative line cycle inductor charging mode

Using Fig. 2c as an example: The operation of the negative half line cycle (neutral > line) is analogous to that of the positive half line cycle (neutral > line), with the exception that the top and bottom switches are switched. S_1 is now the main switch, S_2 is free-wheeling, and S_3 is activated, leaving S_4 dormant. Current flows from $L_1 \rightarrow S_3 \rightarrow S_1$ and then back to L when the primary switch S_1 is switched on. During this time, the inductor L_1 charges current and the output capacitor C_L discharges to keep the output voltage controlling.

Interval 4: Negative line cycle inductor discharging mode

In Fig. 2d, while still in the negative half line cycle, when S_1 is switched off, S_2 is turned on, and current flows via S3 and back to L through S_2 throughout the timeframe $(1 - D)$. The inductor, L1, is discharging current to the output during this time, when the output capacitor, CL, is charging voltage.

Because S_3 is performing all of the time during negative half line cycle operation (intervals 3 and 4), the DC bus VDC+ is tied to N potential. For the duration of the negative half cycle, intervals 3 and 4 loop repeatedly.

2.2 Modeling, Analysis and Design

HPFC converter has two GaN switches (S_1, S_2) and two MOSFETs (S_3, S_4), as shown in Fig. 2 [6, 7]. S_4 is switched on during the positive half-cycle, S_2 is the active switch and S_1 is the synchronous switch. The supply charges the inductor when S_2 is turned on, and when S_1 is turned on the inductor discharges the energy to the capacitor. S_3 and S_1 are the active switches in the negative half cycle, and S_2 is the synchronous switch.

From Fig. 2a in which active switch is ON in positive cycle and inductor is charged by the AC supply, we have state space as given below:

$$\begin{pmatrix} \frac{di_L}{dt} \\ \frac{dv_c}{dt} \end{pmatrix} = \begin{pmatrix} 0 & 0 \\ 0 & \frac{-1}{RC} \end{pmatrix} \begin{pmatrix} i_L \\ v_c \end{pmatrix} + \begin{pmatrix} \frac{1}{L} \\ 0 \end{pmatrix} V_{ac} \tag{1}$$

$$V_O = \begin{pmatrix} 0 & 1 \end{pmatrix} \begin{pmatrix} i_L \\ v_c \end{pmatrix} \tag{2}$$

The coefficient of state-space matrix when the active switch is ON is as follows:

$$A_1 = \begin{pmatrix} 0 & 0 \\ 0 & \frac{-1}{RC} \end{pmatrix} B_1 = \begin{pmatrix} \frac{1}{L} \\ 0 \end{pmatrix} \tag{3}$$

$$C_1 = \begin{pmatrix} 0 & 1 \end{pmatrix} \tag{4}$$

From Fig. 2b in which active switch is OFF in positive cycle and inductor is discharging the energy into dc-link capacitor, we have state-space as given below:

$$\begin{pmatrix} \frac{di_L}{dt} \\ \frac{dv_c}{dt} \end{pmatrix} = \begin{pmatrix} 0 & \frac{-1}{L} \\ \frac{1}{C} & \frac{-1}{RC} \end{pmatrix} \begin{pmatrix} i_L \\ v_c \end{pmatrix} + \begin{pmatrix} \frac{1}{L} \\ 0 \end{pmatrix} V_{ac} \tag{5}$$

$$V_O = \begin{pmatrix} 0 & 1 \end{pmatrix} \begin{pmatrix} i_L \\ v_c \end{pmatrix} \tag{6}$$

The coefficient for the state-space matrix when the synchronous switch is ON is as follows:

$$A_2 = \begin{pmatrix} 0 & \frac{-1}{L} \\ \frac{1}{C} & \frac{-1}{RC} \end{pmatrix} B_2 = \begin{pmatrix} \frac{1}{L} \\ 0 \end{pmatrix} \tag{7}$$

$$C_2 = \begin{pmatrix} 0 & 1 \end{pmatrix} \tag{8}$$

After applying the disturbance on X,U and D,

$$\dot{X} + \dot{\hat{x}} = \left[\left(D + \hat{d} \right) A_1 + \left(1 - D - \hat{d} \right) A_2 \right] \left(X + \hat{x} \right)$$

$$+\left[\left(\mathrm{D}+\hat{\mathrm{d}}\right)\mathrm{B}_1+\left(1-\mathrm{D}-\hat{\mathrm{d}}\right)\mathrm{B}_2\right](\mathrm{U}+\dot{\mathrm{u}})$$

where X, U and D are the steady-state value of the state vector, the input voltage vector and the duty cycle, respectively. $\hat{x}$, $\hat{u}$, $\hat{d}$ are the disturbance of the state vector, the input voltage vector and the duty cycle, respectively.

$$\dot{\mathrm{X}}=[DA_1+(1-\mathrm{D})\mathrm{A}_2]\,\mathrm{X}+[\mathrm{DB}_1+(1-\mathrm{D})\,\mathrm{B}_2]\,\mathrm{U} \tag{9}$$

$$\dot{\hat{\mathrm{x}}}=\mathrm{A}\hat{\mathrm{x}}+\mathrm{B}\hat{\mathrm{u}}+[(\mathrm{A}_1-\mathrm{A}_2)\mathrm{X}+(\mathrm{B}_1-\mathrm{B}_2)\mathrm{U}]\hat{\mathrm{d}} \tag{10}$$

In order to obtain the power level transfer functions should be changed into S-domain form

$$\begin{pmatrix}\dot{\mathrm{I}}_\mathrm{L}\\ \dot{\mathrm{V}}_\mathrm{C}\end{pmatrix}=\begin{pmatrix}0 & \frac{-(1-\mathrm{D})}{\mathrm{L}}\\ \frac{(1-\mathrm{D})}{\mathrm{C}} & \frac{-1}{\mathrm{RC}}\end{pmatrix}\begin{pmatrix}\hat{\mathrm{i}}_\mathrm{L}\\ \hat{\mathrm{v}}_\mathrm{c}\end{pmatrix}+\begin{pmatrix}\frac{1}{\mathrm{L}} & \frac{\mathrm{V_C}}{\mathrm{L}}\\ 0 & \frac{-\mathrm{I_L}}{\mathrm{C}}\end{pmatrix}\begin{pmatrix}\hat{\mathrm{v}}_\mathrm{ac}\\ \hat{\mathrm{d}}\end{pmatrix} \tag{11}$$

$$\begin{pmatrix}\mathrm{I}_\mathrm{L}\\ \mathrm{V}_\mathrm{O}\end{pmatrix}=\begin{pmatrix}1 & 0\\ 0 & 1\end{pmatrix}\begin{pmatrix}\hat{\mathrm{i}}_\mathrm{L}\\ \hat{\mathrm{v}}_\mathrm{c}\end{pmatrix} \tag{12}$$

By using the state-space we derive the gain:

$$\mathrm{G_{id}}=\frac{\widehat{\mathrm{i_L}}}{\widehat{d}}=\frac{(1-\mathrm{D})\mathrm{I_L}+(\mathrm{sC}+\frac{1}{\mathrm{R}})\mathrm{V_O}}{\mathrm{LCs}^2+\frac{\mathrm{L}}{\mathrm{R}}\mathrm{s}+(1-\mathrm{D})^2}\,\text{at}\ \hat{\mathrm{v}}_\mathrm{ac}=0 \tag{13}$$

$$\mathrm{G_{vd}}=\frac{\widehat{\mathrm{v_c}}}{\widehat{\mathrm{d}}}=\frac{(1-\mathrm{D})\mathrm{V_O}-\mathrm{sLI_L}}{\mathrm{LCs}^2+\frac{\mathrm{L}}{\mathrm{R}}\mathrm{s}+(1-\mathrm{D})^2}\,\text{at}\ \hat{\mathrm{i}}_\mathrm{L}=0 \tag{14}$$

(a) **Inductor**

We have to choose inductor size so that the ripple in the input side is of specified limit [8].

$$\mathrm{L}\geq\frac{\mathrm{V_o}\mathrm{D}(1-\mathrm{D})}{f\,\Delta\mathrm{I}}=\frac{400*0.5*(1-0.5)}{500*1000*0.02*20.28}=0.5\,\mathrm{mH}$$

Since here we are taking the ripple to be 2% of the input current, the frequency of the switch is to be 500 kHz. As higher the switching frequency the inductor size is reduced by that proportion. The higher the inductance the less will be the ripple.

(b) **Output capacitor**

The output capacitor was sized to meet both the hold-up time or the AC line voltage period of 20 ms, and the low-frequency voltage ripple requirements. The capacitor value is selected to have the larger value among the two equations given below:

$$C \geq \frac{2 * P_o * t_{hold}}{V_o^2 - V_{o,min}^2} = \frac{2 * 3300 * 20 * 10^{-a}}{400^2 - 340^2} = 2171\,\mu F$$

$$C \geq \frac{P_o}{2\pi * f_{line} * \Delta V * V_o} = \frac{3300}{2\pi * 50\,Hz * 10 * 400} = 2626\,\mu F$$

We will choose the higher value of capacitance, C = 2626 mF.

3 Control Implementation

Since CCM operation was chosen for this design, average current mode control will be used as it is the most convenient method for achieving a CCM operation PFC [9]. Power factor is defined as the ratio of the actual and apparent power of an AC input, as noted in the literature review. PF can be defined as the product of current distortion and phase shift, assuming that the input voltage is a perfect sine wave. The PFC control loop functions are:

- **Control the output voltage**: Making the output voltage equal to the reference value we will implement the voltage control loop. In Fig. 3, v is measured feedback voltage and v^* is our reference voltage. The error value is going to the PI controller, and the output of the PI controller is shown in Fig. 8.
- **Control the input current**: For current to be sinusoidal and maintain the same phase as the input voltage, we implement the current control loop. Here in Fig. 4, i is the measured feedback current which is compared with i^* which is our reference current. The error is going to the PI controller and the output of the PI controller is shown in Fig. 9. For generating the pulse we use the repeating sequence and relation operator (Fig. 5).

  In control scheme we have the following:

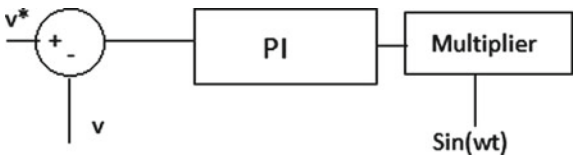

Fig. 3 Voltage control scheme

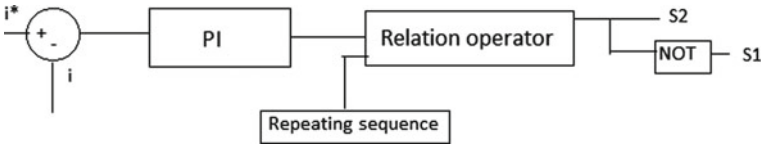

Fig. 4 Current control scheme

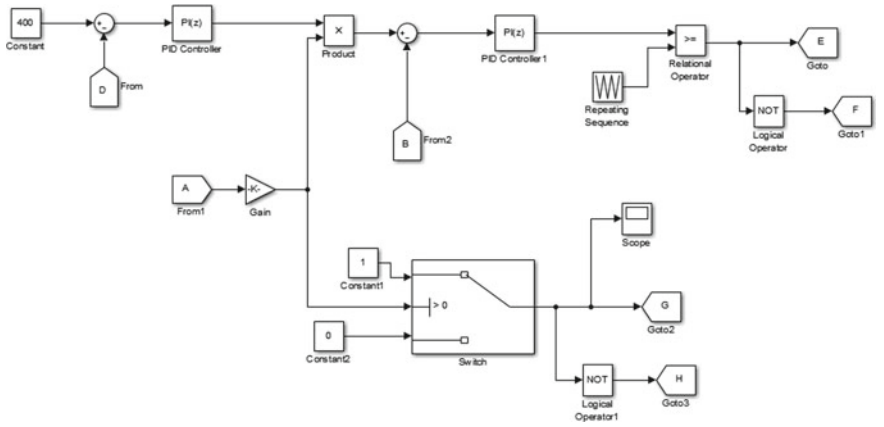

Fig. 5 Power circuit simulation diagram

- **Reduced switching control scheme**: When two switches are GaN switches, the other two are MOS switches operating at power frequency (Figs. 6 and 7).
- **High switching frequency control scheme**: All four switches are high-frequency operating switches.

Voltage control is also called the outer control loop. With the help of voltage control loop, we are keeping the output voltage equal to 400 V.

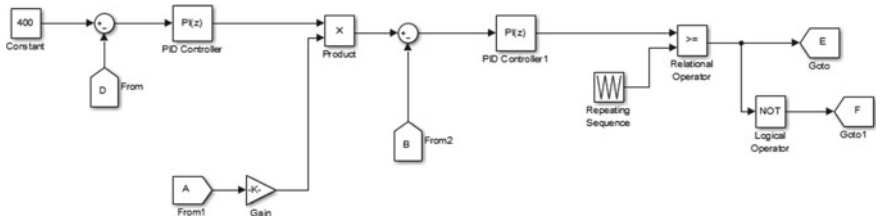

Fig. 6 Control circuit simulation diagram for reduced switching control

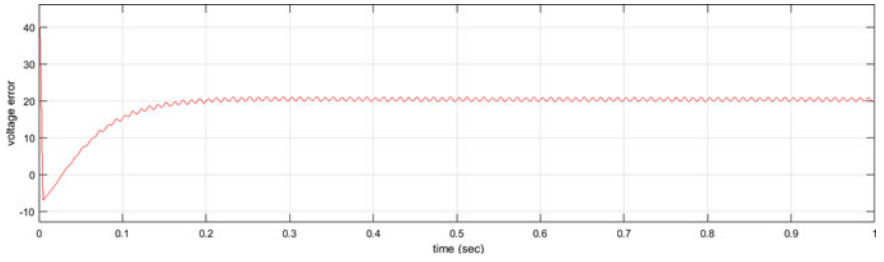

Fig. 7 Control circuit simulation diagram for high switching frequency control

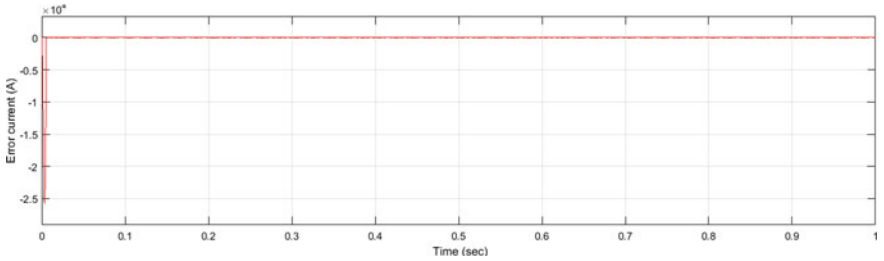

Fig. 8 Output of voltage control loop

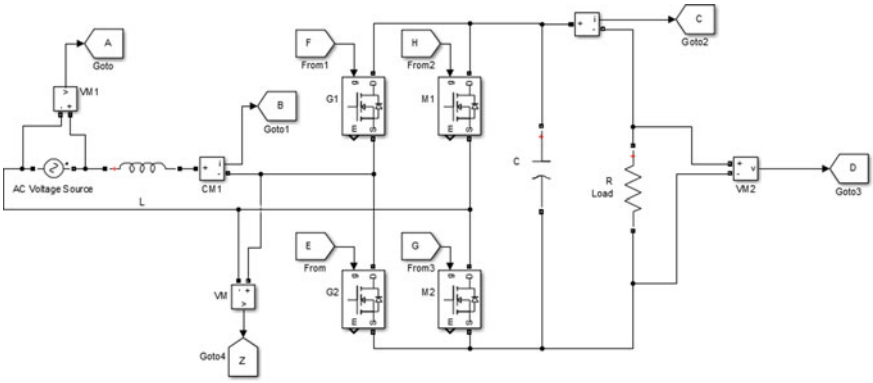

Fig. 9 Output of current control loop

Current control is also the inner control loop. With the help of inner loop control, we are keeping the input current which is also equal to the inductor current in phase with the input voltage (Figs. 8 and 9).

Output of control loop

4 Results and Discussion

4.1 Component Selection for the Power Circuit

Parameter	Value
Input voltage (RMS)	85–265 V
Output voltage	400 V
Output power steady state	3.3 kW

(continued)

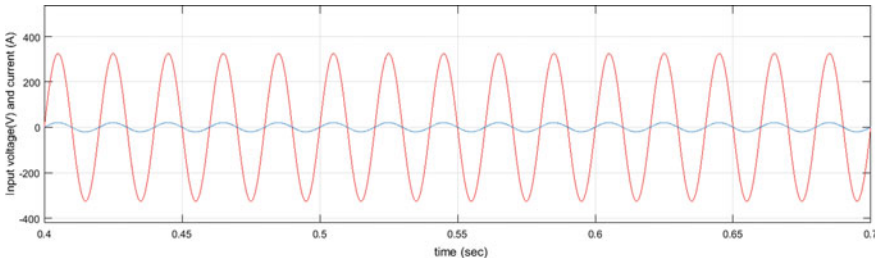

Fig. 10 Input voltage and current for the reduced switching control

(continued)

Parameter	Value
Switching frequency	500 kHz
Output voltage 100 Hz ripple	10 V peak to peak
Power factor	>0.98
Current THD	5% (max)

Reduced Switching Frequency control Scheme

Figure 10 shows input voltage and input current which are in phase with each other, i.e., at unity power factor. Figure 11 shows the output voltage and Fig. 12 shows the pole voltage for the reduced switching frequency.

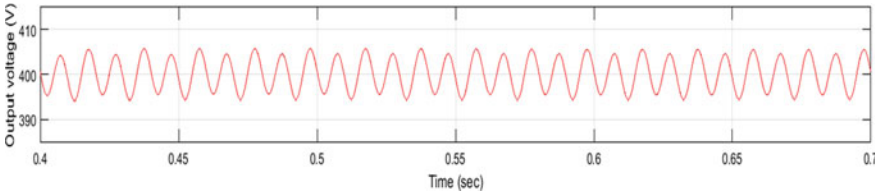

Fig. 11 Output voltage for the reduced switching control

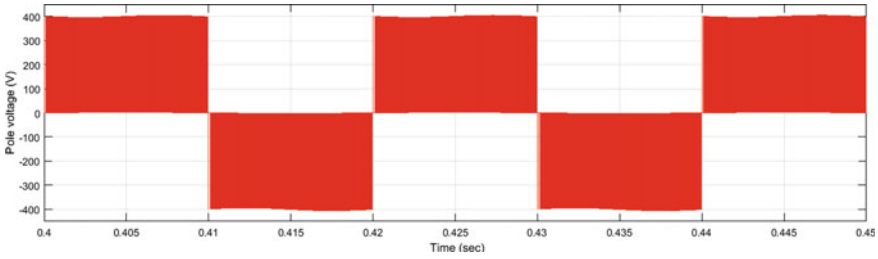

Fig. 12 Pole voltage for the reduced switching control

High switching Frequency Control Scheme

Figure 13 shows that input current and input voltage are in phase, i.e., at unity PF. Figure 14 shows the output voltage and Fig. 15 shows the pole voltage for the high switching frequency scheme.

THD & Input PF

Figures 16 and 17 show the THD for input current of the high switching frequency and reduced switching frequency. Here we show the THD value for two powers at 500 W and at 3.3 kW which are given below.

Figure 18 shows the THD versus power graph for high switching frequency and reduced switching frequency. As observed, the THD value starts decreasing as power increases. For high-frequency switching THD at 3.3 kW is 3.08% and for reduced switching frequency it is 2.27%.

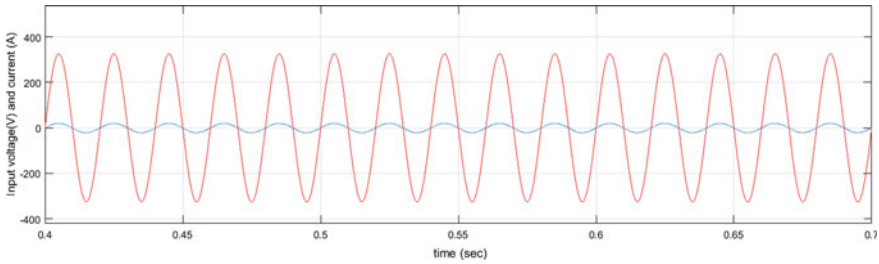

Fig. 13 Input voltage and current for high switching frequency control

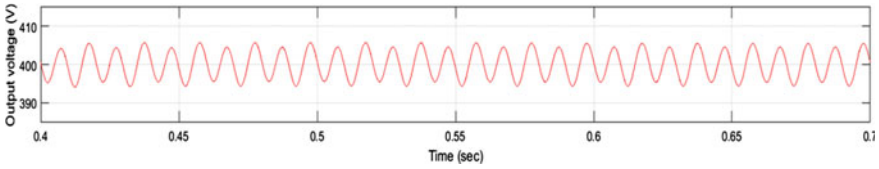

Fig. 14 Output voltage for high switching frequency control

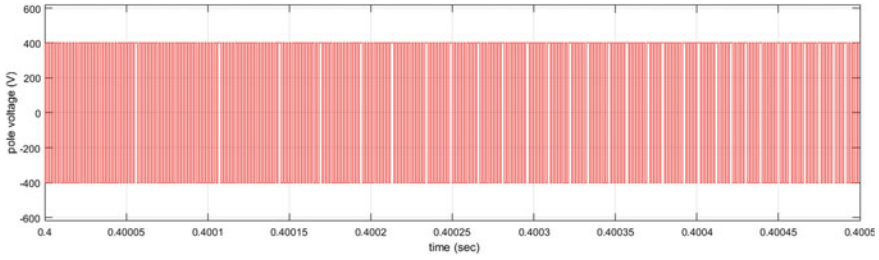

Fig. 15 Pole voltage for high switching frequency control

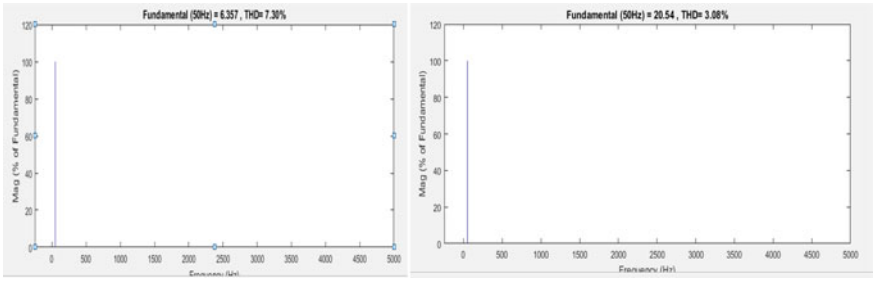

Fig. 16 Current THD for high-frequency switching for 1 and 3.3 kW, respectively

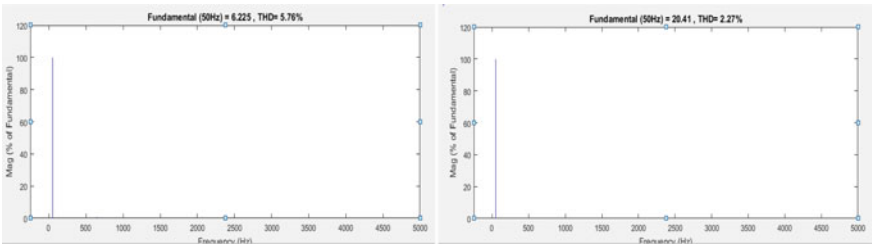

Fig. 17 Current THD for reduced frequency switching for 1 and 3.3 kW, respectively

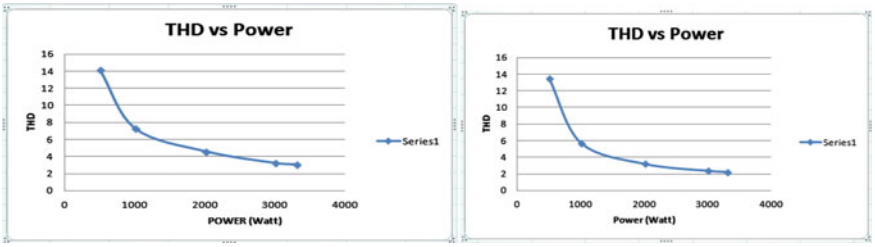

Fig. 18 Current THD versus power for high-frequency switching and reduced frequency switching, respectively

Figure 19 shows the input power factor for the high and reduced frequency switching scheme for the HPFC converter. As observed, the input PF increases as we start increasing the power from 500 W to 3300 kW.

5 Conclusion

Design and modeling of 3.3 kW GaN-based HPFC converter for onboard EV charger is investigated with the software platform. A small-signal analysis of high PFC has

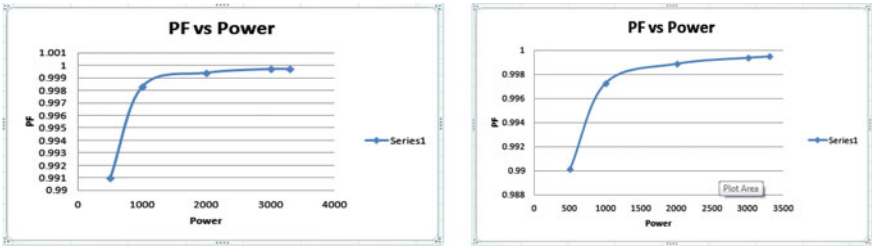

Fig. 19 PF versus power for high-frequency switching and reduced frequency switching, respectively

been carried out. State-space averaging is used to derive the transfer function of the PI controller for the voltage and current loop controller. Two PWM control strategies are implemented to get the desired output. Power quality aspects like input current, THD, and output voltage ripple are investigated in both cases. It can be observed that both the methods are providing nearly sinusoidal input currents.

References

1. Mohanty PR, Panda AK, Das D (2016) An active PFC boost converter topology for power factor correction. Ann IEEE Ind Conf (INDICON)
2. Babu KSH, Holde R, Singh BH (2018) Power factor correction using boost converter operating in CCM for front-end AC to DC conversion. ICSESP
3. Turchi J, Dalal D, Wang P, Jenck L (2014) Power Factor Correction (PFC) handbook. ON Semiconduct
4. GaN Systems, Appl. Note GN001 (2018) Application guide-design with GaN enhancement mode HEMT
5. GaN Systems, Appl. Note GS665BTP-REF rev 170905 (2017) High efficiency CCM bridgeless totem pole PFC design using GaN E-HEMT
6. Erickson RW, Maksimovic D (2001) Fundamentals of power electronics, 2nd edn. Kluwer Academic Publishers, Norwell
7. Mohan N, Undeland TM, Robbins WP (2003) Power electronics: converters, application and design 3rd edn. John Willey & Sons, New York
8. Johnson B, Instrument T (2018) Application Report SLUA896. Power factor correction design for on-board chargers in electric vehicles
9. NXP Semiconductors, Appl. Note DRM174 (2016) Totem-pole bridgeless PFC design using MC56F82748

A Novel Thirteen-Level Two-Fold Gain Inverter Topology with Reduced Voltage Stress

M. S. H. Naidu, C. Sadanala, and S. Patnaik

1 Introduction

Currently, multilevel inverters are playing a very crucial role in developing high power applications like HVDC, traction and propulsion systems, renewable energy sources, electric vehicles, AC drives, etc. [1]. They can withstand higher voltages, operate at high switching frequencies by avoiding higher voltage stresses and produce the stepped sinusoidal wave with low distortions. Also, they can reduce filter size at the output. However, the conventional three-level inverters are not suitable to meet the above demands, so the inverters that can produce multi levels are proposed in the literature [2]. Mainly there are three different configurations for multilevel converters: (1) Neutral point clamped MLI (NPC-MLI), (2) flying capacitor MLI (FC-MLI), and (3) cascaded H bridge MLI (CH-MLI). Besides the advantages of these above converters, there are some drawbacks also mentioned in the literature. In the case of NPC-MLI and FC-MLI, there is a problem of voltage balancing in the capacitors. If the number of levels increases at the output then the requirement of the capacitors also increases in these topologies. In CH-MLI, a large number of DC sources and more number of switches are required which increases the cost of the inverter. So there are a wide variety of topologies available in the literature to encounter the aforementioned problems. In [3], asymmetrical MLI topologies were proposed with less number of switches but multiple DC sources are used. In [4], two sources are used but more number of components are used. In switched capacitor multilevel inverters [5] only one source is used but total standing voltage and maximum blocking voltages are very high, so they are not appropriate for high-voltage applications. In FC-MLIs, TSV and MBV are low but cannot boost the voltage up to the requirements. By considering all the above problems, this paper proposed a hybrid 13-level inverter topology that uses the reduced count of components with low voltage stress on the

M. S. H. Naidu (✉) · C. Sadanala · S. Patnaik
Department of Electrical Engineering, NIT Raipur, Raipur 492010, India
e-mail: naidusaiharsha@gmail.com

S. Kumar et al. (eds.), *Recent Advances in Power Electronics and Drives*, Lecture Notes in Electrical Engineering 852, https://doi.org/10.1007/978-981-16-9239-0_32

switches. It has a gain of 2 and MBV is within Vdc. Moreover, the self-balancing of capacitor voltages will take place without the use of any additional circuitry or control methods.

2 Presented Topology

The presented topology consists of 13 switches (s1–s13), 3 capacitors (C1–C3), and 1 dc input source, as shown in Fig. 1. C1 and C2 are the flying capacitors which will have steady-state voltages in the ratio 1:2 and the other one is switched capacitor used to bring out the intermediate voltage levels. The different voltage levels which are generated by using switching configurations can be seen in Table 1 and the corresponding current paths for positive levels can be understood from Fig. 2.

2.1 Natural Balancing of Capacitors

As per the switching table the voltage levels ±1/3, ±2/3, ±4/3, ±5/3 Vdc, can be produced in three different states. This shows us that these levels have extra switching states which will help in balancing the capacitors in a natural way. The current second balance is used for balancing the capacitor voltage, i.e., the capacitors will reach the steady-state if and only if they maintain the current second balance. The current second balance means the amount of energy stored by the capacitor should be released in one complete switching cycle so that each of the extra switching states for the specified voltage levels in the table should be given to the converter in each cycle for maintaining the current second balance of the capacitors; therefore the flying capacitors are required to be managed in three cycles with respect to fundamental of modulating (reference) wave to maintain the required steady-state voltages. Hence, the time period of the fundamental modulating wave is equal to three times of time

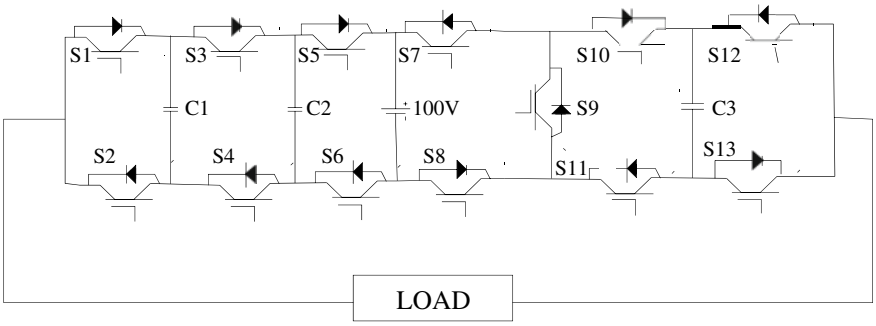

Fig. 1 Circuit diagram for the presented 13-level inverter

Table 1 Switching states for the presented 13-level inverter

O/P voltage level	Capacitor states (Vs, Vc1, Vc2, Vc3)	S1	S2	S3	S4	S5	S6	S7	S8	S9	S10	S11	S12	S13
2 Vdc	$Vs + 0 + 0 + C3$	1	0	1	0	1	0	0	1	1	1	0	0	1
$1\frac{2}{3}$ Vdc	$Vs - C1 - C2 + C3$	1	0	0	1	1	0	0	1	1	1	0	0	1
	$C3 + C2$	1	0	1	0	0	1	0	1	1	1	0	0	1
	$C3 + Vs - V1$	0	1	1	0	1	0	0	1	1	1	0	0	1
$1\frac{1}{3}$ Vdc	$Vs + 0 - C2 + C3$	0	1	0	1	1	0	0	1	1	1	0	0	1
	$C3 + C2 - C1$	0	1	1	0	0	1	0	1	1	1	0	0	1
	$C3 + C1$	1	0	0	1	0	1	0	1	1	1	0	0	1
1 Vdc	Vs	1	0	1	0	1	0	1	1	0	1	1	0	1
$\frac{2}{3}$ Vdc	$Vs + C1 - C2 + 0$	1	0	0	1	1	0	0	1	0	0	1	0	1
	C2	1	0	1	0	0	1	0	1	0	0	1	0	1
	$Vs - C1$	0	1	1	0	1	0	0	1	0	0	1	0	1
$\frac{1}{3}$ Vdc	$Vs - C2 + 0$	0	1	0	1	1	0	0	1	0	0	1	0	1
	$C2 - C1$	0	1	1	0	0	1	0	1	0	0	1	0	1
	C1	1	0	0	1	0	1	0	1	0	0	1	0	1
0		1	0	1	0	1	0	1	0	0	1	0	1	0
$-\frac{1}{3}$ Vdc	$-Vs + 0 + C2 + 0$	1	0	1	0	0	1	1	0	0	1	0	1	0
	$-C2 + C1$	1	0	0	1	1	0	1	0	0	1	0	1	0
	$-C1$	0	1	1	0	1	0	1	0	0	1	0	1	0
$-\frac{2}{3}$ Vdc	$-Vs - C1 + C2 + 0$	0	1	1	0	0	1	1	0	0	1	0	1	0
	$-C2$	0	1	0	1	1	0	1	0	0	1	0	1	0
	$-Vs + C1$	1	0	0	1	0	1	1	0	0	1	0	1	0

(continued)

Table 1 (continued)

O/P voltage level	Capacitor states (Vs, Vc1, Vc2, Vc3)	S1	S2	S3	S4	S5	S6	S7	S8	S9	S10	S11	S12	S13
−1 Vdc	−Vs	0	1	0	1	0	1	1	0	0	1	0	1	0
$-1\ \frac{1}{3}$ Vdc	−Vs + 0 + C2 − C3	1	0	1	0	0	0	1	0	1	0	1	1	0
	−C3 − C2 + C1	1	0	1	0	1	0	1	0	1	0	1	1	0
	−c3 − c1	0	1	1	0	1	0	1	0	1	0	1	1	0
$-1\ \frac{2}{3}$ Vdc	−Vs + C1 + C2 − C3	0	1	1	0	0	1	1	0	1	0	1	1	0
	−C3 − C2	1	0	0	1	1	0	1	0	1	0	1	1	0
	−C3 − Vs + C1	0	1	1	0	1	0	1	0	1	0	1	1	0
−2Vdc	−Vs + 0 + 0 − C3	0	1	0	1	0	1	1	0	1	0	1	1	0

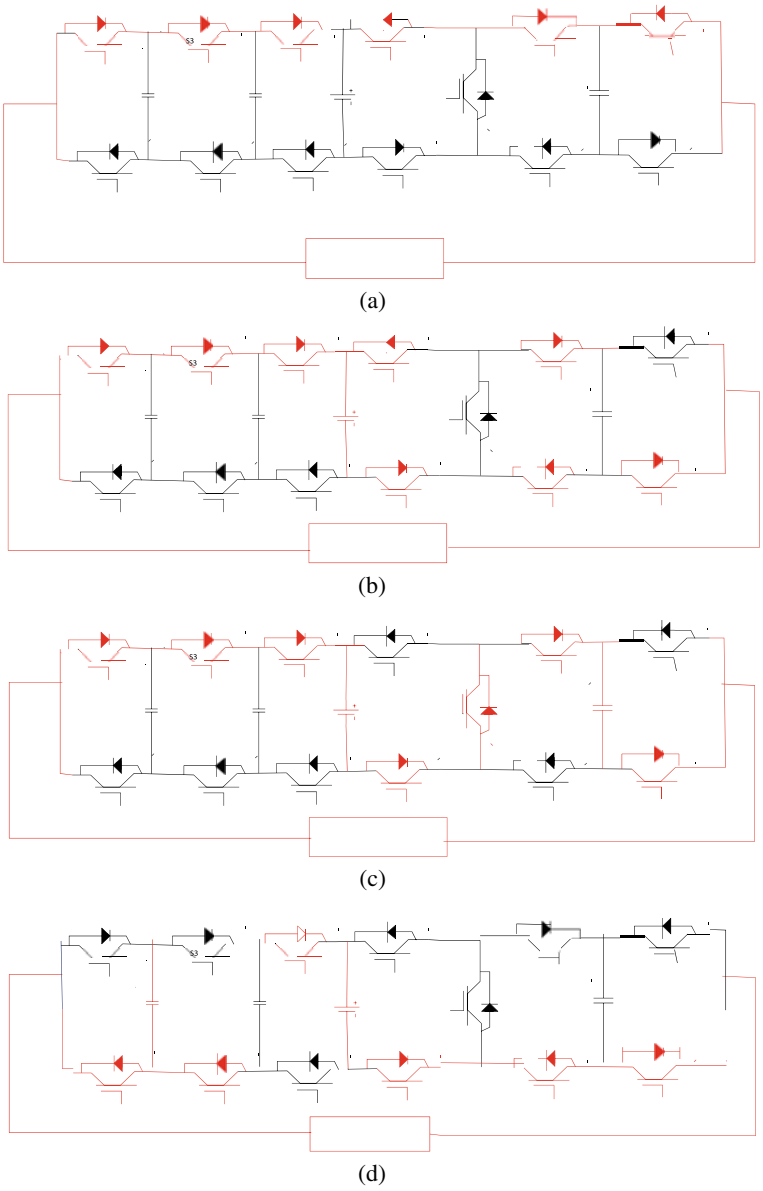

Fig. 2 Switching states of the proposed model

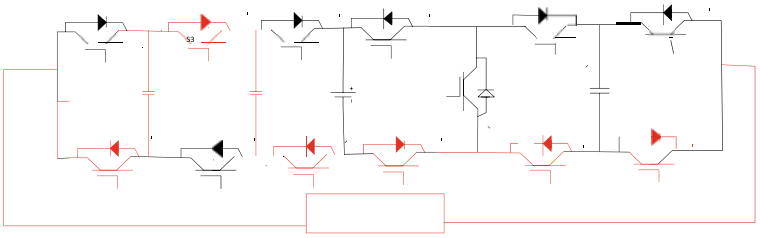

(e)

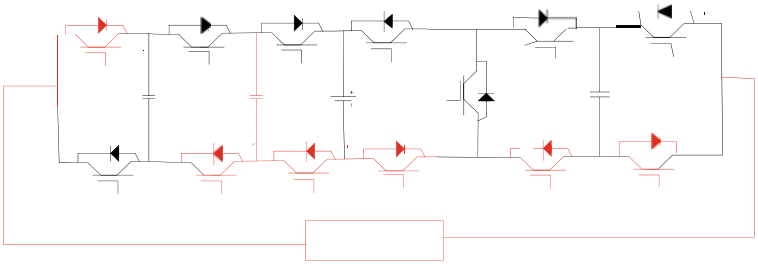

(f)

Fig. 2 (continued)

period of the capacitor voltages. Here the positive value of the capacitor indicates discharging and the negative value indicates charging. The value of voltages across the capacitors can be found by using the time-domain analysis [6].

2.2 Analysis of Voltage Levels

The output voltage levels 0, ±Vdc, ±2 Vdc are the same for all three cycles. Out of those 0, +Vdc, +2 Vdc levels are explained below:

Level 0: Fig. 2a shows the circuit diagram for o/p voltage level 0. It is produced by switching all upper switches or all lower switches.

Level 1: Fig. 2b shows the circuit diagram for o/p voltage level 1 Vdc. It is produced by using switching states S5, S3, S1, S13, S11, S8, S7, S10, and the voltage source provides load current. All the capacitors are disconnected.

Level 2: Fig. 2c explains the circuit diagram for o/p voltage level 2 Vdc. It is produced by using switching states S5, S3, S1, S13, S11, S8, S7, S10, and the input voltage source and switching capacitor C3 supply the load current. Flying capacitors are disconnected.

All the three equivalent circuits (Fig. 2d–f) of the inverter will use different switching configurations to generate the same voltage level. These three different

configurations are applied to the converter in three different cycles for obtaining natural balancing of the capacitors [6]. One-third level in three cycles is explained below.

Cycle 1: Fig. 2d shows the circuit diagram for o/p voltage level 1/3 Vdc. It is produced by using switching states S5, S4, S2, S13, S11, S8, and the input voltage source and capacitor C2 contribute to the output voltage level.

Cycle 2: Fig. 2e explains the circuit diagram for o/p voltage level 1/3 Vdc. It is produced by using switching states S3, S2, S13, S11, S8, and S6. Here the flying capacitors C1 and C2 contribute to the output voltage levels.

Cycle 3: Fig. 2f shows the circuit diagram for o/p voltage level 1/3 Vdc. It is produced by using switching states S1, S13, S11, S8, S6, and S4. Here capacitor C1 contributes to the output voltage level.

2.3 Parameters Comparison

In this module the other recent topologies are compared with the presented topology in terms of the number of active/passive components, TSV, MBV and CF in Table 2. This topology uses single DC source to generate 13 levels and also gives the low value of TSV and cost function (CF) compared to other recent topologies. In [5, 7] the authors use few number of switches but TSV is very high. All the topologies in the table can generate the 13 levels. The CF will evaluate the total cost of the converter [8] which can be expressed as

$$\mathrm{CF} = \frac{\left[Nsw + Ngd + Nd + Ncap + \alpha \mathrm{TSV(p,u)}\right] * \mathrm{Nsources}}{N\,level} \tag{1}$$

where α is the weight coefficient.

3 Simulation Results

The presented model is validated in the simulation environment of MATLAB for R and RL load. A single voltage source of 100 V DC is used at the input side and the output voltage has the maximum value of 200 V which is due to the input voltage source and switched capacitor voltage. Flying capacitors are used for producing the intermediate voltage levels in the waveform. All the capacitors are well balanced at their desired values to produce the 13 levels at the output. The simulation circuit parameters are shown in Table 3. The total harmonic distortion of R load output voltage is found to be 9.48% without using any harmonic filter at the load side. The output voltages and currents from R and RL load and the voltages across the

Table 2 Comparative analysis of 13-level inverters

Paper	Sources	Gatedrivers	Capacitors	Diodes	Switches	Gain	TSV	MBV	Cost function	
									$\alpha = 0.5$	$\alpha = 1.5$
[9]	1	3	4	4	10	6	33	1	2.88	5.42
[10]	1	13	3	2	13	6	32	3	3.61	6.076
[8]	1	12	4	0	12	1.5	6	1	2.38	2.84
[11]	1	14	3	1	14	6	5.50	3	2.67	3.09
[4]	2	9	2	14	14	6	32	6	8.46	9.84
[12]	1	29	5	5	29	6	4.83	1	13.38	19.68
[7]	4	6	0	0	10	1	32	5	5.41	5.78
[5]	1	7	5	0	10	6	59	1	3.96	4.80
[3]	3	8	0	0	8	2	4	5	8.5	7.807
[13]	1	19	5	0	19	6	39	3	4.15	5.07
Proposed	1	9	3	0	13	2	9	1	2.26	2.96

Table 3 Parameters of the presented circuit

Input voltage	100 V
Switching frequency	5 kHz
Peak voltage at the output	200 V
Capacitor values	1200 uF

capacitors are also taken from the simulation. THD analysis is also done for R load output voltage (Fig. 3d).

4 Conclusions

In this paper, a novel 13-level two-fold gain inverter topology is presented with a reduced number of components which aim to reduce the voltage stress on the circuit components. The presented model comprises 13 switches, 3 capacitors and 1 DC input source to produce 13-level output voltage having a gain of 2. Different operating modes and their switching states of the circuit are explained elaborately for the presented model. Capacitor voltage balance will take place in open loop without using voltage or current sensing circuits. The comparison analysis was made between the other recent topologies and the presented topology, and it has been found that the proposed one has the lowest cost function. The voltage and current waveforms for R and RL load are taken from the simulation and the THD analysis is done for R load output voltage.

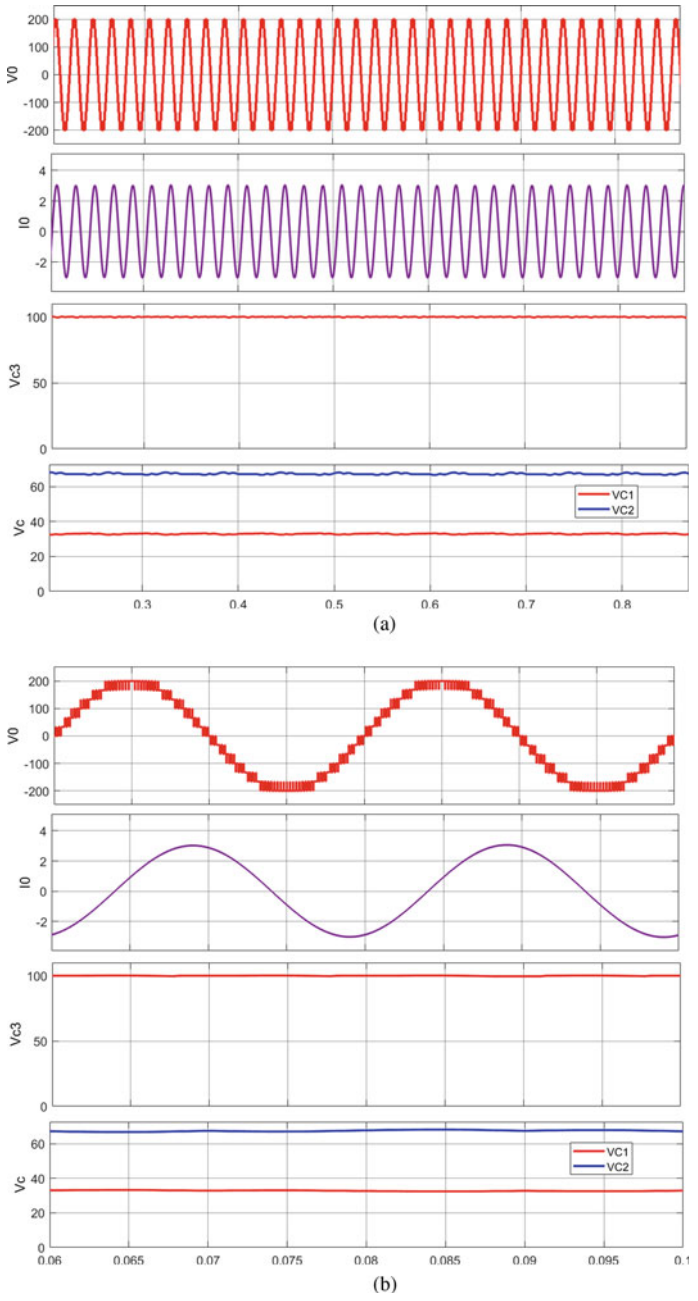

Fig. 3 Output voltages, currents and capacitor voltages for **a** RL load **b** RL load between 0 and 0.1 s **c** R load **d** THD analysis for R load output voltage

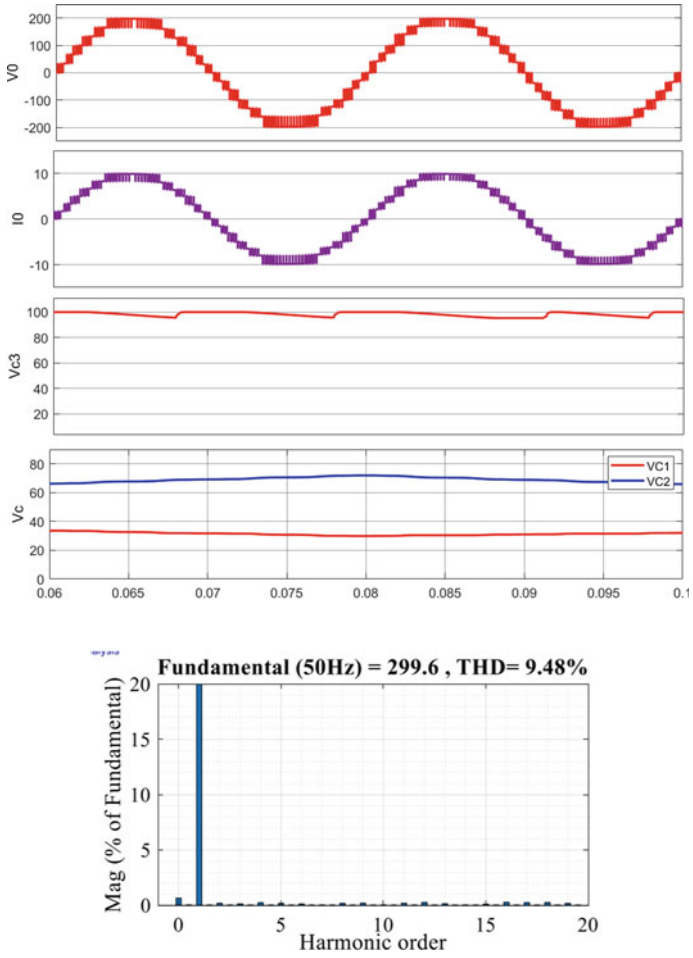

Fig. 3 (continued)

References

1. Rodriguez J, Lai J-S, Peng FZ (2002) Multilevel inverters: a survey of topologies, controls, and applications. IEEE Trans Industr Electron 49(4):724–738. https://doi.org/10.1109/TIE.2002.801052
2. Kouro S et al (2010) Recent advances and industrial applications of multilevel converters. IEEE Trans Industr Electron 57(8):2553–2580. https://doi.org/10.1109/TIE.2010.2049719
3. Siddique MD et al (2019) Low switching frequency based asymmetrical multilevel inverter topology with reduced switch count. IEEE Access 7:86374–86383. https://doi.org/10.1109/ACCESS.2019.2925277
4. Samadaei E, Kaviani M, Bertilsson K (2019) A 13-levels module (K-type) with two DC sources for multilevel inverters. IEEE Trans Industr Electron 66(7):5186–5196. https://doi.org/10.1109/TIE.2018.2868325

5. Ye Y, Cheng KWE, Liu J, Ding K (2014) A step-up switched-capacitor multilevel inverter with self-voltage balancing. IEEE Trans Industr Electron 61(12):6672–6680. https://doi.org/10.1109/TIE.2014.2314052
6. Vasu R, Chattopadhyay SK, Chakraborty C (2020) Seven-level packed U-cell (PUC) converter with natural balancing of capacitor voltages. IEEE Trans Ind Appl 56(5):5234–5244. https://doi.org/10.1109/TIA.2020.3008397.
7. Samadaei E, Gholamian SA, Sheikholeslami A, Adabi J (2016) An envelope type (E-Type) module: asymmetric multilevel inverters with reduced components. IEEE Trans Industr Electron 63(11):7148–7156. https://doi.org/10.1109/TIE.2016.2520913
8. Zeng J, Lin W, Cen D, Liu J (2020) Novel K-type multilevel inverter with reduced components and self-balance. IEEE J Emerg Select Topi Power Electron 8(4):4343–4354. https://doi.org/10.1109/JESTPE.2019.2939562
9. Ye Y, Chen S, Wang X, Cheng K-WE (2021) Self-balanced 13-level inverter based on switched capacitor and hybrid PWM algorithm. IEEE Trans Industr Electron 68(6):4827–4837. https://doi.org/10.1109/TIE.2020.2989716
10. Sandeep N (2021) A 13-level switched-capacitor-based boosting inverter. IEEE Trans Circuits Syst II Express Briefs 68(3):998–1002. https://doi.org/10.1109/TCSII.2020.3017338
11. Kim K-M, Han J-K, Moon G-W (2021) A high step-up switched-capacitor 13-level inverter with reduced number of switches. IEEE Trans Power Electron 36(3):2505–2509. https://doi.org/10.1109/TPEL.2020.3012282
12. Taghvaie A, Adabi J, Rezanejad M (2018) A self-balanced step-up multilevel inverter based on switched-capacitor structure. IEEE Trans Power Electron 33(1):199–209. https://doi.org/10.1109/TPEL.2017.2669377
13. Hinago Y, Koizumi H (2012) A switched-capacitor inverter using series/parallel conversion with inductive load. IEEE Trans Industr Electron 59(2):878–887. https://doi.org/10.1109/TIE.2011.2158768

PV-Array-Integrated UPQC for Power Quality Enhancement and PV Power Injection

Harsh D. Patel, Priyank Gandhi, and Pranav Darji

1 Introduction

Harmonics, unbalanced current, reactive power, voltage dip and swell result in losses, less utilization grid, poor efficiency, tripping of motors, etc. and cause electrical pollution in the distribution system. Also, pollution of the environment is a major concern, therefore the world is shifting toward green energy generation through PV-based solar rooftops in households and commercial buildings [1]. PV array is an intermittent source of energy and connecting a large number of such sources in a weak distribution system may result in a dip and swell in the voltage, consequently resulting in instability of the grid [2]. To improve the power quality and to transmit the green energy, two power electronic-based devices are required. This paper aims to address the function of power quality enhancement and green energy transfer in a distribution system using single power electronic-based device. In order to overcome the power quality issues and integrate clean energy source in the grid, a multifunctional PV-integrated UPQC is discussed in the paper.

A single-stage system is used to deal with power quality issues and it is also performing the function of PV power injection in the three-phase distribution system [3]. In [4], a single-phase system for power quality improvement on the load side and PV power injection is discussed. But the problem with integrating PV system with the shunt filter is that it is not able to achieve unity instantaneous power factor and regulate the voltage of PCC at the same time. In order to fulfill both the purpose that is unity power factor and voltage regulation, UPQC can be used. PV array integration in UPQC can be done to improve the power quality problem and green energy generation. In [5, 6], PV-UPQC has been reported with d-q-o theory, in which single-stage PV-UPQC has been discussed. This has several advantages such as grid

H. D. Patel (✉) · P. Gandhi · P. Darji
Sardar Vallabhbhai National Institute of Technology, Gujarat, Surat 395007, India

P. Darji
e-mail: pra-nav@eed.svnit.ac.in

S. Kumar et al. (eds.), *Recent Advances in Power Electronics and Drives*, Lecture Notes in Electrical Engineering 852, https://doi.org/10.1007/978-981-16-9239-0_33

and load-side power quality improvement, protecting the critical load from a grid-side problem and improving the fault ride-through capacity of the converter. Design and configuration of various distributed flexible AC transmission system (D-FACTS) devices are discussed in [7].

A case study of distribution static compensator (DSTATCOM) having second-order Butterworth low-pass filter to filter out dc component from d-axis and q-axis load current is mentioned in [8]. In [9, 10] moving average filter-based UPQC is implemented to enhance the performance of SRF control, particularly in nonlinear and unbalanced load condition. So in this paper, PV-UPQC having a moving average filter in DSTATCOM control system for extracting dc component is used. In [11, 12] configuration, structure and control of dynamic voltage restorer (DVR) to mitigate supply-side power quality issues is given. In [13, 14] various MPPT algorithms for bringing out maximum power from the PV array are discussed. In [15] performance analysis of PV-UPQC for sensitive load is carried out and it is learned that oscillation in induction motor due to dip and swell in the supply voltage is reduced. A generalized cascaded delay signal cancellation for fundamental frequency positive sequence voltage or current generation for PV-UPQC is discussed and performance anatomization is carried out in [16]. A battery energy storage-based PV-UPQC that can also supply the real power to the grid during cut-off of the supply power with power quality enhancement is discussed in [17].

To control PV-integrated UPQC there are several control strategies for the generation of reference current/voltage and they can be classified in time-domain control strategies and frequency-domain control strategies. Time-domain control strategies consist of unit template generation, instantaneous reactive power theory, SRF theory, etc. Frequency-domain control strategies such are Fourier series theory, discrete Fourier transform theory, etc. [7]. SRF theory is used in this paper to control DSTATCOM and DVR. In the case of unbalanced loading, the d-axis load current contains a double harmonic part. To remove the double harmonic part, a low-pass filter having a very low corner frequency is needed. Since the dynamic response of a low-pass filter during the extraction of an active load component is poor, a moving average filter has been utilized to strain the d-axis load current [5].

In this paper a two-stage PV-UPQC is considered. The first stage is of the boost converter and the second stage of UPQC. The key benefits of the system are as follows:

1. Voltage and current quality improvement.
2. Power quality improvement with PV power penetration.
3. Improvement of dynamic performance during load active current extraction using moving average filter [5].
4. Stable performance under dynamic conditions such as dip, swell, insolation change and different loading condition.

The performance of the system is investigated for different conditions using MATLAB/Simulink.

2 Configuration and Design of the System

The configuration of PV-array-integrated UPQC using MPPT circuit is exhibited in Fig. 1. MPPT circuit consists of a boost converter and MPPT algorithm. PV-UPQC consists of DSTATCOM and DVR which share a common dc-link capacitor and the PV system is connected to the dc-link capacitor using an MPPT circuit. DSTATCOM is connected to the load side and DVR is affixed to the source side. A transformer connected in series with the supply is used to feed the voltage generated by the DVR in order to reduce dip and swell from the supply. A series RC filter (ripple filter) is used to reduce the harmonics of the DVR and DSTATCOM.

2.1 Design of PV-UPQC

PV-UPQC design entails determining the correct PV array rating, dc-link capacitor value, interconnecting inductor value for DVR and DSTATCOM, series transformer rating and dc-link voltage. DSTATCOM is designed to provide active power from PV array, supply reactive power of load and mitigate load harmonics. The DVR's design allows it to minimize up to 30% dip and swell in the voltage [12]. PV array

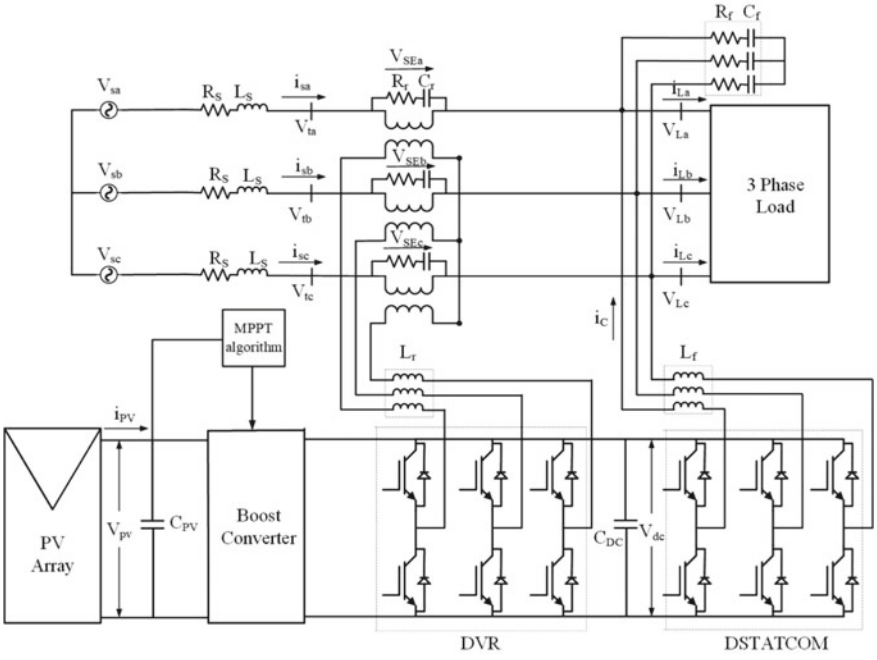

Fig. 1 Layout of PV-UPQC

rating is such that it will supply power to the load and feed the remaining power to the grid. Values of PI controller, PV array specification, ripple filter values, etc. are given in the Appendix.

Voltage magnitude of dc-link: As given in [7], the magnitude of dc-link voltage depends upon the phase voltage of the supply and depth of the modulation. The supply phase voltage (V_{ph}) is 239.6 V and the depth of the modulation (m) is set to 1. The magnitude of the dc-link voltage must be at least twice as high as the peak phase voltage [7].

$$\begin{aligned} V_{dc} &= \frac{2\sqrt{2}V_{ph}}{m} \\ &= 677.69\,\text{V} \end{aligned} \tag{1}$$

The dc-link voltage turns out to be 677.69 V and the value is taken approximately 700 V.

Value of the dc-link capacitor: The voltage magnitude of the dc-link capacitor and the power supplied by DSTATCOM is used to calculate the value of the dc-link capacitor [7]. The value of the capacitor can be found by using the energy balance equation given as follows:

$$\begin{aligned} C_{dc} &= \frac{3kaV_{ph}I_{sh}t}{0.5 * \left(V_{dc}^2 - V_{dc1}^2\right)} \\ &= 9.3\,\text{mF} \end{aligned} \tag{2}$$

where average dc voltage (V_{dc}) is 700 V, lowest dc voltage (V_{dc1}) is 677.7 V, phase voltage (V_{ph}) is 239.60 V, the time required to attain steady-state value (t) is 30 ms, phase current of the DSTATCOM (I_{sh}) is 44.17 A, the factor for considering a variation in the energy during dynamics (K) is 0.1 and the overloading factor (a) is 1.5.

Interconnecting inductor for DSTATCOM: The value of the interconnecting inductor for DSTATCOM depends upon the switching frequency, dc-link voltage, maximum overload and ripple in the current supplied by the DSTATCOM. The value of the interconnecting inductor for the DSTATCOM can be estimated from the below equation [5]. The value of the inductor is chosen as 1 mH.

$$\begin{aligned} L_f &= \frac{\sqrt{3}mV_{dc}}{12af_{sh}I_{rc,pp}} \\ &= 800\,\mu\text{H} \end{aligned} \tag{3}$$

where the depth of modulation index (m) is 1, switching frequency (f_{sh}) is 10 kHz, ripple in the inductor current of DSTATCOM ($I_{rc,pp}$) is 10.52 A and the value of maximum overload (a) is 1.2 pu.

Series feeding transformer for DVR: PV-integrated UPQC given in this paper can compensate 30% dip and swell in the voltage appearing at load which is 71.88 V. So the voltage required to be injected is 71.88 V; hence the series feeding transformer turns ratio required can be given as

$$K_{se} = \frac{V_{vsc}}{V_{se}} = \frac{239.6}{71.88} = 3.33 \tag{4}$$

In order to get the KVA rating of the series feeding transformer, the primary side current of the transformer should be known which is the same as the supply current. With a 30% dip condition it will be 46 A, so the KVA rating is given as.

$$S_{Se} = 3V I_{se,sag} = 3 * 72 * 46 = 10\,\text{KVA} \tag{5}$$

Interconnecting inductor for DVR: The value of the interconnecting inductor for DVR depends on the switching frequency, dc capacitor voltage, depth of modulation and inductor ripple current of DVR [5]. The value of the interconnecting inductor for the DVR can be estimated from the following equation:

$$L_r = \frac{\sqrt{3} m V_{dc} K_{se}}{12 a f_{se} I_r} = 3.6\,\text{mH} \tag{6}$$

where the depth of modulation index (m) is 1, switching frequency (f_{se}) is 10 $_{kHz}$, ripple in the inductor current of DVR (I_r) is 6.9 A, the value of maximum overload in pu (a) is 1.2 and series transformer turns ratio (K_{se}) is 3.

3 Control of PV-UPQC

PV-integrated UPQC consists of DSTATCOM, DVR along with PV array and MPPT circuit to transfer the maximum active power from the PV array. DSTATCOM is connected to the load side and it is used to mitigate power quality problems appearing due to loads, such as unbalanced current, reactive power and harmonics. DSTATCOM also performs the function of transferring real power from the PV array to the grid. DVR is used to mitigate supply-side power quality problems such as dip and swell in the supply voltage.

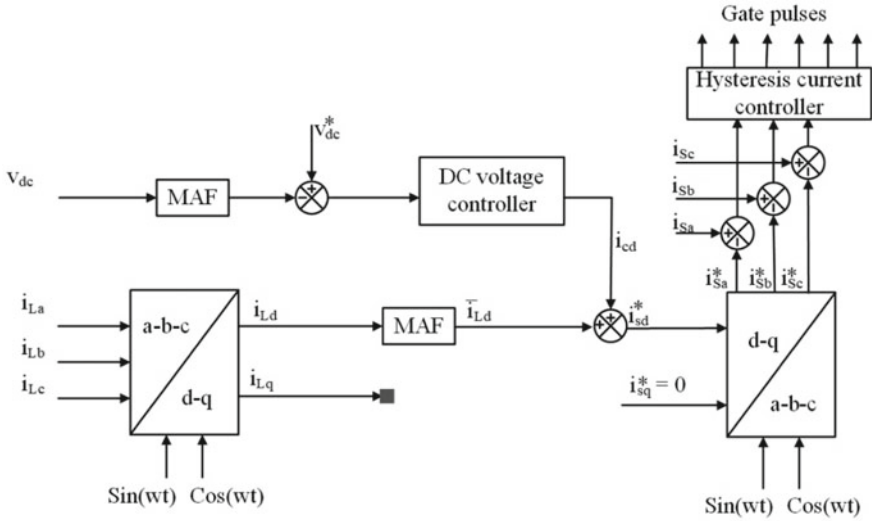

Fig. 2 Control strategy for DSTATCOM

3.1 Control of DSTATCOM

SRF-based control strategy having a moving average filter for DSTATCOM is depicted in Fig. 2. In this control strategy the load current is changed to d-q-o domain from a-b-c domain. PLL is synchronized with PCC voltage. The dc component is extracted from d-axis by using a moving average filter to generate reference compensating current. The dc voltage control loop is provided to control the dc-link capacitor voltage. A low-pass filter having a corner frequency of 10 Hz can be used in place of the moving average filter, but the low-pass filter has a poor dynamic response than the moving average filter [9]. Since the smallest order harmonic in the d-axis load current is having a double harmonic part, the window length (T_w) of the moving average filter is held at 10 ms. The moving average filter's transfer function is given as

$$MAF(s) = \frac{1 - e^{-T_w s}}{T_w s} \tag{7}$$

3.2 Control of DVR

Different control strategies for DVR are discussed in [10, 12] such as in-phase compensation, energy optimal compensation and pre-sag compensation. The control structure for DVR is shown in Fig. 3. To requite for dip and swell in source voltage,

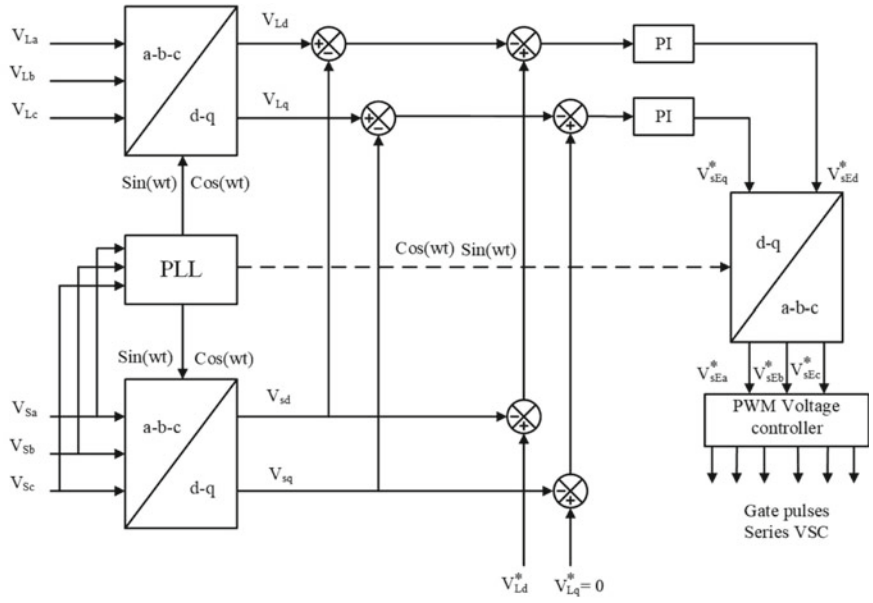

Fig. 3 Control strategy for DVR

DVR injects voltage that is in phase or out of phase with the source voltage. Load and source voltages are converted to d-q-o domain to obtain actual compensating voltage. Reference compensating voltage and actual compensating voltage are compared to produce an error signal. This error signal is then converted back to a-b-c domain and given to pulse width modulation (PWM) voltage control to generate a switching signal. The reference value of d-axis load voltage (VLd*) is taken as reference load voltage peak, while the reference value of q-axis load voltage (VLq*) is taken as zero [10].

3.3 MPPT Circuit

In order to integrate the PV system with UPQC and to transfer the maximum power available with the PV array to the load and source, the MPPT circuit is used. MPPT circuit consists of a boost converter and MPPT algorithm. Perturb and observe (P&O) strategy is utilized in the MPPT algorithm. To be able to transfer the maximal power from PV array to the UPQC, boost converter does the function of impedance matching such that effective impedance across boost converter become equivalent to the impedance of PV array [13]. Impedance matching is done by controlling the duty cycle for the boost converter and it is shown in (Fig. 4). The equation relating the duty cycle and impedance for the boost converter is given as follows:

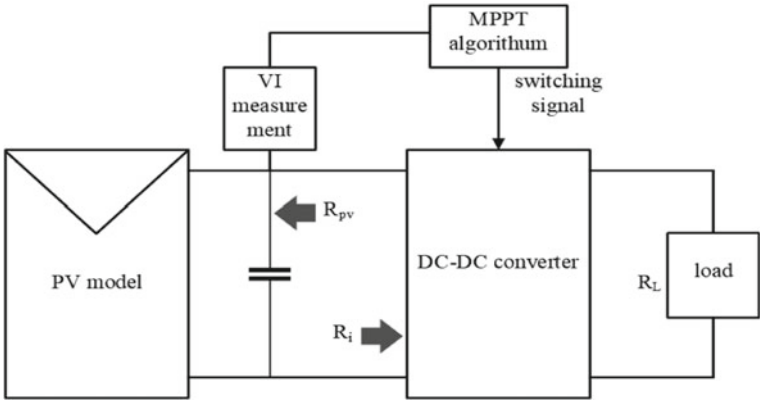

Fig. 4 Block diagram of MPPT

$$R_i = (1 - D)^2 R_l \tag{8}$$

where R_l is load impedance and R_i is input impedance of the boost converter.

The duty cycle for the boost converter is produced via sensing voltage and current of the PV array which is then given to perturb and observe algorithm which will produce suitable duty cycle for the boost converter. Flowchart of the P&O is depicted in Fig. 5.

4 PV-UPQC Simulation Analysis

To investigate the dynamic and steady-state behavior, PV-UPQC as shown in Fig. 1 is considered and its response is analyzed using MATLAB/Simulink. Nonlinear load (diode bridge rectifier) and unbalanced load are taken. The step size considered for the simulation is 1e-5 s. The dynamic conditions such as change of solar radiation, dip in voltage, swell in voltage and load variation are considered. Details of the different parameters are provided in the Appendix.

4.1 Performance Evaluation of PV-UPQC During the steady-State Condition

Figures 6 and 8 are of the system without connecting PV-UPQC and it is clear that the PCC was unbalanced current and contains harmonics. Also, the instantaneous power factor was not unity. After connecting PV-UPQC in the system it is observed in Figs. 7 and 9 that instantaneous power factor has turned out to be unity, harmonics are

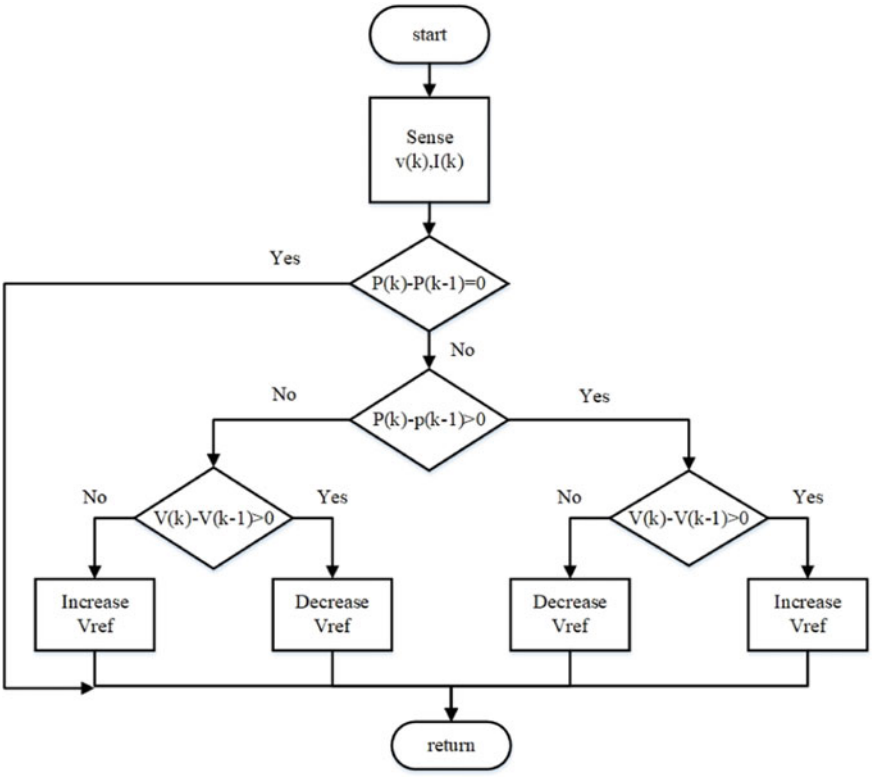

Fig. 5 Flowchart for the perturb and observe algorithm

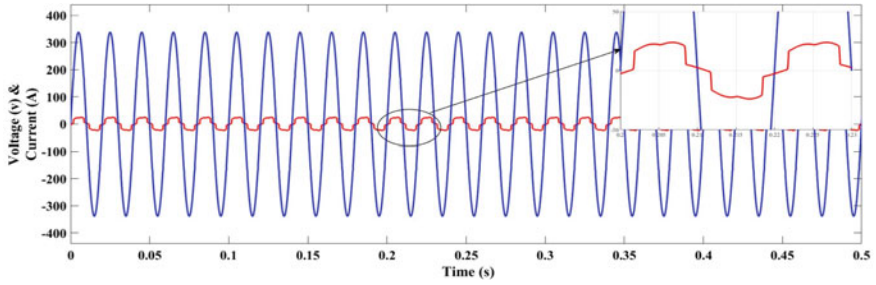

Fig. 6 PCC voltage and source current before connecting PV-UPQC

reduced, unbalanced PCC current has become balance and power is being supplied by PV-UPQC to source and load. As active power is being supplied from PV-UPQC to the source, the current at PCC is 180° out of phase with PCC voltage (Fig. 10).

The dc-link voltage settles at 705 V. THD in the source current before applying the PV-UPQC was 21.61%, which is then reduced to 3.28%.

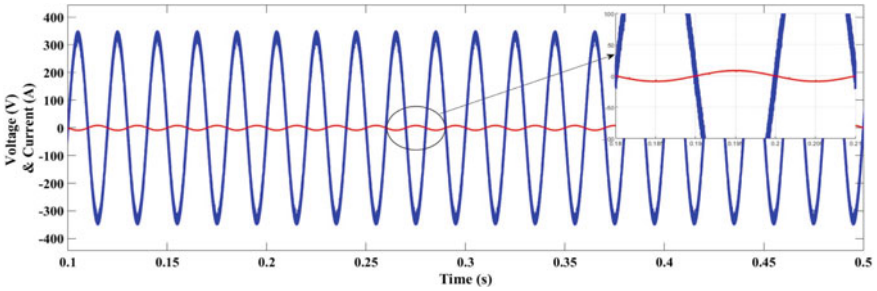

Fig. 7 PCC voltage and source current after connecting PV-UPQC

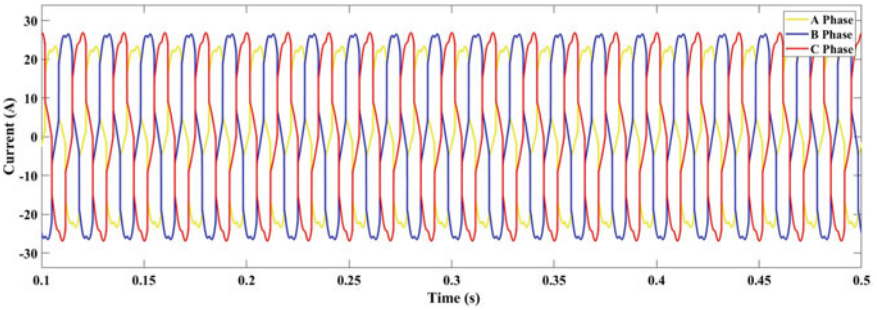

Fig. 8 Load current for nonlinear and unbalanced load

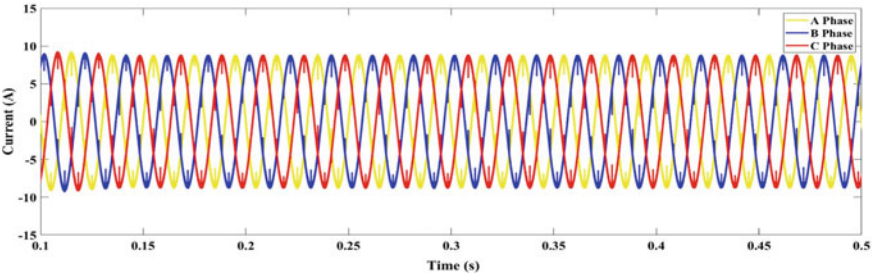

Fig. 9 Source current under steady-state condition

4.2 Change of Solar Radiation

Solar radiation received by the PV array is changed from 1 kW/m^2 to 0.2 between 0.4 and 0.6 s, as shown in Fig. 11 and it is observed in Fig. 12 that MPPT is efficiently tracking the change in the solar radiation. As seen in Figs. 13 and 14, the current supplied by the source increases while the current supplied by the DSTATCOM decreases due to changes in radiation. Because of the change in the power delivered

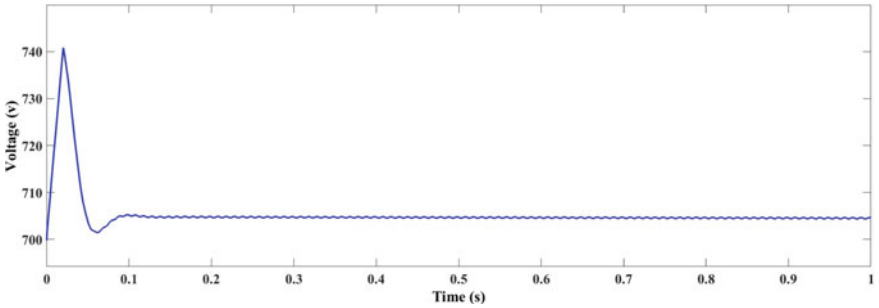

Fig. 10 DC-link voltage under steady-state condition

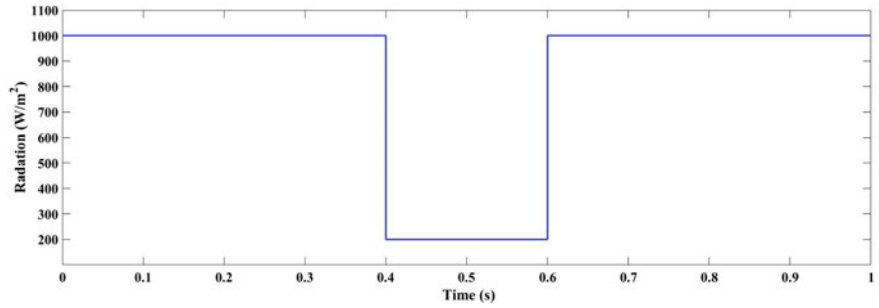

Fig. 11 Change of solar radiation

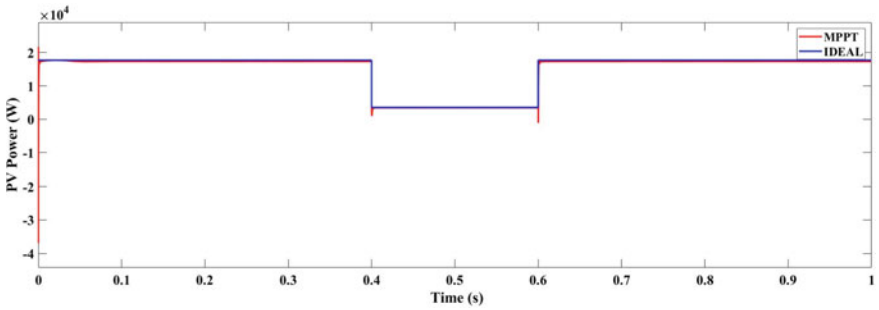

Fig. 12 Ideal and extracted maximum power from PV array

by the PV array, now DSTATCOM is providing power only to the load. Change in radiation has resulted in a small dip in the capacitor voltage, and it is reduced from 705 to 701 V. After checking a few different data points in Fig. 12, the efficiency of the MPPT circuit obtained is around 97–98%, that is 97–98% of maximum power available with PV array is being extracted by MPPT (Fig. 15).

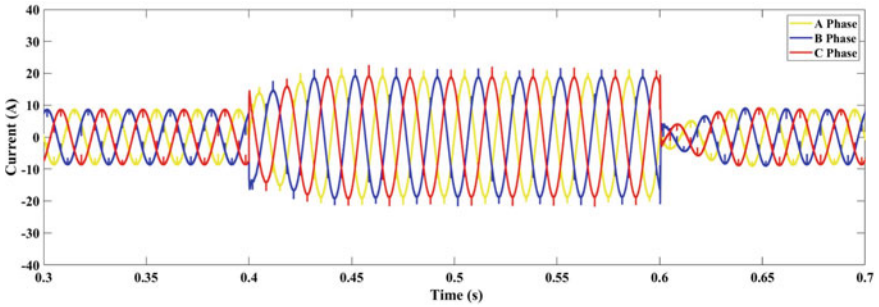

Fig. 13 Current supplied from the source under change in radiation

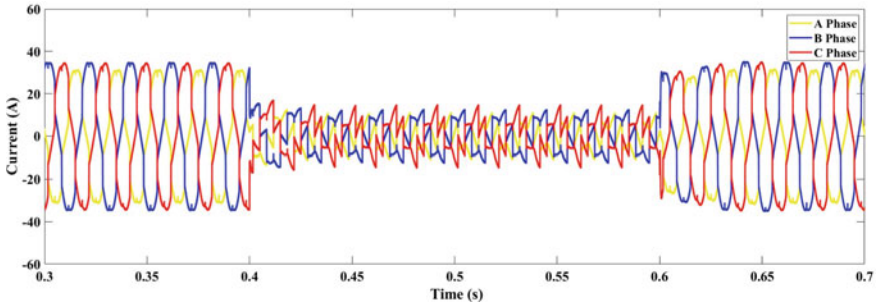

Fig. 14 Current supplied by DSTATCOM under change in radiation

4.3 Dip and Swell in Supply Voltage

The change of supply voltage from 1 pu to 0.8 pu is made between 0.3 and 0.4 s to create a dip in the voltage, and the change of supply voltage from 1 to 1.2 pu is made between 0.4 and 0.5 s to create a swell in the supply voltage as depicted in Fig. 16.

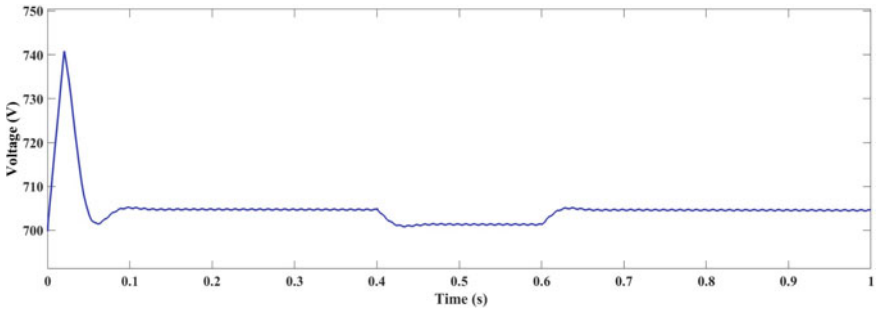

Fig. 15 DC-link voltage under change of radiation

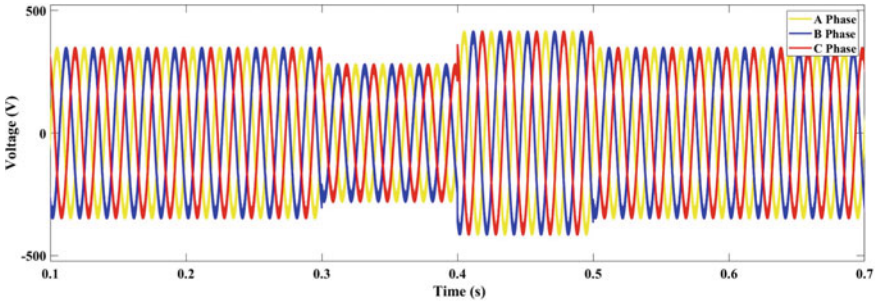

Fig. 16 Source voltage during dip and swell

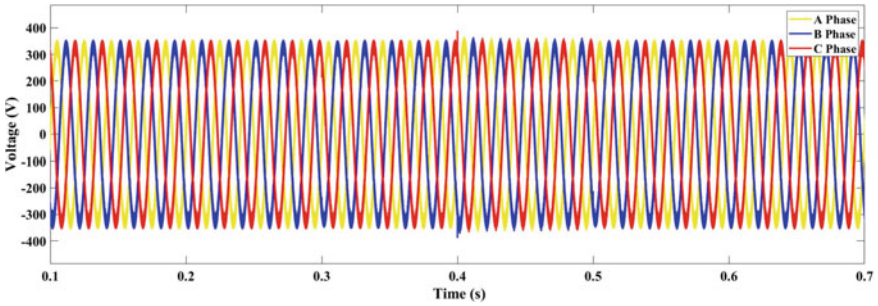

Fig. 17 Load voltage during dip and swell

It is observed in Fig. 17 that the effect of voltage dip and swell is overcome in the load voltage by using PV-UPQC. DVR will supply in-phase voltage to overcome the dip in the supply voltage and DVR will supply 180° out of phase voltage in order to overcome the swell in the voltage as depicted in Fig. 18. Small changes in the capacitor voltage are noticed during the dip and swell condition in the source voltage (Fig. 19).

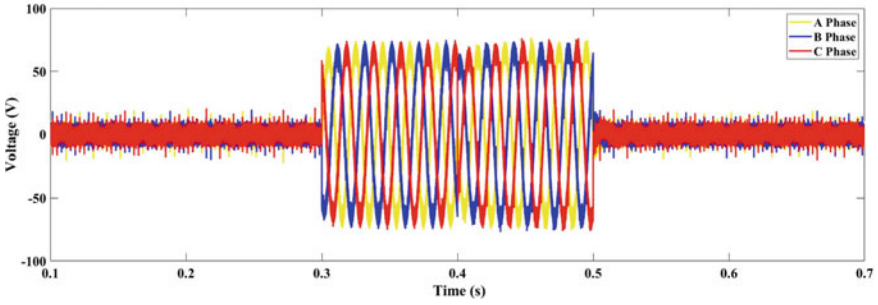

Fig. 18 Voltage supplied by DVR during dip and swell

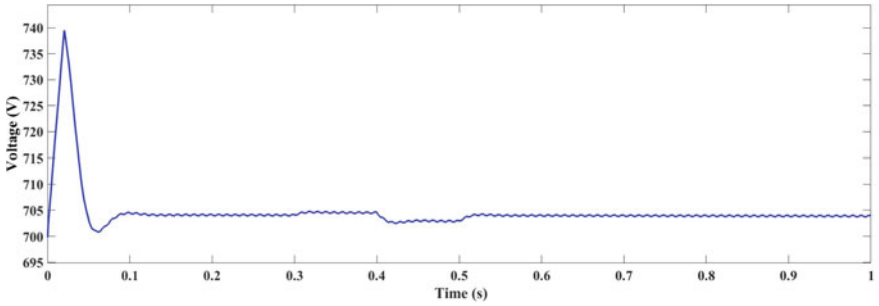

Fig. 19 Voltage of dc-link capacitor during dip and swell

4.4 Dynamic Load Change

Changes in load are made to observe the system's dynamic response. First, a nonlinear load is connected in parallel with the balanced load, then the unbalanced load is introduced in parallel with the existing load at 0.4 s and it is disconnected from the system at 0.6 s. Changes in DSTATCOM current and dc-link voltage caused by a change in load settle in 0.08 s. With the increase in load there is no change in the voltage at the load side due to PV-UPQC and it is maintained at 240 V (Figs. 19, 20, 21, 22).

The voltage across a dc-link capacitor is depicted in Fig. 23, and a negligible change in dc-link capacitor voltage is observed due to change in loading condition.

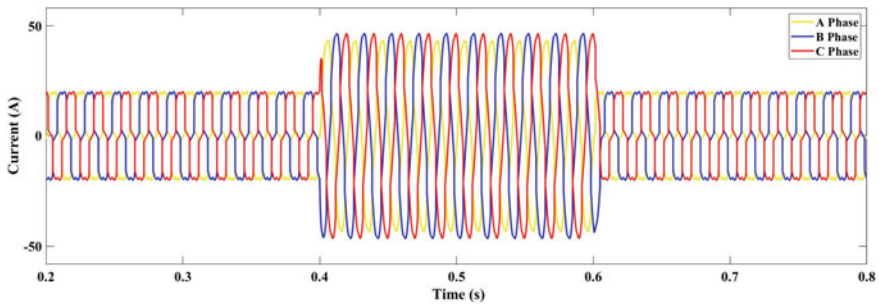

Fig. 20 Load current during change in load

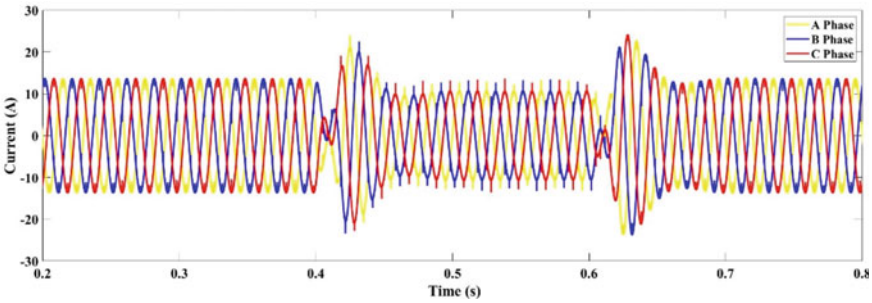

Fig. 21 Source current during change in load

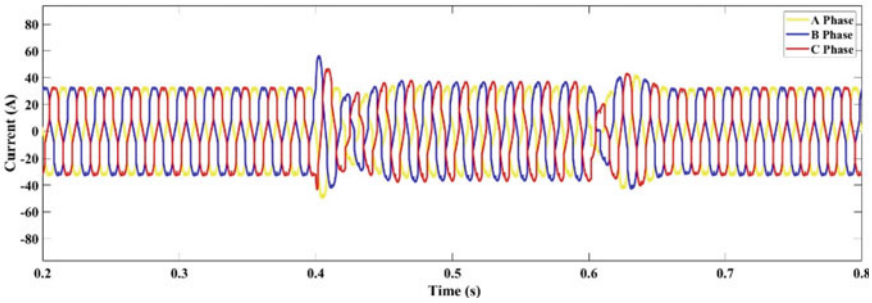

Fig. 22 Current supplied by DSTATCOM during change in load

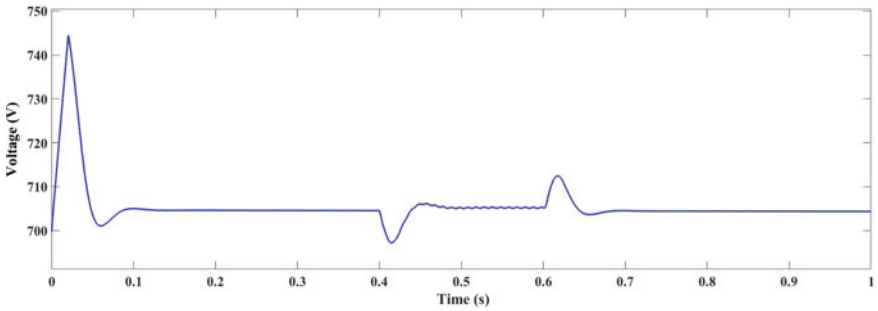

Fig. 23 DC-link voltage under change in load

5 Conclusion

The performance of PV-UPQC is examined under steady-state and diverse circumstances, and the designing of various parameters is done. Simulation studies of PV-UPQC are carried out in MATLAB/Simulink. From the simulation study, it is perceived that PV-UPQC is able to supply reactive power demand of load and hence

achieves unity instantaneous power factor at PCC. It is able to reduce THD in load current from 21.61 to 3.28%. It has made the unbalanced source current balanced. The simulation study revealed that PV-UPQC is capable of reducing power quality issues and supplying real power in diverse circumstances. By the use of an MPPT circuit, PV-UPQC is able to deliver 97–98% of power available with a PV array. It is observed from the simulation study that it is performing well to lessen power quality issues and PV-UPQC appears to be a viable option for injecting green energy through UPQC.

Appendix

Simulation parameter

PCC line voltage is 415 V, diode bridge rectifier load having P = 5000 W Q = 500 Var, unbalance load having P1 = 1000 W, P2 = 2000 W, P3 = 1500 W, Q1 = 400 Var, Q2 = 350 Var, Q3 = 600 Var, C_{dc} = 9.3 mF, switching frequency for DVR is 10 kHz, RC filter with R = 10 Ω and C = 10 μF, PI controller in DSTATCOM having K_p = 1.5 and K_i = 0.1 and PI controller in DVR having K_p = 8 and K_i = 1200, L_s = 0.1 mH, R_s = 0.02 Ω. The PV array model used is having three parallel connected module and 23 series connected module V_{oc} = 864 V, I_{sc} = 62.65 A; V_{mpp} = 701 V; I_{mpp} = 58.94 A; P_{pv} = 41.35 KW.

References

1. Mountain B, Szuster P (2015) Solar, solar everywhere: opportunities and challenges for Australia's rooftop PV systems. IEEE Power Energy Mag 13(4):53–60. https://doi.org/10.1109/MPE.2015.2416113
2. Yang BYY, Enjeti P, Blaabjerg F, Wang H (2015) Wide-scale adoption of photovol-taic energy. IEEE Ind Appl Mag 21–31
3. Singh B, Jain C, Goel S (2014) ILST control algorithm of single-stage dual purpose grid connected solar PV system. IEEE Trans Power Electron 29(10):5347–5357
4. Wu T-F, Nien H-S, Shen C-L, Chen T-M (2005) A single-phase inverter system for PV power injection and active power filtering with nonlinear inductor consideration. IEEE Trans Ind Appl 41(4):1075–1083
5. Dhagate DR, Dhamaal SS, Thakre MP (2020) Design and performance evaluation of 3-phase photovoltaic integrated UPQC. In: 2020 international conference on power, energy, control and transmission systems (ICPECTS), pp 1–7
6. Devassy S, Singh B (2017) Design and performance analysis of three-phase solar PV integrated UPQC. IEEE Trans Ind Appl 54(1):73–81
7. Singh B, Chandra A, Haddad KA (2015) Power quality: problems and mitigation techniques. Wiley, Hoboken, NJ, USA
8. Padiyar KR (2007) FACTS controllers in power transmission and distribution
9. Raja A, Santhosh KNSK (2019) Mitigation of current and voltage harmonics using MAF based UPQC, pp 2436–2441

10. Dash SK, Ray PK (2021) A new PV-open-UPQC configuration for voltage sensitive loads utilizing novel adaptive controllers. IEEE Trans Ind Inf 17(1):421–429
11. Hossain MI, Rahaman I, Rahman MN, Hasan MF, Hasan MM, Sarker RC (2020) Voltage sag compensation in distribution system using dynamic voltage restorer. In: 2020 2nd international conference on advanced information and communication technology (ICAICT), pp 492–497
12. Jayaprakash P, Singh B, Kothari D, Chandra A, Al-Haddad K (2014) Control of reduced-rating dynamic voltage restorer with a battery energy storage system. IEEE Trans Ind Appl 50(2):1295–1303
13. Solanki CS (2015) Solar photovoltaics: fundamentals, technologies and applications. Phi learning pvt. Ltd.
14. Singh R, Yadav R, Varshney L, Sharma S (2021) Analysis and comparison of PV array MPPT techniques to increase output power. Int Conf Adv Comput Innov Technol Eng (ICACITE) 2021:168–172
15. Dheeban SS, Muthu Selvan NB (2020) PV integrated UPQC for sensitive load. In: 2020 international conference on emerging trends in information technology and engineering (ic-ETITE), pp 1–7
16. Kumar K, Ravi K (2019) New performance upgrade grid system with PV Integrated UPQC-S control. In: 2019 international conference on computation of power, energy, information and communication (ICCPEIC), pp 1–7
17. Mansor MA, Hasan K, Othman MM, Noor SZBM, Musirin I (2020) Construction and performance investigation of three-phase solar PV and battery energy storage system integrated UPQC. IEEE Access 8:103511–103538

A Fuzzy-Based Buck-Boost Photovoltaic Inverter for Voltage Stabilization During Mismatched Environmental Conditions

Varun Bhardwaj and Prerna Gaur

Nomenclature

L_1, L_2	Energy storage inductors (mH)
L_g	Filter inductor (mH)
V_{pv}	Photovoltaic array (PVA) voltage (V)
I_{pv}	Photovoltaic array (PVA) current (A)
C_{pv}	Photovoltaic array (PVA) to ground parasitic capacitor (uF)
f_s	Switching frequency (Hz)
C_{o1}, C_{o2}	Voltage ripple reduction capacitors (uF)
V_{co1}, V_{co2}	Rated voltage capacity of the capacitors (V)
P_{co1}, P_{co2}	Rated power capacity of the capacitors (W)
f_g	Grid frequency (Hz)
V_g	Grid voltage (V)
R	Rectified version of unity sinusoidal function
V_m	Amplitude of the grid voltage (V)
V_{dc}	DC-link voltage (V)

1 Introduction

Considering the photovoltaic array as the optimal renewable source of power generation as compared to other renewable sources, it is used in most grid systems [1]. But there is a greater drawback for the photovoltaic array source as the power output is fluctuating from the photovoltaic array modules because the solar insolation is

V. Bhardwaj (✉) · P. Gaur
Instrumentation and Control Engineering Department, Netaji Subhas University of Technology, New Delhi, India

S. Kumar et al. (eds.), *Recent Advances in Power Electronics and Drives*, Lecture Notes in Electrical Engineering 852, https://doi.org/10.1007/978-981-16-9239-0_34

not constant. An array is formed with different PV panels connected in parallel and series combinations which generate variable power and voltage output. In [2], module integrated (MI) inverters are integrated with the ac grid parallelly, and a flyback transformer is used for boosting the voltage. But this configuration results in lower efficiency. In [3], the PV system is integrated with the grid through transformerless H6-type inverter configuration, which is capable of eliminating problems such as common-mode voltage and leakage current associated with the non-isolated system. But to achieve desired voltage at the inverter input terminals, the count of series-connected PV modules increases, due to which the output power from this configuration is not constant during partial shading conditions.

So, various MPPT (maximum power point tracking) techniques were designed for producing maximum output power and boosting voltage during mismatched environmental conditions [4-6]. Some researchers used a power electronic equalizer [7] or a DC–DC converter [7–10] for extracting maximum power and boosting voltage. But there are limitations to these schemes. These schemes require a large number of components; hence the cost and complexity of the system increase. The model presented in [8] uses a DC–DC converter after every PV module to produce maximum power output, but this structure suffers from low efficiency because of the increased converter stages in this. In [11], all the PV modules are split up into two subarrays to reduce the number of overall intermediate converter stages and then MPPT is employed in each subarray. This scheme reduces the number of converter stages, but still the efficiency is low. In conventional topology, the photovoltaic array variable output is stabilized by a DC–DC booster converter [12], followed by an individual inverter that feeds power into the grid. Due to this two-stage operation, there are many conversion losses and losses related to switching included in the topology reducing the system's efficiency. To avoid these losses the photovoltaic array modules are connected to a new single-stage buck-boost inverter which is tied to the grid directly without any transformer connected between the grid and photovoltaic array inverter. Because of this single-stage inverter, the conversion losses and switching losses are reduced, thus improving the system's efficiency [13]. In [14], low-voltage PV modules are integrated with a power-optimized-based converter and voltage source inverter to deliver stable voltage to the grid. These converters are used to enhance the DC voltage and also to produce the rated power by using a control scheme called fuzzy logic in partial shading conditions. The cost and the complexity of this architecture increase because each PV module requires a DC–DC converter to boost the DC voltage. In [15] the authors proposed a methodology that uses a boost converter and five-level neutral point clamped inverter to produce stable DC voltage at the grid in mismatched environmental conditions. But there is a high number of switches requirement in the inverter stage which makes it complex and difficult to use.

In this paper, the introduced inverter is connected in series with two photovoltaic array modules at the input. The two photovoltaic modules are operated at different sun insolation conditions which generate power and voltages at different levels. The buck-boost inverter topology needs to stabilize the output voltage for different operating photovoltaic array modules and convert DC voltage to single-phase AC voltage for grid power injection. The introduced novel dual buck-boost single-phase

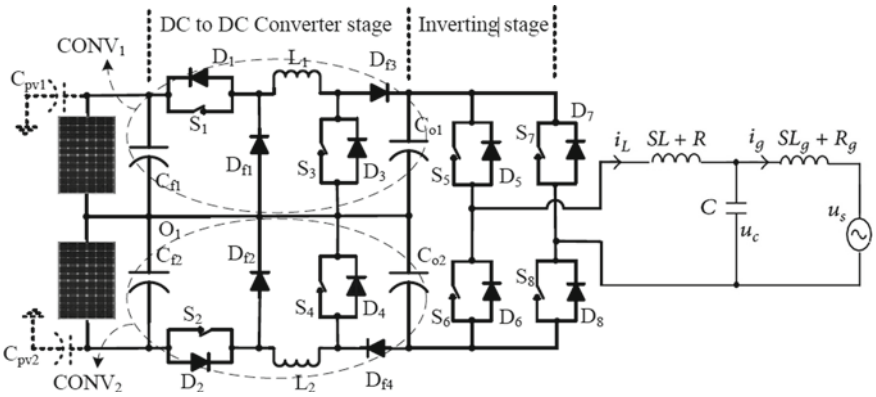

Fig. 1 Introduced novel DBBI topology

inverter (DBBI) topology is presented in Fig. 1 [16]. With the proposed topology in Fig. 1, the number of devices connected can be reduced with a less complicated control structure and improved efficiency.

Organization: This paper includes the working principle of the introduced DBBI (dual buck-boost single-phase inverter) topology in Sect. 2, and control structure modeling for the introduced inverter including the FIS module in Sect. 3. In Sect. 4 simulation results explanation for different operating conditions of PV modules are presented. In Sect. 5 conclusion of the paper along with references are presented.

2 Working Principle DBBI

Figure 1 shows the circuit in which converter 1 has two controlled switches S_1 and S_3 with body diodes D_1 and D_3. These diodes are freewheeling diodes connected anti-parallel to the switches to dissipate the residual energy [17] in the switch during the OFF state to avoid peak voltage generation during switching. Similar to converter 1, converter 2 also includes switches S_2 and S_4 connected with anti-parallel diodes D_2 and D_4. The two converters include individual energy storage inductors L_1 and L_2, respectively, which makes the converter operate in buck mode or boost mode. The inputs of the converters are connected with filter capacitors C_{f1} and C_{f2} in parallel to the photovoltaic array modules which reduce the input voltage ripple [18]. At the outputs of the converters two separate voltage ripple reduction capacitors, C_{o1} and C_{o2} are connected for DC voltage stabilization. The circuit is also included with two freewheeling diodes D_{f1} and D_{f2} which operate during the OFF state of all the switches S_1, S_2, S_3 and S_4. The passive element calculation for the circuit is represented as.

$$L_1 = \frac{V_{pv1}}{4\Delta I_{L1} f s} \tag{1}$$

$$L_2 = \frac{V_{pv2}}{4\Delta I_{L2} f s} \tag{2}$$

In the above equation, V_{pv1} and V_{pv2} have rated photovoltaic array module voltages, ΔI_{L1} and ΔI_{L2} are the allowable current ripple for the inductors L_1 and L_2, which is considered to be 15% of the rated peak current, and f_s is the switching frequency of the switches. The values of C_{o1} and C_{o2} are taken from the expression given in [19].

$$C_{o1} = \frac{x P_{co1}}{2\pi f g V_{co1}^2} \tag{3}$$

$$C_{o2} = \frac{x P_{co2}}{2\pi f g V_{co2}^2} \tag{4}$$

Here, V_{co1} and V_{co2} are the rated voltage capacity of the capacitors [19], P_{co1} and P_{co2} are the rated power capacity of the capacitors, f_g is the grid frequency, and x is the multiplication factor considered to be 2.5%.

With the above passive element calculations, the circuit is modeled and operated as per the requirement. During buck mode [20] of operation of DBBI (dual buck-boost single-phase inverter), only the switches S_1 and S_2 of both the converters are operated with switches S_3 and S_4 being completely in OFF state. In buck mode, there are four states of operation, where two are positive conduction states and two are negative conduction states.

(a) Buck charge positive conduction (mode 1):

In this mode, S_1 and S_2 switches are turned ON charging the L_1 and L_2 inductors. In a positive conduction state the inverter switches S_5 and S_8 are maintained ON conducting current [4] in a positive direction on the grid side. In this mode, the filter diodes D_{f3} and D_{f4} are in forward-biased conditions. The current conduction path for mode 1 is shown in Fig. 2 [16].

(b) Buck discharge positive conduction (mode 2)

In this mode, the switches S_1, S_2 are turned OFF and S5, S8 switches are maintained ON. The charge stored in inductors L_1 and L_2 is discharged to the inverter with positive conduction [21] to the grid. The freewheeling diodes D_{f1}, D_{f2}, D_{f3}, and D_{f4} are in forward-biased condition in this mode. The current conduction path for this mode can be seen in Fig. 3 [16].

Similar to positive conduction modes, the negative conduction modes operate in the same way but the switching of S_6 and S_7 switches are different. The switches S_1 and S_2 are operated at high switching frequency to store energy in inductors L_1 and L_2. The current conduction for the negative conduction mode is shown in Fig. 4 [16].

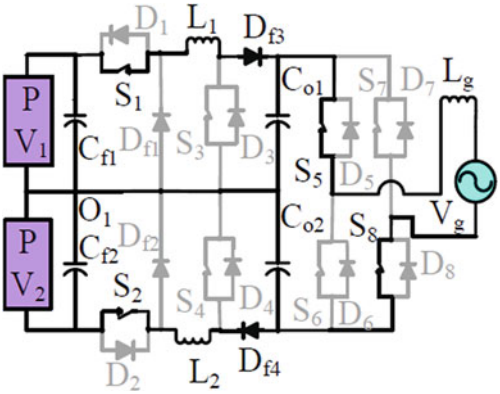

Fig. 2 Buck charge positive conduction mode (mode 1)

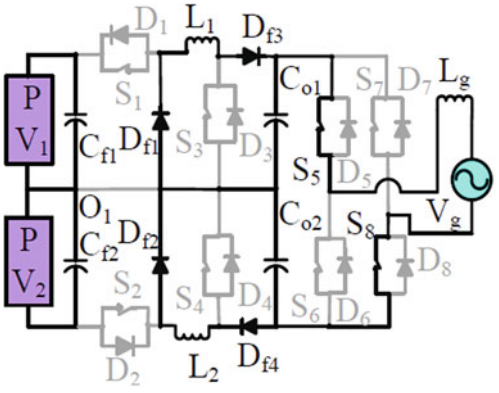

Fig. 3 Buck discharge positive conduction mode (mode 2)

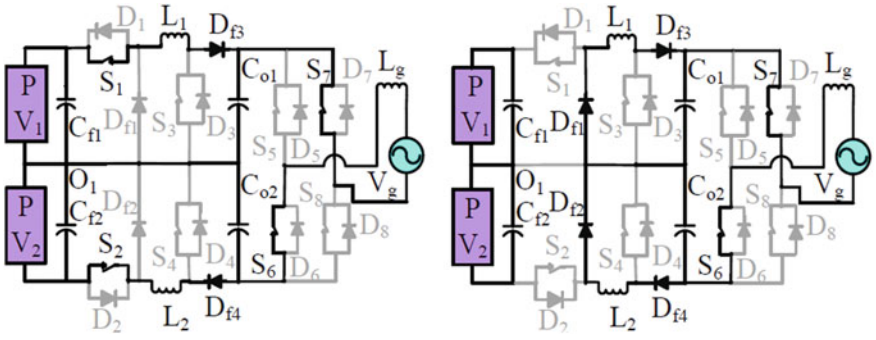

Fig. 4 Buck mode negative conduction modes (mode 3 and mode 4)

(c) Boost charge positive conduction (mode 5)

In this mode of operation, the switches S_1 and S_2 are completely maintained ON with S_3 and S_4 turned ON. Similar to mode 1 the switches S_5 and S_8 of the inverter are turned ON for positive condition to the grid. During this mode of operation, the inductors L_1 and L_2 are charged [8] by the PV module voltages. The current conduction for this mode is shown in Fig. 5 [16].

In this mode, all the diodes are in reverse-biased condition and the output capacitors C_{o1} and C_{o2} provide voltage at the output terminals.

(d) Boost discharge positive conduction (mode 6)

During this mode, the switches S_1 and S_2 are still maintained ON but the switches S_3 and S_4 are turned OFF. In this mode, the freewheeling diodes D_{f3} and D_{f4} are in forward-biased condition and the charged inductors L_1 and L_2 are in series with the photovoltaic array modules [8] adding up the voltage. Therefore, the output voltage is very high making it operate in boost mode. The current conduction for this mode 6 is shown in Fig. 6 [16].

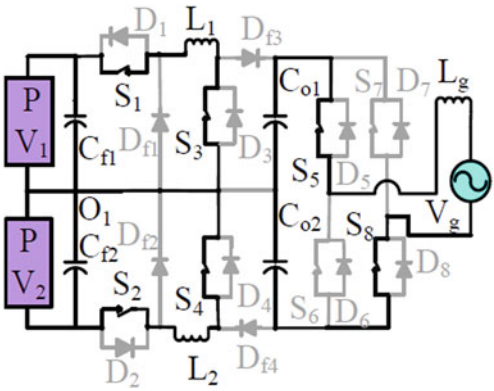

Fig. 5 Boost charge positive conduction mode (mode 5)

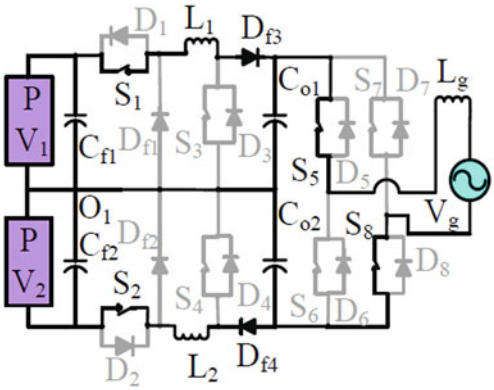

Fig. 6 Boost discharge positive conduction mode (mode 6)

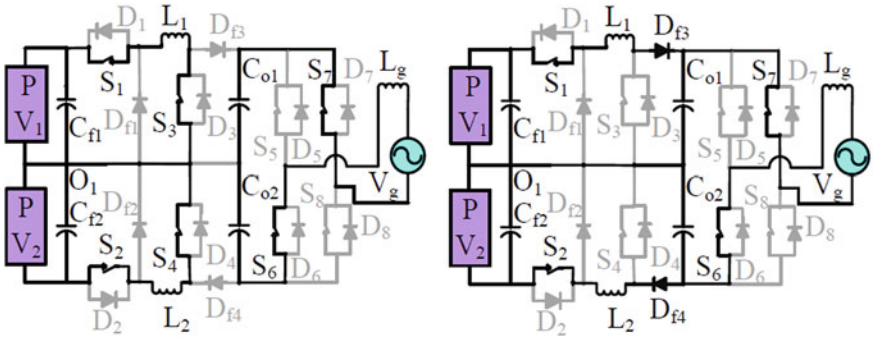

Fig. 7 Boost mode negative conduction modes

After this mode the inverter needs to conduct in a negative direction; therefore, the switching of the switches S_1, S_2, S_3, and S_4 will be the same but the inverter switches S_6 and S_7 are maintained ON [22]. The boost mode negative conduction operations are shown in Fig. 7 [16].

3 Control Structure

For the introduced DBBI (dual buck-boost single-phase inverter) topology, the inverter has to operate in synchronization to the grid voltage. The DC-link voltage of the buck-boost converter needs to be stable even during shaded conditions. For this, an MPPT algorithm [22] is used for the operation of switches S_1, S_2, S_3, and S_4. In the MPPT algorithm, an incremental conductance is adopted into the control structure for the DC voltage stabilization. The complete control structure of the introduced DBBI is shown in Fig. 8.

The MPPT algorithm takes feedback from the photovoltaic array voltage (V_{pvN}) and current (I_{pvN}), where N is the number of photovoltaic array modules. The

Fig. 8 Introduced control structure

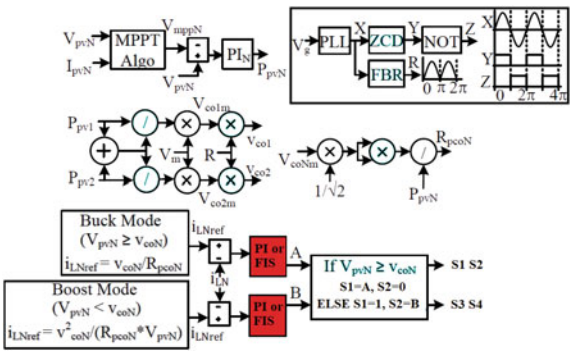

maximum estimated voltage is compared to photovoltaic array voltage V_{pvN} and the error is fed to the PI controller for power output (P_{pvN}) estimation of the photovoltaic array. The pulses for the inverter switches are generated by PLL [23] with feedback taken from grid voltage. During the positive voltage of the grid, switches S5 and S8 are turned ON, and during the negative voltage of the grid, switches S6 and S7 are turned ON. The operating condition of the buck-boost converter depends on the photovoltaic array voltage (V_{pvN}).

If $V_{pvN} \geq V_{coN}$; buck mode ON;

If $V_{pvN} < V_{coN}$; boost mode ON;

V_{coN} is represented as.

$$V_{co1} = \left(\frac{P_{pv1}}{P_{pv1} + P_{pv2}}\right) \cdot Vm \cdot R \tag{5}$$

$$V_{co2} = \left(\frac{P_{pv2}}{P_{pv1} + P_{pv2}}\right) \cdot Vm \cdot R \tag{6}$$

Here 'R' is the rectified version of the unity sinusoidal function, generated from unity sinusoidal function X (Fig. 8), synchronized with grid voltage and 'V_m' is the amplitude of the grid voltage at the output. In any mode inductor current estimation is taken as reference (i_{LNref}) for duty ratio generation of the switches S_1, S_2, S_3, and S_4. The reference inductor current for a buck converter is represented as

$$i_{LNref} = \frac{v_{coN}}{R_{pcoN}} \tag{7}$$

The reference inductor current for boost converter is represented as.

$$i_{LNref} = \frac{v_{coN}^2}{\left(R_{pcoN * V_{pvN}}\right)} \tag{8}$$

Here R_{pcoN} is represented as

$$R_{pcoN} = \frac{\left(\frac{v_{coNm}}{\sqrt{2}}\right)^2}{P_{pvN}} \tag{9}$$

The duty ratio from both the PI controllers [23] is compared with the high-frequency sawtooth waveform-generating pulse A and pulse B. During buck mode, pulse A is fed to switches S_1, S_2, and switches S_3, S_4 are in OFF condition. During boost mode, pulse B is fed to switches S_3, S_4, and switches S_1, S_2 are in ON condition.

The conventional PI controller for the duty ratio generation of buck and boost modes of operation is replaced with a FIS controller [24] with two input variables, i.e., error (E) and change in error (CE), and one output variable (duty ratio D). Each

variable has seven membership functions [25] with output arranged as per the rule base represented in Table 1.

The modeling of membership functions of the input and output variables is shown in Fig. 9.

Table 1 Rule base

E	CE						
	NB	NM	NS	ZE	PS	PM	PB
NB	NB	NB	NB	NM	NS	NS	ZE
NM	NB	NM	NM	NM	NS	ZE	PS
NS	NB	NM	NS	NS	ZE	PS	PM
ZE	NB	NM	NS	ZE	PS	PM	PB
PS	NM	NS	ZE	PS	PS	PM	PB
PM	NS	ZE	PS	PM	PM	PM	PB
PB	ZE	PS	PS	PM	PB	PB	PB

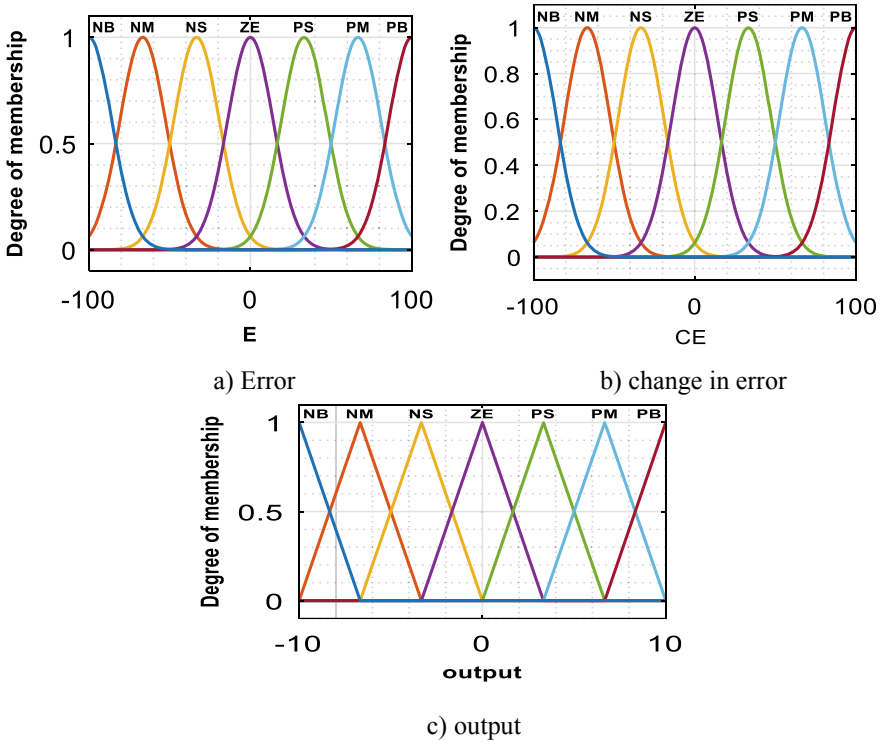

Fig. 9 Inputs (**a**, **b**) and output (**c**) membership functions

The results comparison with PI and FIS controller are represented in Sect. 4 with the simulation of the introduced circuit with different sun insolation conditions on PV_1 and PV_2.

4 Simulation Results Analysis

Figure 10 describes circuit modeling of DBBI (dual buck-boost single-phase inverter) with interconnection to grid through inductor filter Lg for reduction of harmonics in the current injection from the photovoltaic array module. The above test system is modeled with the below parameters given as per Table 2 [16].

The values of L_1 L_2, C_{o1}, and C_{o2} are calculated as per Eqs. (1–4) substituted with given PV rating parameters. The simulation is run for 0.1 s with sun insolation represented for PV1 is 1000 W/mt^2 and with sun insolation represented for PV2 is 700 ^{W}/mt^2 depicts that it is due to the presence of dust particles on PV2 array or a

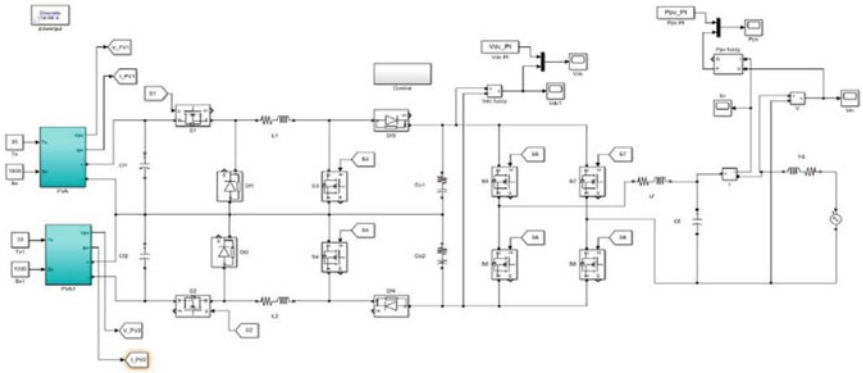

Fig. 10 Modeling of introduced DBBI connected to the grid

Table 2 Parameter values

Passive element parameter	Value
Grid V_g and f_g	230 Vrms 50 Hz
L_1, L_2, L_g	0.6, 0.6, 0.4 mH
C_{o1}, C_{o2}	5, 5 uF
C_{pv1}, C_{pv2}	0.1, 0.1 uF
S1–S4 f_s	50 kHz
S5–S8 f_s	50 Hz
Vmp (voltage of photovoltaic array at maximum power)	116 V
Vdc link voltage	400 V

cloud is intervened between the surface of the PV2 module and Sun. Figure 11 is a single-phase AC voltage waveform at PCC (point of common coupling) where the photovoltaic array module and AC grid are connected.

Figures 12 and 13 show the DC-link voltage with PI and FIS controller of buck-boost converter, respectively, and Fig. 14 shows the DC-link voltage comparison between PI and FIS controller of the buck-boost converter.

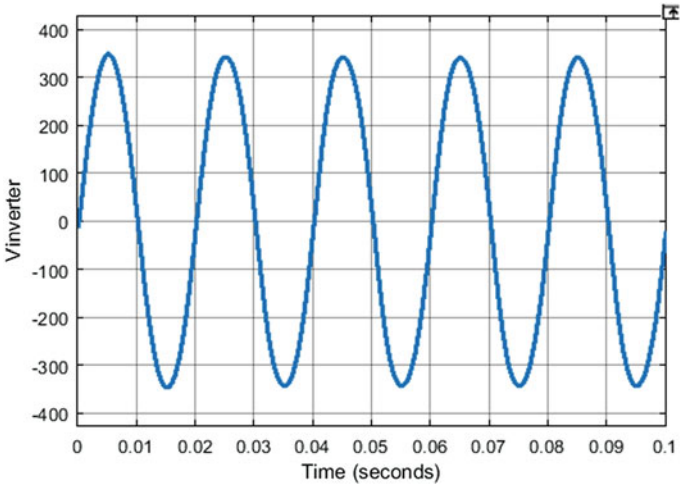

Fig. 11 AC voltage output of inverter

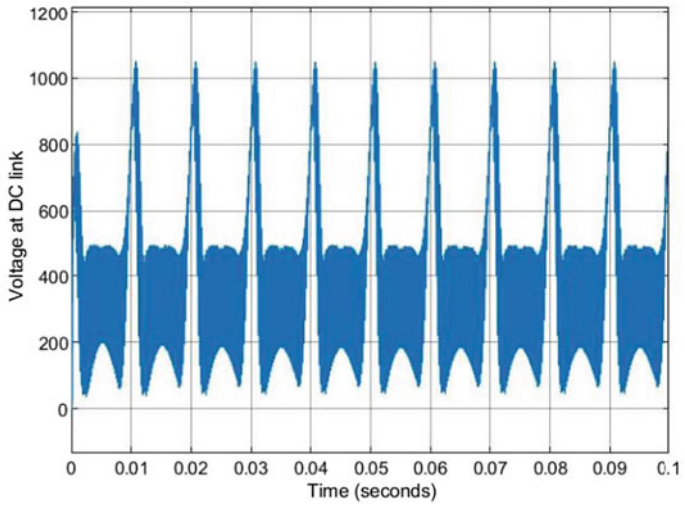

Fig. 12 DC-link voltage with PI controller

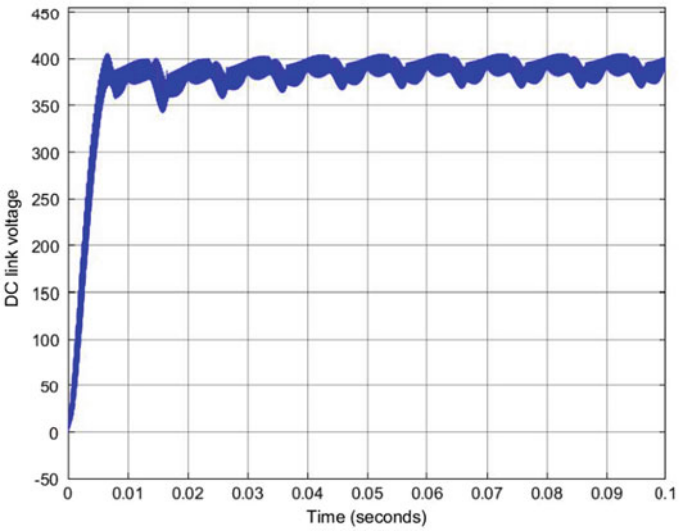

Fig. 13 DC-link voltage with FIS controller

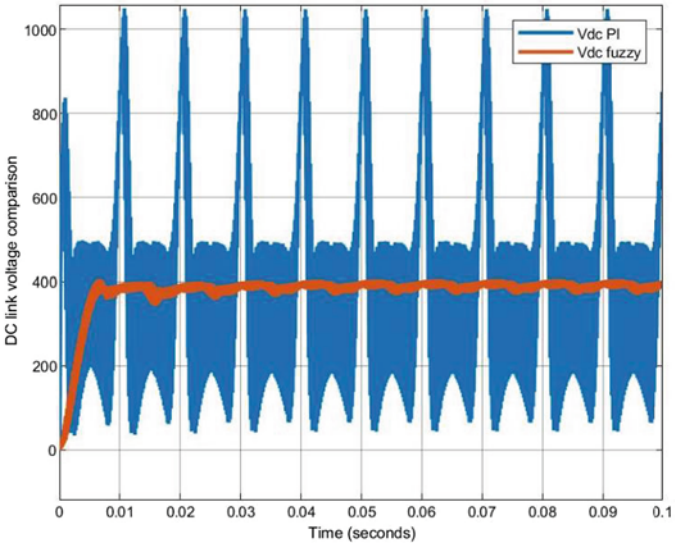

Fig. 14 DC-link voltage comparison between PI and FIS controller

Figure 15 draws the comparison of active power injection from PV array-connected DBBI (dual buck-boost single-phase inverter) for PI and FIS controllers under mismatched environmental conditions. Along with DC-link voltage comparison, the power injection comparison, the THD of PCC (point of common coupling)

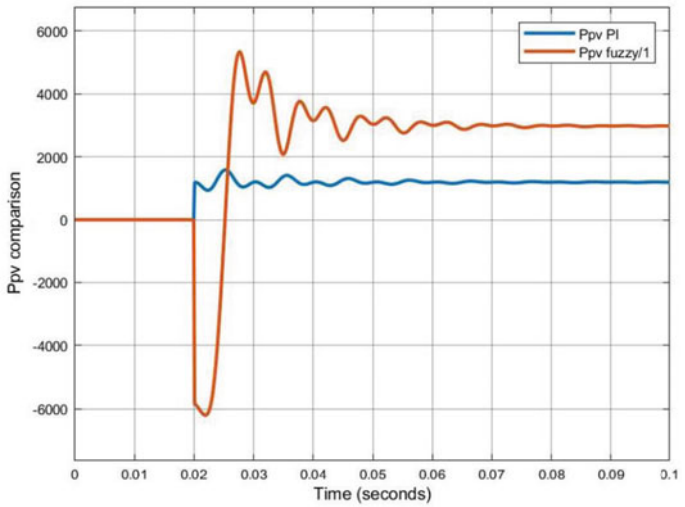

Fig. 15 Active power injection comparison between PI and FIS controller

voltage with PI, and the fuzzy controller is also studied using the FFT analysis toolbox available in the powergui tool. Figures 16 and 17 describe the THDs of the PCC voltages with PI and FIS controllers, respectively.

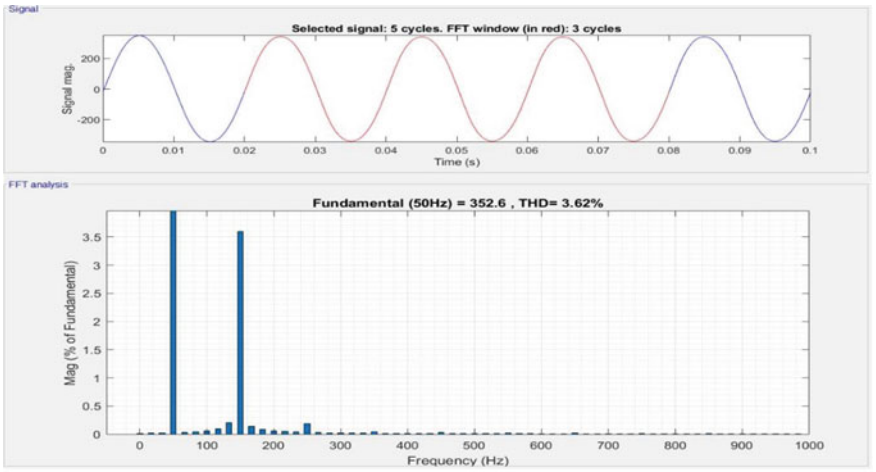

Fig. 16 THD of PCC voltage with PI controller

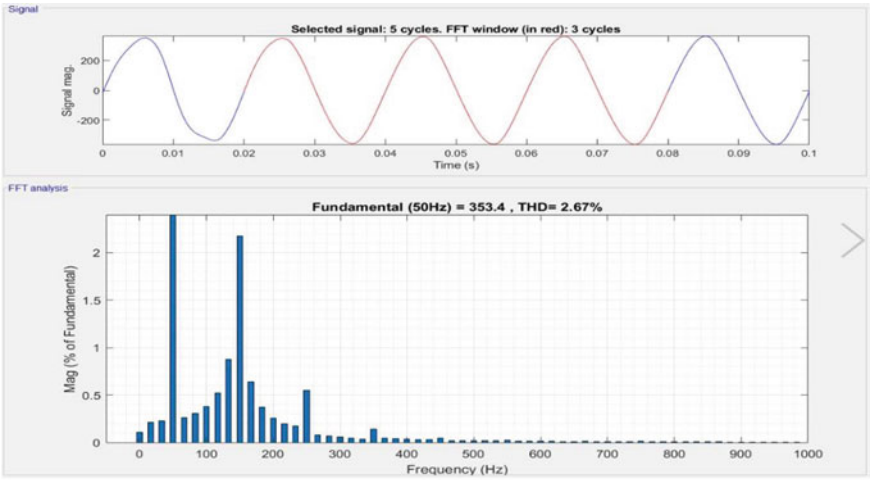

Fig. 17 THD of PCC voltage with FIS controller

5 Conclusion

As per the comparison of the results in Sect. 4, it can be concluded that even during different sun insolation for the photovoltaic array modules representing mismatched environmental conditions, the DC-link voltage is more stable at 400 V for the FIS controller module. The ripple in DC-link voltage with FIS is very less than obtained from the PI controller module. The power injected by DBBI with PI controller is recorded at 1.5 kW, whereas for the FIS controller the DBBI injects 3 kW which is much higher. Therefore, the DBBI module with different sun insolation conditions of PV modules controlled by FIS is more stable and efficient than a conventional PI controller. As the DC-link voltage is stable for the FIS controller, the THD of the PCC voltage is also less for the same. The recorded THD for the PI controller is 3.62% and for the FIS controller is 2.67%. All the results are plotted with time as a reference using the powergui toolbox of MATLAB software.

References

1. Foster R, Ghassemi M, Cota A (2010) Solar energy: renewable energy and the environment. CRC Press Taylor and Francis Group, Inc
2. Umuhoza J, Zhang Y, Liu Y, Moquin J, Farnell C, Mantooth HA (2015) Interleaved flyback based micro-inverter for residential photovoltaic application in remote areas. In: IEEE 16th workshop control and modeling for power electronics (COMPEL) Vancouver BC 1–6
3. Ji B, Wang J, Zhao J (2013) High-efficiency single-phase transformerless PV H6 inverter with hybrid modulation method. IEEE Trans Industr Electron 60(5):2104–2115
4. Bidram A, Davoudi A, Balog RS (2012) Control and circuit techniques to mitigate partial shading effects in photovoltaic arrays. IEEE J Photovoltaics 2(4):532–546

5. Kaushika ND , Gautam NK (2003) Energy yield simulations of interconnected solar PV arrays. IEEE Trans Energy Conver 18(1):127–134
6. Patel H, Agarwal V (2008) Maximum power point tracking scheme for PV systems operating under partially shaded conditions. IEEE Trans Industr Electron 55(4)1689–1698
7. Villa LFL , Ho T-P, Crebier J-C, Raison B (2013) A power electronics equalizer application for partially shaded photovoltaic modules. IEEE Trans Industr Electron 60(3)1179–1190
8. Olalla C, Deline C, Clement D, Levron Y, Rodriguez M, Maksimovic D (2015) Performance of power-limited differential power processing architectures in mismatched PV systems. IEEE Trans Power Electron 30(2):618–631
9. Femia N, Lisi G, Petrone G, Spagnuolo G, Vitelli M (2008) Distributed maximum power point tracking of photovoltaic arrays: novel approach and system analysis. IEEE Trans Industr Electron 55(7):2610–2621
10. Alharbi BM, Alhomim MA, McCann RA (2020) An efficient high voltage gain using two-stage cascaded interleaved boost converter for solar PV system with MPPT technique. In: 2020 IEEE power & energy society innovative smart grid technologies conference (ISGT), pp 1–4
11. Debnath D, Chatterjee K (2016) Maximising power yield in a transformerless single-phase grid connected inverter servicing two separate photovoltaic panels. IET Renew Power Gener 10(8):1087–1095
12. Wai R-J, Wang W-H, Lin C-Y (2008) High-performance stand-alone Photovoltaic generation system. IEEE Trans Industr Electron 55(1):240–250
13. Ankit SK, Sahoo SS, Yanine FF (2018) Review and comparative study of single-stage inverters for a PV system. Renew Sustain Energy Rev 91:962–986
14. Pardhi PK, Sharma SK (2020) Power optimized architecture based converter and its control for single phase grid-tied solar photovoltaic system. IEEE international conference on power electronics, smart grid and renewable energy (PESGRE2020)
15. Abdelkrim T, Bouarroudj N, Lakhdari A, Benlahbib B, Borni A, Benamrane K (2019) Design novel fuzzy logic controller of photovoltaic conversion cascade based five levels inverter for stand-alone applications. In: International conference on environment and electrical engineering (EEEIC)
16. Dutta S, Chatterjee K (2018) A buck & boost based grid connected PV inverter maximizing power yield from two PV arrays in mismatched environmental conditions. IEEE Trans Ind Electron 65(7):5561–5571
17. Faranda R, Leva S, Maugeri V (2018) MPPT techniques for PV systems: energetic and cost comparison. In: 2008 IEEE power and energy society general meeting—conversion and delivery of electrical energy in the 21st century, pp 1–6
18. Liu F, Duan S, Liu F, Liu B, Kang Y (2008) A variable step size INC MPPT method for PV systems. IEEE Trans Industr Electron 55(7):2622–2628
19. Wu W, He Y, Blaabjerg F (2012) An LLCL power filter for single phase grid-tied inverter. IEEE Trans Power Electron 27(2):782–789
20. Araujo SV, Zacharias P, Mallwitz R (2010) Highly efficient single-phase transformerless inverters for grid-connected photovoltaic systems. IEEE Trans Industr Electron 57(9):3118–3128
21. Quesada GV, Gispert FG, Lopez RP, Lumbreras MR, Roca AC (2009) Electrical PV array reconfiguration strategy for energy extraction improvement in grid-connected PV systems. IEEE Trans Ind Electron 56(11):4319–4331
22. Patrao I, Garcera G, Figueres E, Gonzalez-Medina R (2014) Grid tie inverter topology with maximum power extraction from two photovoltaic arrays. IET Renew Power Gener 8(6):638–648

23. Sinha A, Jana KC, Das MK (2018) An inclusive review on different multi-level inverter topologies, their modulation and control strategies for a grid connected photovoltaic system. Sol Energy 170:633–657
24. Won CY, Kim DH, Kim SC, Kim WS, Kim HS (2009) A new maximum power point tracker of photovoltaic arrays using fuzzy controller. In: Proceedings of the 25th annual IEEE power electronics specialists conference, pp 396403
25. Islam MS, Nepal MP, Skitmore M, Attarzadeh M (2017) Current research trends and application areas of fuzzy and hybrid methods to the risk assessment of construction projects. Adv Eng Inform 33:112–131

Modified Hysteresis Current Control Implementation for Three-Phase Grid-Connected Inverter

Mayank Arora and C. Vyjayanthi

1 Introduction

The distributed generation (DG) system is gradually becoming a new development path in the global energy sector. The majority of DG systems utilize advanced technologies such as solar PV systems and wind turbines with an inverter connected to deliver power to the grid.

PV system is cheaper, cleaner, and is provided free from nature. However, it is widely used either in stand-alone or grid-connected systems. The main application of stand-alone [1] is household [2], water pumping [3], electric vehicle charging [4], military applications [5], and street lighting [6], whereas the grid connection is mainly made in the hybrid system.

In a hybrid system like PV grid integration, the power from the PV module is directly fed to the utility grid without using energy storage devices such as a battery. It reduces the overall system investment by reducing the maintenance cost and less space for installing equipment [7]. The integration of the grid requires a controller that is efficient in operation. However, the performance of the inverter controller largely determines the power quality of an inverter connected to the DG system. The most widely used control method for grid-connected inverters is pulse width modulation (PWM). Compared to voltage PWM converter operating in an open loop, the current control PWM technique provides various advantages like a fast response, accurate dc-link voltage stabilization, and protection features [8].

For providing the quick current control with stability, accuracy, and ease of implementation, the hysteresis current control outperforms other current control techniques like sinusoidal PWM. Also, the error in the current can be reduced by changing the bandwidth of the signal, which controls the switching frequency of the system. As the switching frequency increases, the current waveform is improved. But there are limitations to increasing the switching frequency as it increases the switching loss and

M. Arora (✉) · C. Vyjayanthi
National Institute of Technology Goa, Veling, India

S. Kumar et al. (eds.), *Recent Advances in Power Electronics and Drives*, Lecture Notes in Electrical Engineering 852, https://doi.org/10.1007/978-981-16-9239-0_35

problems related to EMI [9]. Hence, this interface system combines the three-phase inverter with the pulse generation using hysteresis current control and power optimizer operating at MPPT, capable of extracting maximal power from the PV system [10, 11]. Therefore, this paper implements a hysteresis current controller with PI for pulse generation of the three-phase inverter while maintaining the constant dc voltage.

This paper is categorized as basic elements involved in grid integration in Sect. 2, and the proposed methodology is presented in Sect. 3. Calculation, results, and discussion are performed in Sects. 4 and 5. And, the conclusion is bestowed in Sect. 6.

2 Basic Elements of Solar PV Grid Integration

The solar PV with the grid integration comprises various elements like PV module of desired rating, power optimizer for increasing or decreasing the voltage as per our applications, inverters, filters, and the utility grid as shown in Fig. 1. There is a unique design in which a battery is also employed at the PCC to enhance the system reliability, but it makes the cost and complexity go high [12].

2.1 PV Module

The solar PV system consists of various cells joined together in series or parallel to form a panel, and multiple panels joined to form an array, and when the number of arrays is combined, it creates a module [13]. However, for high voltage and high power production, various modules are connected and feed power to the grid while maintaining the constant voltage at the dc bus.

Figure 2 shows the equivalent circuit of the PV cell [14].

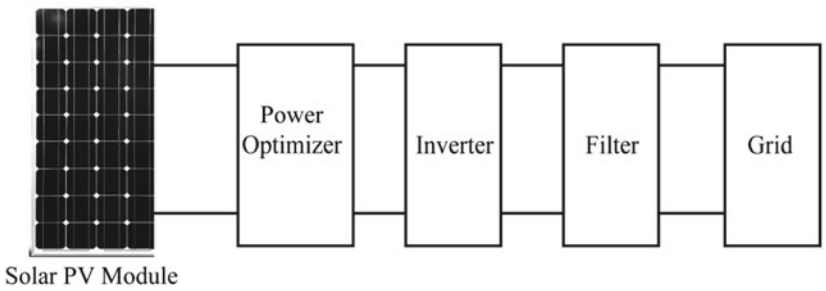

Fig. 1 Elements of solar PV grid integration

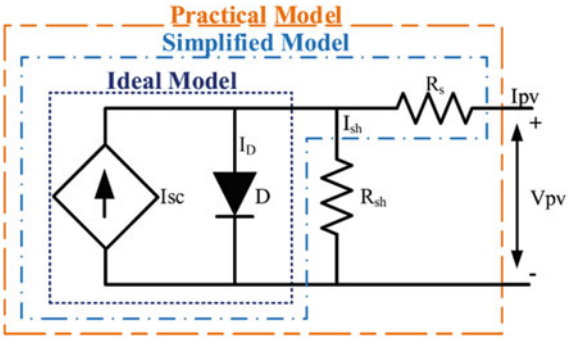

Fig. 2 Mathematical model of solar cell

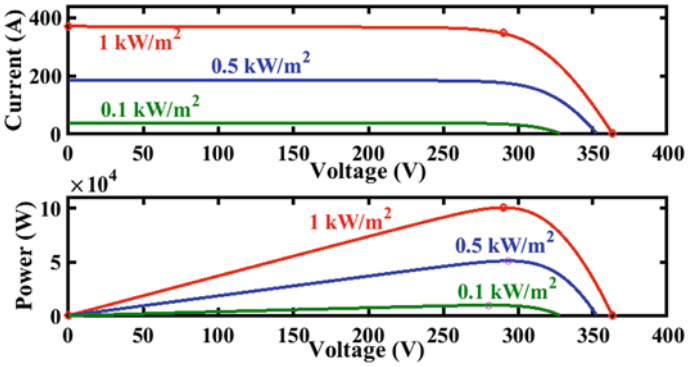

Fig. 3 P–V and I–V curve of solar module

In contrast, Fig. 3 shows the PV module's voltage, current, and power characteristics. Table 1 manifests the panel rating, which is utilized to design hysteresis current control for the implementation of three-phase grid-connected inverter topology.

Table 1 Panel rating for grid integration

S. no	Parameters	Value
1	Voc	36.3 V
2	Isc	7.84 A
3	Cells per module	60
4	Parallel string	47
5	Series connected module	10
6	Maximum power	213.15 W

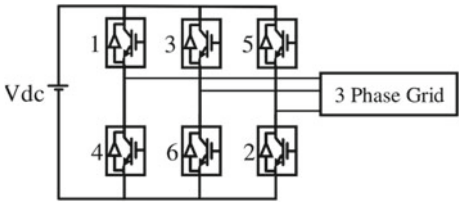

Fig. 4 Three-phase VSI

2.2 Power Optimizer

Various types of power optimizers are available that can be used according to our desired applications. In this three-phase grid connection, the rating of the solar PV system is 363 V at the input and 600 V at the output. So, the converter which can be utilized must be boost, buck-boost, SEPIC, or zeta converter [12].

2.3 Inverter

It is the most critical part of the grid-connected system, which has to be controlled by switching pulses. Switching pulses are generated by using various methods which are available in the literature. In this paper, the hysteresis control technique is employed due to its simplicity and cost-effectiveness [15]. The inverter's primary function is to convert DC from PV array to AC and feed that AC power to the utility grid by maintaining acceptable power quality levels. In this, a three-phase voltage source inverter is utilized for integrating with the grid as shown in Fig. 4. It comprises six switches which are controlled by the pulses given by the hysteresis controller.

2.4 Grid

The grid is connected at the end of the system. A few criteria should be matched before interconnecting the grid with solar PV systems, like the voltage, frequency, and phase sequence matching [16]. If these criteria are ignored, it injects harmonics into the system, which decrease the stability of the interconnected system.

3 Proposed Methodology

The solar PV grid-connected system comprises a solar PV module that produces dc voltage and current under varying solar irradiation. It is connected with the power optimizer operating with the maximum power point tracking technique. This power

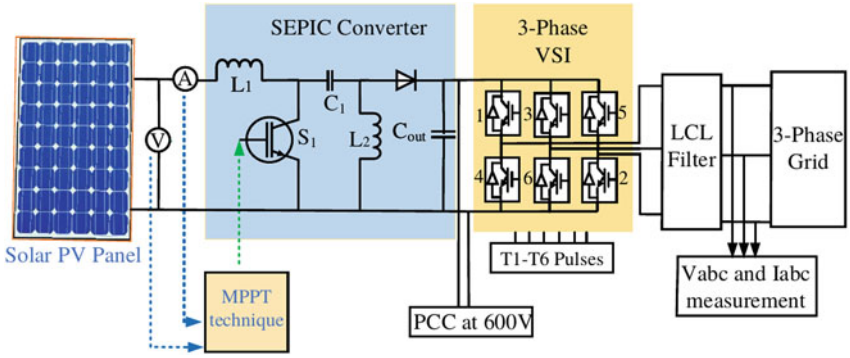

Fig. 5 Model of solar PV with grid integration

optimizer (SEPIC converter) is further connected to a three-phase inverter, which converts DC power into AC to supply power to the connected grid [17], as shown in Fig. 5.

The elements and its operation which are involved in the pulse generation using hysteresis current control are discussed below:

3.1 MPPT

The solar module converts the solar energy from the sun to electrical energy. The solar radiation throughout the day is not constant and varies with time, making our system deviate from MPPT and operate with low efficiency. However, to trace that maximum powerpoint, various MPPT techniques are used, and classified into three, i.e., classical, optimization, and intelligent approach [15]. For this hysteresis control, the P&O algorithm is implemented because of its ease of operation and simplicity [9].

The flowchart of the P&O methodology is shown in Fig. 6.

It senses the current and voltage from the solar PV panel and calculates the change in power and voltage change. If the change in power is greater than 0, check for the change in voltage; if it is greater than 0, increase the Vref and if it is lesser than 0, decrease the Vref. Similarly, if the change in power is lesser than 0, check for a change in voltage; if this change is more than zero, decrease the Vref; otherwise, increase the Vref, where Vref represents the array voltage.

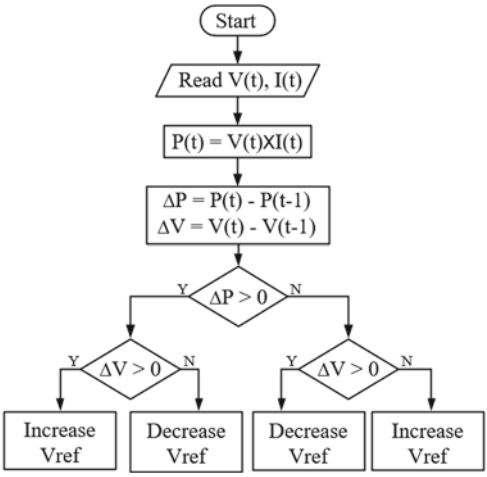

Fig. 6 Perturb and observe MPPT algorithm

3.2 Hysteresis Current Controller

The hysteresis current controller is used to generate pulses for the inverter connected between PV and grid system. It senses the voltage of point of coupling (PCC) and compares it with the voltage that needs to be maintained constant, i.e., 600 V for this system, as shown in Fig. 7.

The error is then fed to the PI controller, which converts the voltage into current quantity. This current is then converted from dq to abc reference frame and compared with the actual grid current, which is further passed through the hysteresis band for the generation of pulses. And these pulses from $T1$ to $T6$ are fed to a three-phase inverter for maintaining the constant voltage at the PCC.

The modified current control technique uses the PI controller with the hysteresis band to reduce the error at the steady-state. The hysteresis controller gives varying switching frequencies when operated alone, which causes noise in the system. Hence,

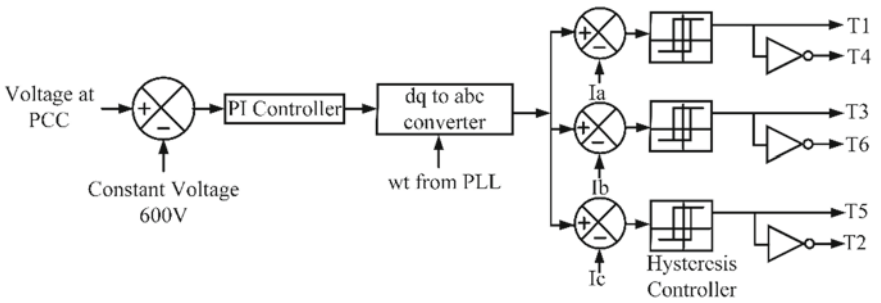

Fig.7 Hysteresis controller design

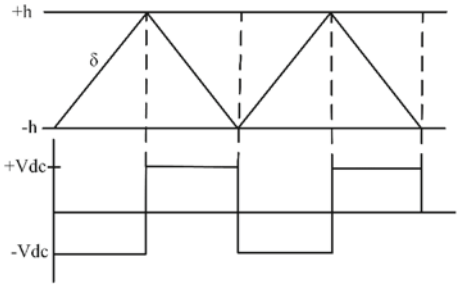

Fig. 8 Hysteresis band pulses

the PI controller is introduced by changing the reference frame that reduces hysteresis controller bandwidth [8].

Figure 8 indicates +h and –h as the limits of the hysteresis band and δ as the slope. In phase a of hysteresis band, as the slope is positive, the controller makes switch $T2$ to turn on and switch $T1$ to turn off, and when the slope is negative, it makes $T1$ as on and $T2$ as off, which is then fed to VSI. Similarly, the same case follows for the phases b and c.

In this case, when the voltage at the dc bus is measured and compared with the constant voltage, it produces an error signal. This error, when given to the PI controller, produces the current. And this current is compared with the grid current which gives error as output. This error is given by the following equations:

When the switch is operating, the dc bus voltage can be written as

$$V_{PCC} = L_{\text{filter}} \frac{di_{\text{output}}}{\text{dt}} + V_{\text{grid}} \tag{1}$$

The error fed to the hysteresis band is

$$\delta = i_{\text{output}} - i_{\text{ref}} \tag{2}$$

As the output current is the phase a current, so substituting Eq. (2) in Eq. (1) we get

$$V_{PCC} = L_{\text{filter}} \frac{d}{\text{dt}} (I_{\text{ref}} + \delta) + V_{\text{grid}} \tag{3}$$

$$V_{PCC} - V_{\text{grid}} = L_{\text{filter}} \frac{d\delta}{\text{dt}} \tag{4}$$

As considering dynamic nature, the change in error is

$$\frac{d\delta}{\text{dt}} = \frac{V_{PCC} - V_{\text{grid}}}{L_{\text{filter}}} \tag{5}$$

The above equation shows the change in error concerning time oscillating between the band for the production of pulses for VSI.

4 Calculations

4.1 Designing of SEPIC Converter

SEPIC converter is designed by considering the following parameters [12]:

Vo = 600 V(PCC voltage), *Vs* = 363 V (solar PV voltage), *P* = 100 KW, *fsw* = 5 kHz

$$\text{Input Current of Inverter } I_{in} = \frac{P_o}{V_S} = \frac{100 * 10^3}{363} = 275.48\,\text{A}$$

$$\text{Output Current of Inverter } I_o = \frac{P_o}{V_o} = \frac{100 * 10^3}{600} = 166.67\,\text{A}$$

$$\text{Duty Cycle of Converter } D = \frac{V_O}{V_S + V_o} = 0.6230 = 62.30\%$$

Average inductor current and change in inductor current is given by [12]

$$I_{L2} = I_{\text{O}} = 166.67\,\text{A}$$

$$I_{L1} = \frac{V_o * I_o}{V_S} = \frac{100 * 10^3}{363} = 275.48\,\text{A}$$

Assuming change in inductor current = 40%

$$\Delta I_{L1} = 0.4 * 275.48 = 110.191\,\text{A}$$

$$\Delta I_{L2} = 0.4 * 166.67 = 66.668\,\text{A}$$

$$\text{Ripple in inductor current is given by } \Delta i_L = \frac{V_s * D}{f * L}$$

$$L_1 = \frac{V_s * D}{f * \Delta i_{L1}} = \frac{363 * 0.6230}{5000 * 110.192} = 410.4\,\text{mH}$$

$$L_2 = \frac{V_s * D}{f * \Delta i_{L2}} = \frac{363 * 0.6230}{5000 * 66.668} = 678\,\text{mH}$$

Table 2 Parameters of SEPIC converter

S. no	Parameters	Value
1	Inductor 1	410.4 mH
2	Inductor 2	678 mH
3	Capacitors	1.735 mF

Now assuming the capacitor ripple voltage to be 2% of output voltage (Table 2).

$$C_1 = C_2 = \frac{D}{R * (\Delta V_O / V_O) * \mathrm{f}} = 1.735\,\mathrm{mF}$$

4.2 Filter Design

Switching frequency = 10 kHz, Fres = Fsw/10 = 1000 Hz.

Calculating for single phase [18]: For 100 KW, 230 V(P–P), 50 Hz

$$C = \frac{0.05 * S}{V^2 * 2 * \pi * f} = 0.05 * \frac{\frac{100 * 10^3}{3}}{230^2 * 2 * \pi * 50} = 100.28\,\mathrm{mF}$$

Grid current in a single phase of the three-phase system is (Table 3)

$$Ig = \frac{100\mathrm{KVA}/3}{230} = 144.92\,\mathrm{A}$$

$Ig(sw) = 0.3\%$ of $Ig = 0.003 * 144.92 = 0.434$ A.
$Vi(sw) = 0.9 * Vg = 0.9 * 230 = 207$ V

$$L = \frac{1}{(w_{SW} * \left(\frac{Ig_{sw}}{Vi_{sw}}\right) * (1 - (w_{sw/w_{\mathrm{res}}})^2))} = 76.68\mathrm{mH}$$

$$L_1 = L_2 = \frac{76.68}{2} = 38.34\mathrm{mH}(\mathrm{MinimumValue})$$

$$L_{\max} = \frac{0.2 * V_{\mathrm{grid}}}{2 * \pi * 50 * I} = \frac{0.2 * 230}{2 * \pi * 50 * 144.92} = 1\mathrm{mH}$$

$$L_1 = L_2 = \frac{1\mathrm{mH}}{2} = 500\,\mu\mathrm{H}(\mathrm{MaximumValue})$$

Table 3 Parameters of filter design

S. no	Parameters	Value
1	Inductor 1	500 mH
2	Inductor 2	500 mH
3	Capacitor	100.28 mF

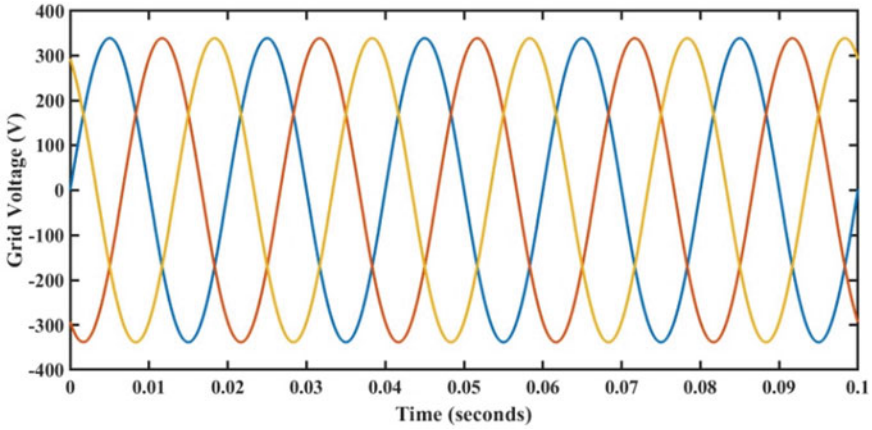

Fig. 9 Grid voltage

5 Results and Discussion

5.1 Simulation at Standard Testing Condition

At STC, i.e., 1000 W/m^2 and 25 °C grid voltage for a three-phase grid connection as shown in Fig. 9 is around 320 V. And the grid current is around 200 A, as shown in Fig. 10.

Figure 11 shows the PCC voltage waveform controlled by the hysteresis controller by maintaining the constant 600 V supply at the dc bus. It operates in a transient state while starting time from 0 to 0.035 s, and after 0.035, it becomes stable at 600 V, the so-called steady-state operation.

Figure 12 shows the active power waveform. Initially, it is in a transient state, and when the PCC voltage reaches the stable region at 0.035 s, active power becomes 100 KW, which is the rating of our grid-connected PV system.

The filter design and fast-acting hysteresis controller effectively reduce the harmonics of grid-side current. Figure 13 shows that the total harmonics distortion is 1.09%, and the magnitude of the fundamental component is 193.5.

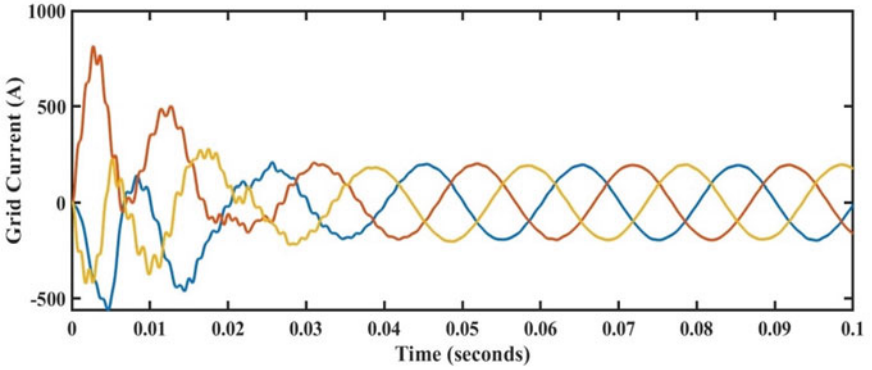

Fig. 10 Grid current

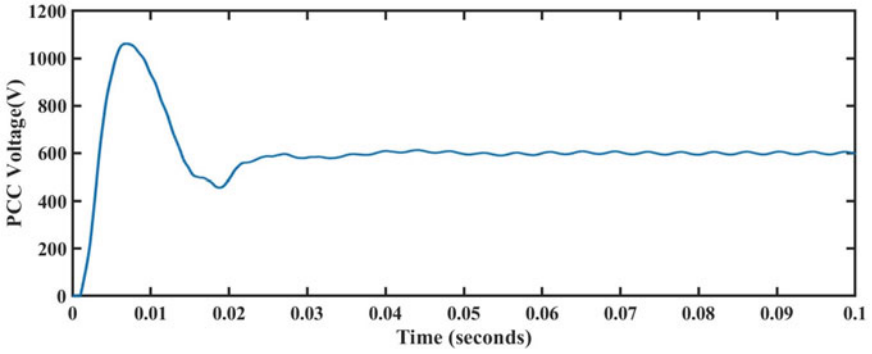

Fig. 11 Voltage at PCC

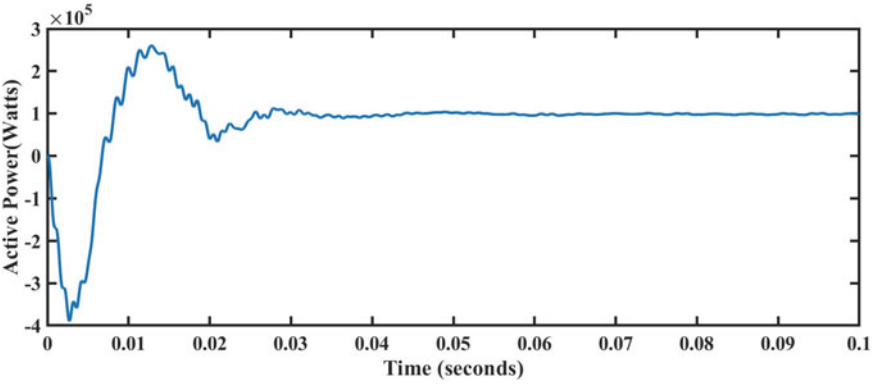

Fig. 12 Active power at the grid

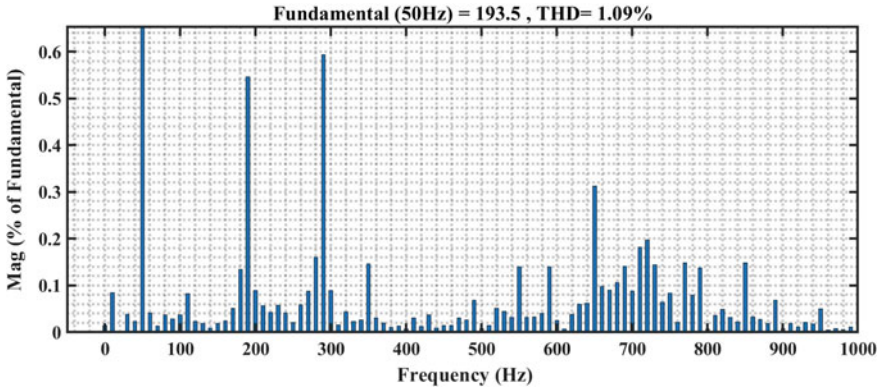

Fig. 13 THD of grid current

6 Conclusion

In this paper, the hysteresis current control technique for the pulse generation of the three-phase inverter is modified, which is simple and efficient in operation as it takes lesser time to track and reach the steady state.

The simulated results prove that the proposed system of current control is efficient in operation while maintaining the MPPT of the power optimizer at all conditions. All the work is carried out in the MATLAB Simulink model, which shows the dynamic behavior and performance of the grid-connected system with the calculation of filter design and the power optimizer, which is chosen to be SEPIC because it provides lesser THD compared to the ZETA converter. Overall, this hysteresis current control of pulse generation is simple, robust, and efficient in operation.

References

1. Al-Waeli AH, Kazem HA, Chaichan M (2016) Review and design of a stand-alone PV system performance. Int J Comput Appl Sci 1–6
2. Dhiman B, Kumar T, Rituraj G, Bhalla K, Chakrabarti D (2019) Study of small scale photovoltaic applications in rural Indian household context. J Phys Conf Ser 1343
3. Patil SS, Zende RM (2017) Solar-powered water pumping system. In: 2017 third international conference on sensing, signal processing and security (ICSSS), Chennai, pp 186–190
4. Porselvi T, Nisha J, Thendral K, Vasantha DP (2019) Solar Pv fed electric vehicle charging system with hybrid energy storage system. In: 2019 international conference on computation of power 2019 energy, information and communication (ICCPEIC), Melmaruvathur, India, pp 202–206
5. Jenkins P, Walters R (2017) Photovoltaic technology for Navy and Marine corps applications. In: 2017 IEEE 60th international midwest symposium on circuits and systems (MWSCAS). Boston, MA, USA, pp 958–961

6. Shivaleelavathi BG, Vinay ME, and Sucheeth V (2018) Solar based smart street lighting system. In: 2018 international conference on electrical, electronics, communication, computer, and optimization techniques (ICEECCOT), Msyuru, India, pp 1479–1483
7. Li Y, Chi Y, Wang X, Tian X, Jianqing J (2019) Practices and challenge on planning with large-scale renewable energy grid integration. In: 2019 IEEE 3rd conference on energy internet and energy system integration (EI2), Changsha, China, pp 118–121
8. Jena S, Babu BC, Naik AK, Mishra G (2011) Performance improvement of single-phase grid—connected PWM inverter using PI with hysteresis current controller. In: 2011 international conference on energy, automation and signal, pp 1–5
9. Rajamohamed S, Jeyanthy A, Devaraj D (2018) Hysteresis-based voltage and current control techniques for grid connected solar photovoltaic systems: comparative study. Int J Electr Comput Eng (IJECE), pp 2671–2681
10. Rajalakshmi B, Soumya U, Kumar AG (2017) Vehicle to grid bidirectional energy transfer: grid synchronization using hysteresis current control. In: 2017 international conference on circuit, power and computing technologies (ICCPCT), Kollam, India, pp 1–6
11. Sabegh MRZ, Bingham CM (2019) Impact of hysteresis control and internal thermal mass on the energy efficiency of IoT-controlled domestic refrigerators. In: 2019 IEEE 7th international conference on smart energy grid engineering (SEGE), Oshawa, Canada, pp 103–107
12. Pachauri RK, Chauhan YK (2016) Modeling and simulation analysis of PV fed Cuk, Sepic, Zeta and Luo DC–DC converter. In: 2016 IEEE 1st international conference on power electronics, intelligent control and energy systems (ICPEICES), pp 1–6
13. Hashimoto J, Ustun TS, Suzuki M, Sugahara S, Hasegawa M, Otani K (2021) Advanced grid integration test platform for increased distributed renewable energy penetration in smart grids. IEEE Access 9:34040–34053
14. Mohammed AY, Mohammed FI, Ibrahim MY (2017) Grid connected photovoltaic system. In: 2017 international conference on communication, control, computing and electronics engineering (ICCCCEE), pp 1–5
15. Bollipo RB, Mikkili S, Bonthagorla PK (2020) Critical review on PV MPPT techniques: classical, intelligent and optimization. IET Renew Power Gener 1433–1452
16. Roselyn Dr, Preetha J, Sen D, Lal P, Purkayastha N, Nithya C (2020) Development of hysteresis current controller for power quality enhancement in grid connected Pv system. Int J Electr Eng Technol 11(4):8–21
17. Mohammed AY, Mohammed FI, Ibrahim MY (2017) Grid connected photovoltaic system. In: 2017 international conference on communication, control, computing and electronics engineering (ICCCCEE), Khartoum, Sudan, pp 1–5
18. Jo J, Liu Z, Cha H (2019) A new design method of LCL filter for single phase grid connected power converter. In: 2019 international symposium on electrical and electronics engineering (ISEE), pp 189–193

A Quasi-Direct Buck-Boost Fuzzy Controlled Rectifier for Rapid Charging of Electric Vehicle Battery

Rohan Jain and M. S. Manisha

1 Introduction

With increase in pollution due to emission of gases from internal combustion vehicles the environment is deteriorating causing climatic disasters. Continuing the same is also causing global warming where the temperature of earth's surface is increasing day by day. To reduce these impacts on environment and to save earth from these climatic disasters, zero emission methods of transportation need to be adopted by us. This can be only achieved by electric vehicles with battery as the source of power for drive train [1]. But utilizing battery, replacing internal combustion is a greater challenge as the battery needs to be charged regularly after discharge because of drive train. There are many ongoing researches running for better charging capabilities of the heavy battery. New technologies [1] are introduced to charge the battery faster at rapid rate with high charging current injection to the battery. In conventional topologies [2] the charging time takes around eight to ten hours, which is a major issue for economy non-commercial vehicles. This charging time needs to be reduced to around 1–2 h for charging the battery full from lowest state of charge (10%).

To solve this issue of slow battery charging a novel circuit topology Quasi-direct buck-boost (QDBB) is introduced in this paper with three-phase AC input. The circuit uses a six IGBT switches controlled rectifier [3] for producing stable DC link voltage. The constant DC voltage is taken as input to the three-legged buck-boost converter which controls the output current fed to the battery. In the three-legged buck-boost converter [4], each leg comprises of two IGBT switches represented as buck and boost switch. The ON and OFF time of these switches determine the charging current of the battery [5]. The proposed QDBB topology is shown in Fig. 1.

As seen in the above proposed circuit the controlled rectifier is connected to three-phase AC supply with LCL filter in between for mitigation of harmonics generated by the rectifier due to high-frequency switching [6]. The rectifier DC voltage Vdc is fed

R. Jain (✉) · M. S. Manisha
Netaji Subhas University of Technology, Delhi, India

S. Kumar et al. (eds.), *Recent Advances in Power Electronics and Drives*, Lecture Notes in Electrical Engineering 852, https://doi.org/10.1007/978-981-16-9239-0_36

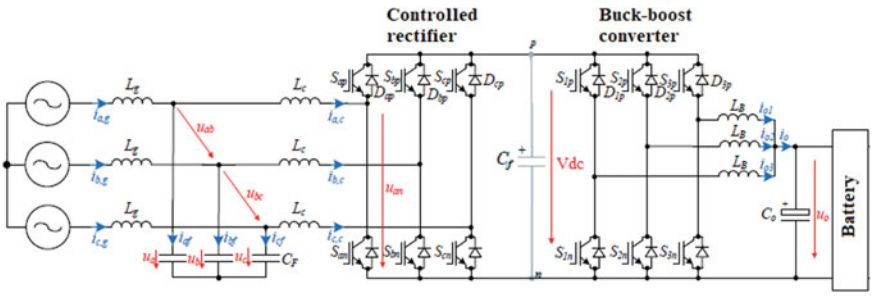

Fig. 1 Proposed QDBB topology with input three-phase supply

to three-legged buck-boost converter as mentioned previously. For ripple reduction in the DC voltages Cf and Co filter capacitances are connected at the outputs of both the converters, respectively. The battery is charged with voltage (uo) controlled by the feedback loop control system.

This paper is included with the working principle of QDBB converter in section II followed by section III with controlled design of the proposed topology and FIS modeling. Section IV has the simulation results of the proposed system providing graphical comparative analysis of QDBB converter with PI and FIS controllers.

2 Working Principle of QDBB Converter

As mentioned previously the QDBB topology includes three-phase controlled rectifier operated by sinusoidal PWM technique. The controlled rectifier has six IGBT power electronic switches connected in three leg format fed from three-phase source terminals through LCL filter [6]. The complete circuit is divided as upper region switches and lower region switches. The positive region switches include Sap, Sbp and Scpand negative region switches include San, Sbn and Scn. The positive region switches and the negative region switches operate alternatively with NOT gate signals connected to the switches. Each IGBT switch is connected with antiparallel diode for energy dissipation in the power IGBT switch during OFF condition to avoid overshoot of voltage at the output [7]. As per the input voltage the switches are operated to generate DC voltage [8]. For AB phase voltage switches Sap Sbn San Sbp are operated. During positive voltage Vab, switches Sap Sbn are turned ON, and during negative voltage Vba, switches Sbp San are turned ON. As similar to the above conduction for BC positive voltage (Vbc), switches SbpScn are turned ON and during negative voltage (Vcb), switches ScpSbn are turned ON. For AC positive voltage (Vac), switches Sap Scn are turned ON and for negative voltage (Vca), switches San Scp are turned ON. The rectification for B phase can be seen in Fig. 2.

In the above circuit the idc is the DC current generated at the output terminals of the controlled rectifier [9]. The filter capacitance Cf is connected at the output

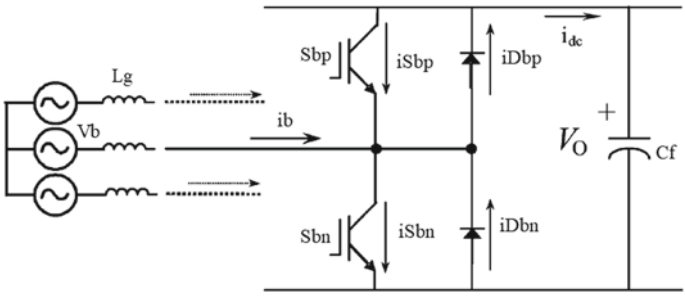

Fig. 2 Rectifier operation for phase B

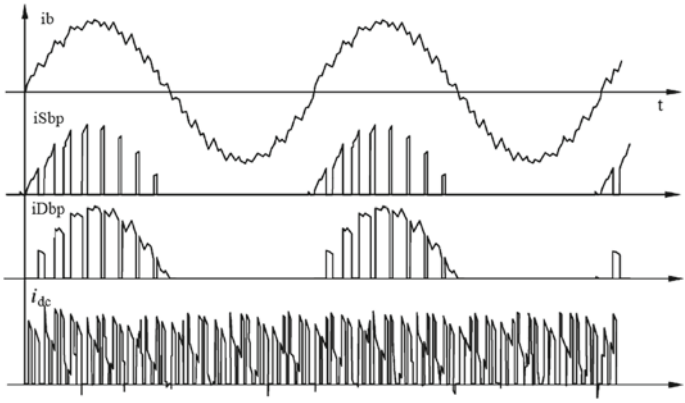

Fig. 3 Current conduction path for phase B positive rectification

terminals to reduce ripple in the DC voltage. The current conduction path for the phase B rectification is shown in Fig. 3.

The pulse generation for the controlled rectifier is explained in detail in Sect. 3. At the output terminals of three-phase rectifier buck-boost converter [10] is connected with three legs connected with individual inductors connected [11, 12] to each leg for energy storage (Fig. 4).

Each inductor Lb has charging currents i_{o1}, i_{o2} and i_{o3} accumulated to io. The complete current is given as

$$i_o = i_{o1} + i_{o2} + i_{o3} \tag{1}$$

As seen in the circuit topology above the switches S1p S2p S3p are the buck switches [13] and switches S1n S2n S3n are the boost switches. The ON time and OFF time of these switches are controlled by voltage feedback PI controller further updated with FIS controller. The control structure of rectifier and buck-boost converter is discussed in Sect. 3.

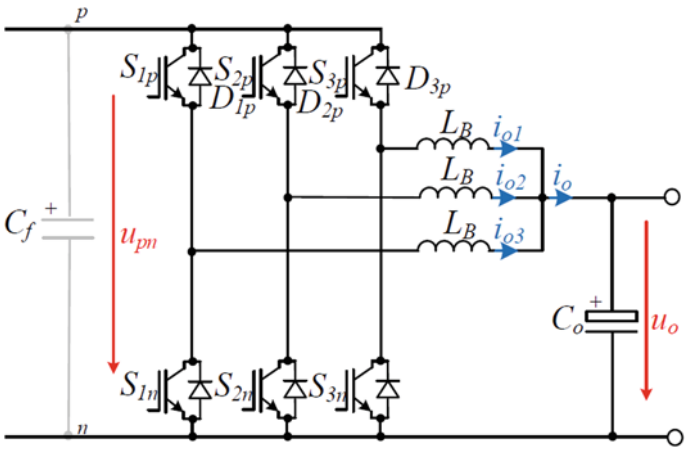

Fig. 4 Three-legged Buck-Boost converter

3 Control Design

The controlled rectifier is operated with sinusoidal PWM technique [14] where reference sin waveform is compared to high-frequency triangular wave for generation of pulses. The control structure of the module is shown in Fig. 5.

A two component current is produced with current feedback from three-phase source (ia, cib, cic, c). The Clarks transformation of the current is given as

$$\begin{bmatrix} i_\alpha \\ i_\beta \end{bmatrix} = \frac{2}{3}\begin{bmatrix} 1 & \frac{-1}{2} & \frac{-1}{2} \\ 0 & \frac{\sqrt{3}}{2} & \frac{-\sqrt{3}}{2} \end{bmatrix}\begin{bmatrix} i_{a,c} \\ i_{b,c} \\ i_{c,c} \end{bmatrix} \tag{2}$$

The measured two iα iβ components are compared to reference components $i_\alpha^* i_\beta^*$. The reference components is given as

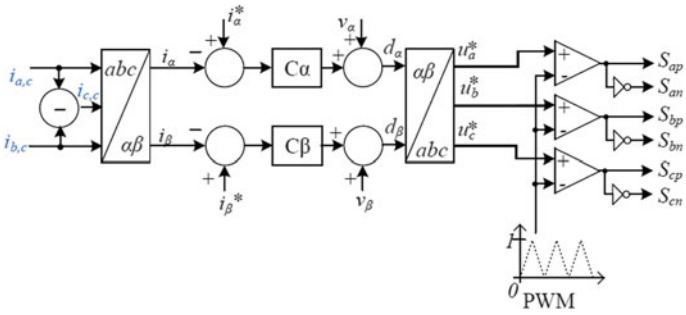

Fig. 5 Controller of controlled rectifier

$$i_{\alpha}^{*} = G^{*}.V_{\alpha} \tag{3}$$

$$i_{\beta}^{*} = G^{*}.V_{\beta} \tag{4}$$

Here, $V_{\alpha}V_{\beta}$ are the two voltage components of the three-phase source voltages $u_a u_b u_c$ [15] generated using Eq. 2. The multiplication factor G* is given as

$$G^{*} = (K_p + \int \frac{K_i}{s})(u_o^{*} - u_o) \tag{5}$$

Here, K_p is the proportional gain, K_i is integral gain of PI controller fed from comparison of output DC voltage (u_o) of the three-legged converter with reference DC voltage value (u^{*}_{o}).

The reference two component duty ratios for the generation of pulse for the rectifier is given as

$$d_{\alpha} = V_{\alpha} + C_{\alpha}(i_{\alpha}^{*} - i_{\alpha}) \tag{6}$$

$$d_{\beta} = V_{\beta} + C_{\beta}(i_{\beta}^{*} - i_{\beta}) \tag{7}$$

The two component reference duty ratios are converted to three signal format given as

$$\begin{bmatrix} u_a^{*} \\ u_b^{*} \\ u_c^{*} \end{bmatrix} = \frac{3}{2} \begin{bmatrix} \frac{2}{3} & 0 \\ \frac{-1}{3} & \frac{\sqrt{3}}{3} \\ \frac{-1}{3} & \frac{-\sqrt{3}}{3} \end{bmatrix} \begin{bmatrix} d_{\alpha} \\ d_{\beta} \end{bmatrix} \tag{8}$$

The above reference voltage signals are compared to high frequency triangular waveform [14] for generation of pulses for $S_{ap}S_{bp}$ and S_{cp}. The lower switches $S_{an}S_{bn}$ and S_{cn}get the complimentary signals through NOT gates.

The three-legged buck-boost converter control structure is shown in Fig. 6.

As per Eq. 5 the reference inductor discharge current ($i_{o,n}^{*}$) is given as

$$i_{o,n}^{*} = G^{*}.u_o^{*} \tag{9}$$

Here, n is the number of the leg of the buck-boost converter. The above reference inductor current is compared to measured inductor current ($i_{o,n}$). The compared error current is fed to PI controller [15] generating required duty ratio change for the buck and boost switches. The final duty ratio is given as

$$m_{Bn} = D_n + m_{buck} \tag{10}$$

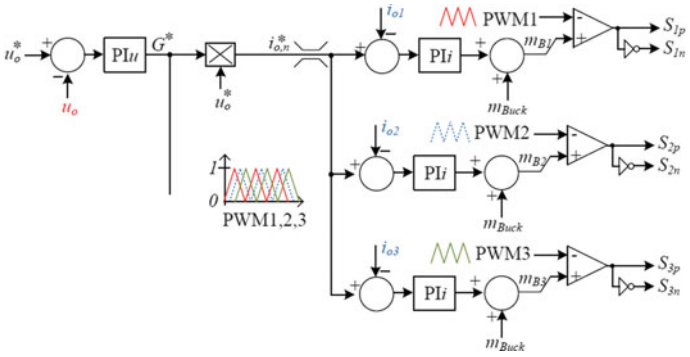

Fig. 6 Controller of buck-boost converter

The above resultant duty ratio is compared to phase shifted high-frequency triangular waveforms for generation of pulses for S1p S2p S3p and the NOT gate signals of the same are fed to S1n S2n S3n.

The PI controller of the DC output voltage comparison [8] as in Eq. 5 is replaced with FIS control structure with seven membership functions two input variables and one output variable with similar membership functions. The input variables are modeled with 'gauss' type membership functions [16] and the output variable is modeled with 'triangular' type membership functions. The FIS modeling is shown in Fig. 7.

In the above figure ZE is zero region, PS is Positive Small region, PM is Positive medium region, PB is positive big region, NS is negative small region, NM is negative medium region, NB is negative big region. The first input variable is error (E) [17] set with a range −400 to 400, and second variable change in error (CE) is set with a range −1 to 1. The output variable is set with a range of -4 to 4. As per the membership functions the rule [17] is given as (Table 1).

With the above If-and-If–then rule base the PI controller is replaced with FIS module and the results are compared in the next section with graphical representation plotted with respect to time.

4 Simulation Results and Analysis

With all the above modules a simulation model is developed using MATLAB Simulink software as shown in Fig. 8.

In the above modeling the input is a three-phase source connected to a step down transformer. The secondary of the transformer is connected to LCL filter for reduction of harmonics as the controlled rectifier operates at high switching frequency injects harmonics into the grid. The simulation is run for 1 s and the possible results are recorded for different operating conditions (Fig. 9).

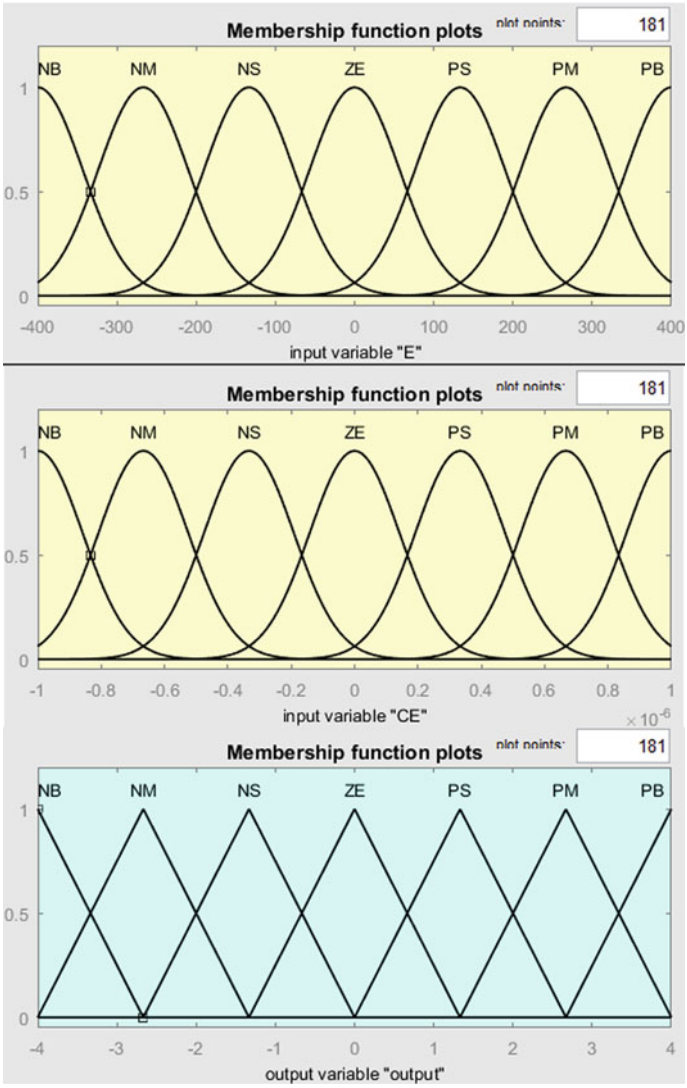

Fig. 7 FIS modeling

The above is the FIS controller modeling with two input variables (E and CE) and one output variable (G*). The reference inductor current is generated by multiplication of G* value with the reference output voltage Vo*. The G* value is specifically limited in a range using saturation block. As per Fig. 6 the reference inductor current io*n is compared to measured current ion and from the error, duty ratio for the switches is generated using PI controllers. For the given reference value below are the three-phase source input voltages and currents for the controlled rectifier (Fig. 10).

Table 1 A 49 rule base

E CE	NB	NM	NS	ZE	PS	PM	PB
NB	NB	NB	NB	NM	NS	NS	ZE
NM	NB	NM	NM	NM	NS	ZE	PS
NS	NB	NM	NS	NS	ZE	PS	PM
ZE	NB	NM	NS	ZE	PS	PM	PB
PS	NM	NS	ZE	PS	PS	PM	PB
PM	NS	ZE	PS	PM	PM	PM	PB
PB	ZE	PS	PS	PM	PB	PB	PB

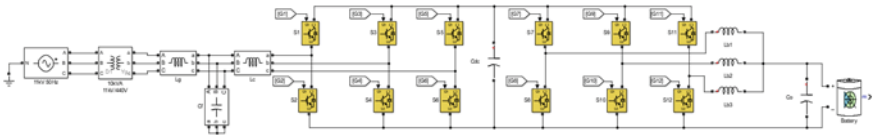

Fig. 8 Simulation modeling of the proposed system

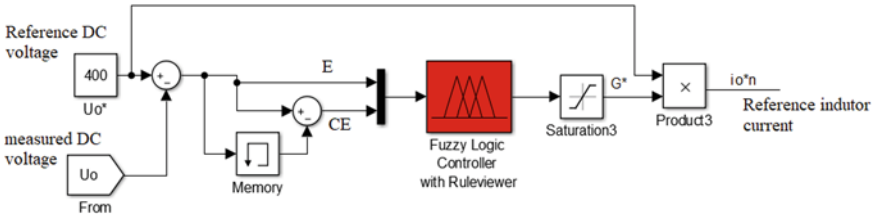

Fig. 9 FIS modeling in controller

As observed the three-phase voltages and currents have very less harmonics in them reduced by the LCL filter connected between the source and the controlled rectifier. Below is the DC link voltage [18] of 380 V generated by the controlled rectifier maintained constant throughout the simulation time of 1 s (Fig. 11).

For the same simulation time the battery charging characteristics like battery voltage, battery current and State of charge (SOC) of the battery are recorded and battery charging currents are compared with PI and FIS controllers [19] (Figs. 12, 13, 14).

In the above figure the charging current comparison is taken and it is observed that the charging current of the battery is higher for FIS controller. Therefore the converter charges the battery faster with FIS control structure reducing the charging time (Fig. 15).

As seen above the power factor of input with FIS is near to unity whereas with PI controller the power factor of the three-phase source is very low.

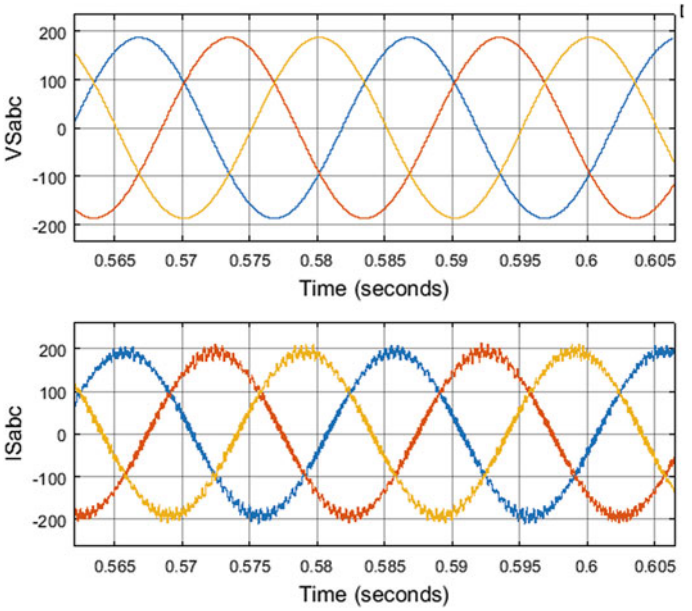

Fig. 10 Three-phase input voltages and currents

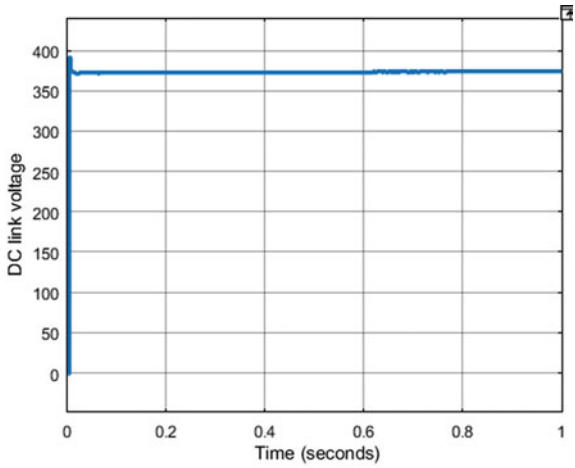

Fig. 11 DC output voltage after controlled rectifier

5 Conclusion

A successful simulation implementation of quasi-direct buck-boost converter is done with different controllers improving the performance of the converter. As per the results compared the DC voltage is more stable and generated with reduced ripple

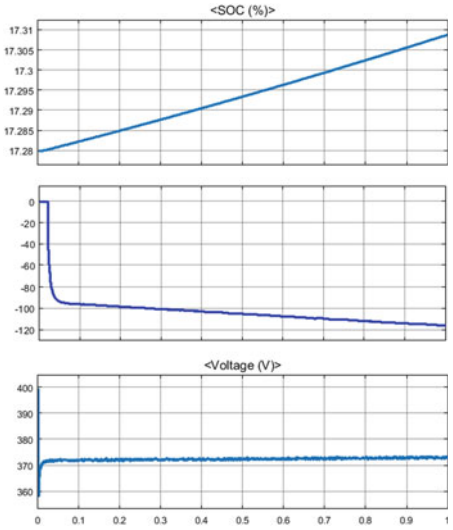

Fig. 12 Battery charging characteristics with PI controller

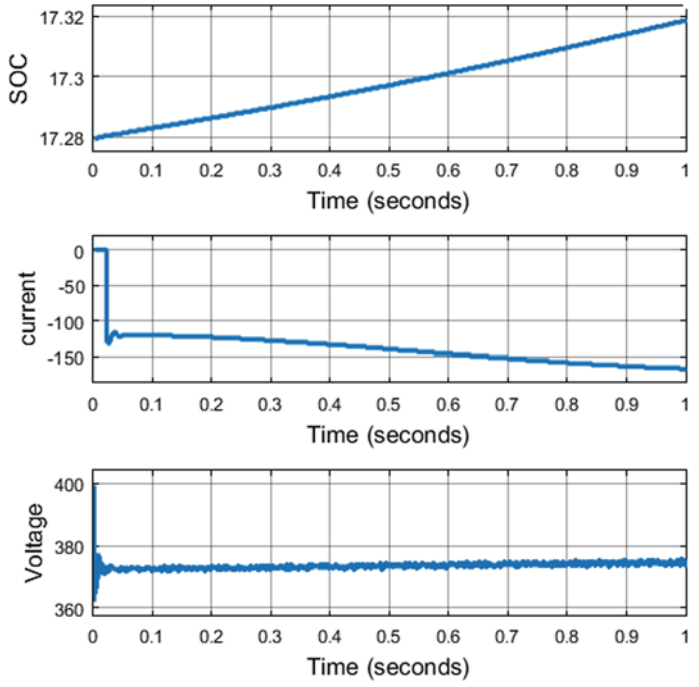

Fig. 13 Battery charging characteristics with fuzzy logic controller

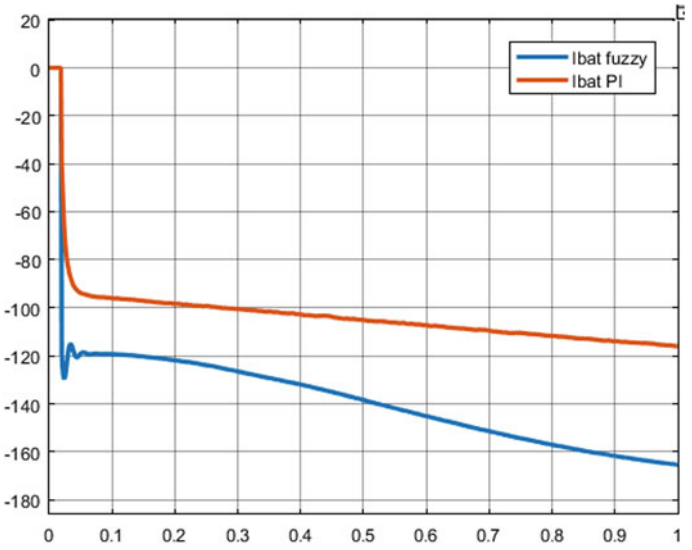

Fig. 14 Battery charging current comparison with PI and FIS controllers

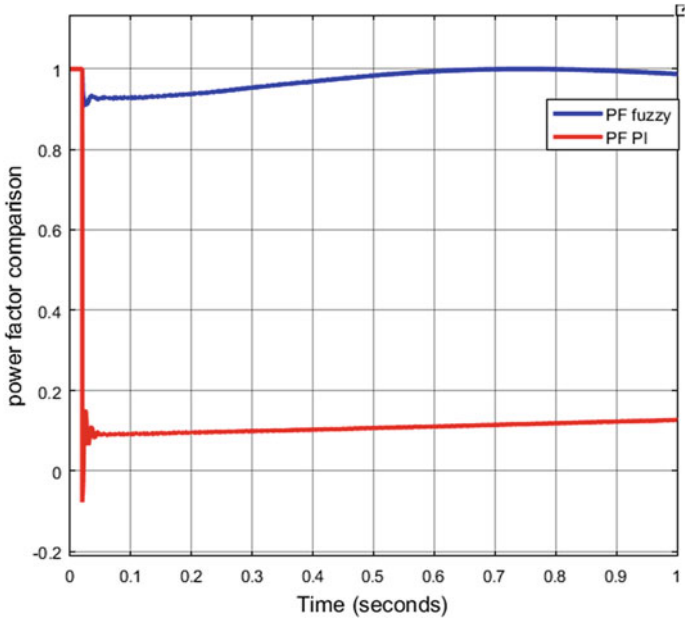

Fig. 15 Power factor comparison with PI and FIS controller

content charging the battery with three-legged buck-boost converter. The generation of better reference inductor signal by the FIS controller makes the battery to charge faster as compared to traditional PI controller. Even the power factor is maintained near to unity with fuzzy controller whereas the power factor with PI controller is low at 0.1. Hence the performance of the converter is improved with FIS controller and the battery is charged rapidly reducing the charging time.

References

1. Mohan N, Undeland T, Robbins W (2002) Power electronics: converters applications and design, 3rd edn. Wiley, NewYork
2. Singh B, Singh BN, Chandra A, Al-Hadad K, Pandey A, Kothari D (2003) Are view of single-phase improved power quality AC-DC converters. IEEE Trans Ind Electron 50(5):962–981
3. Prasad AR, Ziogas P, Manias S (1991) Anactive power factor correction technique for three-phase diode rectifiers. IEEE Trans Power Electron 6(1):83–92
4. Stihiand O, Ooi B (1998) A single-phase controlled-current PW Mrectifier. IEEE Trans Power Electron 3(4):453–459
5. Ooi BT, Dixon JW, Kulkarni AB, Nishimoto M (1998) An integrated AC drive system using a controlled-current PWM rectifier/inverter link. IEEE Trans Power Electron 3(1):64–71
6. Dixonand JW, Ooi BT (1988) Indirect current control of a unity power factor sin usoidal current boost type three-phase rectifier. IEEE Trans Ind Electron 35(4):508–515
7. Pahlevani M, Jain PK (2020) Soft-switching power electronics technology for electrical vehicle: a technology review. IEEE J Emerg Selected Top Indus Electron 1
8. Kuperman A, Levy U, Goren J, Zafransky A, Savernin A (2013) Battery charger for electic vehicle traction battery switch station. IEEE Trans Ind Electron
9. Gomez JC, Morcos MM (2003) Impact of ev battery chargers on the power quality of distribution systems. IEEE Power Delivery
10. Chan CC, Chau KT (1997) An overview of power electronics in electric vehicles. IEEE Trans Ind Electron
11. Chen G, Deng Y, Dong J, Hu Y, Jiang L, He X (2017) Integrated multiple-output synchronous buck converter for electric vehicle power supply. IEEE Trans Vehicular Technol 66(7):5752–5761
12. Ray O, Josyula A, Mishra S, Joshi A (2015) Integrated dual-output converter. IEE Trans Ind Electron 62(1):371–382
13. Vasiladiotis M, Rufer A (2015) A modular multiport power electronic transformer with integrated split battery energy storage for versatile ultrafast ev charging stations. IEEE Trans Ind Electron
14. Menzi D, Bortis D, Kolar JW (2018) Three-phase two-phase-clamped boost-buck unity power factor rectifier employing novel variable dc link voltage input current control. In: Proceedings of 2nd IEEE International power electronics and application conference and exposition (PEAC)
15. Soeiro TB, Bauer P (2019) Three-phase unidirectional quasi-single-stage delta-switch rectifier + dc-dc buck converter. In: Proceedings of 39th annual conference of the industrial electronics and society (IECON)
16. Sugeno M, Nguyen HT, Prasad NR (1999) Fuzzy modeling and control: selected works of M. Sugeno. CRC Press, Boca Raton
17. Passino KM, Yurkovich S (1998) Fuzzy control. Addison Wesley Longman, Menlo Park, CA
18. Wu H, Zhang J, Xing Y (2015) A family of multi-port buck-boost converters based on DC-link-inductors (DLIs). IEEE Trans Power Electron 30(2):735–746
19. Zhai L, Hu G, Lv M, Zhang T, Hou R (2020) Comparison of two design methods of EMI filter for high voltage power supply in DC–DC converter of electric vehicle, vol. 8, pp 66564–66577

Comparative Analysis of Controlling Methods for Doubly Fed Induction Generator Based Wind Energy System

Aftab Ahmed Ansari and Giribabu Dyanamina

1 Introduction

Despite the effects of the COVID-19 recession, the wind industry will continue to advance rapidly and can contribute significantly to future economic crises. The latest market outlook released by Global wind energy council (GWEC) market intelligence predicts that 771.3 GW of wind infrastructure will be set up in 2020 considering the impact of COVID-19, a 6% reduction from pre-COVID Q1 2020 forecasts. The forecast for offshore wind stations in 2020 has increased by 5% from pre-COVID predictions to 6.5 GW, owing to the construction rush in China. From over 348 GW planned to be constructed between 2020 and 2024, the wind farm industry is on target to accomplish record growth in the next five years, bringing global total wind capacity to nearly 1000 GW by the end of 2024, a 54% increase from 2019. In the face of COVID-19, the wind industry's continued growth, despite the fact that other economic sectors, such as coal and oil, have seen varying prices and enormous demand drops, demonstrates its role in building sustainable and reliable economies [1].

The increasing popularity of wind farms in the electrical network has been intrinsically tied to the wind farm research and development in frequent years. Wind turbine electrical systems have become increasingly crucial in the interface between the mechanical systems of wind farms and grids to which wind turbines are connected [2]. Usually, induction machines or synchronous and permanent magnet generators are chosen to transform mechanical power into electrical power. The squirrel-cage induction generator is popularly used due to its simple design, high weight and low cost compared to synchronous generators. Squirrel cage induction generator (SCIG), a device of constant speed wind turbine generators (WTG), which has variety of disadvantages, poor voltage regulation, wind intensity variations reflected in the grid and lower wind energy transformation efficiency. By using variable speed WTGs,

A. A. Ansari (✉) · G. Dyanamina
Maulana Azad National Institute of Technology, Bhopal, India

S. Kumar et al. (eds.), *Recent Advances in Power Electronics and Drives*, Lecture Notes in Electrical Engineering 852, https://doi.org/10.1007/978-981-16-9239-0_37

although most of the drawbacks may be eliminated. With recent advancements in modern power electronics, the DFIG-based wind power plant has attracted great attention.

The DFIG system is an effective system where the power electronic integration manages rotor currents so that the variable speed needed for optimum power capture during fluctuating winds is achieved. DFIG provides the advantages of speed control at lesser cost and lower power loss because the power electronic switches handle only the power of the rotor, usually less than 25% of the total output power. The use of power converters enables the circuit of rotor to provide bidirectional power flow and increases the generator's speed range. By performing MPPT relatively higher range of speed (±30%), robustness against power system disruption, and improved dynamic efficiency are advantages compared with the other turbines [3–5]. These characteristics have made DFIG WECS one of the wind industry's leading advanced technologies today with a share of the market of around 50%.

WECS interconnected to the system is equipped with various sophisticated control methodologies. Among all these techniques field oriented control (FOC) is the widely used approach in DFIG-based WTs because of its some feature like consistent and accurate steady-state performance, lesser converter frequency but it also has some disadvantages such as its dependency on system parameter variation [6] so to overcome this drawback several nonlinear control strategies, such as direct torque control/direct power control (DTC/DPC), have been introduced. The rapid advancement has placed much importance on direct-control techniques for AC machinery due to its simplicity and high dynamic performances. Takashi pioneered the use of direct torque control technique in 1985 [7]. It has outstanding performance characteristics and solid strength with regard to changes in the machine parameters. Its principle is based on controlling the machine's developed torque directly by choosing the appropriate voltage vector using torque and flux information from a table known as a switching table. Hysteresis controllers are used in traditional DTC methods for induction motors to mitigate errors. The usage of hysteresis controllers causes conventional DTC to have certain drawback which includes varying/changing switching frequency, troubles during starting and medium speed operations, unnecessarily high torque ripple. Much advancement in direct-control strategies such as DTC with space-vector modulation was introduced to counteract these disadvantages (DTC-SVM) [8]. Furthermore, the use of smart control methods has been implemented to all places in various industries; the DFIG control system has successfully used the artificial neural system, the sliding-mode control (SMC), the fuzzy logic control (FLC).

In the same way as DTC, another control methodology named direct power control (DPC) is formulated relying on the relatively similar principles as DTC. This approach does not demand any complicated transformations and computation complexity in comparison to the vector control approach. The real and reactive power is controlled by the selection of the most suitable voltage vectors from the switching table directly and without modulation. In this way DPC has a lower dynamic response and sensitivity to system parameters than traditional vector control. Ripple in high power in steady-state operation is the primary disadvantage of the DPC mechanism

[9]. All three of these strategies have distinct characteristics and are widely used. These control methods are reviewed in this article, and their performance at different operating conditions is analyzed and compared using simulation.

This paper is divided into the following sections: Sect. 2 of this paper discusses DFIG's mathematical modeling, whereas Sect. 3 of this paper reviews DFIG's operational control system strategies. Section 4 summarizes the results obtained. Section 5 compares the various operational techniques and finally, the conclusion is Sect. 6.

2 DFIG Mathematical Modeling

The energy transfer is achieved by implementing 2 subsystems: a mechanical power extraction device known as a turbine and an electrical power conversion machine known as a generator. DFIG is an example of a machine with a wound rotor. In the dq reference frame, the space-vector electrical equations for DFIG are written as [10]:

$$V_{sd} = R_s I_{sd} + \frac{d\phi_{sd}}{dt} - \omega_s \phi_{sq} \tag{1}$$

$$V_{sq} = R_s I_{sq} + \frac{d\phi_{sq}}{dt} + \omega_s \phi_{sd} \tag{2}$$

$$V_{rd} = R_r I_{rd} + \frac{d\phi_{rd}}{dt} - \omega_{re} \phi_{rq} \tag{3}$$

$$V_{rq} = R_r I_{rq} + \frac{d\phi_{rq}}{dt} + \omega_{re} \phi_{rd} \tag{4}$$

where,

I_{rd} is the d-axis orientation current of the rotor

I_{rq} is the q-axis orientation current of the rotor

I_{sd} is the d-axis orientation current of the stator

I_{sq} is the q-axis orientation current of the stator

ω_s is the synchronous electrical speed

ω_{re} is the electrical speed of rotor

R_s and R_r are the static and rotating motor windings resistances.

The stator and rotor flux are found to be:

$$\phi_{sd} = L_s I_{sd} + M I_{rd} \tag{5}$$

$$\phi_{sq} = L_s I_{sq} + M I_{rq} \tag{6}$$

$$\phi_{rd} = L_r I_{rd} + M I_{sd} \tag{7}$$

$$\phi_{rq} = L_r I_{rd} + M I_{sd} \tag{8}$$

where the stator flux is ϕ_{sd} and ϕ_{sq} toward the direction of the d and q axes, respectively.

Rotor flux ϕ_{rd}, ϕ_{rq} is direction of the axis d and q.

L_s and L_r are, respectively, leakage inductances.

M is the mutual inductance.

The real and reactive powers of the stator are described as:

$$P_s = V_{sd} I_{sd} + V_{sq} I_{sq} \tag{9}$$

$$Q_s = V_{sq} I_{sd} + V_{sd} I_{sq} \tag{10}$$

For DFIG, the torque equation can be represented as:

$$T_{em} = \frac{pM}{Ls}\left(I_{rd}\phi_{sq} - I_{rq}\phi_{sd}\right) \tag{11}$$

This DFIG electrical model is a widely known model for designing and determining the control objectives of a DFIG wind energy conversion system.

3 DFIG Control Methods

Wind power system research primarily focuses on issues such as cost reduction, improved power quality and simpler system operation to address the unpredictable nature of wind flow [11]. In WECS, control really plays a crucial role in addressing a constantly changing as well as nonlinear characteristic of wind. Different techniques of controlling to resolve this problem have been reviewed in the literature.

3.1 Field-Oriented Control (FOC)

DFIG control systems usually use field-oriented control (FOC) because it controls the speed of the motor quite effectively and also it's lower building cost. The approach uses independent torque and flux control. In general, there is current-oriented control

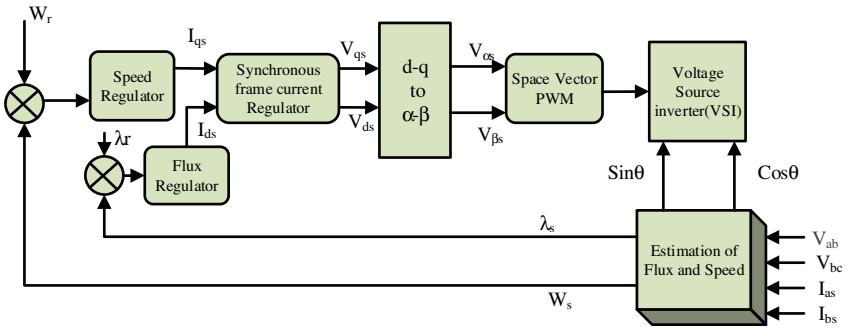

Fig. 1 Field-oriented control

and stator-flux-oriented control. For maximum wind power extraction, the stator-flux-oriented control is extensively used in the DFIG by regulating the power generated by DFIG and it uses the q-axis component of current to control the real power and the reactive power control is offered by the d-axis component of current. A schematic field-oriented control block diagram is shown in Fig. 1. The current of stator in the FOC method is controlled by altering it into a rotary dq reference framework. The real and reactive powers are controlled by RSC, while the DC-link potential difference is controlled by GSC [12].

The sensorless FOC is addressed in [13] on the basis of a model reference observer and its performance will be compared to the open-loop estimator strategy. It is suggested in [14] that a WECS based on DFIG with a DC-link battery energy storage system maintains constant grid power with a stator-flux-oriented control technique. The vector field control allows the decomposition of real and reactive powers on the side of stator. As a consequence, it is possible to gain high-performance control of power. A simulation result for RST and PI controller integrated with FOC for DFIG-based WT is presented in [15] and it also describes two types of control based on the calculation of the angle of flux space vector. FOC can be applied as a direct-field oriented control (DFOC) where the machine's flux model is employed and Indirect-field oriented control (IFOC), which uses the calculated slip frequency and rotor flux to determine the angle of the flux vector. A comparative analysis between the DFOC regulation and the IFOC regulation of the DFIG incorporated in the wind farm is illustrated in [16]. Sensorless positioning FOC control of DFIG requires the use of at least four to six current sensors [17]. Proposes a new rotor positioning and current estimation approach that allow the controlling operation of DFIG only with three current sensors. Eliminating a single current sensor increases hardware reliability by reducing the number of hardware elements that must be used, thus minimizing complexity of the system and cost of the system.

SMC (Sliding-Mode Control) has become extremely popular recently. The machine states are transmitted to the sliding board. Once achieved, SMC maintains the system state in the near vicinity [18]. Numerous papers explored FOC utilizing SMC for DFIG, such as [19], which presents a DFIG-based SMC for wind farm.

In [20], sliding-mode control of second order is employed for the tracking of stator reactive power and electro-mechanical torque desired value is examined. In [21], a Sliding mode block is used to monitor and control the RSC and GSC for a DFIG. In traditional sliding-mode control, the major downside is that the system is responsive to parametric variation; moreover, Chattering can disrupt the performance of the controlled system and create a dangerous high-frequency vibration [22]. However, to actually achieve increased performance of FOC, an accurate understanding of DFIG parameters is necessary; these parameters cannot in practice be exactly known [23].

3.2 Direct Torque Control (DTC)

A further potential alternative to the FOC control strategy is DTC. A schematic direct torque control block diagram is shown in Fig. 2. It uses a lookup table and hysteresis control to regulate the stator flux and electro-magnetic torque. This is basically a dynamic current limiting method. It restricts to some degree the use of crowbar protection during voltage dips [24]. The plural current loops are omitted in the conventional DTC (CDTC) method, and the control pulses are selected straightforwardly via lookup table to control the torque and rotor flux combination. Limitations of the CDTC include high torque pulsation, variable frequency of switching, torque, and flux control problems at low speeds. These adverse effects are reduced in many DTC research papers by the use of the SVM scheme [25, 26] however,

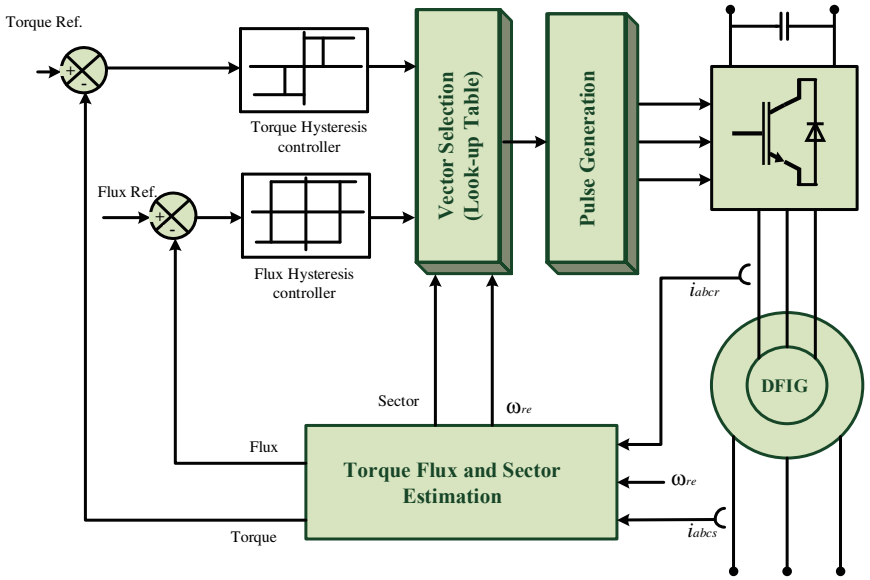

Fig. 2 Direct Torque control

control robustness is scarified. In general, the DTC scheme is preferred because of lower calculation requirements and improving system dynamics. The DTC method implemented for the dc voltage control in [27] is effective in reducing harmonics and is easy to execute. An improved DTC procedure for a wind system DFIG that enhances both the rotor flux position's division accuracy and the number of basic voltage vectors is presented in [28].

In [29] a new robust DTC technique is presented depending on the sliding second-order mode and on the modulation of space vectors of a doubly fed induction generator installed WT system. The DTC technique suggested would reduce the flux, torque, and current ripples depending on the second-order SMC. It also decreases the frequency fluctuations in the control of the induction-machine. To control these surfaces, two separate sliders are used, for example, flux and torque sliding surfaces. Rotor flux control directly does not necessarily ensure reactive power control, as the relationship between them is uncertain. Therefore, a random selection of a flux reference does not, therefore, guarantee good power factor control. An updated DTC method is therefore suggested in [28], to simultaneously handle the stator power factor when regulating the generator's electro-magnetic torque and rotor-flux. The idea presented in this article presented a plan to control the rotor field flux of a wind power converter. The controls are supported by a rotor vector for controlling the rotor flux as well as electro-magnetic torque whereas the power factor at the terminals of stator is kept under control. Direct rotor flux control does not inherently guarantee control of reactive power as the correlation between the reactive power is not evident. The random choice of flux reference, therefore, does not ensure a reasonable control of the power factor. This fuzzy direct torque control scheme is investigated in [30] for a DFIG-based wind turbine. It has become more popular recently because of the high performance it provides over traditional FOC, especially regarding electric machines. In [31] a novel fuzzy DTC system of DFIG was developed to improve DTC performance and high torque characteristics can be attained. This model uses the concept of the fuzzy logic control system and improves the system performance by reducing the ripples of electro-magnetic torque and optimizing the total harmonic distortion (THD) in the electro-magnetic current.

3.3 Direct Power Control (DPC)

DTC performance gets poorer as speed decreases and also at the time of start-up. Direct power control (DPC) was considered as a solution to avoid this problem with the DTC. The background of the DPC is drawn mainly from the DTC. Figure 3 illustrates the DPC block diagram. Direct Power Control is a major beneficial link in regulating the DC-link voltage and adjusting the system reactive power. In DPC, we also often take advantage of the geometrical connection between rotor and stator fluxes and the fact that we can regulate the flux of rotor through the RSC in DPC. In DPC rather than controlling torque and rotor flux directly, we control the impact these magnitudes have on stator's real and reactive power.

The issues related to wind turbines based on DFIG were addressed in [32]. The electro-magnetic torque oscillations could be removed under unbalanced conditions using a simplistic DPC technique, followed with a real and reactive power reference approach, which avoid mechanical stress in wind turbines and exchanges sinusoidal currents with the grid.

Conventional DPC includes methods of switching frequencies of a component, by using an optimal table for the switching transitions. This is an easy and effective strategy which ensures good outcome in applying. But there are several problems with the conventional DPC, which make the wind power generation system based on DFIG hard to use. For instance, the voltages generated by the rotor through a discrete and fixed switching table could not reach an accurate and reactive power control during maximum wind energy extraction. In addition, the vibration of the electro-magnetic torque due to the conventional DPC is much larger than that in the vector control at the same frequency of sampling. Furthermore, the traditional DPC moreover exacerbates the AC filter structure because the switching frequency is variable in DPC. Many redesigned or improved DPC methods have been observed in [33, 34] in order to overcome these limitations. In [39] article addressed three types of DPC strategies with theoretical study and a comprehensive simulation investigation for wind power generation systems based DFIG. A comparative analysis is provided in [36] between the traditional DPC based on the standard position of flux of rotor and the DPC based on the stator flux position for the wind turbine oriented DFIG. Specifically, in [37] the author presented a novel DPC for DFIG with MPPT strategy for wind farm application which is based on hybrid artificial intelligence with fixed switching frequency. A fractional-order sliding-mode control (FOSMC) based DPC Scheme for DFIG-based WECS is proposed in [38]. In order to construct sliding surfaces, the principle of Caputo derivatives is implemented and used. Additionally, a comparative analysis is performed using simulations of FOSMC-based DPC and SMC-based DPC in four different operational scenarios a steady-state environment, variable wind speed, and variable grid-voltage condition. [40] presents a robust and simple enhanced new voltage modulated-DPC control scheme for the DFIG system's BTB converter. The proposed model is a simple feed forward and feedback arrangement that eliminates the use of PLL or Park transformations, thereby reducing computational stress and simplifying the architecture and global exponential stabilization is ensured by the suggested method.

4 Results and Discussion

This paper is a comparative analysis of three of the most successful DFIG control methodologies, namely: field-oriented control (FOC), direct torque control (DTC), and direct power control (DPC). The simulation results are analyzed and descriptive and analytical output comparisons are brought out. In Table 2, the parameters used are mentioned. The DFIG performance for wind speed rises to 12 m/s from 10 m/s in 1.5 s and the current waveform of the stator for FOC, DTC and DPC is shown

in Fig. 4. The stator current waveform has more ripples in the field-oriented control compared to direct-control techniques.

The WECS performance for different parameters such as speed, torque, active and reactive power during starting transient is presented in Fig. 5. The speed of rotor for field-oriented control at the start of the generator has a higher peak overshoot. This high peak overshoot can be minimized by using the DPC controller instead of the FOC controller. The rotor speed varies in all situations depending on the wind velocity, but in the case of FOC the settling requires a long time. Introducing DTC in DFIG-based WECS also tends to improve torque ripples by improving their current waveform.

The behavior of WECS in three control strategies in the course of wind speed changes by a step as shown in Fig. 6. Compared to the two other approaches, the performance of the direct power control is better. The torque and speed of rotor are

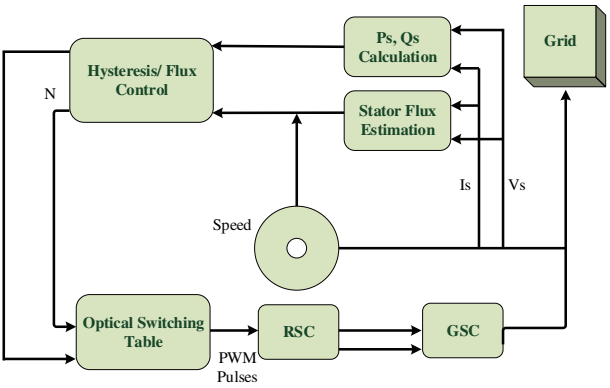

Fig. 3 Direct power control

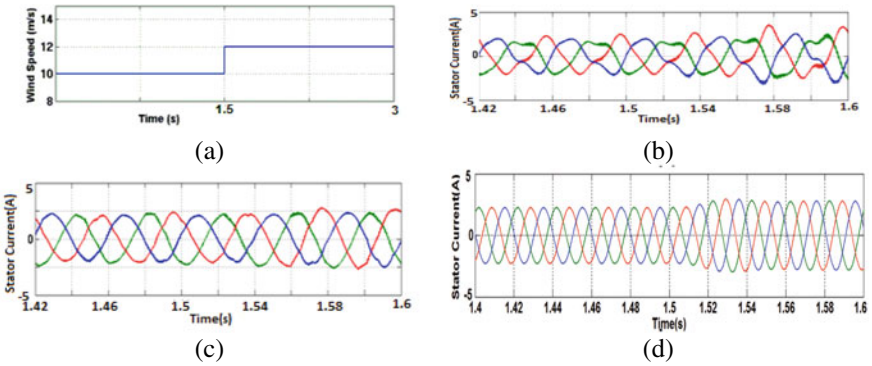

Fig. 4 **a** Variation of Wind Speed, Waveform of the stator current for **b** FOC control of DFIG **c** DTC control of DFIG **d** DPC control of DFIG

adjusted and can be easily settled down for the DPC controller during the gradual shift in wind velocity.

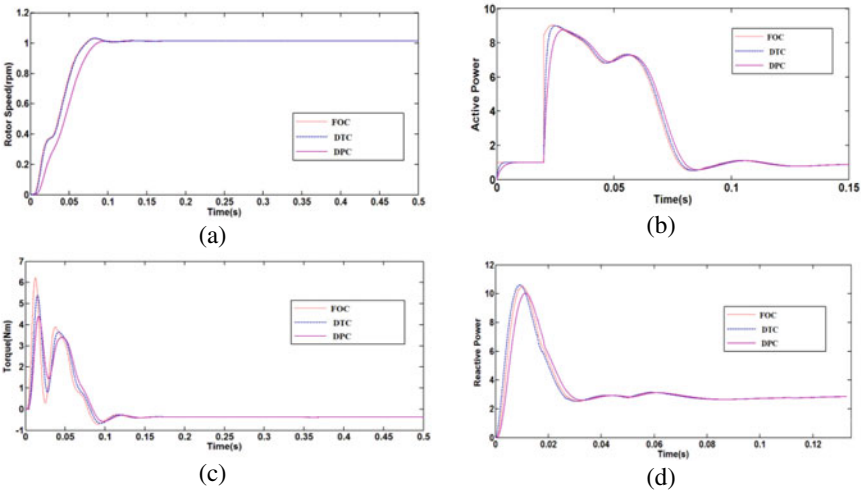

Fig. 5 DFIG's transient performance for three control methods **a** speed, **b** active power, **c** Torque and **d** reactive power

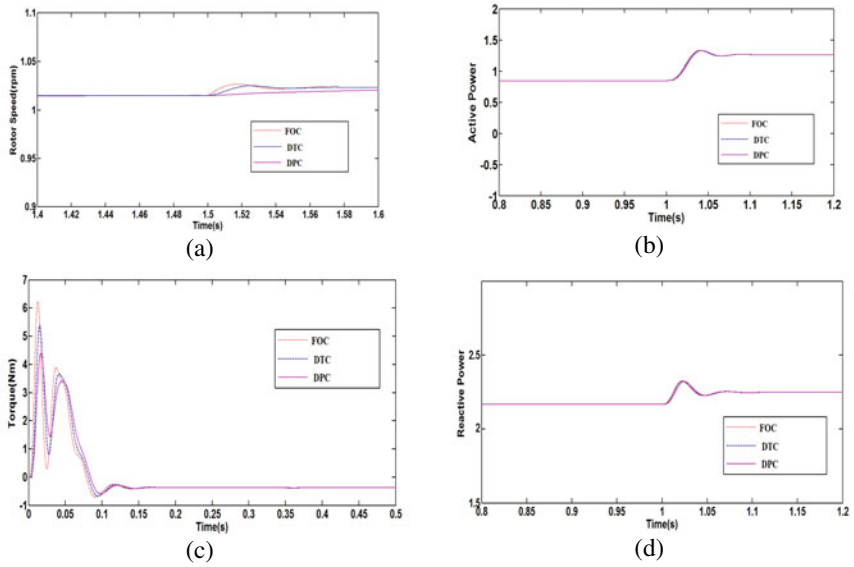

Fig. 6 DFIG performance for three control methods **a** speed **b** active power, **c** torque and **d** reactive power throughout step change in wind velocity at 1.5 s

5 Comparison of Operational Control Strategies for DFIG Based WECS

In last sections, we summarize the comprehensive review of the control strategies and show the simulation results of the reviewed control strategies under transient conditions and at the time of step change in wind velocity. Now, we present a set of descriptive and analytical comparisons that show the advantages and disadvantages of the control method in the DFIG-based WECS application. FOC is indeed the most complicated control strategy due to its advanced applications of reference frame transformations and model-based structure. The DPC, on the other side, emerges out as the least complicated control mechanism with full machine-model independence. In comparison to the FOC requirements, the sampling times related to direct must be shorter and the sensor-bandwidth must be greater: this empowers direct strategies to focus particularly on controlled quantities in order to keep them inside the specified hysteresis bands.

The FOC execution incurs lower instrumentation constraints, although structurally complex. With regard to computational tasks within MATLAB Simulations, FOC seems to be very resource-consuming due to the multiple reference-transformations and model-based nature whereas at the other side the direct techniques involve simplified data handling, mostly using hysteresis comparators and lookup tables so overall implementation complexity of FOC is more. The dynamic reaction of FOC is overcome by both direct-control technologies, although it is fast and performing. A number of references in relation to the operation under FOC of the DFIG [37, 38] concludes that the variability of the reference-currents must be limited in an aim to maintain the control system's stability. The sampling times of up to 200 μs seemed to be possible for VC method before any significant negative impact could be reported on the control. As regards direct methods, the quality or strength of current waveforms at control time exceeding 50 μs was detrimental as the controlled signals were likely to leave the hysteresis belts. Minimizing sampling time doesn't really guarantee better direct-control efficiency: if the sensor-bandwidth is exceeded and the observed signal is not exact, reducing sampling time has negative effects on direct-control methods. We defined robustness as a measurement of the control technique's ability to achieve success in the case of structure disturbances and unsafe conditions along with modeling errors, parameter variations, noise measurement and so on. Section 4 simulation results show that FOC and DPC are fairly robust control systems with different capabilities: Under parameter deviation FOC becomes weaker and DPC is not very successful under noise measurement. The MPPT wind turbine operation mode calls for mechanical parameters to be measured or estimated. Only DPC is insufficient for MPPT, as stated in the control designs for the control methods under review. However, by introducing a position-encoder to DPC control system, this weakness can be quickly overcome. Table 1. is the final comparable overview depending on different results mentioned in this paper.

Table 1 Comparison of Operational Control Strategies for DFIG Based WECS

Performance criteria	FOC	DTC	DPC
Computational complexity	The most complicated control technique is FOC	DTC is the moderate complex control technique	DPC steps out as simplest control method
Machine model dependency	FOC refers to a technique that is more dependent on system parameters	DTC is the strategy that marginally depend on machine parameter	DPC is parameter-independent
Sample time constraint	Low	High	High
Transitory response	Low transitory performance	Medium transitory performance	High transitory performance
Settling time	Medium	Low	Low
Harmonic content	Low	Medium	Medium
Instrumentation constraint	FOC Instrument constraint is Moderate	High	High
Overall implementation complexity	FOC is in fact the most difficult method to implement	DTC is moderately complex strategy to implement	DPC needs only a few signals to be sensed so less complex strategy to implement
Robustness	High	Medium	High
MPPT stability	High	High	Low

Table 2 DFIG ratings and parameters

Variables	Values implemented
Power	$2 * 10^6$ (VA)
Nominal voltage (L-L)	690 (V)
Frequency (Grid)	50 (cycle/second)
Resistance of stator	0.03513 (pu)
Inductance of stator	0.04586 (pu)
Resistance of rotor	0.03488 (pu)
Inductance of rotor	0.04586 (pu)
Mutual inductance	1.352 (pu)
Pairs of pole	2
Factor of friction	0 (pu)

6 Conclusion

All three comparative control methods have demonstrated remarkable performance in both the transient and the step change of wind. The simulations and review yield valuable insights into the benefits and drawbacks of each control scheme. FOC seems

to be the most complicated control strategy due to its lengthy use of frame transformations of reference and model-based structure. On the other hand, DPC manages to stand out as the least complicated control mechanism with full machine method independence. Under parameter deviation VC becomes weaker and DPC is not very successful under noise measurement. The FOC execution incurs lower instrumentation constraints, although structurally complex. With regard to computational tasks within MATLAB Simulations, FOC seems to be very resource-consuming due to the multiple reference-transformations and model-based nature. The direct techniques, on the other side, require simplified data handling, mostly using hysteresis comparators and lookup tables so overall implementation complexity of FOC is more. The simulation results and comparison show that the DPC method, as outlined in this work, performed better than the other two strategies.

References

1. Global Wind Energy Council, Global Wind Energy Council (2021) [Online]. Available: https://gwec.net/. Accessed 29 Jan 2021
2. Yaramasu V, Wu B, Sen PC, Kouro S, Narimani M (2015) High-power wind energy conversion systems: State-of-the-art and emerging technologies. In: Proceedings of the IEEE, vol 103, no. 5, pp 740–788
3. Bhowmik S, Spee R, Enslin JHR (1999) Performance optimization for doubly fed wind power generation systems. IEEE Trans Indus Appl 35(4):949–958
4. Ekanayake J, Jenkins N (2004) Comparison of the response of doubly fed and fixed-speed induction generator wind turbines to changes in network frequency. IEEE Trans Energy Conver 19(4):800–802
5. Flannery PS, Venkataramanan G (2008) A fault tolerant doubly fed induction generator wind turbine using a parallel grid side rectifier and series grid side converter. IEEE Trans Power Electron 23(3):1126–1135
6. Aydin E, Polat A, Ergene LT (2016) Vector control of DFIG in wind power applications. In: 2016 IEEE international conference on renewable energy research and applications (ICRERA), Birmingham, UK, pp 478–483. https://doi.org/10.1109/ICRERA.2016.7884383
7. Takahashi, Noguchi T (1986) A new quick-response and high efficiency control strategy of an induction motor. IEEE Trans Ind Appl IA 22:820–827
8. Lai Y, Chen J (2001) A new approach to direct torque control of induction motor drives for constant inverter switching frequency and torque ripple reduction. IEEE Trans Energy Convers 16:220–227
9. Nian H, Song Y (2014) Direct power control of doubly fed induction generator under distorted grid voltage. IEEE Trans Power Electron 29(2):894–905. https://doi.org/10.1109/TPEL.2013.2258943
10. Golnary F, Moradi H (2019) Dynamic modelling and design of various robust sliding mode controls for the wind turbine with estimation of wind speed. Appl Math Model 65:566–585
11. Jha D (2017) A comprehensive review on wind energy systems for electric power generation: Current situation and improved technologies to realize future development. Int J Renew Energy Res (IJRER) 7(4):1786–1805
12. Karad S, Thakur R (2019) Recent trends of control strategies for doubly fed induction generator based wind turbine systems: a comparative review. Arch Comput Methods Eng 28(1):15–29
13. Esmaeeli MR, Kianinezhad R, Razzaz M (2012) Field oriented control of DFIG in wind energy conversion systems. J Basic Appl Sci Res 2(11):11486–11493

14. Rahul Charles CM, Vinod V, Jacob A (2015) Field oriented control of doubly fed induction generator in wind power system. In: IEEE international conference on computational intelligence and computing research (ICCIC), Madurai, pp 1–5. https://doi.org/10.1109/ICCIC.2015.7435760
15. Poitiers F, Bouaouiche T, Machmoum M (2009) Advanced control of a doubly-fed induction generator for wind energy conversion. Electric Power Syst Res 79(7):1085–1096. https://doi.org/10.1016/j.epsr.2009.01.007
16. Ihedrane Y, El Bekkali C, Bossoufi B (2017) Direct and indirect field oriented control of DFIG-generators for wind turbines variable-speed. In: 14th international multi-conference on systems, signals & devices (SSD), Marrakech, pp 27–32. https://doi.org/10.1109/SSD.2017.8166915
17. Prasad RM, Mulla MA (2019) A novel position-sensorless algorithm for field-oriented control of DFIG with reduced current sensors. IEEE Trans Sustain Energy 10(3):1098–1108. https://doi.org/10.1109/TSTE.2018.2860993
18. Tanvir AA, Merabet A, Beguenane R (2015) Real-time control of active and reactive power for doubly fed induction generator (DFIG)-based wind energy conversion system. Energies 8:10389–10408
19. Barambones O, Cortajarena JA, Alkorta P, Gonzalez de Durana JM (2014) Real-time sliding mode control for a wind energy system based on a doubly fed induction generator. Energies 7:6412–6433
20. Beltran B, Benbouzid M, Tarek AA (2012) Second-order sliding mode control of a doubly fed induction generator driven wind turbine. IEEE Trans Energy Convers 27:261–269
21. Ruiz-Cruz R, Loukianov AG, Sanchez EN (2013) Real-time sliding mode control for a doubly fed induction generator. In: Decision and control (CDC) IEEE 52nd annual conference on 2013, pp 6786–679
22. Patnaik RK, Dash PK, Mahapatra K (2016) Adaptive terminal sliding mode power control of DFIG based wind energy conversion system for stability enhancement. Int Trans Electr Energy Syst 26:750–782
23. Utkin V, Guldner J, Shi J (2009) Sliding mode control in electro-mechanical systems, 2nd edn. CRC Press. https://doi.org/10.1201/9781420065619
24. Naveen G, Sarvesh PKS, Krishna BR (2013) DTC control strategy for doubly fed induction machine. Int J Eng Adv Technol 3(1)
25. Chen SZ, Cheung NC, Wong KC, Wu J (2010) Integral sliding-mode direct torque control of doubly-fed induction generators under unbalanced grid voltage. IEEE T Energy Conver 25:356–368
26. Zhu X, Liu S, Wang Y (2014) Second-order sliding-mode control of DFIG-based wind turbines. In: IEEE 2014 3rd renewable power generation conference, Naples, Italy. IEEE, New York, NY, USA, pp 1–6
27. Gundavarapu A, Misra H, Jain AK (2017) Direct torque control scheme for DC voltage regulation of the standalone DFIG-DC system. IEEE Trans Indus Electron 64(5):3502–3512. https://doi.org/10.1109/TIE.2016.2644623
28. Li Y et al (2016) An improved DTC controller for DFIG-based wind generation system. In: IEEE 8th international power electronics and motion control conference (IPEMC-ECCE Asia), Hefei, pp 1423–1426. https://doi.org/10.1109/IPEMC.2016.7512499
29. Boudjema Z et al (2017) A novel direct torque control using second order continuous sliding mode of a doubly fed induction generator for a wind energy conversion system. Turk J Electr Eng Comput Sci 25:965–975
30. Ayrir W, Ourahou M, Hassouni BE, Haddi A (2020) Direct torque control improvement of a variable speed DFIG based on a fuzzy inference system. Math Comput Simul 167:308–324
31. El Ouanjli N, Motahhir S, Derouich A, Abdelaziz E, Ali C, Mohammed T (2019) Improved DTC strategy of doubly fed induction motor using fuzzy logic controller. 5:271–279. https://doi.org/10.1016/j.egyr.2019.02.001
32. Abad G, Rodríguez MÁ, Iwanski G, Poza J (2010) Direct power control of doubly-fed-induction-generator-based wind turbines under unbalanced grid voltage. IEEE Trans Power Electron 25(2):442–452. https://doi.org/10.1109/TPEL.2009.2027438

33. Escobar G, Stankovic AM, Carraso JM et al (2003) Analysis and design of direct power control (DPC) for a three phase synchronous rectifier via output regulation subspaces. IEEE Trans Power Electron 18(3):8232830
34. Xin W, Yue CD, Yu ZC (2005) A torque ripple minimization scheme in direct torque control of induction motors. Tech Autom Appl 24(8):72–74
35. Xiong L, Wang J, Mi X, Khan MW (2018) Fractional order sliding mode based direct power control of grid-connected DFIG. IEEE Trans Power Syst 33(3):3087–3096. https://doi.org/10.1109/TPWRS.2017.2761815
36. Zhi D, Xu L (2007) Direct power control of DFIG with constant switching frequency and improved transient performance. IEEE Trans Energy Convers 22(1):110–118
37. Fayssal A, Chaiba A (2016) A novel direct power control for grid-connected doubly fed induction generator based on hybrid artificial intelligent control with space vector modulation. Revue Roumaine des Sciences Techniques Serie Electrotechnique et Energetique 61:263–268
38. Petersson A, Thiringer T, Harnefors L, Petru T (2005) Modeling and experimental verification of grid interaction of a DFIG wind turbine. IEEE Trans Energy Convers 20(4):878–886. https://doi.org/10.1109/TEC.2005.853750
39. Heller M, Schumacher W (1997) Stability analysis of doubly-fed induction machines in stator flux reference frame. In: Proceedings of the 7th european conference on power electronics and applications (EPE'97), vol 2, pp 707–710
40. Gao S, Zhao H, Gui Y, Zhou D, Blaabjerg F (2021) An improved direct power control for doubly fed induction generator. IEEE Trans Power Electron 36(4):4672–4685. https://doi.org/10.1109/TPEL.2020.3024620

Adaptive Pitch Control of Wind Turbine Generator to Counter Transient Contingencies in a Multi Machine System

Hailiya Ahsan, Abdul Waheed Kumar, and M. D. Mufti

1 Introduction

With every passing year, as wind power gains significant impetus, it is considered as a mainstream solution to all major energy crisis problems. A number of factors collectively come to its rescue in disguise, viz., hike in fuel costs, fuel crisis, environmental degradation and the urge towards a green Earth. The increasing wind power capacity, however, burdens the existing power systems with an instability threat. In reality, the very intermittent nature of wind is primarily the inherent cause of facilitating staggering power outputs [1]. A highly variable wind speed results in an uneven consumption of reactive VAR's by the reactive power compensation devices like capacitor banks. This digresses the power factor from a unity power factor operating template [2]. It is due to this reason, that the wind turbine generator (WTG) generates fluctuating voltage at its point of common coupling with the grid and thus hampers power quality [3].

Pitch controlled wind turbines are technically encouraged to stabilize the WTG's power outputs, when the wind speed faces excursions [4]. Inefficient pitch control technique determining the turbine blade position can lead to consequential stress on the blades, leading to blade wear and tear and reduced life [3, 5]. In [6], the authors have presented a pitch neuro-control architecture based on neuro-estimators of the effective wind to control the pitch angle. The current wind and the forecasting wind have been included in the controller. A pitch angle control scheme for rapid power control of a permanent magnet synchronous generator based wind power plant has been shown in [7]. The effectiveness of variable pitch sliding mode controller based on disturbance observer to improve dynamic performance and robustness to wind disturbances has been demonstrated in [8]. In [9], the authors have validated

H. Ahsan (✉) · A. W. Kumar · M. D. Mufti
Department of Electrical Engineering, National Institute of Technology, Hazratbal Srinagar, J&K 190006, India
e-mail: waheed_02phd17@nitsri.ac.in

S. Kumar et al. (eds.), *Recent Advances in Power Electronics and Drives*, Lecture Notes in Electrical Engineering 852, https://doi.org/10.1007/978-981-16-9239-0_38

the higher performance nature of Linear Active Disturbance Rejection Control over conventional Proportional-Derivative (PD) control method to improve wind turbine dynamics in a varying wind profile.

In this paper, a novel adaptive pitch control scheme of WTG's is presented with the aim of smoothing the power output as well as the terminal voltage of the machine. The said adaptive control technique is a self tuning scheme, which targets the reduction/mitigation of the driving point variable to zero, which in this case happens to be the network frequency. A trained recursive least squares algorithm is adopted for obtaining the model parameters, at each sampling instant. An optimized control signal is issued by the APC strategy by minimizing a quadratic index serving as the control law [10]. This control signal reflects the blade pitch angle and effectively reduces the driving point frequency error to zero.

The main highlights of this paper are:

1) A self tuned adaptive control scheme determines the pitch angle of a WTG, thereby imparting comprehensive stability to a multi machine system.
2) Detailed mathematical modeling of the WTG is delineated .
3) Modified Newton Raphson load flow technique is outlined in depth.
4) Stability evaluation performed in light of turbulent contingencies (wind as well as 3-ϕ faults) [11, 12].

2 Wind Turbine Generator Fed Multi Machine System

The arrested mechanical power by a variable speed wind turbine can be put forth as [13],

$$P_{wturb} = 0.5\rho\pi R^2 {v_w}^3 C_p(\lambda, \beta) \tag{1}$$

where, P_{wturb} is the arrested mechanical power from the wind, ρ is the density of air in kgm^{-3}, R is the radius of the turbine blade in m, v_w is the speed of the wind in ms^{-1}; and C_p is the function of the tip speed ratio (λ) and the blade pitch angle (β), also known as the power coefficient [14].

The wind turbine power coefficient is mathematically put as (See Fig. 1),

$$C_p = \frac{1}{2}(\lambda - 0.022\beta^2 - 5.6)e^{-0.17\lambda} \tag{2}$$

The lumped one mass model torque equation can be defined as [15],

$$\dot{\omega} = \frac{1}{2H_{wtg}}(P_{wturb}/\omega_B - T_e) \tag{3}$$

In this paper, a squirrel cage induction generator is adopted as the wind turbine generator due to its cost effectiveness and rugged construction [16]. The wind driven induction machine's electrical torque modelling can be done as,

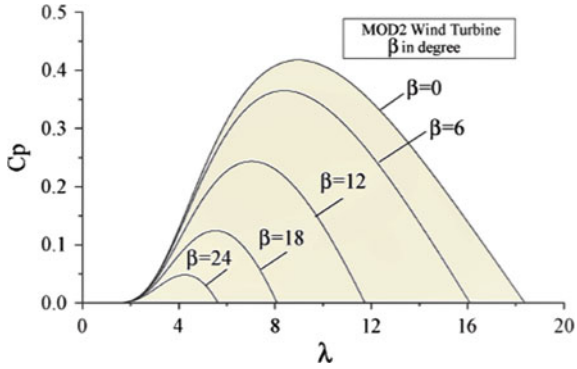

Fig. 1 Relation between $C_p - \lambda$ and varying pitch angles (β)

Table 1 Induction generator data

Parameters	Symbol	Values
Rotor time constant, sec	T_o	0.8871
Stator resistance, p.u.	r_{swtg}	0.0017
Turbine-generator inertia constant, p.u.	H_{wtg}	0.42
Induction machine reactance, p.u.	X	5.0167
Transient reactance, p.u.	X'	0.0333
X-X', p.u.	b_0	4.9834

$$T_{e_{wtg}} = E_{d_{wtg}} I_{d_{wtg}} + E_{q_{wtg}} I_{q_{wtg}} \tag{4}$$

The induction machine has been modelled as an induction motor in the system, running in generating mode, claiming negative slip as well as torque in operation. All induction generator details are given in Table 1 [17].

The stator algebraic equations pertaining to the induction generator at *wtg bus* are:

$$\begin{bmatrix} V_{d_{wtg}} \\ V_{q_{wtg}} \end{bmatrix} = \begin{bmatrix} E_{d_{wtg}} \\ E_{q_{wtg}} \end{bmatrix} + \begin{bmatrix} r_{s_{wtg}} & -X'_{wtg} \\ X'_{wtg} & r_{s_{wtg}} \end{bmatrix} \begin{bmatrix} I_{d_{wtg}} \\ I_{q_{wtg}} \end{bmatrix} \tag{5}$$

The differential set of equations describing the rotor winding dynamics can be put as,

$$\begin{aligned} \begin{bmatrix} \dot{E}_{d_{wtg}} \\ \dot{E}_{q_{wtg}} \end{bmatrix} = \frac{1}{T_o} \left\{ \begin{bmatrix} -E_{d_{wtg}} \\ -E_{q_{wtg}} \end{bmatrix} - \begin{bmatrix} 0 & b_0 \\ b_0 & 0 \end{bmatrix} \begin{bmatrix} I_{d_{wtg}} \\ I_{q_{wtg}} \end{bmatrix} \right\} \\ + \begin{bmatrix} s E_{q_{wtg}} \\ -s E_{d_{wtg}} \end{bmatrix} \omega_o \end{aligned} \tag{6}$$

Steady state analysis using a slightly modified *Newton Raphson load flow* is performed on the system which yields the pre-fault (or pre-disturbance) state values

Table 2 Steady state analysis: modified load flow results

Bus no.	Voltage magnitude	Angle degrees	Generation		Load	
			MW	MVAR	MW	MVAR
1	1.040	0.000	0.000	0.000	21.66	41.60
2	1.025	10.791	0.000	0.000	163.0	9.800
3	1.025	6.157	0.000	0.000	85.00	−7.800
4	1.017	−0.676	0.000	0.000	50.00	−21.50
5	0.989	−2.495	125.0	50.00	0.000	0.000
6	1.006	−2.190	90.00	30.00	0.000	0.000
7	1.024	5.220	0.000	0.000	0.000	0.000
8	1.014	2.214	100.0	35.00	0.000	0.000
9	1.031	3.454	0.000	0.000	0.000	0.000

Induction machine initial slip: −0.0074

of network variables like generator injection currents, bus voltages and injected real and reactive powers at all the buses.

On setting the derivative terms in the induction machine modelling equations to zero, and solving for the real and reactive power contributions of the induction machine, a fourth order equation for machine *slip* computation is obtained. Mathematically, it can be jotted down as

$$S_1 s^4 + S_2 s^3 + S_3 s^2 + S_4 s + S_5 = 0 \tag{7}$$

where,

$$S_1 = a^4 \left({r_{s4}}^3 + X'^2 - r_{s_{wtg}} {V_{wtg}}^2 / P_{wtg} \right)$$

$$S_2 = a^3 b_0 \left(2 r_{s_{wtg}} - {V_{wtg}}^2 / P_{wtg} \right)$$

$$S_3 = a^2 \left({b_0}^2 - 2 r_{s_{wtg}} {V_{wtg}}^2 / P_{wtg} + 2 {r_{s4}}^2 + 2 b_0 X' + 2 X'^2 \right)$$

$$S_4 = a b_0 \left(2 r_{s_{wtg}} - {V_{wtg}}^2 / P_{wtg} \right)$$

$$S_5 = {r_{s_{wtg}}}^2 - {V_{wtg}}^2 / P_{wtg} + 2 b_0 X' + X'^2 + {b_0}^2$$

and

$$b_0 = X - X'$$

$$a = \omega_0 T_0$$

The power contribution can also be inferred from Eq. 4 and can be put in real and reactive terminologies as,

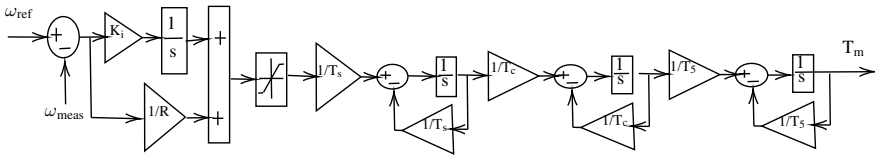

Fig. 2 Governor dynamics' modeling with automatic generation control

$$P_{wtg} = \frac{\beta_1 |V_{wtg}|^2}{(\beta_1{}^2 + \beta_2{}^2)} \tag{8}$$

$$Q_{wtg} = \frac{\beta_2 |V_{wtg}|^2}{(\beta_1{}^2 + \beta_2{}^2)} \tag{9}$$

and simplification terms can be put forth as,

$$\beta_1 = r_{s_{wtg}} + \left(\frac{sab_0}{1 + s^2a^2}\right)$$

$$\beta_2 = X' + \left(\frac{b_0}{1 + s^2a^2}\right)$$

The load flow initiation is done using a flat voltage at the induction machine connected bus. On solving the slip equation, i.e., Eq. (7), the maximum negative value of the slip is taken as the initial slip for the operation of the induction machine. Equation (9) is solved for a flat voltage, initial slip and initial real power status of the machine.

The obtained reactive power is fed to the load flow algorithm, so as to yield a nearly perfect approximation for the reactive power drawn by the induction generator from the capacitor banks or grid. This is the modified load flow algorithm implementation with hybrid topologies of synchronous as well as induction machines. Thenceforth, the regular load flow procedure is followed.

The load flow results of the present system under consideration have been mentioned in Table 2. The initial conditions of the four machines are mentioned in Tables 3 and 4.

The mathematical modeling of the synchronous machines of the multi machine system is given in detail in [18, 19]. All reactances in terms of line, capacitor banks, transformers and so on are translated into an admittance format and the load computation at h nodes is done using [15, 20],

$$Y_h = (P_h - jQ_h)/|V_h|^2 \tag{10}$$

Automatic generation control with governor transient dynamics has been taken into account, and the modeling scheme can be shown as in Fig. 2 [21]. The parameters

Table 3 Initial conditions: synchronous generators

Parameters	SG1	SG2	SG3
I_{SG0}	0.2083 − 0.4007i	1.5800 + 0.2039i	0.8163 + 0.1645i
δ_0	1.0719	61.9350	54.4525
I_{d0}	0.4045	1.2983	0.5686
I_{q0}	0.2008	0.9233	0.6084
E_{d0}'	0.0000	0.6164	0.6132
E_{q0}'	1.0644	0.7986	0.7850
E_{fd0}	1.0989	1.8060	1.4282

Table 4 Initial conditions: WTG

Parameters	Values
E_{D40}	1.0109
E_{Q40}	0.0050
I_{D40}	0.4998
I_{Q40}	0.2053
s_0	−0.0074

Table 5 Governor control parameters

Parameters	SG_1	SG_2	SG_3
R	0.05	0.05	0.05
k_i	0.2362	0.5020	0.2618
T_c	0.40	0.40	0.40
T_5	5	5	5
T_s	0.1	0.1	0.1
T_3	0	0	0
T_4	0	0	0
T_m^{max}	1.6	3.2	1.7
T_m^{min}	0	0	0

of the speed governor control for the three areas of synchronous generators have been given in Table 5. The automatic voltage control has been incorporated using the IEEE-Type I exciter, the details of which can be found in [17].

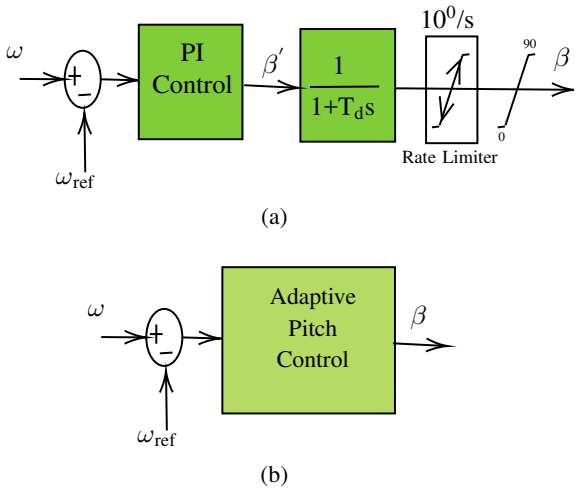

Fig. 3 **a** Conventional pitch control: PI controlled technique, **b** adaptive pitch control technique

3 Adaptive Pitch Control

An adaptive control system may be defined as one that adjusts automatically on-line the parameters of its controller, so as to maintain satisfactory performance when the parameters of the plant(controlled system) vary with time [22].

Problem Formulation

A linear discrete time model of the plant for controller design is required and is assumed to be of the form,

$$z(k) = \sum_{i=1}^{N} m_i z(k-1) + \sum_{i=1}^{N} n_i p(k-1) \tag{11}$$

where, *z(k)* is the deviation of the controlled variable from its nominal value and *p(k)* is the control signal at *k*th sampling instant. In Eq. (11), m_i and n_i are the model parameters for all values of *i*, which are estimated on-line at each sampling instant.

Quadratic Indexed-Control Law

For devising a control law, the following performance index is defined, where

$$\mathscr{W} = [\hat{z}(k+1)]^2 + d[\hat{z}(k+1) - z(k)]^2 + c[p(k) - B^* p(k-1)]^2 \tag{12}$$

The second term can however be approximated easily as,

$$\frac{d}{dt}\{z(k+1)\} = \frac{[z(k+1) - z(k)]}{T}$$

Mathematical conveniences like derivative terms are introduced to impart fast correcting actions and early damping. Similarly, integral correcting action is incorporated with binary constant (B^*) to facilitate inclusion/exclusion of past control signal, as needed. d and c are weighing constants, attached to the controller.

Optimal control signal p(k) is obtained by first replacing $\widehat{z}(k+1)$ in Eq. (12) by z(k+1) obtained from Eq. (11) and then finally setting

$$\frac{\partial \mathscr{W}}{\partial p_k} = 0$$

The optimal control signal is yielded as,

$$p(k) = \frac{[g_1 dz(k) + cB^* p(k-1) - f(k)]}{[c + g_1{}^2(1+d)]} \tag{13}$$

where,

$$f(k) = g_1(1+d)\left[\sum_{i=1}^{N} m_i z(k-i+1) + \sum_{i=1}^{N} n_i p(k-i+1)\right]$$

Figure 3 delineates the difference in the implementation of the conventional pitch control and the proposed APC technqiue.

The system output is assumed to be the digression in network frequency [23]. While regulating this driving point parameter, the pitch angle of the WTG is altered. This is because, the system frequency gets affected when either the wind speed anticipates turbulence or the network entertains some fault scenario.

APC in a Gist

The implementation of the adaptive control scheme requires the following steps in each sampling period:

(1) Sample the system output.
(2) Estimate the model parameters.
(3) Compute and apply the derived control signal.

4 Results and Discussion

In order to assess/illustrate the application of the proposed technique in the Western System Coordinating Council, a simulation was performed. Figure 4 depicts the fault location as implemented in simulation studies. The fault is sustained for 95 milliseconds. The wind generator meets with a staggering wind profile, as shown in Fig. 5.

It can be seen from Fig. 6, that the system parameters converge to their final values in a few milliseconds. This implies the attainment of a steady state, when the adaptive pitch control scheme is in action.

Figure 7 illustrates the WTG responses, when the system is perturbed with a 3-ϕ short circuit [25]. The deviations in power, voltage as well as pitch angle of the induction generator are appreciably lesser with APC equipped WTG than with a conventionally employed PI controlled WTG. The peak overshoot is reduced by over 12.2% in wind power output with APC driven generator. Similarly, the terminal

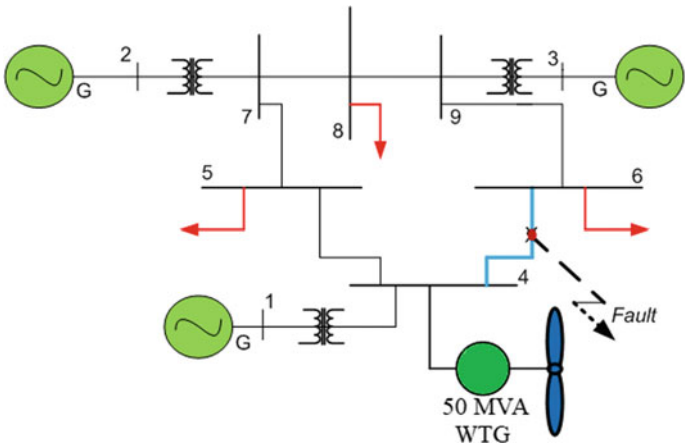

Fig. 4 Wind turbine generator fed Western System Coordinating Council [24]

Fig. 5 Wind perturbation

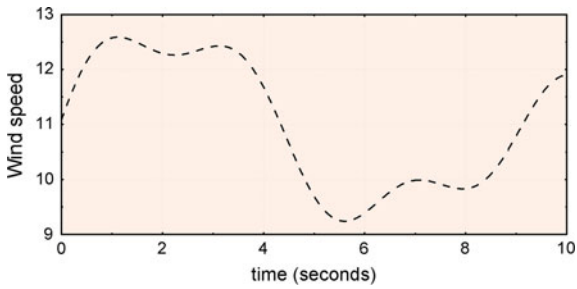

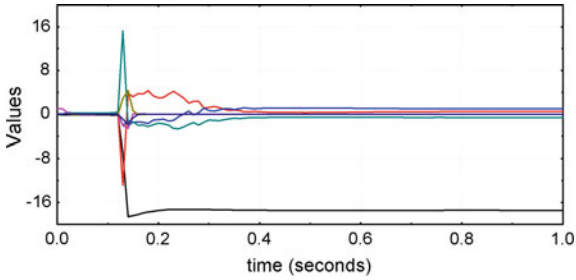

Fig. 6 Evolution of model parameters online

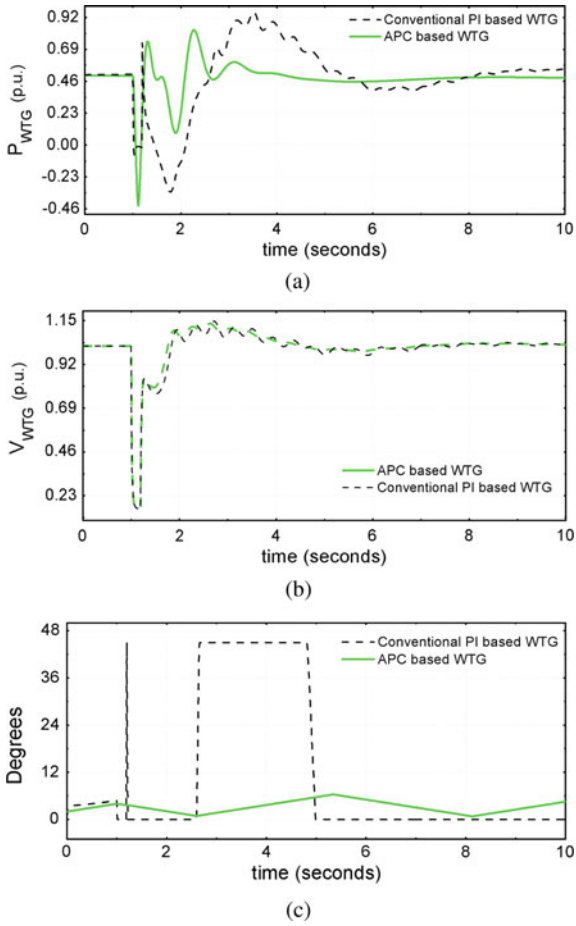

Fig. 7 Simulation results-Wind turbine generator responses: **a** power scene, **b** voltage scene, **c** pitch angle response

WTG voltage reflects considerable smoothing and flat profile, seconds after the fault is aborted. Significant improvement in pitch angle regulation is noticed, where the blade is turned at lower angles as the nature of wind and fault inception changes. Clearly, the APC based blade does not furnish any pitch angle spikes. This means, the blade does not require instantaneous movement. On the contrary, the PI controlled pitch angle shows irregular responses, which might be lethal for the turbine blade.

Some inferences drawn from the simulation study results are:

(1) Even though PI controllers are categorized as one of the simplest controllers, which can be tuned to suit a plethora of operating conditions, but adaptive controllers have a number of key advantages. Firstly, there is no requirement of a transfer function in adaptive control implementation. Secondly, these controllers adapt/self-tune to the changing operating conditions on-line. The variations is system operating states does not allow the PI controllers to modulate their control signal [26, 27]. However, this ability is found in adaptive control stategies.
(2) APC driven WTG robustly handles the turbulent wind and network fault contingency [28].
(3) Comprehensive power and voltage smoothing is witnessed.
(4) Lastly, the blade pitch angle is effectively regulated without any spikes in pitch angle.

5 Conclusion

The development and application of an Adaptive Pitch Control scheme has been proposed for a simple squirrel cage induction generator, which serves as a wind turbine generator in a multi machine power system. Detailed mathematical modeling and load flow implementation is presented. A self tuned adaptive control strategy, which is based on a quadratic index qualified control law, determines the pitch angle of the WTG. Comprehensive stability is accorded to the wind generator, by smoothing the power and voltage profiles, in addition to regulation of the turbine blade angular movement. A fault is simulated in the system model, with a varying wind in the background, and a comparative analysis is carried out between an APC based WTG and a PI based WTG. Simulation studies uphold the potency of the proposed scheme. In future, the aforementioned APC based turbine blade control can also be extended to doubly fed induction generator driven systems, under wind turbines. Also, a drive train model of the wind turbine can also be considered with minimum inertia and damping.

References

1. Farzin H, Fotuhi-Firuzabad M, Moeini-Aghtaie M (2017) A stochastic multi-objective framework for optimal scheduling of energy storage systems in microgrids. IEEE Trans Smart Grid 8(1):117–127
2. Ghofrani M, Arabali A, Etezadi-Amoli M, Fadali M (2013) Energy storage application for performance enhancement of wind integration. IEEE Trans Power Syst 28(4):4803–4811
3. Hasanien HM, Muyeen S (2012) Design optimization of controller parameters used in variable speed wind energy conversion system by genetic algorithms. IEEE Trans Sustain Energy 3(2):200–208
4. Zhang S, Mishra Y, Shahidehpour M (2016) Fuzzy-logic based frequency controller for wind farms augmented with energy storage systems. IEEE Trans Power Syst 31(2):1595–1603
5. Milano F, Dörfler F, Hug G, Hill DJ, Verbič G (2018) Foundations and challenges of low-inertia systems. In: Power systems computation conference (PSCC). IEEE, pp 1–25
6. Sierra-García JE, Santos M (2021) Improving wind turbine pitch control by effective wind neuro-estimators. IEEE Access 9:10 413–10 425
7. Thapa KB, Jayasawal K (2020) Pitch control scheme for rapid active power control of a PMSG-based wind power plant. IEEE Trans Indus Appl 56(6):6756–6766
8. Wan-Jun H, Shi-Yuan H, Yi-Shi J, Xin-Jing C, Song-Qing C, Yan-Hui Q, Zhe L (2018) Variable pitch sliding mode control of wind turbine based on disturbance observer. In: Chinese control and decision conference (CCDC), pp 5221–5225
9. De T, Rashid A, Ying D, Sheng LH (2020) Pitch angle control of modern variable speed variable pitch wind turbine based on linear active disturbance rejection control approach. In: IEEE/IAS industrial and commercial power system Asia (I CPS Asia), pp 1382–1387
10. Arabali A, Ghofrani M, Etezadi-Amoli M, Fadali MS, Baghzouz Y (2013) Genetic-algorithm-based optimization approach for energy management. IEEE Trans Power Delivery 28(1):162–170
11. Chaiyatham T, Ngamroo I (2017) Improvement of power system transient stability by PV farm with fuzzy gain scheduling of PID controller. IEEE Syst J 11(3):1684–1691
12. Ahsan H, Mufti M-UD (2020) Sweeping power system stabilization with a parametric fuzzy predictive control of a generalised energy storage device. IET Gener Transmission Distrib
13. Ahsan H, Mufti M-D (2019) Modelling and stability investigations of an aggregate wind farm–fed multi-machine system. Wind Eng 0309524X19862759
14. Muyeen S, Takahashi R, Ali MH, Murata T, Tamura J (2008) Transient stability augmentation of power system including wind farms by using ecs. IEEE Trans Power Syst 23(3):1179–1187
15. Wang L, Truong D-N (2013) Stability enhancement of DFIG-based offshore wind farm fed to a multi-machine system using a Statcom. IEEE Trans Power Syst 28(3):2882–2889
16. Ahsan H, Mufti M-D (2019) Distributed storage approach versus singular storage approach: a dynamic stability evaluation. Int J Power Energy Syst 39(1)
17. Sauer PW, Pai MA, Chow JH (2017) Power system dynamics and stability: with synchrophasor measurement and power system toolbox. Wiley
18. Ahsan H, Salam Z, Lone SA et al (2017) Modeling and simulation of an energy storage based multi-machine power system for transient stability study. In: Energy Conversion (CENCON), IEEE Conference on 2017. IEEE, pp 78–83
19. Ahsan H, Mufti M-D (2019) Dynamic performance improvement of a hybrid multimachine system using a flywheel energy storage system. Wind Eng 0309524X19849853
20. Ahsan H, Mufti MD (2017) Modeling and simulation of a superconducting magnetic energy storage based multi-machine power system for transient stability study. In: 2017 6th international conference on computer applications in electrical engineering-recent advances (CERA). IEEE, pp 347–352
21. Hosseini S, Etemadi A (2008) Adaptive neuro-fuzzy inference system based automatic generation control. Electric Power Syst Res 78(7):1230–1239
22. Lim C (1989) A self-tuning stabiliser for excitation or governor control of power systems. IEEE Trans Energy Convers 4(2):152–159

23. Ahsan H, Mufti MUD (2020) Systematic development and application of a fuzzy logic equipped generic energy storage system for dynamic stability reinforcement. Int J Energy Res
24. Ahsan H, Mufti MD (2020) Comprehensive power system stability improvement with ROCOF controlled SMES. Electric Power Components Syst 48(1–2):162–173
25. Ghosh S, Kamalasadan S (2017) An energy function-based optimal control strategy for output stabilization of integrated DFIG-flywheel energy storage system. IEEE Trans Smart Grid 8(4):1922–1931
26. Silva-Saravia H, Pulgar-Painemal H, Mauricio JM (2016) Flywheel energy storage model, control and location for improving stability: the Chilean case. IEEE Trans Power Syst 32(4):3111–3119
27. Lee D-J, Wang L (2008) Small-signal stability analysis of an autonomous hybrid renewable energy power generation/energy storage system part i: time-domain simulations. IEEE Trans Energy Convers 23(1):311–320
28. Taj TA, Hasanien HM, Alolah AI, Muyeen SM (2015) Transient stability enhancement of a grid-connected wind farm using an adaptive neuro-fuzzy controlled-flywheel energy storage system. IET Renew Power Gener 9(7):792–800

Detection of Broken Rotor Bar Fault in an Induction Motor Employing Motor Current Signature Analysis

Alok Verma, Pratul Arvind, Somnath Sarangi, Jayendra Kumar, and Anumeha

1 Introduction

The induction motor plays a necessary part in any industrial plant. An early detection of faults in the motor will be very helpful to avoid costly breakdowns in industrial plant.

According to IEEE broken rotor bar fault is one among the supreme faults in an induction motor [1, 2]. Uncontrolled vibrations, greater thermal stress or torque fluctuation as well as poor starting performances are some of the most common faults in a broken rotor bar. For the detection of a broken rotor bar fault, various methods were already used. The diagnosis of the rotor faults in an induction motor can be detected using various sensor signals in which vibration monitoring is a well-known approach [3, 4].

Mechanical systems often exhibit non-linear behaviours, because of vibrations in parameters like friction and damping. Therefore, the normal vibration signals may be changed to a complex and non-linear form [5]. There may have some limitations in

A. Verma (✉)
Advanced Remanufacturing and Technology Centre, Agency for Science, Technology and Research (A*Star), Singapore, Singapore
e-mail: alok_kumar_verma@artc.a-star.edu.sg

P. Arvind
ADGITM, New Delhi, India

S. Sarangi
Indian Institute of Technology, Patna, India
e-mail: somsara@iitp.ac.in

J. Kumar
National Institute of Technology, Jamshedpur, India

Anumeha
Government Women's Polytechnic Jamshedpur, Jamshedpur, India

S. Kumar et al. (eds.), *Recent Advances in Power Electronics and Drives*, Lecture Notes in Electrical Engineering 852, https://doi.org/10.1007/978-981-16-9239-0_39

often applied techniques that include time and frequency domain techniques. Consequently, the techniques for non-linear dynamic parameter estimation are needed that can give a useful option to retrieve the fault-related parameters hidden in the complex as well as non-linear samples [5]. Diverse experiments have already been performed for parameter extraction and fault diagnosis on-linear dynamic data set [6]. However, some literatures used approximate entropy (ApEn) as a fault diagnosis tool for non-linear signals. ApEn has also been described [5, 6] in the fields of the physiological signal and vibration signal processing of the rotating machine. Nevertheless, ApEn showed very close similarity with the time series and self-matching which makes ApEn majorly dependent on the length of time series [7]. Later, a new method for entropy called sample entropy (SampEn) which excludes, self-matches was offered by Richman and Moorman [8] to overcome the limitations of ApEn, and has brought a lot of consideration in this field of work.

In this paper, faults of the broken rotor bars were investigated by employing rotor vibration as diagnostic media. To tackle the non-linear behaviour existing in the rotor bar using vibration, multiscale entropy (MSE) was used which describes the uniformity in the diagnostic information. Despite that, the support vector machine (SVM) was used for the categorization and diagnosis of fault in broken rotor bars. New entropy named multiscale entropy was discussed for the measurement of complexity in the recent literature [9]. Various researchers applied this latest method for making a distinction between healthy and congestive hearts failure of a person [9, 10]. Few works have been done where multiscale entropy (MSE) has been employed in the area of fault diagnosis of the machine and that was only for the vibration signals. Zhang et al. [11] has introduced SVM based intelligent fault diagnosis method by extracting multiple time scale of entropy (MSE) from vibration signal. An approach to differentiate the aligned motor with a misaligned one using vibration was performed by Lin et al. [12]. MSE of vibration signal was used for bearing fault diagnosis using MSE to tackle the nonlinearity that existed with the bearing fault by Zhang et al. [13]. In the later stage, adaptive neuro-fuzzy inference system (ANFIS) was used to diagnose the bearing faults from the system. Several research [14–17] have also been performed to diagnose the machine failures using machine learning techniques.

In this paper, a new approach is proposed to detect the faults in the broken rotor bar by the authors, to tackle the nonlinearity which exists in the vibration of a broken rotor. For the extraction of information from vibration, a new approach of multiscale entropy analysis is being processed that differentiates the fault of broken rotor bars from the healthy rotor bar.

2 Multiscale Entropy

The MSE algorithm is employed in the present work that depends on the SampEn for variety of scales. A statistical method for noisy time series identified as approximate entropy (ApEn) was introduced by Pincus [7] in 1991. This method was used to measure the regularity of time series data. In the presented study, instead of revising

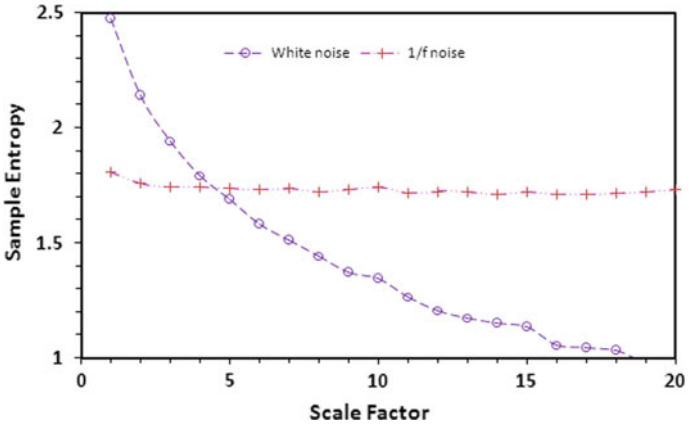

Fig. 1 SampEn with respect to the scale factor for white and 1/f noises time series

the previously used regularity measure ApEn statistical, the MSE algorithm is used for various scales of the similar process. As for refinement of ApEn, SampEn is employed and it measures the regularity in series data. To develop the entropy algorithms, two important parameters such as m and r need to be selected properly; where two m sequences are measured with the tolerance r. SampEn may increase as 'r' decreases; therefore, the determination of these two parameters is important. From the previous works of literature, the presented work selected $r = 0.15 \times$ standard deviation of the time series data, and 'm' $= 2$.

A new algorithm called MSE was proposed by Costa et al. [10], in which SampEn was calculated for multiple scale called scale factor. MSE of the time series X_1,…, X_N can be calculated as

$$y_j^{(\tau)} = \frac{1}{\tau} \sum_{i=(j-1)\tau+1}^{j\tau} X_i \tag{1}$$

where τ is known as scale factor, and j varies from 1 to $\frac{N}{\tau}$. In case of $\tau = 1$, the output of MSE time series is the original series. When τ increases, the length of time series decreases and when the scale factor increases, SampEn of the white noise decreases as shown in Fig. 1. On the other hand, SampEn of $\frac{1}{f}$ noise (pink) remains stable with the rise of scale factor.

3 Experimental Arrangement

As shown in Fig. 2, an experiment is carried on the system. The whole systems consist of three-Φ induction motor, different sensors, data acquisition system, computer/controller, and display as shown in Fig. 2. For the experiment as shown in

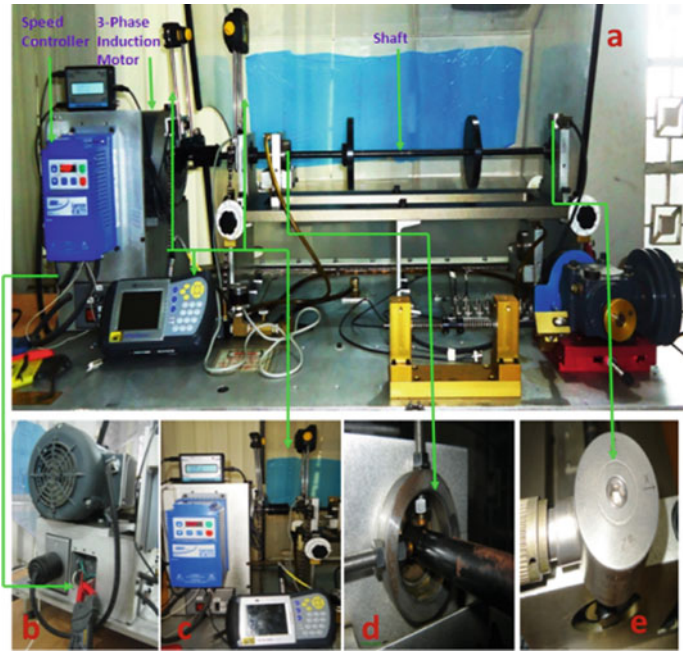

Fig. 2 Experimental test rig set-up: **a** overall experimental setup, **b** 3-Φ induction motor and current sensor used, **c** speed controller/vector drive, **d** proximity sensor, **e** accelerometer

Fig. 2a three phases, 0.75 HP inductions motor without any load was used. Figure 2b shows the data acquisition system. Figure 3 shows the 3-Φ induction motor with broken rotor bar used in the experiments.

An important sensor that is employed in this experiment is the current sensor. Current sensor was clamped on the stator winding of the induction motor as depicted

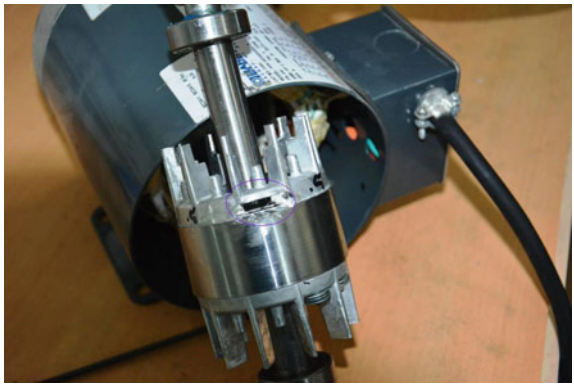

Fig. 3 3-Φ induction motor with broken rotor bar used in the experiments

Table 1 Specifications for experimental components

Sensors/machine	Manufacturer	Sensitivity/specification
Induction motor	Marathon Electric (healthy and broken rotor bars)	0.75 HP, 50 Hz, 2850 RPM
Current probe	Fluke	100 mV/A
Triaxial Accelerometer	Bruel and Kjaer	9.812 mV/(m/s^2)

in Fig. 2d. The overall specifications for the components used in the experiments are represented in Table 1.

3.1 Experimental Procedure

The experimental setup as depicted in Fig. 2 is used to conduct the experiments. For experiments, we have acquired four sets of real-time current signals. The first set of the data was acquired with the healthy motor (N1) running at different speeds from 700 to 1600 rpm with increment of 30 rpm. The second set of the current data was acquired from the motor with broken rotor bar faults (B1) and running at different speeds (700–1600 rpm) by the interchange of the healthy motor to the motor with broken rotor bars. For the collection of the third set of healthy data (denoted by N2), the motors were again interchanged from faulty motor to healthy motor and then data was stored. Finally, the fourth set of the current data was acquired by changing the motor from healthy (N2) to the again motor with broken rotor bar (B2). Total 31 samples were collected for each data set and each trial data has 15,364 signals values which was collected in 3 secs at 5.12 S/s. The control factors and their levels are shown in Table 2.

Wavelet transform is a mostly used method to remove noise from the signals, Although, wavelet transform is used as per the types of the signals. Figure 4 represents the MSE curves (SampEn with respect to scale factor) that is calculated from the current signals with the denoised signals from healthy motor and faulty motor with broken rotor bars, all rotating at 1600 rpm. The idea to use the SampEn to distinguish healthy signals to faulty signals is given by this observation. Diagnosis of fault in the broken rotor bars of an induction motor depends on the method of current measurement which is presented as follows.

The final features were calculated by differentiating the MSE features and the denoised current signals for the detection purpose. A classification algorithm like SVM has used these calculated values as an input to detect motor fault. MSE-related

Table 2 Levels and control factors set for the experiments

	Control factors	Level
A	Motor condition	Normal and faulty
B	Rotational speed	700–1600 rpm

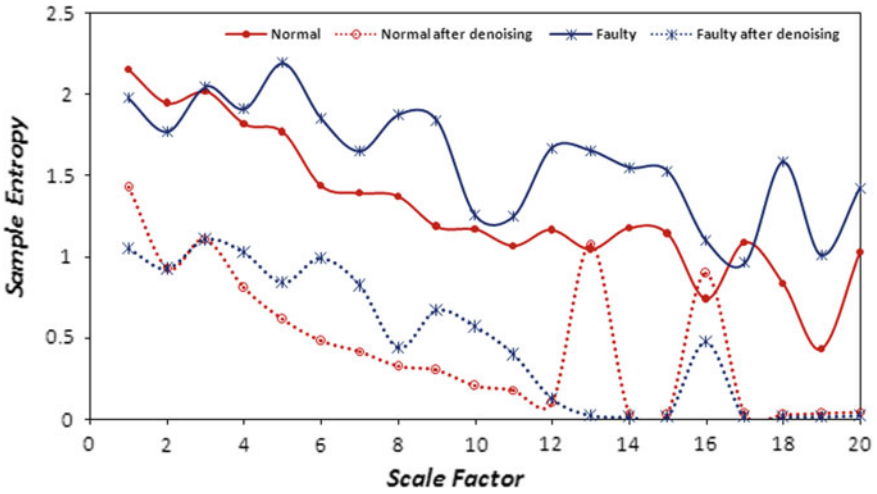

Fig. 4 Sample Entropy at a various Scale factor using motor current from healthy motor and motor with broken rotor bar fault at 1600 rpm before and after denoising

features are discussed in result section which was based on the performance of the classifiers. The Daubechies wavelet transform from the current signals was used to perform the denoising and the algorithm was developed using MATLAB with the parameters settings as (tptr = "rigrsure"; n = "2"; wav = "db4").

4 Results and Discussion

The explained method for broken rotor bar fault detection underlies the concept of statistical analysis. The proposed method employs the use of multiscale entropy in order to tackle the non-linear behaviour that is present in the motor vibration. Also, the regularity in the diagnostic information is explained. Further, the work presented in the paper describes an approach for analysis of multiscale features which easily differentiate the healthy and faulty samples of stator current of the experimental induction motor.

The approaches used for the statistical analysis have been deliberated above. The experimental approach performed the tests in the range of speed between 700 and 1600 rpm with an increase of 30 rpm. Table 2 demonstrates the parameters along with their levels used for the experiment. Further, 03 trials of current samples were performed. The three different tests are further elaborated. For the first trial, 62 current samples of N1 U B1 set were considered. For the second test, 62 current samples of N2 U B2 set were also considered. In both the above cases, 31 samples were used as training and the rest 31 samples were used for the purpose of testing. The third experiment considered the current samples received from N1 U B1 for the purpose

Table 3 Precision value of fault predicted for the training set employing Test 1–3 of current signal (i.e. test-1 = N1 U B1, test-2 = N2 U B2 and test-3 = N3 U B3) that comprises of in total 62 current samples, training set = 31 samples

Test	Training data	Cost function (C)	Gamma(γ)	Cross-validation accuracy (%)	Support vector	Time (secs) approx
1	31	10,000 0000	0.001	91.8	661	2
2	31	10,000 0000	0.001	90.4	448	2
3	31	10,000 0000	0.002	90.1	701	3

Table 4 Precision value of fault predicted for the testing set employing for Test 1–3 of current signal (i.e. test-1 = N1 U B1, test-2 = N2 U B2 and test-3 = N3 U B3) that comprises of total 62 samples, testing set = 31 samples

Test	Testing samples	Accuracy	Time (sec)
1	31	94.68%	2
2	31	94.1%	2
3	31	93.3%	3

of training while the current samples of N2 U B2 were used as testing. Support vector machine using multiscale entropy-related features were used to determine the performance as already discussed.

The inputs considered for the classifier are speed and healthy/faulty current and the output is the detected fault using current. Test-1 resulted in the maximum exactness and performed well for all the three tests. In order to get the optimal accuracy, the classifier has been trained and tested for numerous values. Tables 3 and 4 yield the best value of fault detection obtained by current.

Results assert that the tested current accuracy is about 90.1–94.68% for all the cases from experiments which is quite good. The presented results clearly reveal that the developed SVM model can be trained and tested to predict the broken rotor bar fault using MSE features of current signals at an early stage from failure with reasonable accuracy.

5 Conclusion

A comprehensive information regarding the response of current arising due to the broken rotor bar is presented in this work by using statistical analysis. This experimental investigation is a contribution towards the improvement in the rotor fault

diagnosis by using the multiscale entropy. Following conclusions may derive based on the investigation:

(i) This paper is an important experimental contribution for the analysis of rotor fault on the current signal by using MSE signal.
(ii) Effective modelling of the current using SVM during the rotor fault detection was shown in the results obtained by experiments. The predicted results are within 95% which is promising.

References

1. Bonnet AH (1988) Analysis of rotor failures in squirrel cage induction machines. IEEE Trans Ind Appl 24:1124–1130
2. Bonnet AH, Soukup GC (1992) Cause and analysis of stator and rotor failures in three-phase squirrel-cage induction motors. IEEE Trans Ind Appl 28:921–937
3. Nandi S, Toliyat HA (1999) Fault diagnosis of electrical machine—a review. In: International conference on electric machines and drives, Seattle, WA, pp 219–221
4. Thomson WT, Fenger M (2001) Current signature analysis to detect induction motor faults. IEEE Ind Appl Mag 7:26–34
5. Yan RQ, Gao RX (2007) Approximate entropy as a diagnostic tool for machine health monitoring. Mech Syst Signal Process 21:824–839
6. Yan RQ, Gao RX (1995) Machine health diagnosis based on approximate entropy. In: Instrumentation and measurement technology conference, Italy, pp 2054–2059
7. Pincus SM (1991) Approximate entropy as a measure of system complexity. PNAS 88:2297–2301
8. Richman JS, Moorman JR (2000) Physiological time-series analysis using approximate entropy and sample entropy. Am J Physiol H 278:2039–2049
9. Haitham MA, Alan VS (2002) Use of sample entropy approach to study heart rate variability in obstructive sleep apnea syndrome. IEEE Trans Bio Eng 50:1900–1904
10. Costa M, Goldberger AL, Peng CK (2002) Multiscale entropy analysis of complex physiologictime series. Phys Res Lett 89:68–102
11. Zhang L, Xiong G, Liu H, Zou H, Guo W (2009) An intelligent fault diagnosis method based on multiscale entropy and SVMs. Lect Notes Comput Sci 5553:724–732
12. Lin JL, Liu JYC, Li CW, Tsai LF, Chung HY (2010) Motor shaft misalignment detection using multiscale entropy with wavelet denoising. Expert Syst Appl 37:7200–7204
13. Zhang L, Xiong G, Liu H, Zou H, Guo W (2010) Bearing fault diagnosis using multi-scale entropy and adaptive neuro-fuzzy inference. Expert Syst Appl 37:6077–6085
14. Verma A, Sarangi S, Kolekar M (2016) Misalignment faults detection in an induction motor based on multi-scale entropy and artificial neural network. Electr Pow Compo Sys 44:916–927
15. Verma A, Sarangi S (2015) Fault diagnosis of broken rotor bars in induction motor using multiscale entropy and backpropagation neural network. In: Intelligent computing and applications, vol 343. Springer, New Delhi, pp 393–204
16. Verma A, Sarangi S, Kolekar M (2014) Stator winding fault prediction of induction motors using multiscale entropy and grey fuzzy optimization methods. Comput Electr Eng 2246–2258
17. Arvind P, Maheshwari RP (2012) A wavelet packet transform approach for locating faults in distribution system. In: 2012 IEEE symposium on computers & Informatics (ISCI), Penang, Malaysia, pp 113–118

Performance Analysis of Photovoltaic-Grid Connected System for Electric Vehicle Charging

Manoj Kumar Sharma, Karanbir Singh, and Satish Kansal

1 Introduction

The transportation sector has seen substantial growth in recent years owing to ever increasing population and improving economic conditions. This has led to increased use of internal combustion engines (ICE) vehicles. The ICE vehicles depend on fossil fuels for their operation that adds up to global air pollution substantially. The increasing air pollution and greenhouse effect, caused by the release of CO_2 from the ICE vehicles as well as limited availability of fossil fuels in the future, has necessitated shifting to an alternate clean approach. Electric Vehicles (EVs) being a clean source of transportation are an effective alternative. With features like immediate torque, silent ride and premium performance along with lower fuel and maintenance costs, the acceptance of EVs is on the rise. According to a report, the market share of electric vehicles will increase from 1% in 2015 to 9% in 2025 [1]. As per another forecast, EV market share will rise from 1.1 million worldwide in 2017 to 11 million worldwide by 2025 surging to 20 million by 2030 [2]. Although EVs provide us with a lot of benefits over the ICE vehicles, there are still some economical and technical issues like the stability of the power grid with regard to the usage of high-power chargers, battery management, such as thermal ratings, safety and cell balancing, which need to be addressed. Operating the power plants at their maximum generation range raises many issues regarding their capabilities especially the aging factor and increase in pollution levels by operating coal-fired plants for longer hours. Another issue of charging time for the battery of EVs is a primary concern, as the vehicle needs to absorb power from the grid [3]. The various types of charging

M. K. Sharma (✉) · K. Singh
Department of Electrical and Electronics Engineering, UIET, Panjab University, Chandigarh, India
e-mail: mks_uiet@pu.ac.in

S. Kansal
Department of Electrical Engineering, BHSB Institute of Engineering and Technology, Sangrur, Punjab, India

S. Kumar et al. (eds.), *Recent Advances in Power Electronics and Drives*, Lecture Notes in Electrical Engineering 852, https://doi.org/10.1007/978-981-16-9239-0_40

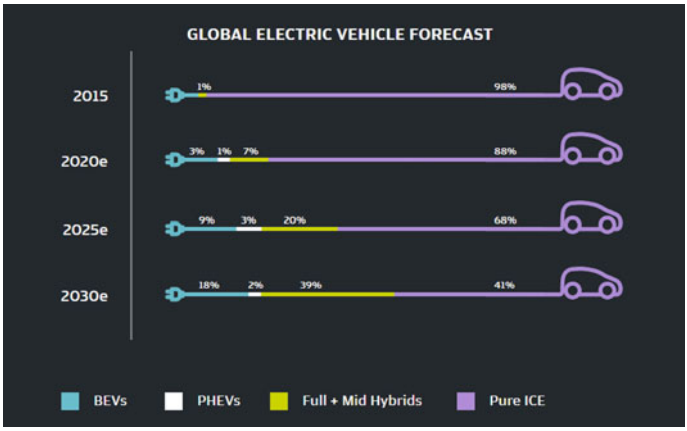

Fig. 1 Percentage penetration forecast of electric vehicles

methods have been compared in [4] to select the most efficient charging method. Ali et al. have modelled hybrid energy storage system using EV batteries and super capacitors for enhancing lifetime of the EV batteries and compared the performance for different optimization strategies [5]. A conceptual architecture and an assessment framework were proposed to explore integration scenarios of EVs and renewable energy generation in distribution networks [6]. The combination of PV energy and EVs in uncontrolled charging and smart charging strategies has been studied [7], as was a two-stage framework for the economic operation of an EV parking deck with renewable energy generation [8]. Most of the researches on charging of EVs and renewable energy generation have focused on design, operation and optimal charging strategies [9–13] (Fig. 1).

The issue of electric vehicle charging and power supply from grid and renewable energy sources is a topic of research worldwide. The integration of PV with the EV charging system has been on the rise due to rapid growth of EVs and concern over the effects of greenhouse gasses. An overview of different charging approaches of EVs is discussed and a PV-grid charging method incorporating a battery management system is elaborated by Bhatti et al. [14, 15]. Khan et al. [16] have presented the charging technologies of EVs, their sustainable development and characteristics. They also forecast the current status, economic assessment, power market operation and control and safety aspects of charging EV system. An electric vehicle charging system incorporating energy storage system (ESS) for power quality improvement and providing fast charging is discussed [17, 18]. A Battery Energy Storage Station (BESS)-based hybrid power station to tackle the disadvantageous unstable power output from PV and wind power generations is elaborated and SOC-based control strategy has been adopted for smoothing the output fluctuation [19]. Mortaz and Valenzuela have modeled a micro grid consisting of renewable energy resources connected within a grid and using EV batteries in the parking facility for energy storage [20]. A rule-based energy management system to provide uninterrupted

constant price charging is proposed. The model incorporates a PV-grid system along with an energy storage unit. A daytime charging system using a PV, an ESU unit and a micro grid with the help of heuristic rule-based strategies is proposed [21, 22]. The model has helped to reduce burden on the micro grid as well as provided efficient cost saving.

A PV-grid system for EV charging using particle swarm optimization PSO algorithm to find optimum size of PV modules and ESU's need has been modeled [23]. The proposed system allows charging EVs at a fixed energy rate without facing economic losses. However, not much has been discussed about the power quality issues related to electric vehicle charging on a PV-Grid system.

In an electric power system, a harmonic is a voltage or current at a multiple of the fundamental frequency of the system, produced by the action of non-linear loads such as rectifiers, discharge lighting or saturated magnetic devices. The Total Harmonic Distortions (THD) occurring in a system can be calculated using Eq. (1).

$$\text{Total Harmonic Distortion, THD} = \frac{\sqrt{V_2^2 + V_3^2 + V_4^2 + \cdots + V_n^2}}{V_1} \tag{1}$$

Harmonic frequencies in the power grid are a frequent cause of power quality problems. Harmonics in power systems result in increased heating in the equipment and conductors, misfiring in variable speed drives, and torque pulsations in motors. Thus it becomes of utmost importance to tackle this problem. The effect of harmonic distortions on the distribution transformers has been analyzed in [24]. To tackle these power quality issues coordinated charging has been proposed in [25] to minimize the power losses and to maximize the main grid load factor. As charging of electric vehicles has led to main power quality issues, thus, in this work an analysis of performance of PV-Grid system for EV charging is done.

In the present paper, a PV-grid system for electric vehicle charging has been designed for four charging stations having eight vehicles each. The battery specifications of EVs considered are same as that of being used in real-life batteries of EVs. The analysis is done for effect of different internal resistances and different SoCs of EVs, total harmonic distortion (THD) and scheduling of PV-grid system. Section 2 of the paper describes the proposed PV-grid model for EV Charging. The description of specified model and its working is given in Sect. 3. The simulations, performance analysis and results are discussed in Sect. 4. Sections 5 and 6 of the paper describe the economic aspect and conclusion, respectively.

2 Proposed PV-Grid Connected Model for EV Charging

One of the most viable and abundant renewable energy sources is solar energy. This solar energy can be harnessed and used for day-to-day power needs. This harnessed energy can be used for the purpose of electric vehicle charging as well. So rather than

depending on the AC grid solely for charging of electric vehicles, the PV module can be scheduled in a way so that maximum energy can be accessed from it for charging during its operation and the rest of the charging needs can be fulfilled from the AC grid. This decreases the overall stress on the grid due to electric vehicle charging.

For this purpose, the model has been designed with four charging stations, each serving eight electric vehicles at a time. The power generated from the PV module will be continuously measured and the shift between PV and grid will take place on the basis of comparison between these measured values and a predefined threshold value of 10 kW.

2.1 Design Parameters

The proposed PV-Grid model is designed in MATLAB/Simulink. The various components along with their ratings, used for designing of the proposed PV-Grid system are given in Table 1:

Table 1 Components and their ratings used in the PV-Grid system

S. no	Component	Ratings	
1	AC grid	3-phase ac source	20 MVA, 13.8 kV, 50 Hz
		3-phase transformer	20 MVA, 13.8/230 kV, 50 Hz
		3-phase active load	5 MW
		3-phase reactive load	500 kVA
2	PV module	PV module rating	236 kW, 480 V
		Temperature	450 °C
		Irradiance	1000 W/m^2
3	Electric vehicles	Battery rating;	48 V, 24 Ah
		Discharge current	10.4348 A
		Capacity Nominal Voltage	21.7 Ah
		Range of initial SOC%	[30%–80%]
4	AC-DC converters	Diodes	6
5	Filters	Resistor	1 Ω
		Capacitor	10 μF

3 Modelling and Description of the Proposed Model

The schematic diagram for the proposed PV-Grid system is shown in Fig. 2. In the proposed model a PV-Grid system has been used in which power is being supplied from the PV module and AC grid to charge the electric vehicles connected to the charging stations. The photovoltaic modules use light energy (photons) from the Sun to generate electricity through the photovoltaic effect. Nominally rated maximum power out (kWp) of a solar array of n modules, each with a maximum power of Wp at STC is given by Eq. (2).

$$kWp = n \times Wp/1000 \tag{2}$$

The available solar radiation (Ema) varies depending on the time of the year and weather conditions. However, based on the average annual radiation for a location and taking into account the efficiency (η) of the cell, the estimation of an average PV system energy yield is obtained as per Eq. (3).

$$Ep = Ema \times kWp \times \eta \tag{3}$$

In the present model, four charging stations are being used to observe the results where each charging station consists of eight charging points for connecting the electric vehicles. Out of these eight charging points, six charging points can be

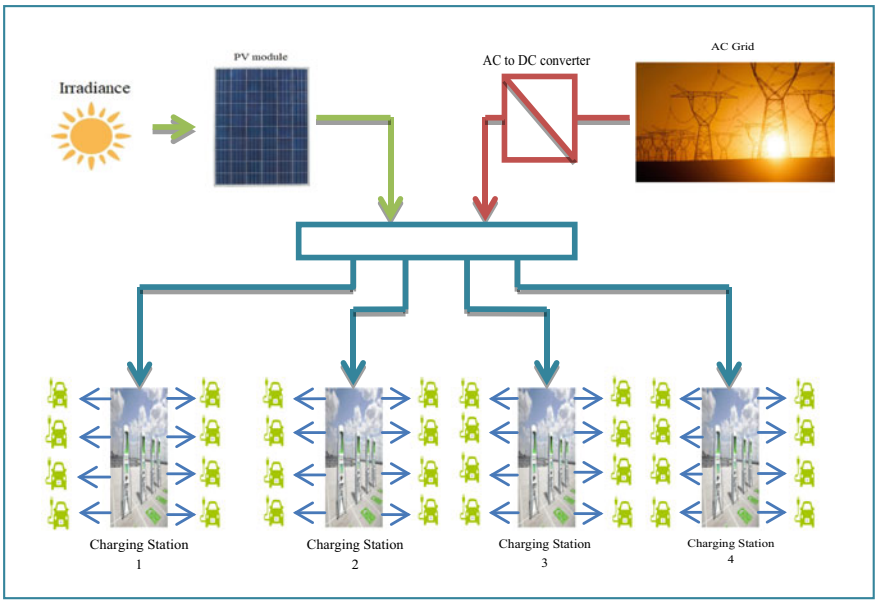

Fig. 2 Schematic diagram for the proposed PV-Grid system for EV charging stations

connected to the grid or PV module. The reason for this is to give provision for backup storage. The two charging points can be Energy Storage Units to prevent any wastage of solar energy in case all the charging points are not being used to supply energy. These Energy Storage Units can then be used to provide supply for charging even when there is no solar energy generation for instance at night.

3.1 Flowchart

The flowchart depicting the entire process of working of the proposed PV-Grid hybrid system is shown in Fig. 3. The process is described as follows:

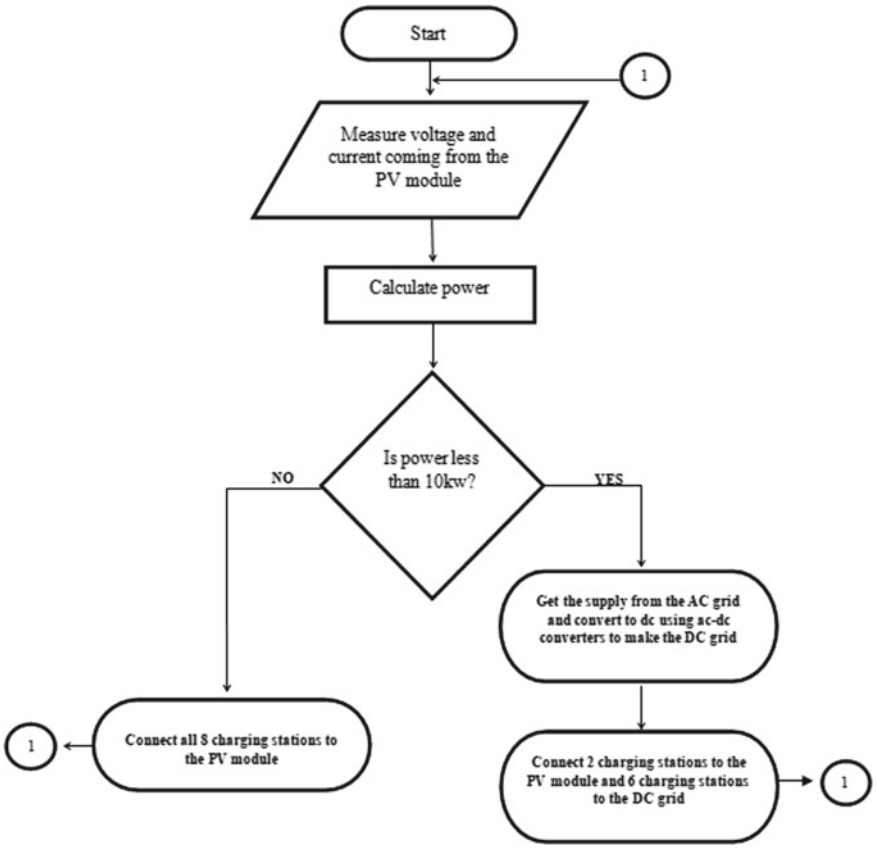

Fig. 3 Flowchart depicting the scheduling process of the PV-grid system

- Initially, when the operation starts, the PV module is being used to charge the EVs. The PV module makes use of irradiance and temperature as inputs to generate the output power.
- As the irradiance is high and power generated is enough to charge the electric vehicle batteries but as time passes the irradiance starts decreasing and so does the power and as a result PV alone is not sufficient to charge the electric vehicle batteries. As a result, all the eight charging points in a charging station are connected to the PV module supply.
- After some time when the power drops below the threshold limit of 10 kW, the electric vehicle charging points are shifted from the PV module supply to the AC grid. The AC supply from the AC grid is converted to DC current using AC-DC converters to form a DC grid.
- Six out of eight charging points are connected to the DC grid whereas two remaining charging points are connected to the PV module exclusively.
- The basis of this operating model is the switching between PV and AC grid. For this purpose, a threshold has to be assigned to the system after which the shift between PV and grid happens.

4 Simulations and Results

4.1 Real-Life Applications

The electric vehicle industry is on the rise and its increasing popularity has drawn many major manufacturing companies to compete in the e-automobile market worldwide. A number of major automobile companies have started implementing EV technology and new electric vehicle products have started emerging. The vehicle manufacturing companies like Hero Electric, Tunwal E-Vehicle, etc. are investing in the EV domain and have come up with various EV products like EV cars, EV bikes, EV scooters, etc. For example, Nyx E5 by Hero Electric is an electric vehicle scooter and Mini Lithino 48 V by Tunwal E-Vehicle with 48 V/28 Ah and 12 V/28 Ah batteries, respectively. The battery specifications used in the present model are same as used in real-life vehicle batteries. Hence, such vehicles can easily be incorporated with the proposed model to provide electric vehicle charging.

4.2 Effect of Different Internal Resistances on Battery Performance

In the real world, all the electric vehicles do not have the same rating. The batteries manufactured by the different manufacturers have varied specifications. To take this into account, batteries with different internal resistances in the range from 0.002 Ω to

Table 2 Internal resistance in terms of percentage of base value

S. no	Battery no	State of charge (%)	Value of internal resistance (ohms)	Percentage of base value (%)
1	Battery 1 & 2	80	0.012 (base value)	100
2	Battery 3	50	0.002	16.67
3	Battery 4	50	0.006	50
4	Battery 5	40	0.010	83.34
5	Battery 6	40	0.014	116
6	Battery 7	30	0.018	150
7	Battery 8	30	0.022	183.34

0.022 Ω have been selected and have been used for simulations. Also, different values of state of charges for batteries have been considered. The base value considered for the batteries is the value of the internal resistance as per default specifications in the Simulink. The range of values taken for internal resistance of batteries and its percentage with respect to the base value of the battery is shown in Table 2. The batteries 1 and 2 with the internal resistance of 0.012 Ω are supplied by the PV alone.

Case 1: Batteries with the same State of Charge

Initially, the same state of charge (SOC) for all the electric vehicles i.e., 80% with different internal resistance is considered. The range of values taken for internal resistance of batteries and its effect on the battery state of charge, battery current and battery voltage is shown in Table 3.

From Table 3 it can be seen that as the internal resistance of the battery increases:-

- The rate of charge of the battery decreases.
- The battery current decreases.
- The battery voltage remains almost constant.

Table 3 Battery performance with different internal resistances and same State of Charge

	Internal resistance (Ω)	Battery SOC (%)	Battery current (A)	Battery voltage (V)
Battery 1 & 2	(0.012)	80.06	−22	50.21
Battery 3	(0.002)	80.14	−35	50.02
Battery 4	(0.006)	80.065	−24	50.02
Battery 5	(0.010)	80.025	−14.5	50.02
Battery 6	(0.014)	80.0175	−42.85	50.02
Battery 7	(0.018)	80.075	−8.5	50.02
Battery 8	(0.022)	80.0012	−6	50.02

Figure 4 shows the relation between internal resistances and the rate of charge of batteries. It can be concluded that as the value of internal resistance increases, the rate of charge of batteries decreases.

Case 2: Batteries with different State of Charge

In this case, electric vehicle batteries with different internal resistances and different state of charge are considered. The range of values taken for internal resistances and its effect on battery state of charge, battery current and battery voltage is shown in Table 4.

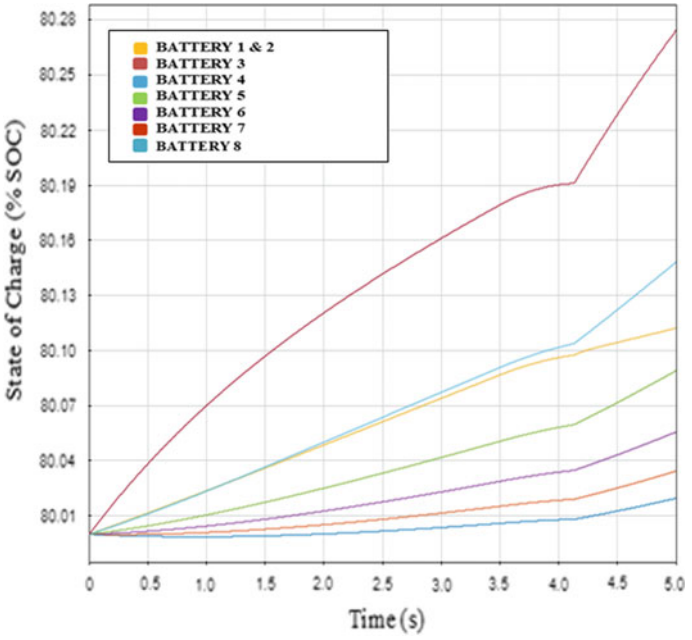

Fig. 4 Rate of charge of batteries with different internal resistances at same SOC

Table 4 Battery performance with different internal resistances and different SOC

	Internal resistance (Ω)	Battery SOC (%)	Battery Current (A)	Battery Voltage (V)
Battery 1 & 2	(0.012)	80.037	−13	50.065
Battery 3	(0.002)	50.155	−44	49.85
Battery 4	(0.006)	50.053	−20.55	49.85
Battery 5	(0.010)	40.041	−16	49.85
Battery 6	(0.014)	40.022	−11	49.85
Battery 7	(0.018)	30.028	−9.5	49.85
Battery 8	(0.022)	30.018	−7.4	49.85

4.3 *Scheduling of Power for Charging Electric Vehicles in the Proposed PV-Grid System*

The proposed model has been run for 5 s (simulation time in Simulink) in Simulink and the various outputs obtained are as follows.

Battery State of Charge (SOC)

Figure 5 shows the variation of State of Charge (SOC) with time for different values of internal resistance of batteries of Electric Vehicles.

From the graph, it can be seen that as the internal resistance of the battery increases, the rate of charge of the battery decreases. Also, it can be seen that the shift from the PV module to the AC grid occurs at time 4.2 s (approximately) when power from the PV module drops below the threshold value of 10 kW.

Battery Voltages

The rate of change of battery voltage w.r.t. time for different 8 values of internal resistance of electrical vehicles is shown in Fig.6.

From Fig. 6 it can be seen that the Battery Voltage remains fairly constant. Batteries 1 & 2 show the graph for the charging point being supplied from the PV alone. It can be seen also that the shift from the PV module to the AC grid occurs at time 4.2 s (approximately) when power from the PV module drops below a threshold value of 10 kW.

Battery Currents

The following are the Time vs Current graphs, which show the rate of change of current of EVs with time. The graphs here are plotted for 8 different values of internal resistance.

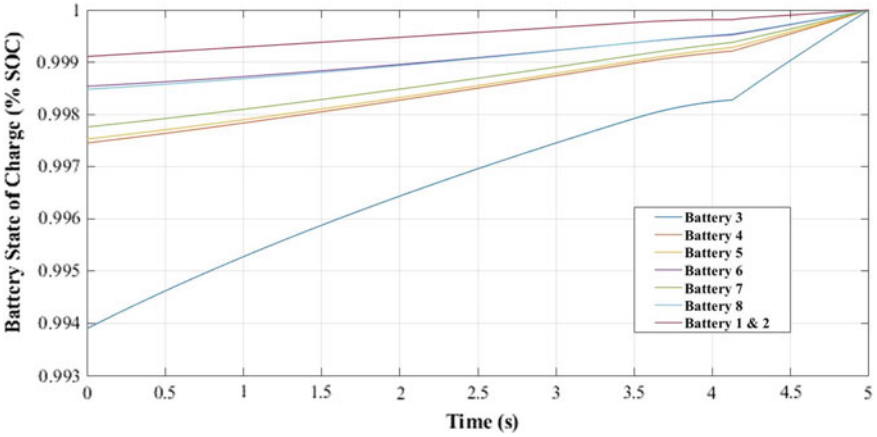

Fig. 5 Battery SOC with Internal Resistance ranging from 0.002 to 0.012 Ω

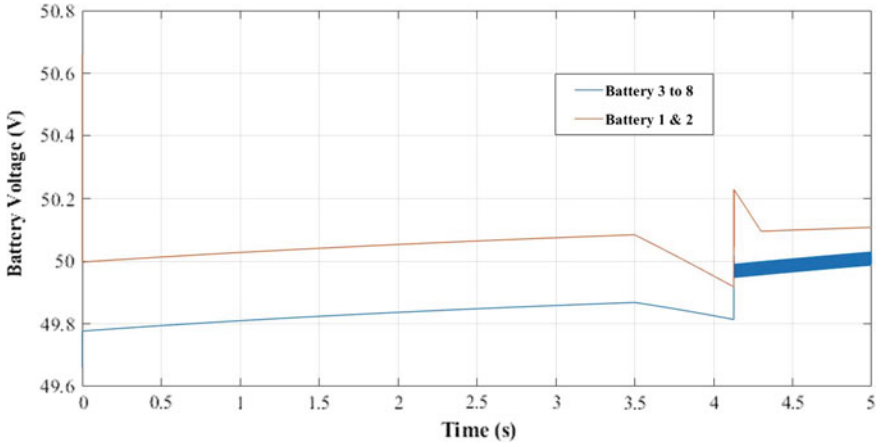

Fig. 6 Rate of change of voltage of batteries 1–8 with different internal resistances

From Fig. 7 it can be seen that the Battery Current decreases as the internal resistance of the battery increases. Batteries 1 & 2 show the graph for the charging point being supplied from the PV alone. Here it can be seen that from Fig. 8, the shift from the PV module to the AC grid occurs near 4.2 s (approximately) when power from the PV module drops below 10 kW.

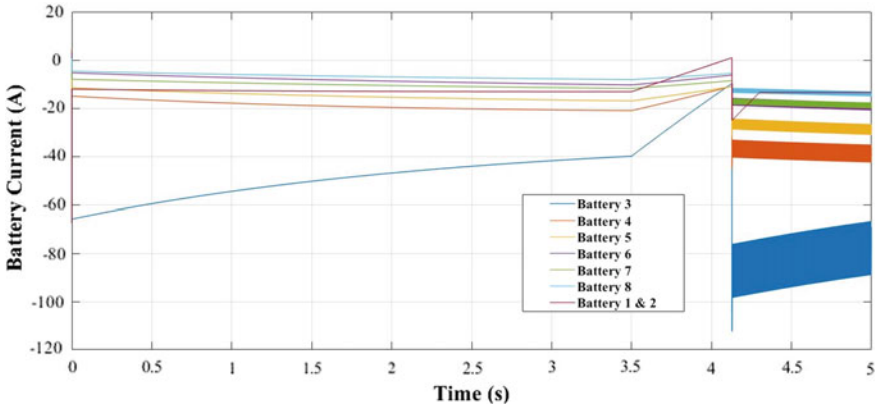

Fig. 7 Rate of change of current of batteries with different internal resistances

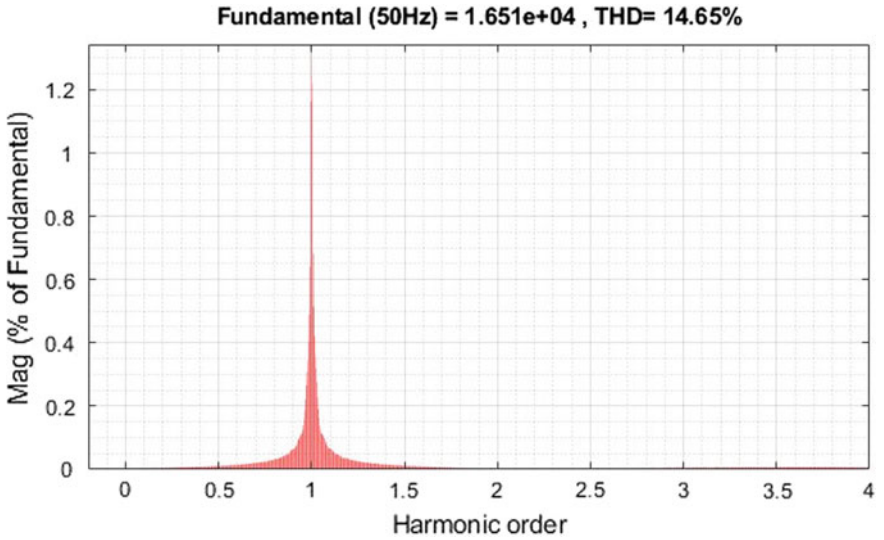

Fig. 8 THD (voltage distortions) injected in the grid caused due to the charging of electrical vehicles

4.4 Electric Vehicle Charging on AC Grid Alone

Electric vehicles are comprised of non-linear loads such as batteries which are known to cause harmonic distortions in the electrical grid. By using an AC grid designed in Simulink the Total Harmonic Distortions occurring in the system have been calculated due to the charging of electric vehicles.

The acceptable THD limit as per standard IEEE 519 is 5%. The results show that the Harmonic Distortion caused by charging electric vehicles through the AC grid is 14.65% for voltage distortions and 6.28% for current distortions as shown in Fig. 8 and Fig. 9, respectively. Hence it is important to reduce these distortions to a minimal value as possible.

4.5 Reduction of THD in the Proposed PV-Grid System

Lower THD in power systems means higher power factor, lower peak currents and higher efficiency. The low THD is an important feature in power systems. The International Standards such as IEC 61,000-3-2 set limits on the harmonic currents of various classes of power equipment. One of the objectives of this model is to control the Total Harmonic Distortions occurring in the system.

To analyze the total harmonic distortions (THD) occurring due to the charging of electric vehicles a PV-Grid system has been designed using MATLAB/Simulink

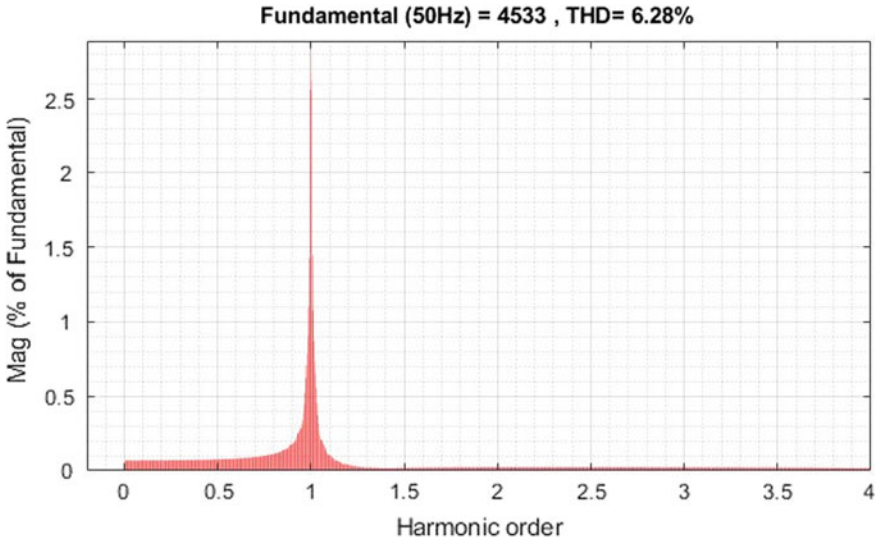

Fig. 9 THD (current distortions) injected in the grid caused due to the charging of electrical vehicles

software and the impact on the proposed system due to electric vehicle charging has been studied.

It is observed that employing low pass filters and scheduling the charging period of electric vehicles in the PV-Grid system helps in tackling THD. During the day when there is an abundant amount of solar energy, the PV module is used to harness this energy and further utilize it to charge the electric vehicles. As the day passes the irradiance decreases and the power generated by the PV module also decreases. When the power generated by the PV module drops below the threshold value of 10 kW the circuit breakers connecting the ac grid to the charging points in the electric vehicle stations close. After the threshold value of 10 kW, both the PV and ac grid are connected to the charging points on the electric vehicle charging stations to provide the power required to charge the electric vehicles.

It is also observed that connecting the electric vehicles solely to the ac grid results in large harmonics entering the system. On the other hand, by incorporating the PV module into the system these harmonics are reduced to a large extent. In this system, the electric vehicles are connected to PV module during the day when there is an abundant amount of solar energy rather than connecting to the ac grid. As a result, when PV supply is available the ac grid is not used for the electric vehicle charging purpose and the load stress imposed on the system is decreased. Hence harmonics entering into the system are reduced to a significant amount. The values of THD are drastically dropped to 0.36% and 1.27% for voltage and current distortions as shown in Fig. 10 and Fig. 11, respectively, when vehicles are charged on the proposed PV-grid system as compared to the 14.65% and 6.28%, respectively, when charged on ac grid alone.

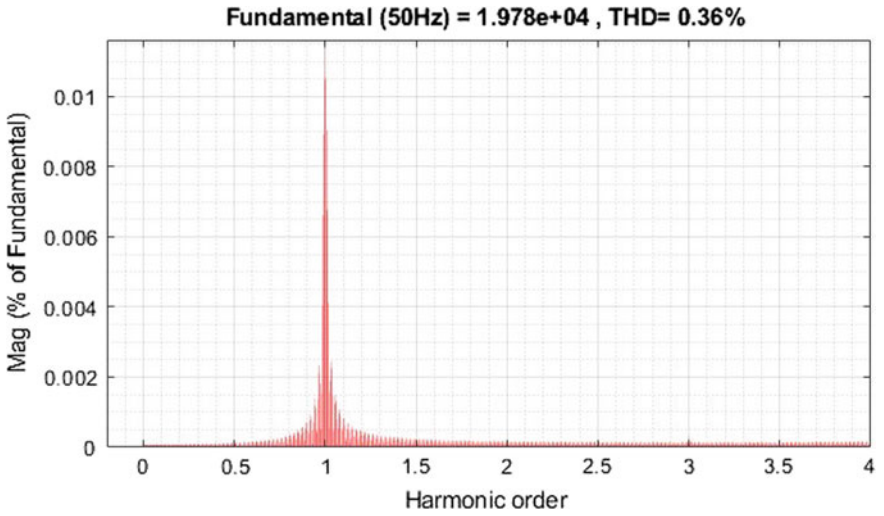

Fig. 10 THD (voltage distortions) injected in the grid due to the charging of electric vehicles by the proposed system

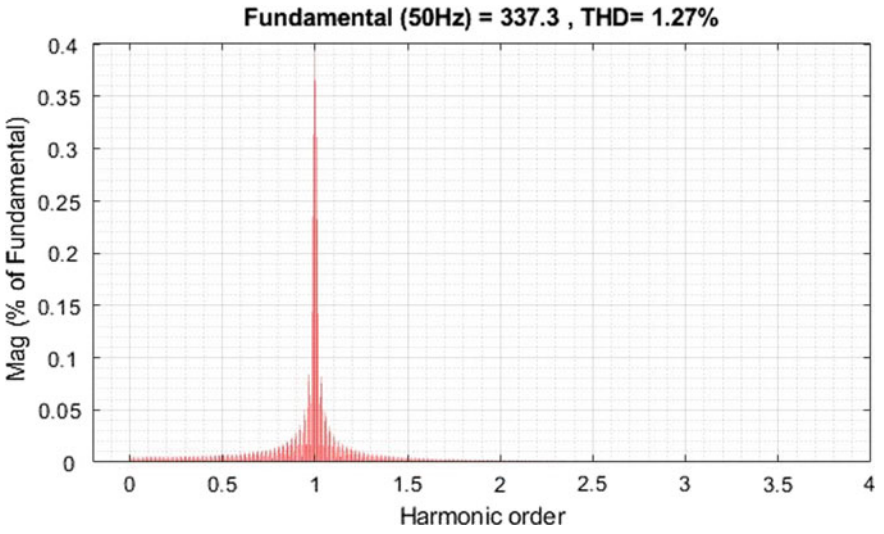

Fig. 11 THD (current distortions) injected in the grid due to the charging of electric vehicles by the proposed system

5 Economic Benefits

The proposed PV-Grid system for charging of the electric vehicles can provide more benefits as compared to charging the vehicles on the grid alone system. During the

peak times of the day when there is an abundant amount of solar energy available, the vehicles are charged on the proposed PV-Grid system in which energy is supplied by the solar modules. The solar energy has the least negative impact on the environment as compared to any other type of energy source. PV modules do not create any noise pollution, which is a major benefit. It does not produce greenhouse gasses and does not pollute the environment and also has the least maintenance cost.

6 Conclusion

Ever-increasing pollution owing to emissions from ICE vehicles and limited fuel sources has shown the importance of shifting to an alternate clean and renewable energy resource. In the proposed work, a PV-Grid system has been developed for the purpose of charging electric vehicles in MATLAB/Simulink. As the electric vehicles manufactured by different industries may have different internal resistances so the effect of different internal resistances on battery performance has been observed for same SOC and different SOC conditions. The passive filters have been designed in the proposed PV-GRID system to further enhance harmonic mitigation. The system performance for various load conditions has been analyzed by employing different charging stations. The system has been designed in such a way that the load on the grid is scheduled for on-peak and off-peak hours i.e., during day and night. This scheduling decreases the stress on the grid that could have been imposed if the grid had been used for the purpose of electric vehicle charging for the entire 24 h period. It is observed that the proposed system has been successfully able to suppress the total harmonic distortions (THD) to a great extent i.e. 14.65% to 0.36% for voltage distortion and from 6.28% to 1.27% for current distortions, respectively. The widespread use of hybrid renewable energy will not only solve the energy issues but also ensure a green planet.

Acknowledgements The corresponding author wishes to thank Prof. Vijay Sood of Ontario Tech University, Canada for his guidance and continuous support during the research work related to the present paper.

References

1. Morgan JP (2018) Driving into 2025: the future of electric vehicles
2. Bloomberg (2018) Electric vehicle outlook
3. Kumar SA, Bharath A, Sukumar K (2010) The challenges and policy options for integrating plug-in hybrid electric vehicle into the electric grid. Electr J 23(3):83–91
4. Sears J, Roberts D, Glitman K (2014) A comparison of electric vehicle level 1 and level 2 charging efficiency. In: IEEE conference on technologies for sustainability (SusTech). IEEE, pp 255–258

5. Castaings W, Lhomme R, Trigui BA (2016) Comparison of energy management strategies of a battery/supercapacitors system for electric vehicle under real-time constraints. Appl Energy 163:190–200
6. Chaouachi A, Bompard E, Fulli G, Masera M, De Gennaro M, Paffumi E (2016) Assessment framework for EV and PV synergies in emerging distribution systems. Renew Sustain Energy Rev 55:719–728
7. Fattori F, Anglani N, Muliere G (2014) Combining photovoltaic energy with electric vehicles, smart charging and vehicle-to-grid. Sol Energy 110:438–451
8. Guo Y, Xiong J, Xu S, Su W (2016) Two-stage economic operation of microgrid-like electric vehicle parking deck. IEEE Trans Smart Grid 7(3):1703–1712
9. Rao W, Zhang X, Xie J, Ju L (2015) Optimizing electric vehicle users' charging behavior in battery swapping mode. Appl Energy 155:547–559
10. Vander Kam M, Van Sark W (2015) Smart charging of electric vehicles with photovoltaic power and vehicle-to-grid technology in a microgrid; a case study. Appl Energy 152:20–30
11. Van Roy J, Leemput N, Geth F, Buscher J, Salenbien R, Driesen J (2014) Electric vehicle charging in an office building microgrid with distributed energy resources. IEEE Trans Sustain Energy 5(4):1389–1396
12. Chandra Mouli GR, Bauer P, Zeman M (2016) System design for a solar powered electric vehicle charging station for workplaces. Appl Energy 168:434–443
13. Schuller A, Flath CM, Gottwalt S (2015) Quantifying load flexibility of electric vehicles for renewable energy integration. Appl Energy 151:335–344
14. Bhatti AR, Salam Z, Aziz MJBA, Yee KP (2016) A comprehensive overview of electric vehicle charging using renewable energy. Int J Power Electron Drive Syst 7(1):114–123
15. Bhatti AR, Salam Z, Aziz MJBA, Yee KP, Ashique RH (2016) Electric vehicle charging using photovoltaic: status and Technological review. Renew Sustain Energy Rev 54(1):34–47
16. Khan S, Shariff S, Ahmad A, Alam MS (2018) A comprephensive review of level 2 charging system for electrical vechicals. J Smart Sci 6(3)
17. Sbordone D, Bertini I, Di Pietra B, Falvo MC, Genovese A, Martirano A (2015) EV fast charging stations and energy storage technologies: a real implementation in the smart micro grid paradigm. Electric Power Syst Res 120:96–108
18. Bansal P (2015) Charging of electrical vehicles: technology and policy implications 6(1)
19. Li X, Hui D, Lai X (2013) Battery energy storage station (BESS)-based smoothing control of photovoltaic (PV) and wind power generation fluctuations. IEEE Trans Sustain Energy 4(2):464–473
20. Mortaz E, Valenzuela J (2017) Microgrid energy scheduling using storage from electric vehicles. Electric Power Syst Res 143:554–562
21. Bhatti AR, Salam Z (2018) A rule-based energy management scheme for uninterrupted electric vehicles charging at constant price using photovoltaic-grid system. Renew Energy 125:384–400
22. Bhatti AR, Salam Z, Ashique RH (2016) Electric vehicle charging using photovoltaic based microgrid for remote islands. Energy Procedia 103:213–218
23. Bhatti AR, Salam Z, Sultana B, Rasheed N, Awan AB, Sultana U, Yuonas M (2019) Optimized sizing of photovoltaic grid-connected electric vehicle charging system using particle swarm optimization. Int J Energy Res 43(1):500–522
24. Gómez JC, Morcos MM (2003) Impact of EV battery chargers on the power quality of distribution systems. IEEE Trans Power Delivery 18(3):975–981
25. Clement-Nyns K, Haesen E, Driesen J (2010) The impact of charging plug-in hybrid electric vehicles on a residential distribution grid. IEEE Trans Power Syst 25(1):371–380

Development of the System of Initial Excitation of the Autonomous Induction Generator

Volodymyr Chenchevoi, Valeriy Kuznetsov, Iurii Zachepa, Oleksii Chornyi, Olga Chencheva, Vitaliy Kuznetsov, Rostyslav Yatsiuk, and Olha Luhova

1 Introduction

Despite numerous works on theoretical and practical studies of autonomous energy source (AES) with induction generator (IG) [1–5], a number of technical issues have not been fully resolved. For example, the factors influencing the conditions of guaranteed excitation of IG are still unknown. The problem of correct choice of parameters and correct design of AES determines the relevance of assessing the impact of changes in generator parameters on the quality of the self-excitation process in standard and emergency modes of operation of the IG [6, 7].

V. Chenchevoi (✉) · I. Zachepa · O. Chornyi
Department of Systems of Automatic Control and Electric Drive Kremenchuk Mykhailo, Ostrohradskyi National University Kremenchuk, Kremenchuk, Ukraine

V. Kuznetsov
Electric Power Department, Railway Research Institute, Chlopickiego str., 50, Warsaw, Poland
e-mail: vkuznetsov@ikolej.pl

O. Chencheva
Manufacturing Engineering Department, Kremenchuk Mykhailo Ostrohradskyi National University Kremenchuk, Kremenchuk, Ukraine

V. Kuznetsov
Department of the Electrical Engineering and Electromechanic, National Metallurgical Academy of Ukraine, Gagarina ave., 4, Dnipro, Ukraine
e-mail: wit1975@i.ua

R. Yatsiuk
Department of Automation and Computer-Integrated Technologies Kremenchuk Mykhailo, Ostrohradskyi National University Kremenchuk, Kremenchuk, Ukraine
e-mail: RostyslavYatsiuk@protonmail.com

O. Luhova
Department of Electric Machines and Devices Kremenchuk, Mykhailo Ostrohradskyi National University Kremenchuk, Kremenchuk, Ukraine

S. Kumar et al. (eds.), *Recent Advances in Power Electronics and Drives*, Lecture Notes in Electrical Engineering 852, https://doi.org/10.1007/978-981-16-9239-0_41

The use of a generating power plant requires solving the problem of determining the deployment time (commissioning)—to take into account the transient processes of self-excitation when changing the parameters of IG to determine the recovery time of critical infrastructure using inductive machine (IM) as IG. Also, the use of a generating power plant requires solving the problem of determining the deployment time (commissioning) after transportation to the connection point.

In power automated installations with IG, additional means are used to ensure reliable self-excitation of the generator.

The most commonly used:

- forced short-term flow of electric current through the stator winding of a stationary machine, by connecting an external power supply, or discharging the battery of charged capacitors;
- connection of pre-charged capacitors to the stator winding during machine rotation.

If the rotor is strongly demagnetized by short-circuit currents, for the occurrence of asynchronous oscillations, it is necessary to influence the IG. The impact is possible in three ways:

- to amplify the shock created by the residual induction of the rotor by short-term supply to the stator winding of a small three-phase or single-phase voltage;
- briefly increase the capacitance of the capacitor, and after setting the asyncronous mode, reduce the capacitance to the initial value;
- increase the shock from the rotor, i.e. increase the residual induction of the rotor.

In the case where it is necessary to use an external power source (for example, to power electronic control circuits), this source is also used to ensure reliable self-excitation of the IG. In wind turbines, capacitors are pre-charged from special microgenerators with permanent magnets, usually located on the axis of the aerometer. Such microgenerators charge a bank of exciting capacitors, which is disconnected from the generator at wind speeds below the lower limit of the wind turbine operating speeds. It turns on when the turbine reaches the operating speed from the operating speed limit.

To increase the residual induction of the rotor, some authors suggest placing a permanent magnet on the stator or on the rotor IG [8–12].

In the absence of additional means to ensure reliable self-excitation of the generator, the main factor that causes the process and significantly affects its course is the residual magnetism. In normal operating modes (absence of overloads and short circuits), the value of the residual magnetism flux sufficient for the generator to re-excite will always be preserved if the load is switched off first and only then the drive is switched off. In the case of emergency modes (excitation caused by overload, short circuit), the residual magnetism decreases many times, and the most unfavorable case is the excitation of the generator caused by overload. In this case, the generator is almost completely demagnetized and its re-excitation, with constant speed of rotation of the rotor and the capacity of the excitation capacitors, is impossible. More acceptable in this regard is a short circuit, after which the flux of residual magnetism decreases by almost twenty times, but in most cases its value remains sufficient for

re-excitation. In this regard, it is promising to create a system that provides reliable self-excitation of the IG [13–17].

The purpose of the work is to develop a model of IG to assess the impact of variations in generator parameters on the quality of the self-excitation process in determining the basic and limit modes of operation and the initial excitation system at constant generator parameters.

2 Research Method and Result

The speed of the generator self–excitation process depends on the capacitance of the excitation capacitors, the value of the voltage to which they are charged, as well as the number of pre–charged capacitors (in one, two or three phases).

To build these dependencies, the self-excitation process was simulated using the developed mathematical model [18–22]. An IM with a short-circuited rotor was modeled for the analysis of IG parameters. Main parameters: $P_{AG} = 2,2\,\text{kW}$; $p = 2$; $I_s = 4,9$; $n = 1430$ rpm; $\cos\phi = 0.825$; $\eta = 81\%$. The simulation results are shown in Figs. 1 and 2.

As a result of the simulation analysis, it is obvious that the rate of increase of the voltage amplitude in the process of self-excitation of the IG significantly depends on the number of phases of pre-charged capacitors. The difference in the duration of the process of self-excitation of the generator for cases where the capacitors of all phases and only one phase is pre-charged is about 200%.

This allows to limit the power of the additional power supply to the amount required to pre-charge the capacitor to only one of the phases.

Studies of the IG self-excitation process have shown that the discharge of excitation capacitors precharged from an external power supply (assuming that residual magnetism is absent and that the rotor speed is constant) provides reliable IG self-excitation.

There is a point of view that one of the reasons of excitation of IG is residual magnetization of a rotor of the car. There are different views on the degree of influence of the residual magnetic flux on self-excitation, but experiments clearly show that the residual magnetization of the rotor affects the excitation conditions: with a magnetized rotor it is easier to excite an asynchronous machine than with its complete demagnetization.

At least two causes leading to demagnetization of the rotor have been experimentally established. First, demagnetization occurs after a three-phase short circuit; secondly, demagnetization occurs after a complete stop of the asynchronous generator without prior disconnection of the excitation capacities and the load.

It was also found that after demagnetization of the rotor it is not possible to excite the IG without changing the previously applied excitation conditions. Further studies have shown that additional magnetization of the generator is required for re-excitation. As a result, it was decided to develop a system that would determine

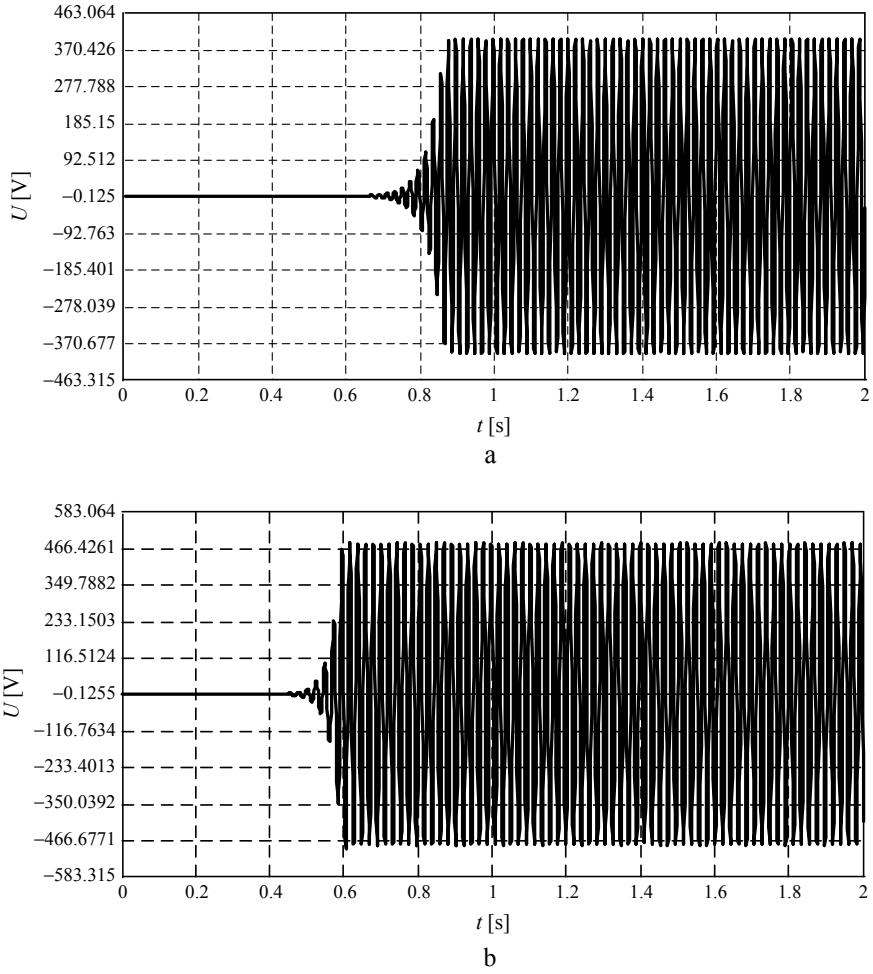

Fig. 1 Time diagrams of the generator output voltage at different excitation powers: **a** C = 100 μF; **b** C = 150 μF

the level of residual magnetization of hypertension and subsequent magnetization with an additional power supply.

As one of the possible options for implementing the system, the scheme shown in Fig. 3. Here, MD—magnetizing device; IG—induction generator; DM—drive motor; C—capacitor block; Z_w—load.

In Fig. 3, capacitor C is connected to the output of the AG generator driven by the motor DM, in each phase, parallel to the load Z_w. With an active load on consumers, the reactive power coming from the capacitors must be equal to the reactive power of the generator required to create a magnetic flux. When the generator is operating

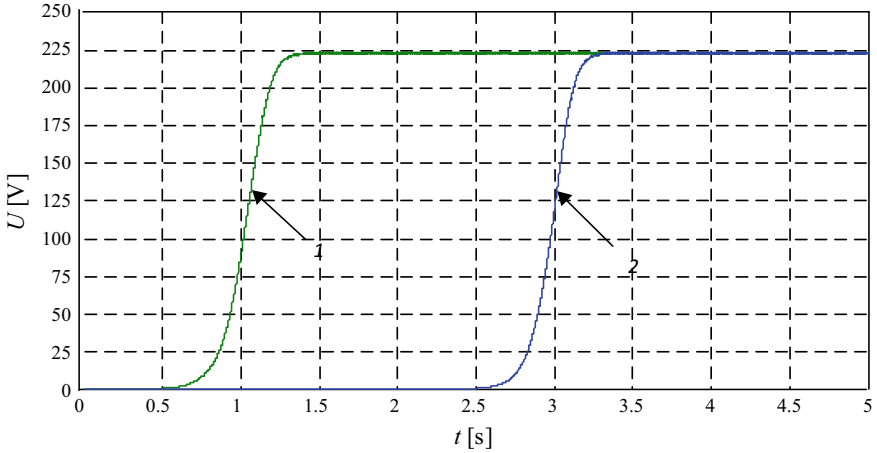

Fig. 2 Time diagrams of the effective value of the phase voltage for different voltage values of the pre-charged capacitor: 1—one of the phases; 2—all phases

Fig. 3 Block diagram of the IG magnetization system

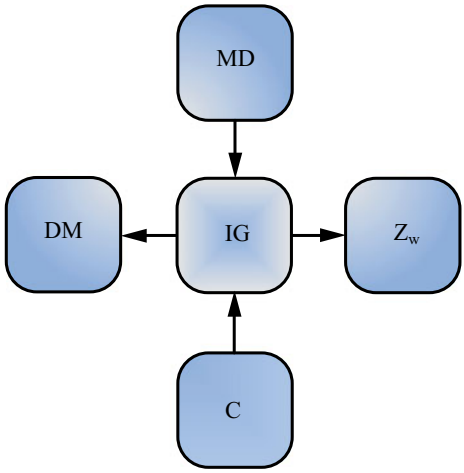

on an active-inductive load, the capacitors must compensate for the reactive power of the machine and the load.

The magnetizing device (MD) must automatically determine the level of residual magnetization (for example, monitors the residual EMF) and, if necessary, briefly connect an additional power supply (battery or capacitor) to the stator windings of the generator. In the case when the level of residual EMF is sufficient, the self-excitation of the generator will occur in the normal mode.

The source of primary energy can be both a direct current source and a pre-charged capacitor. In addition to the presented types of excitation, the source of primary energy can be a solar battery.

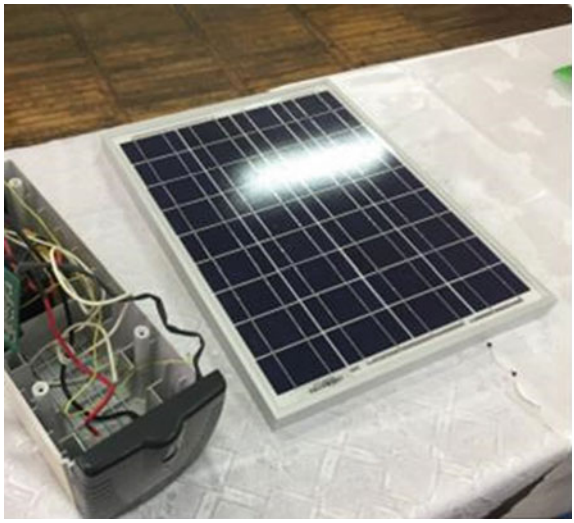

Fig. 4 AXIOMA Energy AX-30P solar module

The advantage of this method of initial excitation of an IG is.

- availability and inexhaustibility of solar radiation as a source of energy
- cost-effectiveness of the process of using photocells
- minimum level of scheduled maintenance and high reliability.

Figure 4 shows the appearance of the solar module of the AXIOMA Energy AX-30P series with a capacity of 30 kW and an output voltage of 18.3 V [23, 24].

Also Fig. 5 shows the I–V characteristics of the solar module and the dependence of the scattering power in the load on the voltage of the module for the level of illumination of the solar cell 100 W/m^2.

The system of initial excitation (Fig. 6) based on application of photoelectric elements is offered. Special converter equipment is required to match the operation of the solar power plant and the generator voltage. As such equipment the active controlled rectifier (ACR) which initial characteristics correspond to the modern standards regulating quality of the electric power is most often used.

The active controlled rectifier is a three-phase bridge on power IGBT transistors with reverse diodes, the input of which is supplied by a solar battery to a DC-DC to DC DC-DC converter. A capacitor of small capacity C1 is connected in parallel with the output of the solar battery. The output clamps of the ACR are connected to the output of the IG. The input circuit of the rectifier includes a capacitor C2, the voltage at which must be higher than the amplitude of the linear voltage of the generator. The energy generated by photocells is enough for the initial impulse of excitation of IG.

Figure 7 shows a model in the software environment Matlab, which implements the initial excitation of the IG. In this model, the generator is based on a three-phase model of an inductive machine [25–28].

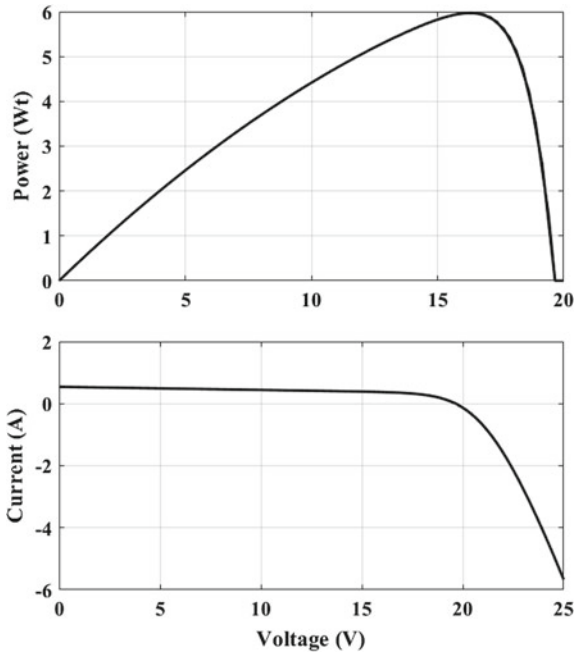

Fig. 5 I–V characteristics of the solar module

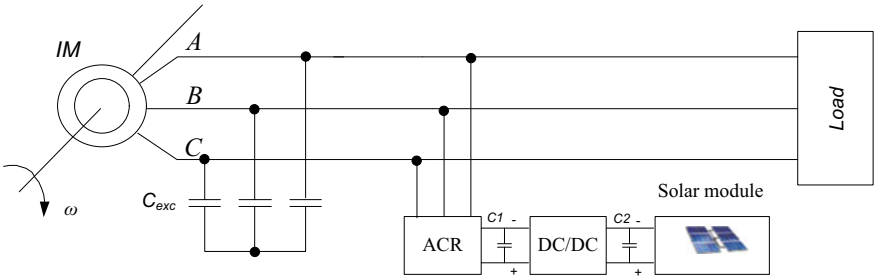

Fig. 6 Autonomous power source based on an IG with an initial excitation system based on photocells

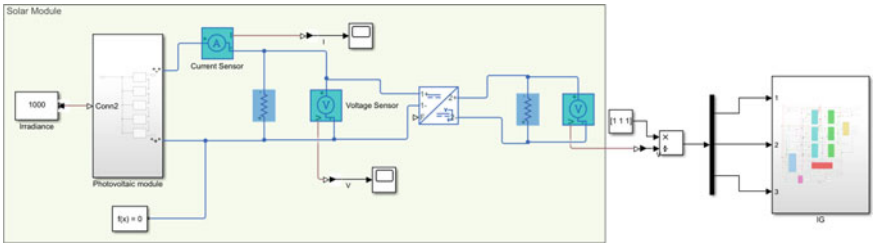

Fig. 7 Simulink model for realization of initial excitation of induction generator by means of the solar module

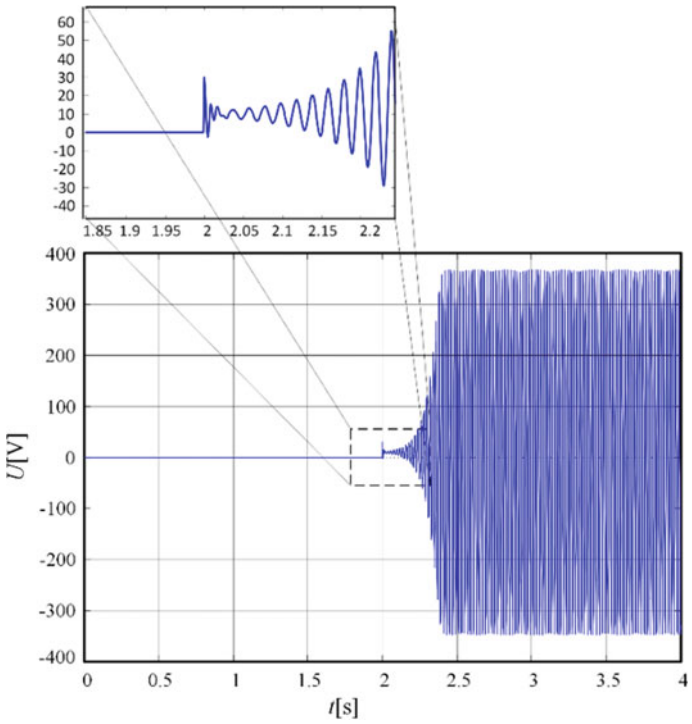

Fig. 8 Time diagram of the output voltage of the induction generator

Figure 8 presents the results of modeling the system of initial excitation of IG on the basis of photocells. Figure 9 shows the dependence of IG excitation time on the level of illumination.

As can be seen from Fig. 9 as the degree of illumination increases, the self-excitation time decreases.

The obtained result of calculating the value of the illumination level for the emergence of capacitor self-excitation can be used to estimate the parameters and requirements for the initial excitation systems capable of providing the required excitation time and conditions.

3 Conclusion

Reliable self-excitation of the generator, regardless of its magnetic state, provides a pre-charge from an external power supply of one of the phase capacitors of the disconnected battery of excitation capacitors and then connecting the whole battery to the stator winding with a rotating rotor. The intensity of self-excitation also depends on the number of pre-charged capacitors, as well as the value of the voltage to which they

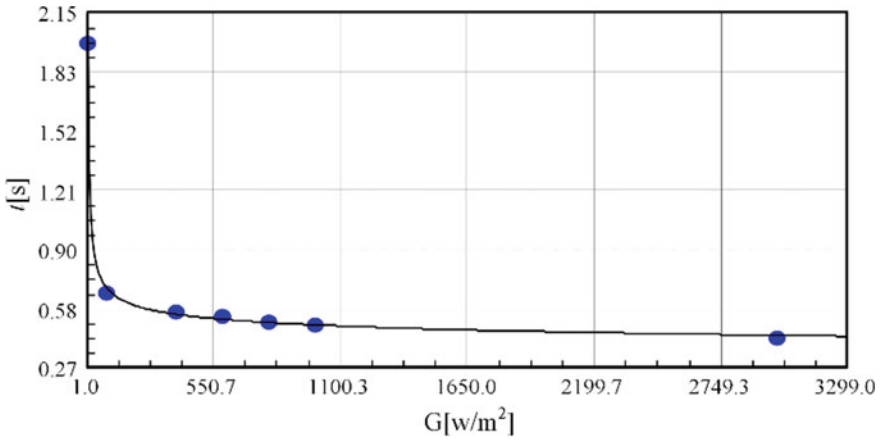

Fig. 9 Dependence of induction generator excitation time on the level of illumination

were charged. The speed of the self-excitation process only largely depends on the connection method and the polarity of the pre-charged excitation capacitors. Satisfactory results are provided by a pre-charge of a single-phase capacitor. This limits the power of the external power supply that is required to pre-charge the capacitors. The system of initial excitation based on application of photoelectric elements that allows to provide reliable self-excitation of IG in case of demagnetization of a rotor is offered. The system allows to provide additional magnetization of the generator after demagnetization of the rotor, without changing the previously applied excitation conditions.

References

1. Vieira RJ, Sliaraf AM, Elgammal A (2011) Design of self-excited induction generators for wind applications. CCECE, IEEE
2. Bansal RC (2005) Three phase self excited induction generators: an overview. IEEE Trans Energy Convers 20(2)
3. Haque MH (2009) A novel method of evaluating performance characteristics of a self-excited induction generator. IEEE Trans Energy Convers 24(2)
4. Malik NH, Al-Bahrani AH (1990) Influence of the terminal capacitor on the performance characteristics of a self excited induction generator. IEE Proceedings 137
5. Murthy SS, Malik OP, Tandon AK (1982) Analysis of self-excited induction generators. IEE Proc 129
6. Toroptsev ND (2004) Asinkhronnyye generatory dlya avtonomnykh energeticheskikh ustanovok [Asynchronous generators for autonomous power installations]. NTF Energoprogres, Moskow, 87 p (in Russian)
7. Kitsis SI (2003) Self-excited asynchronous generator. Energoatomizdat, Moskow, 328 p
8. Diao T (2015) Study on dual-rotor permanent magnet induction motor and performance. Open Electr Electron Eng J 9:584–590. https://doi.org/10.2174/1874129001509010584

9. Qu R, Lipo TA (2003) Dual-rotor, radial wound, permanent-magnet machines. IEEE Trans Ind Appl 39(6):1665–1673
10. Xu L, Zhang Y (2006) Design and evaluation of a dual mechanical port machine and system. In: IEEE 5th international power electronics and motion control conference, Shanghai, China
11. Qu R, Aydin M, Lipo TA (2003) Performance comparison of dual-rotor radial-flux and axial-flux permanent magnet BLDC machines. In: Proceedings of IEEE electric machines and drives conference, Madison, US, pp 1948–1954
12. Roy B (2017) A novel double rotor without stator electric motor: theoretical and functional aspects. J Electr Eng Sci 3(2):1–10. https://doi.org/10.18831/djeee.org/2017021001
13. Nazir R, Syafii AP, Akbar F, Arfan Y (2020) Effect analysis of residual magnetism availability level on the success of voltage generation processes in self-excited induction generators. Int J Power Electron Drive Syst (IJPEDS) 11(3):1211–1219. https://doi.org/10.11591/ijpeds.v11.i3
14. Bansal RC (2005) Three-phase self-excited induction generators: an overview. IEEE Trans Energy Convers 20(2)
15. Nazir R, Syafii AP, Akbar F, Dorinza A (2019) Differences in the impact of harmonic distortion due to the installation of electronic load controller in self-excited induction generator and synchronous generator. Int J Power Electron Drive Syst (IJPEDS) 10(1):104–116
16. Kadhum HH et al (2020) The influence of iron losses on selecting the minimum excitation capacitance for self-excited induction generator (SEIG) with wind turbine. Indonesian J Electr Eng Comput Sci 19(1):11–22
17. Zagirnyak M, Rod'kin D, Romashykhin I, Romashykhina Z, Nikolenko A (2017) Refined calculation of induction motor equivalent circuit nonlinear parameters by an energy method. Eastern-Eur J Enterprise Technol 3(87):4–10. https://doi.org/10.15587/1729-4061.2017.104146
18. I. Romashykhin NR, Kuznetsov V (2017) The possibilities of the energy method for identifying the parameters of induction motor. In: 2017 international conference on modern electrical and energy systems (MEES), Kremenchuk, Ukraine, pp 128–131. https://doi.org/10.1109/MEES.2017.8248869
19. Zagirnyak M, Zachepa Y, Chenchevoi V (2014) Estimation of induction generator overload capacity under connected direct current consumers. Acta Technica, Praga: Institute of Thermomechanics AS CR, 2014, vol. 59, № 2, pp 149–169, ISSN 0001–7043
20. Zagirnyak M, Prus V, Rodkin D, Zachepa I (2019) A refined method for the calculation of steel losses at alternating current. Arch Electr Eng 68(2):295–308
21. Zagirnyak M, Ogar V, Chenchevoi V (2014) Analysis of induction motors features taking into account change of iron properties. Acta Tech 59(1):25–47
22. Chenchevoi V, Zachepa I, Chencheva O, Yatsiuk R (2020) Parameters of guaranteed self-excitation of an induction generator for autonomous electric power sources. In: 2020 IEEE problems of automated electrodrive. Theory and Practice (PAEP) 21–25 Sept. 2020
23. Available at: https://solar-tech.com.ua/solar-electricity/solar-panels/solnechnaya-batareya-axioma-energy-ax-30p.html
24. Available at: https://alfa.solar/ru/solnechnaya-batareya-axioma-ax-10p-id734.html
25. Perdulak J, Kovac D, Kovacova I, Ocilka M, Gladyr A, Mamchur D, Zachepa I, Vince T, Molnar J (2013) Effective utilization of photovoltaic energy using multiphase boost converter in comparison with single phase boost converter. Communications 15(3):32–38
26. Yevheniia K, Vitaliy K, Mykola T, Alisa K, Maksym T, Mykola B (2019) Development and verification of dynamic electromagnetic model of asynchronous motor operating in terms of poor-quality electric power. In: 2019 IEEE international conference on modern electrical and energy systems (MEES), Kremenchuk, Ukraine, pp 350–353. https://doi.org/10.1109/MEES.2019.8896598
27. Kuzenkov O, Kuznetsov V, Tryputen N (2019) Analysis of phase trajectories of the third - order dynamic objects. In: 2019 IEEE 2nd Ukraine conference on electrical and computer engineering (UKRCON), Lviv, Ukraine, pp 1235–1243. https://doi.org/10.1109/UKRCON.2019.8879819
28. Krishnan R, Krishnan R (2010) Electric motor drives—modeling analysis and control [text]. PHI Learning Private Limited, New Delhi, pp 626

Single Phase Five Level Step-Up Switched Capacitor Based Grid Connected Inverter with LCL Filter

Aratipamula Bhanuchandar and Bhagwan K. Murthy

1 Introduction

The concept of Reduced Device Count (RDC) Multilevel Inverters (MLIs) is very popular in Renewable energy Source applications, and these produce stair case waveform with imitation of sinusoidal wave [1]. Conventionally, three types of MLIs have been reported viz., Neutral Point Clamped (NPC), Flying Capacitor (FC), and Cascaded H-Bridge (CHB). Generally for any MLI, the number of switch count, input dc sources, gate drivers, discrete diodes, capacitors, and Total Blocking Voltage (TBV/TSV) are important to decide the size of the inverter and requirement of filter size in grid connection. For generating five level output, the NPC inverter takes more number of diodes, more number of capacitors, and voltage gain becomes unity. Additionally, to balance the capacitors, separate auxiliary circuits or complex control schemes are required [2]. The number of requirement are more as compared with NPC and in this for better operation, the capacitors must be pre-charged [3]. As compared with NPC and FC, CHB MLI has higher modularity but requires more number of isolated dc sources [4]. The TBV is more in [5] for generating five level output with single dc source. Generally in most of MLIs, less TSV has been preferred for reducing the cost. The topology [6] provides five level output with single dc source and single capacitor but TBV becomes more. For generating five level output with single dc source, it takes TSV of $11V_{dc}$ [7]. The topologies [8, 11] produces TBV of 12Vdc with the same number of component count for generating five level output and separate backend H-Bridge is required in [11] for generating negative voltage levels. The topology [9] requires two dc sources with TSV of $10V_{dc}$ for generating five level output but drawback of this topology is unity voltage gain that means there is no boosting ability. For generating five level output, the topologies [10, 13] requires two capacitors and single dc source. Here, both topologies gives TSV of 14Vdc. The topology [12] gives less TBV but requires two dc sources, and there is

A. Bhanuchandar (✉) · B. K. Murthy
Electrical Engineering Department, NIT Warangal, Telangana, India

S. Kumar et al. (eds.), *Recent Advances in Power Electronics and Drives*, Lecture Notes in Electrical Engineering 852, https://doi.org/10.1007/978-981-16-9239-0_42

no boosting ability. To alleviate aforementioned problems, a new five level output inverter topology and its cascade connection have been introduced in this paper and it provides self-balancing of capacitors and boosting ability with single dc source. Conventionally, different types of modulation techniques [15, 16] are available and in this paper a new URCS has been reported in RL load case by taking reference of Nearest Level Control (NLC) technique. For higher ripple attenuation purpose, the LCL filter has been integrated with grid [14].

The rest of the paper work is organized as follows: The operation and control schemes of proposed topology have been presented in Sect. 2. In Sect. 3, the comparative study has been described. The Sect. 4 gives the simulation results for both RL load and grid connected cases. Finally, the conclusion has been presented in Sect. 5.

2 Operation of Proposed Topology and Control Schemes

A. *Operation of Proposed Inverter Topology*

The schematic of single stage PV to grid connected system, RDC of five level inverter topology with LCL filter, and cascade connection of two SC units with 1:5 source configuration have been depicted in Figs. 1, 2, and 3 respectively. In this paper, the dotted portion in Fig. 1 has been considered for grid connection. The

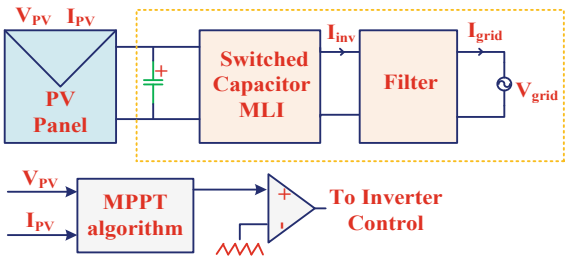

Fig. 1 Single stage PV to grid connected system

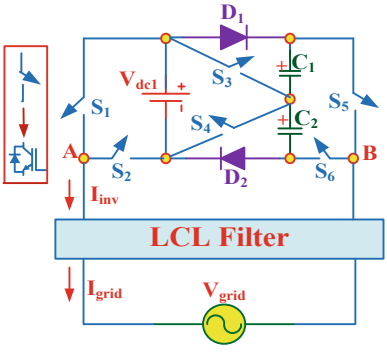

Fig. 2 Proposed five level RSC inverter topology with LCL filter

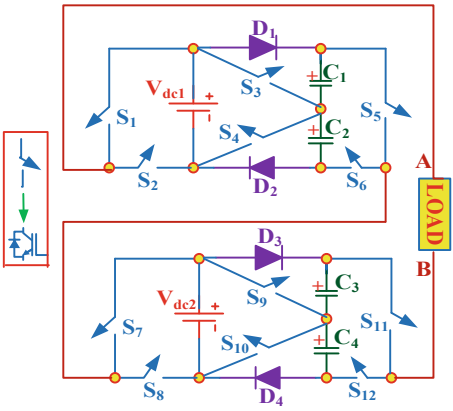

Fig. 3 Cascade connection of two SC units with 1:5. *Source* configuration 25 level O/P

Table 1 Switching arrangement-five level SC inverter

S. no	ON state switches	C_1	C_2	Level
1	$S_1 - S_4 - S_6$	C	D	$+2V_{DC}$
2	$S_1 - S_3 - S_6$	–	C	$+1V_{DC}$
3	$S_2 - S_3 - S_6$	–	C	0
4	$S_2 - S_4 - S_5$	C	–	$-1V_{DC}$
5	$S_2 - S_3 - S_5$	D	C	$-2V_{DC}$

five level inverter topology comprises six unidirectional switches, eight diodes, two switched capacitors (SCs), and one dc source. The operation of five level topology and 25 level topology have been depicted in Tables 1 and 2 respectively. Generally the capacitors are charged in parallel and discharged in series then finally with proper switching action, the capacitors have been self-balanced. From Table 1, it is concluded that this topology provides voltage boosting of two with respect to single stiff dc source. Generally, the voltage stress of each switch is indexed with TBV/TSV. In this topology, the per unit value of TBV becomes four. Based on maximum discharging period (MDP) method, it is possible to get proper switched capacitance value within permissible limits of voltage ripple. However, in this paper little more capacitance value has been considered for making successful operation of grid. As compared with L, LC filters, the LCL filter provides higher ripple attenuation but it suffers from resonance problem and finally system becomes unstable. To alleviate resonance problem, active damping method has been preferred and in this method there is no additional power losses as compared with passive damping method. The PLECS/ PSIM software are very helpful for finding switching, conduction losses of any MLI topology. Lastly, the advantages of proposed topology is that it has less TBV, boosting ability, and self-balanced capacitor with single dc source supply.

Table 2 Switching arrangement-25 level SC inverter

S_1 to S_6	C_1	C_2	S_7 to S_{12}	C_1	C_2	Level
$S_1 - S_4 - S_6$	C	D	$S_7 - S_{10} - S_{12}$	C	D	$12V_{DC}$
$S_1 - S_3 - S_6$	–	C	$S_7 - S_{10} - S_{12}$	C	D	$11V_{DC}$
$S_2 - S_3 - S_6$	–	C	$S_7 - S_{10} - S_{12}$	C	D	$10V_{DC}$
$S_2 - S_4 - S_5$	C	–	$S_7 - S_{10} - S_{12}$	C	D	$9V_{DC}$
$S_2 - S_3 - S_5$	D	C	$S_7 - S_{10} - S_{12}$	C	D	$8V_{DC}$
$S_1 - S_4 - S_6$	C	D	$S_7 - S_9 - S_{12}$	–	C	$7V_{DC}$
$S_1 - S_3 - S_6$	–	C	$S_7 - S_9 - S_{12}$	–	C	$6V_{DC}$
$S_2 - S_3 - S_6$	–	C	$S_7 - S_9 - S_{12}$	–	C	$5V_{DC}$
$S_2 - S_4 - S_5$	C	–	$S_7 - S_9 - S_{12}$	–	C	$4V_{DC}$
$S_2 - S_3 - S_5$	D	C	$S_7 - S_9 - S_{12}$	–	C	$3V_{DC}$
$S_1 - S_4 - S_6$	C	D	$S_8 - S_9 - S_{12}$	–	C	$2V_{DC}$
$S_1 - S_3 - S_6$	–	C	$S_8 - S_9 - S_{12}$	–	C	V_{DC}
$S_2 - S_3 - S_6$	–	C	$S_8 - S_9 - S_{12}$	–	C	0

B. *Proposed Control Schemes*

(i) URCS-RL load case

The new URCS has been applied to the 25 level inverter topology with RL load, and its strategy has been depicted in Fig. 4. The proposed control scheme is the modified version of NLC technique, and it is also called as Unified Rounding Control Scheme (URCS). The URCS has provides less computation time as compared with conventional NLC and SHE PWM techniques.

In this scheme, modulating signal is given to rounding function and it generates aggregated signal (AS). The Switching Table Generation (STG) is taken from Table 2. Because of truncation, there is no need of logic gate requirement for generating gate pulses (GP). This control scheme is basically fundamental switching frequency technique there by switching losses greatly reduces, and it also provides self-balancing of capacitors. It is universally applicable for any MLI topology with valid switching table.

(ii) *dq frame current control strategy-Grid Connected Case*

Fig. 4 Unified rounding control scheme-URCS

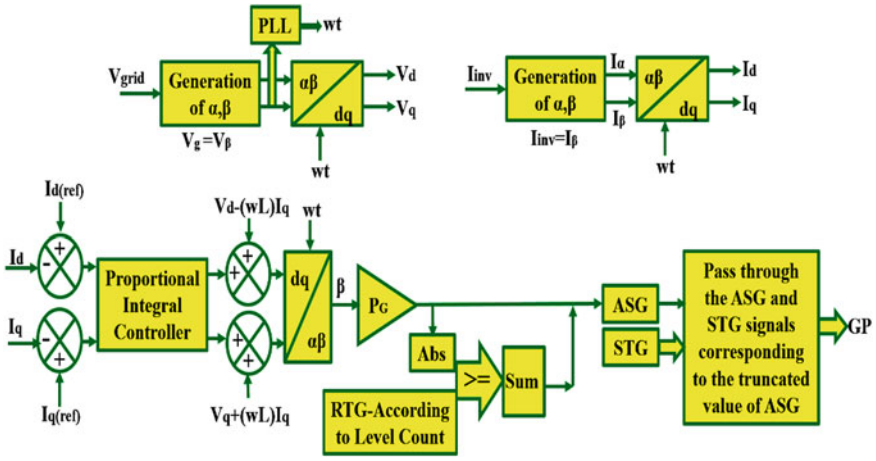

Fig. 5 Proposed dq frame current control scheme

The control strategy for five level SC inverter in grid connected case has been depicted in Fig. 5. Firstly, sense the grid voltage (let, $V_{grid} = V_\beta$) and through proper PLL, the V_d and V_q components have been generated. Here, PLL has been used to generate reference variable for grid synchronization. Similarly, the I_d and I_q components have been generated by sensing inverter current (let, $I_{inv} = I_\beta$). To inject active and reactive power into the grid, $I_{d(ref)}$ and $I_{q(ref)}$ have been used. From decoupling control strategy, the modulating β-component signal has been generated. By using Proper Gain (P_G) value, it is possible to generate desired modulating signal. By taking absolute function, it is possible to curtail the number of high frequency carriers present in Repeating Table Generation (RTG) block. After truncation of ASG and STG, the required switching pulses/gate pulses (GP) have been generated. By taking $I_{q(ref)}$ is equal to zero then it is possible to get UPF operation at grid side.

3 Comparative Study

Table 3 shows the comparative analysis with different conventional five level inverter topologies. From this table, it is concluded that proposed topology gives less TBV with single dc source supply there by the cost requirement of switches can be decreased. Generally, switch requirement reduces means respective protection circuit, gate driver circuit, and heat sink also reduces there by size of inverter can be decreases.

Table 3 Comparative analysis with different conventional five level inverter topologies

S. no	Description	[5]	[6]	[7]	[8]	[9]	[10]	[11]	[12]	[13]	P
1	N_{Levels}	5	5	5	5	5	5	5	5	5	5
2	$N_{Switches}$	12	6	6	8	6	8	8	8	10	6
3	$N_{Drivers}$	12	6	6	8	5	8	8	8	9	6
4	N_{Diodes}	12	8	7	8	6	10	8	10	10	8
5	$N_{Sources}$	1	1	1	2	2	1	2	2	1	1
6	$N_{Capacitors}$	2	1	1	0	0	2	0	0	2	2
7	TSV	20	12	11	12	10	14	12	10	14	8

4 Simulation Results

A. *RL Load Case*

Table 4 shows simulation parameters-1:5 source configuration. The URCS has been applied to the proposed cascaded topology with step change (at $t = 0.05$ s) in Modulation Index (MI) values 1 and 0.7. Figure 6 shows simulation results for 1:5 source configuration inverter with RL load. From this, the capacitors C1 & C2 are self-balanced at 50 V and C3 & C4 are self-balanced at 250 V even if step changes in MI values. With MI = 1 and 0.7, the inverter generates 25 level and 17 level outputs respectively. Figure 7 shows harmonic spectrum of 25 level inverter output voltage with MI = 1.0, and it achieves peak value of 596.6 V at 50Hz.

B. *Grid Connected Case*

Table 5 shows simulation parameters-grid connected case. The LCL filter values have been calculated from [14]. Figure 8 shows simulation results for step changes in $I_{d(ref)}$ from 20 to 10A: UPF operation mode. From Fig. 8, the capacitors C1 & C2 are self-balanced at 200 V and generates five level output then grid voltage and grid current are maintains UPF operation even step changes in $I_{d(ref).}$ By the proposed control strategy of Fig. 5, the grid current exactly reaches the peak value according to $I_{d(ref).}$ Generally, $I_{d(ref)}$ is used to inject active power into the grid. Figures 9 and 10 show harmonic spectrums of inverter output voltage and grid current with respect to $I_{d(ref)} = 20$A.

Table 4 Simulation parameters-1:5 source configuration

S. no	Parameters	Value
1	Vdc1, Vdc2	50 V, 250 V
2	Voltage gain	2
4	R	100 Ω
5	L	30 mH
6	C1 = C2	3400 μF

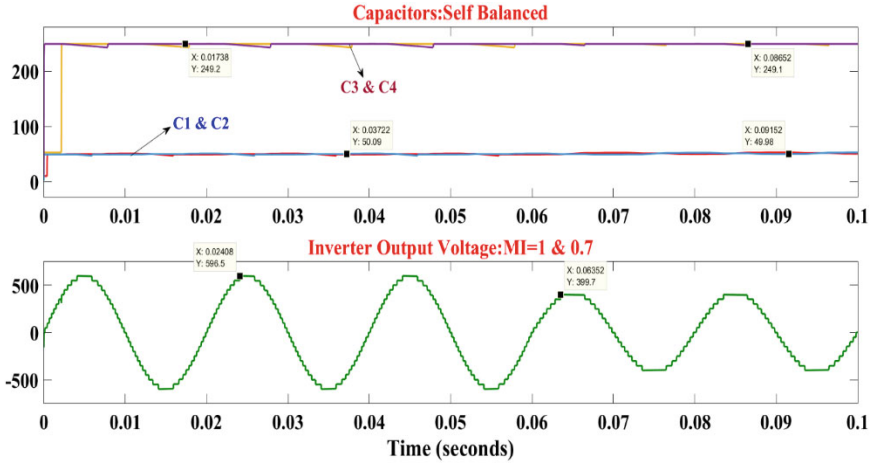

Fig. 6 Simulation results 1:5 source configuration inverter with RL loadL URCS

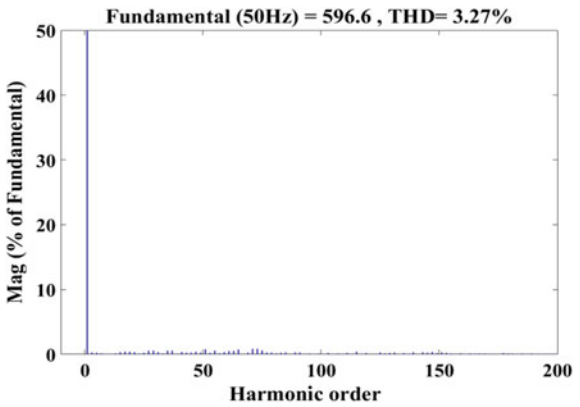

Fig. 7 Harmonic spectrum of 25-level inverter output: MI = 1.0

Table 5 Simulation parameters-grid connected case

S. no	Parameters	Value
1	Grid voltage	230 V (RMS)
2	Switching frequency	10 kHz
3	Grid frequency	50 Hz
4	Resonance frequency	1405 Hz
5	Rated power(S)	2 kVA
6	Vdc	200 V
7	Inverter side inductance	3.98 mH
8	Grid side inductance	4 mH
9	Filter capacitance	5.95 μF
10	Switched capacitors	4700 μF

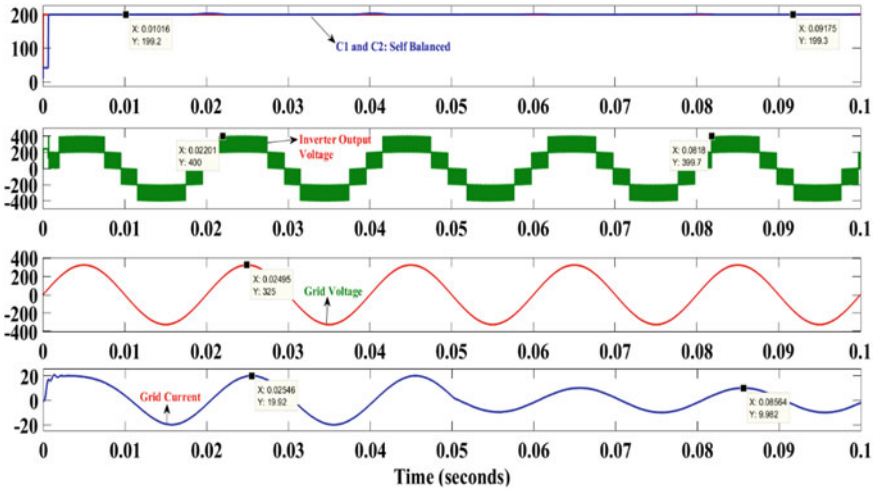

Fig. 8 Step changes in $I_{d(ref).}$: UPF operation mode

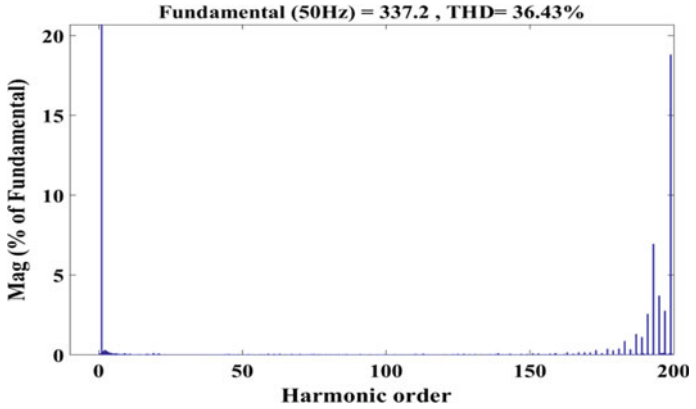

Fig. 9 Harmonic spectrum-five level output voltage

5 Conclusion

The proposed five level SC inverter topology provides four per unit TSV and voltage boosting ability of two with less number of switch count. With cascade connection of two SC units provides 25 level output and it has been elucidated with URCS. In this, the capacitors are self-balanced without need of auxiliary circuits and separate complex control schemes. A comparative study is also done with other conventional five level inverter topologies. With RL load and grid connected cases, the proposed control schemes gives good results in the output. Even if step changes in direct axis reference current values, the grid voltage and grid current still maintains UPF

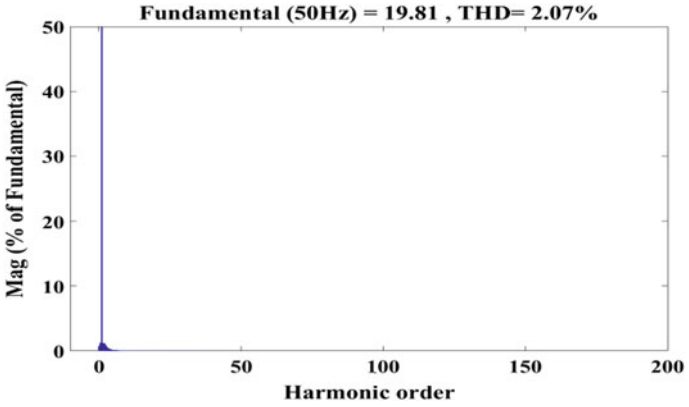

Fig. 10 Harmonic spectrum-grid current with $I_{d(ref)} = 20A$

operation. The drawback of this topology is that it has non-uniform blocking voltage across the switches. This topology is well suitable for photovoltaic and fuel cell based grid connected applications.

References

1. Rodriguez J, Lai J-S, Peng FZ (2002)Multilevel inverters: a survey of topologies, controls, and applications. IEEE Trans Indus Electron 49(4):724–738. https://doi.org/10.1109/TIE.2002.801052
2. Nabae A, Takahashi I, Akagi H (1981) A new neutral-point-clamped PWM inverter. In: IEEE Trans Indus Appl IA-17(5):518–523. https://doi.org/10.1109/TIA.1981.4503992
3. Shukla A, Ghosh A, Joshi A (2007)Capacitor voltage balancing schemes in flying capacitor multilevel inverters. In: 2007 IEEE power electronics specialists conference, Orlando, FL, USA, pp 2367–2372. https://doi.org/10.1109/PESC.2007.4342381
4. Peng FZ, Lai J-S, McKeever J, VanCoevering J (1995) A multilevel voltage-source inverter with separate DC sources for static VAr generation. In: IAS '95. Conference record of the 1995 IEEE industry applications conference thirtieth IAS annual meeting, vol 3, Orlando, FL, USA, pp 2541–2548. https://doi.org/10.1109/IAS.1995.530626
5. Cheng C, He L (2016)Flying-capacitor-clamped five-level inverter based on switched-capacitor topology. In: 2016 IEEE energy conversion congress and exposition (ECCE), Milwaukee, WI, USA, pp 1–5. https://doi.org/10.1109/ECCE.2016.785512
6. Ye Y, Cheng KWE, Liu J, Ding K (2014) A step-up switched-capacitor multilevel inverter with self-voltage balancing. IEEE Trans Indus Electron 61(12):6672–6680. https://doi.org/10.1109/TIE.2014.2314052
7. Barzegarkhoo R, Kojabadi HM, Zamiry E, Vosoughi N, Chang L (2016) Generalized structure for a single phase switched-capacitor multilevel inverter using a new multiple DC link producer with reduced number of switches. IEEE Trans Power Electron 31(8):5604–5617. https://doi.org/10.1109/TPEL.2015.2492555
8. Ruiz-Caballero DA, Ramos-Astudillo RM, Mussa SA, Heldwein ML (2010) Symmetrical hybrid multilevel DC–AC converters with reduced number of insulated DC supplies. IEEE Trans Indus Electron 57(7):2307–2314. https://doi.org/10.1109/TIE.2009.2036636

9. Hari Priya V, Sreenivasarao D, Siva Kumar G (2017) Improved pulse-width modulation scheme for T-type multilevel inverter. IET Power Electron 10(8):968–976. https://doi.org/10.1049/iet-pel.2016.0729
10. Niu D et al. (2019) A novel switched-capacitor five-level T-type inverter. In: 2019 2nd international conference on smart grid and renewable energy (SGRE), Doha, Qatar, pp 1–6. https://doi.org/10.1109/SGRE46976.2019.9021066
11. Su GJ (2005) Multilevel DC-link inverter. IEEE Trans Indus Appl 41(3):848–854. https://doi.org/10.1109/TIA.2005.847306
12. Sivakumar K (2015) A fault-tolerant single-phase five-level inverter for grid-independent PV systems. IEEE Trans Indus Electron 62(12):7569–7577. https://doi.org/10.1109/TIE.2015.2455523
13. Ranjan A, Gupta KK, Kumar L, Jain S (2012)A switched-capacitors based multilevel boost inverter with single input source. In: 2012 IEEE 5th India international conference on power electronics (IICPE), Delhi, India, pp 1–6. https://doi.org/10.1109/IICPE.2012.6450373
14. Ali A, Shanmugham P, Somkun S (2017)Single-phase grid-connected voltage source converter for LCL filter with grid-current feedback. In: 2017 international electrical engineering congress (iEECON), Pattaya, Thailand, pp 1–6. https://doi.org/10.1109/IEECON.2017.8075720
15. Rodriguez J et al (2009) Multilevel converters: an enabling technology for high-power applications. Proc IEEE 97(11):1786–1817. https://doi.org/10.1109/JPROC.2009.2030235
16. Bhanuchandar A, Murthy BK (2021) Single phase nine level switched capacitor based grid connected inverter with LCL filter. In: 2020 3rd international conference on energy, power and environment: towards clean energy technologies, pp 1–5. https://doi.org/10.1109/ICEPE50861.2021.9404491

Single Stage Multiple Source Bidirectional Converter for Electric Vehicles

Siddhant Gudhe and Sanjeev Singh

1 Introduction

With the advancement in power electronics the dependence on the non-renewable energy sources is decreasing exponentially and electric vehicles (EVs) are found to be excellent choice for utilizing the renewable energy sources. Power electronic switches are used to operate and control the EVs. Active research work is being carried out for reconfiguration of the EVs [1]. Pure EV has only the battery as active source while running therefore EVs with the two battery pack have been presented in [1] so that auxiliary loads of the EVs such as AC, lights, horns, and power windows may be operated separately. One battery is used to run traction motor, and other battery is used to supply auxiliary loads. Combination of both the batteries can also be used to supply the load during the high power requirement by the traction motor. One battery replacement by the ultra-capacitor has been reported by [2]. Battery supports high energy requirement and the Ultra-capacitor supports the instantaneous power requirement of the motor. Bidirectional power flow is also possible in Multi-Source Inverter (MSI) during regenerative operation stage of EV. The MSI for Hybrid Electric Vehicles has been presented in [3, 4]. The battery is charged through ICE using generator-rectifier and from main EV motor during regenerative mode.

The concept of using induction motor winding for charging of the EV batteries has been presented in [5] which use single phase supply as shown in Fig. 1 through the interleaved boost converter. Stator windings act as filter inductors. The single phase is supplied through all the windings of the stator and the neutral point created at the midpoint of the capacitors.

For boosting the voltage to charge Li-ion batteries, DC/DC converter has been used. The circuit has the issues variable neutral voltage and the use of DC/DC

S. Gudhe (✉) · S. Singh
Maulana Azad National Institute of Technology, Bhopal, India

S. Singh
e-mail: sschauhan@manit.ac.in

S. Kumar et al. (eds.), *Recent Advances in Power Electronics and Drives*, Lecture Notes in Electrical Engineering 852, https://doi.org/10.1007/978-981-16-9239-0_43

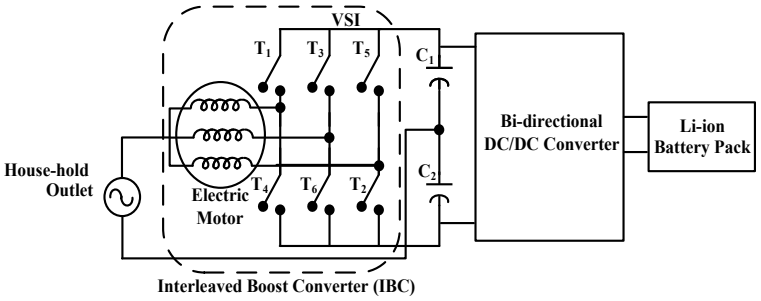

Fig. 1 Integrated charger using the stator winding of the traction motor [5]

Fig. 2 MSBC connected to stator windings and battery connections

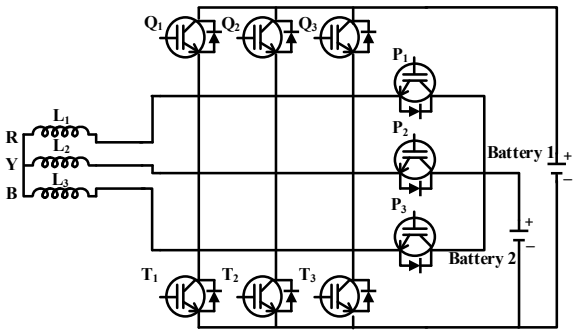

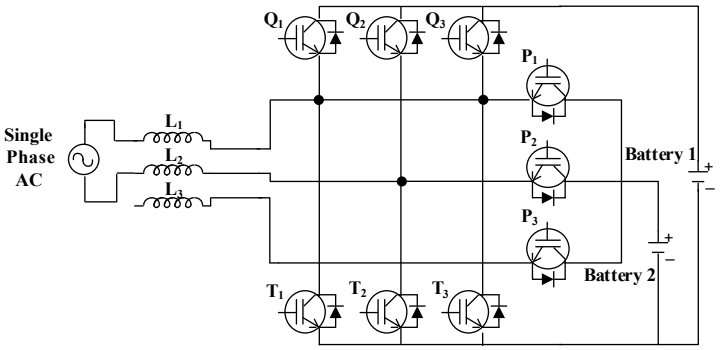

Fig. 3 Charging of batteries with single phase supply

converter. To tackle the issue of additional DC/DC converter, the inverter topology named as Multi source inverter (MSI), patented in 2014 [6], may be used.

The Multi source Inverter (MSI) gives different voltage levels using different combination of switches. The use of the battery for the reactive power compensation is also obtained using one of the two batteries [7, 8]. Boost inverter topology is used in single stage for both boosting and inverting which minimize the ripple components

which reduces the battery life [9]. But the requirement of the reactive power changes with the weather conditions. The requirement of reactive power in summer is more as compared to winter [10].

Integrated charging traction inverter supplied from single phase supply has been patented in [11] but has not been researched extensively. This paper discusses the charging of the multiples batteries using multi source bidirectional converter (MSBC). The basic concept is that this topology connects different DC sources to the single AC supply with not more than single stage of conversion. SO there is no requirement for the DC/DC converter. During traction mode MSBC can act as three level inverter and supply the appropriate voltage to the electrical motor. This power is supplied with main battery which is called as primary battery. Other loads of EV such as electronics loads and fans can be supplied with secondary battery. The voltage rating and size of the secondary battery is almost half compared to main battery. This reduces the converter complications and its control algorithm. Level 1 charger has been used for charging through IM. The simulation to verify the single phase charging of MSBC in MATLAB/Simulink environment has also been presented.

The paper is organized as follows. Operation principle of MSBC, Performance Simulation of proposed MSBC topology, and conclusion are described in the Sects. 2–4.

2 Operation Principle of Multi-Source Bidirectional Converter

Figure 2 shows the diagram for MSBC with battery connection. RYB phase is connected to the stator of the induction motor. Source inductance is represented by L_1, L_2, and L_3. Two batteries are connected in particular configuration. Battery 1 is main battery which is used for supply to induction motor during motoring operation. Battery 2 is auxiliary battery to supply other applications of the EVs. Battery 1 is selected with the voltage rating approximately twice as compared to battery 1 voltage rating. Q_1, Q_2, and Q_3 are the IGBT switches along with the anti-parallel diode at the upper leg. T_1, T_2, and T_3 form the lower leg switches. Similarly switch P_1, P_2, andP_3 forms middle leg.

During charging mode, single phase supply is supplied through any two stator windings L_1, L_2, and L_3. Figure 3 shows the complete charging of both the batteries along with all the switches. Single phase power is supplied through L_1 and L_2 windings. Battery 1 will charge through upper and lower leg switches. Battery 2 will charge through middle leg and lower leg switches. Lower leg switches T1, T2, and T3 forms the common negative path for both the batteries. During discharging mode, winding connection is rearranged through to make stator windings in star connection. The stator windings now will produce rotating magnetic field for the induction motor. During positive half cycle, battery 1 will charge through Q_1-T_2. Battery 2 charges through P_1-T_2 while Q_3, T_3, P_3 will be always off. Similarly during negative half

cycle, Q_2-T_1 charges battery 1 and P_2-T_1 charges battery 2. Voltage across battery 1 is V1, and Voltage across battery 2 is V2.

Figures 4 and 5 show the voltage waveforms during discharging of battery 1 and battery 2. Battery 1 will discharge through Q_1, Q_2, and Q_3, while T_1, T_2, T_3. P_1, P_2, and P_3 remains open. Battery 2 will discharge through P_1, P_2, and P_3, while T_1, T_2, T_3. Q_1, Q_2, and Q_3 remains open. The discussion for the waveforms for the battery 1 discharging is completed while Fig. 1 holds true circuit while discharging with single battery 1 connected in circuit.

Let Q_1-T_2-T_3 are conducting initially, line voltage V_{RY} will be positive, phase Y and B will be short circuited, so the line voltage will be zero and line voltage V_{BR} will have negative voltage. After 60 degrees, T_2 is switched off and the complementary switch Q_2 of the same leg is turned on. So the switches conducting are Q_1-T_2-T_3 for next 60 degrees. Now the Phase R and Y will be short circuited, line voltage V_{YB} will be positive and line voltage V_{BR} will be negative.

Then after again 60 degrees, Q_1 is switched off and complementary switch T1 will be turned on. Similar switching pattern will be followed, and output line voltage as shown in Fig. 4 is obtained. It should be noted that each switch conducts for the period of 180 degrees and turned on at 60 degree interval. Similar switching pattern is obtained for battery 2 but the voltage is called V2, along with the middle and lower leg switches.

When both the batteries are discharging simultaneously, the waveforms and switching pattern obtained is shown in Fig. 5. For this operation, all the lower leg switches T_1, T_2, and T_3 shall remain open. The switching sequence is shown in waveforms. The maximum voltage obtained when both the batteries are operating simultaneously will be difference of both the voltage (V1-V2). Applying similar switching pattern logic, the output line voltage waveforms can be obtained. Obviously, the maximum voltage obtained during this mode will be less than the required

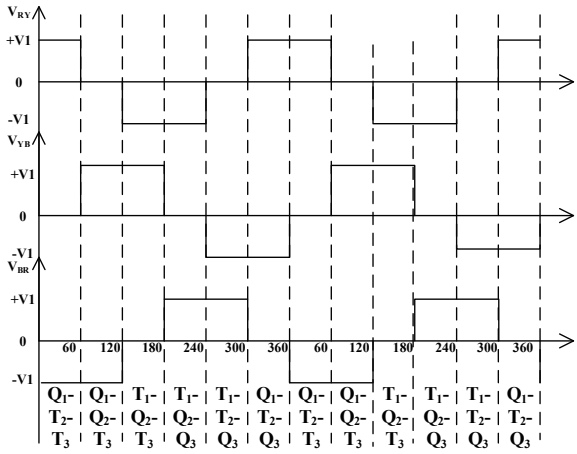

Fig. 4 Voltage waveforms during discharging of Battery 1

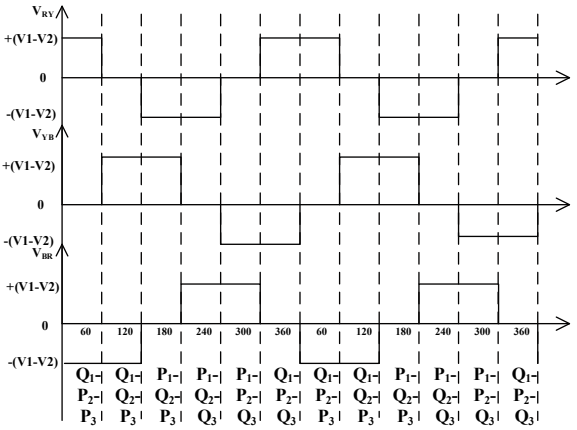

Fig. 5 Voltage waveforms during discharging of Battery 1 and Battery 2 simultaneously

by induction motor. So, for EV application, only battery 1 is specially serving the voltage required by induction motor and battery 2 is used for other application.

The similar charging and discharging principle as presented above is applied this MSBC topology. The charging is provided through any two of the three phase winding L1, L2, and L3. Battery 1 is discharged through the MSBC to create the output voltage similar to the three-level inverter. Figure 6 presents the presented 3 level MSBC for running of the EV traction motor. The stator windings are connected in star to create rotating magnetic field in the induction motor.

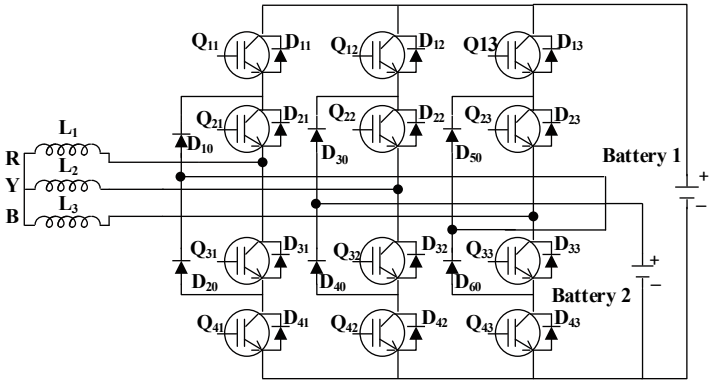

Fig. 6 Discharge of Battery 1 and Battery 2 through MSBC

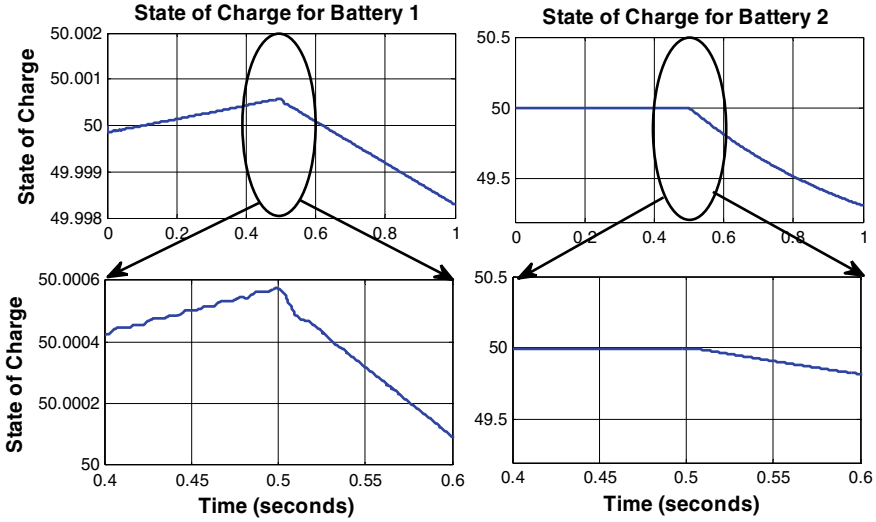

Fig. 7 State of charge during charging and discharging

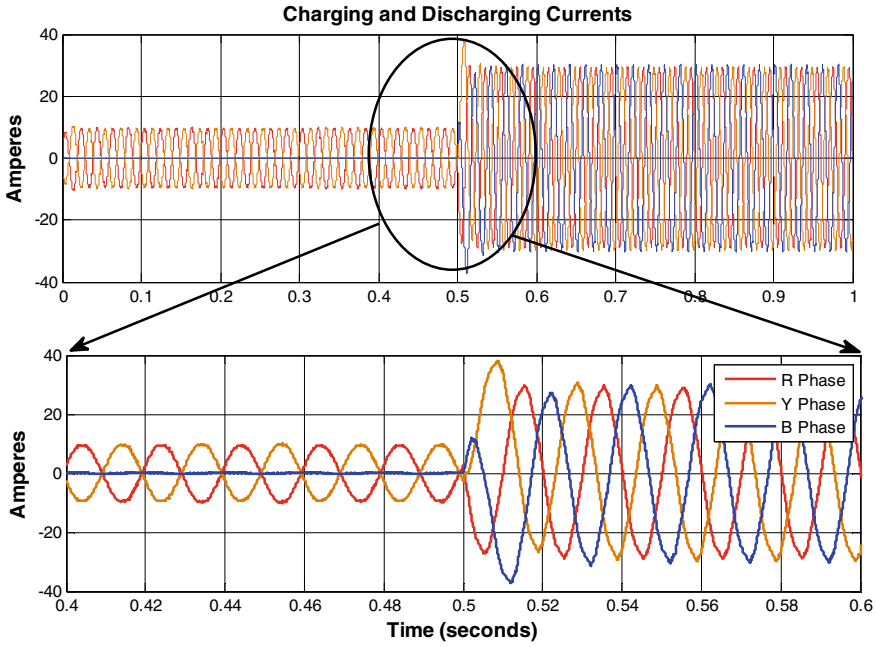

Fig. 8 Current during charging and discharging

3 Performance Simulation of Proposed MSBC Topology

The three-level MSBC is modeled in the MATLAB/Simulink environment. The three phase stator winding are created using RL load with the value of R = 0.435 Ω and L = 4 mH which are the real life values of the 33 Hp, 400 V induction motor. During the battery discharging mode, the load is connected in star to create the rotating magnetic field for the induction motor. Main battery is called as battery 1, and auxiliary battery is called as battery 2. Both the batteries are charged up to 0.5 s and then suddenly discharged till 1 s. Figure 7 shows the simulated performance while charging and discharging state of charge (SOC) of both the batteries. Battery 2 is charging at the slower rate as compared to the battery 1. Battery 1 is discharged through RL load, and battery 2 is discharged to small DC motor.

The current during charging and discharging is shown in Fig. 8. During charging the third leg current is zero because only two legs are used for charging of both the batteries while MSBC acts as a rectifier. During discharging, all the three legs of MSBC, RL load is connected in star configuration. It is also important to observe voltage across and current through the switches. During charging the current through the switches Q_{13}, Q_{23}, Q_{33}, and Q_{43} is zero. Rest all the switches show the current flowing through it. For the verification, the current through switch Q_{11} and voltage across switch Q_{12} waveform for one cycle is shown in Fig. 9. It is important to note that the voltage across and current through the switches does not exceed the rated value. The voltage across the diode shows the similar results. These diodes are called

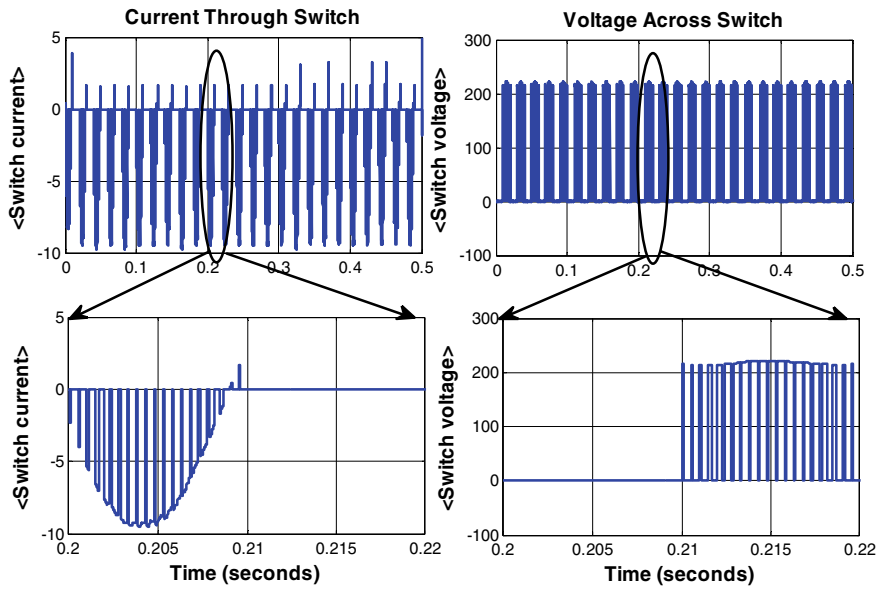

Fig. 9 Current through switch Q_{11} and voltage across switch Q_{12}

as clamping diode, and the above topology is known as Neutral Point Clamped (NPC) topology of the multi-level inverter. Space vector modulation control technique is used during discharging of the batteries, i.e., operation of induction motor for EV.

4 Conclusion

This paper has presented a novel charging method for the two batteries using MSBC. Battery 1 is used to run the traction (induction) motor, and battery 2 has been connected to run a DC motor as an auxiliary load. The charged batteries are used to run induction motor through this MSBC for EV applications.

MATLAB/Simulink results have been presented to validate the proposed concept. The MSBC utilizes battery 1 directly to run induction motor without any additional DC-DC converters. This decreases the magnetic in the electric vehicle. The losses and controlling complexity is reduced. It is concluded that this MSBC shall be useful for new and improved range of EVs.

References

1. Majid P, Jain P (2020) Soft-switching power electronics technology for electric vehicles: a technology review. IEEE J Emerg Select Topics Ind Electron 1(1):80–90
2. Salari O, Nouri M, Zaad KH, Bakshai A, Jain P (2018) A multi-source inverter for electric drive vehicles. In: 2018 IEEE Energy Conversion Congress and Exposition (ECCE)
3. Dorn-Gomba L, Magne P, Danen B, Emadi A (2018) On the concept of the multi-source inverter for hybrid electric vehicle powertrains. IEEE Trans Power Electron 33(9):7376–7386
4. Dorn-Gomba L, Guo J, Emadi A (2019) Multi-source inverter for power-split hybrid electric powertrains. IEEE Trans Veh Technol 68(7):6481–6494
5. Gupta J, Maurya R, Arya S (2020) Improved power quality on-board integrated charger with reduced switching stress. IEEE Trans Power Electron 35(10):10810–10820
6. Emadi A, MAgne P (2014) Power-converter, Patent U.S. 011770 AI
7. Buddika D, Abeywardana W, Acuna P, Hredzak B, Aguilera R (2018) Single-phase boost inverter-based electric vehicle charger with integrated vehicle to grid reactive power compensation. IEEE Trans Power Electron 33(4):3462–3471
8. Sousa T, Hashemi S, Andersen P (2019) Raising the potential of a local market for the reactive power provision by electric vehicles in distribution grids. IET Gener Transm Distrib 13(12):2446–2454
9. Janabi A, Wang B (2020) Switched-capacitor voltage boost converter for electric and hybrid electric vehicle drive. IEEE Trans Power Electron 35(6):5615–5624
10. Yilmaz M, Krein PT (2013) Review of the impact of vehicle-to-grid technologies on distribution systems and utility interfaces. IEEE Trans Power Electron 28(12):5673–5689
11. Rippel WE (1990) Integrated traction inverter and battery charger apparatus, U.S. Patent 4 920 475

Indirect Current Vector Controlled Three-Level Inverter for Induction Motor Driven Electric Vehicle

Paramjeet Singh Jamwal, Sanjeev Singh, and Shailendra Jain

1 Introduction

Electric vehicles (EVs) have number of advantages like good dynamic behavior, higher efficiency, reduced emission, and sustainable alternative but faces number of key issues like short driving range, long charging time, and reduced (passenger and cargo) space [1–3]. Short driving range issue can be resolved by improving the efficiency of battery, inverter, and electric motor of EVs.

Induction motor (IM), permanent magnet (PM) motor, and switched reluctance motor (SRM) are three suitable option of electric motor for EV application as reported in [2, 4]. SRM needs more research for its noise and vibration free operation in EV application. PM motors are facing high-cost issues because of costly rare earth magnet material. IM specially squirrel cage motor has poor efficiency, but still, it is a strong competitor of PM motors and finds application in EVs due to brushless construction and low cost.

Most EVs have two-level inverters (2LIs) for the conversion of battery power to electric motor power. 2LI suffers with the problem like high voltage stress, current stress, voltage total harmonic distortion (THD_v), and current total harmonic distortion (THD_i). To mitigate the issues with 2LIs, an inductor-capacitor (LC) filter is used [5]. Multilevel inverters (MLIs) are giving promising results to resolve the issues faced with 2LIs [6]. Chang et al., has reported [7] the benefits of cascaded h-bridge (CHB) MLI with Si MOSFET switch, over 2LI with IGBT and SiC MOSFET switch. Kersten et al. has reported [8] the benefits of active neutral point clamped three-level

P. S. Jamwal (✉) · S. Jain
Sant Longowal Institute of Engineering and Technology, Longowal, Sangrur, Punjab, India
e-mail: paramjeet_pei1803@sliet.ac.in

S. Singh
Maulana Azad National Institute of Technology, Bhopal, Madhya Pradesh, India
e-mail: sschauhan@manit.ac.in

S. Kumar et al. (eds.), *Recent Advances in Power Electronics and Drives*, Lecture Notes in Electrical Engineering 852, https://doi.org/10.1007/978-981-16-9239-0_44

inverter (NPC-3LI) with MOSFET switch, over 2LI. Guan et al. has reported [9] the loop construction method to provide high frequency isolation in NPC-3LI.

Scalar and vector controls are the two most common schemes to obtain variable speed with IM [10]. Scalar control scheme is easy to implement and has good steady state performance but shows poor dynamic performance. Jamwal et al. has reported [11] the scalar control scheme to generate the switching sequence and operate the switches of CHB-3LI and NPC-3LI for IM drive (IMD). Vector control (VC) is difficult to implement but has good dynamic and steady state performance which suits best for EV application. VC is categorized as direct vector control (DVC) also known as direct field-oriented control (DFOC), indirect vector control (IVC) also known as indirect field-oriented control (IFOC) and direct torque control (DTC) on the basis of magnetic field sensing [12]. In DTC, there is requirement of flux and torque measurement of IM to calculate the field angle [13]. Adigintla and Aware have reported [14] the fractional order proportional-integral controller-based DTC scheme for IMD. In DVC, there is requirement of flux measurement of IM to calculate the field angle, while in IVC, field angle is estimated from voltage or current measurements [15]. Kakodia and Dynamina have reported [16] the comparison of DVC and IVC scheme to generate the switching sequence and operate the switch of NPC-3LI for IMD. IVC is further categorized as indirect voltage vector control (IVVC) and indirect current vector control (ICVC). Nair and Barai have reported [17] the IVVC scheme with space vector modulation (SVM). Krishnatheeram et al. [18] presented the IVVC scheme with continuous SVM and discontinuous SVM in which reference voltage is used to generate the switching sequence and operate the switch of NPC-3LI for IMD.

In this paper, the ICVC scheme in which reference current is used to generate the switching sequence and operate the switch of CHB-3LI and NPC-3LI are used to drive IM for EV application and performance is compared with 2LI. The paper is divided in five major parts. The basic research reported for EVs has been described in the first section. Inverter topology with description is presented in second section. MATLAB Simulink logic of ICVC scheme is described in third section. Performance simulation with discussion is presented in fourth section. Conclusion drawn from the research work is given in fifth section.

2 The Indirect Current Vector Controlled Scheme Fed IMD

The basic block diagram of ICVC scheme for the operation of inverter fed IMD is given in Fig. 1. The control scheme begins with the rotor speed (ω_r) measurement of IM. This measured rotor speed is fed to reference rotor flux generator to estimate rotor flux reference (λ_r). This measured speed is also compared with reference speed to obtain speed error (ω_e).

This speed error is fed to reference torque generator for the estimation of electromagnetic torque reference (T_e). On the basis of estimated electromagnetic torque reference, rotor flux reference, and measured rotor speed, vector controller generates

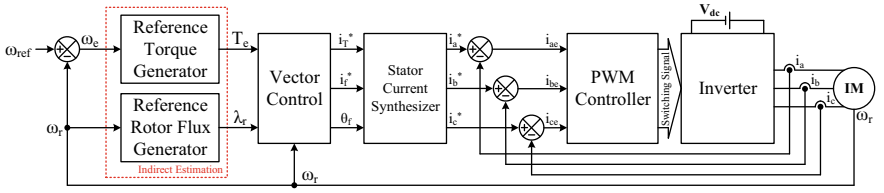

Fig. 1 Block diagram of ICVC scheme operated inverter fed IM

reference torque current (i_T^*), reference field current (i_f^*), and field angle (θ_f) which is fed to stator current synthesizer to generate three-phase reference current (i_a^*, i_b^*, i_c^*). This three-phase reference current is compared with measured three-phase motor current (i_a, i_b, i_c) to obtain error in three-phase current (i_{ae}, i_{be}, i_{ce}). On the basis of three-phase current error, PWM controller generate the switching signal to operate the 2LI as given in Fig. 2a, CHB-3LI as given in Fig. 2b, and NPC-3LI as given in Fig. 2c.

3 The Indirect Current Vector Controller

The logic used for indirect current vector controller is shown below in Fig. 3, as created in MATLAB Simulink.

The indirect current vector control scheme begins with the generation of rotor flux reference from rotor speed. When the rotor speed is between -1430 to 1430 rpm, rotor reference flux generator produces constant rotor flux of 0.85 value. When the speed is greater than 1430 rpm, reference rotor flux generator produces rotor flux of 0.85*(1430/ω_r) value. When the speed is less than −1430 rpm, reference rotor flux generator gives rotor flux of 0.85*(−1430/ω_r) value. Reference torque generator consists of proportional-integral (PI) controller and gain of 9000 value which generates reference electromagnetic torque from speed error. The value of proportional gain (K_p) and integral gain (K_i) is calculated with Ziegler–Nichols method as reported in [19]. These reference rotor flux, reference electromagnetic torque and sensed rotor speed values are fed to vector controller (Eqs. 1–4) which generates reference torque current (i_T^* or iT_ref), reference field current (i_f^* or if_ref), and field angle (θ_f or theta_f).

$$i_T^* = \frac{T_e^*}{\lambda_r^*}\frac{L_r}{L_m}\frac{2}{3}\frac{2}{P} \tag{1}$$

$$i_f^* = \left(1 + p\frac{L_r}{R_r}\right)\frac{\lambda_r^*}{L_m} \tag{2}$$

$$\omega_{sl}^* = \frac{L_m \cdot R_r}{L_r} \cdot \frac{i_T^*}{\lambda_r^*} \tag{3}$$

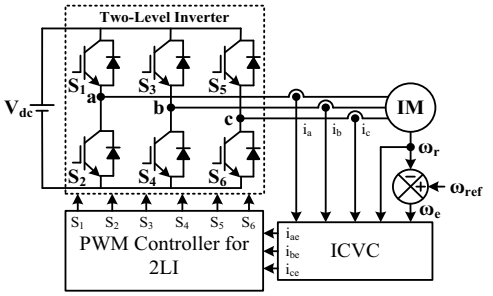

(a) ICVC operated 2LI fed IM.

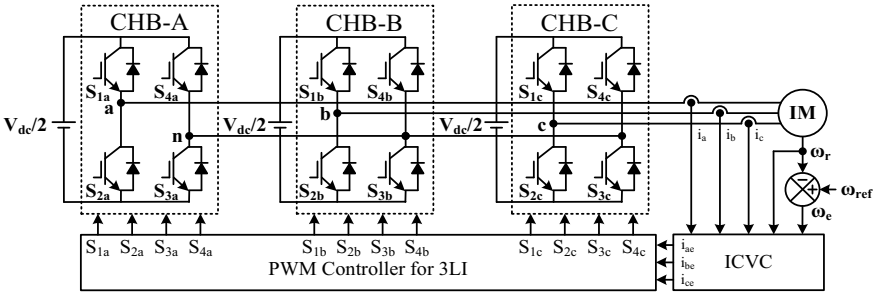

(b) ICVC operated CHB-3LI fed IM.

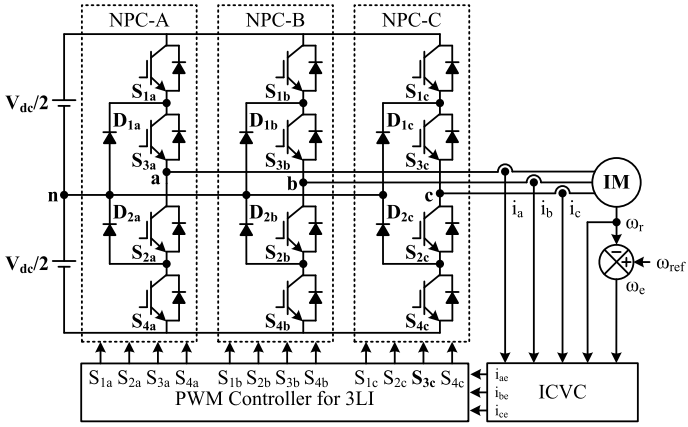

(c) ICVC operated NPC-3LI fed IM.

Fig. 2 Schematic diagram of various topologies for IMD

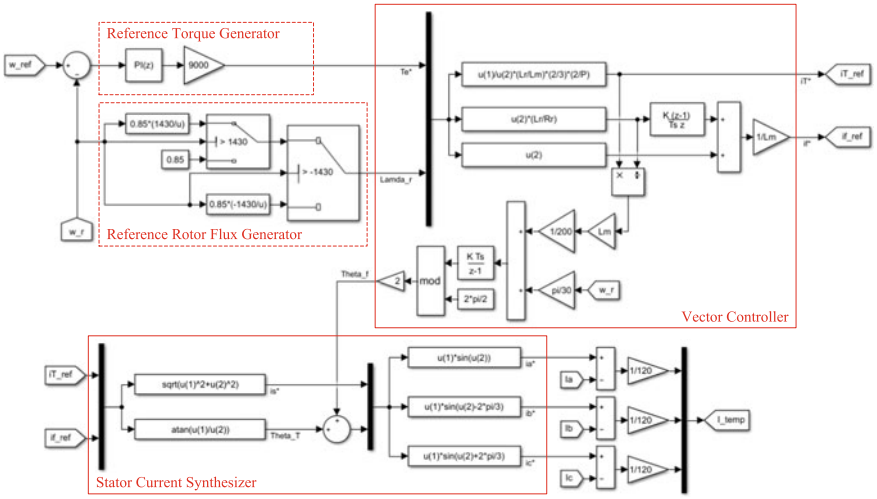

Fig. 3 Logic of ICV controller in MATLAB Simulink

$$\theta_f^* = \int \left(\omega_r + \omega_{sl}^*\right) dt \tag{4}$$

These reference torque current, reference field current, and field angle values are fed to stator current synthesizer which generate three-phase reference currents (i_a^*, i_b^*, i_c^*), which are compared with sensed three-phase currents (i_a, i_b, i_c) to generate current error (i_{ae}, i_{be}, i_{ce}). This current error is divided by a constant (120) to generate unit three-phase current template (I_temp). This unit current template is fed to pulse width modulation (PWM) controller to generate switching sequence and operate the switches of 2LI and 3LIs of IMD [20]. Parameters used in the logic of ICV controller is given in Table 1.

Table 1 ICV controller parameters

Variable	Parameter	Value
Kp	Proportional gain	0.003
Ki	Integral gain	0.04
Lr	Rotor inductance (H)	0.005839
Lm	Mutual inductance (H)	0.1722
P	Number of Poles	4

4 Performance Simulation

The presented ICVC scheme fed IMD are modeled in MATLAB-SIMULINK environment for performance simulation of the complete drive for EV application. Speed-THDv characteristics at 85, 100, and 105% torque with 2LI and 3LIs are obtained and shown in Fig. 4. These torque values are selected to realize the real time loading of the EV as curb weight (80%) of the vehicle with one passenger (5%), with four passengers (20%) and with five passengers (25%). The speed variation has been considered from standstill to rated speed.

From speed-THDv characteristics it is observed that THDv is lesser with both 3LIs as compared with 2LI at all three torques. Speed-Efficiency characteristics at 85, 100, and 105% torque with 2LI and 3LIs is given in Fig. 5.

From speed-efficiency characteristics of IM it is clear that efficiency of IM is better with both 3LIs as compared with 2LI at 85% torque. While efficiency of IM is better with CHB-3LI and same with NPC-3LI as compared with 2LI at 100% torque. Efficiency is same with 3LIs and 2LI at 105% torque. Speed-PF characteristics at 85, 100, and 105% torque with 2LI and 3LIs is given in Fig. 6.

From speed-PF characteristics of inverters it is clear that PF is better with both 3LIs except at 75% speed as compared with 2LI at 85% torque. PF is better with both

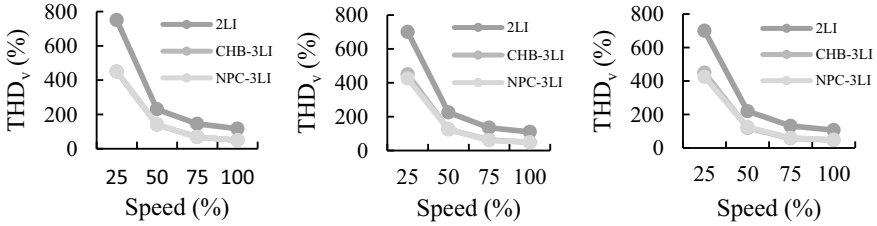

(a) 85% Torque (b) 100% Torque (c) 105% Torque

Fig. 4 Speed-THD_v characteristics of inverters

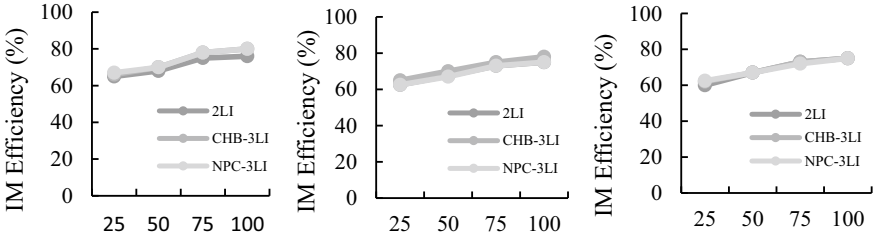

(a) 85% Torque (b) 100% Torque (c) 105% Torque

Fig. 5 Speed-efficiency characteristics of IM

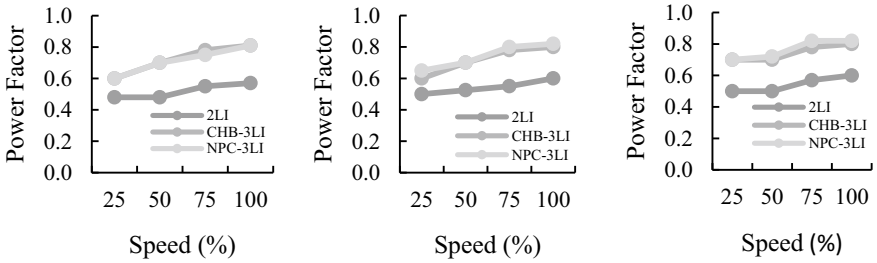

(a) 85% Torque (b) 100% Torque (c) 105% Torque

Fig. 6 Speed-PF characteristics of inverters

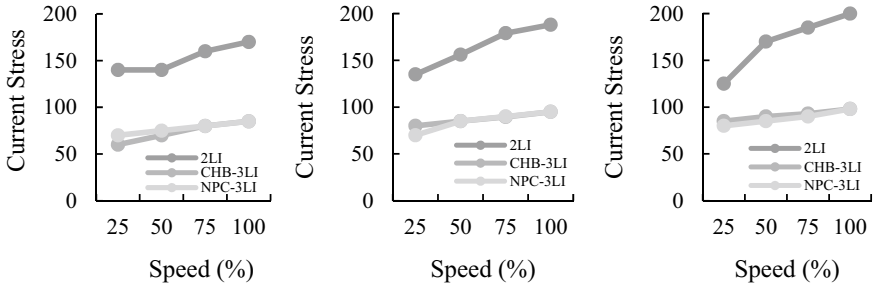

(a) 85% Torque (b) 100% Torque (c) 105% Torque

Fig. 7 Speed-current stress characteristics of inverters

3LIs as compared with 2LI at 100% and 105% torque while PF is better with NPC-3LI as compared with CHB-3LI at 100% and 105% torque. Speed-Current Stress characteristics at 85, 100, and 105% torque with 2LI and 3LIs is given in Fig. 7.

From speed-current stress characteristics of inverters it is clear that current stress (kA/sec) through switch is lesser with both 3LIs as compared with 2LI at 85, 100, and 105% torque. Current stress is lesser with CHB-3LI as compared with NPC-3LI at 85% torque. While current stress is lesser with NPC-3LI as compared with CHB-3LI at 100% and 105% torque. Voltage stress bar graph with 2LI and 3LIs is given in Fig. 8.

From voltage stress bar graph of inverters, it is clear that voltage stress (kV/sec) across the switch is lesser with both 3LIs as compared with 2LI. Line voltage, line current, rotor speed, and electromagnetic torque performance of 2LI fed IMD system, CHB-3LI fed IMD system, and NPC-3LI fed IMD system is given in Fig. 9a, b, and c respectively.

From the speed performance it is clear that ICVC operated 2LI and 3LI fed IMD system is able to follow reference speed at 100% speed, 75% speed, 50% speed, and 25% speed. From the torque performance it is clear that there is reduction in torque ripples with both 3LIs as compared to 2LI fed IMD system.

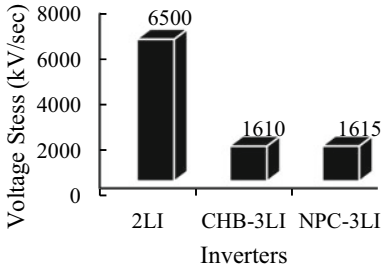

Fig. 8 Voltage stress bar graph of inverters

From the performance simulation results, it is observed that the three level inverters improve the overall performance of the system along with efficiency, thereby, increasing the range of the electric vehicle which is one of the key requirements at present.

5 Conclusions

This paper has presented an indirect current vector controlled three-level inverter for induction motor drive fed electric vehicle with a focus on efficiency and range improvement. The performance of two commonly used topologies i.e., CHB-3LI and NPC-3LI have been compared with 2LI fed IMD system for EV application. The presented performance has demonstrated reduction in total harmonic distortion of inverter output voltage and voltage stress through switch of inverter with both CHB-3LI and NPC-3LI. There is considerable improvement in efficiency of IM with CHB-3LI as compared to NPC-3LI. The improvement in power factor of inverter output with NPC-3LI is more as compared to CHB-3LI. The cost is also low for the squirrel cage Induction motor and the indirect vector control is implementable on low-cost digital signal processors. This shall result in a low cost, efficient and improved range complete drive for induction motor based EVs. It is concluded that NPC-3LI have better performance as compared to CHB-3LI fed IMD system for EV application.

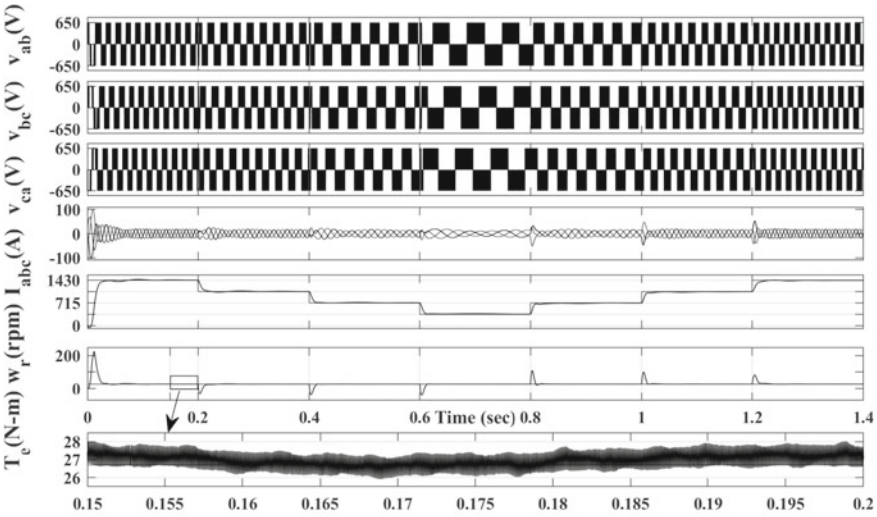

(a) Performance with 2LI fed IMD system.

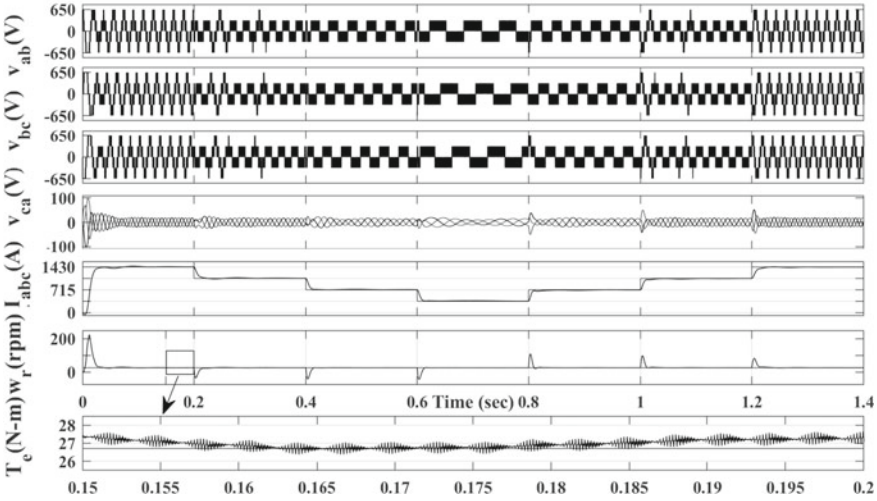

(b) Performance with CHB-3LI fed IMD system.

Fig. 9 Line voltage, line current, rotor speed and electromagnetic torque

Appendix

Battery Voltage (Vdc): 645 V, Frequency: 50 Hz, Friction Factor: 0.002985 N-m-s, Inertia: 0.0131 kg-m^2, Line Voltage: 400 V, Motor Power: 4 kW, Motor Speed: 1430 rpm or 149.75 rad/sec, Motor Torque: 26.71 Nm, Rotor Resistance: 1.395 Ω, and Stator Resistance: 1.405 Ω.

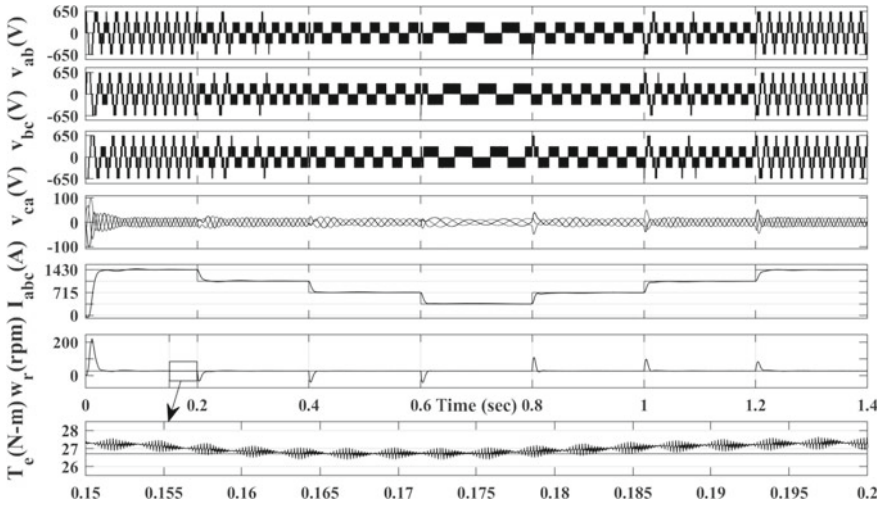

(c) Performance with NPC-3LI fed IMD system.

Fig. 9 (continued)

References

1. Nicoletti L, Brönner M, Danquah B, Koch A, König A, Krapf S, Pathak A, Schockenhoff F, Sethuraman G, Wolff S, Lienkamp M (2020) Review of trends and potentials in the vehicle concept development process. In: 2020 IEEE fifteenth international conference on ecological vehicles and renewable energies (EVER), Monte-Carlo, Monaco
2. Chan CC, Bouscayrol A, Chen K (2010) Electric, hybrid, and fuel-cell vehicles architectures and modeling. In: IEEE Trans Vehicular Technol 59(2):589–598
3. Jain S, Kumar L (2018) Fundamentals of power electronics controlled electric propulsion. In: Rashid MH (eds) Power electronics handbook (4th ed) Butterworth-Heinemann an imprint of Elsevier, pp 1023–1065
4. Rind SJ, Ren Y, Hu Y, Wang J, Jiang L (2017) Configurations and control of traction motors for electric vehicles—a review. Chinese J Elect Eng 3(3):1–17
5. Mishra P, Maheshwari R (2019) Design analysis and impacts of sinusoidal LC filter on pulse width modulated inverter fed induction motor drive. IEEE Trans Ind Electron 67(4):2678–2688
6. Poorfakhraei A, Narimani M, Emadi A (2021) A review of modulation and control techniques for multilevel inverters in traction applications. IEEE Access 9:24187–24204
7. Chang F, Ilina O, Lienkamp M, Voss L (2019) Improving the overall efficiency of automotive inverters using a multilevel converter composed of low voltage Si MOSFETs. IEEE Trans Power Electron 34(4):3586–3602
8. Kersten A, Grunditz E, Thiringer T (2018) Efficiency of active three-level and five-level NPC inverters compared to a two-level inverter in a vehicle. In: 2018 20th European conference on power electronics and applications (EPE'18 ECCE Europe), Riga, Latvia
9. Guan Y, Li L, Zhang J (2020) A novel high frequency isolated three-level inverter and its topological derivation method. In: 2020 15th IEEE conference on Industrial Electronics and Applications (ICIEA), Kristiansand, Norway
10. Ellabban O, Mierlo JV, Lataire P (2011) A comparative study of different control techniques for an induction motor fed by a Z-source inverter for electric vehicles. In: International conference on power engineering, energy and electrical drives, Malaga, Spain

11. Jamwal PS, Singh S, Jain S (2021) Three-level inverters with volt per Hz control for induction motor driven electric vehicles. In: Tiwari M, Shrivastava A, Dwivedi S, Singh S (eds) Proceedings of conference on flexible electronics for electric vehicles, lecture notes in electrical engineering, in press, Springer
12. Mohan H, Dwivedi SK, Pathak MK (2018) Control of induction motor drives—technological advancements. In: 2018 8th IEEE India International Conference on Power Electronics (IICPE), Jaipur, India
13. Naganathan P, Srinivas S (2020) Direct torque control techniques of three-level H-bridge inverter fed induction motor for torque ripple reduction at low-speed operations. IEEE Trans Ind Electron 67(10), 8262–8270
14. Adigintla S, Aware MV (2020) Position control of the induction motor using fractional order controllers. In: 2020 international conference on Power, Instrumentation, Control and Computing (PICC), Thrissur, India
15. Krishnan R (2001) Electric motor drives modeling, analysis, and control. Prentice Hall
16. Kakodia SK, Dynamina G (2020) A comparative study of DFOC and IFOC for IM drive. In: 2020 First IEEE International Conference on Measurement, Instrumentation, Control and Automation (ICMICA), Kurukshetra, India
17. Nair NS, Barai M (2020) A three-level NPC fed induction motor drive with closed loop dc-link voltage balancing algorithm. In: 2020 IEEE international conference on Power, Instrumentation, Control and Computing (PICC), Thrissur, India (2020)
18. Krishnatheeram S, Peter J, Mohammed Shafi KP, Ramchand R (2018) Current error boundary analysis of constant switching frequency voltage controlled three level VSI fed IM drive. In: 2018 IEEE international conference on Power, Instrumentation, Control and Computing (PICC), Thrissur, India
19. Singh S (2019) DC motor drives. In: Rahman MF, Dwivedi SK (eds) Modeling, simulation and control of electrical drives. IET Control, robotics and sensors series vol 118, pp 101–136
20. Jamwal PS, Singh S, Jain S (2021) Three-level inverters for induction motor driven electric vehicles. In: 2020 IEEE 3rd International Conference on Energy, Power and Environment towards clean energy technologies (ICEPE), Shillong, Meghalaya, India

Comparative Analysis of Conventional and Sliding Mode Control Techniques for DC-DC Boost Converter for PV System Under Transient Conditions

Pankaj Swarnkar, Suresh Kumar Gawre, and Gagnesh Akodiya

1 Introduction

The global demand of energy is increasing enormously due to industrialization and urbanization. The existing fossil fuel is limited and causes the global warming effect, this leads to searching for alternate renewable energy sources. PV sources are one of the important power suppliers than other renewable energy sources due to clean, pollution free, and endless. Many methods have been presented to model and simulate a photovoltaic array and to find parameters of the current–voltage equation by adjusting the characteristics at three points: open circuit, maximum power, and short circuit. Effects of irradiation and temperature change on characteristics of PV are also considered to model the PV array [1–3]. To obtain maximum power from solar panel, it needs to operate at maximum operating point. Maximum power point tracking (MPPT) for photovoltaic systems using perturb and observe (P&O) algorithm is the most common technique for this purpose [4]. When MPPT technique is not used then the maximum available power is not being extracted and as a result it leads to the low efficiency of the solar panel and hence the cost per kW of the solar panel is increased. Hence in order to minimize the cost per kW of the solar panel and to improve efficiency various MPPT algorithms are used. Ronn Raedani et al. [5] explore the 'Incremental Conductance' and 'P&O' techniques of MPPT. A comparative analysis on the basis of cost of two techniques is also conducted to perform the comparative analysis between the MPPT techniques. In order to get the constant desired output from a PV array suitable DC-DC boost converter must be designed. Selection of appropriate components of boost converter is also an essential requirement [6, 7]. In order to regulate the output of boost converter specific control technique must be designed. Many conventional and advanced control techniques have been designed and implemented so far to enhance the dynamic characteristic

P. Swarnkar · S. K. Gawre (✉) · G. Akodiya
Maulana Azad National Institute of Technology, Bhopal, India

S. Kumar et al. (eds.), *Recent Advances in Power Electronics and Drives*, Lecture Notes in Electrical Engineering 852, https://doi.org/10.1007/978-981-16-9239-0_45

of DC-DC boost converter which is capable of achieving better transient response is more steady and robust [8–11].

Under classical PI control of DC-DC boost converter, increasing the proportional gain K_p of the controlled variable, advances the system performance and improves the accuracy. However, a high K_p also increases the overshoot and reduces the stability of the system. Increment in integral gain K_i improves the accuracy by reducing the steady-state error but has negligible effect on transient performance. Finally, increasing the derivative control gain K_d reduces the magnitude of oscillation of the response. K_d although does not improve the steady-state accuracy but may increase the noise [11, 12]. Such disadvantages of linear control method made designers to think about nonlinear control methods such as sliding mode control [13–17] which offer better performance under system uncertainties and large perturbations. DC-DC power converters are inherently variable structure systems since at the two switching states, i.e., ON and OFF, they exhibit two different structures. Many adaptive and advance controllers based on AI techniques have also been suggested to overcome the nonlinearity and time varying effect of system [18–20].

In this work the main aim is on regulating the output voltage of boost converter to the desired value by using conventional control technique that is PI control and advanced control technique that is Sliding Model Control. The two control techniques applied for boost converter are simulated for variable input voltage, where input voltage is varied by approx. 10 V difference or so while keeping the load resistance constant. System is also tested for variable load conditions to validate the feasibility of robust control technique over the conventional control.

2 Design of PV Array

The system is designed for normal household application that requires a power of 2000 watts for normal usage. So the PV array designed should be capable of generating 2000 watts of power. The PV module used in simulation is '1Soltech 1sth-235-WH'. Table 1 shows the specifications of a PV array used to feed the boost converter which is considered as plant for designing the control schemes.

Table 1 Specification of PV array

Parameters	Value
Peak power of PV Array	2000 W
Voltage at MPP	104 V
Current at MPP	22.5A
S.C. current	24A
O.C. voltage	135 V
Temperature	60 °C

2.1 Design of Boost Converter

A boost converter steps up the input voltage. A boost converter with a power MOSFET is shown in Fig. 1; Power for the boost converter is taken from solar panel which is denoted by a battery in figure [6–11].

Characterized by switching, DC-DC power converters are inherently variable structure systems since at the two switching states, i.e., ON and OFF, they exhibit two different structures. The working of boost converter can be classified as Operation 1 and Operation 2. Operation 1 is defined for transistor switched on at time t = 0. The input current increases and passes through inductor L and transistor (Fig. 2).

Operation 2 is described for transistor switched off at time $t = t_1$. The input current now flows through L, C, load, and diode D as shown in Fig. 3.

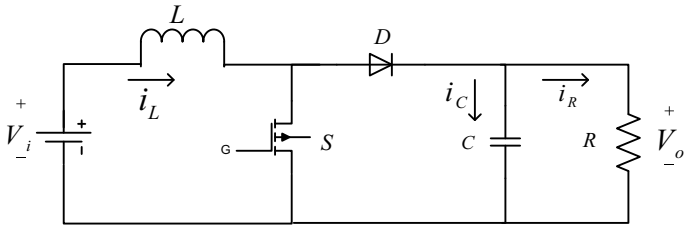

Fig. 1 DC-DC boost converter topology

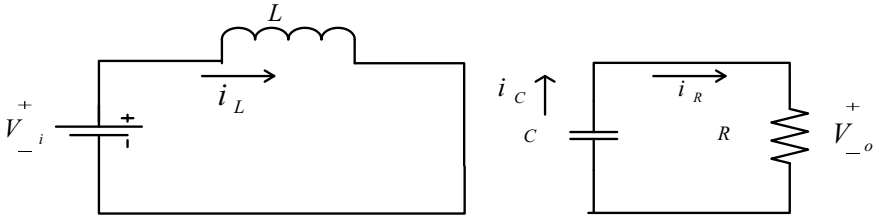

Fig. 2 DC-DC boost converter topology in ON state

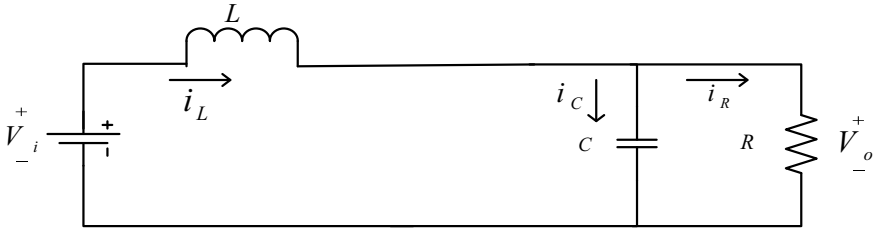

Fig. 3 DC-DC boost converter topology in OFF state

2.2 Calculation of Boost Converter Parameters

The system is designed to give output power of 2000 watts for normal household use. As the aim of this work is to get the constant output voltage of 220 V under any external changes in input voltage or output load resistance, so the value of output voltage can be considered constant at 220 V.

From PV curve of solar module shown in Fig. 4, it is observed that the maximum power is achieved by solar panel at around 100 V so taking minimum output voltage of solar panel to be around 90 V, hence the minimum input voltage of boost converter is also taken as 90 V. Also the switching frequency is taken as 10 kHz for system operation.

So by concluding all some initial values are taken as

$$P_o(output\ \ power) = 2000watts,\ \ f_s(switching\ \ frequency) = 10khz$$

$$V_i(input\ \ voltage) = 90volts,\ \ V_o(output\ \ voltage) = 220volts$$

The other parameters of boost converter are given in Table 2.

Hence the value of load resistance is obtained as 24.2 ohms which can be approximated as 25 ohms. This is the rated value of load resistance for 2000 watts system. Using the values of resistance, inductance and capacitance the DC-DC boost converter is realized and further used to implement the control techniques PIC and SMC.

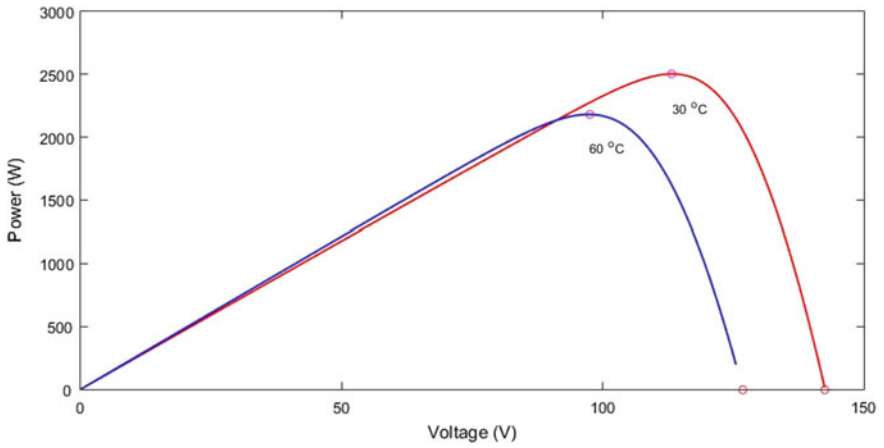

Fig. 4 P–V characteristic of PV array

Table 2 Parameters of boost converter

Parameters	Description	Value
Duty cycle	$d = 1 - \frac{V_i}{V_o} = 1 - \frac{90}{220}$	0.59
Inductance (minimum value to keep the boost converter in continuous conduction mode)	$L_{\min} = \frac{(1-d)^2 \times d \times R}{2 \times f_s}$	0.15 mH
Capacitance (for producing the required output voltage ripple)	$C = \frac{d \times V_o}{R \times f_s \times \Delta V_o}$	0.244 m F
Load Resistance	$R = \frac{V_o^2}{P_o} = \frac{(220)^2}{2000}$	24.2 Ω

2.3 Mathematical Modeling of DC-DC Boost Converter

In this section mathematical model of DC-DC boost converter is presented using in state-space method. This is a generalized time domain representation of system [10]. Dynamics of the converter operating in continuous conduction mode is obtained by applying KVL in the loop containing inductor, DC source, and switch.

$$\frac{dI_L}{dt} = -(1-u)\frac{V_o}{L} + \frac{V_i}{L} \tag{1}$$

Now the KCL is applied on node connecting the capacitor branch, following equation is obtained

$$\frac{dV_o}{dt} = (1-u)\frac{I_L}{C} - \frac{V_o}{RC} \tag{2}$$

By defining state variables as, $x_1 = I_L$ and $x_2 = V_o$, the state equations can be obtained as

$$\dot{x}_1 = -(1-u)\frac{x_2}{L} + \frac{V_i}{L} \tag{3}$$

$$\dot{x}_2 = (1-u)\frac{x_1}{C} - \frac{x_2}{RC} \tag{4}$$

Finally in matrix form,

$$\begin{bmatrix} \dot{x}_1 \\ \dot{x}_2 \end{bmatrix} = \begin{bmatrix} 0 & -(1-u)\frac{1}{L} \\ (1-u)\frac{1}{C} & -\frac{1}{RC} \end{bmatrix} \begin{bmatrix} x_1 \\ x_2 \end{bmatrix} + \begin{bmatrix} \frac{1}{L} \\ 0 \end{bmatrix} V_i \tag{5}$$

where V_o is output capacitor voltage, I_L is inductor current, V_i is input voltage. The control input 'u' represents the ON or OFF state of switch in boost converter, it is a discrete valued function and its values are in set (0,1). It is assumed that the

continuous conduction mode is maintained by keeping inductor value greater than minimum value of inductor as mentioned in Eq. (1).

3 Design of PI Controller

Figure 5 shows the schematic diagram of control scheme for boost converter using PI controller.

In conventional control scheme error signal is generated as the difference between actual and required set point and feed to PI controller. The controller tries to mitigate the error by adjusting the process by introducing a manipulated variable which in boost converters case is its duty cycle. The detection of error is in terms of current, voltage, angle, movement, temperature, etc. for observing the effect of proportional controller only, the integral gain K_i is set to zero.

P-controller tends to generate an offset value and also increase the maximum overshoot of the system. Also too high a value of K_p will lead to the oscillation. The PI controller confirms that the boost converter will deliver a required amount of voltage to the load. The PI control action is defined by the following relation:

$$u(t) = K_p e(t) + K_i \int_0^t e(t)d\tau \tag{6}$$

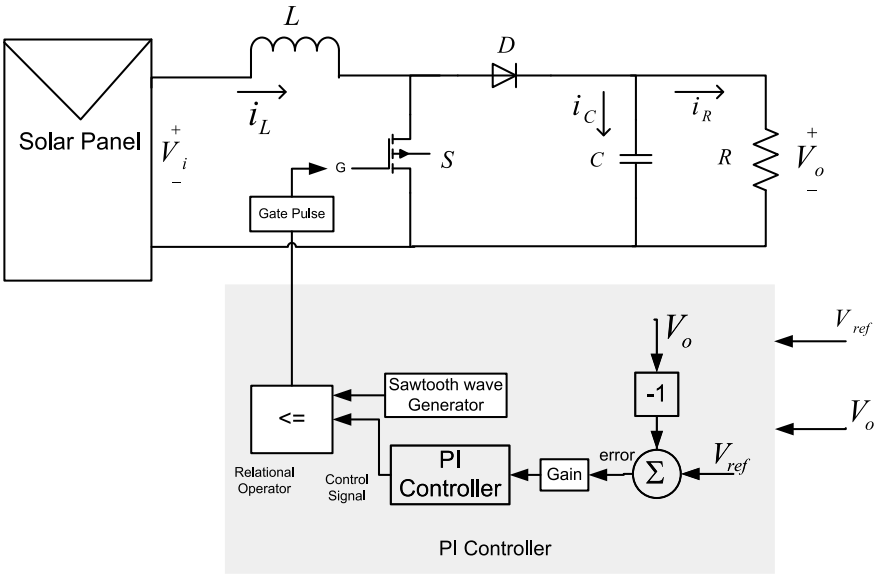

Fig. 5 Schematic diagram of boost converter with PI control

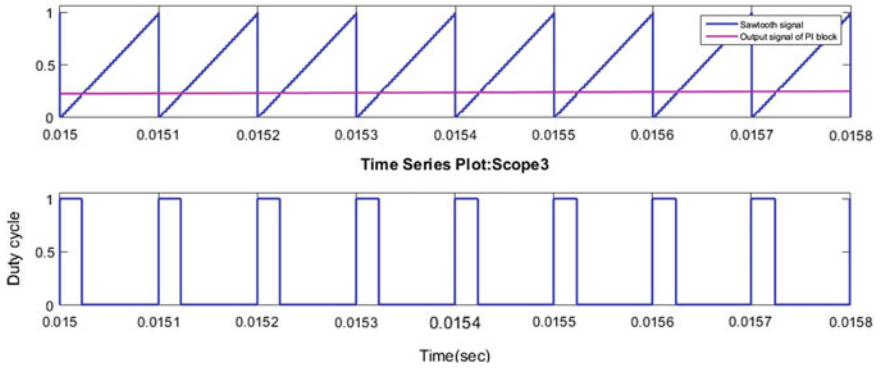

Fig. 6 Duty signal generation of boost converter by PI controller

Here as shown in Fig. 5 variable input voltage is taken from the solar panels for the boost converter. To implement the PI control on boost converter the output voltage of boost converter is compared with the reference value of voltage which in this case is set to 220 V. Error in voltage generated by the comparison is amplified and then it is fed to the PI controller which generates an equivalent control signal as shown in Fig. 6, which is then compared with the saw tooth wave to produce an equivalent duty cycle which is used to drive the switching device of the converter. As long as the control signal is greater than saw tooth signal, switch is in ON state and inductor current rises, and when control signal is less than the saw tooth signal the switch is in OFF state.

4 Sliding Mode Control Design For Boost Converter

The state-space model developed in previous section is used to implement sliding mode control (SMC) on a boost converter. Inductor current and output voltage are chosen as state variables. So state variables $x_1 = I_L$ and $x_2 = V_o$. Now the aim is to achieve a desired constant output voltage V_{ref}. Thus,

$$x_2 = V_{ref} \tag{7}$$

$$\dot{x}_2 = \dot{V}_{ref} = 0 \tag{8}$$

From the conventional SMC theory, the sliding surface is defined as

$$S = x_1 - x_1^* = 0 \tag{9}$$

x_1^* is the reference value.

In order to force the initial variables on the sliding surface S = 0, the ideal control law for the switch is

$$u = \frac{1}{2}(1 - sign(S)) \tag{10}$$

Here the objective is to confirm that the state trajectory of the initial state of system is moved toward the sliding surface S = 0 and slides over it, until it reaches to a stable equilibrium. This is obtained by appropriate design of control law using the reaching condition,

$$S\dot{S} < 0 \tag{11}$$

Since

$$S = x_1 - x_1^*$$

At the equilibrium (generally origin of phase plane), the final values of state variables coincide with the corresponding reference values then

$$x_1^* = 0$$

By Eqs. (9) and (11) we get

$$x_2 > V_i$$

This means existence condition in sliding mode satisfies if the output voltage is greater than the input voltage of boost converter.

Block Diagram of boost converter with SMC is shown in Fig. 7 where V_{ref} represents the reference voltage which is desired at the output of boost converter. The system basically consists of two feedback loops; one is the voltage loop and other one is another current loop. The voltage loop is the slower loop since the change in voltage is slower as compared to the change in current. The system works in two stages, in first the output voltage is compared with the reference voltage and hence the error is generated which is fed to the PI controller which generates the reference inductor current. Hence error (difference between reference and actual inductor current) generated is nothing but the sliding surface for boost converter, now the control signal 'u' of boost converter is achieved by Eq. (10). And hence the sliding mode control of boost converter is achieved.

Figure 8 shows the output voltage of boost converter without any control (open loop). It can be seen that overshoot is 34.09% which is quite large and can cause the instability. It can also be observed that boost converter without any control is able to give the output voltage of 220 V when duty cycle is correctly adjusted. But as the output voltage of solar panel won't remain constant as irradiance and temperature

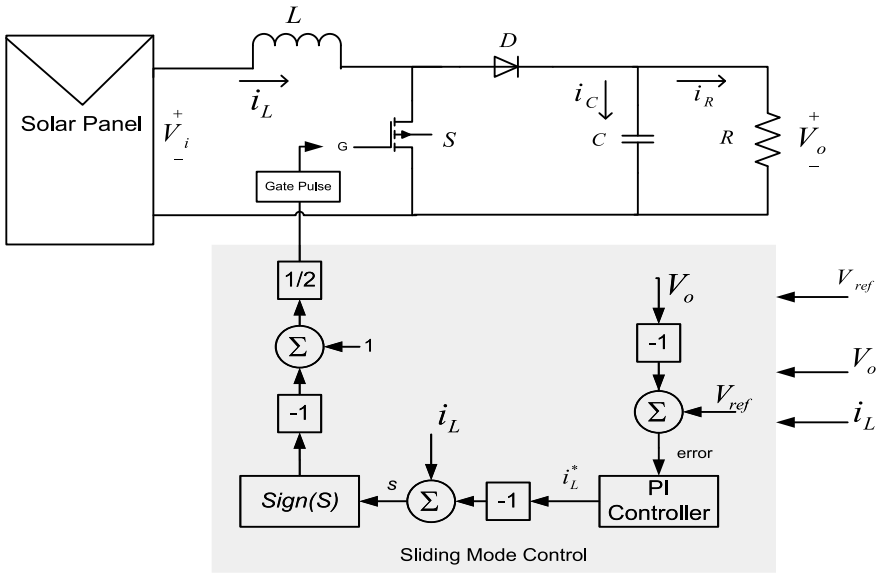

Fig. 7 Schematic Diagram of boost converter with SMC

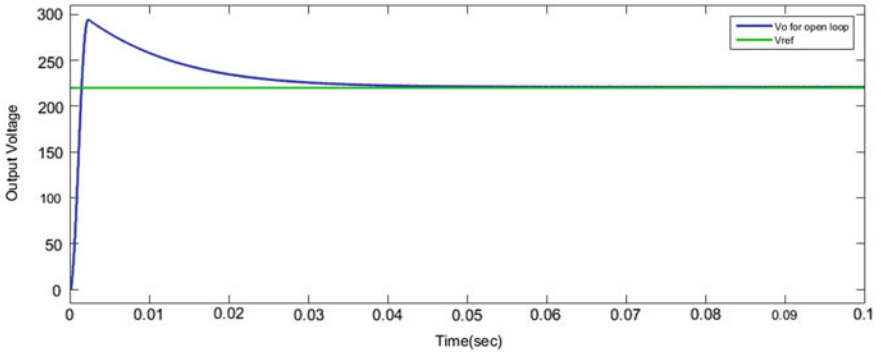

Fig. 8 Simulation results of open-loop boost converter for Vi = 90 V

on solar panels are constantly changing. So in that case it is really necessary to have some controller to regulate the duty cycle to get the desired V_o.

Figure 9 shows the outcomes of boost converter with SMC and PIC when input voltage is set at 90 V and the desired output voltage is set at 220 V. Curves present the comparative analysis of PI control and SM control, Hence the performance can be analyzed in terms of Rise Time (RT), Peak Overshoot (PO), Settling Time (ST), and Steady-state error (SSE) for both control techniques. From figure it can be clearly observed that boost converter with PI control is able to track the V_o of 220 V, and the steady-state value is also close to the desired output voltage. The peak overshoot

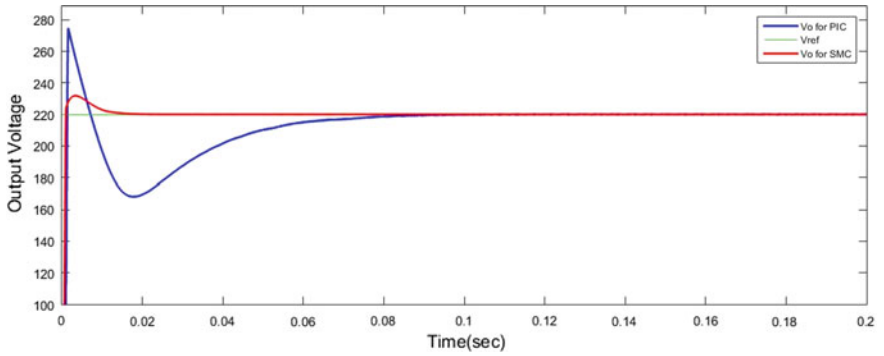

Fig. 9 Simulation results of boost converter with SMC and PI Controller for Vi = 90 V

Table 3 Comparison of different control scheme (input voltage is constant)

Input voltage	Specification	Open loop	PI controller	SMC
90 V	RT	1.5 ms	1.3 ms	0.9 ms
	PO	34.09%	24.9%	5.4%
	ST	0.1 s	0.15 s	0.03 s
	SSE	0.7 V	0.9 V	0.08 V

is reduced as compared to open-loop characteristic hence the system is stable. But curve is having oscillations with large settling time. Now with the application of SMC the overshoot is reduced to permissible limit of 5.4% with no undershoot. Also the settling time is reduced to large extent. So it can be concluded that sliding mode controller performs much better than the PI controller. Table 3 gives the summary of all time response specifications obtained by simulation study with different control schemes.

4.1 Effect of Transients

In this section, the robustness of proposed controller designs is tested under transient conditions. First the system is tested for variation in input voltage (with constant load) and then it is tested for variation in load resistance as well as input voltage. The performance of boost converter is analyzed without any control, with PI control and with SMC for transient condition. In these results the input voltage of boost converter is varied between 90 V and 140 V and the load resistance is varied by ± 5 ohms of its rated value, i.e., 25 ohms (rated). Also the reference value of output voltage is set at 220 V.

4.2 Variation in Input Voltage

The input voltage is varied from 100 to 140 V while keeping the load resistance constant at its rated value of 25 ohms. In previous section the input voltage is kept constant at 90 V, now the further study is done by varying the input voltage to observe the performance of boost converter with different control schemes.

Table 4 gives results of transient analysis for variation in input voltage from $V_i =$ 90 V to $V_i = 140$ V. It can be observed that when the input voltage is increased the performance of boost converter is deteriorated very fast with open loop and PIC. The overshoot of the system is increased beyond the limit and making system unstable. On the other hand, SMC is still able to control the system keeping the specifications at the satisfactory limits.

Table 4 Comparison of different control schemes (input voltage is variable and output resistance Ro = 25 ohms)

Input voltage	Specification	Open loop	PI controller	SMC
90 V	RT	1.5 ms	1.3 ms	0.9 ms
	PO	34.09%	24.9%	5.4%
	ST	0.1 s	0.15 s	0.03 s
	SSE	0.7 V	0.9 V	0.08 V
100 V	RT	1.07 ms	1.16 ms	0.82 ms
	PO	35.45%	34.09%	8.63%
	ST	0.08 s	0.22 s	0.03 s
	SSE	0.65 V	0.8 V	0.2 V
110 V	RT	0.96 ms	1.08 ms	0.76 ms
	PO	40%	43.63%	16.36%
	ST	0.09 s	0.12 s	0.025 s
	SSE	0.65 V	0.8 V	0.15 V
120 V	RT	0.86 ms	1 ms	0.71 ms
	PO	45%	53.63%	23.18%
	ST	0.1 s	0.14 s	0.05 s
	SSE	1.6 V	0.8 V	0.08 V
130 V	RT	1 ms	0.95 ms	0.67 ms
	PO	49.54%	62.72%	30.9%
	ST	0.1 s	0.19 s	0.045 s
	SSE	0.62 V	0.8 V	0.07 V
140 V	RT	0.71 ms	0.89 ms	0.64 ms
	PO	55.45%	72.27%	38.18%
	ST	0.1 s	0.17 s	0.045 s
	SSE	0.55 V	0.7 V	0.07 V

Table 5 Comparison of different control schemes (input voltage is variable and output resistance Ro = 20 ohms)

Input voltage	Specification	PI controller	SMC
90 V	RT	0.129 ms	0.9 ms
	PO	24.54%	4.09%
	ST	0.25 s	0.029 s
	SSE	2.5 V	0.1 V
100 V	RT	1.17 ms	0.82 ms
	PO	33.86%	8.63%
	ST	0.22 s	0.07 s
	SSE	0.9 V	0.1 V
110 V	RT	1.1 ms	0.76 ms
	PO	44.31%	15.9%
	ST	0.12 s	0.035 s
	SSE	0.9 V	0.13 V
125 V	RT	0.98 ms	0.7 ms
	PO	58.63%	26.81%
	ST	0.14 s	0.035 s
	SSE	0.9 V	0.08 V
140 V	RT	0.89 ms	0.65 ms
	PO	71.81%	38.18%
	ST	0.16 s	0.05 s
	SSE	0.9 V	0.09 V

4.3 Variation in Load Resistance

It is important to check the behavior of the boost converter when the load varies from its rated value. Hence load resistance of the boost converter is varied by 20% above and below the rated value of load resistance of 25 ohms. The system is tested with PIC and SMC, when input voltage is also varied for under and over load conditions. The input voltage is varied from 90 to 140 V. The results advocate the superiority of SMC over PIC.

4.4 Load Resistance is Set at 20 Ohms

To study the performance of output voltage when it is loaded under the rated value, the value of load resistance is set at 20 ohms which is 20% below the rated value. Table 5 shows the results for variable input voltage $V_i = 90$ V to $V_i = 140$ V with load resistance $R_o = 25$ ohms. Table 5 compares control schemes on the basis of rise time (RT), peak overshoot (PO), settling time (ST) and steady-state error (SSE).

Table 6 Comparison of different control schemes (input voltage is variable and output resistance $R_o = 30$ ohms)

Input voltage	Specification	PI controller	SMC
90 V	RT	1.28 ms	0.89 ms
	PO	25%	6.136%
	ST	0.12 s	0.03 s
	SSE	0.65 V	0.06 V
100 V	RT	1.2 ms	0.82 ms
	PO	34.54%	9.09%
	ST	0.14 s	0.02 s
	SSE	0.65 V	0.2 V
110 V	RT	1.085 ms	0.75 ms
	PO	45%	16.36%
	ST	0.15 s	0.045 s
	SSE	0.65 V	0.12 V
125 V	RT	1 ms	0.69 ms
	PO	59.09%	27.27%
	ST	0.15 s	0.05 s
	SSE	0.6 V	0.06 V
140 V	RT	0.88 ms	0.64 ms
	PO	72.27%	38.63%
	ST	0.13 s	0.05 s
	SSE	0.7 V	0.065 V

5 Load Resistance is Set at 30 Ohms

To study the performance of output voltage when it is loaded above the rated value, the value of load resistance is set at 30 ohms which is 20% above the rated value. Table 6 gives the comparative analysis of both the control schemes under such variations where input voltage is varied from $V_i = 90$ V to $V_i = 140$ V and converter is overloaded with $R_o = 30$ ohms.

6 Conclusion

This paper presents the PI and Sliding Mode control techniques for solar penal fed boost converter. The system is tested both under steady state and transient conditions. The study shows that both control schemes work satisfactorily under steady-state condition when the system parameters are set at their rated values. As the transients are introduced in the system, the performance of PI controller deteriorates and crosses the acceptable limits while SMC still shows the robustness and keeps the system in

stability limit. So it can be concluded that sliding mode control is a better option because it generated less disturbance in the system and also at the input side.

References

1. Villalva MG, Gazoli JR, Filho ER (2009) Comprehensive approach to modelling and simulation of photovoltaic arrays. IEEE Trans Power Electron 24(5)
2. Krismadinataa, Rahima NA, Pinga HW, Selvaraja J (2013) Photovoltaic module modelling using simulink/matlab. Proc Environ Sci 17:537–546
3. Bellia H, Youcef R, Fatima M (2014) A detailed modeling of photovoltaic module using Matlab. Nriag J Astron Geophys 3(1):53–61
4. Al Sadi S, Al Sayid B (2012) Maximum power point tracking simulation for photovoltaic systems using perturb and observe algorithm. Int J Eng Innov Technol 2(6):80–85
5. Raedani R, Hanif M (2014) Design, testing and comparison of P&O, ICand VSSIR MPPT techniques. Renew Energy Res Appl (ICRERA), pp 322–330
6. Masri S, Chan PW (1990) Design and development of a Dc-Dc converter with constant output voltage. IEEE Trans Power Electron 5(3):323–330
7. Hasaneen BM, Elbaset Mohammed AA (2008) Design and simulation of Dc/Dc boost converter. In: 12th international middle-east power system conference, pp 335–340
8. Mohan N, Undeland TM, Robbins WP (2003) Power electronics: converters, applications, and design, 3rd edn. Wiley, USA
9. Jung D, Ji Y, Park S, Jung Y, Won C, Member S (2011) Interleaved soft-switching boost converter for photovoltaic power-generation system. IEEE Trans Power Electron 26(4):1137–1145, 9
10. Hosseini SH, Haghighian SK, Danyali S, Aghazadeh H (2012) Multi-input Dc boost converter supplied by a hybrid PV/wind turbine power systems for street lighting application connected to the grid. In: Universities Power Engineering Conference, pp 1–6
11. Bakar AA, Utomo WM, Taufik T, Aizam S, Jumadril (2015) Dc/Dc boost converter with PI controller using real-time interface. ARPN J Eng Appl Sci 10(19)
12. Dave MR, Dave KC (2012) Analysis of boost converter using PI control algorithms. Int J Eng Trends Technol 3(2)
13. Abutbul O, Gherlitz A, Berkovich Y, Ioinovici A (2003) Step-up switching-mode converter with high voltage gain using a switched capacitor circuit. IEEE Trans Circuits Syst I, Fundam Theory Appl 50(8):1098–1102
14. Gueldemir H (2005) Sliding mode control of boost converter. J Appl Sci 5(3):588–592
15. Hijazi A, Di Loreto M, Bideaux E, Venet P, Clerc G, Rojat G (2009) Sliding mode control of boost converter: application to energy storage system via super capacitors. In: Electronique, Barcelone, Spain
16. Das S, Qureshi MS, Swarnkar P (2018) Design of integral sliding mode control for DC-DC converter. Material Proc Charact Assoc Mater Today Proc Elsevier J 5(2):4290–4298
17. Qureshi MS, Das S, Swarnkar P, Gupta S (2018) Design and implementation of sliding mode control for uncertain systems. Material Proc Charact Assoc Mater Today Proc Elsevier J 5(2):4299–4308
18. Guo L, Hung JY, Member S, Nelms RM (2009) Evaluation of DSP-based PID and fuzzy controllers for Dc—Dc converters. IEEE Trans Ind Electron 56(6):2237–2248
19. Harsh G, Pankaj S (2019) Investigations on metaheuristic algorithm for designing adaptive PID controller for continuous stirred tank reactor. MAPAN-J Metrol Soc India 34(1):113–119
20. Swarnkar P, Jain S, Nema RK (2014) Adaptive control schemes for improving the control system dynamics: a review. IETE Techn Rev 31(1):17–33

Development of Fault Indicators for Stator Inter-turn Fault Diagnosis of a Synchronous Generator Using Kalman Filter

P. V. Sunil Nag and C. Santhosh Kumar

1 Introduction

With the advancement in civilization, the need for reliable electric power has increased drastically. The workhorse for a typical power system is a synchronous generator and hence the reliability of the synchronous generator is paramount. Reliability can be enhanced using a fault diagnostic system that can identify incipient faults so that early remedial action can be taken, avoiding costly downtime. One of the major faults in the synchronous generator is the stator inter-turn fault which accounts for 30 to 40% of the faults in a machine [1]. This is a seed fault for most of the electrical faults in the synchronous generator. Hence, detecting and diagnosing this fault improves the reliability of the synchronous generator and thus of the power system.

Many strategies have been developed for the fault diagnosis of the stator inter-turn fault. The methods for fault diagnosis, in general, can be classified into 3 categories: signal-based, data-based, and model-based [2]. The model-based approach is superior as it readily makes use of the knowledge of the physics of the machine unlike the other two classes of methods which ignore the physics of the machine involved. One important class of the model-based methods is based on the popular observer/Kalman filter and its variants. One of the important requirements of a fault diagnostic system is its ability to distinguish between a fault and similar disturbing factors [3]. For the stator inter-turn fault of a synchronous generator, one important disturbing factor is the load imbalance [4]. Hence, a fault diagnostic system should be able to produce a fault indicator that can distinguish between the two.

In the recent literature, Kalman filter/observer-based methods have been used for fault diagnosis of the inter-turn fault of electrical machines [3–8] uses a fault indicator

P. V. Sunil Nag (✉) · C. Santhosh Kumar
Department of Electronics and Communication Engineering, Amrita School of Engineering, Amrita Vishwa Vidyapeetham, Coimbatore 641112, Tamil Nadu, India
e-mail: pv_sunil@cb.amrita.edu

S. Kumar et al. (eds.), *Recent Advances in Power Electronics and Drives*, Lecture Notes in Electrical Engineering 852, https://doi.org/10.1007/978-981-16-9239-0_46

namely residual current vector obtained using an observer and sequence component decomposition. Aubert et al. [5] used a joint extended Kalman filter (EKF) to estimate the fault parameters (ratio of the number of shorted turns to the healthy turns) that are used as indicators of the fault. The above works address the issue of load imbalance on the performance of the fault indicator and use a permanent magnet synchronous generator. The model used for the fault diagnosis, in the above works, is capable of detecting a fault in any of the 3 phases and uses the dq0 transformation. El Sayed et al. [6] is similar to the above work but compares the performance of the EKF with unscented Kalman filter but this work does not address the issue of load imbalance. Idrissi et al. [7] uses a linear Kalman filter to diagnose the stator inter-turn fault in a doubly-fed induction generator. The model used is based on a stationary reference (α, β)frame. The proposed diagnostic system can find fault in any of the three phases, but it does not address the issue of load imbalance. Here it is mentioned that the linear Kalman filter is more suitable for hardware implementation. Nadarajan et al. [4] uses a joint extended Kalman filter for fault diagnosis of a Brushless synchronous generator. This work addresses the issues of the effect of load imbalance, further a dq0 model is used. Here fault in the R phase is only addressed. Here it should be mentioned specifically that a brushless synchronous generator is more complex than a permanent magnet synchronous generator, hence the modeling exercise is more difficult. This work uses a combination of time-domain and frequency-domain processing to diagnose the fault. Jaiswal et al. [8] extended the work of [4] for failure prognosis and it uses FEM analysis of the BLSG. This work uses a dq0 model with a fault in a single phase along with an extended Kalman filter.

From the above survey of the recent literature on fault diagnosis of inter-turn fault using Kalman filter and its variants, it could be observed that there is a necessity of a model for fault diagnosis that can accommodate fault in all phases for a synchronous generator. Considering hardware implementation requirements it is desirable if a linear Kalman filter is used for diagnosis. The Kalman filter should also generate a fault indicator that can distinguish between inter-turn fault and load imbalance.

For testing the efficacy of a fault diagnostic algorithm, a fault injection capable machine is required [9]. Developing such a system for a generator with a high current/voltage rating is difficult. The alternative is to develop a simulated system [10, 11]. The best simulation that almost exactly matches the real system is a finite element simulation.

Considering the above conclusions, this work discusses (1) the development of a finite element model-based fault injection capable synchronous generator using ANSYS Maxwell hereafter referred to as a Maxwell. (2) The dq0 model of the synchronous generator along with a fault parameter in all the 3 phases. The model is in the state-space form and this model can be used by a linear Kalman filter for state and parameter estimation. The model developed here is an extension of [4], where the model has been derived for fault in one phase. (3) The process of generating a fault indicator that can identify an inter-turn fault and at the same time exhibit a distinct behavior in case of a load imbalance. Here an important assumption is that a fault can occur in only one phase at a time.

The proposed contributions of this work are the dq0 model with a fault in all three phases an extension of the work given in [4]. Further, a new fault indicator is proposed to identify inter-turn fault using the Kalman filter. This indicator also helps in identifying a load imbalance condition.

Section 2 describes the proposed architecture, Sect. 3 deals with the procedure for obtaining a fault injection capable Maxwell model. Section 4 gives an overview of the derivation of the dq0-based state-space model for the synchronous generator with a fault in all the 3 phases. Section 5 provides the relevant details of how the standard linear Kalman filter algorithm is used to generate the proposed fault indicator. Section 6 gives the results and discussion and the last section provides the conclusion and future work.

2 Block Diagram of the Proposed System

The block diagram of the proposed system is shown in Fig. 1. The fault injection capable synchronous generator is a system in which fault can be injected by closing a switch. It has been designed with split coils.

Terminals from the split coils are brought out and a switch can be used to short the terminals of the particular split. This generator is implemented in Maxwell software. The data from the generator, namely the stator voltages and currents are collected and given to a Joint Kalman filter (a Kalman filter that estimates both states and parameters simultaneously). The Kalman filter uses a dq0-based state- space model.

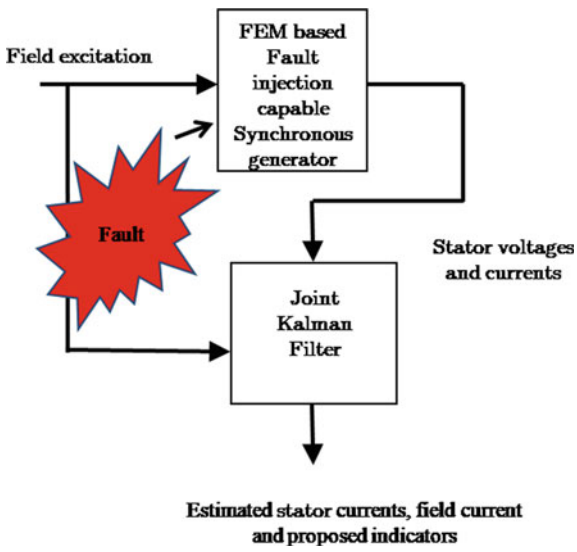

Fig. 1 Block diagram of the proposed system

The Kalman filter in turn estimates the states and indicators for fault diagnosis. The next section describes the fault injection capable generator.

3 Fault Injection Capable Synchronous Generator

As mentioned earlier, building a fault injection capable generator in hardware requires a lot of customization and hence will be costly. A viable alternative for this would be to build a Finite element model (FEM) of the machine. This FEM model is the closest we can get to the actual machine in the simulation domain. Maxwell software was chosen to build the model in this work.

To obtain the model, a 15 kVA synchronous generator was designed using standard procedures [12]. These designed values were entered into the ANSYS RMxprt™ software which will enable easy generation of the FE model in the Maxwell software. After obtaining the Maxwell model of the generator, the FE model was made fault injection capable following the same lines as given in [13]. Each phase of the 15 kVA generator was made up of 12 coils and each coil had 16 turns. Each coil in the phase had a taping at 10 turns. This taping along with the end terminals of each coil was brought out as terminals. The terminals could be shorted externally to simulate an inter-turn short. The next section describes the development of the analytical model called as dq0 model hereafter.

4 Derivation of the Dq0 Based State-Space Model

The schematic shown in Fig. 2 contains the various coils (3 phase coils with inter-turn fault belonging to the stator and 3 coils belonging to the rotor) in the synchronous generator and their relative orientation. Here each phase in the stator winding is split into two parts for example A phase is split into a1 healthy and a2 faulty. To arrive at the state-space model, two types of equations, namely the flux equations and the voltage equations have to be obtained from the coil configurations. A typical flux equation for the coil say a1 is given in Eq. (1), similar equations can be written for other coils, namely a2, b1, b2, c1, c2, fd, kd, and kq. Here the Kirchhoff's current law equations and flux equations for each phase can be written as given in Eqs. (2) to (7). The Eqs. (2) to (7) can be used to manipulate the flux equations that were written for each coil to obtain modified equations. These equations are shown in the matrix form in Eq. (8).

Where ψ_a, ψ_b, and ψ_c are the flux linkages associated with the phases a, b, and c, respectively. Flux linkages of other coils like a1, a2, b1, b2, fd, kd, and kq can be similarly represented. i_a, i_b, and i_c are the currents in the phases a, b, and c, respectively. The currents through other coils like a1, a2, b1, b2, fd, kd, and kq can be similarly represented. Here the inductance L_{x1x2} represents the inductance between coils x1 and x2, for example, L_{a1a2} represents the inductance between the

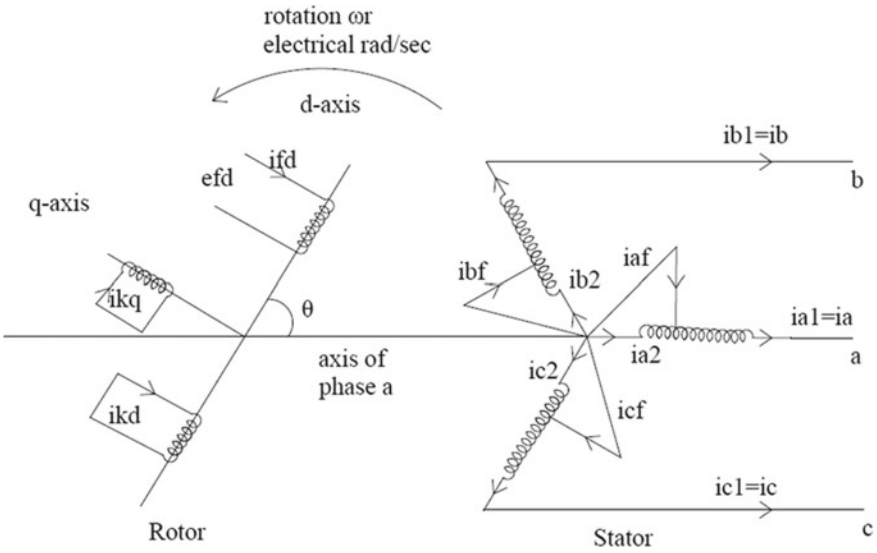

Fig. 2 Schematic of a synchronous generator with a fault in all phases

coils a1 and a2. Parameters μ_1, μ_2, and μ_3 are the ratios of the faulty turns to the total number of turns for the phases A, B, and C, respectively (here A,B,C are used to represent R,Y,B phases interchangeably).

Here it can be observed in Eq. (8) that all the terms of the inductance matrix are time varying. To overcome this park's transformation or dq0 transformation is used for shifting the frame of reference to the rotor reference frame. The simplified inductance matrix obtained after applying the park's transformation in block matrix form is as shown below in Eq. (9)

$$\psi_{a1} = -L_{a1a1}i_{a1} - L_{a1a2}i_{a2} - L_{a1b1}i_{b1} - L_{a1b2}i_{b2} - L_{a1c1}i_{c1} - L_{a1c2}i_{c2} + L_{a1fd}i_{fd} + L_{a1kd}i_{kd} + L_{a1kq}i_{kq} \quad (1)$$

$$i_{a2} = i_{a1} - i_{af} \quad (2)$$

$$i_{b2} = i_{b1} - i_{bf} \quad (3)$$

$$i_{c2} = i_{c1} - i_{cf} \quad (4)$$

$$\psi_a = \psi_{a1} + \psi_{a2} \quad (5)$$

$$\psi_b = \psi_{b1} + \psi_{b2} \quad (6)$$

$$\psi_c = \psi_{c1} + \psi_{c2} \quad (7)$$

$$\begin{bmatrix} \psi_a \\ \psi_b \\ \psi_c \\ \psi_{fd} \\ \psi_{kd} \\ \psi_{kq} \\ \psi_{a2} \\ \psi_{b2} \\ \psi_{c2} \end{bmatrix} = \begin{bmatrix} L_{aa} & L_{ab} & L_{ac} & L_{afd} & L_{akd} & L_{akq} & L_{aaf} & L_{abf} & L_{acf} \\ L_{ba} & L_{bb} & L_{bc} & L_{bfd} & L_{bkd} & L_{bkq} & L_{baf} & L_{bbf} & L_{bcf} \\ L_{ca} & L_{cb} & L_{cc} & L_{cfd} & L_{ckd} & L_{ckq} & L_{caf} & L_{cbf} & L_{ccf} \\ L_{fda} & L_{fdb} & L_{fdc} & L_{fdfd} & L_{fdkd} & L_{fdkq} & L_{fdaf} & L_{fdbf} & L_{fdcf} \\ L_{kda} & L_{kdb} & L_{kdc} & L_{kdfd} & L_{kdkd} & L_{kdkq} & L_{kdaf} & L_{kdbf} & L_{kdcf} \\ L_{kqa} & L_{kqb} & L_{kqc} & L_{kqfd} & L_{kqkd} & L_{kqkq} & L_{kqaf} & L_{kqbf} & L_{kqcf} \\ L_{a2a} & L_{a2b} & L_{a2c} & L_{a2fd} & L_{a2kd} & L_{a2kq} & L_{a2af} & L_{a2bf} & L_{a2cf} \\ L_{b2a} & L_{b2b} & L_{b2c} & L_{b2fd} & L_{b2kd} & L_{b2kq} & L_{b2af} & L_{b2bf} & L_{b2cf} \\ L_{c2a} & L_{c2b} & L_{c2c} & L_{c2fd} & L_{c2kd} & L_{c2kq} & L_{c2af} & L_{c2bf} & L_{c2cf} \end{bmatrix} * \begin{bmatrix} i_a \\ i_b \\ i_c \\ i_{fd} \\ i_{kd} \\ i_{kq} \\ i_{af} \\ i_{bf} \\ i_{cf} \end{bmatrix} \tag{8}$$

$$\begin{bmatrix} \psi_{sdq0} \\ \psi_{rabc} \\ \psi_{fdq0} \end{bmatrix} = \begin{bmatrix} Z_1 & Z_2 & Z_3 \\ Z_4 & Z_5 & Z_6 \\ Z_7 & Z_8 & Z_9 \end{bmatrix} * \begin{bmatrix} i_{sdq0} \\ i_{rabc} \\ i_{fdq0} \end{bmatrix} \tag{9}$$

where

$$\psi_{sdq0} = \begin{bmatrix} \psi_{sd} \\ \psi_{sq} \\ \psi_{s0} \end{bmatrix}; \psi_{rabc} = \begin{bmatrix} \psi_{fd} \\ \psi_{kd} \\ \psi_{kq} \end{bmatrix}; \psi_{fdq0} = \begin{bmatrix} \psi_{df} \\ \psi_{qf} \\ \psi_{0f} \end{bmatrix};$$

$$i_{sdq0} = \begin{bmatrix} i_{sd} \\ i_{sq} \\ i_{s0} \end{bmatrix}; i_{fdq0} = \begin{bmatrix} i_{df} \\ i_{qf} \\ i_{0f} \end{bmatrix} i_{rabc} = i_{rdq0} = \begin{bmatrix} i_{fd} \\ i_{kd} \\ i_{kq} \end{bmatrix}$$

Z_1 to Z_9 in equation (9) can be obtained as follows

$$Z_1 = \begin{bmatrix} -L_d & 0 & 0 \\ 0 & -L_q & 0 \\ 0 & 0 & -L_0 \end{bmatrix}; Z_3 = -Z_7 = \begin{bmatrix} \mu_1 L_d & 0 & 0 \\ 0 & \mu_2 L_q & 0 \\ 0 & 0 & \mu_3 L_0 \end{bmatrix} \tag{10}$$

$$Z_2 = \begin{bmatrix} L_{afd} & L_{akd} & 0 \\ 0 & 0 & L_{akq} \\ 0 & 0 & 0 \end{bmatrix}$$

$$Z_4 = \begin{bmatrix} -\frac{3}{2}L_{afd} & 0 & 0 \\ -\frac{3}{2}L_{akd} & 0 & 0 \\ 0 & -\frac{3}{2}L_{akq} & 0 \end{bmatrix} Z_6 = \begin{bmatrix} \frac{3}{2}L_{afd}\mu_1 & 0 & 0 \\ \frac{3}{2}L_{akd}\mu_1 & 0 & 0 \\ 0 & \frac{3}{2}L_{akq}\mu_2 & 0 \end{bmatrix}$$

$$Z_5 = \begin{bmatrix} L_{fdfd} & L_{fdkd} & 0 \\ L_{fdkd} & L_{kdkd} & 0 \\ 0 & 0 & L_{kqkq} \end{bmatrix} Z_8 = \begin{bmatrix} L_{afd}\mu_1 & L_{akd}\mu_1 & 0 \\ 0 & 0 & L_{akq}\mu_2 \\ 0 & 0 & 0 \end{bmatrix}$$

$$Z_9 = \begin{bmatrix} {\mu_1}^2(L_d - L_0) + \mu_1 L_0 & 0 & 0 \\ 0 & {\mu_2}^2(L_q - L_0) + \mu_2 L_0 & 0 \\ 0 & 0 & \mu_3 L_0 \end{bmatrix} \tag{11}$$

$$Z = \begin{bmatrix} -(L_{ad}+L_l) & 0 & 0 & L_{ad} & L_{ad} & 0 & \mu_1(L_{ad}+L_l) & 0 & 0 \\ 0 & -(L_{aq}+L_l) & 0 & 0 & 0 & L_{aq} & 0 & \mu_2(L_{aq}+L_l) & 0 \\ 0 & 0 & -L_0 & 0 & 0 & 0 & 0 & 0 & \mu_3 L_0 \\ -L_{ad} & 0 & 0 & L_{fdfd} & L_{fdkd} & 0 & L_{ad}\mu_1 & 0 & 0 \\ -L_{ad} & 0 & 0 & L_{fdkd} & L_{kdkd} & 0 & L_{ad}\mu_1 & 0 & 0 \\ 0 & -L_{aq} & 0 & 0 & 0 & L_{kqkq} & 0 & L_{aq}\mu_2 & 0 \\ -\mu_1(L_{ad}+L_l) & 0 & 0 & L_{ad}\mu_1 & L_{ad}\mu_1 & 0 & P & 0 & 0 \\ 0 & -\mu_2(L_{aq}+L_l) & 0 & 0 & 0 & L_{aq}\mu_2 & 0 & Q & 0 \\ 0 & 0 & -\mu_3 L_0 & 0 & 0 & 0 & 0 & 0 & R \end{bmatrix}$$

$$where P = {\mu_1}^2(L_{ad}+L_l-L_0)+\mu_1 L_0;\ Q = -{\mu_2}^2(L_{aq}+L_l-L_0)+\mu_2 L_0;\ R = \mu_3 L_0 \tag{12}$$

Converting the above set of Eq. (9) into the per-unit form and writing Z (where Z is the matrix containing Z_1 to Z_9) the expression in Eq. (12) is obtained. So the Eq. (9) with the value of Z given by Eq. (12) forms the final set of flux equations. The various terms in the Eq. (12) are defined in Table 1 in Appendix A

Next, the equations for the voltage induced in the coils are derived. Figure 2 can be redrawn as shown in Fig. 3. A typical voltage equation for the coil say a1 is given in Eq. (16). Similar equations can be written for other coils, namely a2, b1, b2, c1, c2, fd, kd, and kq. Here the Kirchhoff's current law equations for each phase can be written as given in Eqs. (2) to (4). Other Eqs. (13) to (15) can be used to manipulate the voltage equations that were written for each coil to obtain modified equations. These equations are shown in the matrix form in Eq. (17). Applying the park's transformation to Eq. (17), we obtain the Eq. (19).

$$\begin{aligned} r_a = r_b = r_c = r_s;\ r_{a1} = (1-\mu_1)r_s;\ r_{a2} = \mu_1 r_s; \\ r_{b1} = (1-\mu_2)r_s;\ r_{b2} = \mu_2 r_s;\ r_{c1} = (1-\mu_3)r_s;\ r_{c2} = \mu_3 r_s; \end{aligned} \tag{13}$$

$$v_{a2} = -r_{af} i_{af};\ v_{b2} = -r_{bf} i_{bf};\ v_{c2} = -r_{cf} i_{cf}; \tag{14}$$

$$v_a = v_{a1} + v_{a2};\ v_b = v_{b1} + v_{b2};\ v_c = v_{c1} + v_{c2}; \tag{15}$$

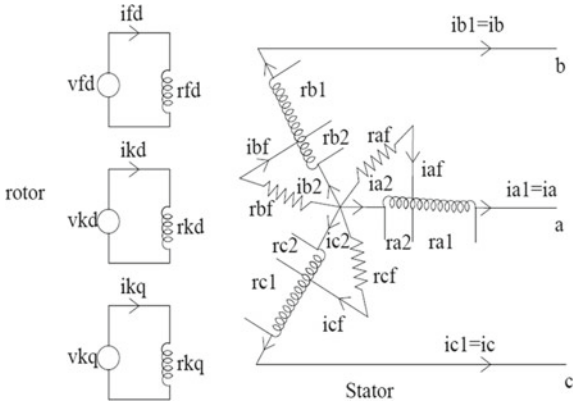

Fig. 3 Modified Schematic of a synchronous generator with fault in all phases

$$v_{a1} = -r_{a1} i_{a1} + \frac{d\Psi_{a1}}{dt} \tag{16}$$

$$\begin{bmatrix} v_{sabc} \\ v_{rabc} \\ 0 \end{bmatrix} = \begin{bmatrix} -R_s & O & \mu_{abc} R_s \\ O & R_r & O \\ -\mu_{abc} R_s & O & \mu_{abc} R_s + R_f \end{bmatrix} * \begin{bmatrix} i_{sabc} \\ i_{rabc} \\ i_{fabc} \end{bmatrix} + \frac{d}{dt} \begin{bmatrix} \psi_{sabc} \\ \psi_{rabc} \\ \psi_{fabc} \end{bmatrix} \tag{17}$$

where

$$\begin{aligned} &\psi_{sabc} = \begin{bmatrix} \psi_a \\ \psi_b \\ \psi_c \end{bmatrix}; \psi_{rabc} = \begin{bmatrix} \psi_{fd} \\ \psi_{kd} \\ \psi_{kq} \end{bmatrix}; \psi_{fabc} = \begin{bmatrix} \psi_{a2} \\ \psi_{b2} \\ \psi_{c2} \end{bmatrix}; i_{sabc} = \begin{bmatrix} i_a \\ i_b \\ i_c \end{bmatrix}; \\ &i_{rabc} = \begin{bmatrix} i_{fd} \\ i_{kd} \\ i_{kq} \end{bmatrix}; i_{fabc} = \begin{bmatrix} i_{af} \\ i_{bf} \\ i_{cf} \end{bmatrix}; v_{sabc} = \begin{bmatrix} v_a \\ v_b \\ v_c \end{bmatrix}; \\ &v_{rabc} = \begin{bmatrix} v_{fd} \\ v_{kd} \\ v_{kq} \end{bmatrix}; 0 = \begin{bmatrix} 0 \\ 0 \\ 0 \end{bmatrix}; R_s = diag[r_s \ r_s \ r_s]; R_r = diag[r_{fd} \ r_{kd} \ r_{kq}]; \\ &R_f = diag[r_f \ r_f \ r_f]; \mu_{abc} = diag[\mu_a \ \mu_b \ \mu_c]; \text{O is 3X3 nullmatrix} \end{aligned} \tag{18}$$

$$\begin{aligned} \begin{bmatrix} v_{sdq0} \\ v_{rdq0} \\ 0 \end{bmatrix} = &\begin{bmatrix} P & O & O \\ O & I_3 & O \\ O & O & P \end{bmatrix} \begin{bmatrix} -R_s & O & \mu_{dq0} R_s \\ O & -R_r & O \\ -\mu_{dq0} R_s & O & \mu_{dq0} R_s + R_{fdq0} \end{bmatrix} * \\ &\begin{bmatrix} P^{-1} & O & O \\ O & I_3 & O \\ O & O & P^{-1} \end{bmatrix} \begin{bmatrix} i_{sdq0} \\ i_{rdq0} \\ i_{fdq0} \end{bmatrix} + \begin{bmatrix} P & O & O \\ O & I_3 & O \\ O & O & P \end{bmatrix} \frac{d}{dt} \begin{bmatrix} \psi_{sabc} \\ \psi_{rabc} \\ \psi_{fabc} \end{bmatrix}; \end{aligned} \tag{19}$$

$$\text{Where } \mu_{dq0} = P^{-1} diag[\mu_a \ \mu_b \ \mu_c] P; \ R_{fdq0} = diag[r_f \ r_f \ r_f] \tag{20}$$

Where

$$\begin{aligned} &\psi_{sabc} = \begin{bmatrix} \psi_a \\ \psi_b \\ \psi_c \end{bmatrix}; \psi_{rabc} = \begin{bmatrix} \psi_{fd} \\ \psi_{kd} \\ \psi_{kq} \end{bmatrix}; \psi_{fabc} = \begin{bmatrix} \psi_{a2} \\ \psi_{b2} \\ \psi_{c2} \end{bmatrix}; i_{sdq0} = \begin{bmatrix} i_{sd} \\ i_{sq} \\ i_{s0} \end{bmatrix}; \\ &i_{rdq0} = \begin{bmatrix} i_{fd} \\ i_{kd} \\ i_{kq} \end{bmatrix}; i_{fdq0} = \begin{bmatrix} i_{df} \\ i_{qf} \\ i_{0f} \end{bmatrix}; v_{sdq0} = \begin{bmatrix} v_{sd} \\ v_{sq} \\ v_{s0} \end{bmatrix}; v_{rdq0} = \begin{bmatrix} v_{fd} \\ v_{kd} \\ v_{kq} \end{bmatrix}; 0 = \begin{bmatrix} 0 \\ 0 \\ 0 \end{bmatrix}; \end{aligned} \tag{21}$$

$$\begin{bmatrix} v_{sdq0} \\ v_{rdq0} \\ 0 \end{bmatrix} = \begin{bmatrix} -PR_sP^{-1} & O & P\mu_{dq0}R_sP^{-1} \\ O & -R_r & O \\ -P\mu_{dq0}R_sP^{-1} & O & P(\mu_{dq0}R_s + R_{fdq0})P^{-1} \end{bmatrix} \begin{bmatrix} i_{sdq0} \\ i_{rdq0} \\ i_{fdq0} \end{bmatrix} + \begin{bmatrix} P & O & O \\ O & I_3 & O \\ O & O & P \end{bmatrix} \frac{d}{dt} \begin{bmatrix} \psi_{sabc} \\ \psi_{rabc} \\ \psi_{fabc} \end{bmatrix}; \tag{22}$$

simplifying further the Eq. (22) is obtained. The derivative part of the Eq. (22) can be simplified to an expression as given in Eq. (23)

$$\begin{bmatrix} v_{sdq0} \\ v_{rdq0} \\ 0 \end{bmatrix} = \begin{bmatrix} -PR_sP^{-1} & O & P\mu_{dq0}R_sP^{-1} \\ O & -R_r & O \\ -P\mu_{dq0}R_sP^{-1} & O & P(\mu_{dq0}R_s + R_{fdq0})P^{-1} \end{bmatrix} \begin{bmatrix} i_{sdq0} \\ i_{rdq0} \\ i_{fdq0} \end{bmatrix} + \frac{d}{dt} \begin{bmatrix} \psi_{sdq0} \\ \psi_{rdq0} \\ \psi_{fdq0} \end{bmatrix} + \begin{bmatrix} \dot{P}P^{-1} & O & O \\ O & O & O \\ O & O & \dot{P}P^{-1} \end{bmatrix} \begin{bmatrix} \psi_{sdq0} \\ \psi_{rdq0} \\ \psi_{fdq0} \end{bmatrix}; \tag{23}$$

From the parks transformation matrices, the value of $\dot{P}\,P^{-1}$ can be obtained as below in Eq. (24)

$$\dot{P}\,P^{-1} = \frac{2}{3}\omega \begin{bmatrix} -\sin\theta & -\sin\left(\theta - \frac{2\pi}{3}\right) & -\sin\left(\theta + \frac{2\pi}{3}\right) \\ -\cos\theta & -\cos\left(\theta - \frac{2\pi}{3}\right) & -\cos\left(\theta + \frac{2\pi}{3}\right) \\ 0 & 0 & 0 \end{bmatrix} * \begin{bmatrix} \cos\theta & -\sin\theta & 1 \\ \cos\left(\theta - \frac{2\pi}{3}\right) & -\sin\left(\theta - \frac{2\pi}{3}\right) & 1 \\ \cos\left(\theta + \frac{2\pi}{3}\right) & -\sin\left(\theta + \frac{2\pi}{3}\right) & 1 \end{bmatrix} \tag{24}$$

Using standard identities [14], we can simplify the Eq. (24) as in Eq. (25). Using Eq. (25) in Eq. (23), the Eq. (26) is obtained

$$\dot{P}\,P^{-1} = \begin{bmatrix} 0 & \omega & 0 \\ -\omega & 0 & 0 \\ 0 & 0 & 0 \end{bmatrix} \tag{25}$$

$$V = RI + \dot{\psi} + Q\psi \tag{26}$$

where

$$Q = \begin{bmatrix} 0 & \omega & 0 & 0 & 0 & 0 & 0 & 0 & 0 \\ -\omega & 0 & 0 & 0 & 0 & 0 & 0 & 0 & 0 \\ 0 & 0 & 0 & 0 & 0 & 0 & 0 & 0 & 0 \\ 0 & 0 & 0 & 0 & 0 & 0 & 0 & 0 & 0 \\ 0 & 0 & 0 & 0 & 0 & 0 & 0 & 0 & 0 \\ 0 & 0 & 0 & 0 & 0 & 0 & 0 & 0 & 0 \\ 0 & 0 & 0 & 0 & 0 & 0 & 0 & \omega & 0 \\ 0 & 0 & 0 & 0 & 0 & 0 & -\omega & 0 & 0 \\ 0 & 0 & 0 & 0 & 0 & 0 & 0 & 0 & 0 \end{bmatrix}$$

$$R = \begin{bmatrix} -r_s & 0 & 0 & 0 & 0 & 0 & \mu_1 r_s & 0 & 0 \\ 0 & -r_s & 0 & 0 & 0 & 0 & 0 & \mu_2 r_s & 0 \\ 0 & 0 & -r_s & 0 & 0 & 0 & 0 & 0 & \mu_3 r_s \\ 0 & 0 & 0 & r_{fd} & 0 & 0 & 0 & 0 & 0 \\ 0 & 0 & 0 & 0 & r_{kd} & 0 & 0 & 0 & 0 \\ 0 & 0 & 0 & 0 & 0 & r_{kq} & 0 & 0 & 0 \\ -\mu_1 r_s & 0 & 0 & 0 & 0 & 0 & \mu_1 r_s + r_f & 0 & 0 \\ 0 & -\mu_2 r_s & 0 & 0 & 0 & 0 & 0 & \mu_2 r_s + r_f & 0 \\ 0 & 0 & \mu_3 r_s & 0 & 0 & 0 & 0 & 0 & \mu_3 r_s + r_f \end{bmatrix} \tag{27}$$

Substituting the value of ψ from Eq. (9) in Eq. (26) and collecting terms, the Eq. (28) is obtained. When PU conversion is done, the form of the Eq. (28) remains the same. The final set of differential equations or the dq0 model describing the synchronous generator is given in Eq. (28). This set of equations can be further rearranged to obtain the state-space model shown in Eq. (30). Here it should be mentioned specifically that the model used here is similar to the model in [4], but the model in the quoted work was done for a fault in a single phase the same has been extended here for fault in all three phases using the fault parameters μ_1, μ_2 and μ_3. The next section describes the Kalman filter used in this work.

$$V = Z\dot{I} + (R + QZ)I \tag{28}$$

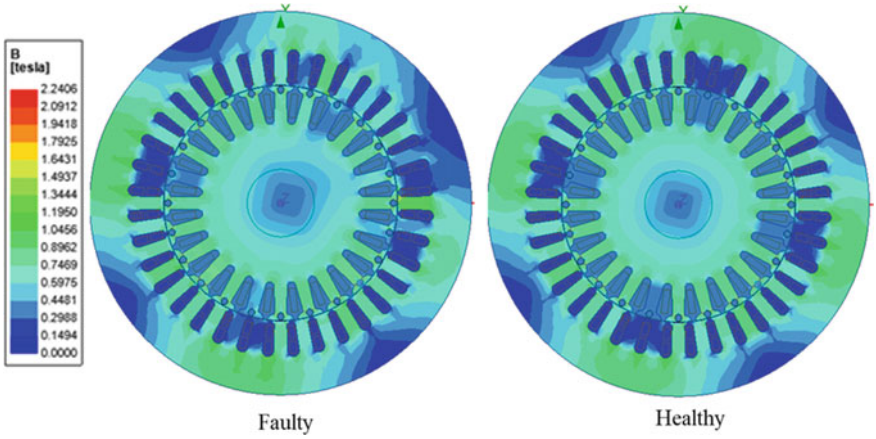

Fig. 4 Flux map during healthy and faulty conditions

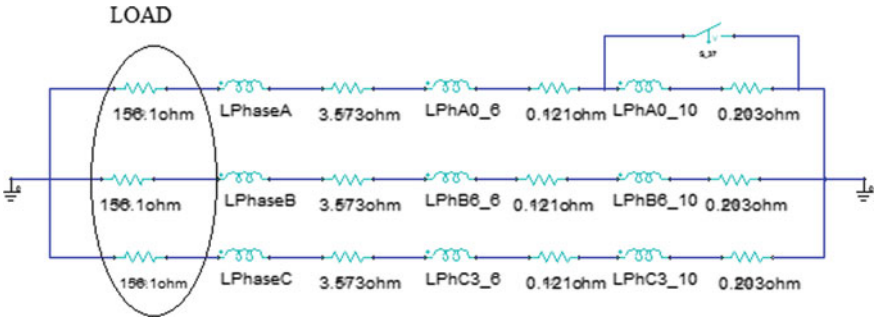

Fig. 5 Generator winding connection with the load

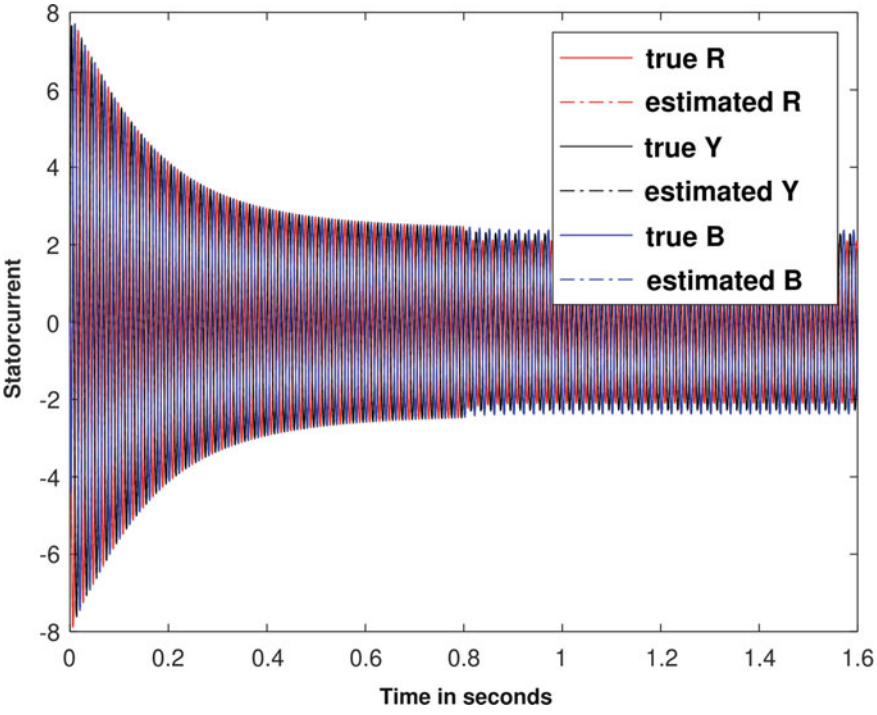

Fig. 6 Plot of the stator currents actual and estimated with fault introduced at 0.8 s

Where

$$R + QZ =$$

$$\begin{bmatrix} -r_s & -\omega(L_{aq}+L_l) & 0 & 0 & 0 & L_{aq}\omega & \mu_1 r_s & \mu_2\omega(L_{aq}+L_l) & 0 \\ \omega(L_{ad}+L_l) & -r_s & 0 & -L_{ad}\omega & -L_{ad}\omega & 0 & -\mu_1\omega(L_{ad}+L_l) & \mu_2 r_s & 0 \\ 0 & 0 & -r_s & 0 & 0 & 0 & 0 & 0 & \mu_3 r_s \\ 0 & 0 & 0 & r_f & 0 & 0 & 0 & 0 & 0 \\ 0 & 0 & 0 & 0 & r_d & 0 & 0 & 0 & 0 \\ 0 & 0 & 0 & 0 & 0 & r_q & 0 & 0 & 0 \\ -\mu_1 r_s & -\mu_2\omega(L_{aq}+L_l) & 0 & 0 & 0 & L_{aq}\mu_2\omega & r_{af}+\mu_1 r_s & N & 0 \\ \mu_1\omega(L_{ad}+L_l) & -\mu_2 r_s & 0 & -L_{ad}\mu_1\omega & -L_{ad}\mu_1\omega & 0 & M & r_{af}+\mu_2 r_s & 0 \\ 0 & 0 & -\mu_3 r_s & 0 & 0 & 0 & 0 & 0 & r_{af}+\mu_3 r_s \end{bmatrix}$$

where $M = -\mu_1\omega(L_0+(L_{ad}+L_l)\mu_1 - L_0\mu_1)$ and $N = \mu_2\omega(L_0+L_q\mu_2 - L_0\mu_2)$

(29)

$$\dot{x}(t) = Ax(t) + Bu(t)$$

Where

$$A = -\begin{bmatrix} -(L_{ad}+L_l) & 0 & 0 & L_{ad} & L_{ad} & 0 \\ 0 & -(L_{aq}+L_l) & 0 & 0 & 0 & L_{aq} \\ 0 & 0 & -L_0 & 0 & 0 & 0 \\ -L_{ad} & 0 & 0 & L_{fdfd} & L_{fdkd} & 0 \\ -L_{ad} & 0 & 0 & L_{fdkd} & L_{kdkd} & 0 \\ 0 & -L_{aq} & 0 & 0 & 0 & L_{kqkq} \end{bmatrix}^{-1}$$

$$\begin{bmatrix} -r_s & -\omega(L_{aq}+L_l) & 0 & 0 & 0 & L_{aq}\omega \\ \omega(L_{ad}+L_l) & -r_s & 0 & -L_{ad}\omega & -L_{ad}\omega & 0 \\ 0 & 0 & -r_s & 0 & 0 & 0 \\ 0 & 0 & 0 & r_f & 0 & 0 \\ 0 & 0 & 0 & 0 & r_d & 0 \\ 0 & 0 & 0 & 0 & 0 & r_q \end{bmatrix} \tag{30}$$

$$B = \begin{bmatrix} -(L_{ad}+L_l) & 0 & 0 & L_{ad} & L_{ad} & 0 \\ 0 & -(L_{aq}+L_l) & 0 & 0 & 0 & L_{aq} \\ 0 & 0 & -L_0 & 0 & 0 & 0 \\ -L_{ad} & 0 & 0 & L_{fdfd} & L_{fdkd} & 0 \\ -L_{ad} & 0 & 0 & L_{fdkd} & L_{kdkd} & 0 \\ 0 & -L_{aq} & 0 & 0 & 0 & L_{kqkq} \end{bmatrix}^{-1}$$

$$x(t) = \begin{bmatrix} i_{sd} - \mu_1 i_{df} \\ i_{sq} - \mu_2 i_{qf} \\ i_{s0} - \mu_3 i_{0f} \\ i_{rd} \\ i_{rq} \\ i_{r0} \end{bmatrix}; u(t) = \begin{bmatrix} v_{sd} \\ v_{sq} \\ v_{s0} \\ v_{fd} \\ v_{kd} \\ v_{kq} \end{bmatrix}$$

5 Linear Kalman Filter and the Proposed Indicator

The standard linear Kalman filter has two steps, namely the prediction step and correction step [15, 16]. In this work, the linear Kalman filter uses the state-space model given in (30), but here the measurements are the stator currents. So to obtain the stator currents from the state vector in the model, a joint Kalman filter with the extended state vector as given in (31) is required. The resultant Am, Bm, and Cm, matrices of the state-space model used by the joint kalman filter are given in (32). The above model is a continuous-time state-space model, to obtain a discretized model, the standard procedure for discretization is used. Here it should be noted that the new system with the extended state vector is linear as the matrices Am, Bm, and Cm are independent of the state vector, hence a linear Kalman filter can be used making the system computationally efficient.

$$x(t) = \left[i_{sd} - \mu_1 i_{df}\ i_{sq} - \mu_2 i_{qf}\ i_{s0} - \mu_3 i_{0f}\ i_{rd}\ i_{rq}\ i_{r0}\ \mu_1 i_{df}\ \mu_2 i_{qf}\ \mu_3 i_{0f}\right]^T \quad (31)$$

$$A_m = \begin{bmatrix} A & 0 \\ 0 & I \end{bmatrix}; B_m = \begin{bmatrix} B \\ 0 \end{bmatrix}; C_m = \begin{bmatrix} I & O & I \end{bmatrix} \quad (32)$$

$$\begin{aligned} &\text{Fault Indicator 1}=\mu_1 i_{df}\cos(\theta_r) - \mu_2 i_{qf}\sin(\theta_r) + \mu_3 i_{0f} \\ &\text{Fault Indicator 2}=\mu_1 i_{df}\cos(\theta_r - 2\pi/3) - \mu_2 i_{qf}\sin(\theta_r - 2\pi/3) + \mu_3 i_{0f} \\ &\text{Fault Indicator 3}=\mu_1 i_{df}\cos(\theta_r + 2\pi/3) - \mu_2 i_{qf}\sin(\theta_r + 2\pi/3) + \mu_3 i_{0f} \end{aligned} \quad (33)$$

In [4], a fault indicator μ_{ifs} has been proposed. This indicator can detect the fault in only one phase since, in this work, the model has been extended to all the 3 phases, 3 sets of indicators are proposed as shown in Eq. (33). To get a proper indicator a 200 pt moving RMS was taken. These indicators can thus indicate a fault in any one of the three phases and in addition, it has been observed that these three indicators react differently to load imbalance in the 3 phases and hence can be also used as indicators for load imbalance. The experiments performed and the results with conclusions are provided in the next section.

6 Results and Discussion

Simulation experiments were done with the fault injection capable generator that was built in Maxwell. As shown in Fig. 5, the generator had a star connected stator, and each phase was split to create fault injection capability as described earlier. The stator windings were connected to a star connected resistive load. For the simulation experiments, the value of the load current was fixed at around 1.5 A. A set of nine experiments were conducted. One set of 3 experiments involved shorting 10 turns of each phase (namely R, Y, and B) in turn and collecting the stator currents, stator

voltages, and field current. The next set of 3 experiments involved shorting of 6 turns for each phase and collecting the data. The final set of 3 experiments involved introducing a load imbalance in each phase and collecting the data. Each experiment involved running the generator for 1.6 s and fault or load imbalance was introduced at 0.8 s. The 2D transient FE simulation was run on a High performance computing cluster. A time step of 0.0001 s was used. The data obtained from the simulations were given to the linear Kalman filter implemented in MATLAB. The Kalman filter generated fault indicators that were described in the previous section

The first thing that has to be proved is the correctness of the FEM. Figure 4 shows the flux map captured during the run of the simulation in healthy and faulty conditions. It shows clearly that asymmetry has been introduced in the flux pattern due to the inter-turn fault. This asymmetry leads to variation in the currents observed due to the inter-turn fault.

Next, to check the validity of the proposed dq0 model, the estimated stator currents from the Kalman filter and the actual stator currents are plotted. It can be seen from Figs. 6 and 7 that the Kalman filter using the dq0 model was able to track the actual stator currents in both the healthy and faulty conditions. As a further confirmation, the frequency spectra of the actual stator currents and the estimated stator currents were obtained and the same is shown in Figs. 8 and 9. The Fig. 8 contains the frequency spectra of the stator currents for the no-fault case both estimated and actual infact the estimated and actual current spectra overlap perfectly. The Fig. 9 contains the frequency spectra of the stator currents for 10 turn fault in R-phase, both estimated and actual, here too both the spectra overlap confirming that the dq0 model was able to exactly capture the features of the system. Further, by comparing Figs. 8 and 9,

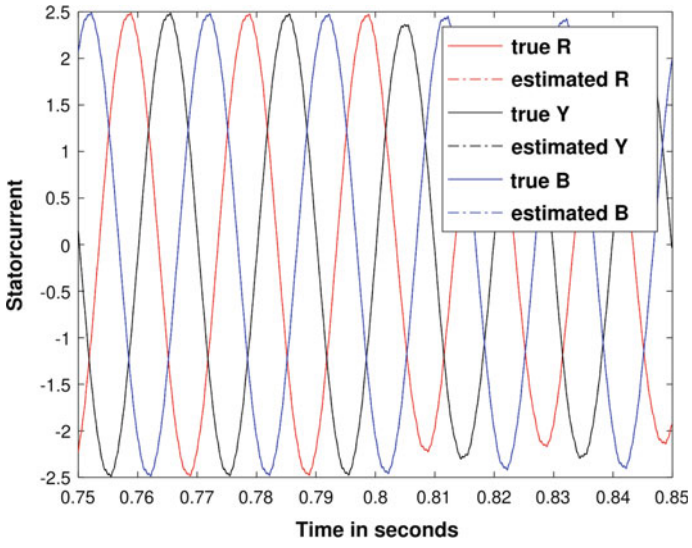

Fig. 7 Zoomed version of Fig. 6

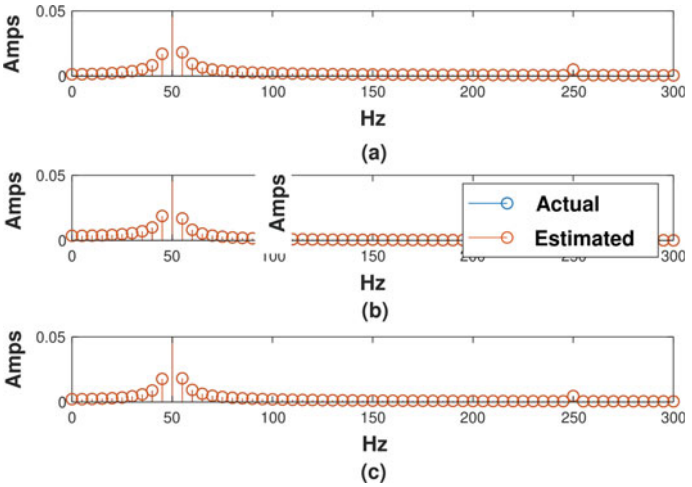

Fig. 8 Frequency spectrum of the stator currents estimated and actual No-fault case (**a**) R-phase (**b**) Y-phase (**c**) B-phase

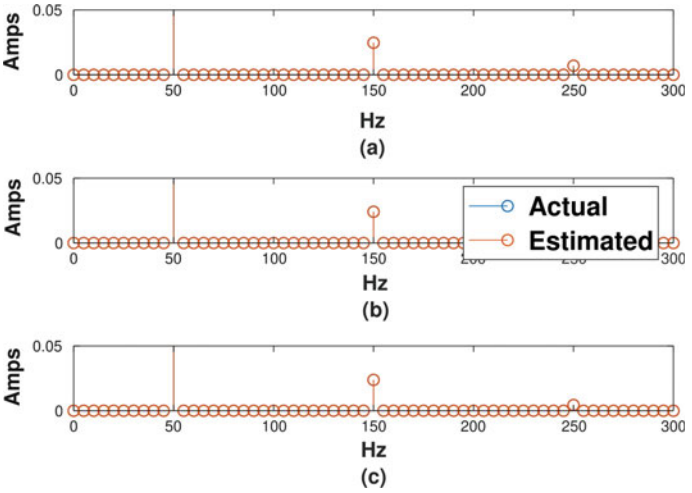

Fig. 9 Frequency spectrum of the stator currents estimated and actual With 10 turn fault in R-phase (**a**) R-phase (**b**) Y-phase (**c**) B-phase

we see that there is a significant change in the third harmonic component due to fault confirming that the FE simulation data confirms the theoretical behavior of inter-turn faults [17].

Next, the data from the 9 sets of simulation experiments mentioned earlier were fed to the Kalman filter and the indicators developed in Eq. (33) were plotted. The results are shown in Figs. 10, 11, and 12. Figure 10 is a subplot showing the three

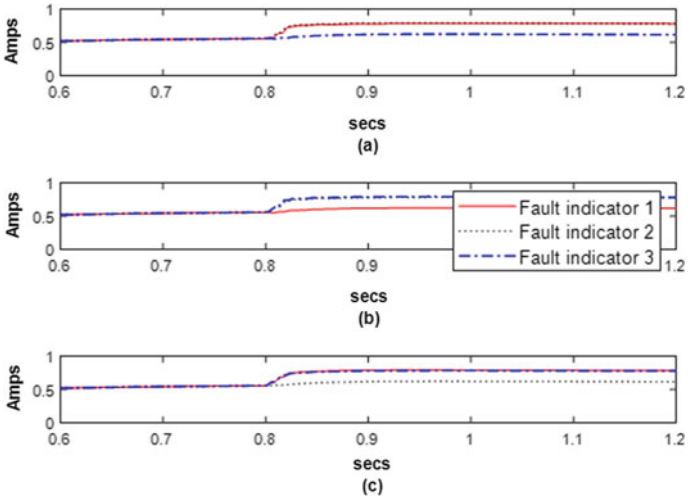

Fig. 10 Fault indicators with 6 turn fault at 0.8 s introduced in (**a**) R-phase (**b**) Y-phase (**c**) B-phase

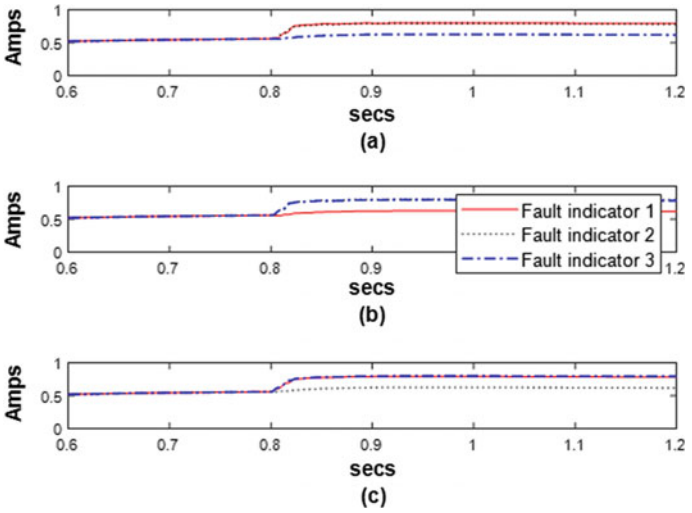

Fig. 11 Fault indicators with 10 turn fault at 0.8 s introduced in (**a**) R-phase (**b**) Y-phase (**c**) B-phase

indicators when a 6 turn fault is introduced in the various phases. The subplot (a) shows the three fault indicators when 6 turn fault is introduced in R phase. It can be seen that all the indicators increase in value from the no-fault conditions but the Fault indicator-3 has the minimum deviation. Similarly, from the subplots(b) and (c), it can be concluded that for a fault in the Y phase the increase will be minimum in the Fault indicator-1, and for a fault in the B phase increase will be minimum in the Fault indicator-2. Figure 11 leads to the same conclusions but for 10 turn fault.

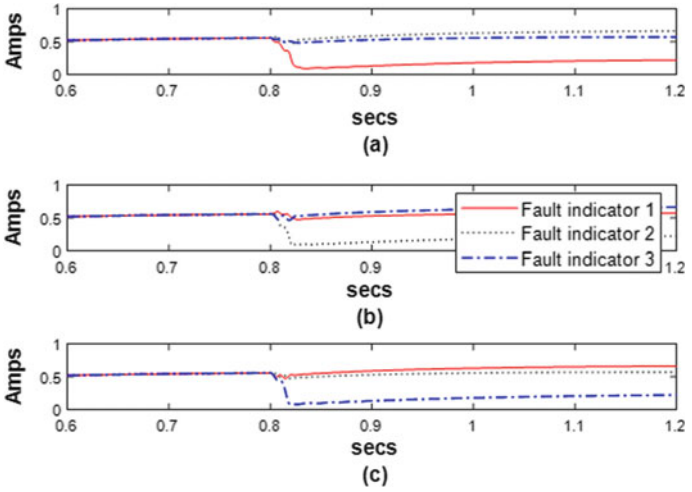

Fig. 12 Fault indicators with load imbalance at 0.8 s introduced in (**a**) R-phase (**b**) Y-phase (**c**) B-phase

Figure 12 (a) shows the indicators when there is a load imbalance in the R phase where it can be observed that almost all the indicators reduced in magnitude. The maximum reduction occurs in the Fault indicator-1. Similarly, from subplots (b) and (c), it can be concluded that imbalance in the Y phase will produce a maximum decrease in Fault indicator-2 and imbalance in the B phase will produce a maximum decrease in Fault indicator-3. Hence, we can conclude that this novel indicator can identify an inter-turn fault and at the same time distinguish the condition from a load imbalance condition.

7 Conclusions and Future Work

Considering the importance of stator inter-turn fault diagnosis in the reliable operation of a synchronous generator, this work proposed an improved way to model a generator so that fault can be diagnosed in all three phases. Further, fault indicators are proposed to identify the phase in which the inter-turn fault has occurred. This indicator also indicates the presence of a load imbalance which can often lead to a faulty diagnostic conclusion regarding the presence of an inter-turn fault. This work assumes that only one of the conditions, either the fault or load imbalance, can occur at a given instant, it is also assumed that fault can occur in one of the phases. These can be taken up for future research.

8 Appendix

Table 1 Terms defined

Variable	Meaning
L_{ad}	mutual inductance between stator and d-axis rotor ckts
L_{aq}	mutual inductance between stator and q-axis rotor ckts
L_l	leakage inductance
L_{fdfd}	self -inductance of the field winding
L_{fdkd}	mutual inductance between field and d-axis damper
L_{kdkd}	self-inductance of the d-axis damper
L_{kqkq}	self-inductance of the q-axis damper
r_s	armature winding resistance
r_f	field winding resistance
r_d	d-axis damper winding resistance
r_q	q-axis damper winding resistance
i_{sd}	d-axis stator current
i_{df}	faulty d-axis stator current
i_{sq}	q-axis stator current
i_{qf}	faulty q-axis stator current
i_{s0}	0-axis stator current
i_{0f}	faulty 0-axis stator current
i_{rd}	d-axis damper current
i_{rq}	q-axis damper current
i_{r0}	0-axis damper current
v_{sd}	d-axis stator voltage
v_{sq}	q-axis stator voltage
v_{s0}	0-axis stator voltage
v_{fd}	field voltage
v_{kd}	d-axis damper voltage
v_{kq}	q-axis damper voltage

References

1. Kliman G, Premerlani W, Koegl R, Hoeweler D (1996) A new approach to on-line turn fault detection in ac motors. In: IAS '96 Conference Record of the 1996 IEEE industry applications conference thirty-first IAS annual meeting, vol 1, pp 687–693. https://doi.org/10.1109/IAS.1996.557113
2. Gao Z, Cecati C, Ding SX (2015) A survey of fault diagnosis and fault-tolerant techniques-part i: fault diagnosis with model-based and signal-based approaches. IEEE Trans Ind Electron 62(6):3757–3767

3. Mazzoletti MA, Bossio GR, De Angelo CH, Espinoza-Trejo DR (2017) A model-based strategy for interturn short-circuit fault diagnosis in pmsm. IEEE Trans Ind Electron 64(9):7218–7228. https://doi.org/10.1109/TIE.2017.2688973
4. Nadarajan S, Panda SK, Bhangu B, Gupta AK (2016) Online model-based condition monitoring for brushless wound-field synchronous generator to detect and diagnose stator windings turn-to-turn shorts using extended kalman filter. IEEE Trans Ind Electron 63(5):3228–3241
5. Aubert B, Regnier J, Caux S, Alejo D (2015) Kalman-filter-based indicator for online interturn short circuits detection in permanent-magnet synchronous generators. IEEE Trans Ind Electron 62(3):1921–1930. https://doi.org/10.1109/TIE.2014.2348934
6. El Sayed W, Abd El Geliel M, Lotfy A (2020) Fault diagnosis of pmsg stator inter-turn fault using extended kalman filter and unscented kalman filter. Energies 13(11). https://doi.org/10.3390/en13112972
7. Idrissi I, El Bachtiri R, Chafouk H, Khanfara M (2019) Fault diagnosis of stator inter-turn short circuit in doubly fed induction generator of wind turbine. In: 2019 6th international conference on control, decision and information technologies (CoDIT), pp 1313–1318. https://doi.org/10.1109/CoDIT.2019.8820697
8. Jaiswal V, Wang D, Kumar PS (2020) Winding fault diagnosis and failure prognosis technique for brushless synchronous generator. Electr Power Compon Syst 48(11):1159–1170. https://doi.org/10.1080/15325008.2020.1831652
9. Gopinath R, Nambiar T, Abhishek S, Pramodh SM, Pushparajan M, Ramachandran K, Kumar CS, Thirugnanam R (2013) Fault injection capable synchronous generator for condition based maintenance. In: 2013 7th international conference on intelligent systems and control (ISCO), pp 60–64. https://doi.org/10.1109/ISCO.2013.6481123
10. Naveen P, Praveen Kumar N, Sriganesh K, Rajesh T, Sushmitha K (2019) Stator fault analysis of permanent magnet synchronous motor using finite element method. In: 2019 4th international conference on recent trends on electronics, information, communication technology (RTEICT), pp 655–660. https://doi.org/10.1109/RTEICT46194.2019.9016771
11. Prasob K, Kumar NP, Isha T (2017) Inter-turn short circuit fault analysis of pwm inverter fed three-phase induction motor using finite element method. In: 2017 international conference on circuit, power and computing technologies (ICCPCT), pp 1–6. IEEE.
12. Sawhney A (2014) Electrical machine design, 6th edn. Dhanpat Rai & Sons, New Delhi (2014)
13. Chen Y, Wang L, Wang Z, Rehman AU, Cheng Y, Zhao Y, Tanaka T (2015) Fem simulation and analysis on stator winding inter-turn fault in dfig. In: 2015 IEEE 11th international conference on the properties and applications of dielectric materials (ICPADM), pp 244–247. IEEE
14. Krause PC, Wasynczuk O, Sudhoff SD (2013) Analysis of electric machinery and drive systems, 3rd edn. IEEE Press, New York (2013)
15. Simon D (2006) Optimal State Estimation: Kalman, H Infinity, and Nonlinear Approaches. Wiley-Interscience, USA
16. Nag PS, Kumar CS, Thampatty KS, Isha T (2018) A modified approach for application of augmented extended kalman filter for stator interturn fault diagnosis of a synchronous generator. In: 2018 4th international conference on electrical energy systems (ICEES), pp 465–469. https://doi.org/10.1109/ICEES.2018.8442354
17. Sottile J, Trutt F, Leedy A (2006) Condition monitoring of brushless three-phase synchronous generators with stator winding or rotor circuit deterioration. IEEE Trans Ind Appl 42(5):1209–1215. https://doi.org/10.1109/TIA.2006.880831

Grid Integration of Wind Energy Conversion System Through Parallel Inverter Topology for Power Quality Enhancement

M. E. Aswathi, C. M. Nirmal Mukundan, M. V. Manoj Kumar, and P. Jayaprakash

1 Introduction

Development of renewable energy sources (RES) has been enlarged in recent years [1]. Among these RES wind energy is one of the widest rising technologies. Because of their high energy efficiency, wind energy conversion systems (WECS) with variable-speed and its maximum power point tracking (MPPT) control have attracted a lot of attention [2]. The efficient operation of wind energy conversion system is dependent on the proper design of power converters and controllers (WECS) [1]. The intermittent nature, as well as equipment damage due to abrupt source and load variations, are challenging the reality of wind energy converters. For regulating voltage, frequency, real and reactive powers, and MPPT, a diode rectifier with a DC-DC converter is used [3].

Voltage source inverter (VSI) is used to regulate voltage and frequency, load balancing and leveling, and harmonics mitigation at PCC. To attach to the grid, it must first filter the harmonic content for the feeding of a sinusoidal current to the grid. The grid-connected WECS offers additional functions such as load compensation, power quality enhancement, active, and reactive power flow control with suitable control strategies. Since the entire operation is performed by a single inverter at a time, the inverter would be burdened [3].

Parallel inverter technology is a fine and reliable scheme and some favor points of parallel scheme are briefly defined, such as how each inverter's design, development, installation, maintenance become much more simple and adaptable [3]. The current study looks at how parallel inverters can be used to compensate for reactive and harmonic currents. The following are some of the benefits of the suggested method: (i) using a lower switching frequency or reducing current ripple, (ii) because of the shared connection, there will be less stress on the DC link capacitor, (iii) paralleling

M. E. Aswathi (✉) · C. M. Nirmal Mukundan · M. V. Manoj Kumar · P. Jayaprakash
Department of Electrical and Electronics Engineering, Government College of Engineering Kannur, Kannur, Kerala, India

S. Kumar et al. (eds.), *Recent Advances in Power Electronics and Drives*, Lecture Notes in Electrical Engineering 852, https://doi.org/10.1007/978-981-16-9239-0_47

allows for more effective performance for high-power applications, (iv) use of smaller passive components and various modulation techniques to minimize electromagnetic interference (EMI).

2 System Configuration

The schematic diagram of the grid-tied wind energy conversion system is shown in Fig. 1a. A wind turbine unit is connected with a permanent magnet synchronous generator. The output voltage of PMSG is transformed from AC to DC by operating an uncontrolled diode bridge rectifier. The output side of the rectifier is connected to a DC link capacitor. The main action of this capacitor is to reduce the ripples in the signal and also helps to keep a constant DC link voltage. Employment of a DC-DC converter that is a boost converter helps to increase the voltage magnitude for grid integration and also tracks maximum power point. A perturb and observe (P&O) algorithm controls the boost converter to extract the maximum power point. Rather than sensing the wind speed, a sensorless MPPT technique is implemented. Electrical parameters such as DC link voltage and DC link current are sensed here, and the duty ratio is varied by using the P&O algorithm. This technique helps to bring out the maximum wind power and also promotes keeping the power co-efficient C_p [4]. This paper deals with a parallel inverter structure that is used to increase the performance of the system and empowers the grid to exchange the power generated by the wind energy conversion system. The main purposes of parallelly coupled inverters (inverter 1 and inverter 2) are active power injection and reactive power compensation, respectively. This topology helps to reduce the burden of a single inverter and increase the life span of inverters. Synchronous reference frame theory (SRFT)-based control algorithms are used to function the grid-tied parallel inverter scheme. The design of DC-DC converter and parameters selection are employed [5] and [6].

2.1 Wind Turbine Unit (WTU)

Wind turbine rotor blades are used for the transformation of wind force to mechanical power. PMSG is used to transform mechanical power into electrical power. Through a gearbox, WTU is connected to the PMSG shaft.

The following is the mathematical relationship that shows the extraction of mechanical power from the wind:

$$P_t = C_p(\lambda, \beta)\frac{\rho A}{2}V^3 \tag{1}$$

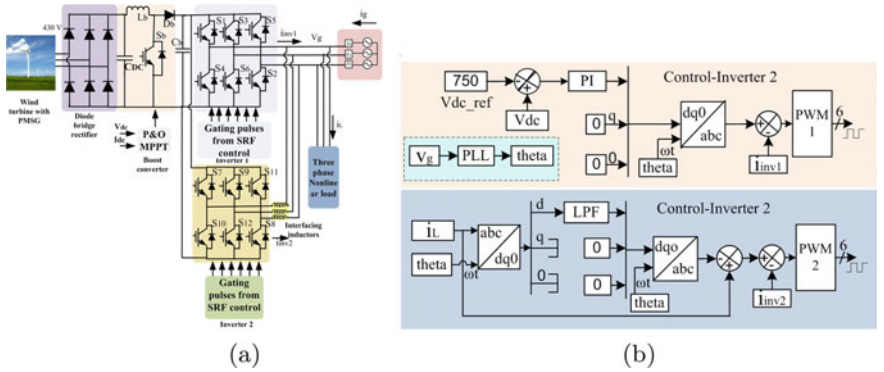

Fig. 1 **a** Schematic diagram of grid-connected WECS **b** SRF control of parallel inverter for WECS

where P_t is the extracted power from the wind, ρ is the air density (kg/m^3), and C_p represents the power co-efficient, which is a function of both tip speed ratio λ and blade pitch angle β (deg) [1].

The power co-efficient C_p is given by

$$C_p(\lambda, \beta) = C_1\left(\frac{C_2}{\lambda_i} - C_3\beta - C_4\right).exp\left(\frac{C_5}{\lambda_i}\right) \tag{2}$$

$$\lambda_i = \left[\left(\frac{1}{\lambda + 0.089} - \frac{0.035}{\beta^3 + 1}\right)\right]^{-1} \tag{3}$$

The coefficients of the wind turbine characteristic C_1 to C_5 are $C_1 = .5$, $C_2 = 98$, $C_3 = .4$, $C_4 = 5$, $C_5 = 16.5$.

T_{mech} is the rotor mechanical torque can be expressed as $T_{mech} = \left(\frac{P_{mech}}{\omega_r}\right)$ ω_r is the rotor angular velocity.

3 Control Configuration of WECS

Converter and inverter control are critical for the operation of the grid integrated WECS. For the control of boost converter, P&O algorithm-based MPPT control is used, and it extracts the maximum available wind power through the WTU. To realize the grid synchronization through the inverter, an SRF-based control technique is used. These control algorithms are explained in this section. Figure 1b shows block diagram representation of the inverter control.

3.1 MPPT Control

The perturb and observe algorithm is the widely used MPPT technique [7]. This algorithm produces the duty ratio that is used to operate the converter. A wind speed-sensorless MPPT technique is implemented instead of conventional MPPT logic. Here, electrical parameters like DC link voltage and current are measured for boost converter control.

3.2 Parallel Converter Control

The topology is made up of two identical three-phase PWM inverters coupled in parallel. A DC-capacitor that is shared for the inverters [8–11]. Figure 1b shows the SRF-based control diagram of the parallel inverter scheme. Inverter 1 and inverter 2 are two inverters that are connected in parallel, and SRF control is used to generate gating pulses. Inverter 1 is used to inject active power, and inverter 2 is used to compensate for the reactive power and harmonics. The corresponding control techniques are applied to those inverters.

For inverter 1, first find out the difference of reference DC link voltage (V_{dcref}) and DC link voltage (V_{dc}). V_{dcref} is considered as 750 V [4]. Only the direct axis component is used to control inverter 1, while the quadrature axis component is ignored. As a result, active power injection takes place. As a result of the d-axis component being converted from dqo to abc frame, reference inverter current is generated. The reference inverter current is compared with current through inverter 1, the gating pulse for controlling inverter 1 is created.

For inverter 2, the three-phase load current (i_L) is extracted and converted from abc to dq0 frames. A low-pass filter, which helps to extract the low-frequency component from the load current and gives out the fundamental component. The reference fundamental component is generated by converting the fundamental DC component from dq0 to abc frame. The subtraction of a fundamental component from the load current aids in the development of harmonics and reactive power. These harmonics and reactive power are compared with current through inverter 2, the gating pulses for controlling inverter 2 are produced [12–15].

4 Results and Discussion

The wind energy conversion system has been simulated in the MATLAB/Simulink for various conditions such as active power injection, reactive power and harmonic compensation, sag, swell, load unbalance whose results are listed below. Wind speed is continuously changed from 12 to 10 m/s.

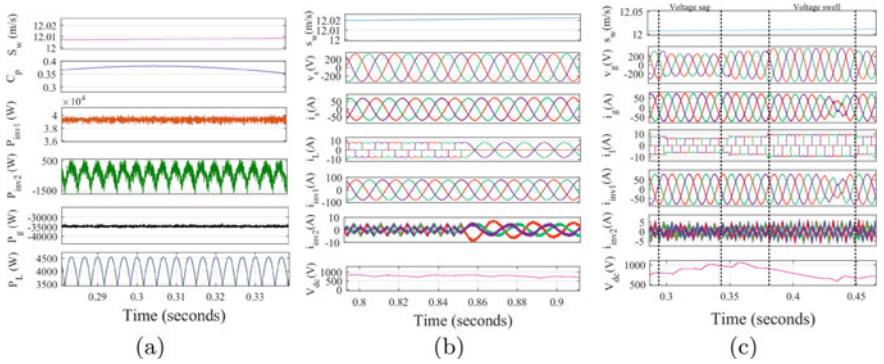

Fig. 2 Waveforms of grid-connected WECS: **a** Power characteristics of WECS under steady state operation **b** Performance under the varying load **c** Performance at grid voltage sag and swell

As the wind speed changes, wind power is also changed. Figure 2a shows the power characteristics of WECS under steady-state condition.The power co-efficient (C_p) is a measure of a system performance. C_p ranged from 0.41 to 0.49 depending on the design. The plot value of C_p is around 0.4. From this figure, it is clear that input power is considered as 40kW and it is given by the wind turbine unit. By observing the grid power, it indicates that the power is injected to the grid.

The performance characteristics of WECS under steady-state operation and together the unbalanced load condition is shown in Fig. 2b. Even at the load is unbalanced, the grid currents must be balanced. Any one of the inverters can generate an unbalanced current in order to achieve balanced grid currents. Inverter 2 assists in the processing of unbalanced currents and ensures that grid currents are balanced. During this time, inverter 1 will inject active power without causing any disturbance. The inverter 2 of WECS compensates for the unbalance in the load which in turn gives the balanced sinusoidal grid currents. So during the unbalanced load condition, a satisfied performance is achieved without altering the maximum extracted power point of the wind energy conversion system.

Grid side voltage variations were applied in sequence of sag, normal voltage, and then swell. Sag is applied for 0.3 to 0.35 s, then normal grid voltage occur. Then swell was applied for the next seconds as shown in Fig. 2c. Grid side currents rise as the voltage difference increases in a voltage sag, and vice versa in a swell state.

During the entire operation, parallel inverter system maintains the grid voltage and current quality within the IEEE 519 standard even at adverse load condition.

5 Conclusion

A parallel inverter topology-based wind energy conversion system has been presented in this work. The active power injection from the wind turbine unit has been achieved along with power quality improvement. The system performances are tested at vari-

ous operating conditions such as grid voltage sag, swell and reactive nonlinear and unbalanced loads. Wind turbine unit with speed-sensorless MPPT technique is used to enhance the power capturing capacity of the whole system. The theoretical claims are validated with simulation proofs with MATLAB/Simulink software. The wind energy conversion system is well suited for the long-term use of renewable energy grid integration. One of the major failure reasons of WECS is the malfunction of the mechanical anemometer, which is avoided here. Moreover, the active power injection and nonlinear power support are achieved through different inverters, increases the service life of the system.

References

1. George T, Pychadathil J (2020) Maximum power tracking and power sharing in grid connected WECS using modified PFC rectifier and PR controlled inverter. Electr Power Compon Syst 48(14–15):1584–1597
2. Ibrahim AM, Gawish SA, El-Amary NH, Sharaf SM (2019) STATCOM controller design and experimental investigation for wind generation system. IEEE Access 7:150453–150461
3. Asiminoaei L, Aeloiza E, Kim JH, Enjeti P, Blaabjerg F, Moran L, Sul SK (2006) Parallel interleaved inverters for reactive power and harmonic compensation. 1–7
4. Busawon K, Jovanovic M, Dodson L (2006) Power coefficient estimation in a wind energy conversion system. 1873–1877
5. Hasaneen BM, Elbaset Mohammed AA (2008) Design and simulation of DC, DC boost converter. In: 12th international middle-east power system conference, vol 2008. Aswan, Egypt, pp 335–340
6. Sridhar JP, Prakash R (2017) Power quality issues and its mitigation by unified power quality conditioner. 887–894. https://doi.org/10.21647/ICCTEST/2017/49081
7. Thongam J, Ouhrouche M (2011) MPPT control methods in wind energy conversion systems. https://doi.org/10.5772/21657
8. Broeck H, Boeke U (1998) A simple method for parallel operation of inverters. 143–150
9. Abuhamdia A (2018) Grid connected three phase inverter. 1–18
10. Zhong Q-C, Hornik T (2012) Parallel PI voltage-current control of a neutral leg. In: Control of power inverters in renewable energy and smart grid integration, IEEE, pp 219–231
11. Zhong Q-C, Hornik T (2012) Parallel operation of inverters. In: Control of power inverters in renewable energy and smart grid integration, IEEE, pp 297–333
12. Wu B, Narimani M (2017) PWM current source inverters. In: High-power converters and AC drives, IEEE, pp 225–256
13. Tuladhar A, Jin H, Unger T, Mauch K (2000) Control of parallel inverters in distributed AC power systems with consideration of line impedance effect. IEEE Tran Ind Appl 36(1):131–138
14. Zhang C, Guerrero JM, Vasquez JC, Coelho EAA (2016) Control architecture for parallel-connected inverters in uninterruptible power systems. IEEE Tran Power Electr 31(7):5176–5188
15. Jin L, He Z, Zhang Y, Nie J, Zhang M (2016) A new virtual impedance method for parallel inverters with droop control. IEEE Vehicle Power Propuls Conf (VPPC) 2016:1–4

Improvement in Quality of Power of Grid-Connected Wind Energy System Through STATCOM—A Review

Manisha Priyadarsani Nayak, Suresh Kumar Gawre, and Shailendra Kumar

1 Introduction

Wind energy is known to be a clean and environmentally friendly renewable energy source as it reduces our dependency on fossil fuels. Nowadays, it has become very famous and is being utilized in every sector as it does not emit any harmful gases such as CO_2 [1]. The global wind report 2019 highlights a positive growth of wind energy having a total installed capacity of 650GW and the wind installation surpassed 60GW in 2019. The individual units present in the distribution network have a capacity of about 2 MW. Nowadays, more than 3,41,320 wind turbines are successfully working worldwide. From the total number; 14,384 offshore wind turbines are there across the world.

When a wind energy system is coupled with an existing power system, it creates many difficulties. Wind turbine gives rise to a changeable and irregular output power due to the fluctuation in wind speed, and it results in fluctuation in the electrical power and in voltage [2]. The power quality has a vital role in the power system and it is greatly affected by the addition of renewable energy like wind into the grid. Power quality is defined as "Any issue and quality degradation of voltage, current, and frequency which results in improper functioning or operational error in equipment" [3].

These issues of power quality can be classified as voltage swell, sag, voltage dips, flickers, harmonics, variation in real and reactive power, etc. Induction generators are the most preferable machine to run a wind generating system due to these advantages.

- Simple and rugged construction
- Low maintenance
- Cheaper as compared to other motors
- Self-starting nature

M. P. Nayak (✉) · S. K. Gawre · S. Kumar
Department of Electrical Engineering, Maulana Azad National Institute of Technology, Bhopal, Madhya Pradesh, India

S. Kumar et al. (eds.), *Recent Advances in Power Electronics and Drives*, Lecture Notes in Electrical Engineering 852, https://doi.org/10.1007/978-981-16-9239-0_48

To establish magnetic flux, reactive power is required by an induction generator. The active power, reactive power and terminal voltage vary a lot, and system gets disturbed due to the varying wind nature. So to balance the reactive power, the application of FACTS device is introduced. Here, we will use a VSC-based STATCOM to improve the power system stability and performance as it has much better performance and transient response than the static var compensator [4]. A battery energy storage (BESS) is needed to manage the fluctuations caused by wind turbines. Importance of STATCOM in a grid-connected system is discussed below [5]:

- Power factor improvement(unity) at source side
- Control of dynamic voltage, active power and reactive power with help of BESS
- Power oscillation damping can be improved in system
- Voltage flicker control issue can be resolved
- Fast dynamic response due to Bang Bang controller
- No requirement of additional shunt reactor and capacitor bank

In paper [1], the power quality issue, consequences, grid coordination rule, power quality improvement and its topology, control scheme, and its performance are discussed. In paper [2, 3, 5], the voltage unbalance, voltage fluctuation, inter harmonics and controller of STATCOM are discussed. Paper [4] describes the topology for power quality improvement, types of controller of STATCOM, i.e. Bang Bang controller and fuzzy logic controller. In paper [6, 7, 8], the power quality issue, role of STATCOM and equivalent representation are discussed. Paper [9] represents the role of different FACT devices in improving power quality in wind energy systems. Paper [10, 11] describe the use of STATCOM and PID controller for stability enhancement in grid-connected wind farms.

Using D-STATCOM, how the power quality is improved in a hybrid power system is discussed in [12, 13, 14]. In paper [15, 16], power quality improvement using a doubly-fed induction generator is discussed. This generator faces severe voltage instability problems during grid faults, and STATCOM is mainly helpful to resolve this problem [17]. We can also compensate for the real and reactive power without adding any type of storage system [18, 19].

Power quality improvement by new techniques of STATCOM is developing day by day is discussed in [20, 21]. The reactive power flow management in renewable energy with low and high voltage ride through is discussed [24]. Using sinusoidal PWM technique, the voltage sag and swell of D-STATCOM can be controlled very easily and getting popular nowadays [25]. To maintain the voltage within the limit mainly corrective, coordinated and preventive voltage control methods are used [27]. By using cascaded STATCOM, the efficiency to improve the voltage stability will increase very much [29].

Huge energy storage devices are needed in case of more fluctuation so to solve this problem STATCOM with a low pass filter can be used for the generation of line power reference [33]. Hybrid energy storage system along with supercapacitor can also be used to smooth the variation of wind as it has a longer life cycle [34].

Wind farm connected with permanent magnet synchronous generator needs a STATCOM as it reduces the chance of losing a great portion of wind generation [36]. To analyze the performance of static compensator; a proportional resonant controller can be connected to it [37, 38]. Sub-synchronous resonance (SSR) is the major problem of wind power systems and STATCOM is very much efficient to mitigate this problem. It increases the grid stiffness by decreasing the grid impedance and resolving the SSR issue [39].

But nowadays, UPFC is getting more popular than STATCOM because UPFC can improve the low voltage ride through (LVRT) better than STATCOM [40].

Contents and the summary of all the papers are discussed in Table 1.

2 Issues in Power Quality

2.1 Voltage Fluctuation

Voltage variation takes place due to error in pitch, error in yaw and fluctuation of wind speed. It is related to variations in real and reactive power. Fluctuation in voltage should be within + /5%. The classifications in voltage variation are [1]:

- Voltage swell
- Voltage sag
- Voltage dips
- Long duration voltage variation
- Voltage variation in short duration

Frequency range for voltage fluctuation is 10–35 Hz.

2.2 Harmonics

Harmonics results due to the addition of converter and nonlinear load into the system [2]. Effect of harmonics is a major cause to degrade the power. As per the IEC-61400-36 guideline, the harmonic voltage should be within limit and each harmonic current source can allow only a limited value. The continuous operation of switch reduces lower order harmonics, but high frequency current is present in output current, which can be filtered out easily.

Table 1 Summary of papers

Reference paper	Contents discussed	Summary
[1]	STATCOM based on Bang Bang controller to improve power quality in grid	• Cancel out the load current with harmonics and improve the power factor • No limit to the switching frequency is a great disadvantage
[2, 3]	Hysteresis current-controlled technique is used	• Provides fast switching signal to the STATCOM • The hysteresis error is more than the maximum error
[4]	Comparison of Bang Bang controller and Fuzzy logic controller is discussed	• THD in the Fuzzy logic controller is less than the Bang Bang controller • Fuzzy logic controller is more simple and faster than Bang Bang controller
[5, 8]	Power quality issues and consequences are discussed	• Voltage sag, swell, harmonics are the major issues in wind energy systems connected to grid
[6, 7]	Power quality improvement using different FACTS devices	• STATCOM, UPFC, IPFC and SSSC play an important role in better power quality
[9]	Power quality improvement comparison between STATCOM and UPQC	• The System connected to UPQC provides better performance than STATCOM, because THD in UPQC is less than STATCOM
[10, 11]	STATCOM and PID controller-based stability enhancement	• PID controller and PWM technique are used for control of STATCOM
[12, 13, 14]	Active power compensation using D STATCOM is discussed	• D-STATCOM reduces the power loss and improves the stability of system
[16, 17]	Power quality improvement in doubly-fed induction generator. -	• STATCOM and BESS help in compensation of generator rotor angle oscillation • It improves the overall stability and dynamic behavior
[19]	Power quality improvement without adding a storage system	• A system without any storage system is less effective than system having a storage system because BESS stores the energy and stabilizes the system

(continued)

Table 1 (continued)

Reference paper	Contents discussed	Summary
[20–23]	Different control techniques of STATCOM are discussed	• LVRT method, nonlinear adaptive coordinating neuro control, optimal power flow, resonant regulators and DFT synchronization algorithm are very popular control methods of STATCOM
[25]	Modeling and simulation of D-STATCOM using SPWM technique	• VSC is developed using the SPWM technique • D-STATCOM provides good voltage regulation and robust
[26, 2728]	Application of STATCOM in wind energy generated system and optimal voltage control of it	• To avoid number of STATCOM; optimal voltage control can be used. It is cost- effective. This is applicable in the offshore cable system
[29, 30]	Wind Farm voltage stability using cascade STATCOM is discussed	• Cascaded STATCOM is quicker and more reliable and has better efficiency
[31, 32]	Stabilization of multi-machine power system using STATCOM	• In a multimachine power system, STATCOM reduces the frequency oscillation
[33]	Regulation of terminal voltage using STATCOM	• A low pass filter when integrated with STATCOM increases the power factor
[34]	Role of HESS in wind power generation	• Super capacitor with hybrid energy storage system reduces variation of wind
[35, 36]	Use of STATCOM with high penetration of wind generation	• In permanent magnet synchronous generator, STATCOM helps to improve power
[38]	Mitigating power quality issues by STATCOM with resonant controller	• Resonant controller can analyze the performance of static compensators
[39]	Control strategy of STATCOM to improve sub-synchronous resonance (SSR)	• SSR can be reduced by increasing the grid stiffness. By adding STATCOM, the grid impedance decreases and stiffness improves. So SSR can be reduced
[40]	Role of Cascaded H Bridge (CHB) STATCOM	• CHB STATCOM can maintain the grid voltage by regulating the Negative sequence Output Admittance (NSOA)

2.3 Reactive Power

When induction generator and capacitor used for compensation of reactive power are added to the wind energy; the wind turbine may get self-excited, after disconnecting the wind turbine from the nonlinear load. The capacitor connected helps in reactive power compensation.

2.4 Switching Operation

Voltage fluctuation such as voltage sag swell caused due to switching operation. According to IEC 61,400-3-7, the switching operation should be within 10 min to 2 h.

3 Consequences of Issues

The voltage deviation and dips, transient, flicker, harmonics make the following dysfunction of equipment [5].

- Tripping of protection devices and contractors
- Computer, PLC system may get stop and the process may stop working and even can damage many pieces of equipment.
- Due to these issues power quality degrades in the grid.

4 Components of Grid-Connected System to Improve Power Quality

The wind energy system connected to grid is shown in Fig. 1, consists of a nonlinear load, induction generator, wind generating system and STATCOM with a shunt connected BESS.

To settle issues involved in power quality and for refinement of power quality, STATCOM along with its control scheme and with a BESS is connected. The STATCOM provides a current that will nullify the reactive and harmonic component of nonlinear load and induction generator current so that the source current is free from harmonics, and it has a desired value of phase angle with the STATCOM and the power factor improves, and hence quality of power also improves in the system.

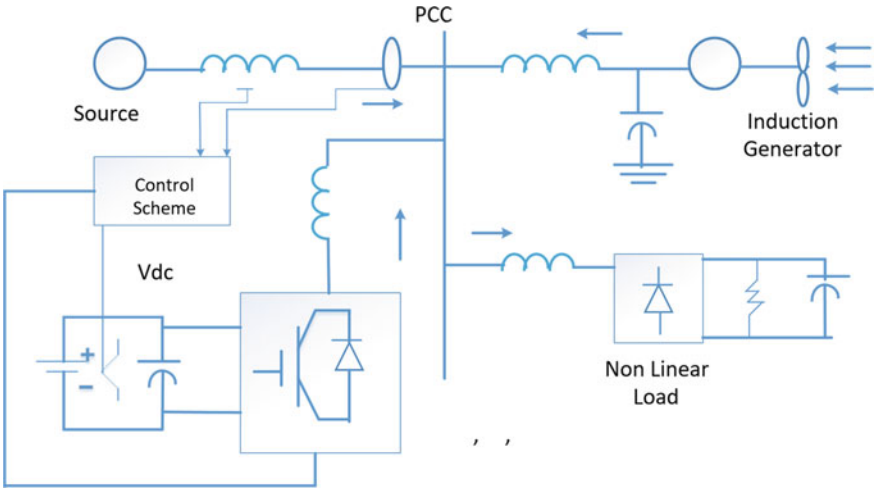

Fig. 1 Grid-connected wind energy System with its component [3]

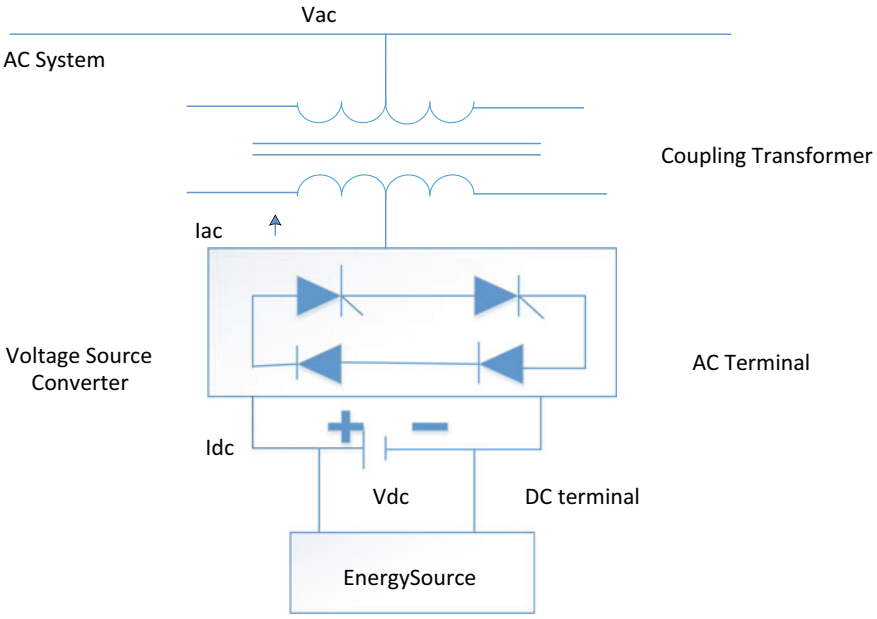

Fig. 2 Block diagram of STATCOM [1]

4.1 STATCOM and BESS

The STATCOM shown in Fig. 2, is a three-phase voltage source converter connected at the common coupling point. The voltage source converter is connected with a DC capacitor source and converts the DC energy to AC energy, which is again fed to the coupling transformer. This coupling transformer is a constant frequency device and it transfers the AC energy from STATCOM to the AC system line and neutralizes harmonics. When the control scheme gives a switching signal to the STATCOM, it will supply a harmonic free current (I) of changing magnitude and frequency component. Also a harmonic filter is present in a STATCOM that attenuates the harmonics and high-frequency component [18].

The battery energy storage system (BESS) and DC capacitor are connected in parallel and it helps in storage of energy. The main functions of BESS are:

- To stabilize the grid system, BESS injects the reactive power to the system.
- In case of need when the reactive power of system is less than the STATCOM, it supplies power and it absorbs power when reactive power of system is more than static compensator; by this charging and discharging operation.
- It balances the voltage regulation.
- It maintains the DC capacitor voltage constant.
- It controls the transmission and distribution system very rapidly.

4.2 Wind Energy Generating System

Wind turbines in wind generating system have a great role as it turns the kinetic energy into clean electrical energy. Wind generating system has a rectifier which converts the AC to DC power and that DC energy stored in battery and supplied to controller in case of need. Then inverter converts the DC energy to AC energy. This energy is supplied to the ac system box or grid. When wind turbine blades rotate due to flow of wind the rotor captures the kinetic energy and converts this mechanical energy to electrical energy. The power equation of wind energy system is formulated as [9] (Fig. 3).

$$pwind = 0.5\rho AV^3 \tag{1}$$

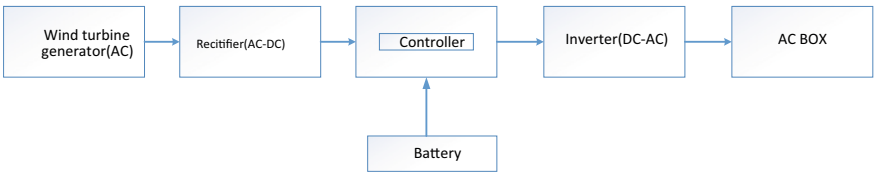

Fig. 3 Wind energy generating system

where

$$\rho(kg/m^3) = Density\ of\ air$$
$$A(m^2) = area\ of\ turbine\ blade$$
$$V(mtr/s) = Speed\ of\ wind$$

The mechanical power can be derived from the kinetic power is given by:

$$pmech = Cp * pwind \tag{2}$$

where (Cp) is the power coefficient. Now the mechanical power generated by wind turbine is [9]

$$pmech = 0.5\rho\pi r^2 V^3 Cp \tag{3}$$

where r = Radius of blade.

4.3 System Operation

STATCOM with parallel connected battery system is connected at the point of common coupling with induction generator and non-linear load in grid system. The output of STATCOM is varied to maintain a good quality of power in grid system. The hysteresis current control strategy has a crucial role in the control scheme, which operates the switching ON/OFF mechanism of the STATCOM compensator in the grid. The block diagram of control scheme of the system is given in Fig. 4 [5].

The current limiter used in this scheme does not allow signal above a specified value and similarly the voltage controller limits the voltage for a predetermined value.

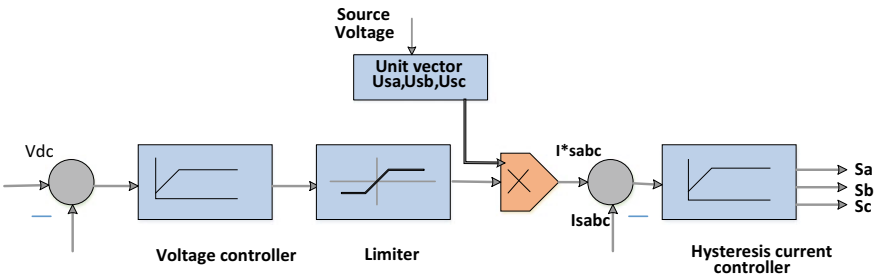

Fig. 4 Control Scheme [5]

5 Control Scheme

The control scheme used here to supply suitable harmonics free currents into the grid is known as "Bang Bang controller", which is also called as on–off controller. In this controller, hysteresis current controlled technique is used, which is a nonlinear method. This technique has a specified hysteresis area and it maintains the variable between its boundary and gives desired signal to turn on the STATCOM to inject the current into grid.

With the help of sensor, we need to measure the source current i_s and DC voltage Vdc. The current control block that is shown in Fig. 3 receives the reference current i_{sabc}, which we have to calculate from the source phase voltage, and actual current i_{sabc} and the difference between the two currents are provided to the hysteresis current controller to start up the operation of STATCOM.

5.1 Controller of STATCOM

In a three-phase balanced system, by using the source phase voltages (Vsa, Vsb, Vsc), the amplitude of RMS source voltage is calculated and known as sampled peak voltage (Vsm):

$$Vsm = \sqrt{\{2/3(Vsa^2 + Vsb^2 + Vsc^2)\}} \tag{4}$$

By using the voltage of each phase and RMS value of unit vector, the in-phase unit vectors are derived as shown below [3].

$$Usa = Vsa/Vsm \tag{5}$$

$$Usb = Vsb/Vsm \tag{6}$$

$$Usc = Vsc/Vsm \tag{7}$$

Due to in-phase unit voltage template, the in-phase reference current is generated and shown below [2].

$$i * sa = I * Usa,\ i * sb = I * Usb, i * sc = I * Usc \tag{8}$$

where 'I' has a proportionate relation with the source voltage magnitude for respective phases, which indicates that the source current is sinusoidal to make the ref current a sinusoid one.

5.2 *Bang Bang Controller*

The Bang Bang current controller working activates the STATCOM by providing an error into the system, which is calculated by adjusting a variable x to some reference value or setpoint x_{set} [5] and keeping it there and error is calculated as

$$Error = X - XS \tag{9}$$

If Error > HB output u = 1

If Error < HB output u = 0

To provide the error of the ref current and source current into the hysteresis controller, the reference current is calculated using phase RMS voltage, and actual current is sensed by a current sensor and it is compared with the hysteresis band to turn ON/OFF the STATCOM.

To turn off the IGBT of STATCOM the condition is:

$$If\ i_{sa} < (i_{*sa} - HB)\ then\ S_A = 0$$

To turn on the IGBT of STATCOM to inject a current; the condition is:

$$If\ i_{sa} > (i_{*sa} - HB)\ then\ S_A = 1$$

Similarly, S_B andS_C can be obtained for phase b and phase c and HB can be taken as small as possible for less ripple in the input current. Here, in this configuration, HB can be taken as 0.08.

6 Simulation and Result

In this paper, to analyze the working of STATCOM in wind farm, wind turbines are taken that uses squirrel cage induction generator. The design comprises six wind turbines of 1.5 MW. A distribution system of 25 kV is connected to the wind turbine and supplies power to a 120 kV grid through a feeder. The system is simulated using Simulink tool of Matlab 2017B (Figs. 5, 6, and 7; Table 2).

Capacitor bank connected to the wind turbine compensates the reactive power, but not completely. So STATCOM of 3-Mvar is there to maintain the reactive power at bus.

To realize the importance of STATCOM, the model is simulated first without connecting the STATCOM and then it is added to the system and run for 20 s.

From Fig. 8, we can see how the STATCOM supplies the reactive power in a wind farm.

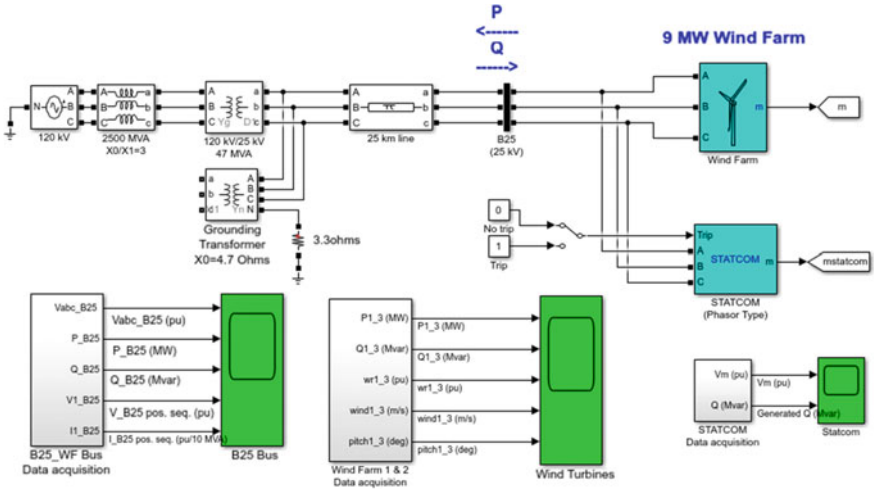

Fig. 5 Simulation model

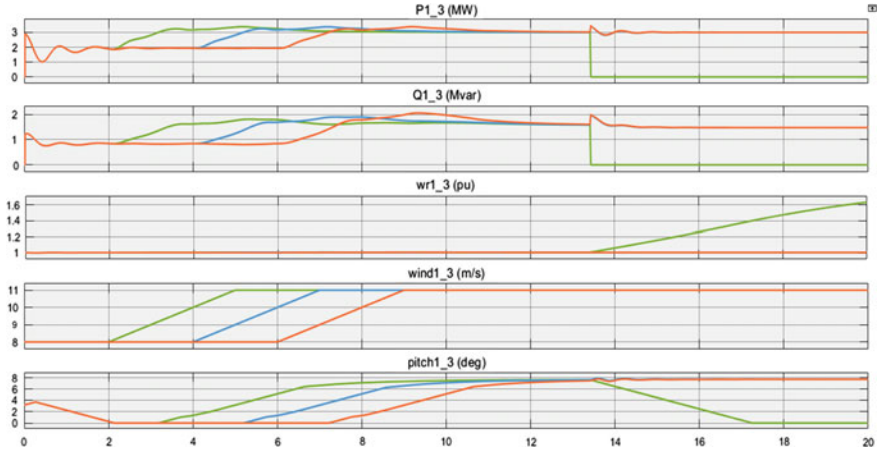

Fig. 6 Active power, reactive power, wind speed and pitch angle variation at wind turbine without STATCOM

- Figures 6 and 9 represent the waveform of active power, reactive power, wind speed and pitch angle of wind turbine without STATCOM and with STATCOM respectively.
- By comparing these two figures, we can conclude that the reactive power and active power improve by using STATCOM (refer Fig. 9). Also, STATCOM is very efficient to control the system during wind speed variation.
- Figures 7 and 10 show the waveform of voltage, current and power at the bus without STATCOM and with STATCOM, respectively.

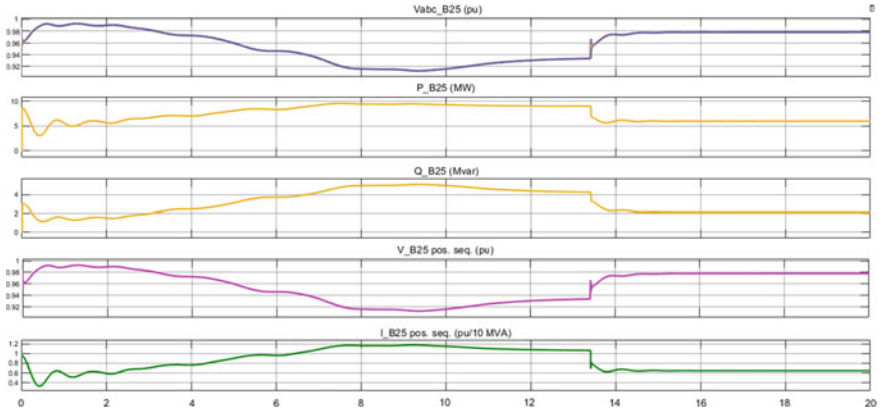

Fig. 7 Voltage, active power, reactive power at bus without STATCOM

Table. 2 Wind turbine specification

Parameters	Symbol	Value
Base power of wind turbine	S	1.5 MW
Nominal wind speed	V	9 m/s
Nominal mechanical power	P	1pu (3 MW)
Grid frequency	F	60 Hz
Pitch angle controller gain	Kp. Ki	5.25
Pitch angle (maximum)	θ	45°
Simulation time	T	20 s

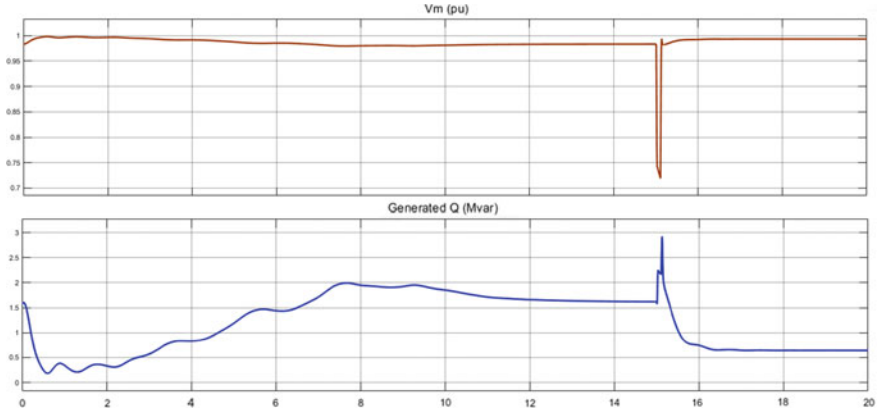

Fig. 8 Voltage and reactive power injected by static compensator

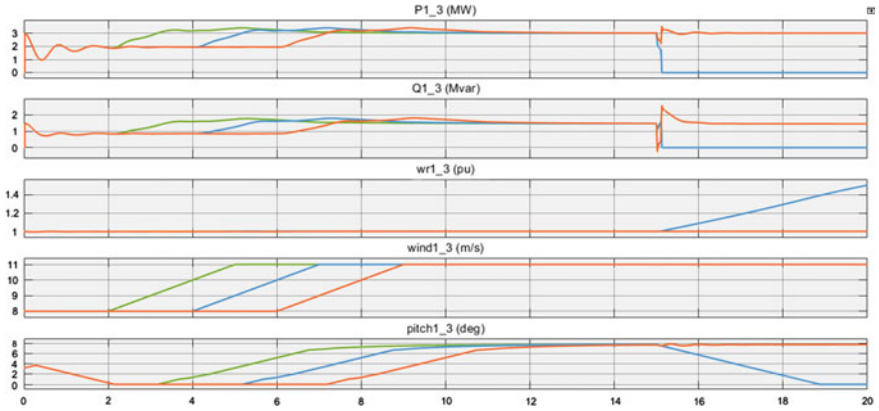

Fig. 9 Active power, reactive power, wind speed and pitch angle variation at wind turbine with STATCOM

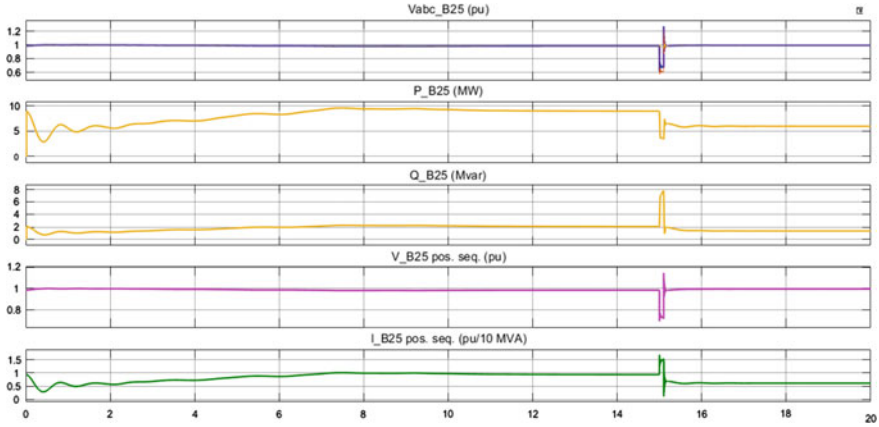

Fig. 10 Voltage, active power, reactive power at bus with STATCOM

- The voltage, current and power have minimum deviation and have a smooth conduction by using STATCOM at bus, which is shown in Fig. 10.

7 Conclusion and Future Scope

STATCOM injects current to nullify reactive and harmonic component of the load and improves the power factor and quality of the overall system.

Hysteresis control helps in generating a switching signal for STATCOM and the choice of hysteresis band should be narrow to improve the current quality in the system and to reduce the ripple in the system. Hysteresis current control provides a

good reliability and stability. It has good speed and correct accuracy so it is widely accepted. Although it is popular for its easy implementation, it has no limit to the switching frequency; so the upper and lower limits of frequency make the hysteresis band error very high as hysteresis band error is twice the maximum error.

By using capacitors in wind farm, the sub-synchronous resonance (SSR) increases. So in future, we can use PV-STATCOM to mitigate this problem. In this technique, the solar farm will act as a PV-STATCOM, which will maintain the voltage stability and compensate the power very efficiently.

References

1. Sunil TP, Loganathan N (2012) Power quality improvement of a grid-connected wind energy conversion system with harmonics reduction using FACTS device. In: IEEE-International Conference on Advances in Engineering, Science and Management (ICAESM-2012), Nagapattinam, Tamil Nadu, pp 415–420
2. Devabalaji KR, Ravi K (2014) Power quality improvement in wind farm connected to grid using STATCOM. In: 2014 International Conference on Advances in Electrical Engineering (ICAEE), Vellore, 2014, pp 1–5. https://doi.org/10.1109/ICAEE.2014.6838508
3. Nirmala N, Suresh Kumar V (2013) A STATCOM-control scheme for wind energy system to improve power quality. In: 2013 International Conference on Information Communication and Embedded Systems (ICICES), Chennai, pp 1108–1113. https://doi.org/10.1109/ICICES.2013.6508175
4. George SK, Chacko FM (2013) Comparison of different control strategies of STATCOM for power quality improvement of grid connected wind energy system. In: 2013 International Mutli-Conference on Automation, Computing, Communication, Control and Compressed Sensing (iMac4s), Kottayam, pp 650–655. https://doi.org/10.1109/iMac4s.2013.6526394
5. Mohod SW, Aware MV (2010) A STATCOM-control scheme for grid connected wind energy system for power quality improvement. IEEE Syst J 4(3):346–352. https://doi.org/10.1109/JSYST.2010.2052943
6. Yuvaraj V, Raj EP, Mowlidharan A, Thirugnanamoorthy L (2011) Power quality improvement for grid connected wind energy system using FACTS device. In: Proceedings of the Joint INDS'11 & ISTET'11, Klagenfurt, pp 1–7. https://doi.org/10.1109/INDS.2011.6024828
7. Patel DM, Nagera AR, Roy KC (2012) Application of static compensator to improve the power quality of grid connected induction generator based wind farm. In: IEEE-International Conference On Advances In Engineering, Science And Management (ICAESM-2012), Nagapattinam, Tamil Nadu, pp 1–4
8. Shanthini K, Verappan N (2012) Power quality enhancement of wind generators connected to grid. In: 2012 International Conference on Emerging Trends in Electrical Engineering and Energy Management (ICETEEEM), Chennai, pp 398–403. https://doi.org/10.1109/ICETEEEM.2012.6494474
9. Amita A, Sinha AK (2018) Power quality comparison of grid connected wind energy system with STATCOM and UPQC. In: 2018 International Conference on Intelligent Circuits and Systems (ICICS), Phagwara, pp 355–360. https://doi.org/10.1109/ICICS.2018.00079
10. Fayek A et al (2019) STATCOM and PID controller based stability enhancement of a grid connected wind farm. In: 2019 International Conference on Energy and Power Engineering (ICEPE), Dhaka, Bangladesh, pp 1–4. https://doi.org/10.1109/CEPE.2019.8726728
11. Mienski R, Pawelek R, Wasiak I (2002) Application of STATCOM controllers for power quality improvement - modeling and simulation. In: 10th International Conference on Harmonics and Quality of Power. Proceedings (Cat. No.02EX630), Rio de Janeiro, vol 2, pp 620–625. https://doi.org/10.1109/ICHQP.2002.1221507

12. Parija B, Behera S, Pattanayak R, Behera S (2019) Power quality improvement in hybrid power system using D-STATCOM. In: 2019 3rd International Conference on Computing Methodologies and Communication (ICCMC), Erode, India, pp 564–567. https://doi.org/10.1109/ICCMC.2019.8819656
13. Saradva PM, Kadivar KT, Pandya MH, Rana AJ (2016) Reactive and real power compensation in distribution line using D-STATCOM with energy storage. In: 2016 International Conference on Computation of Power, Energy Information and Communication (ICCPEIC), Chennai, pp 726–732. https://doi.org/10.1109/ICCPEIC.2016.7557316
14. Kulkarni HR, Virulkar VB (2017) Mitigation of flicker in a distribution-connected wind farm with STATCOM. In: 2017 International Conference on Energy, Communication, Data Analytics and Soft Computing (ICECDS), Chennai, pp 2208–2212. https://doi.org/10.1109/ICECDS.2017.8389844
15. Lei L, Shengtie W, Guizhen T (2016) Grid power quality improvement with STATCOM/HESS for wind turbine with squirrel-cage induction generator. In: 2016 IEEE 11th Conference on Industrial Electronics and Applications (ICIEA), Hefei, pp 2552–2557. https://doi.org/10.1109/ICIEA.2016.7604023
16. Ghorbanian MJ, Goodarzvand F, Poudaryaei A, Mahadi WNL (2014) Power quality improvement of grid connected doubly fed induction generator using STATCOM and BESS. In: 2014 4th International Conference on Engineering Technology and Technopreneuship (ICE2T), Kuala Lumpur, pp 110–115. https://doi.org/10.1109/ICE2T.2014.7006229.
17. Fazli M, Shafighi AR, Fazli A, Shayanfar HA (2010) Effects of STATCOM on wind turbines equipped with DFIGs during grid faults. In: 2010 World Non-Grid-Connected Wind Power and Energy Conference, Nanjing, 2010. https://doi.org/10.1109/WNWEC.2010.5673205
18. Muthusamy M, Kumar CS (2014) New STATCOM control scheme for power quality improvement in wind farm. In: 2014 International Conference on Green Computing Communication and Electrical Engineering (ICGCCEE), Coimbatore, pp 1–5. https://doi.org/10.1109/ICGCCEE.2014.6922323
19. Rekik M, Abdelkafi A, Krichen L (2013) Power quality improvement of a wind farm without adding any type of storage system. In: 14th International Conference on Sciences and Techniques of Automatic Control & Computer Engineering—STA'2013, Sousse, 2013, pp 132–135. https://doi.org/10.1109/STA.2013.6783118
20. Aboul-Seoud T, Jatskevich J (2008) Improving power quality in remote wind energy systems using battery storage. In: 2008 Canadian conference on electrical and computer engineering, Niagara Falls, ON, 2008, pp 001743–001746. https://doi.org/10.1109/CCECE.2008.4564842
21. Rezaeipour R, Kiani B (2009) Review of novel control techniques for STATCOM and its effects on a wind farm. In: 2009 International Conference on Sustainable Power Generation and Supply, Nanjing, , pp 1–5. https://doi.org/10.1109/SUPERGEN.2009.5348152
22. Ma Y, Huang A, Zhou X (2015) A review of STATCOM on the electric power system. In: 2015 IEEE International Conference on Mechatronics and Automation (ICMA), Beijing, pp 162–167. https://doi.org/10.1109/ICMA.2015.7237475.
23. Subramanian SB et al (2018) Control of STATCOMs—a review. In: 2018 IEEE Power & Energy Society General Meeting (PESGM), Portland, OR, pp 1–5. https://doi.org/10.1109/PESGM.2018.8586479
24. Sarkar MNI, Meegahapola LG, Datta M (2018) Reactive power management in renewable rich power grids: a review of grid-codes, renewable generators, support devices, control strategies and optimization algorithms. IEEE Access 6:41458–41489. https://doi.org/10.1109/ACCESS.2018.2838563
25. Madhusudan R, Ramamohan Rao G (2012) Modeling and simulation of a distribution STATCOM (D-STATCOM) for power quality problems-voltage sag and swell based on Sinusoidal Pulse Width Modulation (SPWM). In: IEEE-International Conference On Advances In Engineering, Science And Management (ICAESM -2012), Nagapattinam, Tamil Nadu, 2012, pp 436–441
26. Castaneda J, Enslin J, Elizondo D, Abed N, Teleke S (2010) Application of STATCOM with energy storage for wind farm integration. In: IEEE PES T&D 2010, New Orleans, LA, 2010, pp 1–6. https://doi.org/10.1109/TDC.2010.5484308

27. Wu Q, Solanas JIB, Zhao H, Kocewiak ŁH (2016) Wind power plant voltage control optimization with embedded application of wind turbines and STATCOM. In: 2016 Asian Conference on Energy, Power and Transportation Electrification (ACEPT), Singapore, 2016, pp 1–5. https://doi.org/10.1109/ACEPT.2016.7811534
28. Roy C, Sengupta A † (2015) Implementation of STATCOM to overcome disturbances in grid connected Windfarm. In: 2015 international conference on energy, power and environment: towards sustainable growth (ICEPE), Shillong, 2015, pp 1–4. https://doi.org/10.1109/EPETSG.2015.7510150
29. Shengqing L, Wenxiang X, Weizhou, Huanyue Z (2013) Wind farm grid voltage stability researching based on cascade STATCOM. In: 2013 3rd international conference on intelligent system design and engineering applications, Hong Kong, 2013, pp 1610–1613. https://doi.org/10.1109/ISDEA.2012.387
30. Bubshait AS, Mortezaei A, Simões MG, Busarello TDC (2017) Power quality enhancement for a grid connected wind turbine energy system. IEEE Trans Ind Appl 53(3):2495–2505. https://doi.org/10.1109/TIA.2017.2657482
31. Muyeen SM, Ali MH, Takahashi R, Murata T, Tamura J (2007) Stabilization of wind farms connected with multi machine power system by using STATCOM. In: 2007 IEEE Lausanne power tech, Lausanne, 2007, pp 299–304. https://doi.org/10.1109/PCT.2007.4538333
32. Chavhan ST, Bhattar CL, Koli PV, Rathod VS (2015) Application of STATCOM for power quality improvement of grid integrated wind mill. In: 2015 IEEE 9th International Conference on Intelligent Systems and Control (ISCO), Coimbatore, 2015, pp 1–7. https://doi.org/10.1109/ISCO.2015.7282295
33. Sheikh MRI, Eva F, Motin MA, Hossain MA (2012) Wind generator output power smoothing and terminal voltage regulation by using STATCOM/SMES. In: 2nd International Conference on the Developments in Renewable Energy Technology (ICDRET 2012), Dhaka, Bangladesh, 2012, pp 1–5
34. Han Y, Xu Y, Li Y (2015) Research on application of STATCOM/HESS in wind power integrated to the grid. In: 2015 IEEE 2nd International Future Energy Electronics Conference (IFEEC), Taipei, Taiwan, 2015, pp 1–6. https://doi.org/10.1109/IFEEC.2015.7361566
35. Jamil E, Qurratulain, Hameed S (2017) STATCOM-Based Voltage Regulation in Grid Integrated Wind Farm under Variable Loading Conditions. In: 2017 14th IEEE India Council International Conference (INDICON), Roorkee, India, pp 1-6https://doi.org/10.1109/INDICON.2017.8488062
36. Pereira RMM, Pereira AJC, Ferreira CMM, Barbosa FPM (2016) STATCOM to improve the voltage stability of an electric power system with high penetration of wind generation. In: 2016 51st international Universities Power Engineering Conference (UPEC), Coimbra, Portugal, pp 1–5. https://doi.org/10.1109/UPEC.2016.8114142
37. Tanaka T, Ma K, Wang H, Blaabjerg F (2019) Asymmetrical reactive power capability of modular multilevel cascade converter based STATCOMs for offshore wind farm. IEEE Trans Power Electron 34(6):5147–5164. https://doi.org/10.1109/TPEL.2018.2866398
38. Avudai Lakshmi B, Karpagam R (2015) Resonant controller based STATCOM used in wind farms to mitigate power quality issues. In: 2015 IEEE international conference on electrical, computer and communication technologies (ICECCT), Coimbatore, India, 2015, pp 1–5. https://doi.org/10.1109/ICECCT.2015.7226003
39. Li G, Chen Y, Luo A, Wang H (2020) An enhancing grid stiffness control strategy of STATCOM/BESS for damping sub-synchronous resonance in wind farm connected to weak grid. IEEE Trans Ind Inf 16(9):5835–5845. https://doi.org/10.1109/TII.2019.2960863
40. Peng Y et al (2021) Coordinated control strategy of PMSG and cascaded H-Bridge STATCOM in dispersed wind farm for suppressing unbalanced grid voltage. IEEE Trans Sustain Energy 12(1):349–359. https://doi.org/10.1109/TSTE.2020.2995457

A Computational Intelligence-Based Novel Bearing Defect Detection Method

Arpana Singh, K. R. Satyajit, and Papia Ray

1 Introduction

A machine element has a bearing that constrains the relative motion only to the desired motion, hence decreases friction between the moving parts. Prevent motion by controlling forces of normal vector in moving parts is one of the features of the design of bearing. Bering design also helps in a linear movement or free rotation around an axis. Hence, the elements of rolling are the vital components. Working under different operational and environmental conditions is the job of rotary elements, which leads to numerous defects over the operating surfaces of the components of bearing. In this paper, two techniques are implemented to reduce the fault occurring at the bearing. The fault is diagnosed by the method bispectrum analysis, EMD and EEMD.

In this paper, it has been seen that noise is of two types to be eliminated, i.e. Gaussian and non-Gaussian. The Gaussian noise is removed easily because of its zero mean value but the non-Gaussian noise cannot be removed easily. Hence, two computational intelligence methods (EMD and EEMD) have been adopted to eradicate the non-Gaussian noise from the bearings. Further, it has been noticed that EMD possesses issues like mode mixing, which makes it difficult to swipe noise from the signal whereas EEMD and masking EMD overcome this issue. So, in this paper, EEMD and masking EMD have been suggested to determine bearing defect.

A. Singh · K. R. Satyajit · P. Ray (✉)
Department of Electrical Engineering, Veer Surendra Sai University of Technology, Burla, Sambalpur, Odisha, India
e-mail: papiaray_ee@vssut.ac.in

S. Kumar et al. (eds.), *Recent Advances in Power Electronics and Drives*, Lecture Notes in Electrical Engineering 852, https://doi.org/10.1007/978-981-16-9239-0_49

1.1 Literature Review

Only Gaussian can be completely removed from bispectrum analysis [1]. The higher order spectrum of the signal gets impeded due to the presence of non-Gaussian noise. It also adversely influences the examination of default features. Hence, the elimination of noise that is not Gaussian in the present signal is done before the bispectrum analysis. The Ensemble Empirical Mode Decomposition (EEMD) is a technique that is a self-adaptive signal decomposition method [2]. Like EMD, EEMD can also break the signals into a series of higher-to-lower frequency bands [3]. The various components of frequency of the given signal are firstly segregated then removal of the non-Gaussian noise present in the signal is done. EEMD is one of the noise-assisted data analysis methods that easily prevents the mode mixing process caused by EMD. To prevent this mode, mixing phenomenon addition of white noise is done to the signal. In contrast to the EMD, the intrinsic property of the signal can be disclosed better in IMFs generated by EEMD. Over time, the diagnosis of the mechanical fault is done extensively by the EEMD [4–6]. Wang et al. [7] also use EEMD with the method of correlation dimension for distinguishing the failures of diesel engines. This paper shows the advantages of EMD and EEMD done for detecting the noise in the rolling bearing. Firstly, the decomposition of signal is carried out by EMD and numerous IMFs are generated, but EMD has a mode mixing phenomena problem so we use the FFT method to eliminate the mode mixing phenomena. Further again EEMD is performed, and we get the true IMFs as well as false IMFs. Now a day, audits and diagnosis of faults in the equipment are of huge discussion in each industrial sector. Maintenance costs for emergencies used for the fault diagnosis saved a huge amount of money. Rolling element bearings is an important element due to their excessive wear and tear, which causes the prevention of failures in the whole system. The accurate working of these elements of a machine is crucial in the industry to completely eradicate long-term brutal accidents. To prevent machinery performance degradation, faults, or devastating failures, online machinery condition monitoring system is used [8]. Therefore, we need upgraded technologies to detect the performance of bearings. Bearings are of two types, i.e. sliding and rolling bearing. Both the bearings are called rolling bearings and are extensively seen in the elements of machines. The bearings of rolling elements permit the rotary motion to the shafts in the machinery for huge applications such as bicycles, electric motors, power transmission aircraft gas turbines, rolling mills, handpieces, polishing filling, etc. The methods used for defect detection are bispectrum analysis, EMD and EEMD. These methods will help in eliminating the Gaussian and non-Gaussian signals in fixed and nonlinear signals. EMD is an adjustable time, space analysis method used for analyzing the series that are fixed and non-linear. Noise from the signal is hence eliminated [9]. Whereas EEMD is a noise-assisted data analysis method in which a white noise signal is added. White noise is important to force the ensemble to exhaust all possible solutions in the shifting process, thus making the different scale signals collate in proper intrinsic mode functions.

The contribution of the paper is to obtain a self-changeable technique to study the characteristics of the simulated signal based on the EMD method. The analysis done in the paper is to show the removal of non-Gaussian noise in the rolling bearing of the machine with the method EMD. As we get the mode mixing problem so FFT masking is performed for the removal of it. Another method, i.e. EEMD is also obtained to reduce the number of frequency scales in the EMD. EEMD also deals with the mode mixing phenomenon problem.

The first part of the paper (Sect. 2) talks over the method of the decomposition of signals, i.e. Empirical Mode Decomposition and Ensemble Empirical Mode Decomposition. The second part (Sect. 3) deals with the analysis and performance evaluation of the decomposition methods of the simulated signal. The third part (Sect. 4) shows the masking technique to remove the mode mixing phenomenon and lastly (Sect. 5) deals with the conclusion.

2 Methods of Defect Decomposition

2.1 Empirical Mode Decomposition

IMFs can be reduced in components called Intrinsic Mode Functions because of its self-changeable data decomposition method EMD. This method helps in decaying a nonlinear and fixed signal. Basically, in the EMD algorithm, IMFs are pulling out from a given time series through a shifting process. Hence, it allows decaying the nonlinear and fixed signal into various IMFs. It is extensively used in denoising in certain areas like biomedical signals, acoustic signals. However, the potency of the EMD method is influenced by the mode mixing phenomenon (modal aliasing) [10–12]. While the breakdown of the signals into various components, EMD can be realized with other methods such as Fourier transform and Wavelet transform. In the decomposition methods, the first IMF has the most oscillating (high-frequency) components, it can be rejected to eradicate the high-frequency components (e.g., random noise). EMD is the most adjustable and systematic method for decomposition. The EMD method decomposed a simulated signal into several IMFs that must satisfy to conditions, which are also shown in Fig. 1.

Step 1—Find out the local minima and maxima of the signal f(t).
Step 2—Interpolate between maxima to get an upper envelope and maxima to get a lower envelope.
Step 3—Compute the mean of the upper and lower envelope.
Step 4—Extract IMF.

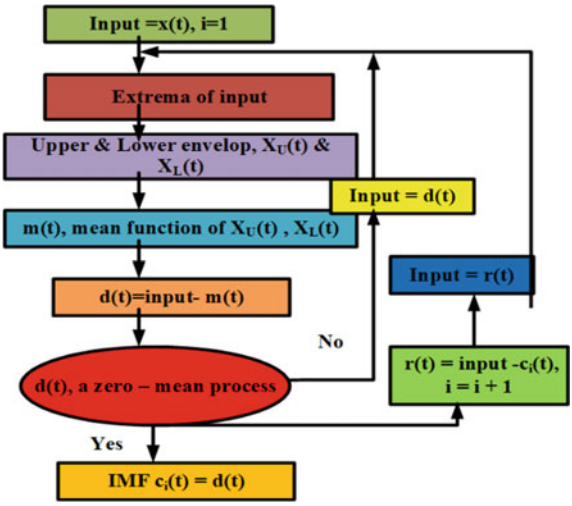

Fig. 1 EMD Algorithm

2.2 Ensemble Empirical Mode Decomposition

The mode mixing problem can be eradicated by the EEMD by inducing white noise at various times in it. In a background space that is filled with white noise, a decomposed signal is applied, then calculating the average of white noise followed by calculating the zero-mean noise making the signal stable by canceling the noise with each other [13–15]. Ensemble empirical mode decomposition (EEMD) is one of the most important tools for processing signals with intermittency. But, a problem exists in the EMD method, which is the mode mixing phenomena made better by the addition of white noise should be enough for the simulated signal. EEMD method was formulated to deal mainly with the signals containing noise. The next step is to measure the performance of the EEMD method using a noisy simulated signal. The results proved that the EEMD method could lessen the problem to a large extent concerning the EMD method. In addition to the above, the reports very well pointed that the EEMD method could act as an improvement for the EMD method. The steps for the calculation of EEMD (as shown in Fig. 2) are as mentioned below:

1. The addition of white noise with normal distribution is carried into the decomposed signal.
2. On the signal, EMD is done, and several white noises are added to acquire IMFs.
3. Repeat the above process by adding white noise in every step.
4. The average value of IMFs calculated is considered as the final output.

The basic principle of the EEMD can be described as: the whole time–frequency space is uniformly populated by the white noise that is added with the comprising components of variable scales set apart by the filter bank. In addition to the signal to this white background that is uniformly distributed, the bits of the signal of variable scales are automatically extrapolated onto the definite scales of reference, which is

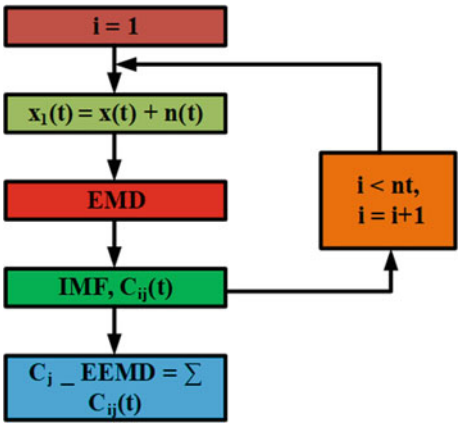

Fig. 2 EEMD algorithm

established by the background white noise. Undoubtedly, each trial produces very noisy results, and each noise-added decomposition consists of the signal and white noises that are added. As separate trials consist of variable noise in each trial, it gets canceled out in the ensemble mean of most of the trials.

3 Analysis of Decomposition Methods

The non-Gaussian noise is to be removed before the bispectrum analysis. HUANG proposed the ensemble empirical mode decomposition method, which is a changeable signal decomposition method. Bispectral analysis, EMD, EEMD based on the signal, can decay signals into a band of different frequencies. The mode mixing phenomenon is removed by EEMD, which occurs by the EMD method if white noise is added to the signal. The intrinsic characteristic of the signal is revealed by the IMFs pulled out by EEMD as compared to EMD. The areas of mechanical fault correction and diagnosis are using this method EEMD [16]. The methods will be analyzed step by step, that is firstly the bispectrum analysis will be done to analyze the Gaussian Noise (as in Fig. 3) and then the EMD will be performed to extract the IMFs and reduce the non-Gaussian noise. This method deals will problems of different frequency modes, i.e. mode mixing problems that are again then dealt with the ensemble empirical mode detection method.

Rayleigh distribution as given in Fig. 4 is a continuous probability distribution for nonnegative valued random variables.

Superposition of the three signals is taken in the signal X(t). The non-Gaussian Noise is eradicated by the analysis of the simulated signal.

The proposed signal is given as.

$$X(\mathrm{t}) = f(\mathrm{t}) + g(\mathrm{t}) + r(\mathrm{t})$$

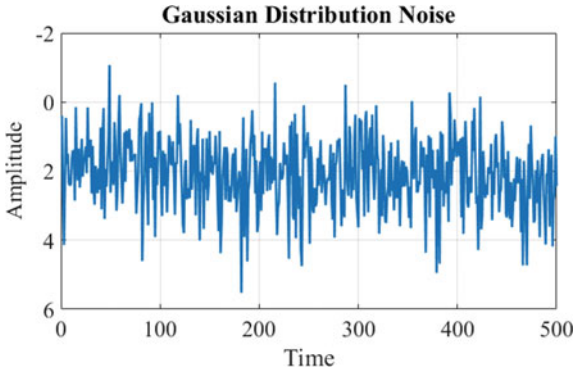

Fig. 3 Gaussian distribution

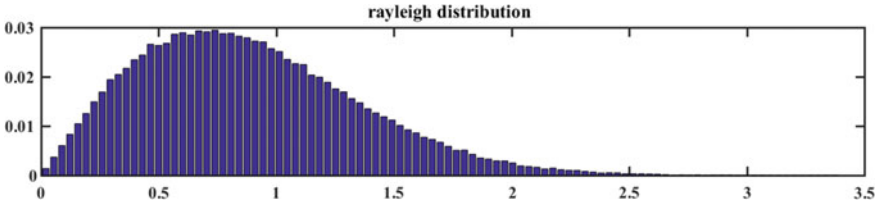

Fig. 4 Rayleigh distribution

$$= \sin(20 * \text{pi} * \text{t}) + \sin(60 * \text{pi} * \text{t}) + \sin(100 * \text{pi} * \text{t}) + n(\text{t}) + r(\text{t}) \quad (1)$$

Equation (1) consists of:
f(t) : It has three sine wave signals frequencies of 10Hz, 30Hz and 50Hz,
g(t) : consists of random signal with Gaussian Distribution
r(t) : consists of random signal with Rayleigh distribution
The sampling rates of f(t), g(t) and r(t) are 1000 Hz.

Figure 5 shows the superposition of the signal of three sine-wave signals, i.e. 10, 30 and 50 Hz. It also shows the signal with Gaussian distribution and signal with Rayleigh distribution and the summation of all the signals is the output of the simulated signal.

3.1 Empirical Mode Decomposition

The signal X(t) is decomposed into Intrinsic Mode Functions (IMFs) by intrinsic mode signal decomposition (EMD) algorithm as shown in Fig. 6. The signal X(t) has three sinusoidal frequencies 10 Hz, 30 Hz and 50 Hz. The ratio of the above IMFs in the figure is much larger than the below IMFs. The real IMFs can be effectively identified, while the false IMFs are removed.

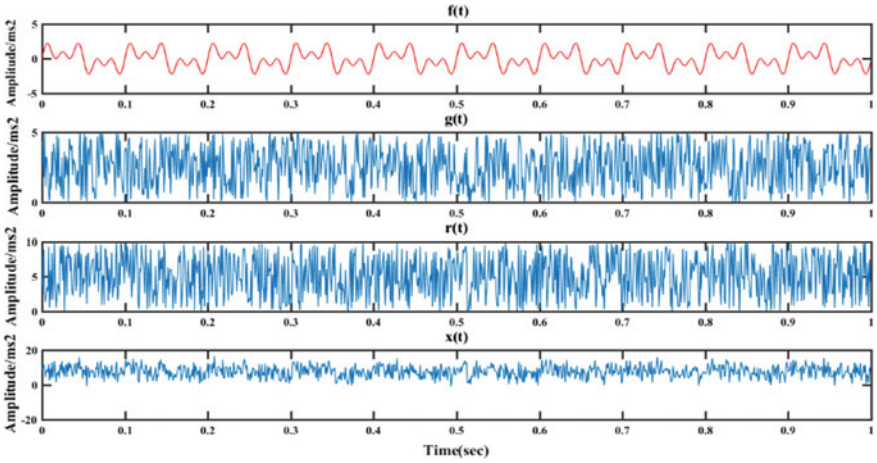

Fig. 5 Simulated signal x(t)

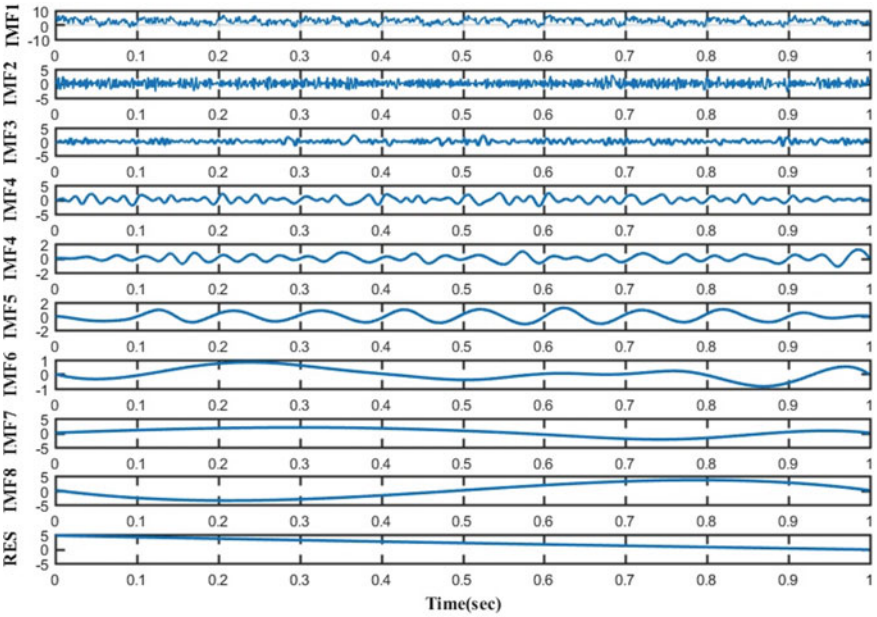

Fig. 6 Signal Decomposition by EMD

In Fig. 6, we have taken the output of the simulated signal X(t) and decomposed the signal using EMD. From the fig, we can extract information from IMF 1, 2, 3, 4 and 5 and hence these are true IMFs and from IMF 6, 7, no information is extracted.

3.2 *Ensemble Empirical Mode Decomposition*

The IMFs of the EMD method consist of coupled oscillations in each IMF. Hence, it also suffers from the mode mixing problem. To solve this problem and identify the time scale, EEMD is used. The proposed method is explained in Fig. 7. The results shown in Fig. 8 make it clear that the synchronizations between corresponding IMF pairs have improved a lot, specifically for the IMF components.

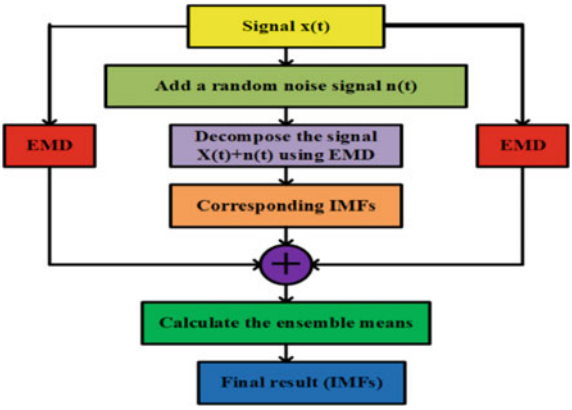

Fig. 7 Proposed method

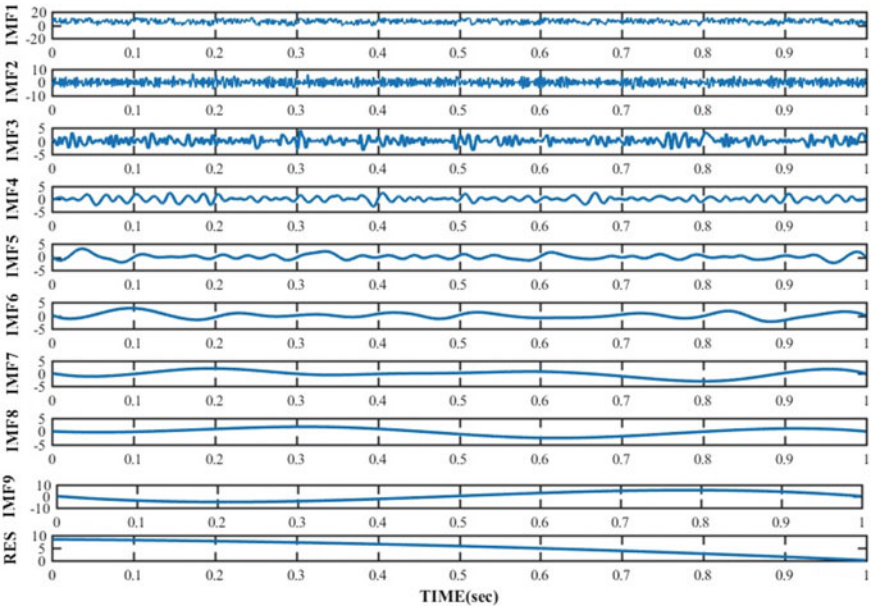

Fig. 8 Signal decomposition by EEMD

In Fig. 8, we can see that IMF has fewer frequency components than in the case of IMF in EMD, and hence noise is eliminated. Also, we can extract information from the IMF1, 2, 3, 4 & 5 but unable to extract it from the IMF 6, 7 and 8 because they are false IMFs.

3.3 Performance Evaluation of Decomposition Methods

Three different sinusoidal signals with frequencies of 10 Hz, 30 Hz and 50 Hz are produced.g(t) is Random signal with Gaussian distribution, r(t) is random signal with Rayleigh distribution. f(t), g(t) and r(t) have sampling rates of 1000 Hz. We denoise the signal for eliminating the non-Gaussian noise, and non-Gaussian noise is eliminated by using EMD. Due to the issue caused by mode mixing phenomena, the noise was not eliminated effectively in this method. A sudden change occurs in the time-scaled decomposed signal containing huge noise. Single IMF has a large number of frequency components. So we choose a different decomposition method EEMD affecting the decomposition by the addition of the white noise, which cancels each other. IMFs produce both false and true one, the false one gets eliminated and true significantly reduces the chance of mode mixing. EEMD helps for reaching the ultimate goal of data analysis for extracting the true signals. The EEMD utilizes the characteristic of noise and effectively is a better method than EMD.

4 Modified Masking in Empirical Mode Decomposition

Separation of mode frequencies by EMD (Empirical Mode Decomposition) present in an octave is not possible due to the problem of mode mixing. Thus, to effectively improve the mode mixing issue, the technique of noise-assisted EMD is implemented. The following section discusses the estimation methods of closely spaced low-frequency modes through masking signals and the mode mixing problem of standard EMD [16].

4.1 FFT-Based Masking Technique

Extension of standard EMD by using masking signal refines the differentiation of the original EMD yet appears to be insignificant to separate the closely spaced modes. Different modes of oscillations can be distinguished by the method of masking signals. It filters out the frequency signal of weak frequencies and later it is removed out during the process of EMD. Selecting the masking signal properly improves the mode extraction potential of the masking method. Thus, the masking technique through FFT improves the mode separation capability of EMD.

4.2 FFT of Standard EMD

Assume a test signal "S" representing two components of a very low frequency 10 and 30, where the magnitude of the higher frequency component is notably lower than the low-frequency component as given in Fig. 9.

$$S(t) = \sin(2 \times \text{pi} \times 30 \times t) + 5 \times \sin(2 \times \text{pi} \times 10 \times t) \quad (2)$$

Examination of mode mixing of EMD is carried out by a synthetic test signal. The figure given below represents the extracted IMFs form of the signals as mentioned in (10) with the help of the original EMD. It is observed that the IMF 1 and 2 shown in Fig. 8 do not show any duplication with the component of the original signal. For better physical interpretation, Hilbert transform can be used because IMF 1 suffers mode mixing problem and is not monotonic. The mode separation process of EMD is rectified by the masking signal. The method is implemented to remove any uncertainty and mode mixing of unseparated and closely spaced frequencies. Hence, in-depth analysis and technical usage of the masking method with the EMD are proposed. The drawback of the method yet observed is that it is not able to examine multiple low-frequency components of oscillating signals.

Step 1: To locate the components of different frequencies f1, f2, f3,… fn from the given FFT S(t), the signal.
Step 2: Construct the masking signals: mask2, mask3, mask4, mask5, …, maskn, such that: maskn(t) = Mn × [sin (2π (f n + f n − 1) t].
Step 3: Construct the signal by addition and subtraction of the masking signals from S(t). Where, S(t) + maskn & S(t) − maskn.
Step 4: Evaluate EMD as shown in the steps (1to7) in the expression: S(t) + maskn and S(t) − maskn to get the value of first IMF Hence after calculating C(t) = [(IMF +) + (IMF −)]/2.
Step 5: Calculate the residue, r(t). Where r(t) = [S(t) − C(t)].
Step 6: The steps from 3 to 4 are repeated by replacing S(t) with residue r(t) until the second last IMF containing components of frequency f2, f3, …, fn are obtained and the final residue comes in the form of f1 component.

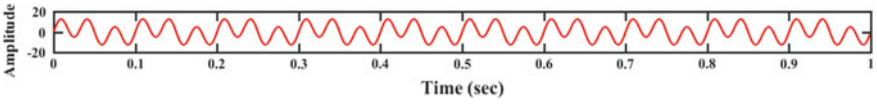

Fig. 9 Sum of 10 and 30 Hz freq sine signal

4.3 FFT of EMD by Masking Technique

In Fig. 10, EMD is performed on the signal given in Fig. 9, and IMF 1 IMF2 and IMF 3 are true IMFs, i.e. we can extract the information about the signal and the rest IMFs ignored. For the enhancement of the mode separation phenomenon ability of the EMD, the masking signal-based approach was used to mask the signal, and hence the FFT frequency spectrum is used. Imprecise and inexact information of frequency is seen for the FFT of the signal that is distorted. Analyzing the signal that exhibits non-linearity and non-stationary is a major concern. Hence, the IMF we got with masking signal done with FFT has two frequency components, called mode mixing problem. The mode estimation by FFT-based masking signal is performed below for seeing the mode mixing problem.

We take the signal S(t) and obtain the frequency spectrum. The frequency spectrum in Fig. 11 gives the value 9.766 and 29.79 as we have the signal of a frequency of 10 and 30 Hz.

Figure 11 shows the amplitude spectrum of the sine wave signal having frequencies 29.79 Hz and 9.799 Hz.

In Fig. 12, we can observe that the different frequency modes of the signal S(t) and again by decomposing IMF1 obtained from the EMD we can see that in Fig. 12a and b, two different frequencies can be obtained causing the mode mixing problem and then by masking technique, we apply the FFT to remove the different frequency mode and mode mixing.

Again now in Fig. 13a and b, we note that the mode mixing is eradicated and we get one frequency in both the figures. In Fig. 13a, we get a frequency of 4 Hz and in Fig. 13b, we get the frequency in 8 Hz. These figures mention that the different frequency that is mode mixing issue is eradicated from the signal to get the picture of true IMFs. We perform FFT on IMF 1 to obtain the Fourier spectrum of the IMF 1 evaluated by the EMD. Hence, the extracted signal has two component frequencies

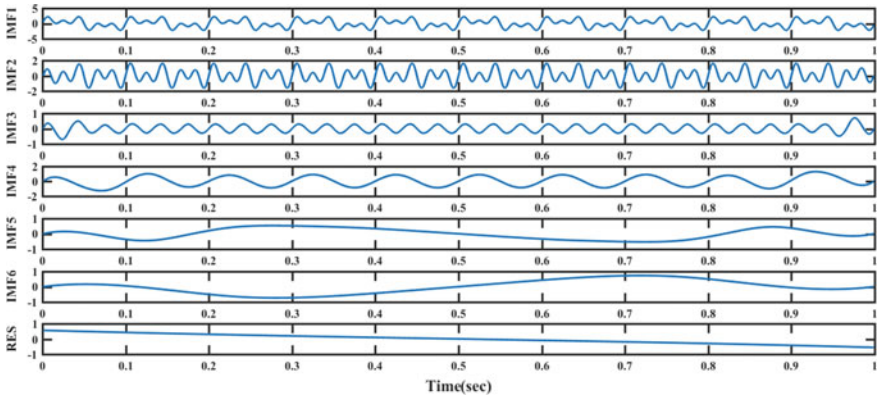

Fig. 10 EMD of the signal S(t)

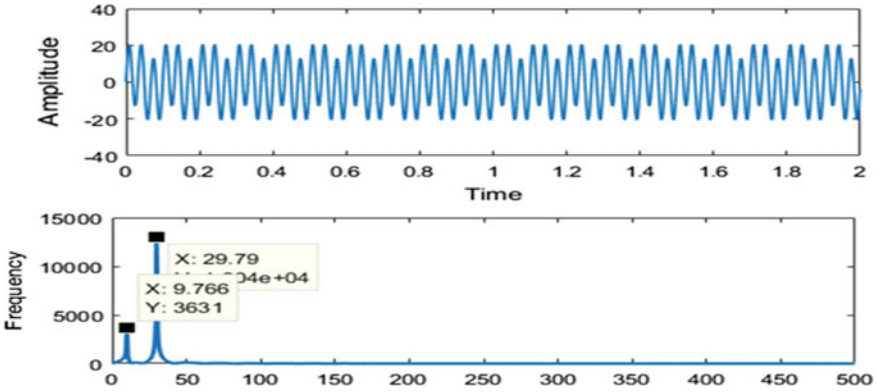

Fig.11 Amplitude spectrum of S(t)

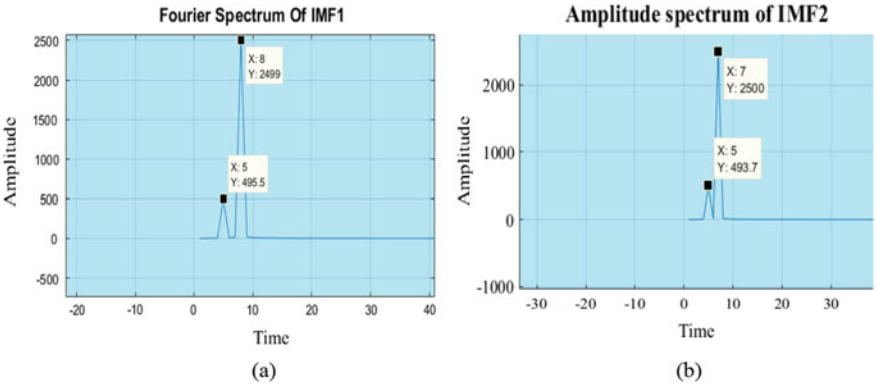

Fig. 12 Fourier spectrum of IMF (**a**) IMF1 (**b**) IMF 2

in which one frequency higher than (8 Hz) and one less than that (5 Hz). As the frequencies are packed closely so the process is more evident. In the second figure, we can see that by the masking technique, we can remove this mode mixing problem that arose in the EMD method and got just one frequency, i.e. (4 Hz), and again the same is repeated with the IMF 2. This masking EMD separates modes of closely spaced frequencies efficiently. The method reconstructs the analysis signal so that the masking method works effectively. Preprocessing of original data using EMD is done before masking EMD on the given data. Original signal EMD produces IMFs and trend signal as residue. Henceforth, all of the significant amplitude IMFs were summed. To obtain different modes of frequencies in the signal, FFT was applied to the IMFs. It suggests extracting a single mode at a time rather than extracting all modes at a single period.

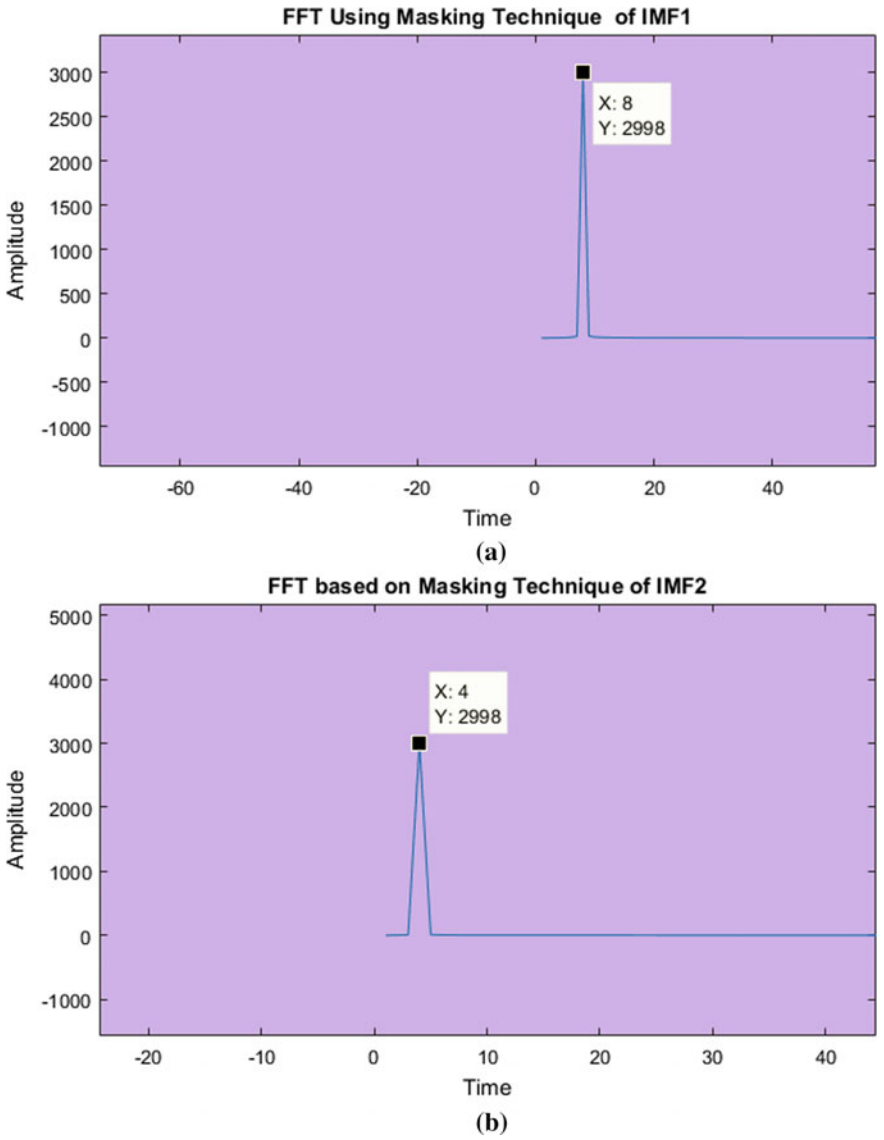

Fig. 13 FFT-based masking technique of IMF (**a**) IMF1 (**b**) IMF2

4.4 Performance Evaluation of Methods

The Fast Fourier Transform method employing masking signal upgrades the EMD ability for mode separation. We take the signal S(t) and obtain the frequency spectrum. The frequency spectrum in Fig. 11 gives the value 9.766 and 29.79 as we have a signal

of a frequency of 10 and 30 Hz. We perform FFT on IMF 1 to extract from the Fourier spectrum of the IMF 1 came from the EMD. As a result, the signal has two component frequencies that are one higher frequency (8 Hz) and one less than that (5 Hz) as given in Fig. 12. This phenomenon is seen when the frequencies are closely packed. In Fig. 12, we can see that by the masking technique we can remove this mode mixing problem that arose in the EMD method and got just one frequency, i.e. (7 Hz) and again the same is repeated with the IMF 2. Hence, the masking of EMD separates closely spaced modes of frequencies systematically. Similarly in Fig. 13, we can observe that a single value of frequency of 8 and 4 Hz of IMFs is obtained.

5 Conclusion

This paper proposes the decomposition methods to eradicate the non-Gaussian noise. The output of the simulated signal is therefore evaluated with the decomposition methods EMD and EEMD. With the EMD method, true IMF information is extracted and the rest of the IMFs are referred to as false IMFs. With the addition of the white noise to EMD, EEMD was performed and here it is seen that signal with fewer frequency components is present. Hence, noise is eliminated successfully by EEMD and better IMFs are produced. So by the noise added in the EEMD eases, the mode mixing problem is caused by EMD and hence produces a signal with effectively reduced noise. Further, we can also go with other better methods for noise assistance for true IMF signals, i.e. Complete Ensemble Empirical Decomposition with Adaptive Noise (CEEMDAN). Further, in the paper FFT method, the signal is taken to obtain the frequency spectrum. A masking signal was used to eradicate the mode mixing. FFT masking technique was done to give the single component for the IMFs. As a result, the extracted signal has two components of frequency in which one is a higher frequency and the other one is less. By masking one single frequency is found and the mode mixing problem is eradicated. It is concluded that by EEMD and masking technique, we can remove this mode mixing problem that arose in the EMD method and got just one frequency for the IMFs.

References

1. Liu H, Liang J, Hu YH (2005) Research on parametric bispectrum of heart sound signal analysis method based on wavelet transform domain. Signal Process 20(1):5–9
2. Huang NE, Shen Z, Long SR, Wu MC, Shih HH, Zheng Q (1998) The empirical mode decomposition and the Hilbert spectrum for nonlinear and non-stationary time series analysis. Proc Math Phys Eng Sci 454(1971):903–995
3. Wu ZH, Huang NE (2012) Ensemble empirical mode decomposition: a noise-assisted data analysis method. Adv Adapt Data Anal 1(1):1–41
4. Wei ZL, Robbersmyr KG, Karimi HR (2017) An EEMD aided comparison of time histories and its application in vehicle safety. IEEE Access 5:519–528

5. Qi YM, Shen CQ, Wang D, Shi JJ, Jiang XX, Zhu ZK (2017) Stacked Sparse autoencoder-based deep network for fault diagnosis of rotating machinery. IEEE Access 5:15066–15079
6. Xiang JW, Zhong YT (2017) A fault detection strategy using the enhancement ensemble empirical mode decomposition and random decrement technique. Microelectron Reliab 75:317–326
7. Wang X, Liu C, Bi F, Bi X, Shao K (2013) Fault diagnosis of diesel engine based on adaptive wavelet packets and EEMD-fractal dimension. Mech Syst Signal Process 41(1–2):581–597
8. Gu F, Shao Y, Hu N, Naid A, Ball AD (2011) Electrical motor current signal analysis using a modified bispectrum for fault diagnosis of downstream mechanical equipment. Mech Syst Signal Proc 25(1):360–372
9. Li W, Zhang G, Shi T, Yang S (2004) Gear crack early diagnosis using bispectrum diagonal slice. Chinese J Mech Eng 16(2):193–196
10. Jiang Y, Tang C, Zhang X, Jiao W, Li G, Huang T (2020) A novel rolling bearing defect detection method based on bispectrum analysis and cloud model-improved EEMD. IEEE Access 8:24323–24333
11. Ray P, Lenka RK, Mohanty BK (2017) A modified noise assisted EMD to extract low frequency modes present in a WAMS data of dynamic power system. IEEE Calcutta Conf CALCON 2017:2–3
12. Tang B, Dong S, Ma J (2013) Study on the method for eliminating mode mixing of empirical mode decomposition based on independent component analysis. Chinese J Sci Inst 33(7):1477–1482
13. Li L, Dang R, Fan Y (2014) Modified EEMD de-noising method and its application in multiphase flow measurement. Chinese J Sci Inst 35(10):2365–2371
14. Cheng Y, Wang ZH, Chen BY, Zhang WH, Huang GH (2019) An improved complementary ensemble empirical mode decomposition with adaptive noise and its application to rolling element bearing fault diagnosis. ISA Trans 91(21):218–234
15. Liu D, Xiao ZH, Hu X, Zhang CX, Malik OP (2019) Feature extraction of rotor fault based on EEMD and curve code. Measurement 135(73):712–724
16. Han T,Jiang D, Wang N (2016) The fault feature extraction of rolling bearing based on EMD and difference spectrum of singular value. Hindawi 5957179:1–14